Small molecule reactivity of zirconocene hydrazides, imides and silylamides

Archibald McNeillis

MChem

St Edmund Hall



Thesis submitted to the University of Oxford for the degree of Doctor of Philosophy in Inorganic Chemistry, July 2020.

The work described in this Thesis was carried out in the Chemistry Research Laboratory, University of Oxford from October 2016 to March 2020 under the supervision of Professors Philip Mountford and Dermot O'Hare. All work is my own unless stated to the contrary and has not previously been submitted for any degree at this or any other university.



Archie McNeillis

July 2020

Abstract

This thesis reports the reactivity of zirconocene hydrazides, imides and silylamides, as well as the reactivity of titanium permethylpentalene complexes. Particular focus is paid to the reactions of hydrazides and imides with boranes and silanes, and reactions of silylamides with terminal alkynes, boranes and silanes.

Chapter One provides a background on Group 4 imido and hydrazido complexes, as well as silylamido complexes containing β-Si–H···M agostic interactions. The Chapter focuses on the synthesis, structure and reactivity, both stoichiometric and catalytic, of these complexes.

Chapter Two describes first the reactions of the zirconocene hydrazide $Cp_2Zr(NNPh_2)(DMAP)$ with boranes and silanes, resulting in 1,2-addition products. Comparisons, supported by DFT calculations, are made to reactions with carbon monoxide and isocyanates, which result in reductive N_α–N_β cleavage. The reactions of the zirconocene imides $Cp_2Zr(N^tBu)(THF)$ and $Cp_2Zr(NXyl)(THF)$ with silanes, resulting in the formation of hydride silylamido complexes, are described.

Chapter Three describes the reactions of the β-agostic silylamido complexes $Cp_2Zr(H)\{N(^tBu)Si(\mu\text{-}H)HPh\}$ and $Cp_2Zr(H)\{N(^tBu)Si(\mu\text{-}H)Me_2\}$ with terminal alkynes. These result in hydride β-hydrogen abstraction followed by insertion into or C–H activation across the Zr–Si bond of transient η^2-silanimine species. Kinetic studies are presented, with supporting DFT studies. Reactions with ethylene and a mixed feedstock of ethylene and hydrogen, resulting in ethylene hydrogenation, are also described.

Chapter Four describes the reactions of both β-agostic and non agostic silylamido complexes with boranes and silanes. With boranes, κ^2- or κ^1-borohydrides are first

formed and, in some cases, further reaction *via* dihydrogen elimination is observed. Kinetic studies to elucidate the mechanism of this intriguing reactivity are described, with supporting DFT studies. With silanes, multiple reaction pathways are observed.

Chapter Five first provides an overview of Group 4 pentalene chemistry. Subsequently, reactions of titanium permethylpentalene complexes with a variety of alkyl metal reagents and small molecules are described.

Chapter Six presents experimental procedures and characterising data for novel complexes.

Appendix contains supporting figures.

Acknowledgements

I must first extend my sincere gratitude to Prof. Philip Mountford for giving me the opportunity to study in Oxford and work on some really stimulating projects, as well as for all the guidance, kinetic discussions and DFT calculations. Also to Prof. Dermot O'Hare for welcoming me into his group and his guidance. Included in this thanks is of course that which goes to Zoë and JC for their supervision of S3.

To the members of the Mountford group I would like to offer a great thanks for the two years we spent together. To Simona, Ben and Bowen for holding my hand when I entered S2. To Bowen, Martin, Wilf and David for extensive kinetic discussions that were truly invaluable and unashamedly enthralling, the many trips to the open market, and your ridiculous humour. To Andrey and Bowen for teaching me the language of crystals. To the aforementioned, Natalia and Peace for their great friendship.

To the members of the O'Hare group a huge thanks for your two years. In particular to the 12pm lunchtime team – Jess, Maureen, Peace, Phil, Rebecca, Tom and Part IIs – what ludicrous conversations we had. To Justin, Sam and Issie for the climbing trips too.

Away from the lab I must thank pole vault, as a sport, for keeping me sane and the OUAC pole vault team – Chris, Rowan, Sam, Nik and Jake (and Justin, despite being a sprinter) – for all the great laughs, training and road trips. Breaking the varsity record was definitely my greatest achievement in Oxford and a special mention must go to Jacqui, Kieran, Roisin and Sam for coming to watch that day.

Out of Oxford, to my parents and family for supporting and encouraging me in everything I do. To Rosena and Karl for hosting me nearly every weekend and providing me with the most amazing of meals. Lastly, to Roisin – you're *absolutely* fantastic.

Contents

	Declaration	i
	Abstract	ii
	Acknowledgements	iv
	Contents	v
	Abbreviations	x
	Notes	xv

Chapter One: Introduction

1.1	General Introduction	1
1.2	Group 4 imido complexes	2
1.2.1	The imido ligand	2
1.2.2	Synthesis of titanium imido complexes	3
1.2.3	Synthesis of zirconium and hafnium imido complexes	6
1.2.4	Stoichiometric reactions	8
1.2.5	Catalytic hydroamination	14
1.3	Group 4 hydrazido complexes	16
1.3.1	The hydrazido ligand	16
1.3.2	Synthesis of titanium hydrazido complexes	16
1.3.3	Synthesis of zirconium and hafnium hydrazido complexes	18
1.3.4	Stoichiometric reactions with unsaturated substrates involving the $M{=}N_{\alpha}$ bond	20
1.3.5	Stoichiometric reactions with unsaturated substrates involving the $N_{\alpha}{-}N_{\beta}$ bond	23
1.3.6	Reactions with boranes and silanes	26
1.3.7	Catalytic reactions	29
1.4	β-Agostic silylamido complexes	32
1.4.1	Synthesis and structure	32
1.4.1.1	Group 4 β-agostic silylamido complexes	32
1.4.1.2	Group 5 and 6 β-agostic silylamido complexes	36
1.4.1.3	Alkaline and rare earth β-agostic silylamido complexes	38

1.4.2		Reactions of β-agostic silylamido complexes	40
	1.4.2.1	Group 4 β-agostic silylamido complexes	40
	1.4.2.2	Group 6 β-agostic silylamido complexes	46
1.5		Summary and outlook	49
1.6		References	50

Chapter Two: Small molecule reactivity of zirconocene hydrazides and imides

2.1		Introduction	57
2.2		Reaction of $Cp_2Zr(NNPh_2)(DMAP)$ (**2.3**) with pinacol borane (HBPin)	61
2.3		Reactions of $Cp_2Zr(NNPh_2)(DMAP)$ (**2.3**) with silanes	69
2.4		Reaction of $Cp_2Zr(NNPh_2)(DMAP)$ (**2.3**) with chlorophenylsilane	78
2.5		Reactions of $Cp_2Zr(NNPh_2)(DMAP)$ (**2.3**), $Cp_2Zr(N^tBu)(THF)$ (**2.1**) and $Cp_2Zr(N^tBu)(DMAP)$ (**2.13**) with H_2	82
2.6		Reactions of $Cp_2Zr(NNPh_2)(DMAP)$ (**2.3**) with CO and XylNC	84
2.7		Reactions of zirconocene imides with silanes	88
	2.7.1	Reactions of $Cp_2Zr(N^tBu)(THF)$ (**2.1**) with silanes	88
	2.7.2	Reactions of $Cp_2Zr(NXyl)(THF)$ (**2.2**) with silanes	97
	2.7.3	Reaction of $Cp_2Zr(N^tBu)(THF)$ (**2.1**) with chlorophenylsilane	102
	2.7.3.1	Computational study of bonding in a zirconocene chloride-silylamide	108
	2.7.3.2	Mechanism of reaction	111
	2.7.4	Reaction of $Cp_2Zr(NXyl)(THF)$ (**2.2**) with chlorophenylsilane	114
2.8		Other reactions	118
2.9		Conclusions	119
2.10		References	122

Chapter Three: Reactions of zirconocene hydride silylamides with terminal alkynes and ethylene

3.1	Introduction	126
3.2	Reactions of $Cp_2Zr(H)\{N(^tBu)Si(\mu\text{-}H)HPh\}$ (**6**) and $Cp_2Zr(H)\{N(^tBu)Si(\mu\text{-}H)Me_2\}$ (**3.3**) with terminal alkynes	130
3.2.1	Reactions of $Cp_2Zr(H)\{N(^tBu)Si(\mu\text{-}H)HPh\}$ (**6**) and $Cp_2Zr(H)\{N(^tBu)Si(\mu\text{-}H)Me_2\}$ (**3.3**) with $HCCC_6F_5$	130
3.2.2	Reactions of $Cp_2Zr(H)\{N(^tBu)Si(\mu\text{-}H)HPh\}$ (**6**) and $Cp_2Zr(H)\{N(^tBu)Si(\mu\text{-}H)Me_2\}$ (**3.3**) with HCC^tBu	136
3.2.3	Kinetic study of the reaction of $Cp_2Zr(H)\{N(^tBu)Si(\mu\text{-}H)HPh\}$ (**6**) with HCC^tBu	143
3.2.3.1	Summary of the kinetic study	157
3.2.4	DFT studies of the reactions of $Cp_2Zr(H)\{N(^tBu)Si(\mu\text{-}H)HPh\}$ (**6**) with HCC^tBu and $HCCC_6F_5$	158
3.2.5	DFT studies of dihydrogen elimination from $Cp_2Zr(H)\{N(Xyl)SiH_2Ph\}$ (**8**)	168
3.3	Reactions of $Cp_2Zr(H)\{N(^tBu)Si(\mu\text{-}H)HPh\}$ (**6**) with ethylene	170
3.4	Other reactions	174
3.5	Conclusions	176
3.6	References	178

Chapter Four: Reactions of zirconocene hydride silylamides with boranes and silanes

4.1	Introduction	182
4.2	Reactions of hydride silylamides with boranes	185
4.2.1	Reactions of $Cp_2Zr(H)\{N(^tBu)Si(\mu\text{-}H)HPh\}$ (**6**) and $Cp_2Zr(H)\{N(Xyl)SiH_2Ph\}$ (**8**) with thexylborane	186
4.2.2	Reactions of $Cp_2Zr(H)\{N(^tBu)Si(\mu\text{-}H)HPh\}$ (**6**), $Cp_2Zr(H)\{N(^tBu)Si(\mu\text{-}H)Ph_2\}$ (**7**) and $Cp_2Zr(H)\{N(^tBu)Si(\mu\text{-}H)Me_2\}$ (**4.5**) with $BH_3{\cdot}SMe_2$	193
4.2.3	Thermal decomposition of $Cp_2Zr\{(\mu\text{-}H)_2BH_2\}\{N(^tBu)SiH_2Ph\}$ (**21**),	201

	$Cp_2Zr\{(\mu\text{-}H)BH_3\}\{N(^tBu)Si(\mu\text{-}H)Ph_2\}$ (**22**) and $Cp_2Zr\{(\mu\text{-}H)BH_3\}\{N(^tBu)Si(\mu\text{-}H)Me_2\}$ (**23**)	
4.2.4	Kinetic studies of the thermal decomposition of $Cp_2Zr\{(\mu\text{-}H)BH_3\}\{N(^tBu)Si(\mu\text{-}H)Me_2\}$ (**23**)	210
4.2.5	Kinetic studies of the thermal decomposition of $Cp_2Zr\{(\mu\text{-}H)_2BH_2\}\{N(^tBu)SiH_2Ph\}$ (**21**)	218
4.2.6	DFT studies on the thermal decompositions of $Cp_2Zr\{(\mu\text{-}H)_2BH_2\}\{N(^tBu)SiH_2Ph\}$ (**21**) and $Cp_2Zr\{(\mu\text{-}H)BH_3\}\{N(^tBu)Si(\mu\text{-}H)Me_2\}$ (**23**)	226
4.2.7	Reaction of $Cp_2Zr(H)\{N(Xyl)SiH_2Ph\}$ (**8**) with $BH_3{\cdot}SMe_2$	231
4.3	Reactions of hydride silylamides and silylhydrazides with silanes and chlorosilanes	234
4.3.1	Reactions of $Cp_2Zr(H)\{N(Xyl)SiH_2Ph\}$ (**8**) and $Cp_2Zr(H)\{N(Xyl)SiHPh_2\}$ (**9**) with silanes, chlorosilanes and dihydrogen	234
4.3.2	Reactions of $Cp_2Zr(H)\{N(^tBu)Si(\mu\text{-}H)HPh\}$ (**6**), $Cp_2Zr(H)\{N(^tBu)Si(\mu\text{-}H)Ph_2\}$ (**7**) with silanes and chlorosilanes	241
4.3.3	Reactions of $Cp_2Zr(H)\{N(NPh_2)SiH_2Ph\}$ (**2**) and $Cp_2Zr(H)\{N(NPh_2)SiHPh_2\}$ (**3**) with silanes and chlorosilanes	244
4.4	Conclusions	245
4.5	References	247

Chapter Five: Titanium permethylpentalene chemistry

5.1	Introduction	251
5.1.1	Overview	251
5.1.2	Nomenclature	251
5.1.3	Synthesis of pentalene and pentalene-derivatives	252
5.1.4	Pentalene coordination chemistry	253
5.1.5	Selected synthesis and small molecule reactivity of Group 4 pentalene complexes	256
5.1.6	Group 4 metallocene alkylidene chemistry	259
5.2	Synthesis of $[Pn^*TiBr(\mu\text{-}Br)]_2$ (**28**)	262

5.3	Reactions of titanium permethylpentalene complexes with alkylaluminium reagents	265
5.3.1	Reactions of [Pn*TiCl(μ-Cl)]$_2$ (**5.7**) and [Pn*TiBr(μ-Br)]$_2$ (**28**)	265
5.3.2	Synthesis of [Pn*TiMe(μ-Br)]$_2$ (**30**)	268
5.3.3	Reactions of [Pn*TiMe(μ-Cl)]$_2$ (**5.8**) and [Pn*TiMe(μ-Br)]$_2$ (**30**)	272
5.4	Thermolysis of titanium permethylpentalene bis(alkyl) complexes	273
5.5	Small molecule reactivity of titanium permethylpentalene alkyl complexes	275
5.6	Conclusions	280
5.7	References	282

Chapter Six: Experimental details and characterising data

6.1	General methods and instrumentation	286
6.2	Literature preparations	287
6.3	X-ray data collection and processing parameters	287
6.4	Computational details	288
6.5	Experimental details and characterising data for Chapter Two	289
6.6	Experimental details and characterising data for Chapter Three	299
6.7	Experimental details and characterising data for Chapter Four	309
6.8	Experimental details and characterising data for Chapter Five	323
6.9	References	327

Appendix 329

Abbreviations

General

Å	Angstrom(s)
atm	atmosphere
ca.	*circa*, about
cf.	*confer*, compared to
CSD	Cambridge Structural Database
°	degrees
°C	degrees Celcius
d	day(s)
Δ	delta, change in
DFT	density functional theory
e	elementary charge
FA	fold angle
G	Gibbs free energy
g	grams
H	enthalpy
h	hour(s)
HOMO	highest occupied molecular orbital
η	hapticity
K	Kelvin
kcal mol^{-1}	kilocalorie(s) per mole
LUMO	lowest unoccupied molecular orbital
M	molarity, mol dm^{-3}
mbar	millibar(s)
mins	minutes
mmol	millimoles
MO	molecular orbital
NWT	non-wingtip
RDS	rate determining step
RT	room temperature

S	entropy
s	seconds
$t_{1/2}$	half life
TS	transition state
μ	bridging
VE	valence electrons
vs	versus
WT	wingtip
ZPE	zero point energy

Chemical

9-BBN	9-borabicyclo[3.3.1]nonane
Ad	adamantyl
Ar	aryl group
Ar’	2,6-$C_6H_3{}^iPr_2$
Bn	benzyl
bipy	2,2’-bipyridine
Cat	1,2-benzediol
cent	ring centroid
COT	cyclooctatetraene
Cp	C_5H_5
Cp*	C_5Me_5
Cp’	C_5H_4Me
Cp”	1,3-$C_5H_3(SiMe_3)_2$
Cy	cyclohexyl
DMAP	4-dimethylaminopyridine
E	generic element to be defined
EIE	equilibrium isotope effect
Et	ethyl
H_2Me_4taa	tetramethyl dibenzotetraaza[14]annulene
Hpypyr	2-(2’-pyridyl)-3,5-dimethylpyyrole

^{i}Pr	*iso*-propyl
KIE	kinetic isotope effect
L	supporting ligand
Me	methyl
Me_2pz	3,5-dimethylpyrazolyl
Me_3[6]aneN_3	1,3,5-trimethyltriazacyclohexane
Me_3[9]aneN_3	1,4,7-trimethyltriazacyclononane
Mes	2,4,6-$C_6H_2Me_3$
N_2N^R	generic diamide-amine ligand
N_2N^{py}	MeC(2-C_5H_4N)(CH_2NSiMe_3)$_2$
$N_2^{SiMe3}N^{Me}$	MeN($CH_2CH_2NSiMe_3$)$_2$
$N_2^{C_6F_5}N^{Me}$	MeN($CH_2CH_2NC_6F_5$)$_2$
N_2N^{SiMe3}	$Me_3SiN(CH_2CH_2NSiMe_3)_2$
$N_2^{iPr}N^{Me}$	MeN($CH_2CH_2N^{i}Pr$)$_2$
$N_2^{TBS}N^{py}$	MeC(2-C_5H_4N){$CH_2N(Si^{t}BuMe_2)$}$_2$
$N_2^{3,5\text{-}Xyl}N^{py}$	MeC(2-C_5H_4N){CH_2NH(3,5-$C_6H_3Me_2$)}$_2$
$N^{3,5\text{-}Xyl}N^{pyr}$	2-(3,5-dimethylphenylamino)pyrrolinato
$N_2^{pyr}N^{Me}$	*N*,*N*-di(pyrrolyl-α-methyl)-*N*-methylamine
Ph	phenyl
Pin	2,3-dimethyl-2,3-butanediol
Pn	pentalene
Pn†	1,5-$C_8H_6(Si^{i}Pr_3)$
Pn*	permethylpentalene
py	pyridine
py'	4-pyrrolidinopyridine
R	generic aryl or alkyl
^{t}Bu	*tert*-butyl
Tex	*tert*-hexyl
THF	tetrahydrofuran
TMEDA	N,N,N',N'-tetramethylethylenediamine
Tol	4-C_6H_4Me

X	generic anionic ligand
Xyl	2,6-$C_6H_3Me_2$
‡	transition state or activation parameter

Nuclear Magnetic Resonance Spectroscopy

$^{13}C\{^1H\}$	proton-decoupled ^{13}C
$^{11}B\{^1H\}$	proton-decoupled ^{11}B
$^{19}F\{^1H\}$	proton-decoupled ^{19}F
$^1H\{^{11}B\}$	boron-decoupled ^1H
br.	broad
COSY	correlation spectrocopy
d	doublet
HMBC	heteronuclear multiple-bond correlation
HSQC	heteronuclear single quantum correlation
Hz	Hertz
i	*ipso*
J	coupling constant
m	*meta*
m	multiplet
MHz	Megahertz
NMR	nuclear magnetic resonance
o	*ortho*
p	*para*
ppm	parts per million
q	quartet
quint.	quintet
s	singlet
sept.	septet
t	triplet
VT	variable temperature
δ	chemical shift in ppm

Infrared Spectroscopy

br.	broad
FT-IR	fourier transform infrared
IR	infrared
cm^{-1}	wavenumber
m	medium
s	strong
w	weak
υ	frequency

Notes

Literature compounds described in this Thesis are numbered **1.x**, **2.x**, **3.x**, **4.x**, **5.x** according to the Chapter. The novel compounds described in this Thesis are numbered **1** – **33**. Density functional theory (DFT) calculated compounds are clearly identified in the text.

X-ray crystallography data was collected by either Dr Benjamin Clough, Dr Bowen Xie or Dr Zoë Turner and solved and refined by either the Author, with the help and guidance of Prof. Philip Montford, or Dr Zoë Turner. Molecular drawings were produced by either Prof. Philip Mountford, the Author or Dr Zoë Turner.

The Density Functional Theory calculations reported throughout this Thesis were performed by Dr Eric Clot (Institut Charles Gerhardt, Université de Montpellier) and/or Professor Philip Mountford (University of Oxford). The principal calculations were performed with the Gaussian09 package at the B3PW91/Def2-SVP (for geometry optimisations) or B3PW91/Def2-TZVP (single point calculations on optimised geometries) levels, incorporating dispersion corrections (for geometry optimisation) and solvent effects (for single point calculations), where appropriate. Full details are provided in Chapter 6, Section 6.4.

Chapter One

Introduction

1.1 General introduction

Transition metal–ligand multiple bond chemistry has, for over four decades, been a field of study for many researchers in both inorganic and organometallic chemistry.[1] Of particular relevance to work presented in this Thesis are transition metal–nitrogen multiple bonds. Work on such systems was initiated by the proposal of imido (M=NR) and hydrazido ($M=NNR_2$) moieties as key intermediates in the biological, transition metal–catalysed, transformation of dinitrogen to ammonia. Since, transition metal imido and hydrazido chemistry has grown beyond these confines with the structure and bonding of these ligands being well understood and a host of academic and industrially applicable stoichiometric and catalytic reactions being discovered. To date, these include the stoichiometric and catalytic reduction of dinitrogen,[2–7] olefin polymerisation,[8–11] carbodiimide metathesis,[12] MOCVD (Metal-Organic Chemical Vapour Deposition),[9,13,14] dehydrocoupling of amine-boranes[15] and new C–N bond-forming reactions, such as hydroamination and hydrohydrazination (N–H bond addition across the CC multiple bonds of alkynes, alkene, allenes and carbodiimides).[16–29] Chapter 2 of this Thesis looks to extend the catalogue of Group 4 imido and hydrazido reactivity through reactions with silanes and boranes, of which there have been few reports.[30–33]

Also of relevance to the work presented in this Thesis is the synthesis and reaction chemistry of β-Si–H···M agostic transition metal–silylamide complexes. Complexes of this type contain several characteristic spectroscopic and structural features and have shown notable reactivity that includes β-hydrogen abstraction and elimination, γ-hydrogen abstraction and catalytic hydrosilylation.[34–50] Importantly, such abstraction and elimination reactions lead to metallacyclic intermediate species that can react with a wide range of unsaturated substrates. To this end, zirconocene-based systems have been

the most extensively studied. Chapters 3 and 4 of this Thesis look to expand upon this chemistry through reactions of β-agostic zirconocene silylamides with terminal alkynes, boranes and silanes.

The following sections of this Chapter will focus first on Group 4 imido and hydrazido chemistry before discussing the synthesis and reaction chemistry of β-agostic silylamido complexes.

1.2 Group 4 imido complexes

1.2.1 The imido ligand

Since the late 1950s, terminal imido ligands of transition metal complexes ($(L)_nM{=}NR$, R = alkyl or aryl) have been the subject of continued research.[1,51–54] The imido ligand can function as either an innocent spectator ligand or as the centre of reactivity. The former scenario is generally found for late transition metal complexes, while the latter is often found for early transition metal (Group 3 – 5) complexes, with the increased reactivity credited to the increased M=N bond polarity. The M=N bonds are considered to contain one σ-bond and either one or two π-bonds, as summarised in Figure 1.1.[52]

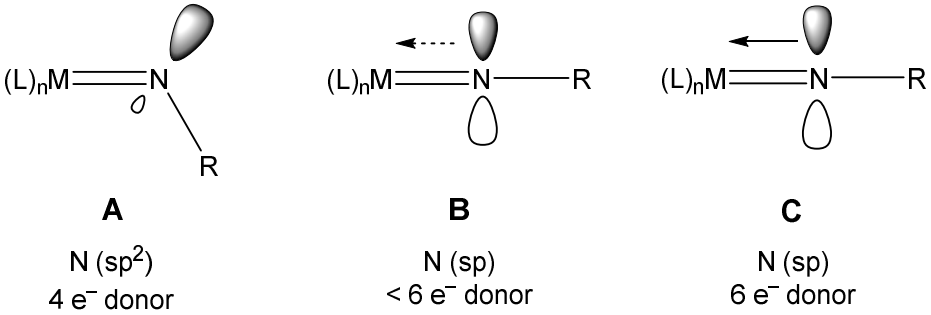


Figure 1.1: Bonding modes of the terminal imido ligand, with hybridisation of the N atom and the ionic valence electron count.

In bonding mode **A** the M=N–R linkage is bent, with an sp^2 hybridised nitrogen and a M=N double bond ($\sigma^2\pi^2$). The lone pair of the nitrogen resides in the sp^2 orbital and does not interact with the metal centre. One example of this rare bonding mode can be found

in the molybdenum bis(imide) $Mo(NPh)_2(S_2CNEt_2)_2$ (**1.1**), in which one imido ligand is near-linear (Mo–N–C = 169.4(4)°) and the other bent (139.4(4)°, Figure 1.2).[55] Most imido linkages are near-linear and correspond to bonding modes **B** or **C**. Here, the nitrogens are sp hybridised and the lone pair resides in a 2p orbital. In bonding mode **B** ($\sigma^2\pi^n$, $2 < n < 4$) the lone pair cannot effectively donate to the metal centre due to a poor energy match or a lack of metal orbitals of the correct symmetry. This situation arises in "π-loaded" metallocene imides, such as $Cp_2Ti(N^tBu)(py)$ (**1.2**) and $Cp_2Zr(N^tBu)(THF)$ (**1.3**), where full donation of the lone pair would result in a twenty valence electron complex. The lone pair of the nitrogen is, however, in competition with the π-donating orbitals of the Cp ligands, preventing full donation.[56,57] The most common bonding mode of the imido ligand is that of **C**, where the lone pair of the nitrogen can effectively donate to the metal centre and act as a six electron donor with a formally triple ($\sigma^2\pi^4$) bond to the metal. Imido and imido-derivative linkages will be drawn as a double bond throughout this Thesis for convenience and to represent the dianionic nature of the ligand, not the bond order.

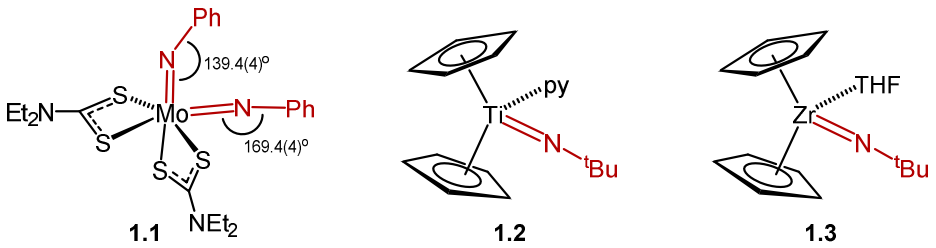
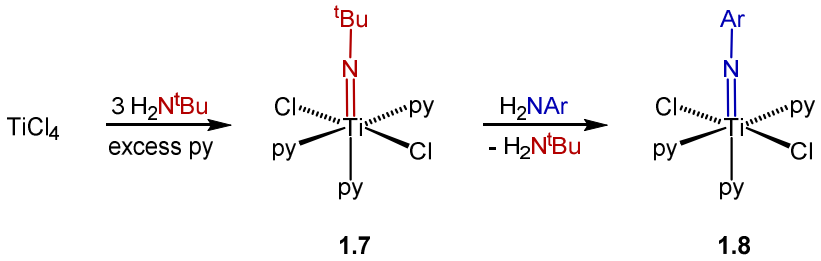


Figure 1.2: Examples of bent (**1.1**) and "π-loaded", linear (**1.2** and **1.3**) imido complexes.[55–57]

1.2.2 Synthesis of titanium imido complexes

The first structurally authenticated titanium imido complexes, namely $Ti(NPh)(Ar'O)_2(py')_2$ (**1.4**, py' = 4-pyrrolidinopyridine) and $Ti\{NP(S)Ph_2\}Cl_2(py)_3$ (**1.5**), were reported in 1990 by the groups of Rothwell and Roesky, respectively.[58,59] Soon after, Wolczanski and co-workers reported the synthesis of the transient imide

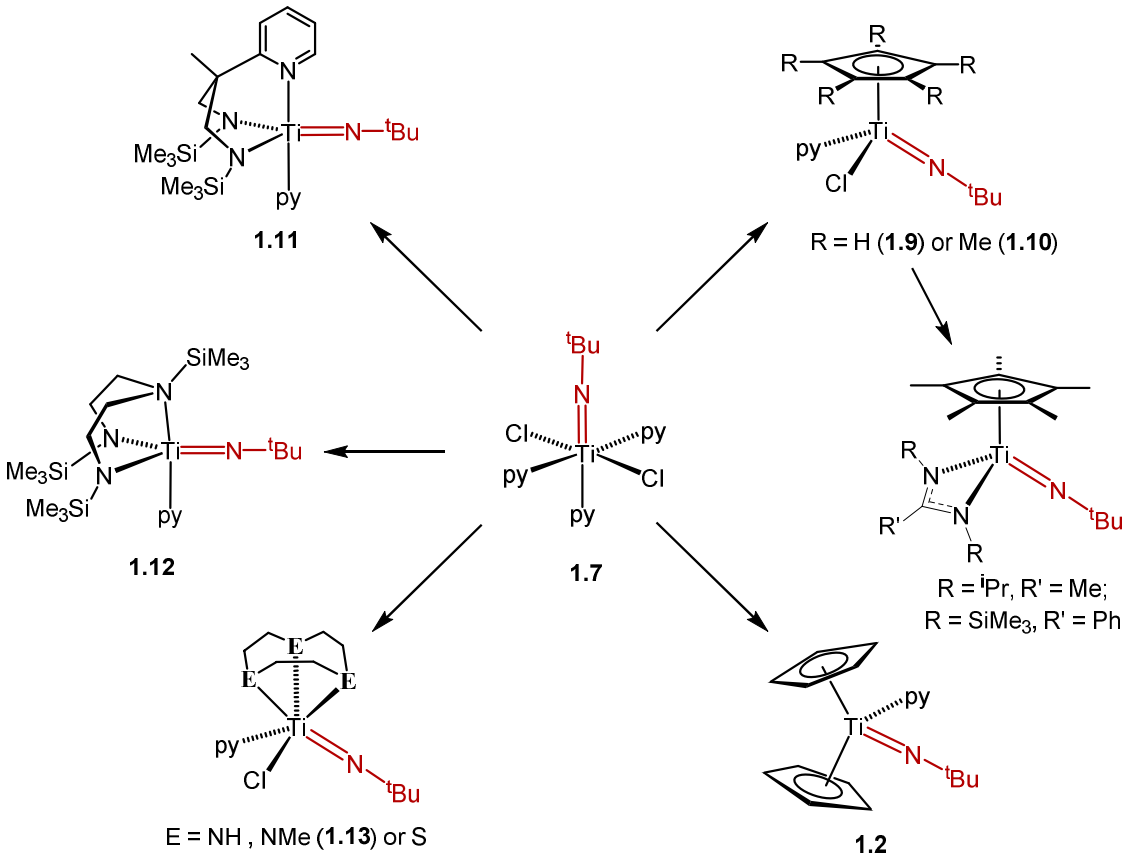
$Ti(NHSi^tBu_3)_2(NSi^tBu_3)$ (**1.6**), *via* thermolysis of $Ti(NHSi^tBu_3)_3(Me)$ or $Ti(NHSi^tBu_3)_4$, which could be trapped by Et_2O or THF.[60] Oxidative routes involving addition of azides or azo compounds to Ti(II) complexes and reactions of $(L)_nTiCl_2$ with 2 equivalents LiNHR to furnish titanium imides have also been reported.[12,61–63] In 1994, Mountford and co-workers published the convenient multigram synthesis of the widely used imido synthons $Ti(N^tBu)Cl_2(py)_3$ (**1.7**) and $Ti(NAr)Cl_2(py)_3$ (**1.8**, Ar = Ph, Xyl (2,6-$C_6H_3Me_2$) and Tol (4-C_6H_4Me), Scheme 1.1).[64]



Scheme 1.1: Synthesis of titanium imido complexes of the type $Ti(NR)Cl_2(py)_3$ (R = ^{t}Bu (**1.7**) or aryl (**1.8**)).[64]

$TiCl_4$ was reacted with H_2N^tBu and excess pyridine to furnish **1.7**, with subsequent reaction with anilines (H_2NAr) yielding **1.8** *via* amine/imide exchange. Attempts to directly form the arylimides by reaction of $TiCl_4$ with anilines were unsuccessful. From these synthons, a wide range of titanium alkyl- and arylimido compounds were swiftly synthesised *via* addition of various lithiated or sodiated ancillary ligands.[12,54,56,64–68] For example, the sandwich complex $Cp_2Ti(N^tBu)(py)$ (**1.2**) and half-sandwich complexes $CpTi(N^tBu)Cl(py)$ (**1.9**) and $Cp^*Ti(N^tBu)Cl(py)$ (**1.10**) were obtained by reaction of **1.7** with either NaCp or LiCp*.[56] Analogously, salt metathesis reactions between **1.7** and lithiated diamide-amine ligands $Li_2N_2N^{py}$ (N_2N^{py} = (2-C_5H_4N)$CMe(CH_2NSiMe_3)_2$) and $Li_2N_2N^{TMS}$ (N_2N^{TMS} = $Me_3SiN\{(CH_2)_2NSiMe_3\}_2$) furnish $Ti(N_2N^{py})(N^tBu)(py)$ (**1.11**) and $Ti(N_2N^{TMS})(N^tBu)(py)$ (**1.12**), respectively.[69,70] The half sandwich complex $Cp^*Ti(N^tBu)Cl(py)$ (**1.10**) also proved a useful synthon, with addition of anilines forming complexes of the type $Cp^*Ti(NAr)Cl(py)$ (Ar = Ar', 2,6-$C_6H_3Br_2$, 2-$C_6H_4{}^tBu$,

2-$C_6H_4{}^iPr$). From here, addition of lithiated amidinate ligands furnished cyclopentadienyl-amidinate titanium imido complexes.[71–75] *tert*-Butyl imido complexes of this type could also undergo aniline/imide exchange and further complexes of this type have been synthesised from cyclopentadienyl-amidinate titanium dichlorides and amidinate titanium imido chlorides.[20,76]



Scheme 1.2: Selected examples of titanium *tert*-butylimides synthesised from $Ti(N^tBu)Cl_2(py)_3$ (**1.7**).[12,54,56,64–70,72–75]

The diamide compound $Ti(NMe_2)Cl_2$ has also proven a useful entry point to a host of imides by reaction with anilines or alkylamies to yield the corresponding imide of the type $Ti(NR)Cl_2(NHMe_2)_2$ (R = alkyl or aryl).[77,78] Ancillary ligands could then be installed; in particular, addition of neutral tridentate ligands furnish a variety of dichloride imides. For example, compounds of the type $Ti(NR)Cl_2(Me_3[9]aneN_3)$ (R = alkyl (**1.13**) or aryl, $Me_3[9]aneN_3$ = 1,4,7-trimethyltriazacyclononane) have been synthesised by simple addition of $Me_3[9]aneN_3$.[8] Additionally, entry to several previously unknown

tris(pyridine) imides of the type **1.7** and **1.8** was gained through exchange of the dimethylamine ligands of $Ti(NR)Cl_2(NHMe_2)_2$ with pyridine. Recently, double deprotonation of the Ti–C bonds of bis(η^5:η^1-ademantylidenerentafulvene)titanium with amine has been reported as an entry route to the titanocene-derivative titanium imido complexes $(CpAd)_2Ti(NR)(py)$ (R = ^{t}Bu or Ar').[79]

1.2.3 Synthesis of zirconium and hafnium imido complexes

Despite the synthesis of the first monomeric zirconium imido complexes preceding titanium complexes there have been fewer reported compounds and a lack of a synthon comparable in use to $Ti(N^tBu)Cl_2(py)_3$ (**1.7**). In 1988, Bergman and co-workers reported the thermolysis of the methyl-amido complexes $Cp_2Zr(Me)(NHR)$ (R = ^{t}Bu, Xyl and 4-$C_6H_4{}^t$Bu) to give the transient imido species $Cp_2Zr(NR)$ (R = ^{t}Bu (**1.14**), Xyl (**1.15**) and 4-$C_6H_4{}^t$Bu (**1.16**), Figure 1.3).[80] These were found to rapidly dimerise in hydrocarbon solution to give bridging imido complexes. Thermolysis in THF solution, however, gave the monomeric THF adducts $Cp_2Zr(N^tBu)(THF)$ (**1.3**) and $Cp_2Zr(NXyl)(THF)$ (**1.17**) for the *tert*-butyl- and xylylimides, respectively.[57,80] The same group also reported this route for the synthesis of the analogous mixed-sandwich complex, $Cp^*CpZr(N^tBu)(THF)$.[81] Dimeric, bridging imido zirconium and hafnium complexes were reported 9 years prior to the monomeric zirconium imides, by Nugent and Harlow, from the reaction of $Zr(NMe_2)_4$ or $Hf(NMe_2)_4$ with H_2N^tBu.[82] The larger radius of zirconium and hafnium, with respect to titanium, means the reactive M=N bond requires more steric protection to yield monomeric, terminal imides.

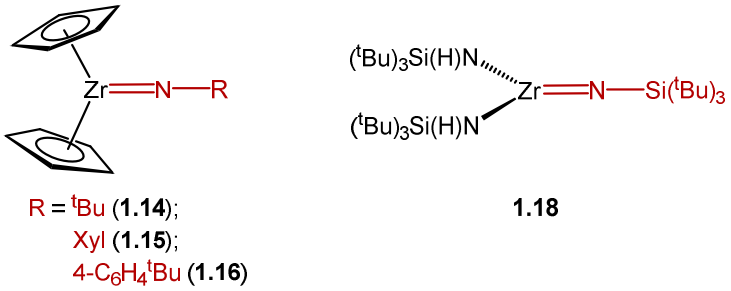


Figure 1.3: Early examples of transient, monomeric zirconium imido complexes.[80,83]

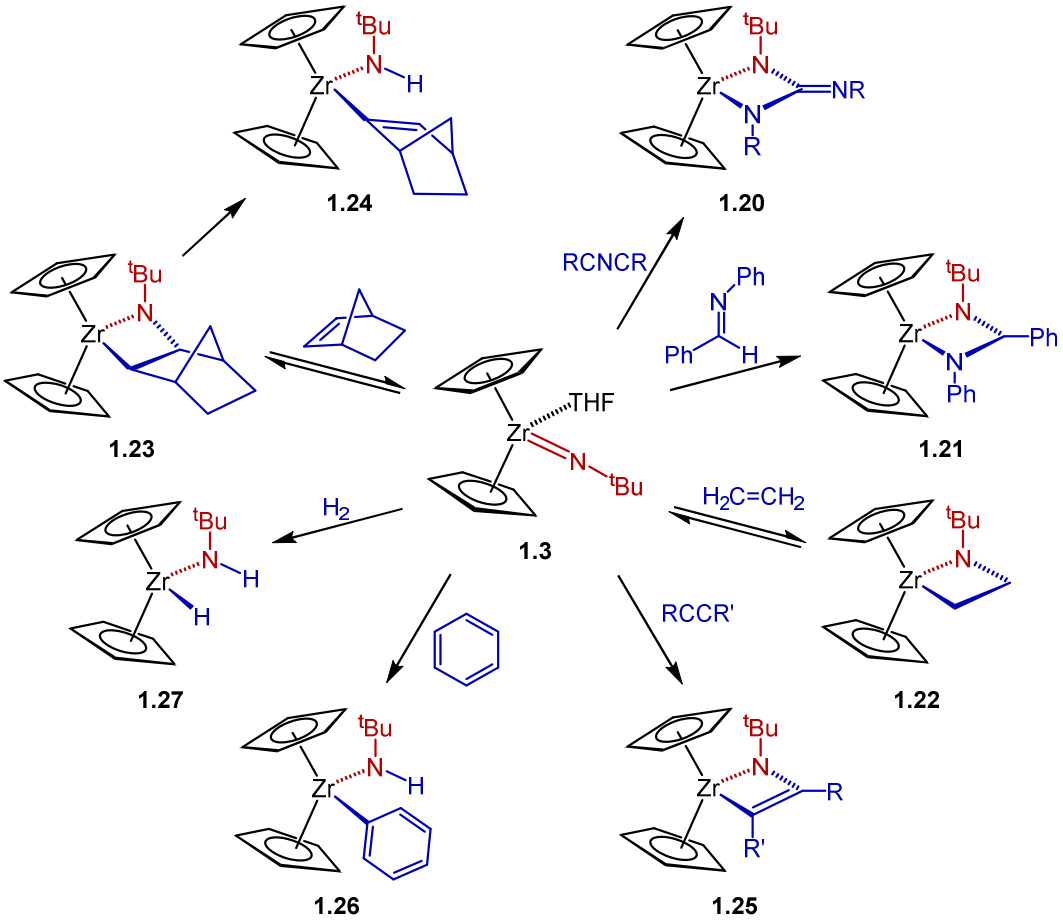
Wolczanski and co-workers, analogous to Bergman, prepared the transient bis(amide)imide [Zr(NSi^{t}Bu$_3$){N(H)Si^{t}Bu$_3$}$_2$] (**1.18**, Figure 1.3) by thermolysis of the tris(amide)methyl complex.[83] Again, the monomeric THF adduct Zr(NSi^{t}Bu$_3$){N(H)Si^{t}Bu$_3$}$_2$(THF) could be isolated by thermolysis in THF solution. Wigley and co-workers reported the zirconium imide synthon Zr(NAr')Cl$_2$(py)$_3$ (**1.19**), isolated from the reaction of ZrCl$_4$(THF)$_2$ with LiNHAr', pyridine and, subsequently, Me$_3$SiCl.[84] Unlike the titanium analogue Ti(NAr)Cl$_2$(py)$_3$ (**1.8**), these reactions were not general and a wider range of alkyl- and arylimido functionalities could not be installed. In the absence of pyridine, Zr(NAr')Cl$_2$(THF)$_2$ was formed, with later crystallographic characterisation showing this to be a dimeric, bridging imido species.[84,85] Similar reactions were conducted for hafnium analogues. From complex **1.19**, the dimeric bridging imido compounds [(η^8-C$_8$H$_8$)Zr(μ-NAr')]$_2$ and [Cp'ZrCl(μ-NAr')]$_2$ (Cp' = η^5-C$_5$H$_4$Me) were synthesised. Furthermore, our research group has used the synthon to furnish various zirconium 2,6-diisopropylphenylimido complexes, such as Zr(N$_2$N^{py})(NAr')(py).[70,86]

Attempts to find zirconium synthons that allow for installation of a wider range of alkyl- and arylimido ligands have been made within our research group.[78] While protonolysis reactions of a range of alkylamines and anilines with Zr(CH$_2$SiMe$_3$)$_2$Cl$_2$(OEt$_2$)$_2$ and Zr(NMe$_2$)$_2$Cl$_2$(THF)$_2$ has provided entry to a variety of dimeric bridging imido dichloride compounds, the synthesis of the corresponding

monomeric imides could not be realised by addition of pyridine or lithiated ancillary ligands. Monomeric zirconium and hafnium compounds have, however, been synthesised from dichloride precursors.[87,88] For example, $Zr(N_2NN')(N^tBu)(py)$ (N_2NN' = $(2\text{-}C_5H_4N)CH_2N(CH_2CH_2NSiMe_3)_2$) has been synthesised by reaction of $Zr(N_2NN')Cl_2$ and 2 equivalents $LiCH_2SiMe_3$, followed by H_2N^tBu and pyridine.[88]

1.2.4 Stoichiometric reactions

The hallmark of Group 4 imido chemistry is the [2+2] cycloaddition of unsaturated substrates across the M=N multiple bond. This being said, examples of C–H, H–H, S–H, N–H and B–H activation across the M=N bond have also been reported. Bergman's zirconocene imido complex $Cp_2Zr(N^tBu)(THF)$ (**1.3**) and the base-free, transient analogue $Cp_2Zr(N^tBu)$ (**1.14**) have exhibited rich reaction chemistry towards small molecules. Selected reactions are shown in Scheme 1.3 and discussed below. Further examples are discussed later in this Section. Similar reactions have been shown for other Group 4 metallocene imides, such as $Cp^*_2Ti(NPh)$.[89]



Scheme 1.3: Selected reactions of $Cp_2Zr(N^tBu)(THF)$ (**1.3**).[57,80,90–96]

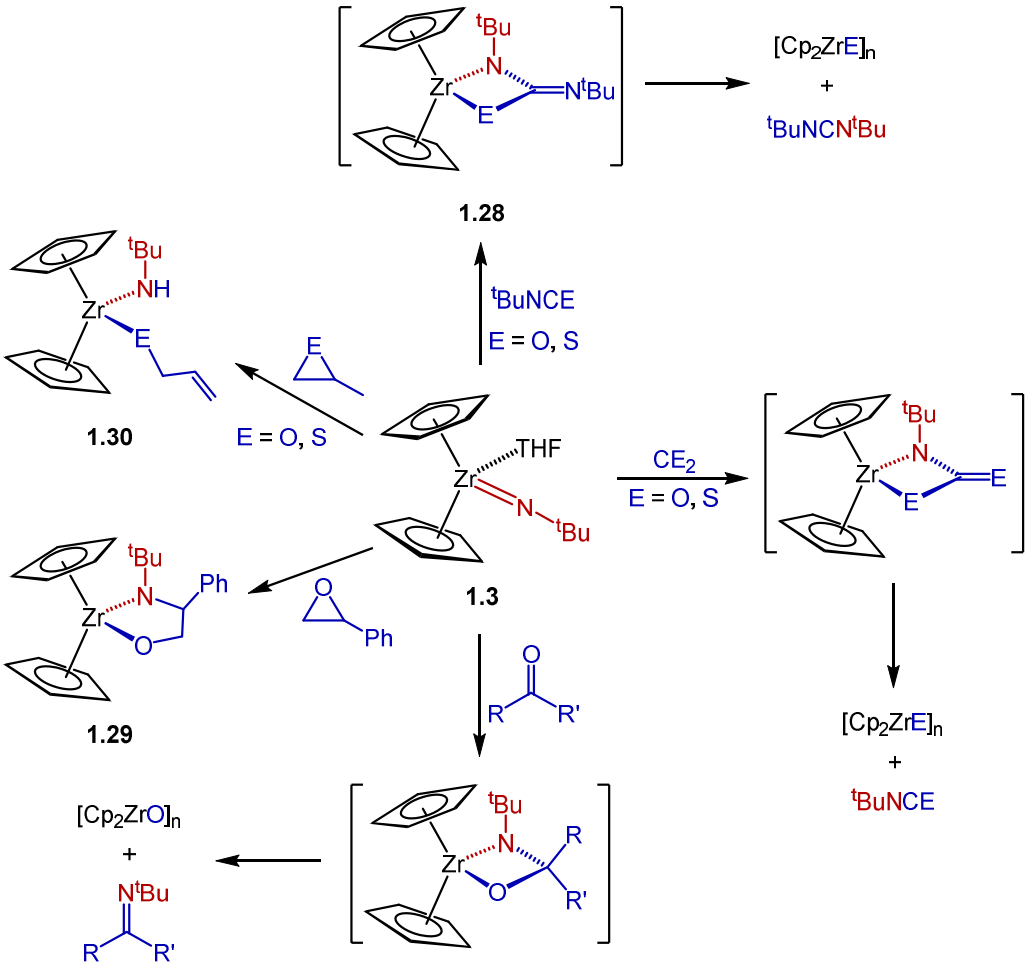
Reaction of both $Cp_2Zr(N^tBu)(THF)$ (**1.3**) and $Cp_2Zr(NXyl)(THF)$ (**1.17**) with carbodiimides were found to give β-iminodiazazirconacyclobutanes of the type $Cp_2Zr\{N(R)C(NR')N(R')\}$ (**1.20**, R' = ^{t}Bu, $SiMe_3$, ^{i}Pr or aryl).[90,91] Stoichiometric reaction of **1.3** with the imine PhC(H)=NPh yielded the diazazirconacyclobutane complex $Cp_2Zr\{N(^tBu)C(H)(Ph)N(Ph)\}$ (**1.21**).[81,92,93] Notably, addition of further equivalents of the imine at elevated temperatures gave the symmetrically substituted diazazirconacyclobutane complex $Cp_2Zr\{N(Ph)C(H)(Ph)N(Ph)\}$ and the imine $PhC(H)=N^tBu$ *via* $[Cp_2Zr(NPh)]$. Reversible cycloaddition was observed for the olefins ethylene and norbornene to give **1.22** and **1.23**, respectively, with heating to 45 °C leading to irreversible sp^2 C–H activation to give **1.24** in the case of norbornene.[57,94] Compound **1.3** was found to undergo [2+2] cycloaddition with both terminal and internal alkynes to

give zirconacyclobutenes of the type $Cp_2Zr\{N(^tBu)C(R)C(R')\}$ (**1.25**, R, R' = H, Me or aryl). Identical reactions were also reported for **1.17**.[57,95]

Beyond [2+2] cycloaddition, the sp^2 C–H activation ability of **1.3** towards olefins has not only been presented with norbornene, but other olefins as well, such as cyclopentene.[97] Furthermore, reaction with benzene, *via* $[Cp_2Zr(N^tBu)]$ (**1.14**) led to the formation of $Cp_2Zr(NH^tBu)(Ph)$ (**1.26**).[80] Notably, $[Cp_2Zr(NXyl)]$ (**1.15**) did not react with benzene under any conditions. Analogous reactions were observed for the transiently generated zirconium and titanium imides $[M(NSi^tBu_3)\{N(H)Si^tBu_3\}_2]$ (M = Zr (**1.18**), Ti) with benzene and sp^3 hybridised methane, forming $M(R)\{N(H)Si^tBu_3\}_3$ (M = Zr or Ti, R = Ph or Me).[60,83] Activation of dihydrogen has recently been reported for **1.3**, forming $Cp_2Zr(H)(NH^tBu)$ (**1.27**).[96] Identical reaction with dihydrogen has been observed for titanocene-derivative imido complexes as well.[62] C–H bond activation of terminal alkynes has also been showcased for Group 4 imides. Compound **1.3** was reported to give a mixture of [2+2] cycloaddition and C–H activation products with $HCCC_6F_5$.[96] Changing of the coordinative base from THF to pyridine or DMAP led to quantitative formation of the C–H activation product $Cp_2Zr(NH^tBu)(CCC_6F_5)$. The homologous imide $Cp^*CpZr(N^tBu)(THF)$ underwent C–H activation with HCC^tBu to give $Cp^*CpZr(NH^tBu)(CC^tBu)$, and likewise for $Cp^*_2Ti(NPh)$ with HCC^tBu and $Cp^*Ti(N^{3,5\text{-}Xyl}N^{pyr})(N^tBu)(NH_2{}^tBu)$ ($N^{3,5\text{-}Xyl}N^{pyr}$ = 2-(3,5-dimethylphenylamino)pyrrolinato) with HCCAr (Ar = Ph or Tol).[20,89,97]

[2+2] Cycloaddition reactions of $Cp_2Zr(N^tBu)(THF)$ (**1.3**) have also extended to isocyanates, heteroallenes and carbonyls (Scheme 1.4). These reactions have provided novel synthetic routes for a host of organo-nitrogen ligands. Reaction of **1.3** with *tert*-butylisocyanate (^{t}BuNCO) provided di-*tert*-butylcarbodiimide and insoluble, oligomeric $[Cp_2Zr{=}O]_n$, allowing for facile purification of the carbodiimide.[57] This was

proposed to proceed *via* a transient, N,O-bound isocyanate adduct (**1.28**), with subsequent cycloreversion.

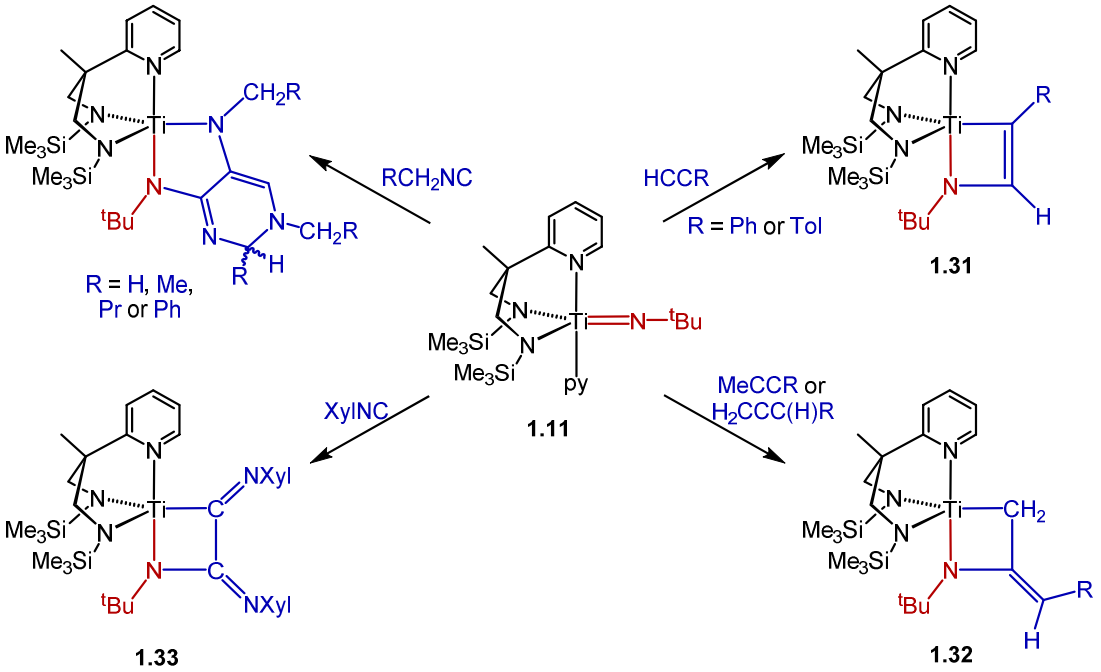


Scheme 1.4: Selected reactions of $Cp_2Zr(N^tBu)(THF)$ (**1.3**) with isocyanates, heterocumulenes, carbonyls, epoxides and episulphides.[57,91,92,94,98,99]

Woo and co-workers have presented an analogous reaction for the zirconium imide Zr(NAr')(TTP) (TTP^{2-} = *meso*-terta-*p*-tolylporphyrinato dianion), though in this instance the N,O-bound isocyanate adduct intermediate was able to be isolated.[87] In contrast, Mountford and co-workers have reported the cycloaddition of the N=C bond of ^{t}BuNCO with the imide Zr(Me$_4$taa)(NAr')(py) to give Zr(Me$_4$taa){N(Ar')C(O)N(^{t}Bu)}.[67] Reaction of **1.3** with heteroallenes and carbonyls, namely benzaldehyde and benzophenone, are analogous as isocyanate reactions.[91,94,98] Compound **1.3** has also been reacted with epoxides and episulphides (Scheme 1.4).[57,99] These are found to undergo ring-opening insertion to give azaoxazirconacyclopentanes (**1.29**). In the absence of

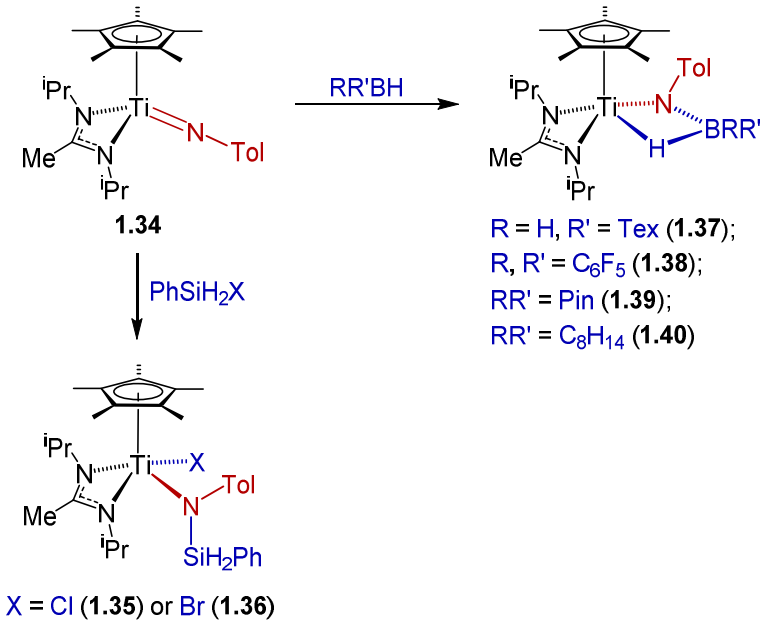
accessible β-hydrogens these are stable, but undergo β-hydrogen elimination to give allylic oxide or sulphide complexes (**1.30**) when β-hydrogens are accessible to the nitrogen. Reactions of **1.3** with amines and azides also centre around the Zr=N bond.[57,92,94]

Scheme 1.5 shows selected transformations of the titanium diamide-amine imido complex Ti(N_2N^{py})(N^tBu)(py) (**1.11**), which has exhibited rich reaction chemistry.[12,68,100–104] Compound **1.11** reacts with terminal alkynes through [2+2] cycloaddition to give compounds of the type **1.31**.[101] Notably, reaction with methyl-substituted alkynes, or allenes, gave titanaazetidines of the type **1.32**.[100,103] Conversely, reaction of the methyl-substituted internal alkynes MeCC(4-$C_6H_4CF_3$) and MeCC(4-C_6H_4F) with Ti($N^{iPr}{}_2N^{py}$)(NXyl)(py) ($N^{iPr}{}_2N^{py}$ = (2-C_5H_4N)CMe($CH_2N^iPr)_2$) led to activation of the *ortho*-hydrogen of the phenyl rings after [2+2] cycloaddition to give *ortho*-metallated vinylamide complexes.[105] Reaction of **1.11** with 2 equivalents XylNC gave the titancycle **1.33**, formed by coupling of the two isocyanides.[102] Further isocyanide coupling was observed on reaction with isocyanides of the type RCH_2NC (R = H, Me, Pr or Ph), bearing α-hydrogens.



Scheme 1.5: Selected reactions of Ti(N_2N^{py})(N^tBu)(py) (**1.11**) with unsaturated substrates.[100–103]

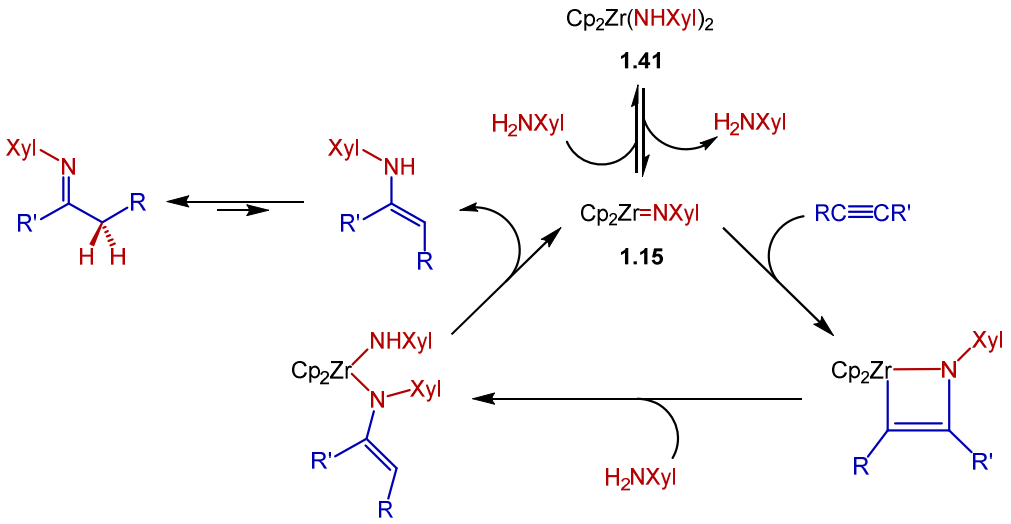
Further to reactions of various unsaturated substrates, C–H and N–H bonds, and dihydrogen, reactions of Group 4 imides with S–H, Si–X (X = Cl or Br) and B–H bonds have been reported. $Cp_2Ti(N^tBu)(py)$ (**1.2**) was shown to react with 2 equivalents MeSH to give $Cp_2Ti(SMe)_2$, with concomitant release of H_2N^tBu, and with SH_2 to give either $[Cp_2Ti]_2(\mu\text{-}S)_2$ or $Cp_2Ti(SH)_2$ depending on the reaction stoichiometry.[106] The cyclopentadienyl-amidinate titanium imido complex Cp*Ti{$MeC(N^iPr)_2$}(NTol) (**1.34**) underwent 1,2-addition of the Si–X bond of $PhSiH_2X$ to give halide silylamide complexes Cp*Ti{$MeC(N^iPr)_2$}(X){$N(Tol)SiH_2Ph$} (X = Cl (**1.35**) or Br (**1.36**)), though these were unstable in solution (Scheme 1.6).[31] There have been no reports of reactions of Group 4 imides with Si–H bonds. With boranes H_2BTex (Tex = *tert*-hexyl), $HB(C_6F_5)_2$, HBPin (Pin = pinacol) and 9-BBN ($[\mu\text{-}H)BC_8H_{14}]_2$), compound **1.34** was recently reported to form hydride-bridged adducts **1.37** – **1.40** without B–H bond cleavage (Scheme 1.6).[33]



Scheme 1.6: Reactions of Cp*Ti{MeC(N^{i}Pr)$_2$}(NTol) (**1.34**) with boranes and silanes.[31,33]

1.2.5 Catalytic hydroamination

Group 4 metal complexes have been extensively studied as catalysts for hydroamination – the addition of an N–H bond across an unsaturated C–C bond to form new C–N bonds in an atom-economical manner. Three general mechanisms have been discovered, the most common of which is the "imido route".[23,28,29,94,107–114] Here, [2+2] cycloaddition of the C–C multiple bond at the M=N bond occurs initially, followed by double protonolysis by an incoming amine to release, in the case of alkyne hydroamination, an enamine or, in the case of an alkene, an amine.[115,116] This enamine can then tautomerise to give an imine. Scheme 1.7 shows this mechanism using the precatalyst Cp$_2$Zr(NHXyl)$_2$ (**1.41**) as an example.[117,118]



Scheme 1.7: Catalytic cycle for the hydroamination of alkynes using the precatalyst $Cp_2Zr(NHXyl)_2$ (**1.41**) *via* the "imido route".[117,118]

In 1992, Bergman and co-workers produced seminal work on zirconium catalysts for the hydroamination of alkynes, alkenes and allenes, reporting hydroamination of diphenylacetylene, 2-butyne and allene with H_2NXyl using the bis(amido) complex $Cp_2Zr(NHXyl)_2$ (**1.41**) as a precatalyst at 3 mol% loading at 95 – 120 °C.[117,118] Other examples of effective zirconium precatalysts include $Cp_2Zr(NMe_2)_2$, $Zr(NMe_2)_4$ and sulphonamide-supported complexes.[119] By comparison, there have been few reports of hafnium complexes being employed as hydroamination catalysts.[120–122] In all reports, the hafnium catalysts were found to be much less active than the zirconium analogues, presumably due to hafnium forming stronger M–E bonds. A host of titanium complexes have also been reported for catalytic hydroamination, *via* the imido route.[20,23,24,109,110,119,123,124]

1.3 Group 4 hydrazido complexes

1.3.1 The hydrazido ligand

Initial research into transition metal hydrazido complexes centred on their relevance to nitrogen fixation in biology. To this end, Group 6 complexes received the most attention. More recently, Group 4 hydrazido complexes have come to the fore with research focussed on their rich reaction chemistry with organic substrates. The presence of the β-nitrogen and reducible N_α–N_β bond, on top of the M=N_α imide linkage for η^1-hydrazido(2–) bonding mode, has allowed for observation of more diverse reactivity than their imido counterparts. Furthermore, the β-nitrogen allows for several possible bonding modes of the hydrazido ligand to metal centres (Figure 1.4).[24] Bonding modes differ depending on the formal –1 or –2 charge of the ligand, which depends on the presence of an N_α-substituent, and coordination of the β-nitrogen. Hydrazido ligands described in this Thesis will be η^1-hydrazido(2–) ligands, unless stated otherwise, and are isoelectronic with the imido ligand.[125–127]

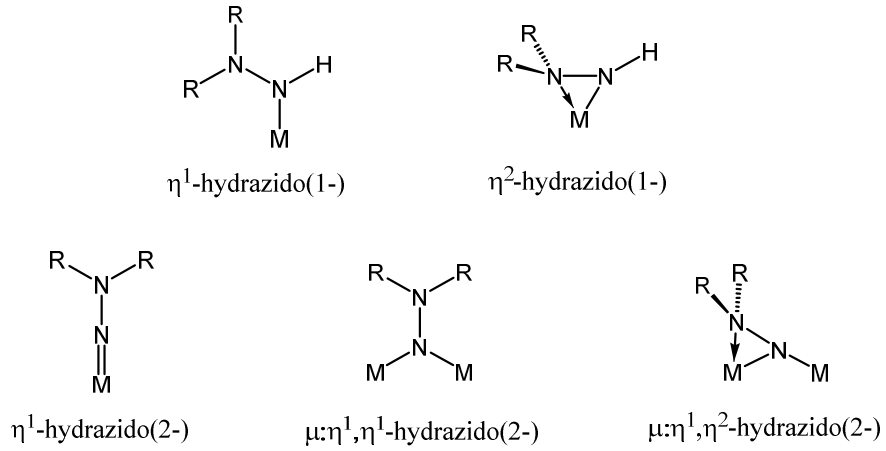
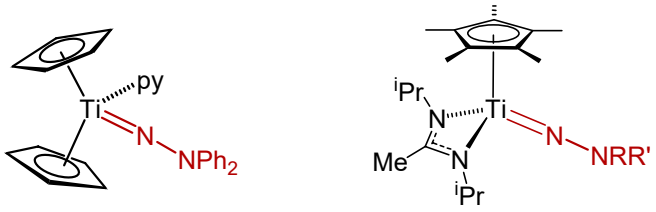


Figure 1.4: Bonding modes of hydrazido ligands.

1.3.2 Synthesis of titanium hydrazido complexes

In 1978, Wiberg and co-workers reported the synthesis of the first monomeric terminal titanium hydrazido complex $Cp_2Ti\{NN(SiMe_3)_2\}$.[128] Only in 1999 was the second such

complex reported – namely, $Ti(NNPh_2)(Me_4taa)$ – formed by simple imide/hydrazine exchange of $Ti(N^tBu)(Me_4taa)$ with H_2NNPh_2 (*cf.* imide/aniline exchange discussed in Section 1.2.2).[67] The first structurally characterised terminal titanium hydrazide, $Ti(N_2^{pyr}N^{Me})(NNMe_2)(^tBu\text{-bipy})$ (^tBu-bipy = 4,4'-di-*tert*-butyl-2,2'-bipyridine) was reported in 2004 by Odom and co-workers.[24] The first hydrazide synthons, $Ti(NNPh_2)Cl_2(py)_3$ (**1.42**) and $Ti(NNPh_2)Cl_2(NHMe_2)_2$ (**1.43**) were reported by Mountford and co-workers, formed by imide/hydrazine exchange with the relevant *tert*-butylimide.[126,129] Indeed, *tert*-butylimide/hydrazine exchange has proved a powerful synthetic route to various titanium hydrazides. Some Cp-supported hydrazides synthesised *via* this route are shown in Figure 1.5.[125,130] The Cp-amidinate-supported hydrazides $Cp^*Ti\{MeC(N^iPr)_2\}(NNRR')$ (R = R' = Me (**1.45**) or Ph (**1.46**); R = Me, R' = Ph (**1.47**)) have provided particularly fruitful reactivity.

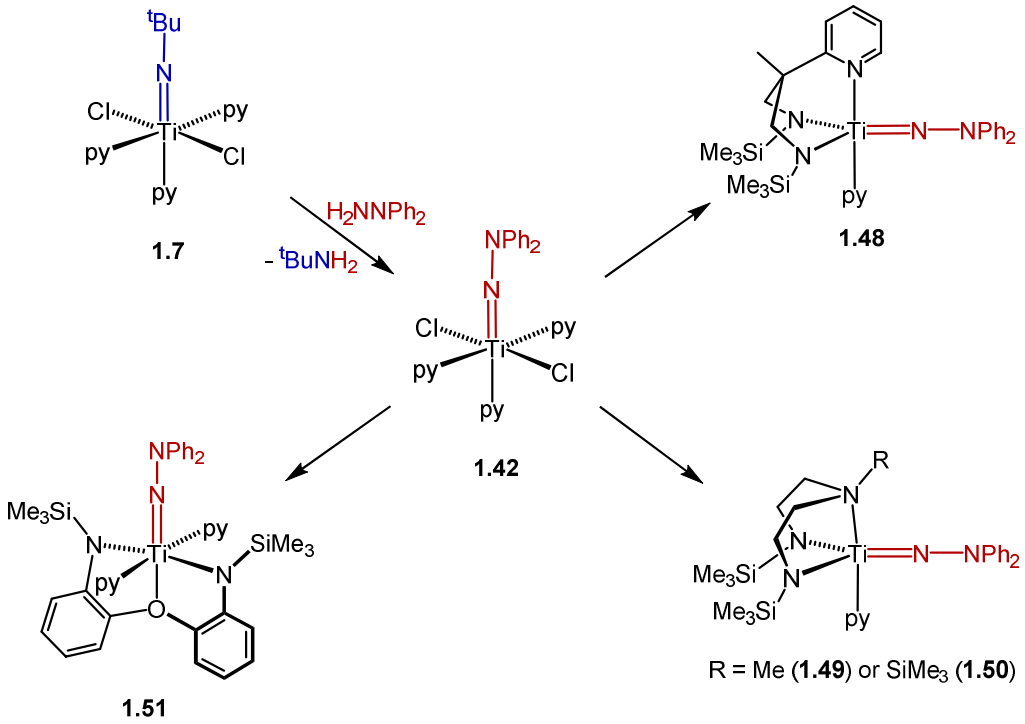


1.44

R = R' = Me (**1.45**) or Ph (**1.46**);
R = Me, R' = Ph (**1.47**)

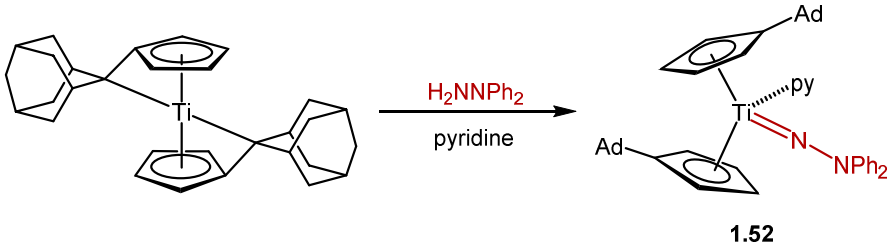
Figure 1.5: Exemplar Cp-supported titanium hydrazides synthesised by *tert*-butylimide/hydrazine exchange.[125,130]

As mentioned, $Ti(NNPh_2)Cl_2(py)_3$ (**1.42**) acts as a synthon allowing access to several hydrazido complexes with varying ancillary ligands *via* salt metathesis. The advent of tridentate N- or O-donor ligands, such as those seen in compounds **1.48** – **1.51** (Scheme 1.8), has led to titanium hydrazides that exhibit rich reaction chemistry.[129] Attempts to synthesise the dimethylhydrazido analogues of synthons **1.42** and **1.43** led to formation of hydrazido-bridged dimers.[126,129]



Scheme 1.8: Synthesis of $Ti(NNPh_2)Cl_2(py)_3$ (**1.42**) and examples of subsequent salt metathesis reactions with lithiated N- or O- donor tridentate ligands to furnish compounds **1.48** – **1.51**.[129]

Recently, Beckhaus and co-workers, in an identical manner to the synthesis of analogous imido complexes, reported the synthesis of $(Cp^{Ad})_2Ti(NNPh_2)(py)$ (**1.52**) *via* double deprotonation of bis(η^5:η^1-ademantylidenerentafulvene)titanium by diphenylhydrazine in the presence of pyridine (Equation 1.1).[79,131]

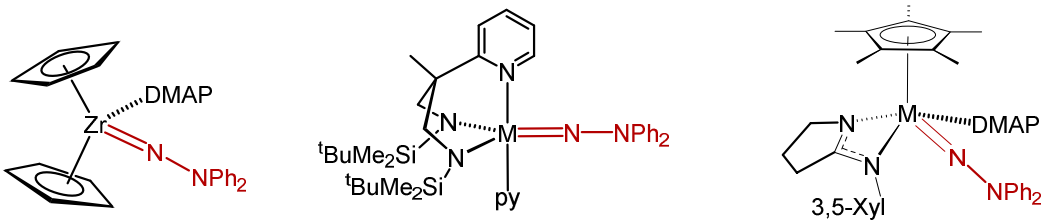


Equation 1.1[131]

1.3.3 Synthesis of zirconium and hafnium hydrazido complexes

Bergman and co-workers reported the first structurally characterised terminal zirconium hydrazide in 1991.[127] Thermolysis of the alkylhydrazido(1–) complex $Cp_2Zr(NHNPh_2)(CH_2CH_2{}^tBu)$ generated the transient hydrazido complex

[$Cp_2Zr(NNPh_2)$] (**1.53**), with concomitant release of 2,2-dimethylbutane. With DMAP present, the monomeric hydrazide $Cp_2Zr(NNPh_2)(DMAP)$ (**1.54**) was isolated. In the absence of base this transient complex formed an unsymmetrical dimer with bridging hydrazido ligands. Structurally, compound **1.54** contains a similar $Z{=}N_\alpha$ bond distance to that of $Cp_2Zr(NAr')(THF)$ (1.873(7) and 1.888(2) Å, respectively) consistent with the hydrazido ligand being isolobal with the imido ligand.[94]



1.54 M = Zr (**1.55**) or Hf (**1.56**) M = Zr (**1.57**) or Hf (**1.58**)

Figure 1.6: Examples of monomeric terminal zirconium and halfnium hydrazido complexes.[127,132–134]

Unlike for imides and titanium hydrazides, no zirconium hydrazide synthon to which a host of ancillary ligands can be added has been found to date. Therefore pre-installation of the target ancillary ligands has been required prior to addition of the hydrazido ligand. To this end, Gade and co-workers have employed several tridentate diamide-pyridine ligands.[132,133,135–137] In 2007, $Zr(N_2^{TBS}N^{py})(NNPh_2)(py)$ (**1.55**, $N_2^{TBS}N^{py}$ = $MeC(2\text{-}C_5H_4N)(CH_2NSiMe_2{}^tBu)_2$) was synthesised by dehydrohalogenation of $Zr(N_2^{TBS}N^{py})Cl(NHNPh_2)$, formed *in situ* by addition of $LiNHNPh_2$ to $Zr(N_2^{TBS}N^{py})Cl_2$, by $LiN(SiMe_3)_2$.[132] The hafnium congener $Hf(N_2^{TBS}N^{py})(NNPh_2)(py)$ (**1.56**) was prepared in an identical manner.[133] Analogously, the half sandwich zirconium and hafnium hydrazido complexes $Cp^*M(N^{3,5\text{-}Xyl}N^{pyr})(NNPh_2)(DMAP)$ (M = Zr (**1.57**) or Hf (**1.58**), $N^{3,5\text{-}Xyl}N^{pyr}$ = 2-(3,5-dimethylphenylamino)pyrrolinato) were synthesised from $Cp^*M(N^{3,5\text{-}Xyl}N^{pyr})Cl_2$, $LiNHNPh_2$ and subsequent hehydrohalogenation by $LiN(SiMe_3)_2$.[134] As well as addition of lithiated hydrazides to diamide-pyridine or Cp*-amidinate supported dichlorides, addition of hydrazines to diamide-pyridine

supported bis(amides) has also been employed as a synthetic pathway to terminal zirconium hydrazides. Addition of two equivalents of the cyclic hydrazines H_2NNR_2 (R_2 = C_9H_{10} or $C_{12}H_8$) to $Zr(N_2^{3,5\text{-}Xyl}N^{py})(NMe_2)_2$ in the presence of DMAP yielded the terminal hydrazides $Zr(N_2^{3,5\text{-}Xyl}N^{py})(NNR_2)(DMAP)_2$.[135]

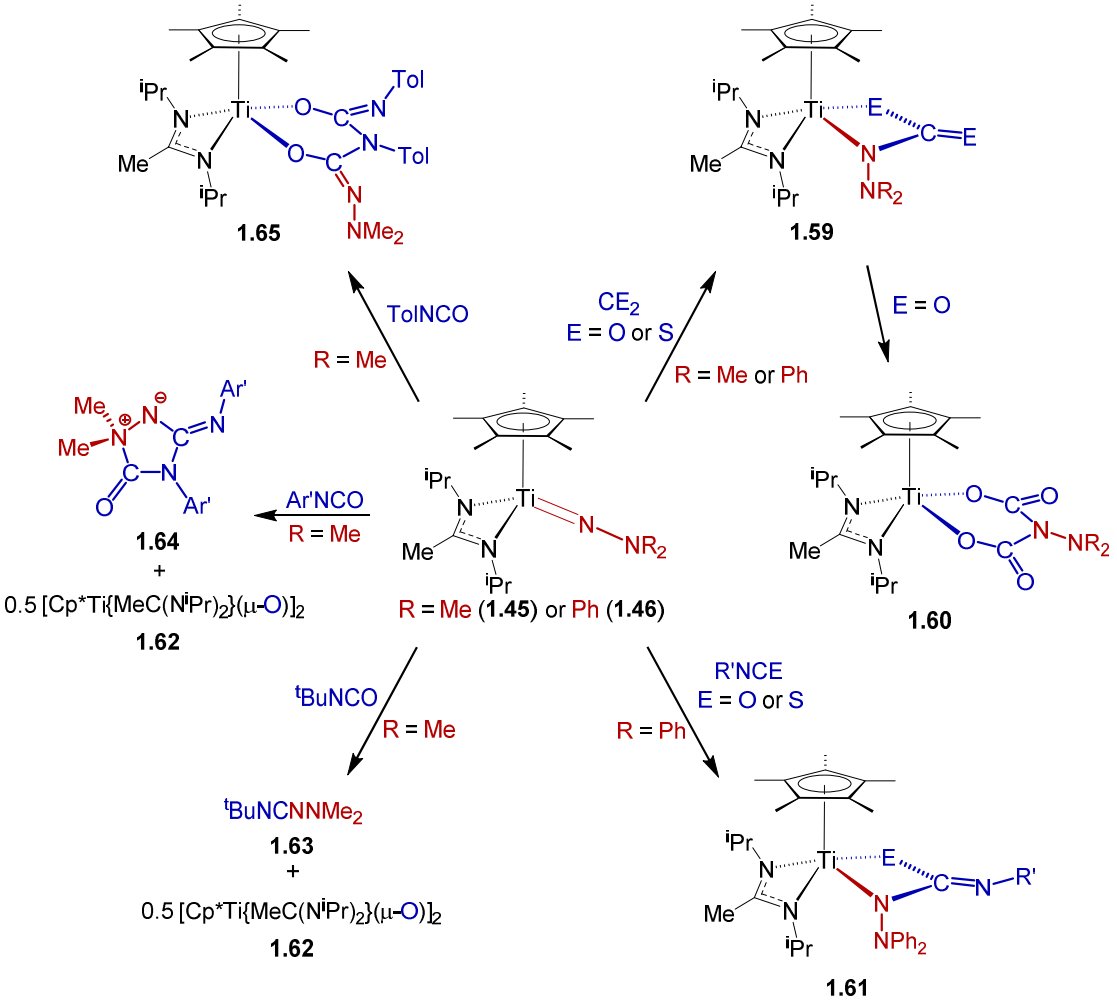
1.3.4 Stoichiometric reactions with unsaturated substrates involving the M=N$_\alpha$ bond

Group 4 hydrazides have shown a wealth of reactivity with small molecules, with the large majority of reports involving reactivity with unsaturated substrates. Reactions predominantly proceed first *via* [2+2] cycloaddition at the M=N$_\alpha$ bond. The possibilities hereafter are the root of the diverse reactivity reported for Group 4 hydrazido complexes and include: cleavage of the now single M–N$_\alpha$ bond by a second substrate or intramolecularly to eliminate an organic compound or; reductive cleavage of the N$_\alpha$–N$_\beta$ bond. This Section will discuss reactivity concerning only the Zr–N$_\alpha$ linkage.

In 1999, Mountford and co-workers reported the first examples of isolated [2+2] cycloaddition reaction products, from reactions of $Ti(NNPh_2)(Me_4taa)$ with CO_2 and TolNCO.[67] Only 9 years later, however, was the first structurally authenticated [2+2] cycloaddition product reported, namely $Cp_2Ti\{N(NPh_2)C(^tBu)P\}$, formed by reaction of $Cp_2Ti(NNPh_2)(py)$ (**1.44**) with the phosphoalkyne ^{t}BuCP.[138] Soon after, interest in the stoichiometric reactivity of Group 4 hydrazides increased and selected examples are discussed below.

Cyclopentadienyl-amidinate supporting ligand frameworks proved to be a robust platform on which the reactivity of the M=N$_\alpha$ bond of the hydrazido ligand could be well showcased.[125] Selected reactions of the compounds $Cp^*Ti\{MeC(N^iPr)_2\}(NNR_2)$ (R = Me (**1.45**) and Ph (**1.46**)) are shown in Scheme 1.9. Reaction with CE_2 (E = O or S) led to

[2+2] cycloaddition to give the carbamate-type compounds **1.59**. With CO_2 a second insertion occurred at the now Ti–N_α single bond to give complexes of the type **1.60**. Interestingly, compounds **1.45** and **1.46** gave different reaction products with isocyanates. Diphenylhydrazide **1.46** gave only cycloaddition products of the type **1.61** with both alkyl and aryl isocyanates. Analogous reactions were observed between isocyanates and both $Cp_2Zr(NNPh_2)(DMAP)$ (**1.54**) and $Zr(N_2^{TBS}N^{py})(NNPh_2)(py)$ (**1.55**), the latter of which also gave cycloaddition products with isothiocyanates, allenes and organic azides, by [2+3] cycloaddition.[139–141]



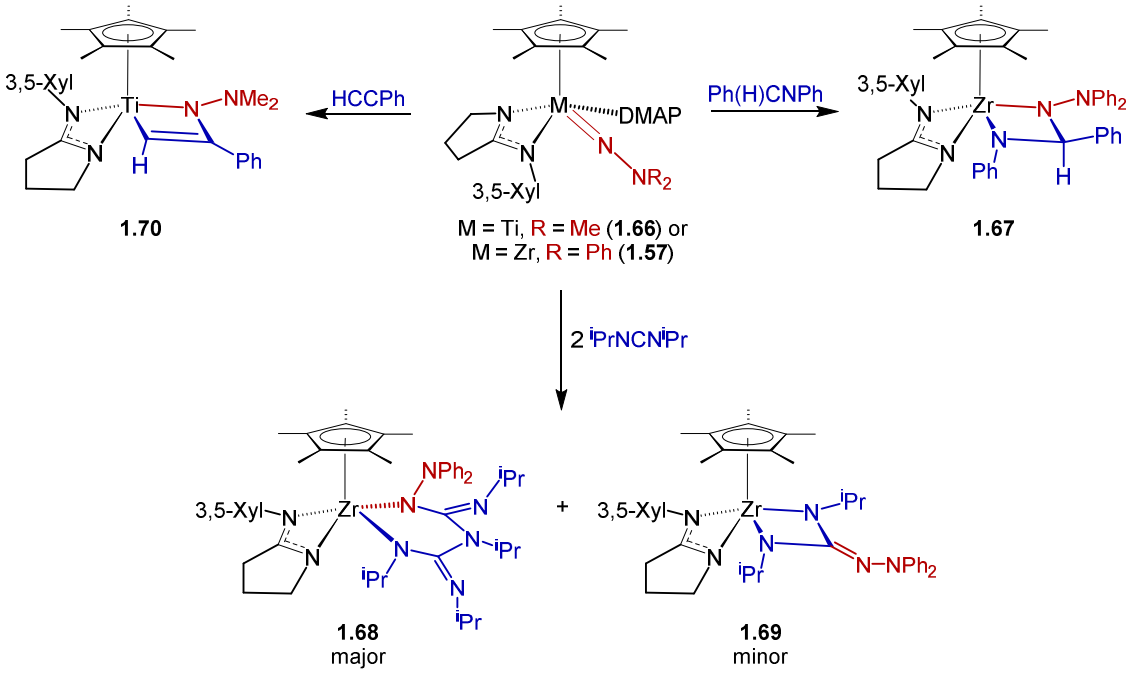
Scheme 1.9: Reactions of $Cp^*Ti\{MeC(N^iPr)_2\}(NNR_2)$ (R = Me (**1.45**) or Ph (**1.46**)) with unsaturated substrates.[125]

Dimethylhydrazide **1.45** with ^{t}BuNCO or Ar'NCO gave the oxo-bridged dimer $[Cp^*Ti\{MeC(N^iPr)_2\}(\mu\text{-}O)]_2$ (**1.62**) and ^{t}BuNCNNMe$_2$ (**1.63**) or cyclic

$N(Me)_2NC(NAr')N(Ar')C(O)$ (**1.64**), respectively, as the result of elimination from inherently unstable cycloaddition products of the type **1.61**.[125] Reaction of TolNCO with **1.45** initially followed the same reaction pathway. After elimination of $TolNCNNMe_2$, however, dimerisation of the titanium-oxo monomer did not occur, but rather cycloaddition with $TolNCNNMe_2$ to form $Cp^*Ti\{MeC(N^iPr)_2\}\{N(Tol)C(NNMe_2)O\}$ (not observed), which then underwent reaction with a second equivalent of TolNCO across the Ti–N bond to give the observed product $Cp^*Ti\{MeC(N^iPr)_2\}\{OC(NNMe_2)N(Tol)N(NTol)O\}$ (**1.65**). Notably, compounds **1.45** and **1.46** did not react with alkynes.

Gade and co-workers also presented interesting reactivity with the cyclopentadienyl-amidinate supported hydrazides $Cp^*M(N^{3,5\text{-}Xyl}N^{pyr})(NNR_2)(DMAP)$ (M = Ti, R = Me (**1.66**) or M = Zr, R = Ph (**1.57**), Scheme 1.10).[19,134] **1.57** was found to react with imine Ph(H)CNPh to give the [2+2] cycloaddition product **1.67** and with carbodiimide $^iPrNCN^iPr$ to give a mixture of products. The major product, **1.68**, is the result of initial [2+2] cycloaddition, followed by an insertion even at the Zr–N(^{i}Pr) bond. The minor product, **1.69**, is the result of initial [2+2] cycloaddition with subsequent elimination and re-cycloaddition of $^iPrNCNNPh_2$, akin to what occurred on route to **1.65**. While compounds **1.45** and **1.46** did not react with alkynes, compound **1.66** reacted with HCCPh to give $Cp^*Ti(N^{3,5\text{-}Xyl}N^{pyr})\{N(NMe_2)C(Ph)C(H)\}$ (**1.70**).[19,125] Here, the Markonikov regioisomer, with the C(H) carbon bound to the metal centre, is isolated due to steric preference, despite being calculated to be electronically unfavourable over the anti-Markovnikov regioisomer (C(Ph) bound to titanium). In contrast, $Ti(N_2N^{py})(NNPh_2)(py)$ (**1.48**) has been found to react with terminal alkyne $HCCC_6F_5$ and internal alkyne MeCCPh, by [2+2] cycloaddition, to give azametallacyclic compounds

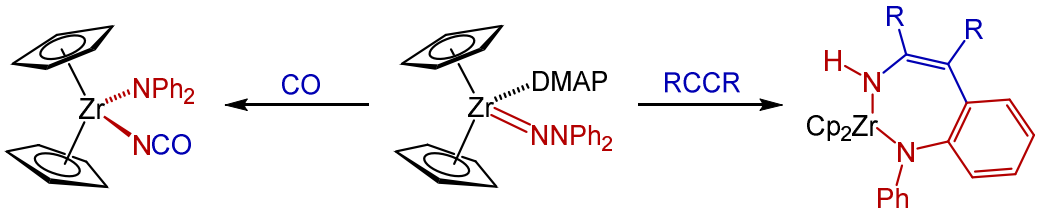
$Ti(N_2N^{py})\{N(NPh_2)C(H)C(C_6F_5)\}$ and $Ti(N_2N^{py})\{N(NPh_2)C(Me)C(Ph)\}$, respectively, with anti-Markovnikov regiochemistry.[142]



Scheme 1.10: Reactions of $Cp^*Zr(N^{3,5\text{-}Xyl}N^{pyr})(NNPh_2)(DMAP)$ (**1.57**) with Ph(H)CNPh and $^{i}PrNCN^{i}Pr$, and $Cp^*Ti(N^{3,5\text{-}Xyl}N^{pyr})(NNMe_2)(DMAP)$ (**1.66**) with HCCPh.[19,134]

1.3.5 Stoichiometric reactions with unsaturated substrates involving the N_α–N_β bond

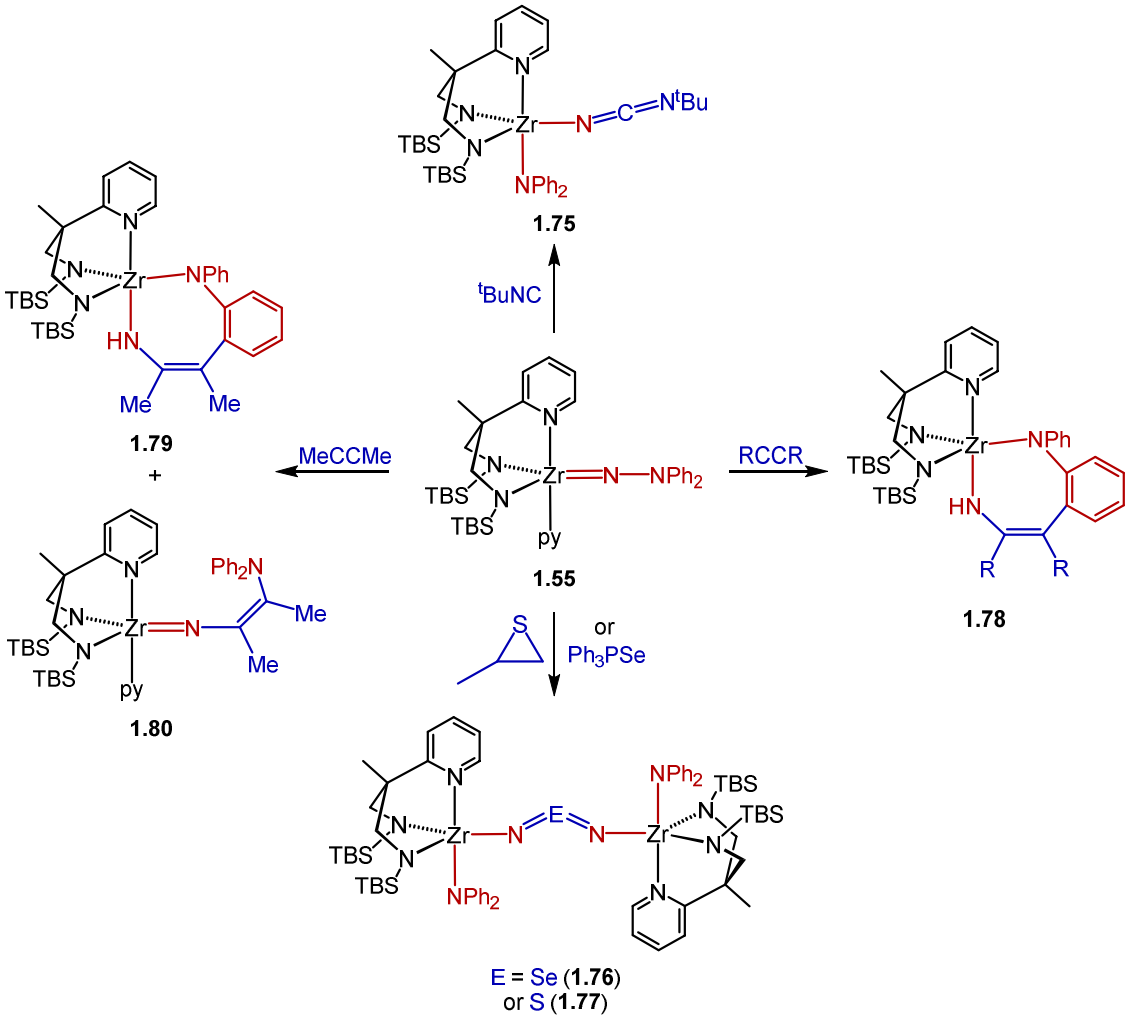
In addition to rich chemistry at the M=N_α bond, the hydrazide ligand sets itself apart from the imido ligand and other imido-derivatives by exhibiting reductive cleavage of the N_α–N_β bond by oxidisable substrates, the majority of which have been unsaturated. The first example of this reactivity was reported in 1991 by Bergman and co-workers with the zirconocene hydrazide $Cp_2Zr(NNPh_2)(DMAP)$ (**1.54**, Scheme 1.11).[127] **1.54** reacted with CO to give the amide-isocyanate $Cp_2Zr(NCO)(NPh_2)$ (**1.71**). While the product could not be isolated from the reaction mixture, independent synthesis and structural characterisation of **1.71** confirmed its assignment. Analogous reaction with CO was exhibited recently by the titanocene hydrazide $(Cp^{Ad})_2Ti(NNPh_2)(py)$ (**1.52**).[131]



1.71 **1.54** R = Et (**1.72**); Ph (**1.73**); Tol (**1.74**)

Scheme 1.11: Reductive N_α–N_β cleavage reactions of $Cp_2Zr(NNPh_2)(DMAP)$ (1.54).[127,139]

This reaction has been mimicked multiple times since, with isolobal isocyanides. In 2007, Gade and co-workers reported the reductive N_α–N_β bond cleavage of the diamide-donor-supported hydrazide $Zr(N_2^{TBS}N^{py})(NNPh_2)(py)$ (**1.55**) by ^{t}BuNC to form $Zr(N_2^{TBS}N^{py})(NPh_2)(NCN^tBu)$ (**1.75**, Scheme 1.12).[132] The titanium complexes $Ti(N_2N^{py})(NNPh_2)(py)$ (**1.48**) and $Ti(N_2N^{Me})(NNPh_2)(py)$ (**1.49**, N_2N^{Me} = $MeN\{(CH_2)_2NSiMe_3\}_2$) both reacted with XylNC in an identical manner.[143] DFT calculations showed the reaction to proceed initially *via* pyridine dissociation and formation of an isocyanide adduct, prior to formation of a three membered Ti–N_α–C ring containing intermediate which is stabilised somewhat by coordination of N_β to Ti. Ti–C and N_α–N_β bond cleavage, to give the final product, then proceeds in a facile manner. $Ti(N_2^{SiMe_3}O)(NNPh_2)(py)_2$ reacted with ^{t}BuNC to give N_α–N_β cleavage product, but could also react with a second equivalent of isocyanide, undergoing insertion into one of the ligand N–$SiMe_3$ bonds.[144] As shown in Scheme 1.12, compound **1.55** also undergoes N_α–N_β bond cleavage when reacted with Ph_3PSe and propylene sulphide, forming the dimeric compounds $\{Zr(N_2^{TBS}N^{py})(NPh_2)\}_2(\mu\text{-}N_2E)$ (E = Se (**1.76**) or S (**1.77**)).[132]



Scheme 1.12: N_α–N_β bond cleavage reactions of $Zr(N_2^{TBS}N^{py})(NNPh_2)(py)$ (**1.55**).[132,137]

The reactions of hydrazido complexes with alkynes can also lead to reductive N_α–N_β bond cleavage, as shown in Schemes 1.11 and 1.12. The zirconocene hydrazide **1.54** reacts with internal alkynes to give the seven-membered zirconacycle-containing complexes **1.72** – **1.74**.[127] Kinetic and computational experiments showed these reactions proceed *via* cycloaddition of the alkyne, followed by N_α–N_β bond cleavage and subsequently C–H bond activation.[139] Analogous reactivity was showcased by $Zr(N_2^{TBS}N^{py})(NNPh_2)(py)$ (**1.55**) for multiple internal alkynes (**1.78**, Scheme 1.12).[137] Exceptionally, in the case of MeCCMe an almost 1:1 mixture of two products was observed: the seven-membered zirconacycle-containing complex **1.80**, analogous to other alkyne reaction products, and the vinylimido complex $Zr(N_2^{TBS}N^{py})\{NC(Me)=C(Me)NPh_2\}(py)$. Reaction of

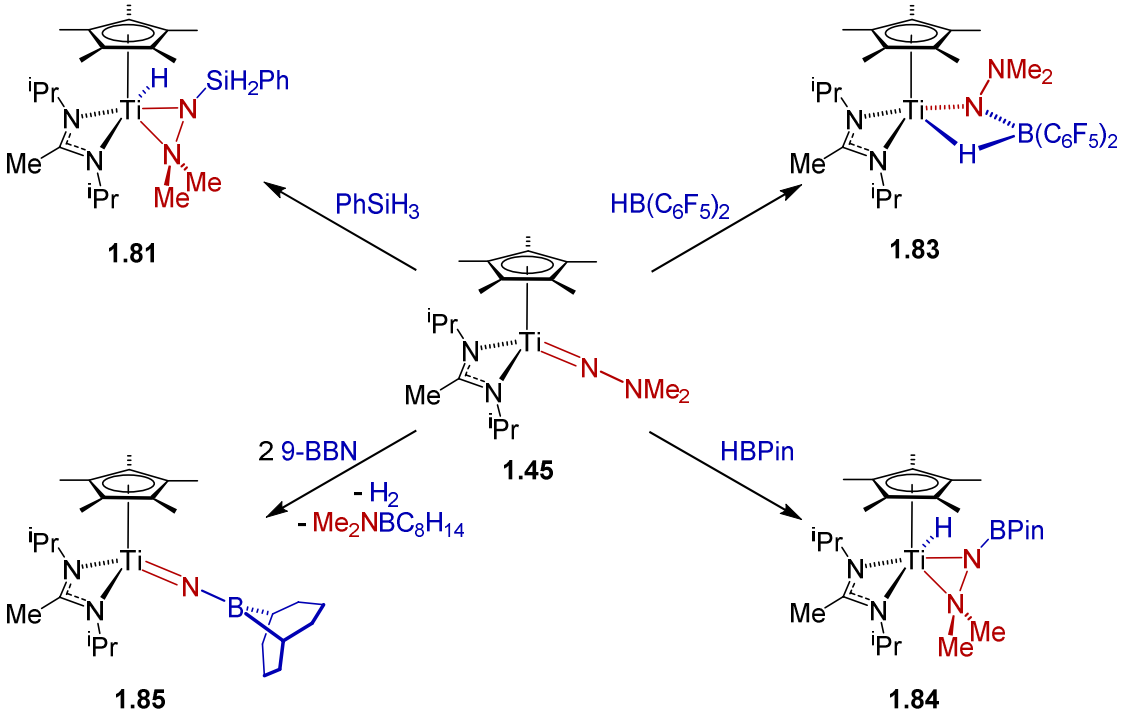
$Ti(N_2N^{Me})(NNPh_2)(py)$ (**1.49**) with several internal alkynes gave quantitative conversion to vinylimido compounds of the type $Ti(N_2N^{Me})\{NC(R)=C(Me)NPh_2\}(py)$ (R = alkyl or aryl), and mixtures of the vinylimido and metallacyle products for reactions with PhCCMe and 4-$MeOC_6H_4CCMe$.[139,142] Analogous vinylimido formation was also observed for the reaction of $Ti(N_2N^{py})(NNPh_2)(py)$ (**1.48**) with PhCCMe.[138] As described in the previous Section, the first formed product is the azametallacyclic complex $Ti(N_2N^{py})\{N(NPh_2)C(Me)C(Ph)\}$, which, after heating to 60 °C for 3 hours, gave the vinylimido complex $Ti(N_2N^{py})\{NC(Ph)=C(Me)NPh_2\}(py)$.

1.3.6 Reactions of with boranes and silanes

The reactions of Group 4 hydrazides, concerning both the $M=N_\alpha$ and $N_\alpha–N_\beta$ bonds, have been predominantly conducted with unsaturated substrates, as discussed in Sections 1.3.4 and 1.3.5, and have been the subject of interest for the past *ca.* 30 years. In contrast, E–H bond activation reactions (E = B and Si) have only recently begun to be investigated, showing rich and diverse reaction outcomes.[30,32,33,131] It is notable, however, that these E–H bond reactions with Group 4 hydrazides are more well developed than those of their imido counterparts.[33]

In 2011, Mountford and co-workers reported the formation of the titanium hydride silylhydrazide(1–) $Cp^*Ti(MeC(N^iPr)_2\}(H)\{N(NMe_2)SiH_2Ph\}$ (**1.81**) by 1,2-addition of the Si–H bond of $PhSiH_3$ across the $Ti=N_\alpha$ bond of $Cp^*Ti(MeC(N^iPr)_2\}(NNMe_2)$ (**1.45**, Scheme 1.13).[30] This addition was found to be reversible under vacuum, in contrast to the 1,2-addition of the Si–Cl bond of $PhSiH_2Cl$ to form $Cp^*Ti(MeC(N^iPr)_2\}(Cl)\{N(NMe_2)SiH_2Ph\}$ (**1.82**), which was irreversible. Further reactivity of these compounds with deuterium labelled silanes confirmed the reversibility of Si–H addition, as well as σ-bond metathesis between Si–H/D and Ti–H/D bonds. Much

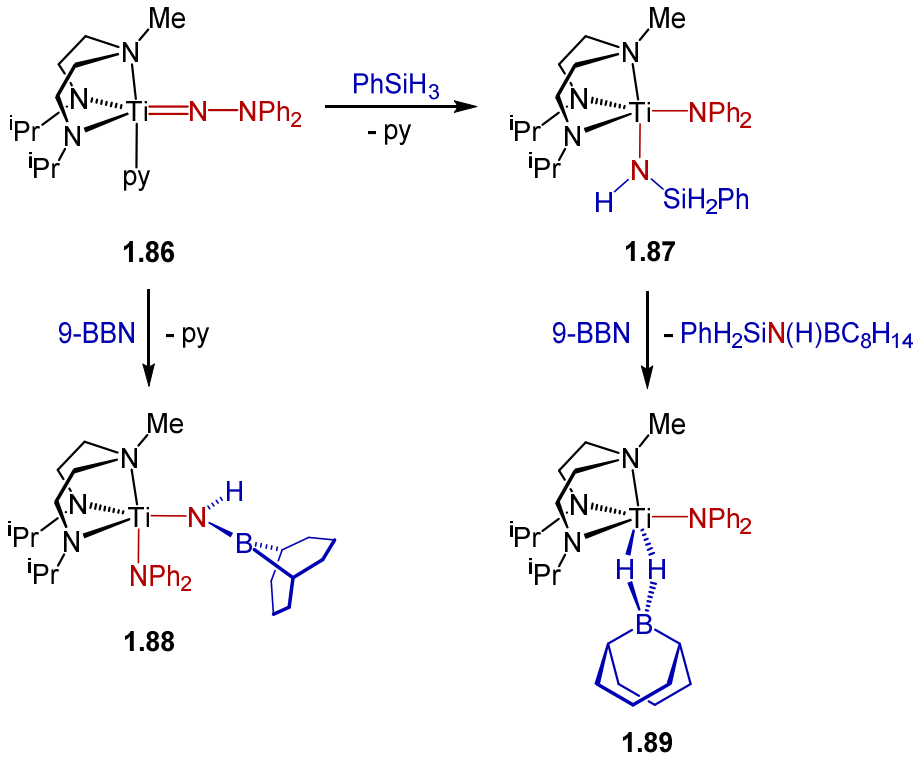
earlier, in 1998, the titanocene alkylidene hydrazide Cp*$_2$Ti(η^2-NNCHTol) underwent a similar 1,2-addition of $PhSiH_3$ and Ph_2SiH_2 to form alkylidene hydrazide(1–) hydrides.[145]



Scheme 1.13: Reactions of Cp*Ti{MeC(N^{i}Pr)$_2$}(NNMe$_2$) (**1.45**) with silanes and boranes.[30,33]

In 2015, the diamide-amine-supported hydrazido complex Ti(N$_2$^{iPr}N^{Me})(NNPh$_2$)(py) (**1.86**) was reported to undergo reductive N$_\alpha$–N$_\beta$ bond cleavage when reacted with silanes giving silylamide amide complexes of the type **1.87** (Scheme 1.14).[32] Kinetic and computational studies showed the reactions proceeded *via* pyridine dissociation and 1,2-addition to give a titanium hydride analogous to **1.81**, followed by migration of the hydride to the N$_\alpha$ atom with N$_\alpha$–N$_\beta$ bond cleavage. The boranes 9-BBN ([μ-H)BC$_8$H$_{14}$]$_2$) and HBMes$_2$ (Mes = 2,4,6-C$_6$H$_2$Me$_3$) exhibit identical reactivity to that of silanes with **1.86** forming borylamide amide complexes Ti(N$_2$^{iPr}N^{Me}){N(H)BC$_8$H$_{14}$}(NPh$_2$) (**1.88**) and Ti(N$_2$^{iPr}N^{Me}){N(H)BMes}(NPh$_2$), respectively. These reductive N$_\alpha$–N$_\beta$ bond cleavage reactions were the first of their kind for silane and borane addition to any hydrazido compound. Compound **1.87** was able to react with further silane equivalents to give exchange products and with 9-BBN to give Ti(N$_2$^{iPr}N^{Me}){(μ-H)$_2$BC$_8$H$_{14}$}(NPh$_2$) (**1.89**),

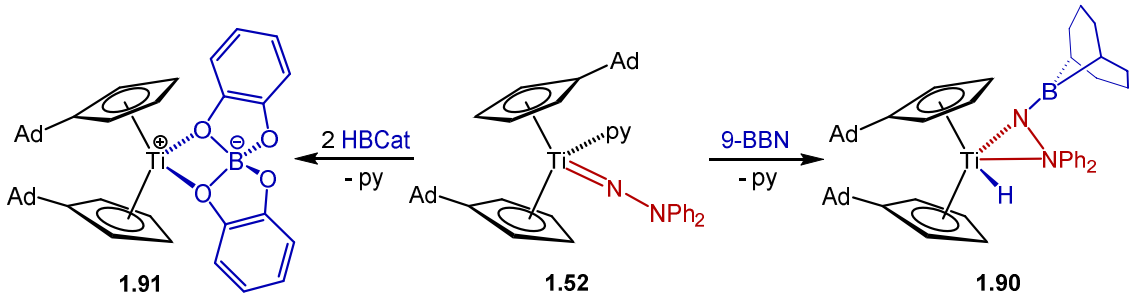
as well as the silylaminoborane $PhH_2SiN(H)BC_8H_{14}$, *via* the hydride $Ti(N_2^{iPr}N^{Me})(H)(NPh_2)$ (Scheme 1.14).



Scheme 1.14: Reactions of $Ti(N_2^{iPr}N^{Me})(NNPh_2)(py)$ (**1.86**) with silanes and boranes.[32]

$Cp^*Ti(MeC(N^iPr)_2\}(NNMe_2)$ (**1.45**) exhibited a range of reactivity with secondary boranes (Scheme 1.13).[33] Reaction with $HB(C_6F_5)_2$ gave the hydride-bridged adduct $Cp^*Ti\{MeC(N^iPr)_2\}\{N(NMe_2)B(C_6F_5)_2(\mu\text{-}H)\}$ (**1.83**), analogous to the reactions of $Cp^*Ti\{MeC(N^iPr)_2\}(NTol)$ (**1.34**) with secondary boranes. With HBPin, 1,2-addition and B–H bond cleavage was observed, yielding the hydride borylhydrazido(1–) complex $Cp^*Ti(MeC(N^iPr)_2\}(H)\{N(NMe_2)BPin\}$ (**1.84**), analogous to the reaction of **1.45** with $PhSiH_3$. Addition of 1 equivalent 9-BBN dimer to **1.45** gave the borylimide **1.85**, dihydrogen and the aminoborane $Me_2NBC_8H_{14}$. Despite kinetic and computational studies, the full mechanism for the formation of this borylimide could not be established, though 1,2-addition and reductive N_α–N_β bond cleavage are thought to occur.

Identical reactivity to that of **1.45** with HBPin was reported by Beckhaus and co-workers for the reaction of $(Cp^{Ad})_2Ti(NNPh_2)(py)$ (**1.52**) and 9-BBN, which resulted in the formation of the hydride borylhydrazido(1–) complex $(Cp^{Ad})_2Ti(H)\{N(NPh_2)BC_8H_{14}\}$ (**1.90**) by 1,2-addition of the B–H bond across the Ti=N_α bond (Scheme 1.15).[131] No N_α–N_β bond cleavage was observed and the reported connectivity of **1.90** places N_β in the central coordination site of the titanocene, which assumedly forms by isomerisation of a first-formed product that contains the N_α in the central coordination site. Terminal titanium(IV) hydrides are relatively uncommon and here the large adamantyl moieties provide steric protection for the hydride. Additionally, **1.52** was reacted with two equivalents catechol borane (HBCat, Cat = 1,2-$O_2C_6H_4$) to quantitatively form a highly unstable titanium(III) species $[(Cp^{Ad})_2Ti^{III}][(O_2C_6H_4)_2B]$ (**1.91**).

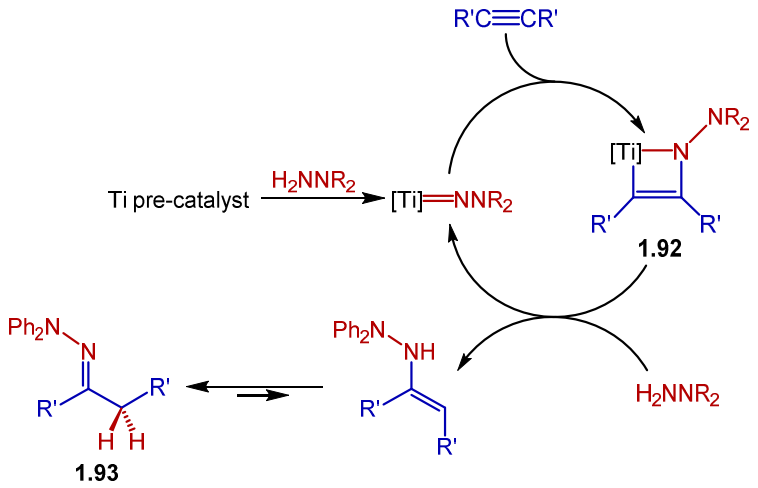


Scheme 1.15: Reactions of $(Cp^{Ad})_2Ti(NNPh_2)(py)$ (**1.52**) with boranes.[131]

1.3.7 Catalytic reactions

The use of Group 4 imido complexes as hydroamination catalysts was described in Section 1.2.5. Accordingly, Group 4 hydrazido complexes have received much attention as hydrohydrazination catalysts, with several systems reported.[16–19,24,109,110] Hydrohydrazination is a direct extension of hydroamination: here, the N–H bonds of an N,N-disubstituted hydrazine, such as H_2NNPh_2, add across an alkyne to form a hydrazone. The mechanism of the metal-catalysed hydrohydrazination catalysis reactions discussed below are proposed to proceed initially *via* [2+2] cycloaddition of the alkyne

across the M=N$_\alpha$ bond of the hydrazide catalyst, which may be formed *in situ*,[16–18,109] to form complexes of the type **1.92** followed by double protonolysis by incoming hydrazine, *via* a transient mixed bis(hydrazido(1–)) intermediate, to form hydrazones (**1.93**) and reform the hydrazide catalyst (Scheme 1.16). This is analogous to the "imido route" for hydroamination shown in Scheme 1.7.[117,118]

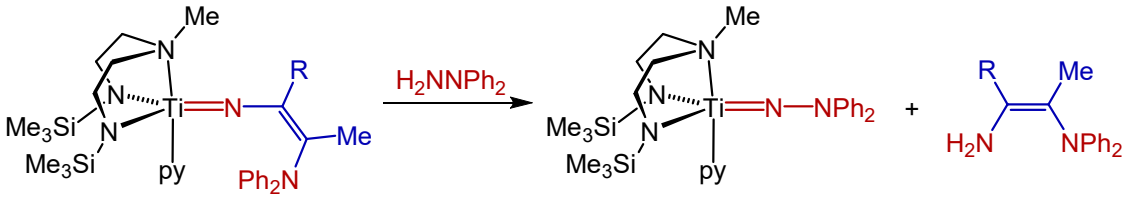


Scheme 1.16: Catalytic cycle for the hydrohydraziination of alkynes using a nominal titanium hydrazido precatalyst.[16–19,24,109,110]

Gade and co-workers reported the compounds Cp*Ti(N$^{3,5\text{-Xyl}}$N^{pyr})(NNRR')(L) (R = R' = Ph or Me, or R = Ph, R' = Me; L = py, DMAP or NH$_2$^{t}Bu) as effective catalysts for hydrohydrazination with a range of alkynes.[19] At 5 mol% loading and room temperature, the reactions were quantitative after just 1 hour, with >99% selectivity for the Markovnikov regioisomer. Most systems require elevated temperatures and long reaction times.[16–18,24,25,109] In some systems, further reaction of the hydrazones to form other organics, such as indoles, has been reported.[17,24,25,109,110] This proceeds *via* a cyclisation reaction that usually requires addition of an external Lewis acid, such as $ZnCl_2$. Bergman and co-workers first showed stoichiometric indole synthesis in this manner by addition of acid to the seven-membered zirconacycle containing complexes **1.72** – **1.74**.[127]

Iminohydrazination, the coupling of an alkyne, hydrazine and organic isocyanide in a single reaction to form a 1,3-iminohydrazone, has also been developed by Odom and co-workers using pre-catalysts $Ti(NMe_2)_2(dap)_2$ (dap = 2-(*N*,*N*-dimethylaminomethyl)pyrrolyl) and $Ti(NMe_2)_3(bap)$ (bap = bis-2,5-(*N*,*N*-dimethylaminomethyl)pyrrolyl).[27,146] Here, the isocyanide inserts into the Zr–C bond of the four-membered metallacyle intermediate (**1.92**) prior to double protonolysis. Furthermore, the coupling of alkynes, monosubstituted hydrazines and isonitriles to form pyrazoles has been achieved by the same research group, using the pre-catalyst $Ti(NMe_2)_2(pypyr)_2$ (pypyr = 2-(2'-pyridyl)-3,5-dimethylpyrrolyl).[147]

The formation of vinylimido complexes, such as **1.80** (Scheme 1.12) or **1.94**, from the reaction of hydrazides such as $Zr(N_2{}^{TBS}N^{py})(NNPh_2)(py)$ (**1.55**) or $Ti(N_2N^{Me})(NNPh_2)(py)$ (**1.49**), respectively, and internal alkynes through net insertion into the N_α–N_β bond was described in Section 1.3.5.[137,142] Addition of H_2NNPh_2 to complexes of the type **1.94** was found to generate **1.49** and the 1,2-diamination products $H_2NC(R)C(Me)NPh_2$ (**1.95**, R = alkyl or aryl, Equation 1.2).[105,129,139,142] This stoichiometric reaction was able to be performed catalytically using either **1.49** or **1.94**. Notably, it was shown that use of $Ti(N_2{}^{iPr}N^{Me})(NNPh_2)(py)$ (**1.86**), with less sterically encumbering ^{i}Pr groups in place of $SiMe_3$ groups on the N_{amide} atoms of the ancillary ligand, led to hydrohydrazination catalysis rather than 1,2-diamination.[148]



1.94 **1.49** **1.95**

Equation 1.2[142]

1.4 β-Agostic silylamido complexes

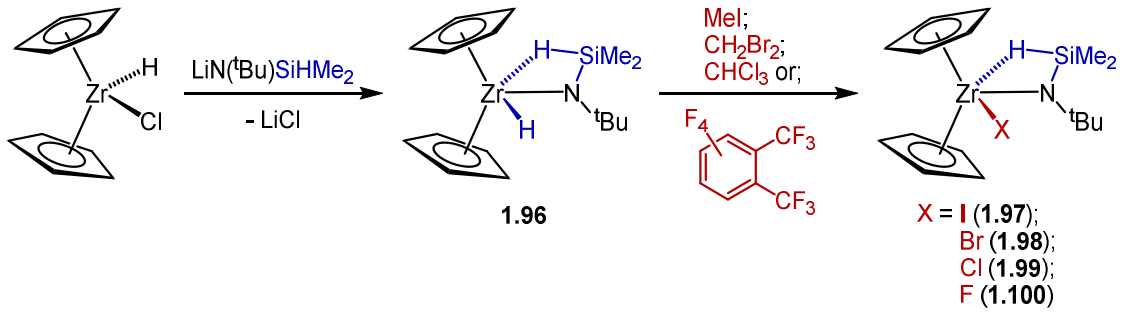
Additional to organometallic imido and hydrazido chemistry, another class of chemistry of relevance to the work presented in this Thesis is that of organometallic silylamide compounds. The silylamide ligand is widely used in organometallic chemistry with substitution at both the silyl and amide positions rendering silylamides sterically and electronically tuneable. While often acting as spectator ligands, a particular subset of silylamide ligands – those containing β-Si–H···M agostic interactions – have exhibited interesting reaction chemistry and are the focus of this Section. Particular attention will be paid to zirconocene-based systems and isolobal Group 5 and 6 analogues.

1.4.1 Synthesis and structure

β-Agostic silylamide complexes are known for a host of transition, rare earth and alkaline earth metals and are predominantly synthesised by salt metathesis or ligand exchange reactions. Examples discussed here are those that have exhibited notable reactivity (see Section 1.5.2) or highlight notable structural features of β-agostic interactions and the effects ancillary ligands have on these.

1.4.1.1 Group 4 β-agostic silylamido complexes

The first β-agostic silylamide was a zirconocene hydride silylamide complex synthesised in 1991 by Berry and co-workers.[34] Stoichiometric reaction of $LiN(^tBu)SiHMe_2$ with Schwarz's reagent ($[Cp_2ZrHCl]_n$) gave $Cp_2Zr(H)\{N(^tBu)Si(\mu\text{-}H)Me_2\}$ (**1.96**) in an 86% isolated yield on a multi-gram scale (Scheme 1.17). Further to this, reaction of **1.96** with iodoform, dibromomethane, chloroform or perfluoro-*o*-xylene afforded the halide analogues $Cp_2Zr(X)\{N(^tBu)Si(\mu\text{-}H)Me_2\}$ (X = I (**1.97**), Br (**1.98**), Cl (**1.99**) or F (**1.100**)).[35]



Scheme 1.17: Synthesis of $Cp_2Zr(H)\{N(^tBu)Si(\mu\text{-}H)Me_2\}$ (**1.96**) and the halide analogues $Cp_2Zr(X)\{N(^tBu)Si(\mu\text{-}H)Me_2\}$ (X = I (**1.97**), Br (**1.98**), Cl (**1.99**) or F (**1.100**)).[34,35]

As can be seen from the connectives of complexes **1.96** – **1.100** (Scheme 1.17) the structural motif and bonding of the complexes facilitates the formation of the β-agostic interactions. In the absence of the β-agostic interaction the zirconium centre contains 16 VE and a vacant bonding orbital lying in the plane of the Cp_2Zr bent metallocene.[149] Given the placement of this site of Lewis acidity on the metal centre, it is geometrically accessible to the Si–H bond – a key prerequisite to the formation of agostic interactions.[150,151] Furthermore, formation of the agostic interaction gives the zirconium centre a valence electron count of 18, and the negative hyperconjugation, which the M–N σ-bond undergoes into the σ* orbital of the Si–H bond, lowers the energy of the M–N bond. While the negative hyperconjugation is somewhat stifled by the π-character of the M–N bond, the competition for π-donation by the Cp ligands reduces this effect, further facilitating agostic interaction.[151] These factors more than offset any increase in free energy associated with the now restricted rotation of the system and so the agostic interaction is formed.

Notably, Berry and co-workers reported several spectroscopically and structurally identifying features of the β-Si–H···Zr interaction of **1.96**, which have been echoed by all other β-agostic silylamides.[34,35] These not only gave insight into the nature of the agostic interaction, but also allowed comparisons with related agostic β-C–H···M

interactions of amides and alkyls. The ^{1}H NMR shifts of the SiH proton (1.21 ppm) was seen to be dramatically shifted upfield, with respect to the free silylamine (4.83 ppm), as was the ^{29}Si shift. In addition, the $^{1}J_{SiH}$ coupling constant was found to be greatly reduced in the agostic complex. For a terminal Si–H bond $^{1}J_{SiH}$ would be expected to be ~200 Hz, but is reduced to 113 Hz in **1.96**. This was noted to correlate to a weakening of the Si–H bond, and a similar phenomenon has been observed for β-C–H···M interactions.[152]

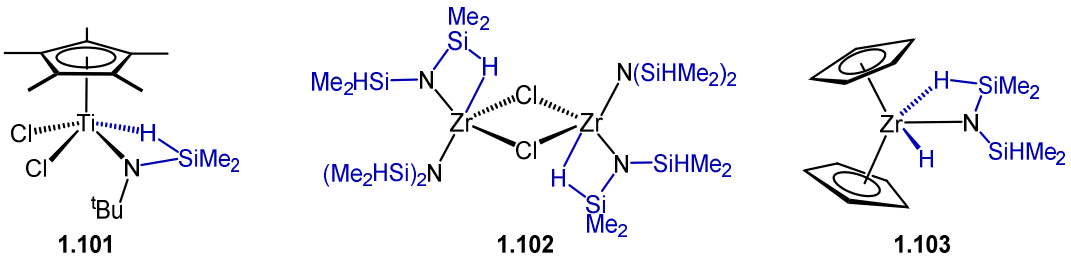
The IR stretch of the Si–H bond also showed weakening, with the stretching frequency reduced from an expected value between 2080 and 2280 cm^{-1} to 1912 cm^{-1}.[153] In the solid state structure, the Zr–N–Si angle was found to be just 95.1(2)° (*cf.* ~120° in a non-agostic silylamide with a planar nitrogen) indicating bending of the silicon towards the zirconium centre, with a short Zr–Si distance of 2.857(2) Å. Furthermore, the Zr, N, Si and idealised zirconium–hydrogen and silicon–hydrogen atoms lie in the plane of the zirconocene. The small M–N–Si angle here, and in other β-agostic silylamide ligands, falls in-between the acute values found for the analogous M–C_{α}–C_{β} angles of β-agostic alkyl ligands and the larger (typically >100°) M–N–C angles of β-agostic amide ligands.[151] The SiH hydrogen was idealised and so no conclusions were drawn on the effect on the length of the Si–H bond. However, it has subsequently been found that the Si–H bond distance experiences a minor or negligible increase on interaction with a metal centre.[37,49,50,154–159]

Using the halide series **1.96** – **1.100**, Berry and co-workers noted these spectroscopic and structural features to correlate to the strength of the agostic interaction.[35] The strength of the agostic interaction followed the trend H>I>Br>Cl>F, rationalised by π-donation of the halide competing with the agostic interaction for donation into the vacant metal orbital. The greater this π-donation the weaker the agostic interaction, which was manifested in a higher stretching frequency of the Si–H bond, a larger M–N–Si angle, a more downfield shifted SiH proton resonance and a larger $^{1}J_{SiH}$ coupling constant.

Okazaki and Ebina synthesised the β-agostic titanium silylamide $Cp^*Ti(Cl)_2\{N(^tBu)Si(\mu\text{-}H)Me_2\}$ (**1.101**, Figure 1.7), featuring the same silylamide ligand as in **1.96** – **1.100**, by salt metathesis of $LiN(^tBu)SiHMe_2$ with Cp^*TiCl_3.[154] The chemical shift of the SiH proton of **1.101** appeared at a resonance of 4.63 ppm, with a $^1J_{SiH}$ coupling constant of 142 Hz, indicating a weak agostic interaction. Indeed, the proton resonances of the methyl groups of the $SiMe_2H$ moiety appeared as a single resonance at room temperature and only decoalesced at 223 K, implying lability of the weak agostic interaction on the NMR timescale at room temperature. The solid state structure showed a Ti–H distance of 2.1370(2) Å and a Ti–N–Si angle of 97.65(5)°, consistent with an agostic interaction. Notably, the chloride ligands here are not thought to have such a weakening effect on the agostic interaction as the complex contains only 14 valence electrons.[40]

Analogous to aforementioned syntheses, in 1992 Herrmann and co-workers synthesised the dimeric zirconium complex $[\{(Me_2HSi)_2N\}Zr\{N(SiHMe_2)Si(\mu\text{-}H)Me_2\}(\mu\text{-}Cl)Cl]_2$ (**1.102**, Figure 1.7) by salt metathesis reaction of $LiN(SiHMe_2)_2$ with zirconium tetrachloride.[153] This complex contained only one agostic interaction per zirconium centre, as judged by IR spectroscopy and X-ray crystallography. Subsequently, the bis(dimethylsilyl)amide ligand has been utilised in a variety of systems, often exhibiting β-agostic interactions. Sadow and co-workers reported the synthesis of the zirconocene hydride bis(dimethylsilyl)amide complex $Cp_2Zr(H)\{N(SiHMe_2)Si(\mu\text{-}H)Me_2\}$ (**1.103**, Figure 1.7) by reaction of Schwarz's reagent with $LiN(SiHMe_2)_2$.[46,47] IR spectroscopy showed two bands for Si–H bond stretches at 1907 and 2047 cm^{-1}, indicating one agostic and one non-agostic SiH moiety. This was echoed in the solid state structure, which exhibited Zr–N–Si angles of 101.60(9) and 130.51(10)° and Zr–Si distances of 2.98 and 3.50 Å. Notably, the N–Si distance was found to be longer for that of the agostic silicon

(1.68(3) vs. 1.710(2) Å), an equivalent phenomenon is observed for β-agostic alkyl ligands and has been related to their reactivity (*vide infra*). In solution, ^{1}H NMR spectroscopy showed the two SiH protons to be equivalent with a time-averaged resonance appearing at 3.78 ppm, with a $^{1}J_{SiH}$ coupling constant of 161 Hz. The resonances could be decoalesced at low temperatures showing parameters typical of agostic and non-agostic SiH moieties. Other β-agostic zirconocene bis(dimethylsilyl)amide complexes have been reported by the same group.[45–48]

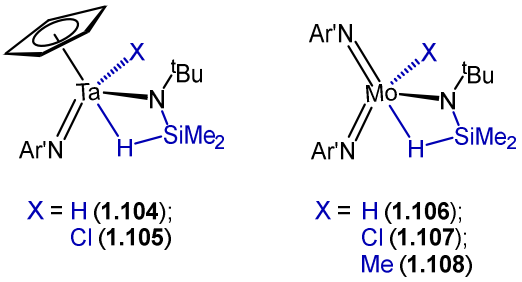


1.101 **1.102** **1.103**

Figure 1.7: Selected examples of Group 4 β-agostic silylamide complexes.[46,47,153,154]

1.4.1.2 Group 5 and 6 β-agostic silylamido complexes

Nikonov and co-workers have published a series of reports based on the synthesis and reactivity of Group 5 and 6 β-agostic silylamido complexes.[37,38,40–42,49,50,160] In 2016, the group prepared a series of Ta and Mo d^0 complexes isolobal to Berry's zirconocene complexes **1.96** – **1.100**.[40] Salt metathesis reactions afforded the tantalum complexes Cp(Ar'N)Ta(X){N(^{t}Bu)Si(μ-H)Me$_2$} (Ar' = 2,6-diisopropylphenyl, X = H (**1.104**) and Cl (**1.105**)). Here, the imido ligand acts as an isolobal analogue of Cp when considered as a 6 electron donor. As with Berry's hydride and chloride compounds, the chloride **1.105** was observed to have a weaker agostic interaction than in **1.104**.



X = H (**1.104**); Cl (**1.105**)

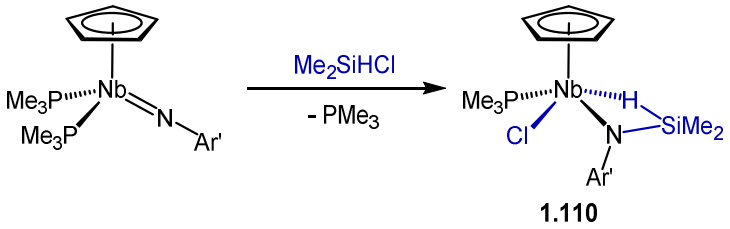
X = H (**1.106**); Cl (**1.107**); Me (**1.108**)

Figure 1.8: Tantalum and molybdenum β-agostic silylamide complexes isolobal with $Cp_2Zr(H)\{N(^tBu)Si(\mu\text{-}H)Me_2\}$ (**1.96**).[40]

Similarly, the molybdenum silylamide hydride, chloride and methyl complexes $(Ar'N)_2Mo(X)\{N(^tBu)Si(\mu\text{-}H)Me_2\}$ (X = H (**1.106**), Cl (**1.107**) and Me (**1.108**)) were synthesised by salt metathesis. The alkoxide complex $(Ar'N)_2Mo(OBn)\{N(^tBu)SiHMe_2\}$ (**1.109**) was further synthesised by addition of benzaldehyde to **1.106**. Analysis of the molybdenum series showed the hydride **1.106** to contain the strongest agostic interaction, with chloride **1.107** and methyl **1.108** containing weak agostic interactions of similar strength. For **1.107** this is expected due to competitive π-donation of the chloride. For **1.108**, the weaker agostic interaction with respect to **1.106** was attributed to the sterics of the methyl ligand. Though not structurally characterised, NMR spectroscopy indicated the alkoxide **1.109** contained no agostic interaction, with a $^1J_{SiH}$ coupling constant of 198 Hz (*cf.* 125 Hz in **1.106**). This was attributed to the π-donor characteristics and sterics of the OBn ligand.

Prior to these complexes containing metal centres with d^0 configurations, Nikonov and co-workers synthesised several Groups 5 and 6 β-agostic silylamide complexes with the metal centre in the d^2 configuration.[37,38,41,42,49,50,160,161] This change in electron configuration was found to impact the agostic interaction greatly. For example, the niobium silylamide $CpNb(Cl)\{N(Ar')Si(\mu\text{-}H)Me_2\}(PMe_3)$ (**1.110**) exhibited a proton resonance at –5.67 ppm attributed to the Si–H–Nb proton (*cf.* 4.13 ppm in **1.106**) and a $^1J_{SiH}$ coupling constant of 97 Hz (*cf.* 125 Hz in **1.106**).[42] The solid state structure of **1.110**

revealed the Nb–N–Si angle to be acute, at 89.1(2)°, similar to in η^2-silanimines, with a short Nb–Si distance of 2.646(1) Å.[34,154] Furthermore, the Nb–H distance was found to be short, at 1.91(5) Å, and the Si–H distance, at 1.52(5) Å, to be elongated, with respect to the free silylamine. These parameters implied a large degree of Si–H bond breaking and Nb–H and Nb–Si bond formation, and is more akin to what is observed for β-agostic alkyl complexes, which are viewed as intermediates towards β-hydrogen elimination.[150,151]



1.110

Equation 1.3[42]

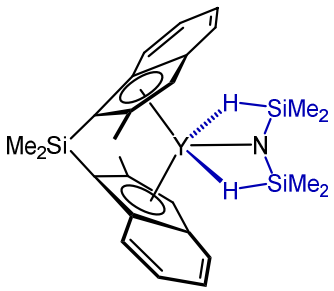
Notably, **1.110** was synthesised by addition of chlorodimethylsilane to the imido compound CpNb(NAr')$(PMe_3)_2$, similar to the addition of silanes to the Group 4 hydrazides discussed in Section 1.3.6, though the reactions were found to proceed *via* a different mechanism (Equation 1.3).[49] Other examples of β-agostic silylamides synthesised by addition of a silane to an imide include the molybdenum complexes (RN)Mo(Cl){N(R)Si(μ-H)Me_2}$(PMe_3)_2$ (**1.111**, R = ^{t}Bu, Xyl, Ar') and (Ar'N)Mo(SiH_2Ph){N(Ar')Si(μ-H)HPh}(PMe_3) (**1.112**)[37,38,41,50] and the tungsten complexes (Ar'N)W(Cl){N(R)Si(μ-H)MeX}$(PMe_3)_2$ (**1.113**, R = Xyl and Ar', X = Cl and Me).[37] The spectroscopic and structural parameters of these systems lie in-between those of **1.110** and more typical β-agostic silylamides.

1.4.1.3 Alkaline and rare earth β-agostic silylamido complexes

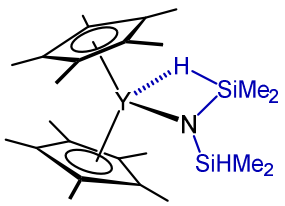
The bis(dimethylsilyl)amide ligand, as an extension of the much used bis(trimethylsilyl)amide ligand, is found repeatedly in Group 2 and 3 and lanthanide

β-agostic silylamide complexes.[155,162–164] Anwander and co-workers and Bubrin and Niemeyer have reported the rare earth bis(dimethylsilyl)amide complexes of the type $M(N(SiMe_3)_2\}_3(THF)_x$ (**1.114**, M = Sc, Y, La, Ce, Pr, Nd, Sm, Er and Lu), synthesised by salt metathesis reactions with the relevant metal trichlorides.[158,165,166] These have proved useful synthons to a host of silylamide complexes bearing β-agostic interactions. Several sterically crowded metallocene and *ansa*-metallocene complexes of the type $(Cp^{R_n})_2M\{N(Si(\mu\text{-}H)Me_2)_2\}$, such as $\{(\eta^5\text{-}C_9H_5\text{-}2\text{-}Me)_2SiMe_2\}Y\{N(Si(\mu\text{-}H)Me_2)_2\}$ (**1.115**, Figure 1.9) and $Cp^*_2Y\{N(SiHMe_2)Si(\mu\text{-}H)Me_2\}$ (**1.116**, Figure 1.9), have been synthesised *via* protonation of two silylamide ligands by cyclopentadienes.[156,157,159]

Notably, the solid state structures of **1.115** and **1.116** revealed the bis(dimethylsilyl)amide ligand of the less crowded *ansa*-metallocene complex, **1.115**, to contain two symmetrical agostic interactions, while that of the more crowded metallocene complex, **1.116**, contained only one agostic Si–H bond. This was judged by the Y–N–Si angles, which were found to be both 103.4(1)° in **1.115** and 99.7(1) and 124.9(1)° in **1.116**, the Si–N–Si angles, 153.3(2) and 134.8(1), respectively, and Y–H distances, 2.54(2) Å in **1.115** and 2.40(3) and 3.37(3) Å in **1.116**. This highlighted the impact of steric factors on the formation of β-agostic interactions. Other silylamide ligands, such as $–N(^tBu)SiHMe_2$, $–N(Ph)SiHMe_2$ and $–N(Ar')SiHMe_2$, have also been utilised in rare earth systems.[164,167,168]



1.115



1.116

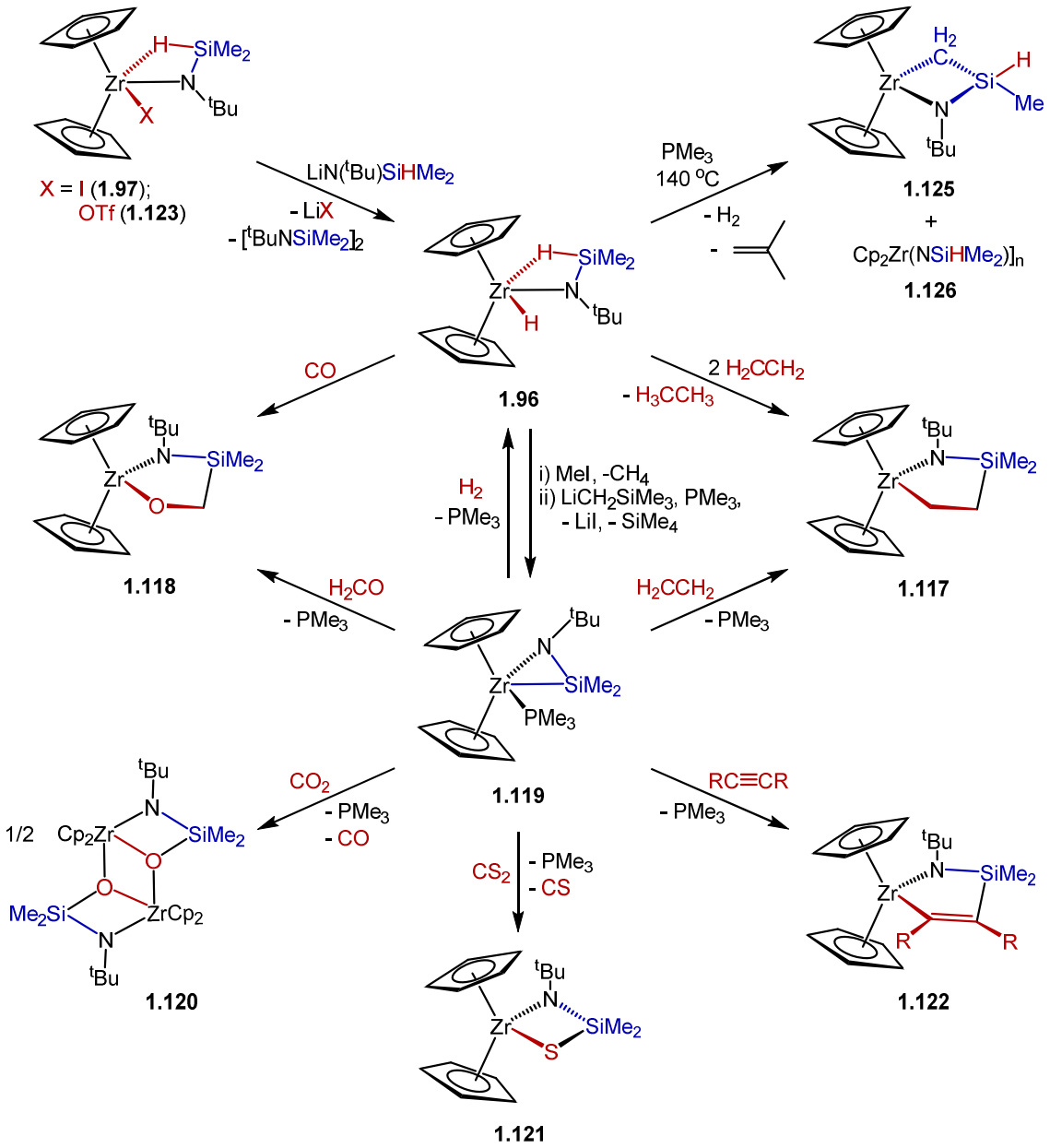
Figure 1.9: Examples of yttrocene β-agostic silylamides containing one or two β-agostic interactions.[156,157,159]

1.4.2 Reactions of β-agostic silylamido complexes

The hallmark of reaction chemistry concerning β-agostic silylamide ligands is the abstraction or, in certain cases, elimination of the β- or γ-hydrogen to form metallacyclic intermediates that can undergo reaction with small, usually unsaturated molecules. To this end, Group 4 systems have shown the most diverse reaction chemistry and Group 6 systems have exhibited reactivity through β-hydrogen abstraction. Sadow and co-workers recently reported the hydrosilylation of acetophenone with the β-agostic yttrium silylamide $Y\{N(Ar')Si(\mu\text{-}H)Me_2\}_3$, but beyond this alkaline and rare earth systems have exhibited very limited reaction chemistry pertaining to their β-agostic silylamide ligands.[167] Notably, the slow or lack of β-hydrogen elimination of the $–N(SiHMe_2)_2$ ligand has been attributed to its utility in these systems.[151,156,157,162,169] Therefore, this Section contains an overview of the reactivity of Group 4 and 6 systems.

1.4.2.1 Group 4 β-agostic silylamido complexes

Berry and co-workers published the first reports on the reactivity of β-agostic silylamide complexes in 1991.[34,43,44] The hydride silylamide $Cp_2Zr(H)\{N(^tBu)Si(\mu\text{-}H)Me_2\}$ (**1.96**) was found to react with ethylene to form the zirconacycle $Cp_2Zr\{N(^tBu)SiMe_2CH_2CH_2\}$ (**1.117**) and ethane (Scheme 1.18). The reaction was proposed to proceed by insertion of ethylene into the Zr–H bond to transiently form $Cp_2Zr(CH_2CH_3)\{N(^tBu)Si(\mu\text{-}H)Me_2\}$, followed by abstraction of the β-hydrogen by the ethyl ligand to form ethane and the transient η^2-silanimine $Cp_2Zr\{\eta^2\text{-}N(^tBu)SiMe_2\}$, with subsequent insertion of a second equivalent of ethylene into the Zr–Si bond. Similarly, compound **1.96** reacted with CO to form the zirconocycle $Cp_2Zr\{N(^tBu)SiMe_2CH_2O\}$ (**1.118**), *via* insertion of CO into the Zr–H bond, followed by β-H abstraction and insertion of the eliminated formaldehyde into the transiently formed Zr–Si bond.



Scheme 1.18: Reactions of the β-agostic zirconocene silylamide complexes $Cp_2Zr(X)\{N(^tBu)Si(\mu\text{-}H)Me_2\}$ (X = H (**1.96**), I (**1.97**) and OTf (**1.123**)) and the η^2-silanimine $Cp_2Zr\{\eta^2\text{-}N(^tBu)SiMe_2\}(PMe_3)$ (**1.119**).[34,43,44,46]

The base-stabilised η^2-silanimine $Cp_2Zr\{\eta^2\text{-}N(^tBu)SiMe_2\}(PMe_3)$ (**1.119**) was able to be synthesised *via* transient formation of the alkyl silylamide $Cp_2Zr(CH_2SiMe_3)\{N(^tBu)Si(\mu\text{-}H)Me_2\}$, which spontaneously underwent β-H abstraction at room temperature, in the presence of PMe_3 (Scheme 1.18). Notably, the η^2-silanimine **1.119** was observed to react with dihydrogen, ethylene and formaldehyde to form **1.96**, **1.117** and **1.118**, respectively. Furthermore, compound **1.119** could react

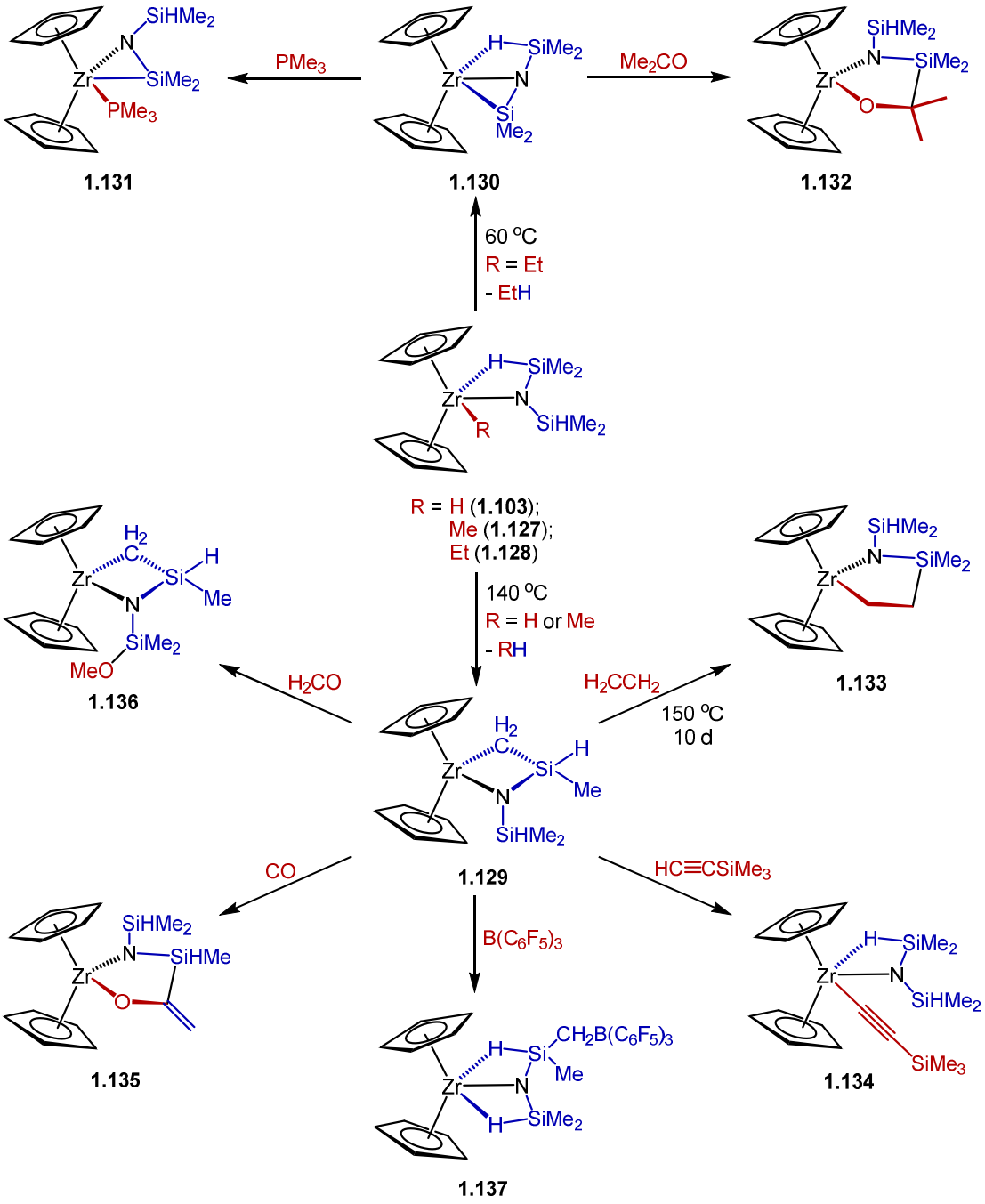
with CO_2, CS_2 and internal alkynes by addition of the unsaturated bonds across the Zr–Si bond. Okazaki and Ebina reported similar β-H abstraction of a titanium silylamide.[154] Upon methylation of Cp*Ti(Cl)$_2${N(^{t}Bu)Si(μ-H)Me$_2$} (**1.101**), in the presence of PMe_3, spontaneous β-H abstraction, to eliminate methane and give the η^2-silanimine Cp*Ti(Cl){η^2-N(^{t}Bu)SiMe$_2$}(PMe_3), occurred.

In 2012, Sadow and co-workers extended the reactivity of Berry's Cp$_2$Zr(X){N(^{t}Bu)Si(μ-H)Me$_2$} system.[46] Remarkably, addition of one equivalent LiN(^{t}Bu)SiHMe$_2$ to either Cp$_2$Zr(I){N(^{t}Bu)Si(μ-H)Me$_2$} (**1.97**) or Cp$_2$Zr(OTf){N(^{t}Bu)Si(μ-H)Me$_2$} (**1.123**) at room temperature yielded the hydride silylamide Cp$_2$Zr(H){N(^{t}Bu)Si(μ-H)Me$_2$} (**1.96**), LiX salt (X = I or OTf) and the dimeric silanimine [^{t}BuNSiMe$_2$]$_2$ (Scheme 1.18). Similarly reaction of two equivalents LiN(^{t}Bu)SiHMe$_2$ with Cp$_2$ZrCl$_2$ or Cp$_2$HfCl$_2$ gave **1.96** or Cp$_2$Hf(H){N(^{t}Bu)Si(μ-H)Me$_2$} (**1.124**), LiCl and [^{t}BuNSiMe$_2$]$_2$ under identical reaction conditions. These reactions proceeded *via* direct β-hydrogen elimination from the transiently formed bis(silylamide) Cp$_2$Zr{N(^{t}Bu)SiHMe$_2$}$_2$. Such β-hydrogen eliminations had not previously been observed for silylamides, are rare for amides and are more commonly associated with β-agostic alkyl species.[151,170–172] Alternatively, addition of the lithiated bis(trimethylsilyl)amide LiN(SiMe$_3$)$_2$, lacking β-hydrogens, to **1.123** in the presence of PMe_3 gave the η^2-silanimine Cp$_2$Zr{η^2-N(^{t}Bu)SiMe$_2$}(PMe_3) (**1.119**), formed by β-hydrogen abstraction by the bis(trimethylsilyl)amide ligand.

In the same report, γ-hydrogen abstraction by the hydride ligand of **1.96** was observed, despite the presence of a β-hydrogen.[46] Heating of a mixture of **1.96** and PMe_3 at 140 °C for 6 hours led to the formation of a mixture of the 4-membered zirconacycle Cp$_2$Zr{N(^{t}Bu)Si(H)(Me)CH$_2$} (**1.125**) and the oligomeric bridged imide [Cp$_2$Zr(NSiHMe$_2$)]$_n$ (**1.126**), as well as dihydrogen and isobutene (Scheme 1.18).

Compound **1.125** formed by abstraction of a γ-hydrogen of the SiMe groups, while **1.126** was formed by abstraction of a γ-hydrogen of the ^{t}Bu group and subsequent isobutene elimination.

Sadow and co-workers also produced a series of reports on the reactivity of zirconocene bis(dimethylsilyl)amido compounds.[45–48] Similar to the thermal decomposition of **1.96** in the presence of PMe_3, the bis(dimethylsilyl)amide complexes $Cp_2Zr(R)\{N(SiHMe_2)Si(\mu\text{-}H)Me_2\}$ (R = H (**1.103**) or Me (**1.127**)) underwent γ-hydrogen abstraction when heated to 140 °C to give the 4-membered zirconacycle $Cp_2Zr\{N(SiHMe_2)Si(H)(Me)CH_2\}$ (**1.129**, Scheme 1.19). In contrast, the ethyl analogue $Cp_2Zr(Et)\{N(SiHMe_2)Si(\mu\text{-}H)Me_2\}$ (**1.128**) underwent β-hydrogen abstraction when heated to 60 °C to give the η^2-silanimine $Cp_2Zr\{\eta^2\text{-}N(Si(\mu\text{-}H)Me_2)SiMe_2\}$ (**1.130**). Compound **1.130** was found to be stabilised by a β-agostic interaction, though addition of PMe_3 could break this interaction in favour of coordination of PMe_3, giving $Cp_2Zr\{\eta^2\text{-}N(SiHMe_2)SiMe_2\}(PMe_3)$ (**1.131**). Mimicking the reaction of formaldehyde with the η^2-silanimine **1.119**, acetone was also seen to react with **1.130**, forming the 5-membered zirconoacycle $Cp_2Zr\{N(SiHMe_2)SiMe_2CMe_2O\}$ (**1.132**) by insertion into the Zr–Si bond.



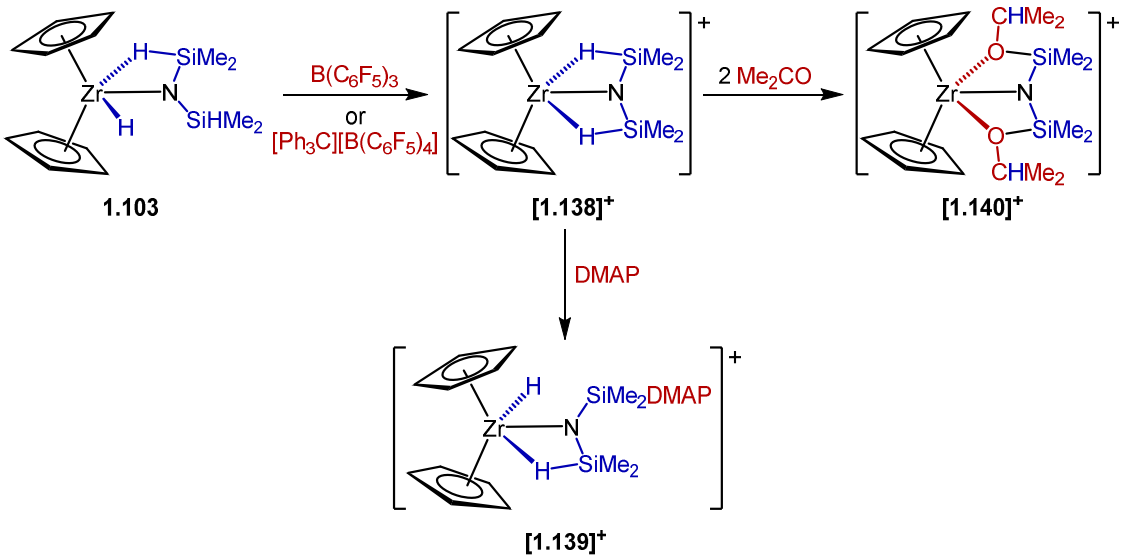
Scheme 1.19: Selected reactions of zirconocene bis(dimethylsilyl)amido complexes.[45,48]

The zirconacycle **1.129** was found to react with several small molecules, as shown in Scheme 1.19.[45,48] Addition of ethylene at 150 °C for an extended period gave the 5-membered zirconacycle $Cp_2Zr\{N(SiHMe_2)SiMe_2CH_2CH_2\}$ (**1.133**). The reaction was found to proceed by C–H activation across the Zr–C bond to form the ethenyl intermediate $Cp_2Zr(CHCH_2)\{N(SiHMe_2)Si(\mu\text{-}H)Me_2\}$ which could undergo β-H abstraction to give ethylene and a transient η^2-silanimine, followed by insertion of

ethylene into the Zr–Si bond. C–H activation was explicitly showed by the addition of trimethylsilylacetylene to **1.129** to give the acetylide $Cp_2Zr(CCSiMe_3)\{N(SiHMe_2)Si(\mu\text{-}H)Me_2\}$ (**1.134**). Compound **1.134** was not reported to undergo β-H abstraction.

Addition of CO to **1.129** gave the 5-membered zirconacycle $Cp_2Zr\{N(SiHMe_2)Si(H)(Me)C(=CH_2)O\}$ (**1.135**), formed by 1,1-insertion of CO to give an acyl intermediate, with subsequent rearrangement to give the observed product. Formaldehyde was observed to insert into the pendant Si–H bond of **1.129** leading to the unexpected formation of $Cp_2Zr\{N(Si(OMe)Me_2)Si(H)(Me)CH_2\}$ (**1.136**). No reaction with the Zr–C bond was observed and, as the Si–H bond does not interact with the metal centre, rationale for the reaction could not be provided. In contrast, reaction of formaldehyde with **1.96** gave insertion into the Zr–H bond and no reaction was observed with **1.125**.

Reaction with $B(C_6F_5)_3$ led to formation of the diagostic, zwitterionic complex $Cp_2Zr\{N(Si(\mu\text{-}H)Me_2)Si(\mu\text{-}H)(Me)CH_2B(C_6F_5)_3\}$ (**1.137**). Similarly, reaction of **1.103** with $B(C_6F_5)_3$ or $[Ph_3C][B(C_6F_5)_4]$ gave the cationic diagostic complex $[Cp_2Zr\{N(Si(\mu\text{-}H)Me_2)_2\}]^+$ (**[1.138]**$^+$, Scheme 1.20).[47] The SiH protons of **[1.138]**$^+$ appeared at –0.48 ppm in the ^{1}H NMR spectrum and the $^1J_{SiH}$ coupling constant was found to be just 89 Hz. The Si–H bond stretches were observed at 1738 and 1659 cm^{-1}, indicating significant bond weakening. Furthermore, in the solid state structure the Si–H bonds were found to be elongated and the N–Si bonds shortened.



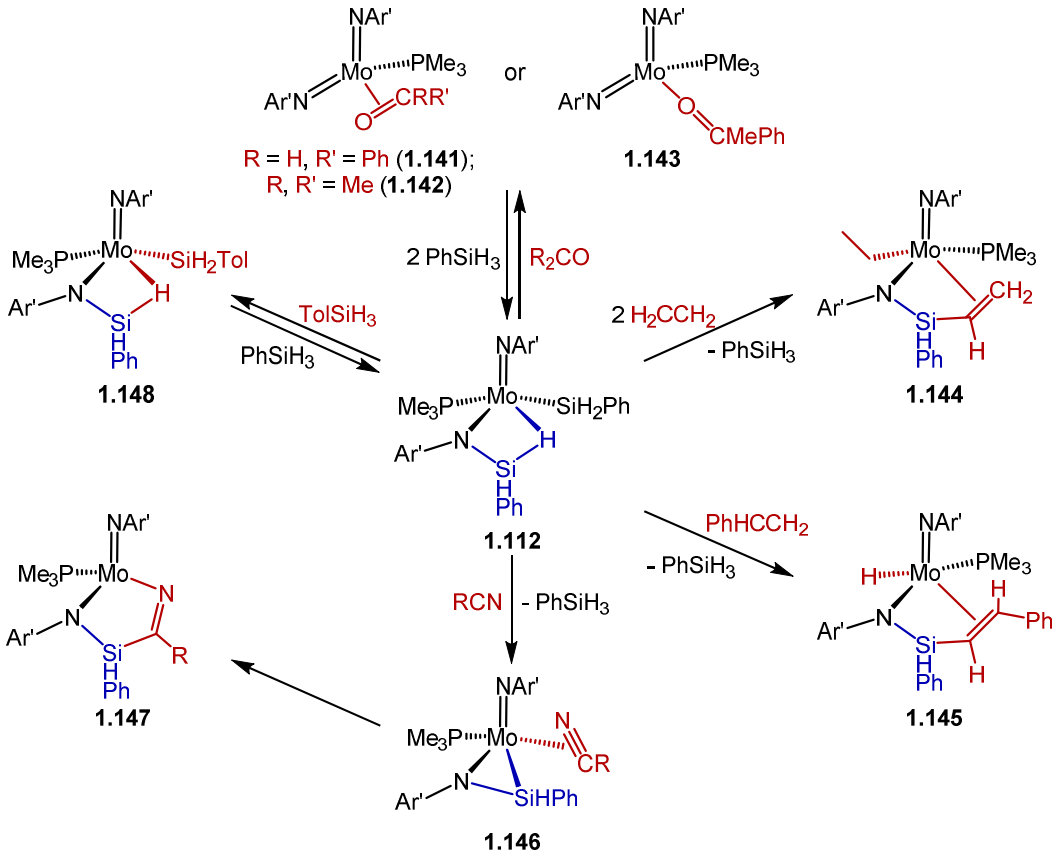
Scheme 1.20: Synthesis and selected reactions of the cationic, diagostic complex $[Cp_2Zr\{N(Si(\mu\text{-}H)Me_2)_2\}]^+$ (**[1.138]**$^+$).

Confirming the large degree of Si–H bond activation in **[1.138]**$^+$, addition of DMAP led to Si–H bond cleavage and the formation of $[Cp_2Zr(H)\{N(SiMe_2DMAP)Si(\mu\text{-}H)Me_2\}]^+$ (**[1.139]**$^+$, Scheme 1.20). Furthermore, addition of two equivalents acetone led to hydrosilylation by both Si–H bonds to give $[Cp_2Zr\{N(Si((\mu\text{-}O)CHMe_2)Me_2)_2\}]^+$ (**[1.140]**$^+$, Scheme 1.20). This reaction was proposed to proceed by coordination of acetone to silicon, with concomitant Si–H bond cleavage and subsequent insertion of the C=O bond into the transiently formed Zr–H bond.

1.4.2.2 Group 6 β-agostic silylamide complexes

Nikonov and co-workers reported on the reactivity of the molybdenum silylamide $(Ar'N)Mo(SiH_2Ph)\{N(Ar')Si(\mu\text{-}H)HPh\}(PMe_3)$ (**1.112**).[50] Reaction with benzaldehyde, acetone or acetophenone led to the formation of the adducts $(NAr')_2Mo(\eta^2\text{-}OCRR')(PMe_3)$ (R = H, R' = Ph (**1.141**) or R, R' = Me (**1.142**)) or $(NAr')_2Mo(\eta^1\text{-}OCMePh)(PMe_3)$ (**1.143**), with elimination of phenylsilane and unknown silicon-containing by-products (Scheme 1.21). Compound **1.112** reacted with two equivalents ethylene to form the ethyl-vinylsilylamide

(Ar'N)Mo(Et){η^3-N(Ar')Si(H)(Ph)CHCH$_2$}(PMe$_3$) (**1.144**), with elimination of phenylsilane. The reaction was found to proceed initially by β-hydrogen elimination of the silylamide ligand by the silyl ligand to eliminate phenylsilane and form a transient η^2-silanimine.[38] Insertion of ethylene into the Mo–Si bond followed, forming a metallacycle analogous to Cp$_2$Zr{N(SiHMe$_2$)SiMe$_2$CH$_2$CH$_2$} (**1.133**). This metallacycle could then undergo β-C–H elimination to form a hydride-vinylsilylamide, followed by insertion of the second equivalent of ethylene into the Mo–H bond to give **1.144**. Styrene underwent a similar reaction, forming the hydride-vinylsilylamide (Ar'N)Mo(H){η^3-N(Ar')Si(H)(Ph)CHCH$_2$}(PMe$_3$) (**1.145**), though a second equivalent of styrene was not observed to insert into the Mo–H of **1.145**. Notably, ethylene could insert into the Mo–H bond of **1.145**.



Scheme 1.21: Selected reactions of (Ar'N)Mo(SiH$_2$Ph){N(Ar')Si(μ-H)HPh}(PMe$_3$) (**1.112**).[38,50]

Further to stoichiometric reactions with alkenes, compound **1.112** was reported to catalyse the hydrosilylation of ethylene by phenylsilane.[38] The mechanism was proposed to proceed from **1.112** to **1.144** followed by hydrogenation of the vinyl moiety by the ethyl ligand and silane, forming the intermediate species (Ar'N)Mo(SiH_2Ph){N(Ar')Si(μ-H)EtPh}(η^2-CH_2CH_2). This species could then undergo ligand exchange and silane exchange to reform **1.112** and give $PhEtSiH_2$. Additionally, the hydride silylamide (Ar'N)$_2$Mo(H){N(^{t}Bu)Si(μ-H)Me_2} (**1.106**) was reported to catalyse the hydrosilylation of carbonyls.[40] While the mechanism of this catalysis could not be established, it was clear that insertion of the carbonyl into the Mo–H bond did not occur.

Reaction of **1.112** with silanes led to exchange of the silyl ligand and use of deuterium labelling showed hydrogen-deuterium exchange at the Si–H sites of the silylamide ligand (Scheme 1.21).[38,50] This was proposed to occur *via* one of two possible mechanisms, one of which involved β-hydrogen abstraction and an η^2-silanimine intermediate. With nitriles, **1.112** underwent β-hydrogen abstraction by the silyl ligand to form η^2-silanimine-η^2-nitrile species of the type (Ar'N)Mo{η^2-N(Ar')SiHPh}(η^2-NCR)(PMe_3) (**1.146**, Scheme 1.21). Whether coordination of the nitrile occurred before or after β-H abstraction was not clear and these compounds were found to be unstable towards insertion of the nitrile into the Mo–Si bond to form metallacycles of the type (Ar'N)Mo{N(Ar')Si(H)(Ph)C(R)N}(PMe_3) (**1.147**).

1.5 Summary and outlook

The first half of this Chapter provided an overview of the chemistry of Group 4 imido and hydrazido complexes, ranging from their synthesis to their stoichiometric and catalytic reactivity. While the reaction chemistry of these complexes has been intensely studied, it is clear reactions with E–H (E = B, Si) bonds are underdeveloped with respect to with unsaturated bonds. Few reports have been made for the reactions of boranes with Group 4 imides and hydrazides and only Group 4 hydrazides have been reported to react with silanes. Furthermore, only one report on the reactions of B–H bonds with a metallocene hydrazide has been published to date. As such, the first focus of this Thesis is to extend the scope of these reactivity studies using zirconocene imides and hydrazides, which have received little attention in recent years. This work is presented in Chapter 2.

In the second half of this Chapter, the synthesis, structure and reactivity of transition metal silylamido complexes containing β-Si–H···M agostic interactions was reviewed. These complexes contain several notable structural features, which can be characterised, and the reaction chemistry observed has been wide scoping. Reactions can proceed through β- or γ-hydrogen elimination or abstraction, often forming species that can react onwards with small molecules. However, this intriguing reactivity has been not been fully investigated and onward reactivity predominantly involves insertion of unsaturated bonds to M–E bonds. Therefore, the second focus of this Thesis is to extend the reactivity studies of β-Si–H···M agostic zirconocene silylamides through addition of terminal alkynes, B–H bond containing boranes and silanes. In doing so, the list of ligands that can facilitate β-hydrogen abstraction from such complexes is extended to the hydride ligand. This work is presented in Chapters 3 and 4.

1.6 References

1 W. A. Nugent and J. M. Mayer, *Metal-ligand multiple bonds*, Wiley-Interscience, New York, 1988.
2 J. Chatt, A. J. Pearman and R. L. Richards, *J. Chem. Soc., Dalton Trans.*, 1977, 2139–2142.
3 M. Hidai, *Coord. Chem. Rev.*, 1999, **185**–**186**, 99–108.
4 R. R. Schrock, *Acc. Chem. Res.*, 2005, **38**, 955–962.
5 D. V. Yandulov and R. R. Schrock, *Inorg. Chem.*, 2005, **44**, 1103–1117.
6 W. W. Weare, X. Dai, M. J. Byrnes, J. M. Chin, R. R. Schrock and P. Müller, *Proc. Natl. Acad. Sci. U. S. A.*, 2006, **103**, 17099–17106.
7 R. R. Schrock, *Angew. Chem., Int. Ed.*, 2008, **47**, 5512–5522.
8 N. Adams, H. J. Arts, P. D. Bolton, D. Cowell, S. R. Dubberley, N. Friederichs, C. M. Grant, M. Kranenburg, A. J. Sealey, B. Wang, P. J. Wilson, A. R. Cowley, P. Mountford and M. Schröder, *Chem. Commun.*, 2004, **4**, 434–435.
9 P. Bolton and P. Mountford, *Adv. Synth. Catal.*, 2005, **347**, 355–366.
10 H. R. Bigmore, M. A. Zuideveld, A. M. Kowalczyk, A. R. Cowley, M. Kranenburg, E. J. L. McInnes and P. Mountford, *Inorg. Chem.*, 2006, **45**, 6411–6423.
11 H. R. Bigmore, S. R. Dubberley, M. Kranenburg, S. C. Lawrence, A. J. Sealey, J. D. Selby, M. A. Zuideveld, A. R. Cowley and P. Mountford, *Chem. Commun.*, 2006, 436–438.
12 N. Hazari and P. Mountford, *Acc. Chem. Res.*, 2005, **38**, 839–849.
13 C. H. Winter, P. H. Sheridan, T. S. Lewkebandara, M. J. Heeg and J. W. Proscia, *J. Am. Chem. Soc.*, 1992, **114**, 1095–1097.
14 T. S. Lewkebandara, P. H. Sheridan, M. J. Heeg, A. L. Rheingold and C. H. Winter, *Inorg. Chem.*, 1994, **33**, 5879–5889.
15 M. Slusarczyk, DPhil Thesis, University of Oxford, 2018.
16 J. S. Johnson and R. G. Bergman, *J. Am. Chem. Soc.*, 2001, 123, 2923–2924.
17 C. Cao, Y. Shi and A. L. Odom, *Org. Lett.*, 2002, **4**, 2853–2856.
18 S. Banerjee, E. Barnea and A. L. Odom, *Organometallics*, 2008, **27**, 1005–1014.
19 K. Weitershaus, H. Wadepohl and L. H. Gade, *Organometallics*, 2009, **28**, 3381–3389.
20 K. Weitershaus, B. D. Ward, R. Kubiak, C. Müller, H. Wadepohl, S. Doye and L. H. Gade, *J. Chem. Soc., Dalton Trans.*, 2009, 4586–4602.
21 P. D. Schweizer, H. Wadepohl and L. H. Gade, *Organometallics*, 2013, **32**, 3697–3709.
22 I. Bytschkov and S. Doye, *European J. Org. Chem.*, 2003, **2003**, 935–946.
23 S. Doye, *Synlett*, 2004, 2004, 1653–1672.
24 Y. Li, Y. Shi and A. L. Odom, *J. Am. Chem. Soc.*, 2004, **126**, 1794–1803.
25 L. Ackermann and R. Born, *Tetrahedron Lett.*, 2004, **45**, 9541–9544.
26 V. Khedkar, A. Tillack, M. Michalik and M. Beller, *Tetrahedron Lett.*, 2004, **45**, 3123–3126.
27 S. Banerjee, Y. Shi, C. Cao and A. L. Odom, *J. Organomet. Chem.*, 2005, **690**, 5066–5077.
28 A. V. Lee and L. L. Schafer, *Eur. J. Inorg. Chem.*, 2007, **2007**, 2245–2255.
29 T. E. Müller, K. C. Hultzsch, M. Yus, F. Foubelo and M. Tada, *Chem. Rev.*, 2008, **108**, 3795–3892.
30 P. J. Tiong, A. Nova, E. Clot and P. Mountford, *Chem. Commun.*, 2011, **47**,

3147.
31 P. J. Tiong, A. Nova, A. D. Schwarz, J. D. Selby, E. Clot and P. Mountford, *Dalton Trans.*, 2012, **41**, 2277.
32 L. C. Stevenson, S. Mellino, E. Clot and P. Mountford, *J. Am. Chem. Soc.*, 2015, **137**, 10140–10143.
33 S. Mellino, L. C. Stevenson, E. Clot and P. Mountford, *Organometallics*, 2017, **36**, 3329–3342.
34 L. J. Procopio, P. J. Carroll and D. H. Berry, *J. Am. Chem. Soc.*, 1991, **113**, 1870–1872.
35 L. J. Procopio, P. J. Carroll and D. H. Berry, *J. Am. Chem. Soc.*, 1994, **116**, 177–185.
36 S. K. Ignatov, N. H. Rees, A. A. Merkoulov, S. R. Dubberley, A. G. Razuvaev, P. Mountford and G. I. Nikonov, *Chem. Eur. J.*, 2008, **14**, 296–310.
37 S. K. Ignatov, A. Y. Khalimon, N. H. Rees, A. G. Razuvaev, P. Mountford and G. I. Nikonov, *Inorg. Chem.*, 2009, **48**, 9605–9622.
38 A. Y. Khalimon, R. Simionescu and G. I. Nikonov, *J. Am. Chem. Soc.*, 2011, **133**, 7033–7053.
39 A. Y. Khalimon, O. G. Shirobokov, E. Peterson, R. Simionescu, L. G. Kuzmina, J. A. K. Howard and G. I. Nikonov, *Inorg. Chem.*, 2012, **51**, 4300–4313.
40 N. A. McLeod, L. G. Kuzmina, I. Korobkov, J. A. K. Howard and G. I. Nikonov, *Dalton Trans.*, 2016, **45**, 2554–2561.
41 S. K. Ignatov, N. H. Rees, S. R. Dubberley, A. G. Razuvaev, P. Mountford and G. I. Nikonov, *Chem. Commun.*, 2004, **4**, 952–953.
42 G. I. Nikonov, P. Mountford, J. C. Green, P. A. Cooke, M. A. Leech, A. J. Blake, J. A. K. Howard and D. A. Lemenovskii, *Eur. J. Inorg. Chem.*, 2000, **2000**, 1917–1921.
43 L. J. Procopio, P. J. Carroll and D. H. Berry, *Organometallics*, 1993, **12**, 3087–3093.
44 L. J. Procopio, P. J. Carroll and D. H. Berry, *Polyhedron*, 1995, **14**, 45–55.
45 K. Yan and A. D. Sadow, *Chem. Commun.*, 2013, **49**, 3212–3214.
46 K. Yan, A. Ellern and A. D. Sadow, *J. Am. Chem. Soc.*, 2012, **134**, 9154–9156.
47 K. Yan, J. J. Duchimaza Heredia, A. Ellern, M. S. Gordon and A. D. Sadow, *J. Am. Chem. Soc.*, 2013, **135**, 15225–15237.
48 K. Yan, A. Pindwal, A. Ellern and A. D. Sadow, *Dalton Trans.*, 2014, **43**, 8644–8653.
49 G. I. Nikonov, P. Mountford, S. K. Ignatov, J. C. Green, M. A. Leech, L. G. Kuzmina, A. G. Razuvaev, N. H. Rees, A. J. Blake, J. A. K. Howard and D. A. Lemenovskii, *J. Chem. Soc., Dalton Trans.*, 2001, 2903–2915.
50 A. Y. Khalimon, R. Simionescu, L. G. Kuzmina, J. A. K. Howard and G. I. Nikonov, *Angew. Chem., Int. Ed.*, 2008, **47**, 7701–7704.
51 W. A. Nugent and B. L. Haymore, *Coord. Chem. Rev.*, 1980, **31**, 123–175.
52 D. E. Wigley, *Progress in inorganic chemistry*, Wiley-Interscience, New York, 1994.
53 M. H. Chisholm and I. P. Rothwell, in *Comprehensive Coordination Chemistry*, Pergamon Press, Oxford, 1987, pp. 161–184.
54 P. Mountford, *Chem. Commun.*, 1997, 2127–2134.
55 B. L. Haymore, E. A. Maatta and R. A. D. Wentworth, *J. Am. Chem. Soc.*, 1979, **101**, 2063–2068.
56 S. C. Dunn, P. Mountford and D. A. Robson, *J. Chem. Soc., Dalton Trans.*, 1997, 293–304.

57 P. J. Walsh, F. J. Hollander and R. G. Bergman, *Organometallics*, 1993, **12**, 3705–3723.
58 J. E. Hill, R. D. Profilet, P. E. Fanwick and I. P. Rothwell, *Angew. Chem., Int. Ed.*, 1990, **29**, 664–665.
59 H. W. Roesky, H. Voelker, M. Witt and M. Noltemeyer, *Angew. Chem., Int. Ed.*, 1990, **29**, 669–670.
60 C. C. Cummins, C. P. Schaller, G. D. Van Duyne, P. T. Wolczanski, A. W. E. Chan and R. Hoffmann, *J. Am. Chem. Soc.*, 1991, **113**, 2985–2994.
61 R. Duchateau, A. J. Williams, S. Gambarotta and M. Y. Chiang, *Inorg. Chem.*, 1991, **30**, 4863–4866.
62 T. E. Hanna, I. Keresztes, E. Lobkovsky, W. H. Bernskoetter and P. J. Chirik, *Organometallics*, 2004, **23**, 3448–3458.
63 A. R. Fout, U. J. Kilgore and D. J. Mindiola, *Chem. Eur. J.*, 2007, **13**, 9428–9440.
64 A. J. Blake, P. E. Collier, S. C. Dunn, W. S. Li, P. Mountford and O. V. Shishkin, *J. Chem. Soc., Dalton Trans.*, 1997, 1549–1558.
65 S. C. Dunn, A. S. Batsanov and P. Mountford, *J. Chem. Soc., Chem. Commun.*, 1994, 2007–2008.
66 D. Swallow, J. M. McInnes and P. Mountford, *J. Chem. Soc., Dalton Trans.*, 1998, 2253–2259.
67 A. J. Blake, J. M. McInnes, P. Mountford, G. I. Nikonov, D. Swallow and D. J. Watkin, *J. Chem. Soc., Dalton Trans.*, 1999, 379–391.
68 L. H. Gade and P. Mountford, *Coord. Chem. Rev.*, 2001, **216**–**217**, 65–97.
69 P. E. Collier, S. M. Pugh, H. S. C. Clark, J. B. Love, A. J. Blake, F. G. N. Cloke and P. Mountford, *Inorg. Chem.*, 2000, **39**, 2001–2005.
70 A. J. Blake, P. E. Collier, L. H. Gade, P. Mountford, J. Lloyd, S. M. Pugh, M. Schubart, M. E. G. Skinner and D. J. M. Trösch, *Inorg. Chem.*, 2001, **40**, 870–877.
71 P. J. Stewart, A. J. Blake and P. Mountford, *J. Organomet. Chem.*, 1998, **564**, 209–214.
72 A. E. Guiducci, C. L. Boyd and P. Mountford, *Organometallics*, 2006, **25**, 1167–1187.
73 A. E. Guiducci, C. L. Boyd, E. Clot and P. Mountford, *J. Chem. Soc., Dalton Trans.*, 2009, 5960–5979.
74 A. E. Guiducci, A. R. Cowley, M. E. G. Skinner and P. Mountford, *J. Chem. Soc., Dalt. Trans*, 2001, 1392–1394.
75 B. A. Clough, S. Mellino, A. V. Protchenko, M. Slusarczyk, L. C. Stevenson, M. P. Blake, B. Xie, E. Clot and P. Mountford, *Inorg. Chem.*, 2017, **56**, 10794–10814.
76 P. J. Stewart, A. J. Blake and P. Mountford, *Organometallics*, 1998, **17**, 3271–3281.
77 M. Froneman, D. L. Cheney and T. A. Modro, *Phosphorus. Sulfur. Silicon Relat. Elem.*, 1990, **47**, 273–281.
78 N. Adams, H. R. Bigmore, T. L. Blundell, C. L. Boyd, S. R. Dubberley, A. J. Sealey, A. R. Cowley, M. E. G. Skinner and P. Mountford, *Inorg. Chem.*, 2005, **44**, 2882–2894.
79 M. Manßen, S. De Graaff, M. F. Meyer, M. Schmidtmann and R. Beckhaus, *Organometallics*, 2018, **37**, 4506–4514.
80 P. J. Walsh, F. J. Hollander and R. G. Bergman, *J. Am. Chem. Soc.*, 1988, **110**, 8729–8731.

81 R. L. Zuckerman, S. W. Krska and R. G. Bergman, *J. Am. Chem. Soc.*, 2000, **122**, 751–761.
82 W. A. Nugent and R. L. Harlow, *Inorg. Chem.*, 1979, **18**, 2030–2032.
83 C. C. Cummins, S. M. Baxter and P. T. Wolczanski, *J. Am. Chem. Soc.*, 1988, **110**, 8731–8733.
84 D. J. Arney, M. A. Brack, S. R. Huber and D. E. Wigley, *Inorg. Chem.*, 1992, **31**, 3749–3755.
85 S. R. Dubberley, S. Evans, C. L. Boyd and P. Mountford, *Dalton Trans.*, 2005, 1448–1458.
86 A. J. Blake, P. Mountford, G. I. Nikonov and D. Swallow, *Chem. Commun.*, 1996, 1835–1836.
87 J. L. Thorman, I. A. Guzei, V. G. Young and L. K. Woo, *Inorg. Chem.*, 1999, **38**, 3814–3824.
88 M. E. G. Skinner, T. Toupance, D. A. Cowhig, B. R. Tyrrell and P. Mountford, *Organometallics*, 2005, **24**, 5586–5603.
89 J. L. Poise, R. A. Andersen and R. G. Bergman, *J. Am. Chem. Soc.*, 1998, **120**, 13405–13414.
90 R. L. Zuckerman and R. G. Bergman, *Organometallics*, 2001, **20**, 1792–1807.
91 R. L. Zuckerman and R. G. Bergman, *Organometallics*, 2000, **19**, 4795–4809.
92 K. E. Meyer, P. J. Walsh and R. G. Bergman, *J. Am. Chem. Soc.*, 1995, **117**, 974–985.
93 K. E. Meyer, P. J. Walsh and R. G. Bergman, *J. Am. Chem. Soc.*, 1994, **116**, 2669–2670.
94 A. P. Duncan and R. G. Bergman, *Chem. Rec.*, 2002, **2**, 431–445.
95 Sun Yeoul Lee and R. G. Bergman, *Tetrahedron*, 1995, **51**, 4255–4276.
96 B. Xie, DPhil Thesis, University of Oxford, 2018.
97 H. M. Hoyt and R. G. Bergman, *Angew. Chem., Int. Ed.*, 2007, **46**, 5580–5582.
98 S. Y. Lee and R. G. Bergman, *J. Am. Chem. Soc.*, 1996, **118**, 6396–6406.
99 S. A. Blum, V. A. Rivera, R. T. Ruck, F. E. Michael and R. G. Bergman, *Organometallics*, 2005, **24**, 1647–1659.
100 D. J. M. Trösch, P. E. Collier, A. Bashall, L. H. Gade, M. McPartlin, P. Mountford and S. Radojevic, *Organometallics*, 2001, **20**, 3308–3313.
101 B. D. Ward, A. Maisse-François, P. Mountford and L. H. Gade, *Chem. Commun.*, 2004, **4**, 704–705.
102 A. Bashall, P. E. Collier, L. H. Gade, M. McPartlin, P. Mountford, S. M. Pugh, S. Radojevic, M. Schubart, I. J. Scowen and D. J. M. Trösch, *Organometallics*, 2000, **19**, 4784–4794.
103 A. Bashall, P. E. Collier, L. H. Gade, M. McPartlin, P. Mountford and D. J. M. Trösch, *Chem. Commun.*, 1998, 2555–2556.
104 S. M. Pugh, D. J. M. Trösch, D. J. Wilson, A. Bashall, F. G. N. Cloke, L. H. Gade, P. B. Hitchcock, M. McPartlin, J. F. Nixon and P. Mountford, *Organometallics*, 2000, **19**, 3205–3210.
105 L. C. Stevenson, DPhil Thesis, University of Oxford, 2015.
106 P. Mountford, *J. Organomet. Chem.*, 1997, **528**, 15–18.
107 S. Tobisch, *Chem. Eur. J.*, 2008, **14**, 8590–8602.
108 K. Hultzsch, *Adv. Synth. Catal.*, 2005, **347**, 367–391.
109 A. L. Odom, *Dalton Trans.*, 2005, 225–233.
110 A. Tillack, H. Jiao, I. Garcia Castro, C. G. Hartung and M. Beller, *Chem. Eur. J.*, 2004, **10**, 2409–2420.
111 B. F. Straub and R. G. Bergman, *Angew. Chem., Int. Ed.*, 2001, **40**, 4632–4635.

112 S. Tobisch, *Dalton Trans.*, 2006, 4277–4285.
113 S. Tobisch, *Chem. Eur. J.*, 2007, **13**, 4884–4894.
114 C. Müller, R. Koch and S. Doye, *Chem. Eur. J.*, 2008, **14**, 10430–10436.
115 F. Pohlki and S. Doye, *Angew. Chem., Int. Ed.*, 2001, **40**, 2305–2308.
116 L. E. N. Allan, G. J. Clarkson, D. J. Fox, A. L. Gott and P. Scott, *J. Am. Chem. Soc.*, 2010, **132**, 15308–15320.
117 P. J. Walsh, A. M. Baranger and R. G. Bergman, *J. Am. Chem. Soc.*, 1992, **114**, 1708–1719.
118 A. M. Baranger, P. J. Walsh and R. G. Bergman, *J. Am. Chem. Soc.*, 1993, **115**, 2753–2763.
119 L. Ackermann, R. G. Bergman and R. N. Loy, *J. Am. Chem. Soc.*, 2003, **125**, 11956–11963.
120 J. Cho, T. K. Hollis, E. J. Valente and J. M. Trate, *J. Organomet. Chem.*, 2011, **696**, 373–377.
121 L. Luconi, A. Rossin, G. Tuci, S. Germain, E. Schulz, J. Hannedouche and G. Giambastiani, *ChemCatChem*, 2013, **5**, 1142–1151.
122 K. Manna, W. C. Everett, G. Schoendorff, A. Ellern, T. L. Windus and A. D. Sadow, *J. Am. Chem. Soc.*, 2013, **135**, 7235–7250.
123 D. Duncan and T. Livinghouse, *Organometallics*, 1999, **18**, 4421–4428.
124 L. Ackermann and R. G. Bergman, *Org. Lett.*, 2002, **4**, 1475–1478.
125 P. J. Tiong, A. Nova, L. R. Groom, A. D. Schwarz, J. D. Selby, A. D. Schofield, E. Clot and P. Mountford, *Organometallics*, 2011, **30**, 1182–1201.
126 T. B. Parsons, N. Hazari, A. R. Cowley, J. C. Green and P. Mountford, *Inorg. Chem.*, 2005, **44**, 8442–8458.
127 P. J. Walsh, M. J. Carney and R. G. Bergman, *J. Am. Chem. Soc.*, 1991, **113**, 6343–6345.
128 N. Wiberg, H.-W. Häring, G. Huttner and P. Friedrich, *Chem. Ber.*, 1978, **111**, 2708–2715.
129 J. D. Selby, C. D. Manley, A. D. Schwarz, E. Clot and P. Mountford, *Organometallics*, 2008, **27**, 6479–6494.
130 J. D. Selby, M. Feliz, A. D. Schwarz, E. Clot and P. Mountford, *Organometallics*, 2011, **30**, 2295–2307.
131 M. Manßen, M.-F. Meyer, M. Schmidtmann and R. Beckhaus, *Organometallics*, 2018, **37**, 4515–4520.
132 H. Herrmann, J. Lloret Fillol, H. Wadepohl and L. H. Gade, *Angew. Chem., Int. Ed.*, 2007, **46**, 8426–8430.
133 H. Herrmann, J. L. Fillol, T. Gehrmann, M. Enders, H. Wadepohl and L. H. Gade, *Chem. Eur. J.*, 2008, **14**, 8131–8146.
134 P. D. Schweizer, H. Wadepohl and L. H. Gade, *Organometallics*, 2014, **33**, 1726–1739.
135 S. A. Scholl, H. Wadepohl and L. H. Gade, *Organometallics*, 2013, **32**, 937–940.
136 S. A. Scholl, G. T. Plundrich, H. Wadepohl and L. H. Gade, *Inorg. Chem.*, 2013, **52**, 10158–10166.
137 T. Gehrmann, S. A. Scholl, J. L. Fillol, H. Wadepohl and L. H. Gade, *Chem. Eur. J.*, 2012, **18**, 3925–3941.
138 J. D. Selby, C. Schulten, A. D. Schwarz, A. Stasch, E. Clot, C. Jones and P. Mountford, *Chem. Commun.*, 2008, 5101.
139 A. D. Schofield, DPhil Thesis, University of Oxford, 2012.
140 T. Gehrmann, G. T. Plundrich, H. Wadepohl and L. H. Gade, *Organometallics*, 2012, **31**, 3346–3354.

141 T. Gehrmann, J. Lloret Fillol, H. Wadepohl and L. H. Gade, *Angew. Chem., Int. Ed.*, 2009, **48**, 2152–2156.
142 A. D. Schofield, A. Nova, J. D. Selby, C. D. Manley, A. D. Schwarz, E. Clot and P. Mountford, *J. Am. Chem. Soc.*, 2010, **132**, 10484–10497.
143 A. D. Schofield, A. Nova, J. D. Selby, A. D. Schwarz, E. Clot and P. Mountford, *Chem. Eur. J.*, 2011, **17**, 265–285.
144 J. Unruangsri, H. Morgan, A. D. Schwarz, A. D. Schofield and P. Mountford, *Organometallics*, 2013, **32**, 3091–3107.
145 A. W. Kaplan, J. L. Polse, G. E. Ball, R. A. Andersen and R. G. Bergman, *J. Am. Chem. Soc.*, 1998, **120**, 11649–11662.
146 S. Banerjee and A. L. Odom, *Organometallics*, 2006, **25**, 3099–3101.
147 A. A. Dissanayake and A. L. Odom, *Chem. Commun.*, 2012, **48**, 440–442.
148 A. D. Schwarz, C. S. Onn and P. Mountford, *Angew. Chem., Int. Ed.*, 2012, **51**, 12298–12302.
149 J. C. Green, *Chem. Soc. Rev.*, 1998, **27**, 263.
150 W. Scherer, V. Herz and C. Hauf, *Struct. Bond.*, 2012, **146**, 159–207.
151 W. Scherer, D. J. Wolstenholme, V. Herz, G. Eickerling, A. Brück, P. Benndorf and P. W. Roesky, *Angew. Chem., Int. Ed.*, 2010, **49**, 2242–2246.
152 M. Brookhart, M. L. H. Green and L.-L. Wong, *Prog. Inorg. Chem.*, 1988, **36**, 1–124.
153 W. A. Herrmann, N. W. Huber and J. Behm, *Chem. Ber.*, 1992, **125**, 1405–1407.
154 M. Okazaki and S. Ebina, *Chem. Lett.*, 2014, **43**, 1089–1091.
155 Y. Sarazin, D. Roşca, V. Poirier, T. Roisnel, A. Silvestru, L. Maron and J. F. Carpentier, *Organometallics*, 2010, **29**, 6569–6577.
156 W. A. Herrmann, J. Eppinger, M. Spiegler, O. Runte and R. Anwander, *Organometallics*, 1997, **16**, 1813–1815.
157 M. G. Klimpel, H. W. Görlitzer, M. Tafipolsky, M. Spiegler, W. Scherer and R. Anwander, *J. Organomet. Chem.*, 2002, **647**, 236–244.
158 R. Anwander, O. Runte, J. Eppinger, G. Gerstberger, E. Herdtweck and M. Spiegler, *J. Chem. Soc., Dalton Trans.*, 1998, 847–858.
159 J. Eppinger, M. Spiegler, W. Hieringer, W. A. Herrmann and R. Anwander, *J. Am. Chem. Soc.*, 2000, **122**, 3080–3096.
160 S. K. Ignatov, N. H. Rees, A. A. Merkoulov, S. R. Dubberley, A. G. Razuvaev, P. Mountford and G. I. Nikonov, *Organometallics*, 2008, **27**, 5968–5977.
161 G. I. Nikonov, *J. Organomet. Chem.*, 2001, **635**, 24–36.
162 B. Liu, T. Roisnel, J.-P. Guégan, J.-F. Carpentier and Y. Sarazin, *Chem. Eur. J.*, 2012, **18**, 6289–6301.
163 B. Liu, T. Roisnel, J.-F. Carpentier and Y. Sarazin, *Chem. Eur. J.*, 2013, **19**, 2784–2802.
164 J. Y. Corey, *Chem. Rev.*, 2016, 116, 11291–11435.
165 I. Nagl, W. Scherer, M. Tafipolsky and R. Anwander, *Eur. J. Inorg. Chem.*, 1999, **1999**, 1405–1407.
166 D. Bubrin and M. Niemeyer, *Inorg. Chem.*, 2014, **53**, 1269–1271.
167 K. C. Boteju, S. Wan, A. Venkatesh, A. Ellern, A. J. Rossini and A. D. Sadow, *Chem. Commun.*, 2018, **54**, 7318–7321.
168 N. Eedugurala, Z. Wang, K. Yan, K. C. Boteju, U. Chaudhary, T. Kobayashi, A. Ellern, I. I. Slowing, M. Pruski and A. D. Sadow, *Organometallics*, 2017, **36**, 1142–1153.
169 J. F. Hartwig, *J. Am. Chem. Soc.*, 1996, **118**, 7010–7011.
170 J. M. Mayer, C. J. Curtis and J. E. Bercaw, *J. Am. Chem. Soc.*, 1983, **105**, 2651–

2660.
171 J. S. Figueroa and C. C. Cummins, *J. Am. Chem. Soc.*, 2003, **125**, 4020–4021.
172 Y. C. Tsai, M. J. A. Johnson, D. J. Mindiola, C. C. Cummins, W. T. Klooster and T. F. Koetzle, *J. Am. Chem. Soc.*, 1999, 121, 10426–10427.

Chapter Two

Small molecule reactivity of zirconocene hydrazides and imides

2.1 Introduction

As discussed in Chapter 1, Group 4 imido compounds of the type (L)M(NR) (L = supporting ligand set; R = alkyl or aryl) have been the subject of considerable attention for the past *ca.* 30 years, with investigations into structure, bonding, and reactivity being explored.[1–11] Group 4 hydrazides (L)N(NNR_2) have also received much attention,[12–23] while, more recently, other classes of heteroatom substituted imido analogues, such as *tert*-butoxyimides (L)M(NO^tBu)[24–26] and borylimides (L)M(NBR_2),[22,23,27–30] have received growing attention. In general, the reactivity of imido and imido-type compounds centres around addition or insertion of unsaturated compounds into the formally triple ($\sigma^2\pi^4$) M–N_α bond. Group 4 imides have also been used as catalysts for hydroamination,[7,31,32] and, more recently, dehydrocoupling reactions,[33] by exploiting the reactivity of the M–N_α bond. In addition to M–N_α bond reactivity, hydrazido compounds set themselves apart from their imido analogues by undergoing reductive cleavage of the N_α–N_β bond with oxidisable substrates such as CO, alkynes or isonitriles, as well as catalytic 1,2-diamination of alkynes *via* reductive insertion into the N_α–N_β bond.[34–36]

Some of the first systems studied for small molecule reactivity were the zirconocene imides $Cp_2Zr(N^tBu)(THF)$ (**2.1**) and $Cp_2Zr(NXyl)(THF)$ (**2.2**), and hydrazide $Cp_2Zr(NNPh_2)(DMAP)$ (**2.3**).[5,12,37–41] Reports have shown rich reactivity at the Zr=N bond with a host of unsaturated substrates, as well as with amines and dihydrogen for the imides. Reactivity studies of Group 4 imides and imido-analogues have somewhat moved away from the aforementioned zirconocene systems in recent years, focussing on titanium-based systems or alternative ancillary ligands, such as diamide-pyridine ligands or Cp*-amidinate ligand sets.[19–22,34,36,42,43] However, they have continued to be dominated by addition of unsaturated substrates and C–H bond activation.[7,16,19,29,35,39,40]

In contrast, E–H bond activation reactions (E = B and Si) of Group 4 imido and imido-type compounds are still poorly developed, with most work in this area focussing on hydrazide reactivity.[20,22,23] The first example of B–H addition to an imide of any kind was reported by Chen *et al*., in 2014, for a scandium imide reacting with 9-BBN to give a scandium hydride, which formed an adduct with a second equivalent of 9-BBN.[44] Since then, our group has reported hydride-bridged adduct formation with titanium imides. Titanium hydrazides have reacted further to give 1,2-addition of the B–H bond (**2.4**), reductive N_α–N_β bond cleavage **(2.5**) and the formation of a borylimide (**2.6**, Figure 2.1). Most recently, Beckhaus and co-workers reported 1,2-addition of 9-BBN across the Ti=N_α bond of $(Cp^{Ad})_2Ti(NNPh_2)(py)$ (**2.7**, Cp^{Ad} = η^5-C_5H_4Ad) to form the hydride borylhydrazido(1–) compound **2.8** (Figure 2.1).[15]

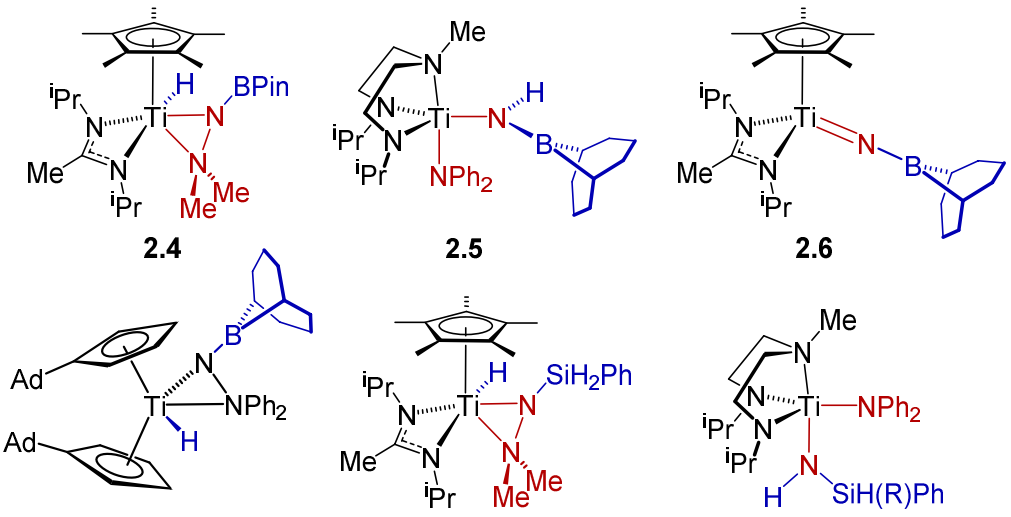


Figure 2.1: Products of the reactions of Group 4 hydrazides with silanes and boranes.

For the reactions of silanes, no Si–H addition reactions to Group 4 imides have been observed and there is only one example of Si–Cl and Si–Br addition, though the products were unstable and characterised by NMR spectroscopy only.[45] In contrast to Group 4 imides, there have been examples of Si–H 1,2-addition to a strained tantalum imide[46] and a scandium imide, albeit in equilibrium,[47] to form hydride silylamide complexes.

Furthermore, there have been reports of halosilane additions to Group 5 and 6 imido compounds, though *via* a different mechanism.[48–50] For Group 4 hydrazides, reversible Si–H 1,2-addition to Cp*Ti{MeC(N^{i}Pr)$_2$}(NNMe$_2$) has been observed forming **2.9** and irreversible Si–Cl addition of PhSiH$_2$Cl to form the chloride analogue. Furthermore, the diamide-amine-supported hydrazido complex Ti(N$_2$^{iPr}N^{Me})(NNPh$_2$)(py) underwent reductive N$_\alpha$–N$_\beta$ bond cleavage, giving **2.10** (Figure 2.1).[22] Kinetic and computational studies showed the reaction proceeded *via* pyridine dissociation, followed by 1,2-addition, to give a titanium hydride analogous to **2.9**, and subsequent migration of the hydride to the N$_\alpha$ atom with N$_\alpha$–N$_\beta$ bond cleavage.

Overall, Si–H and B–H bond activation reactions of Group 4 imides and hydrazides are underdeveloped with respect to the reactions of unsaturated molecules. Though the details of these reactions have begun to be investigated, with much of the work being carried out in this research group, the scope of this intriguing reactivity has not been fully investigated and nor have the factors controlling the reductive N$_\alpha$–N$_\beta$ bond cleavage. No Group 4 imides have been reported to form stable 1,2-addition products with silanes, there have been no reported reactions of silanes with Group 4 metallocene imides or hydrazides and there has been only one report of reactions of a Group 4 metallocene hydrazide with boranes.[15]

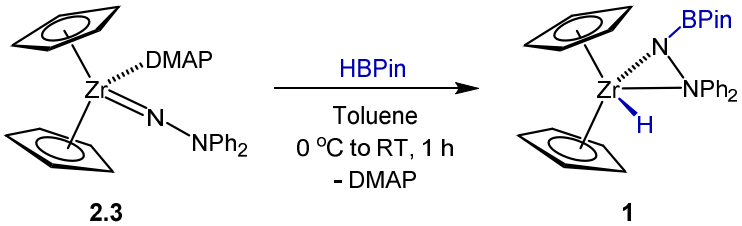
As such, this Chapter will explore the B–H, Si–H and Si–Cl bond activation reactions of the zirconocene hydrazido compound **2.3**. For comparison, reactions of **2.3** with CO, conducted previously by Bergman and co-workers, and isocyanides, which have previously been shown to induce N$_\alpha$–N$_\beta$ bond cleavage in a variety of systems, will be presented.[34,36,51,52] Complementary Density Functional Theory (DFT) calculations will aid discussion. The reactions of the zirconocene imido compounds **2.1** and **2.2** with silanes will also be discussed and were targeted in particular as the literature precedent

would suggest these reactions would form zirconocene silylamido compounds. Such compounds have previously synthesised by the research groups of Berry and Sadow and have shown interesting reaction chemistry, which could be expanded upon.[53–60]

It can be noted that all DFT calculations discussed in this chapter were performed by either Dr Eric Clot (Institut Charles Gerhardt, Université de Montpellier) or Professor Philip Mountford (University of Oxford). Full details of these calculations are provided in Chapter 6, Section 6.4.

2.2 Reaction of $Cp_2Zr(NNPh_2)(DMAP)$ (2.3) with pinacol borane (HBPin)

Reactions of $Cp_2Zr(NNPh_2)(DMAP)$ (**2.3**) with one or two equivalents of several different primary or secondary boranes, including 9-BBN, thexyl borane (H_2BTex, Tex = *tert*-hexyl), $HBAr^F_2$ ($Ar^F = C_6F_5$), dicyclohexyl borane ($HB(C_6H_{11})_2$), dimesityl borane and catechol borane (HBCat), gave intractable mixtures in every case. Reactions of each borane with the base-free hydrazide [$Cp_2ZrNNPh_2$] (**2.3_int**), *via* thermolysis of the alkyl-amide $Cp_2Zr\{N(H)NPh_2\}(CH_2CH_2{}^tBu)$ (**2.11**) in the presence of borane, yielded similarly intractable mixtures. In contrast, stoichiometric reaction of **2.3** with pinacol borane (HBPin) in C_6D_6 gave rapid and quantitative conversion to the hydride borylhydrazido(1–) compound $Cp_2Zr(H)\{N(NPh_2)BPin\}$ (**1**) and dissociated DMAP at room temperature on the NMR tube scale. On the preparative scale (Equation 2.1), **1** was isolated as pale yellow crystals in 73% yield and characterised by NMR spectroscopy, IR spectroscopy, elemental analysis and X-ray analysis. It is notable that this reaction is analogous to the reaction of $(Cp^{Ad})Ti(NNPh_2)(py)$ (**2.7**) with 9-BBN.[15]



2.3 **1**

Equation 2.1

The identification of **1** as a hydride borylhydrazido(1–) compound, formed by 1,2-addition of the B–H bond across the Zr–N multiple bond, was initially achieved through inspection of the ^1H and ^{11}B NMR spectra. The ^1H NMR spectrum reveals a single Cp resonance at 5.67 ppm and a single set of resonances attributed to two equivalent phenyl moieties, indicating the compound is C_s symmetric in the solution

phase. A singlet resonance at 5.22 ppm is assigned to the ZrH environment; the ^{11}B NMR spectrum shows a singlet resonance at 26.1 ppm, indicative of a three-coordinate boron environment.[23] This, along with the ZrH resonance, shows that, while the B–H bond has been cleaved to give a hydride borylhydrazido(1–) compound, the reaction has not proceeded further to give N_α–N_β bond cleavage. The fact the chemical shifts of the phenyl environments differ greatly to those of $Cp_2Zr(NCO)(NPh_2)$ (**2.12**) may support this observation.[12]

With the identification of **1** as a hydride borylhydrazide(1–), the isomeric preference of **1** must also be considered and there are three isomers possible for such a species. Either the borylhydrazide(1–) moiety can be κ^1- or κ^2-bound, and in the κ^2-bound state either the α- or β-nitrogen can reside in the central coordination site. While the κ^2-bound isomers would be 18 VE and the κ^1-bound 16 VE, significant strain would be present in the three membered Zr–N–N rings of the former isomers. Diffraction-quality crystals of **1** were grown from a saturated solution of hexane at 4 °C, allowing identification of the isomeric preference of **1** – that shown in Equation 2.1. The solid state structure of **1** is shown in Figure 2.2 and selected bond distances and angles in Table 2.1.

Compound **1** adopts a typical bent metallocene geometry with the β-nitrogen (N(2)) occupying the central coordination site of the zirconocene and H(1), N(1), N(2) and B lying in the equatorial plane. Though there are inherent inaccuracies regarding the location of hydrides in heavy atom structures such structures as **1**, the hydride was located in the Fourier difference map and positionally and isotropically refined. The Zr–H bond distance of 1.80(2) Å falls within the range of previously characterised zirconocene hydrides (1.64(5) – 1.97(8) Å).[61–63] Furthermore, the Zr–N(1) bond distance (2.1200(11) Å) is typical of a Zr–N single bond of three-membered zirconacycles and the lone pair of

the trigonal planar N(1) is oriented such that there is minimal interaction with the three planar bonding orbitals of the zirconocene.[64–66]

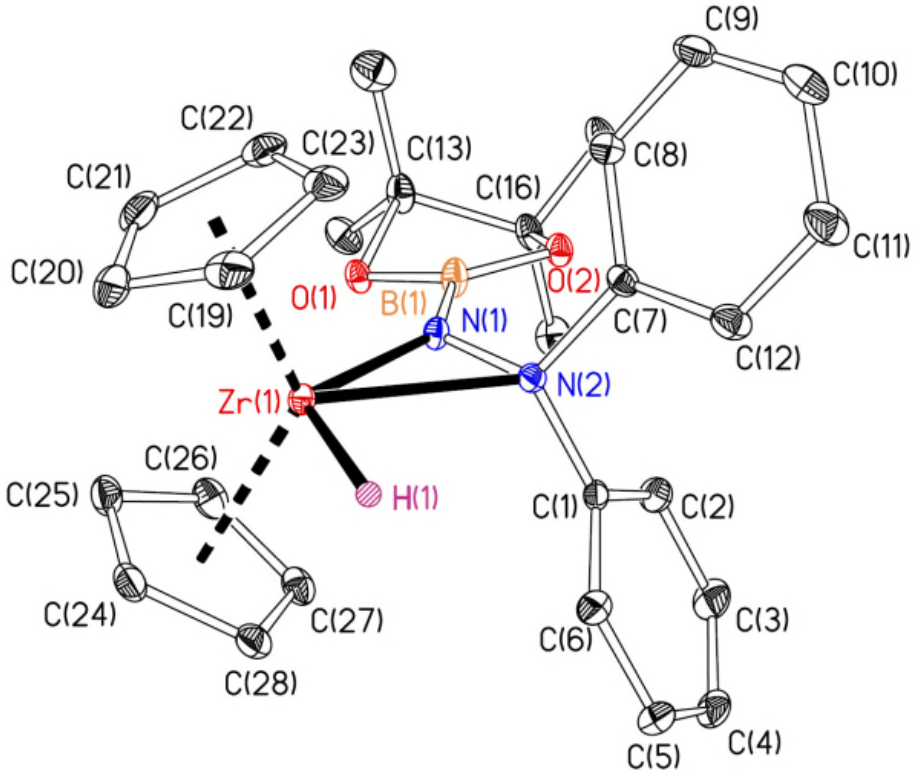


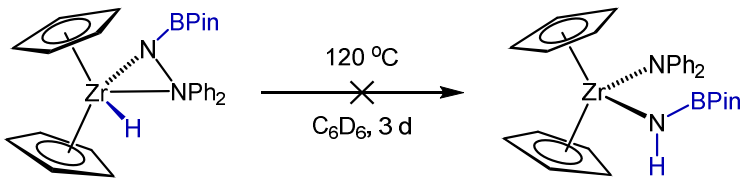
Figure 2.2: Displacement ellipsoid plots (20% probability) of $Cp_2Zr(H)\{N(NPh_2)BPin\}$ (**1**). C–H atoms are omitted for clarity. H(1) is drawn as a sphere of arbitrary radius.

Table 2.1: Selected bond distances (Å) and angles (°) for $Cp_2Zr(H)\{N(NPh_2)BPin\}$ (**1**). $Cp_{cent(1)}$ and $Cp_{cent(2)}$ refer to the computed Cp ring centroids for the "upper" and "lower" Cp rings, respectively, as depicted in Figure 2.2.

Zr(1)-N(1)	2.1200(11)	N(1)-Zr(1)-H(1)	116.8(6)
Zr(1)-N(2)	2.4182(11)	N(1)-Zr(1)-N(2)	35.89(4)
Zr(1)-H(1)	1.80(2)	N(2)-Zr(1)-H(1)	81.1(6)
$Zr(1)-Cp_{cent(1)}$	2.22	Zr(1)-N(1)-N(2)	83.52(7)
$Zr(1)-Cp_{cent(2)}$	2.23	Zr(1)-N(1)-B(1)	148.56(10)
N(1)-N(2)	1.4269(16)	B(1)-N(1)-N(2)	127.87(11)
N(1)-B(1)	1.397(2)	Zr(1)-N(2)-N(1)	60.59(6)
B(1)-O(1)	1.409(3)	N(1)-B(1)-O(1)	117.04(16)
B(1)-O(2)	1.3782(19)	O(1)-B(1)-O(2)	112.76(17)
		O(2)-B(1)-N(1)	128.53(14)
		$Cp_{cent(1)}-Zr(1)-Cp_{cent(2)}$	129.1

Compound **1** is structurally analogous to Cp*Ti{MeC(N^{i}Pr)$_2$}(H){N(NMe$_2$)BPin} (**2.4**, Figure 2.1), containing a κ^2-borylhydrazide(1–) moiety.[23] The two three-membered metallacycles are geometry similar, with the N(1)-M(1)-N(2) angle of **1** slightly smaller than in **2.4** (35.89(4) vs. 39.69(4)°) and the M(1)-N(1)-N(2) slightly larger (83.52(7) vs. 79.58(6)°). These differences are concurrent with the difference between the M–N$_\alpha$ and M–N$_\beta$ bond distances being larger in **1** than in **2.4** (0.2983(16) vs. 0.2509(15) Å), while the N$_\alpha$–N$_\beta$ bond distances are similar in both (1.4269(16) vs. 1.4399(14) Å).

It is notable that while the reactions of **2.3** with CO (to give **2.12**, Scheme 2.2) and Ti(N$_2^{iPr}$N^{Me})(NNPh$_2$)(py) with 9-BBN (to give **2.5**, Figure 2.1) both gave reductive N$_\alpha$–N$_\beta$ bond cleavage at room temperature, **1** does not proceed to undergo reductive N$_\alpha$–N$_\beta$ bond cleavage, similar to the titanocene analogue **2.8**.[12,15,22] Compound **1** is stable up to 80 °C and forms an intractable mixture upon heating to 120 °C (Equation 2.2). Despite this, the DFT computed relative free energy of the product of reductive N$_\alpha$–N$_\beta$ bond cleavage Cp$_2$Zr{N(H)BPin}(NPh$_2$) (**1_cleave**) is –45.0 kcal mol^{-1} with respect to **1**. This indicates that, though strongly thermodynamically favourable, the barrier to cleavage is inaccessible. Given these observations, the full mechanism of the reaction of **2.3** with HBPin to give **1** was calculated by DFT (Figure 2.3). Additionally, the mechanism of the inaccessible hydride transfer to N$_\alpha$ and reductive N$_\alpha$–N$_\beta$ bond cleavage of **1** to give **1_cleave** *via* **Int3_B** and **Int4_B** is also included in Figure 2.3.



1 **1_cleave**

Equation 2.2

As is common for reactions of base-stabilised hydrazido and imido compounds with small molecules such as boranes, the reaction proceeds *via* dissociation of DMAP to form **2.3_int**, with a barrier of 17.1 kcal mol^{-1}.[22,23,29,36,39,67,68] Notably, addition of HBPin to a C_6D_6 solution of DMAP reveals a shift in the ^{11}B NMR resonance of HBPin to a lower chemical shift, indicating that an equilibrium between a DMAP·HBPin adduct and the free molecules is established and the coordination of DMAP to HBPin is fluxional on the NMR timescale. As such, HBPin may thermodynamically aid dissociation of DMAP from **2.3**.

1,2-Addition of B–H to the Zr=N$_\alpha$ bond is facile, proceeding *via* the adduct **Int2_B** (G_{rel} = 4.1 kcal mol^{-1}) and **TS1_B** (4.3 kcal mol^{-1}). The Zr–H distance of **Int2_B** is 1.914 Å, compared to 1.80(2) Å in the solid state structure of **1**, showing significant interaction between zirconium and the hydride. Meanwhile, the B–H bond distance is significantly longer than that calculated for HBPin (1.453 Å *vs.* 1.190 Å), showing a large degree of bond breaking. Accordingly, the N–B distance is relatively short at 1.580 Å, with significant lengthening of the Zr=N$_\alpha$ bond (1.980 Å vs. 1.874 Å in **2.3_int**). Such a short N$_\alpha$–E (E = B or Si) is not calculated for **Int2_Si** (2.564 Å, see Section 2.3). This shows relatively strong donation from the $Cp_2ZrNNPh_2$ HOMO into the 2p orbital of the boron. Furthermore, these parameters are in line with those found for the intermediate adduct on the pathway of the reaction of Cp*Ti{MeC(N^{i}Pr$_2$)$_2$}(NNCPh$_2$) with HBPin.[23]

Subsequent to 1,2-addition of HBPin, three possible conformations of the hydride borylhydrazide(1–) can be directly formed: **1**, a κ^2-borylhydrazide(1–) with N$_\beta$ occupying the central coordination site; **Int4_B**, a κ^2-borylhydrazide(1–) with N$_\alpha$ occupying the central coordination site, or; **Int3_B**, a κ^1-borylhydrazide(1–) in which the lone pair of the α-nitrogen lies in the plane of the zirconocene. Their free energies are calculated to be –16.6, –11.5 and –10.0 kcal mol^{-1}, respectively, and **Int3_B** is found to be the

first-formed product from **TS1_B**. The free energy barrier between the putative first-formed intermediate **Int3_B** and **1** is calculated to be just 1.0 kcal mol^{-1}, consistent with no such intermediate being observed upon following the reaction by ^{1}H NMR spectroscopy. The transition state towards formation of **Int4_B**, **TS3_B**, lies 1.3 kcal mol^{-1} higher in energy than **TS2_B**, and **Int4_B** is only found on the reaction pathway towards hydride transfer and reductive N_α–N_β bond cleavage.

Interrogating the energies of **1** and **Int4_B**, the central coordination site of zirconocene is known to be less sterically hindered than the outer two sites,[69] and was also calculated to be a slightly weaker coordination site. Therefore, to probe whether the 6.6 kcal mol^{-1} energy difference between **1** and **Int4_B** is a steric or electronic phenomenon, the geometries and energies of sterically-reduced model systems, replacing the phenyl groups with hydrogen atoms and the pinacol moiety with $–OCH_2CH_2O–$, were calculated. The two isomers were shown to have similar energies (ΔE = 1.4 kcal mol^{-1}), indicating the origin of the energetic difference is primarily steric in nature.

Overall on the reaction pathway between **2.3** and **1**, DMAP dissociation is rate determining and subsequent steps are relatively facile. Such facile B–H activation of HBPin has also been found for reactions with Cp*Ti{$MeC(N^iPr_2)_2$}($NNCPh_2$) and Cp*Ti{$MeC(N^iPr_2)_2$}($NNMe_2$).[23,70]

Attention is now turned to the pathway of hydride transfer to N_α and reductive N_α–N_β bond cleavage of **1** to give the non-observed **1_cleave**. Initially, **1** isomerises to form **Int4_B** *via* **Int3_B** with a barrier of 7.4 kcal mol^{-1}. Of the three isomers of **1**, only **Int4_B** pertains the correct geometry, with the hydride adjacent to N_α and N_β coordinated to zirconium, to allow for the reaction to take place and such geometries are invariably found as intermediates on analogous reaction pathways.[22,23,36,39,68] Subsequent hydride

transfer and reductive bond cleavage occurs with a thermally inaccessible energy barrier of 39.3 kcal mol^{-1} relative to **1**, consistent with the reaction not being observed upon heating to 120 °C, despite the final product **1_cleave** lying 45.0 kcal mol^{-1} lower in energy than **1** and the transition state **TS4_B** having a relative energy of 22.7 kcal mol^{-1} with respect to **2.3** and HBPin.

An identical phenomenon was calculated for the reaction of Cp*Ti{$MeC(N^iPr_2)_2$}($NNMe_2$) with HBPin.[23,70] While the relative energy of the transition state for reductive N_α–N_β bond cleavage was calculated to be just 20.6 kcal mol^{-1}, with respect to the starting compounds, the relative energy of the 1,2-addition product, Cp*Ti{$MeC(N^iPr_2)_2$}(H)($N(NMe_2)BPin$) (**2.4**), was calculated to be –16.7 kcal mol^{-1}, giving an inaccessible barrier of 37.3 kcal mol^{-1}. These observations show the stability of 1,2-addition product is a key factor in rendering reductive N_α–N_β bond cleavage inaccessible. Comparisons will be made to the reaction of **2.3** with CO later in this Chapter (Section 2.6).

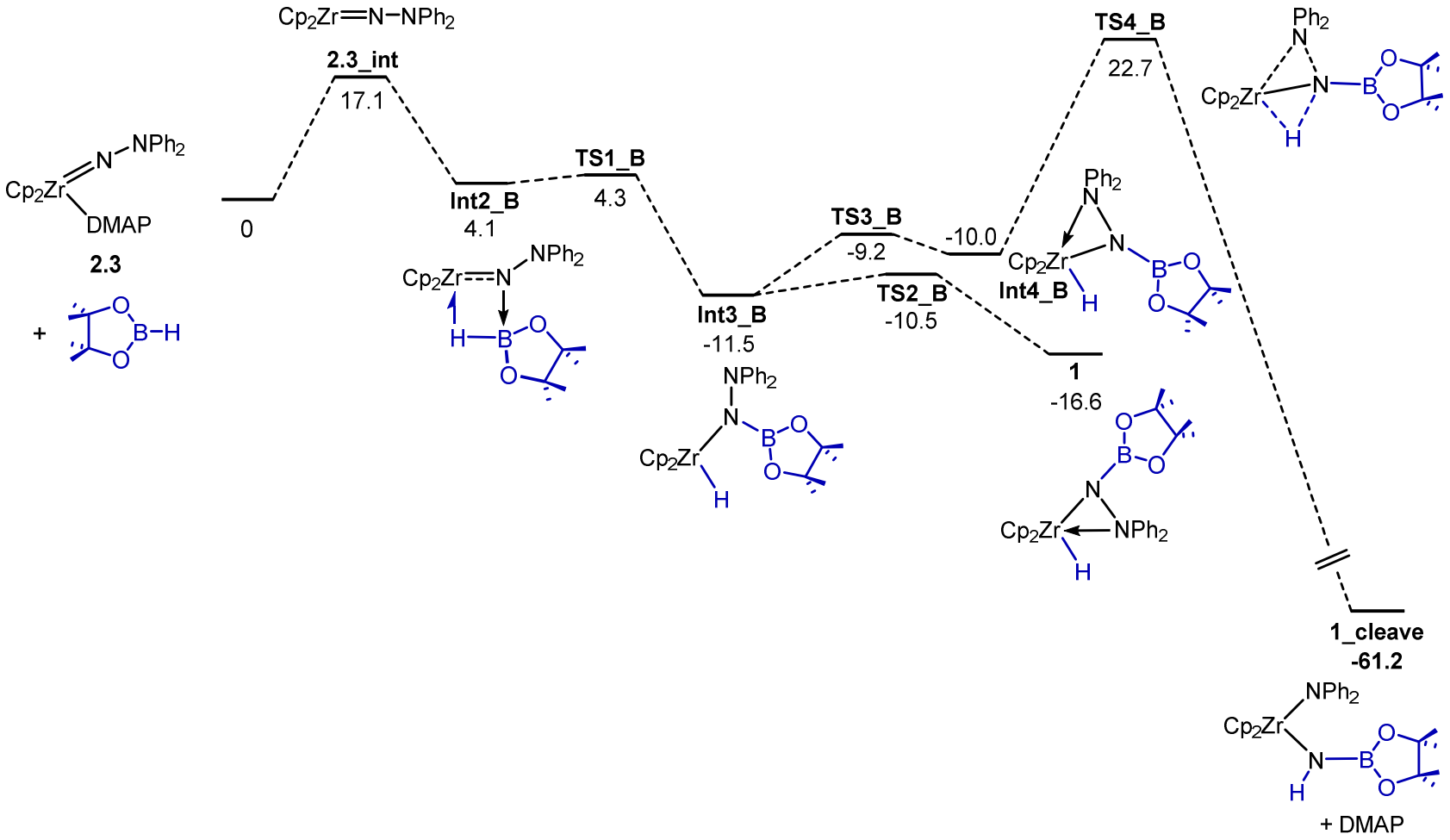
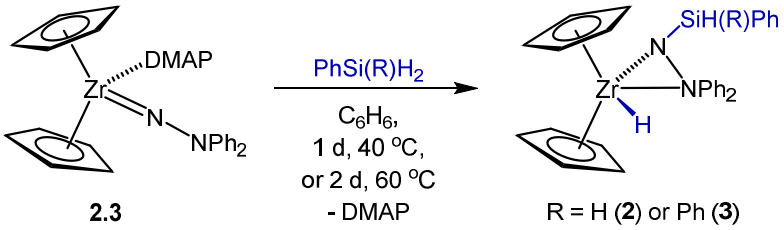


Figure 2.3: DFT (B3PW91/Def2-TZVP/d3-bj/SCRF) mechanism for the reaction of **2.3** with HBPin forming **1** and DMAP, as well as the inaccessible reaction of **1** to give **1_cleave**. Gibbs free energies (kcal mol^{-1}, T = 298.15 K) for minima, maxima and transition states (labelled **Intx_B** or **TSx_B**) are shown in bold relative to **2.3** and HBPin.

2.3 Reactions of $Cp_2Zr(NNPh_2)(DMAP)$ (2.3) with silanes

On the NMR tube scale, stoichiometric reactions of $Cp_2Zr(NNPh_2)(DMAP)$ (**2.3**) with several silanes, including $PhSiH_3$, Ph_2SiH_2 and $^nBuSiH_3$, in C_6D_6, gave quantitative conversion to hydride silylhydrazido(1–) compounds of the type $Cp_2Zr(H)\{N(NPh_2)SiHRR'\}$, formed by 1,2-addition of the Si–H bond across the Zr–N_α multiple bond. Only reactions of **2.3** with $PhSiH_3$ and Ph_2SiH_2 were carried out on the preparative scale, where mixtures of **2.3** with $PhSiH_3$ or Ph_2SiH_2 were stirred in benzene for 1 day at 40 °C or 2 days at 60 °C, respectively. $Cp_2Zr(H)\{N(NPh_2)SiH_2Ph\}$ (**2**) and $Cp_2Zr(H)\{N(NPh_2)SiHPh_2\}$ (**3**) were isolated as yellow powders with one equivalent DMAP in 65 and 61% yield, respectively (Equation 2.3). Both compounds **2** and **3** were characterised by NMR spectroscopy, IR spectroscopy and X-ray analysis.



2.3 R = H (**2**) or Ph (**3**)

Equation 2.3

The increase in temperature and time required for the reaction of **2.3** with Ph_2SiH_2 compared to with $PhSiH_3$ is attributed to the increased steric bulk of the secondary silane. Such an increase in steric bulk presumably increases the energy barrier of addition to the Zr=N_α bond. Indeed, no reaction was observed upon addition of the tertiary silane Et_3SiH to **2.3**, even in excess and at 80 °C. Such a phenomenon has previously been observed with the addition of Ph_2SiH_2 and Et_3SiH to $Cp^*Ti\{MeC(N^iPr)_2\}(NNMe_2)$, where an equilibrium was observed in the case of Ph_2SiH_2 and no reaction was observed for Et_3SiH.[20,45] It can also be noted that exhaustive attempts were made to remove DMAP by crystallisation, sublimation and washing with hexane and pentane, though were

unsuccessful and led to incomplete removal of DMAP and decomposition of the target compounds.

The ^{1}H, $^{13}C\{^{1}H\}$ and ^{29}Si NMR spectra of **2** and **3** are consistent with the proposed structures shown in Equation 2.3, which have been confirmed by X-ray crystallography (*vide infra*). Similar to **1**, the ^{1}H NMR spectrum of both **2** (Figure 2.4, top) and **3** reveal resonances at 5.03 and 5.02 ppm, respectively, attributed to ZrH environments. Furthermore, the phenyl resonances of both compounds appear at similar chemical shifts to those of **1**, indicating coordinated NPh_2 moieties. The SiH_2 and SiH environments of **2** and **3** appear at 5.53 and 6.25 ppm, and ^{29}Si-^{1}H gradient experiments reveal one-bond interactions between the singlets at 5.53 and 6.25 ppm and ^{29}Si resonances at –32.9 ($^{1}J_{SiH}$ = 202 Hz) and –20.7 ppm ($^{1}J_{SiH}$ = 201 Hz), respectively. This large $^{1}J_{SiH}$ coupling (>200 Hz) indicates no interaction of the SiH bonds with Zr, as was seen by Berry and co-workers, who reported a $^{1}J_{SiH}$ coupling of 113 Hz for a zirconocene silylamido compound containing a β-Si–H···Zr agostic interaction, and as is observed later in this Chapter for similar β-agostic silylamido compounds.[53] The synthesis of $Cp_2Zr(D)\{N(NPh_2)SiD_2Ph\}$ (**2-*d*$_3$**) confirms the assignments of the ZrH and SiH_2 resonances of **2** (Figure 2.4, bottom).

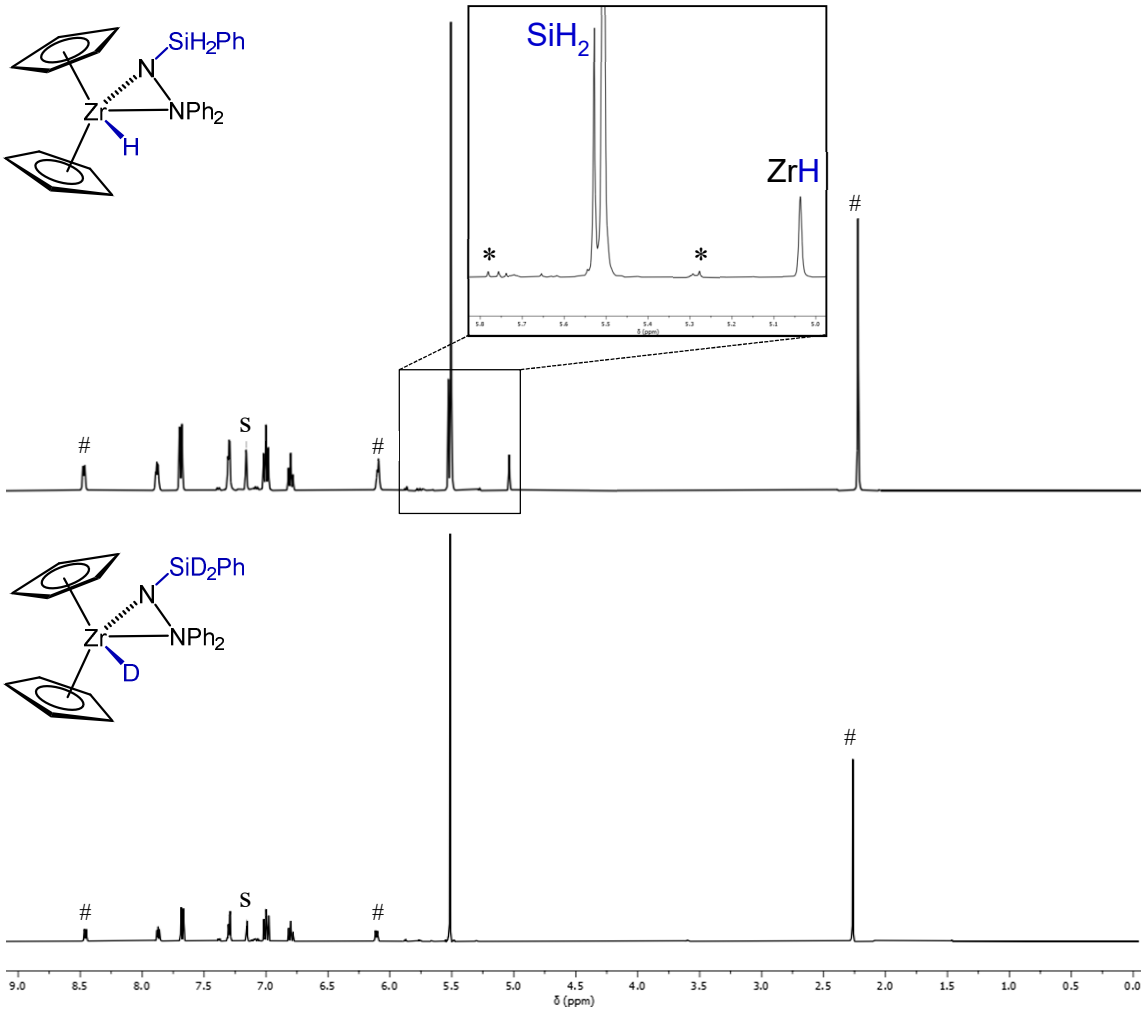


Figure 2.4: ^{1}H NMR spectra (C_6D_6, 400.1 MHz, 298 K) of $Cp_2Zr(H)\{N(NPh_2)SiH_2Ph\}$ (**2,** top) and $Cp_2Zr(D)\{N(NPh_2)SiD_2Ph\}$ (**2-*d*$_3$**, bottom) with ZrH and SiH, with ^{29}Si satellites (*), resonances enlarged. (# indicates resonances attributable to DMAP).

Along with the NMR spectra of **2** and **3**, the solid state IR spectra (Nujol mull) of both are consistent with hydride silylhydrazido(1–) compounds, exhibiting bands at 1584 and 1586 cm^{-1}, assigned to ν(Zr–H), and at 2110 and 2072 (symmetric and antisymmetric combinations), and 2125 cm^{-1}, assigned to ν(Si–H). These Si–H stretches are consistent with terminal Si–H stretches (ν(Si–H$_t$)) rather than agostic Si–H stretches (ν(Si–H$_b$)), which appear at much lower stretching frequencies due to the weakening of the Si–H bond.[53,58]

Diffraction-quality crystals of **2** and **3** were grown from saturated solutions of benzene at room temperature, confirming the connectivity shown in Equation 2.3. The solid state

structures of **2** and **3** are shown in Figure 2.5 and selected bond distances and angles in Table 2.2. Both **2** and **3** are structurally analogous to **1**, adopting bent metallocene geometries with the β-nitrogens of the κ^2-silylhydrazide(1–) moieties occupying the central coordination site of the zirconocene. While the parameters of both compounds three-membered zirconacycles are similar to that of **1**, Si(1) of **2** lies slightly out of the plane of the zirconocene in which Zr(1), N(1), N(2) and H(1) lie. Indeed, the angles about N(1) sum to 352.7(9)° in **2** (vs. 359.4(2) and 360.0(3)° for **3** and **1**, respectively). Both the Zr–H and Si–H bond distances of **3** lie within the typical ranges for such bonds, while those of **2** were subject to bond distance restraints.[63]

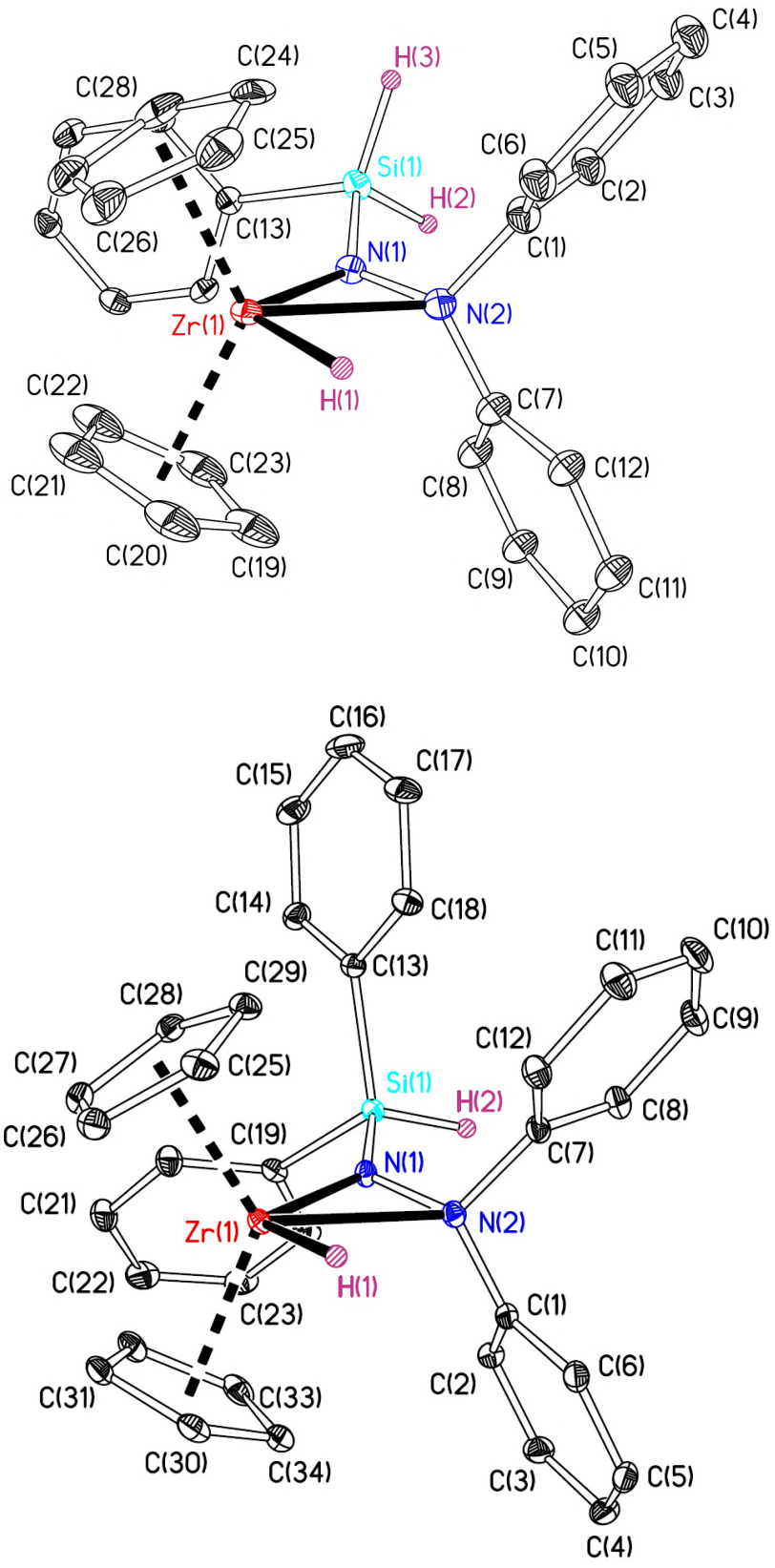


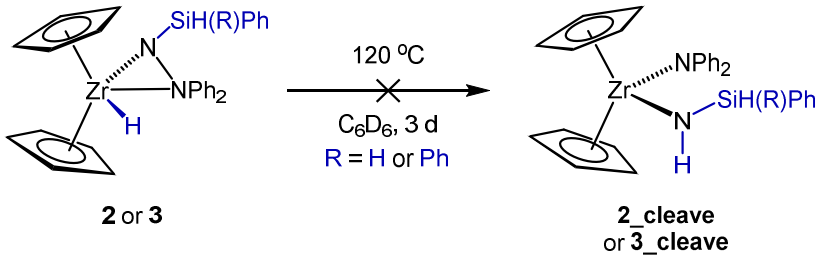
Figure 2.5: Displacement ellipsoid plots (20% probability) of $Cp_2Zr(H)\{N(NPh_2)SiH_2Ph\}$ (**2**, top) and $Cp_2Zr(H)\{N(NPh_2)SiHPh_2\}$ (**3**, bottom). C–H atoms are omitted for clarity and other H atoms are drawn as spheres of an arbitrary radius.

Table 2.2: Selected bond distances (Å) and angles (°) for $Cp_2Zr(H)\{N(NPh_2)SiH_2Ph\}$ (**2**) and $Cp_2Zr(H)\{N(NPh_2)SiHPh_2\}$ (**3**). $Cp_{cent(1)}$ and $Cp_{cent(2)}$ refer to the computed Cp ring centroids for the "upper" and "lower" Cp rings, respectively, as depicted in Figure 2.5.

Parameter	**2**	**3**
Zr(1)-N(1)	2.122(4)	2.1227(11)
Zr(1)-N(2)	2.374(5)	2.4217(11)
Zr(1)-H(1)	1.849(5)	1.91(2)
$Zr(1)-Cp_{cent(1)}$	2.23	2.25
$Zr(1)-Cp_{cent(2)}$	2.23	2.24
N(1)-N(2)	1.420(6)	1.4393(15)
N(1)-Si(1)	1.728(4)	1.7178(11)
Si(1)-H(2)	1.400(5)	1.375(19)
Si(1)-H(3)	1.399(5)	-
N(1)-Zr(1)-H(1)	109.9(18)	115.7(6)
N(1)-Zr(1)-N(2)	36.28(16)	36.18(4)
N(2)-Zr(1)-H(1)	73.6(18)	80.4(6)
Zr(1)-N(1)-N(2)	81.6(3)	83.30(6)
Zr(1)-N(1)-Si(1)	142.3(3)	146.34(6)
Si(1)-N(1)-N(2)	128.8(3)	129.78(8)
Zr(1)-N(2)-N(1)	62.1(2)	60.52(6)
$Cp_{cent(1)}$-Zr(1)-$Cp_{cent(2}$	127.1	126.5

The reactions of **2.3** with primary and secondary silanes are analogous to those reactions of $Cp^*Ti\{MeC(N^iPr)_2\}(NNMe_2)$ with primary silanes, including $PhSiH_3$, and the reaction of **1** with HBPin (Equation 2.1).[20] In contrast, the reactions differ from the reactions of $Ti(N_2^{iPr}N^{Me})(NNPh_2)(py)$ with primary silanes, including $PhSiH_3$, in which reductive N_α–N_β bond cleavage is observed.[22] Compounds **2** and **3** are not observed to undergo reductive N_α–N_β bond cleavage, even with extensive heating up to 120 °C (Equation 2.4). This is despite the fact that the related N_α–N_β bond cleavage product of **2**, **2_cleave**, is calculated to have a relative free energy of –48.1 kcal mol^{-1}. To probe this

further, the energy barrier and mechanism for reductive N_α–N_β bond cleavage of **2**, as well as for the formation of **2** from **2.3** and $PhSiH_3$, was calculated by DFT (Figure 2.6).



2 or **3** — **2_cleave** or **3_cleave**

Equation 2.4

The reaction of **2.3** with $PhSiH_3$ proceeds in an identical manner to that with HBPin. Initially, DMAP dissociates from **2.3** to leave **2.3_int** (G_{rel} = 17.1 kcal mol^{-1}). 1,2-addition of the Si–H bond then proceeds *via* the adduct **Int2_Si**, which has a significantly higher relative energy than the equivalent adduct in the HBPin reaction (G_{rel} = 12.7 *vs.* 4.1 kcal mol^{-1}). In **Int2_Si**, the phenyl of the silane is positioned *trans* to N_α, preventing steric repulsion with the phenyl groups of the hydrazide.

The bonding parameters of **Int2_Si** are similar to those observed previously.[22] The Zr–H distance of 1.934 Å is only slightly longer than in **2** (1.849(5) Å) and the bridging Si–H distance is 0.119 Å longer than the terminal Si–H distances (1.603 *vs.* 1.484 Å). It can also be noted that whilst the silicon has undergone a rehybridization to accommodate donation of the N_α lone pair, the N_α–Si is significantly longer than in **2** (2.564 *vs.* 1.728(4) Å, respectively). This implies that the silane is weakly bound, unlike for HBPin in its reaction with **2.3** which contains a relatively short N_α–B distance 1.580 Å in **Int2_B** (*cf.* 1.397(2) Å in **1**). This is consistent with silicon being a poorer acceptor than boron and so **Int2_B** being lower in energy than **Int2_Si**.

From adduct **Int2_Si**, the barrier to 1,2-addition of the Si–H bond is only 2.5 kcal mol^{-1} and the first-formed product is found to be the κ^2-silylhydrazido(1–) compound **Int3_Si** (G_{rel} = –3.4 kcal mol^{-1}), which contains N_α in the central coordination site. Rotation about

the Zr–N_α bond then gives the κ^1-silylhydrazido(1–) compound **Int4_Si** (G_{rel} = –4.7 kcal mol^{-1}) with a barrier of 0.5 kcal mol^{-1}. Further rotation gives the experimentally observed and final product **2** (G_{rel} = –7.5 kcal mol^{-1}) with a barrier of 1.9 kcal mol^{-1}. This is in contrast to the formation of **1**, which is calculated to proceed *via* only the κ^1-borylhdrazido(1–) compound **Int3_B**.

Looking next at the hydride transfer and reductive N_α–N_β bond cleavage of **2** to give **2_cleave**, **2** initially undergoes isomerisation to **Int3_Si** *via* **Int4_Si**. With the hydride adjacent to N_α, hydride transfer and reductive N_α–N_β bond cleavage would proceed with an inaccessible barrier of 35.6 kcal mol^{-1}, forming the highly thermodynamically favourable cleavage product **2_cleave** (ΔG = –48.1 kcal mol^{-1}). This contrasts with the 17.3 kcal mol^{-1} barrier calculated for the conversion of $Ti(N_2^{iPr}N^{Me})(H)\{N(NPh_2)SiH_2Ph\}$ to $Ti(N_2^{iPr}N^{Me})\{N(H)SiH_2Ph\}(NPh_2)$.[22] One contributing factor to the high, inaccessible barrier calculated for the conversion of **2** to **2_cleave** is the isomeric rearrangement required of **2** prior to hydride migration. Another factor could be the contrasting geometries and sizes of the Zr and Ti centres rendering orbital overlap poorer in the **TS4_Si** than the transition state of the $Ti(N_2^{iPr}N^{Me})$ system and required displacements of moieties larger.

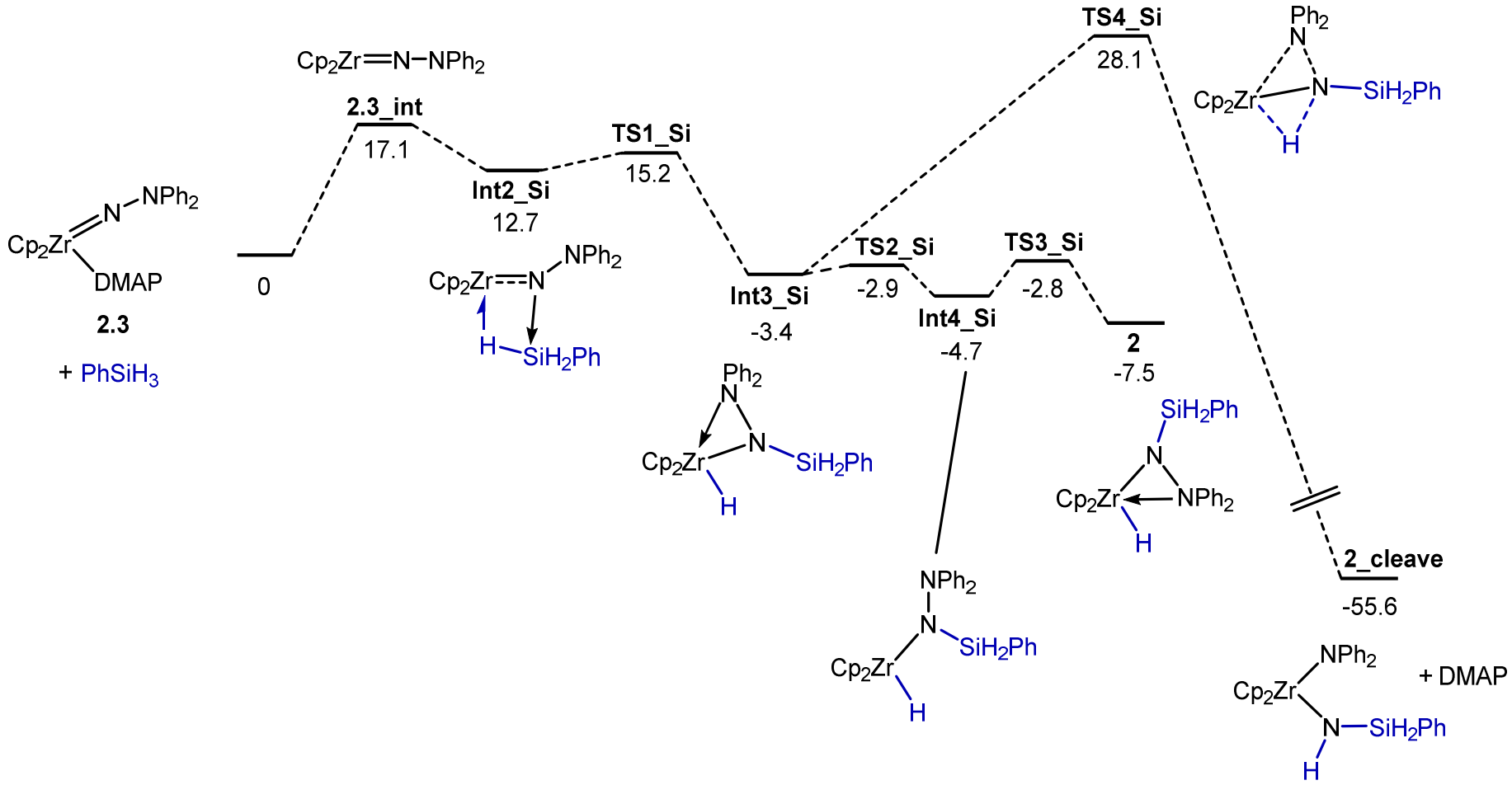
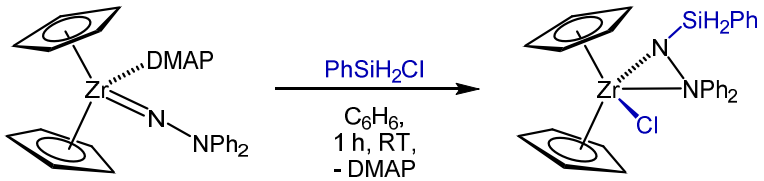


Figure 2.6: DFT (B3PW91/Def2-TZVP/d3-bj/SCRF) mechanism for the reaction of **2.3** with $PhSiH_3$ forming **2** and DMAP, as well as the inaccessible reaction of **2** to give **2_cleave**. Gibbs free energies (kcal mol^{-1}, T = 298.15 K) for minima, maxima and transition states (labelled **Intx_Si** or **TSx_Si**) are shown in bold relative to **2.3** and $PhSiH_3$.

2.4 Reaction of $Cp_2Zr(NNPh_2)(DMAP)$ (2.3) with chlorophenylsilane

Stoichiometric reaction of **2.3** with $PhSiH_2Cl$ gave quantitative conversion to the chloride silylhydrazido(1–) compound $Cp_2Zr(Cl)\{N(NPh_2)SiH_2Ph\}$ (**4**). Compound **4**, the chloride analogue of the hydride **2**, was isolated with one equivalent DMAP as an orange powder in 71% yield on the preparative scale and was characterised by NMR spectroscopy, IR spectroscopy and X-ray analysis (Equation 2.5). The ^1H NMR and IR spectra of **4** are similar to that of **2**, except for the absence of a resonance/band attributable to a ZrH environment. The SiH_2 resonance appears at 5.42 ppm (*cf.* 5.53 ppm for **2**) and the IR spectrum exhibits two bands at 2142 and 2102 cm^{-1} for the symmetric and antisymmetric ν(Si–H) modes, supporting the formation of a chloride. The ^{29}Si NMR resonance of **4** is also very similar to that of **2** (–29.9 *vs*. –32.9 ppm) with comparable $^1J_{SiH}$ couplings (208 *vs*. 202 Hz).



2.3 **4**

Equation 2.5

Diffraction-quality crystals of **4** were grown from a saturated solution of benzene at room temperature, confirming the connectivity shown in Equation 2.5. The solid state structure of **4** is shown in Figure 2.7 and selected bond distances and angles in Table 2.3. The molecular structure of **4** is similar to that of compounds **1**, **2** and **3** (Figure 2.2 and Figure 2.5). As with these complexes N_β occupies the central coordination site of the zirconocene, presumably due mainly to steric reasons, as was calculated for **1**. The Zr–N(1) bond distance of **4** is slightly longer than in **1**, **2** and **3**, which may be due to π-donation of the chloride ligand to the same orbital on zirconium as the nitrogen bonds

through – a similar phenomenon is observed later in this Chapter (see Section 2.7.3) and has been discussed in the literature.[53] Also, the N(1)–Zr–X(1) (X = H or Cl) angle is significantly larger in **4** than **2** (118.32(6)° vs. 109.9(18)°). The opening of this angle would lead to poorer orbital overlap for N(1) and so could cause the increase in bond distance. As with **2**, Si(1) lies out of plane of the zirconocene in which Zr(1), N(1), N(2) and Cl(1) lie, and the angles about N(1) sum to 345.2(4)° (*cf.* 352.7(9)° in **2**). The origin of this greater deviation from trigonal planar exhibited by N(1) of **4** than of **2** could be attributed to poorer π-donation from N(1) to the metal centre, due to the competitive chloride, rendering a planar orientation about N(1) less stable.

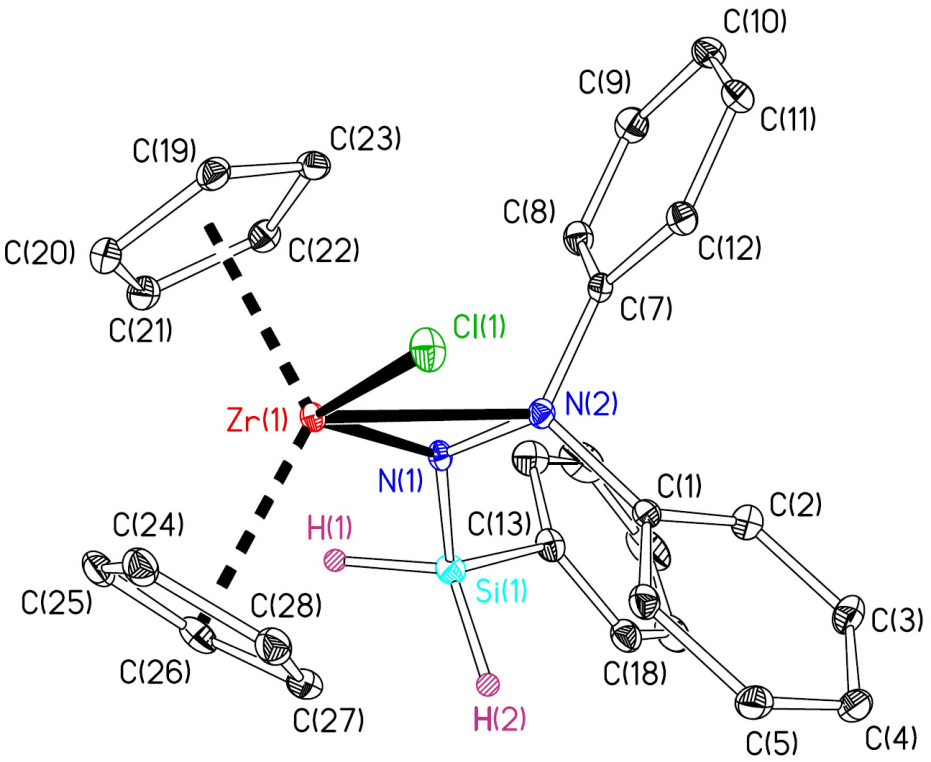


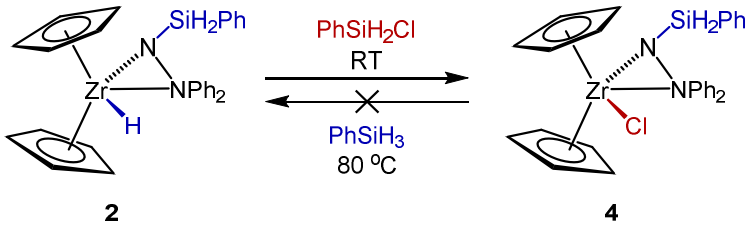
Figure 2.7: Displacement ellipsoid plot (20% probability) of $Cp_2Zr(Cl)\{N(NPh_2)SiH_2Ph\}$ (**4**). C–H atoms are omitted for clarity. H(1) and H(2) are drawn as spheres of an arbitrary radius.

Table 2.3: Selected bond distances (Å) and angles (°) for $Cp_2Zr(Cl)\{N(NPh_2)SiH_2Ph\}$ (**4**). $Cp_{cent(1)}$ and $Cp_{cent(2)}$ refer to the computed Cp ring centroids for the "upper" and "lower" Cp rings, respectively, as depicted in Figure 2.7.

Zr(1)-N(1)	2.142(2)	N(1)-Zr(1)-Cl(1)	118.32(6)
Zr(1)-N(2)	2.396(6)	N(1)-Zr(1)-N(2)	36.24(9)
Zr(1)-Cl(1)	2.5450(7)	N(2)-Zr(1)-Cl(1)	82.29(6)
$Zr(1)-Cp_{cent(1)}$	2.24	Zr(1)-N(1)-N(2)	81.58(13)
$Zr(1)-Cp_{cent(2)}$	2.26	Zr(1)-N(1)-Si(1)	136.10(12)
N(1)-N(2)	1.432(3)	Si(1)-N(1)-N(2)	127.51(17)
N(1)-Si(1)	1.730(2)	Zr(1)-N(2)-N(1)	62.18(12)
Si(1)-H(2)	1.36(4)	$Cp_{cent(1)}$-Zr(1)-$Cp_{cent(2}$	124.6
Si(1)-H(3)	1.37(3)		

No evidence of the hydride silylhydrazido(1–) compound $Cp_2Zr(H)\{N(NPh_2)SiH(Cl)Ph\}$, which would form from 1,2-addition of the Si–H bond across the Zr–N_α multiple bond, was found upon following the reaction by ^{1}H NMR spectroscopy. Furthermore, **4** is immediately formed, by Si–Cl/Zr–H σ-bond metathesis, upon reaction of **2** with $PhSiH_2Cl$ (Equation 2.6, this reaction will be discussed in more detail in Chapter 4, Section 4.3). Meanwhile, $PhSiH_3$ does not react with **4**, even when heated to 80 °C. Consistent with this, the DFT computed Δ_rG values for formation of **4** and **2** from **2.3** are –25.4 and –7.5 kcal mol^{-1}, leading to Δ_rG(**4** + $PhSiH_3$ → **2** + $PhSiH_2Cl$) = –17.9 kcal mol^{-1} at room temperature and –15.9 kcal mol^{-1} at 80 °C. It is notable that chlorotrimethylsilane elimination from transition metal chloride silylamide complexes has been employed as a synthetic strategy towards imido compounds, but no evidence of chlorosilane elimination is found here, which is unsurprising given the magnitude of Δ_rG(**2.3** + $PhSiH_2Cl$ → **4** + DMAP).[9,71–73] This establishes overall Si–Cl addition to Zr=$NNPh_2$ as thermodynamically preferable over Si–H addition, as has been observed

previously for reactions of titanium hydrazides and Group 5 and 6 imides with halosilanes.[20,45,48–50,74,75]



2 **4**

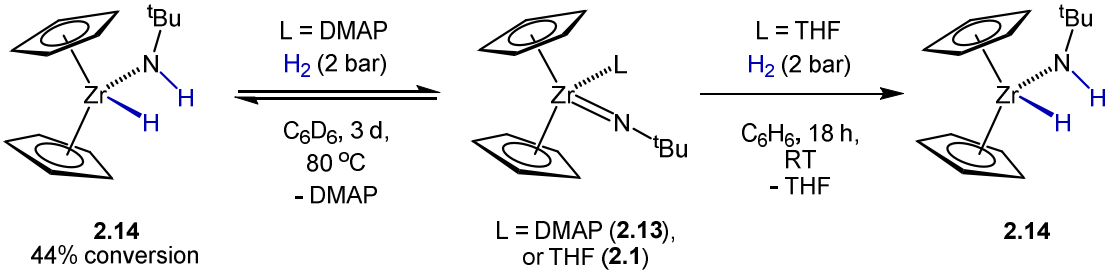
Equation 2.6

It can also be noted that the reaction of **2.3** with $PhSiH_2Cl$ proceeds much faster than with $PhSiH_3$, implying that Si–Cl addition is kinetically favoured. However, it could be the case that Si–H addition occurs first to give $Cp_2Zr(H)\{N(NPh_2)SiH(Cl)Ph\}$, followed by rapid conversion to **4**. This is observed for the reaction of $PhSiH_2Cl$ with **2.1** (see Section 2.7.3), but does not account for the increase in rate of reaction between $PhSiH_2Cl$ and $PhSiH_3$. Therefore, it follows that 1,2-addition of the Si–Cl bond across the Zr–N_α multiple bond does occur and is both kinetically and thermodynamically favoured over Si–H addition.

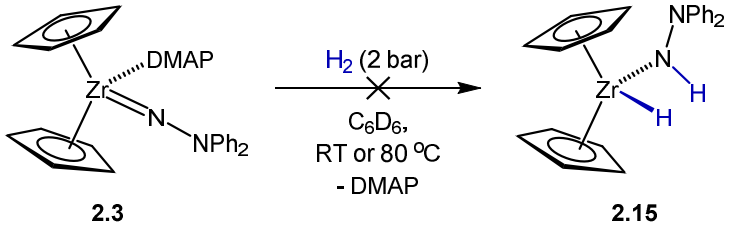
In the presence of excess chlorophenylsilane, the Zr–N bond of the amidinate ligand of $Cp^*Ti\{MeC(N^iPr)_2\}(Cl)\{N(NMe_2)SiH_2Ph\}$ was found to react with the Si–Cl bond of excess silane to form the dichloride silylhydrazide(1–) $Cp^*Ti\{N(NMe_2)SiH_2Ph\}Cl_2$.[45] Similarly, reactions of dichlorosilanes formed dichloride complexes and chlorosilanes activated across the Zr–N bonds of the diamideamine ligand of $Ti(N_2{}^{iPr}N^{Me})(NNPh_2)(py)$.[76] In contrast and as expected due to the relatively inert Cp–Zr coordination, addition of excess chlorophenylsilane to **4** gave no reaction. Reactions of **2.3** with $Ph_2MeSiCl$, $PhSiCl_3$, $MeSiCl_3$, $SiCl_4$ and $PhSiH_2F$ were also attempted, but gave only intractable mixtures.

2.5 Reactions of $Cp_2Zr(NNPh_2)(DMAP)$ (2.3), $Cp_2Zr(N^tBu)(THF)$ (2.1) and $Cp_2Zr(N^tBu)(DMAP)$ (2.13) with H_2

Following the reactions of silanes, which are often studied as dihydrogen mimics, with **2.3**, the reaction with H_2 was attempted. Several Group 4 complexes containing metal-ligand multiple bonds have been reported to undergo H–H bond addition, including the imido complex $Cp_2Zr(N^tBu)(THF)$ (**2.1**, Scheme 2.1).[40] However, there have been no reported cases of dihydrogen addition to Group 4 hydrazido complexes, with both $Cp^*Ti\{MeC(N^iPr)_2\}(NNMe_2)$ and $Ti(N_2^{iPr}N^{Me})(NNPh_2)(py)$ proving inert to dihydrogen.[45,76] Consistent with this, reaction of **2.3** with 1 bar overpressure H_2 gave no reaction (Equation 2.7).



Scheme 2.1: Reactions of zirconocene imides **2.1** and **2.13** with dihydrogen.[40]



Equation 2.7

Despite a lack of reaction, the DFT mechanism was calculated and is shown in Figure 2.8. As with previous reactions, DMAP dissociates initially to leave the base-free hydrazide $[Cp_2ZrNNPh_2]$. The formation of dihydrogen σ-adduct **Int2_H** leads to an incresae in free energy (G_{rel} = 19.1 kcal mol^{-1}) and subsequent H–H addition, *via* **TS1_H**, is further "uphill" in free energy (23.9 kcal mol^{-1}). This is attributed to the lack of acceptor

ability of H_2, resulting in reduced stabilisation upon coordination of H_2 *vs.* boranes or silanes. Although formation of **2.15** is slightly thermodynamically favourable according to DFT, the calculated Δ_rG (–1.4 kcal mol^{-1}) is at the limits of accuracy of the model, rationalising why no reaction is observed. Furthermore, Δ_rG for both **2.15** and **Int3_H_iso** is less exergonic than for **Int4_Si** and **2**, respectively, most likely due to the strong H–H bond, consistent with experimental observation. As for hydride transfer and reductive N_α–N_β bond cleavage, the reaction is again thermodynamically very favourable (ΔG = –45.1 kcal mol^{-1}), however is thermally inaccessible with a free energy of activation of 40.3 kcal mol^{-1} from **2.15**.

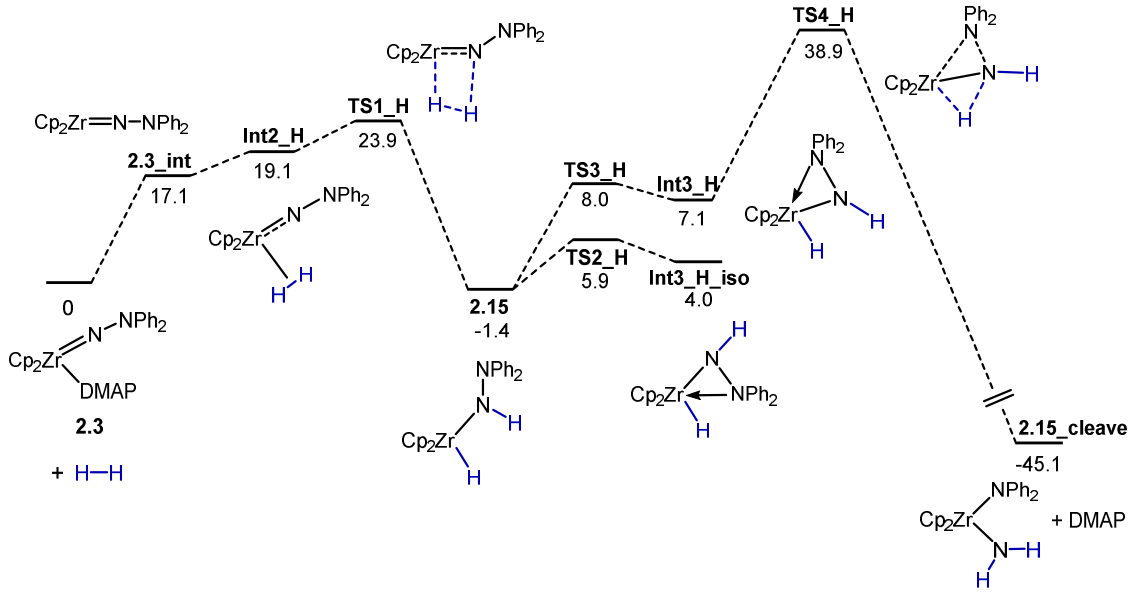
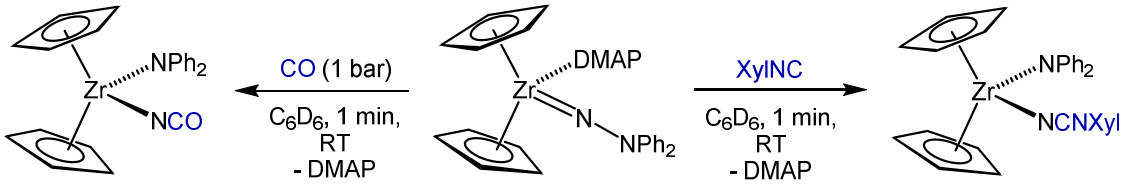


Figure 2.8: DFT (B3PW91/Def2-TZVP/d3-bj/SCRF) mechanism for the reaction of **2.3** with H_2 forming **2.15** and DMAP, as well as the reaction of **2.15** to give $Cp_2Zr(NPh_2)(NH_2)$. Gibbs free energies (kcal mol^{-1}, T = 298.15 K) for minima, maxima and transition states (labelled TSx) are shown in bold relative to **2.3** and H_2.

It is notable that a large portion of the activation energy for dihydrogen addition is attributable to DMAP dissociation. Indeed, while the reaction of 1 bar overpressure H_2 with $Cp_2Zr(N^tBu)(THF)$ goes to completion,[40] reaction with $Cp_2Zr(N^tBu)(DMAP)$ was found to occur in equilibrium, reaching 44% conversion, highlighting the importance of the Lewis base in these reactions (Scheme 2.1).

2.6 Reactions of $Cp_2Zr(NNPh_2)(DMAP)$ (2.3) with CO and XylNC

Following the reactions of **2.3** with boranes and silanes, and the absence of any with H_2, it was of interest to further investigate reactions with CO and isolobal analogues in order to probe the factors governing reductive N_α–N_β cleavage. Consistent with literature,[51] reaction of CO (1 bar overpressure) with **2.3** gave instant, quantitative conversion to the zirconocene amide cyanate $Cp_2Zr(NPh_2)(NCO)$ (**2.12**), as judged by ^{1}H NMR spectroscopy. Correspondingly, reaction of **2.3** with XylNC (Xyl = 2,6-$C_6H_3Me_2$) gave instant, quantitative conversion to a single product, proposed to be the zirconocene amide carbodiimide $Cp_2Zr(NPh_2)(NCNXyl)$ (**5**, Scheme 2.2). Analogous reactivity was observed by Gade and co-workers when reacting $(N_2^{TBS}N^{py})Zr(NNPh_2)(py)$ with ^{t}BuNC to form $(N_2^{TBS}N^{py})Zr(NCN^tBu)(NPh_2)$.[36]



2.12 **2.3** **5**

Scheme 2.2: Reactions of **2.3** with CO (left) and XylNC (right) to give $Cp_2Zr(NPh_2)(NCO)$ (**2.12**) and $Cp_2Zr(NPh_2)(NCNXyl)$ (**5**), respectively.

Compound **5** was found to be highly sensitive to vacuum, forming an intractable species, and was not able to be isolated on the preparative scale. A similar phenomenon was reported by Bergman and co-workers for **2.12**.[12] The ^{1}H NMR spectrum of **5** (Figure 2.9, bottom) exhibits singlet resonances attributable to the two Cp moieties and the two Me groups of the xylyl moiety, as well as a single set of resonances for the Ph groups, indicating C_s symmetry. These Ph resonances range between 7.15 – 7.11 and 6.90 – 6.86 ppm, considerably different to those of zirconocene hydrazido(1–) complexes and similar to those of **2.12** (Figure 2.9, top), consistent with formation of an amide.

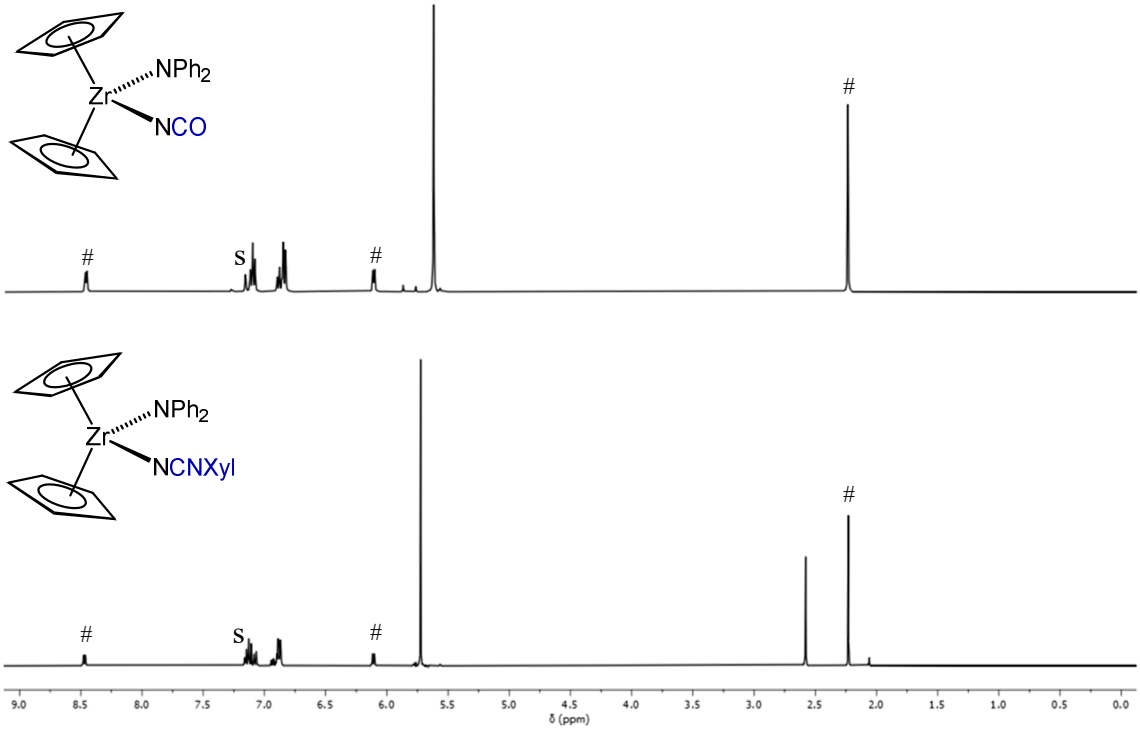


Figure 2.9: ^{1}H NMR spectra (C_6D_6, 400.1 MHz, 298 K) of $Cp_2Zr(NPh_2)(NCO)$ (**2.12**, top) and $Cp_2Zr(NPh_2)(NCNXyl)$ (**5**, bottom). (# indicates resonances attributable to DMAP).

To further probe the facile reductive cleavage of **2.3** upon reaction with CO and XylNC, the energy barrier and mechanism for the formation of **2.12** from **2.3** and CO was calculated (Figure 2.10). The reaction proceeds with a barrier of 27.5 kcal mol^{-1} from **Int2_CO**. While such a barrier is indicative of a rather slow reaction at room temperature, errors within these calculations means this value could fall within the realms of that of a rapid room temperature reaction and the key observation to be made is that the barrier is significantly lower than those calculated for the reductive cleavage reactions of **2.3** with HBPin, $PhSiH_3$ and H_2 (39.3, 35.6 and 40.3 kcal mol^{-1}, respectively).

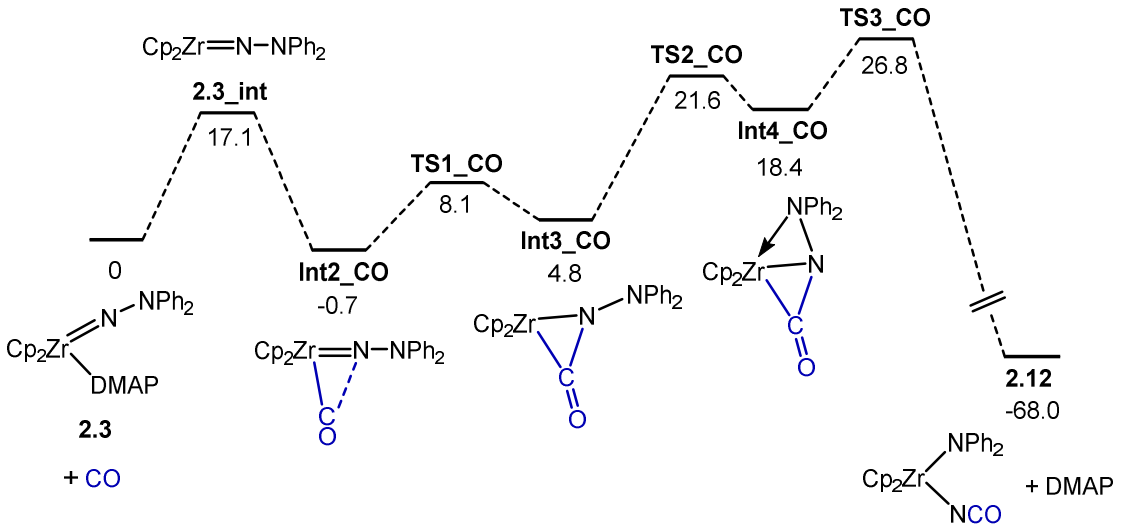


Figure 2.10: DFT (B3PW91/Def2-TZVP/d3-bj/SCRF) mechanism for the reaction of **2.3** with CO forming **2.12** and DMAP. Gibbs free energies (kcal mol^{-1}, T = 298.15 K) for minima, maxima and transition states (labelled **Intx_CO** or **TSx_CO**) are shown in bold relative to **2.3** and CO.

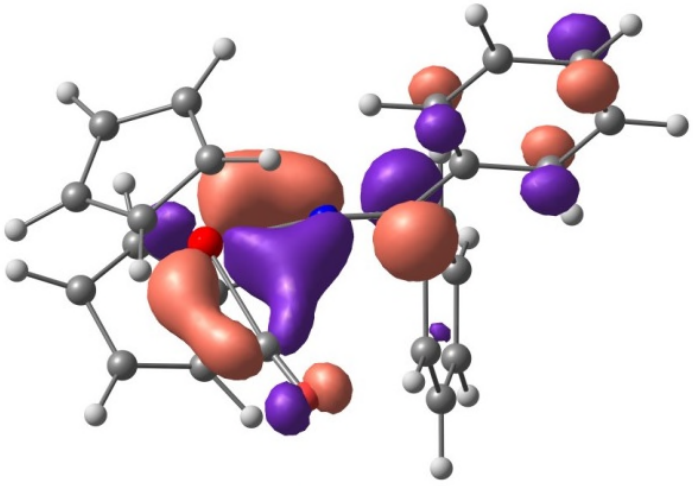


Figure 2.11: Isosurface of the HOMO of the DFT (B3PW91/Def2-TZVP/d3-bj/SCRF) model compound **Int2_CO**.

As with previous reactions, DMAP initially dissociates to give **2.3_int** (G_{rel} = 17.1 kcal mol^{-1}). CO then coordinates to the metal centre to give **Int2_CO** with G_{rel} = –0.7 kcal mol^{-1}. Analysis of the HOMO of **Int2_CO** (Figure 2.11) reveals significant electron transfer from the HOMO of $Cp_2ZrNNPh_2$ to the LUMO of CO ($Zr{=}N_\alpha$ π / N_α–N_β π* → CO π*), rationalising the stability of **Int2_CO**. Furthermore, this transfer also rationalises the facile nature of insertion of CO into the $Zr{=}N_\alpha$ bond to give **Int3_CO** ($\Delta G^{\ddagger}$ = 8.8 kcal

mol^{-1}), given the necessary orbitals already have significant interaction with one another and geometric changes are relatively small throughout insertion.

Whilst **Int3_CO**, containing a strained three-membered ring, is the analogue of the κ^1-borylhydrazide(1–) **Int3_B** and κ^1-silylhydrazide(1–) **Int4_Si**, its relative energy is much higher than that of both **Int3_B** and **Int4_Si** (4.8 *vs*. –11.5 and –4.7 kcal mol^{-1}, respectively). Unlike in the previous reactions, only one κ^2-hydrazide(1–) isomer of **Int3_CO** can possibly be formed – **Int4_CO**, which forms *via* **TS2_CO** with a barrier of 22.3 kcal mol^{-1}, relative to **Int2_CO**. **Int4_CO** is highly strained, high in energy (G_{rel} = 18.4 kcal mol^{-1}), and directly precedes reductive N_α–N_β cleavage, which occurs *via* **TS3_CO** (G_{rel} = 26.8 kcal mol^{-1}) to form the thermodynamically stable zirconocene amide cyanate **2.12** (Δ_rG = –68.0 kcal mol^{-1}).

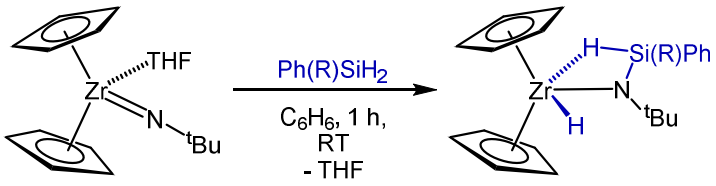
It can be noted that the relative energy of **TS3_CO** is similar to the analogous transition states **TS4_B** and **TS4_Si** relative to **2.3** and the starting materials. However, the barrier to cleavage is significantly lower for reaction with CO than HBPin and $PhSiH_3$ as no stable intermediates (*cf*. **1** and **2**) are found on the reaction pathway. Indeed, **TS3_CO** is geometrically similar to **Int4_CO**, due to the pre-existence of a C–N_α bond and of N_β–Zr coordination, and, accordingly, they are of similar energy. Comparatively, no interaction between the hydride and α-nitrogen is found before the transition state in either reaction with HBPin or $PhSiH_3$, and so the advent of the C–N_α bond, along with a lack of stable intermediate, appear key driving forces for the observed reactivity.

2.7 Reactions of zirconocene imides with silanes

Following 1,2-addition reactions of silanes and halosilanes with the Zr=N_α bond of **2.3**, it was of interest to investigate the reactivity of zirconocene imides with silanes and halosilanes. As mentioned previously, there have been no reports of Si–H addition reactions to Group 4 imides and only one example of Si–Cl and Si–Br addition.[45] Furthermore, zirconocene hydride silylamides, which would be the products of Si–H addition to zirconocene imides, have previously exhibited interesting small molecule reactivity.[54–59]

2.7.1 Reactions of $Cp_2Zr(N^tBu)(THF)$ (2.1) with silanes

On the NMR tube scale, reaction of $Cp_2Zr(N^tBu)(THF)$ (**2.1**) with $PhSiH_3$ or Ph_2SiH_2, in C_6D_6 at room temperature, gave quantitative conversion to the hydride silylamide compounds $Cp_2Zr(H)\{N(^tBu)Si(\mu\text{-}H)RPh\}$ (R = H (**6**) or Ph (**7**)), formed by 1,2-addition of the silane across the Zr–N multiple bond. On the preparative scale, the mixture of **2.1** and $PhSiH_3$ or Ph_2SiH_2 in benzene was stirred for 1 h at RT, and **6** and **7** were isolated as yellow and colourless powders in 43 and 51% yield, respectively (Equation 2.8). Both compounds **6** and **7** were characterised by NMR spectroscopy, IR spectroscopy, elemental analysis and X-ray analysis. As mentioned previously, Berry and co-workers synthesised the related compound $Cp_2Zr(H)\{N(^tBu)Si(\mu\text{-}H)Me_2\}$ (**2.16**) by a salt metathesis reaction from Schwarz's reagent, $[Cp_2ZrHCl]_n$, and $Li[N(^tBu)SiHMe_2]$.[53]



2.1 R = H (**6**) or Ph (**7**)

Equation 2.8

The ^{1}H NMR spectrum of **6** (Figure 2.12, top) shows a single Cp resonance at 5.75 ppm and a single resonance at 3.30 ppm for the SiH_2 protons, indicating the compound is fluxional and C_s symmetric in the solution phase and the two SiH proton environments, terminal and β-agostic (β-Si–H···Zr), are rapidly exchanging on the NMR timescale at RT. The ZrH resonance appears at 5.69 ppm, similar to that of **2.16** at 5.53 ppm, with the synthesis of $Cp_2Zr(D)\{N(^{t}Bu)Si(\mu\text{-}D)DPh\}$ (***6-d₃***) confirming assignment of both ZrH and SiH_2. The SiH_2 protons average resonance at 3.30 ppm is at a significantly lower frequency when compared to terminal SiH_2 resonances (*c.f.* 5.53 ppm in **2**). However, is at a higher frequency with respect to the β-Si–H···Zr proton resonance displayed by **2.16** at 1.21 ppm, reflecting that the resonance observed for **6** arises from fluxionality between terminal and β-Si–H···Zr environments.[53]

A ^{29}Si-^{1}H gradient experiment reveals a one-bond interaction between the singlet at 3.30 ppm and a ^{29}Si resonance at –95.1 ppm ($^{1}J_{SiH}$ = 173 Hz). This coupling constant is in between the reported values for terminal (*ca.* 200 Hz) and β-agostic (e.g. 113 Hz for **2.16**), again reflecting the fluxional nature of the SiH_2 environment.[48,49,53,59,60,77,78] The decrease in $^{1}J_{SiH}$ coupling constants has been attributed lengthening and weakening or rehybridisation of the Si–H bond, with similar observations made for agostic C–H bonds.[79] Similar such fluxionality has been observed by Sadow and co-workers, with the two SiH proton resonances of $Cp_2Zr(H)\{N(Si(\mu\text{-}H)Me_2)(SiHMe_2)\}$ (**2.17**) appearing as one multiplet at 3.78 ppm in C_6D_6, with $^{1}J_{SiH}$ = 161 Hz.[58]

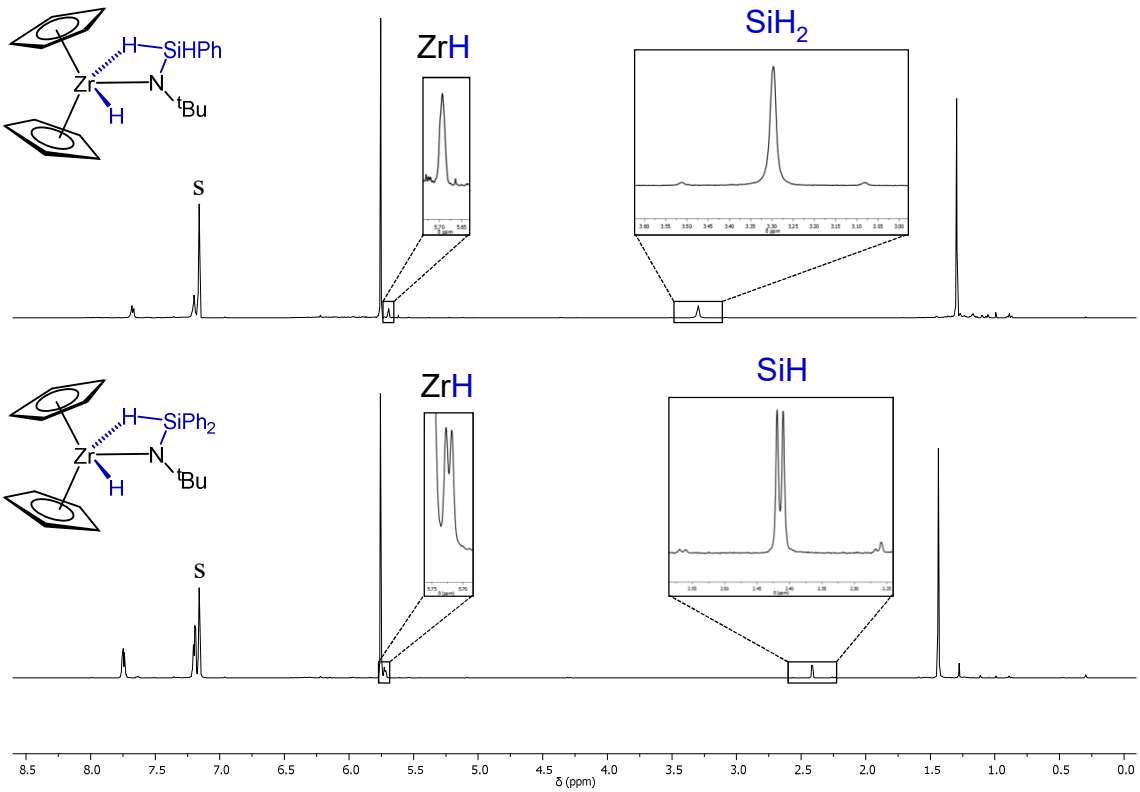


Figure 2.12: ^{1}H NMR spectra (C_6D_6, 400.1 MHz, 298 K) of $Cp_2Zr(H)\{N(^tBu)Si(\mu\text{-}H)HPh\}$ (**6**, top) and $Cp_2Zr(H)\{N(^tBu)Si(\mu\text{-}H)Ph_2\}$ (**7**, bottom) with ZrH and SiH, with ^{29}Si satellites, resonances enlarged.

Upon cooling a toluene-d_8 solution of **6** to 185 K (–88 °C) the SiH_2 resonance decoalesces. However, the two SiH resonances, appearing at 4.57 and 1.74 ppm for the terminal and β-agostic environments respectively, are observed as broad singlets, as is the ZrH resonance, indicating the slow-exchange limit had not been reached (see Appendix, Figure A1). Despite this, coupling between the ZrH and β-Si–H···Zr environments was observed through a ^{1}H-^{1}H COSY experiment at 185 K. Furthermore, the coalescence temperature of the SiH resonances was observed to be 218 ± 5 K, giving a $\Delta G^{\ddagger}$ value of 9.2 ± 0.3 kcal mol^{-1}. Sadow and co-workers were also able to observe decoalescence of the two SiH resonances of $Cp_2Zr(H)\{N(SiHMe_2)_2\}$ at 191 K, with resonances at 4.99 and 2.13 ppm being assigned to the terminal and β-agostic environments, respectively.[58]

The ^{1}H NMR spectrum of **7** (Figure 2.12, bottom) exhibits mutually coupled doublets at 5.72 and 2.41 ppm ($^{2}J_{HH}$ = 3.7 Hz) assigned to the ZrH and β-Si–H···Zr environments, respectively. A ^{29}Si-^{1}H gradient HMBC experiment reveals a one-bond interaction between the doublet at 2.41 ppm and a ^{29}Si resonance at –81.1 ppm ($^{1}J_{SiH}$ = 121 Hz). The $^{1}J_{SiH}$ coupling constant and the coupling between β-Si–H···Zr and ZrH resonances indicate the agostic interaction is not fluxional on the NMR timescale, as is observed for **6**. Although the β-Si–H···Zr resonance appears at a higher frequency than that of **6** at –88 °C, the difference between the SiH resonance of **6** and **7** and the respective free silanes is similar in **6** and **7** (Δδ = 2.49 and 2.67 ppm, respectively) indicating the agostic interactions are of a similar strength. The two coupling constants observed are also comparable to that of **2.16** ($^{1}J_{SiH}$ = 113 Hz and $^{2}J_{HH}$ = 3.1 Hz).[53]

The solid state IR spectrum of **6** is consistent with a β-agostic silylamido compound and exhibits bands at 2089, 1941 and 1576 cm^{-1}, assigned to ν(Si–H$_t$), ν(Si–H$_b$) and ν(Zr–H), respectively. A DFT calculated IR spectrum of **6** confirmed the assignments, with the calculated bands appearing at 2087, 1934 and 1600 cm^{-1}, respectively. These bands were also absent in the IR spectrum of **6-*d*$_3$** with corresponding bands observed at 1521, 1410 and 1128 cm^{-1}, in reasonable agreement with the predictions made by the harmonic oscillator model (1502, 1396 and 1120 cm^{-1}) and DFT (1501, 1388 and 1137 cm^{-1}). The observation of distinct terminal and agostic Si–H stretches shows that the SiH$_2$ moiety is not fluxional in the solid state, in contrast to solution phase. This is also in agreement with what is seen by Berry and Sadow,[53,58] with the agostic Si–H bond displaying a significantly reduced stretching frequency and therefore weaker bond. The IR spectrum of **7** exhibits bands at 1893 and 1614 cm^{-1}, assigned to ν(Si–H$_b$) and ν(Zr–H), respectively. A DFT calculated IR spectrum, with ν(Si–H$_b$) and ν(Zr–H) appearing at 1907 and 1590 cm^{-1}, respectively, confirmed these assignments. The stretching frequency

of Si–H_b for **7** is comparable to, but slightly lower than, that of **6**, **2.16** (1912 cm^{-1}) and **2.17** (1907 cm^{-1}).[53,58]

Diffraction-quality crystals of both **6** and **7** were grown from saturated solutions of benzene at room temperature and hexane at –30 °C, respectively, confirming the connectivity shown in Equation 2.8. The solid state structure of **6** and **7** are shown in Figure 2.13 and selected bond distances and angles in Table 2.4. Both **6** and **7** adopt typical bent metallocene geometries, with the nitrogen occupying the central coordination site of zirconocene and H(1), N, Si, H(2) and C(1) lying in the equatorial plane, as was found for Berry's compound **2.16**.[53] Though there are inherent inaccuracies regarding location of hydrogens in heavy atom structures such as that of **6** and **7**, the zirconium and silicon hydrides were located in the Fourier difference map and positionally and isotropically refined. Only the Si–H(3) bond of **6** was subject to a bond distance restraint. The Zr–H bond distance is significantly longer in **6** than **7** (1.90(5) and 1.69(3) Å, respectively). However, both fall within the range of previously structurally characterised terminal zirconocene hydrides (1.64(5) – 1.97(8) Å).[61–63]

The Zr–N bond distances of **6** and **7** (2.169(3) and 2.1782(16) Å, respectively) are slightly longer than those of analogous compounds, for example 2.143(6) Å in **2.16**.[53] While the nitrogen in both **6** and **7** has planar geometry, the Zr–N–Si angle is small (*ca.* 98°), similar to the angle observed for the four-membered ring of $[Cp_2Zr(OSiMe_2N^tBu)]_2$ (96.31(8)°),[55] and the Zr–N–C(1) angle large (*ca.* 134 – 136°) showing the silicon is bent towards the metal. Furthermore, the Zr–Si distance of *ca.* 2.92 Å is only slightly longer than structurally characterised Zr–Si single bonds, such as those of $Cp_2Zr(Cl)\{Si(SiMe_3)_2C(Me)_2{}^iPr\}$ (2.853(2) Å) and $Cp_2Zr(SiMe_3)(S_2CNEt_2)$ (2.815(1) Å).[63,80,81] These findings are consistent with the previously structurally characterised β-Si–H···Zr agostic containing neutral zirconocene silylamides of Berry and Sadow, as

well as other β-Si–H···Zr agostic containing compounds.[53,58,59,82,83] For **2.16**, $Cp_2Zr(Cl)\{N(^tBu)Si(\mu\text{-}H)Me_2\}$ (**2.18**) and $Cp_2Zr(OTf)\{N(^tBu)Si(\mu\text{-}H)Me_2\}$ (**2.19**) the Zr–N–Si angle ranges between *ca.* 95 and 99° while the Zr–Si distance ranges between *ca.* 2.86 and 2.93 Å.

The Zr–H(2) distances of 2.16(4) and 2.17(2) Å for **6** and **7**, respectively, are within the expected range of bridging zirconocene hydrides.[53,59,84,85] Though the agostic silicon hydride of **2.16** and **2.19** were not able to be located in the Fourier difference map or positionally and isotropically refined, the idealised position and Si–H bond length led to a Zr–H distance of *ca.* 2.1 Å for **2.16** and **2.19** in good agreement with **6** and **7**. The agostic silicon hydride of the chloride **2.18** was able to be located in the Fourier difference map and successfully refined giving a longer Zr–H distance of 2.266(30) Å, for reasons which will be discussed later in this Chapter.

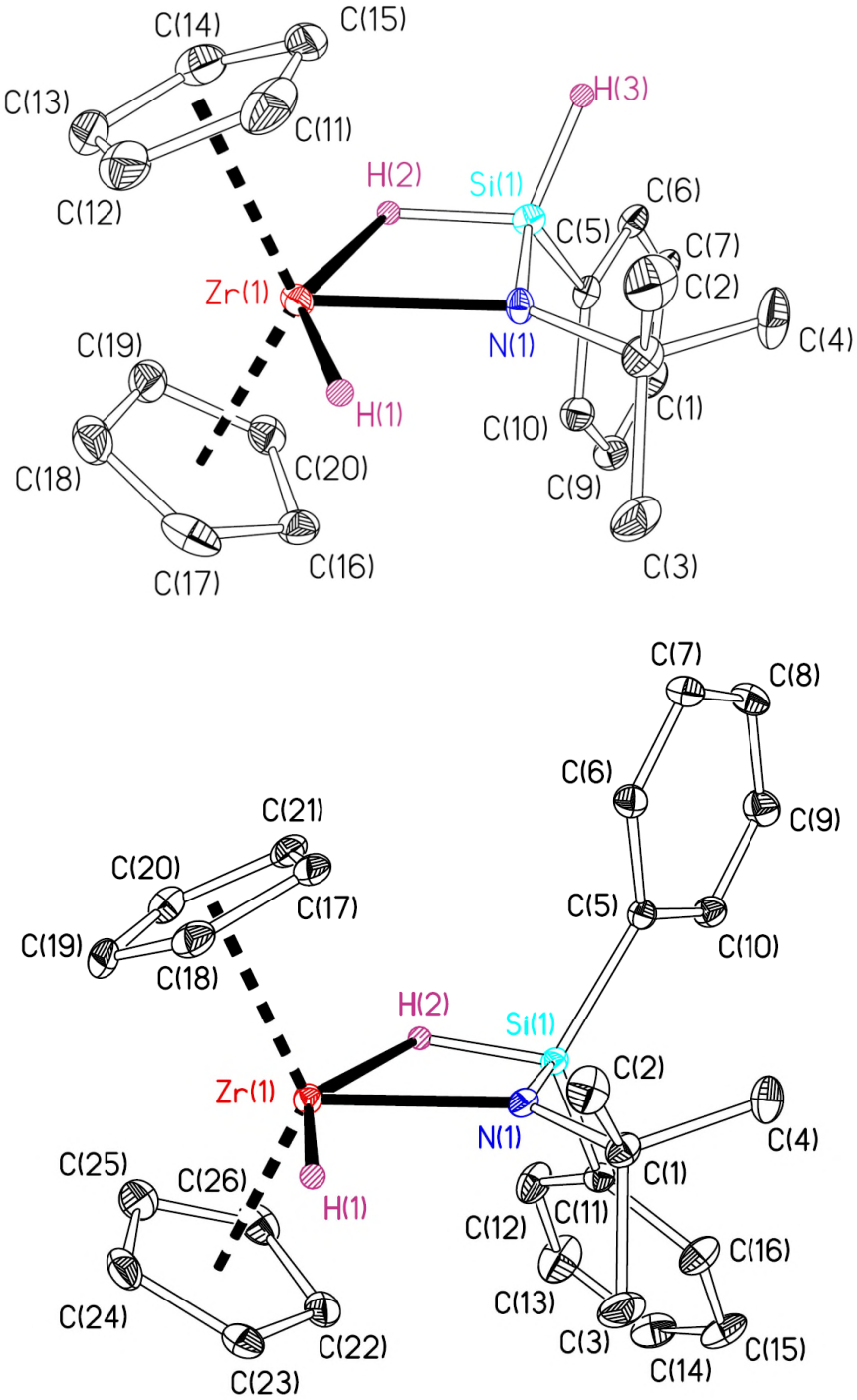


Figure 2.13: Displacement ellipsoid plots (20% probability) of $Cp_2Zr(H)\{N(^tBu)Si(\mu\text{-}H)HPh\}$ (**6**, top) and $Cp_2Zr(H)\{N(^tBu)Si(\mu\text{-}H)Ph_2\}$ (**7**, bottom). C–H atoms are omitted for clarity and other H atoms are drawn as spheres of an arbitrary radius.

Table 2.4: Selected bond distances (Å) and angles (°) for $Cp_2Zr(H)\{N(^tBu)Si(\mu\text{-}H)HPh\}$ (**6**) and $Cp_2Zr(H)\{N(^tBu)Si(\mu\text{-}H)Ph_2\}$ (**7**). $Cp_{cent(1)}$ and $Cp_{cent(2)}$ refer to the computed Cp ring centroids for the "upper" and "lower" Cp rings, respectively, as depicted in Figure 2.13.

Parameter	6	7
Zr(1)-N(1)	2.169(3)	2.1782(16)
Zr(1)-H(1)	1.90(5)	1.69(3)
Zr(1)-H(2)	2.16(4)	2.17(2)
Zr(1)-Si(1)	2.9185(10)	2.9256(6)
$Zr(1)\text{-}Cp_{cent(1)}$	2.23	2.23
$Zr(1)\text{-}Cp_{cent(2)}$	2.22	2.23
N(1)-Si(1)	1.672(3)	1.6807(16)
Si(1)-H(2)	1.48(4)	1.50(2)
Si(1)-H(3)	1.400(5)	-
H(1)-Zr(1)-H(2)	141.8(18)	144.6(11)
Zr(1)-N(1)-Si(1)	98.07(12)	97.77(8)
N(1)-Si(1)-H(2)	92.9(17)	93.1(9)
Si(1)-H(2)-Zr(1)	105(2)	104.1(12)
H(2)-Zr(1)-N(1)	63.7(12)	64.4(6)
H(1)-Zr(1)-N(1)	78.2(14)	80.7(9)
Zr(1)-N(1)-C(1)	136.4(2)	134.30(13)
C(1)-N(1)-Si(1)	125.2(2)	127.29(14)
$Cp_{cent(1)}\text{-}Zr(1)\text{-}Cp_{cent(2)}$	128.6	128.9

While **6** and **7** adopt typical bent metallocene geometries, with the nitrogen occupying the central coordination site of zirconocene and the agostic and terminal hydride in the outer coordination sites, there exists two other isomeric possibilities for these compounds. One containing no agostic interaction (**6_int**, see Appendix, Figure A2) and one placing the agostic hydride in the central coordination site of the zirconocene and the nitrogen and terminal hydride in the outer coordination sites (**6_alt**). To investigate the relative energies of these isomers and their sequence of formation on the pathway of reaction of

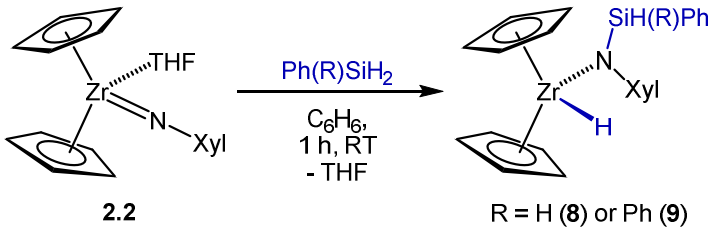
2.1 with silane, the full mechanism of the reaction of **2.1** with $PhSiH_3$ was calculated by DFT (see Appendix, Figure A2).

Addition of $PhSiH_3$ to **2.1** proceeds in an analogous manner to with $Cp_2Zr(NNPh_2)(DMAP)$ (**2.3**). THF is first lost before formation the silane adduct **Int1**, *via* **TS1**, followed by 1,2-addition *via* **TS2** with a free energy barrier of 8.5 kcal mol^{-1}. The transition state, **TS1**, and its free energy were not able to be located. From Δ_rH, the upper bound for the free energy of **TS1** is calculated to be 18.2 kcal mol^{-1}. Notably, the first formed product is the non-agostic isomer **6_int** (G_{rel} = –15.6 kcal mol^{-1}). From **6_int** rotation about the Zr–N bond forms either **6_alt** (G_{rel} = –16.5 kcal mol^{-1}) with a barrier of 2.1 kcal mol^{-1}, or **6** (G_{rel} = –19.3 kcal mol^{-1}) with a barrier of 13.2 kcal mol^{-1} (14.1 kcal mol^{-1} from **6_alt**). Consistent with experimental observation **6** is calculated to be the thermodynamic product of the reaction. Notably, **6_alt** represents the kinetic product of the reaction. Attempts to observe **6_alt** on following the reaction by ^1H NMR spectroscopy at –30 °C were unsuccessful.

To probe the origin of the 2.8 and 3.7 kcal mol^{-1} energy difference between **6** and **6_alt** and **6_int**, respectively, the free energies of the analogous isomers of the methyl analogue $Cp_2Zr(H)\{N(Me)SiH_2Ph\}$ were calculated (see Appendix, Figure A3 (b)). The two agostic isomers were found to be identical in free energy and slightly higher in free energy (0.6 kcal mol^{-1}) than the non-agostic isomer. This shows the isomeric preference of **6** most likely arises due to sterics, with the central coordination site of zirconocene being the least sterically encumbered.[86] Furthermore, the favourability of the non-agostic isomer for $Cp_2Zr(H)\{N(Me)SiH_2Ph\}$ most likely arises due to the less electron donating character of the methyl group, with respect to ^tBu, which would lead to a lesser degree of negative hyperconjugation of the Zr–N bond into the Si–H σ* orbital (see Section 2.7.2), with steric factors having little influence here.

2.7.2 Reactions of $Cp_2Zr(NXyl)(THF)$ (2.2) with silanes

On the NMR tube scale, reaction of $Cp_2Zr(NXyl)(THF)$ (**2.2**) with $PhSiH_3$ or Ph_2SiH_2, in C_6D_6 at room temperature gave quantitative conversion to the hydride silylamide compounds $Cp_2Zr(H)\{N(Xyl)SiHRPh\}$ (R = H (**8**) or Ph (**9**)), formed by 1,2-addition of the silane across the Zr–N multiple bond. On the preparative scale, mixtures of **2.2** and $PhSiH_3$ or Ph_2SiH_2 in benzene were stirred for 1 h at RT, and **8** and **9** were isolated as waxy, yellow solids in 44 and 58% yields, respectively (Equation 2.9). However, an impurity, which could not be removed from the starting material **2.2**, could not be removed from **8** or **9** and prevented the confirmation of bulk purity of the compounds by elemental analysis. Attempts to wash or extract the products with hexane or ether were unsuccessful and also led to significant amounts of decomposition of the products. Compounds **8** and **9** were also found to decompose under exposure to high vacuum for several hours, though were stable in solution for several days and at temperatures up to 80 °C. Attempts to grow diffraction-quality crystals of **8** and **9** were unsuccessful.



2.2 R = H (**8**) or Ph (**9**)

Equation 2.9

The ^1H NMR spectrum of **8** (Figure 2.14) shows a single Cp resonance at 5.70 ppm, a single resonance for the methyl groups of the xylyl moiety at 2.12 ppm and a single resonance at 5.26 ppm for the SiH_2 protons, indicating the compound is C_s symmetric in solution. The ZrH resonance appears at 5.49 ppm, similar to that of **6** at 5.69 ppm and **2.16** at 5.53 ppm, with the synthesis of $Cp_2Zr(D)\{N(Xyl)SiD_2Ph\}$ (**8-*d*$_3$**) confirming assignment of both the ZrH and SiH_2 resonances. The SiH_2 chemical shift of 5.26 ppm is at significantly higher frequency to that of **6**, **2.16** and **2.17**, and is more indicative of a

terminal SiH_2 resonance than an SiH_2 resonance that is fluxional between terminal and agostic SiH resonances, as is seen for **6**.[53,58,60] Furthermore, $^1J_{SiH}$ coupling between the singlet at 5.26 ppm and a ^{29}Si resonance at –31.4 ppm was found, by a ^{29}Si-^{1}H gradient experiment, to be 206 Hz. This $^1J_{SiH}$ coupling constant is typical of a terminal SiH_2 resonance. The ^{1}H and ^{29}Si NMR of **9** are similar to those of **8**, with single Cp and Me resonances, ZrH, SiH and Si resonances of 5.56 (^{1}H), 6.01 (^{1}H) and –20.0 ppm, respectively, and a $^1J_{SiH}$ coupling of 205 Hz.

Given the apparent lack of agostic interactions in **8** and **9**, rotation about the Zr–N and N–C bonds must be fast on the NMR timescale to account for the observation of single Cp and single methyl resonances. Upon cooling a toluene-d_8 solution of **8** to –80 °C the Cp, methyl and SiH_2 resonances decoalesce. The Cp resonance is seen to decoalesce between –60 and –70 °C, while the methyl and SiH_2 resonances decoalesce between –70 and –80 °C. Unlike with **6**, where the two SiH resonances decoalesce to 4.57 and 1.74 ppm, the SiH resonances of **8** decoalesce to between 5.55–5.35 (determination of the chemical shift was obscured by overlap with the broad Cp resonance) and 5.13 ppm. This indicates no agostic interaction is present in **8** even at low temperatures in solution. The ZrH resonance remains a sharp singlet with no coupling observed to the SiH_2 resonances in an ^{1}H-^{1}H COSY experiment at –80 °C, showing there is no interaction between the metal and silicon hydrides.

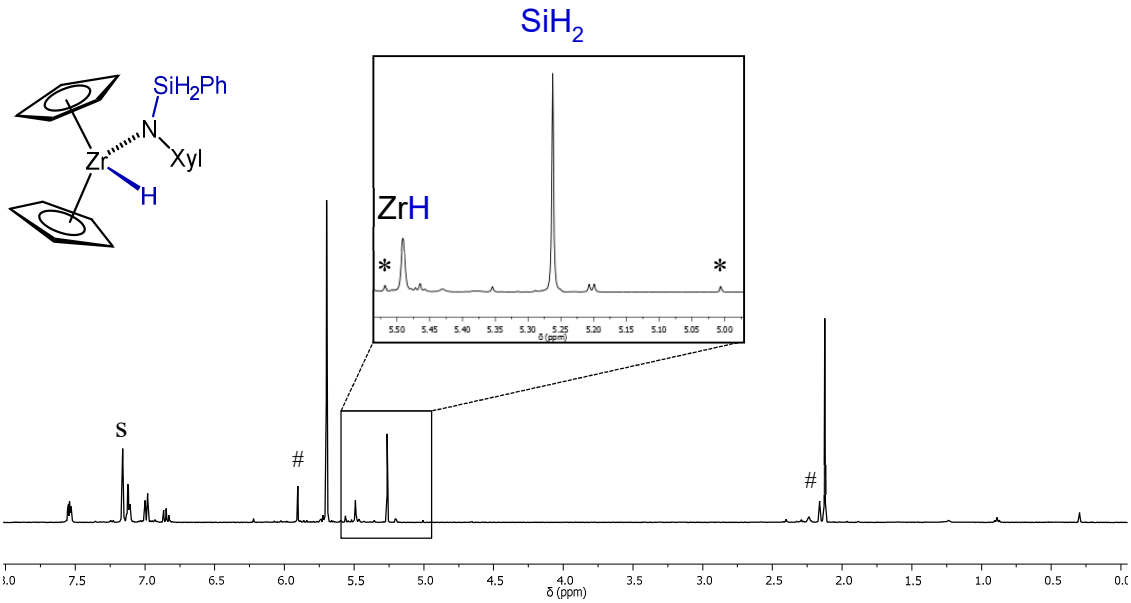


Figure 2.14: ^{1}H NMR spectrum (C_6D_6, 400.1 MHz, 298 K) of $Cp_2Zr(H)\{N(Xyl)SiH_2Ph\}$ (**8**) with ZrH and SiH, with ^{29}Si satellites (*), resonances enlarged. (# indicates the impurity from the starting material **2.2**).

The solid state IR spectrum of **9** is consistent with the compound containing a terminal SiH moiety, exhibiting a band assigned to $\nu(Si–H_t)$ at 2126 cm^{-1}.[22,53] This stretching frequency is significantly higher than $\nu(Si–H_b)$ of **6** and **7** (1941 and 1893 cm^{-1}, respectively), but similar to $\nu(Si–H_t)$ of **6** (2089 cm^{-1}), indicating there is no β-Si–H···Zr agostic interaction in the solid state. The structures of **8** and **9** were computed by DFT and are shown in Figure 2.15. Both structures contain no β-agostic interaction and support the connectivity shown in Equation 2.9. The calculated $\nu(Si–H_t)$ of 2100 cm^{-1} for **9** is in reasonable agreement with that found experimentally. Furthermore, $\nu(Zr–H)$ was calculated to be 1588 cm^{-1}, in excellent agreement with that found experimentally (1587 cm^{-1}). Additional to the structures of **8** and **9**, the two possible agostic isomers of $Cp_2Zr(H)\{N(Xyl)SiH_2Ph\}$, namely **8_alt** and **8_alt1**, and $Cp_2Zr(H)\{N(Xyl)SiHPh_2\}$, namely **9_alt** and **9_alt1**, were computed by DFT (see Appendix, Figure A3 (c) and (e)), as was the full mechanism for the reaction of **2.2** with $PhSiH_3$ (Figure A4).

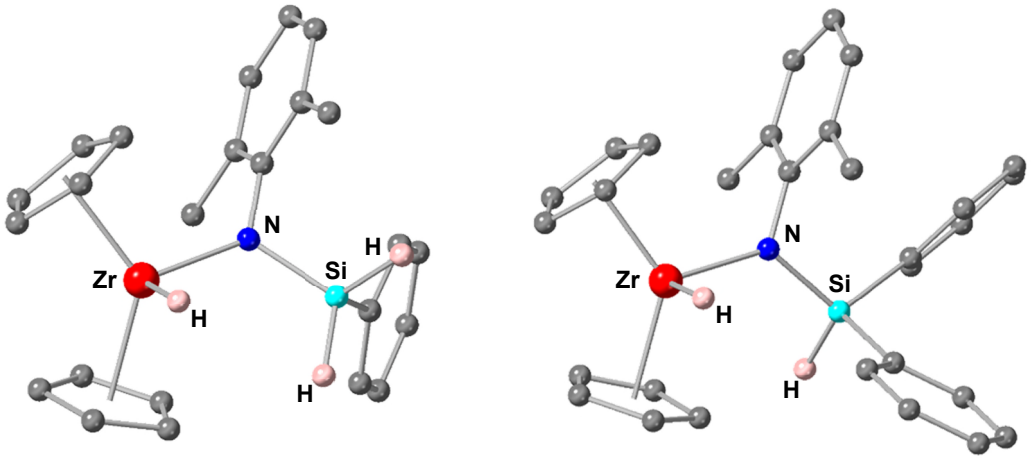


Figure 2.15: DFT (B3PW91/Def2-TZVP/d3-bj/SCRF) structures of $Cp_2Zr(H)\{N(Xyl)SiH_2Ph\}$ (**8**, left) and $Cp_2Zr(H)\{N(Xyl)SiHPh_2\}$ (**9**, right). C–H atoms are omitted for clarity.

The mechanism of reaction is analogous to that of both **2.1** and **2.3** with $PhSiH_3$, proceeding by dissociation of THF followed by adduct formation and subsequent 1,2-addition. Notably, the first-formed product is **8**, which is calculated to be 6.8 kcal mol^{-1} lower in free energy than **8_alt**, the agostic isomer containing nitrogen in the central coordination site (geometry analogous to **6**), and 13.2 kcal mol^{-1} lower than **8_alt1**, the agostic isomer containing the agostic hydrogen in the central coordination site (geometry analogous to **6_alt**). Similarly, the non-agostic isomer **9** was calculated to be 7.9 and 12.1 kcal mol^{-1} more stable than the agostic isomers **9_alt** and **9_alt1** (Figure A3 (e)). Silylamido ligands bearing β-Si–H bonds are often observed to have non-classical β-agostic interactions with their metal centre, with examples extending to β-agostic alkaline-earth, rare-earth, niobium, tantalum and molybdenum silylamides, marking **8** and **9** as oddities.[48–50,60,87–97] The one difference between compounds **6** and **8**, and **7** and **9**, is the group bound to the nitrogen of the silylamido moiety (*tert*-butyl or xylyl). As such, there must be a steric and/or electronic difference between the *tert*-butyl and xylyl groups that causes one to favour an agostic conformation and the other a non-agostic conformation.

Two factors chiefly influence whether β-agostic interactions will form, and their strength.[98] First, whether a locally induced site of Lewis acidity on the metal is present that is geometrically accessible for the β-hydrogen to approach the metal centre. Second, the propensity of the M–E_α bond (the Zr–N bond in compounds **6** – **9**) to undergo negative hyperconjugation into the σ* orbital of the E_β–H_β bond (the Si–H bond in compounds **6** – **9**). Negative hyperconjugation acts as a means to stabilise the M–E_α bonding orbital and so the higher the energy of M–E_α bonding orbital the greater the ability to undergo negative hyperconjugation.

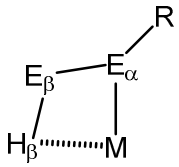


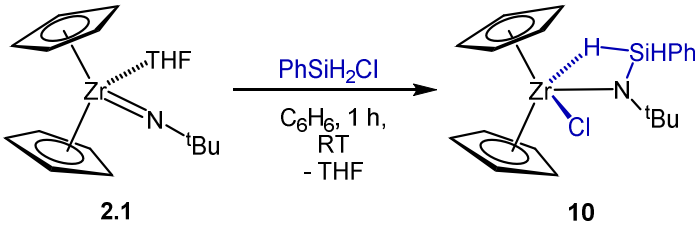
Figure 2.16: General structure of a compound containing a β-E–H···M agostic interaction.

With regards to the first factor described, compounds **6** – **9** all contain Lewis acidic sites (vacant bonding orbitals) that are geometrically accessible for the β-hydrogen. However, the xylyl group is sterically bulkier than the *tert*-butyl group and this may contribute to the agostic isomers being unfavourable. Indeed, analysis of the DFT structures of the agostic isomers shows significant clashes between the xylyl group and Cp groups or hydride. Furthermore, substitution of the xylyl group for the electronically similar, but sterically reduced, phenyl group ($Cp_2Zr(H)\{N(Ph)SiH_2Ph\}$) leads to significant changes in the isomeric preference (Figure A3 (d)). Here, the agostic isomer analogous to **6** is only 4.2 kcal mol^{-1} higher in free energy than the non-agostic isomer and, notably, the agostic isomer analogous to **6_int** is 2.1 kcal mol^{-1} lower in energy than the non-agostic isomer. This implies that the steric profile of the R group greatly affects the isomeric preference of these compounds. Steric factors have been attributed to the weakening or absence of β-agostic interactions in similar silylamide compounds.[60,95]

With regards to the second factor described, the xylyl group is less strongly σ-donating than the *tert*-butyl group. A strongly σ-donating R group will act to raise the energy of the Zr–N bonding orbital and so facilitate negative hyperconjugation and β-agostic interactions. As such, the negative hyperconjugation in compounds **8** and **9** may not be significant enough to lead to the formation of a β-agostic interaction. As previously discussed, the slight preference of the methyl analogue of **6**, $Cp_2Zr(H)\{N(Me)SiH_2Ph\}$ to adopt a non-agostic isomer was attributed to the less electron donating capacity of the methyl group, with respect to ^{t}Bu. However, Nikonov and co-workers previously observed β-agostic interaction in the molybdenum compound $(ArN)Mo(SiH_2Ph)(PMe_3)\{N(Ar)Si(\mu\text{-}H)HPh\}$ (Ar = 2,6-diisopropylphenyl), indicating the σ-donation of aromatic groups is sufficient to facilitate β-agostic interactions.[93] Furthermore, the phenyl analogue of **8**, $Cp_2Zr(H)\{N(Ph)SiH_2Ph\}$, is calculated to favour an agostic isomer. This indicates while electronic differences do somewhat influence the isomeric preference of these compounds, the dominating factor is the steric profile of the R group bound to the nitrogen.

2.7.3 Reaction of $Cp_2Zr(N^tBu)(THF)$ (2.1) with chlorophenylsilane

On the NMR tube scale, reaction of $Cp_2Zr(N^tBu)(THF)$ (**2.1**) with $PhSiH_2Cl$, in C_6D_6 at room temperature, gave quantitative conversion to the chloride silylamide compound $Cp_2Zr(Cl)\{N(^tBu)Si(\mu\text{-}H)HPh\}$ (**10**) after 5 minutes. On the preparative scale, the mixture of **2.1** and $PhSiH_2Cl$ in benzene was stirred for 1 h at RT, and **10** was isolated as an orange powder in 49% yield (Equation 2.10). Compound **10** was characterised by NMR and IR spectroscopy, elemental analysis and X-ray analysis.



2.1 **10**

Equation 2.10

The ^{1}H NMR spectrum of **10** (Figure 2.17) is analogous to that of compound **6**, with a single Cp resonance at 6.01 ppm and a single resonance at 4.33 ppm for the SiH_2 protons, indicating a fluxional compound with C_s symmetry in the solution phase. No proton resonance in the region expected for a hydride was observed, consistent with the formation of a zirconium chloride. The single resonance at 4.33 ppm for the SiH_2 protons indicates that the two SiH proton environments, terminal and β-agostic, are fluxional on the NMR timescale at RT, in an identical manner to **6**. However, the resonance is at a higher frequency than that of **6** (*cf.* 3.30 ppm) by 1.03 ppm, indicating a weaker agostic interaction. The one-bond interaction ($^{1}J_{SiH}$) between this SiH_2 resonance and a ^{29}Si resonance at –69.7 ppm was found to be 182 Hz, consistent with a fluxional β-agostic SiH_2 moiety though 9 Hz larger than that of **6**, again indicating a weaker agostic interaction. Upon cooling of **10** to –88 °C in toluene-d_8, the SiH_2 resonance decoalesces to two broad singlets at 4.84 and 3.61 ppm for the terminal and β-agostic SiH environments, respectively. This β-agostic SiH resonance at –88 °C is at a significantly higher frequency than that of **6** (1.74 ppm) at the same temperature.

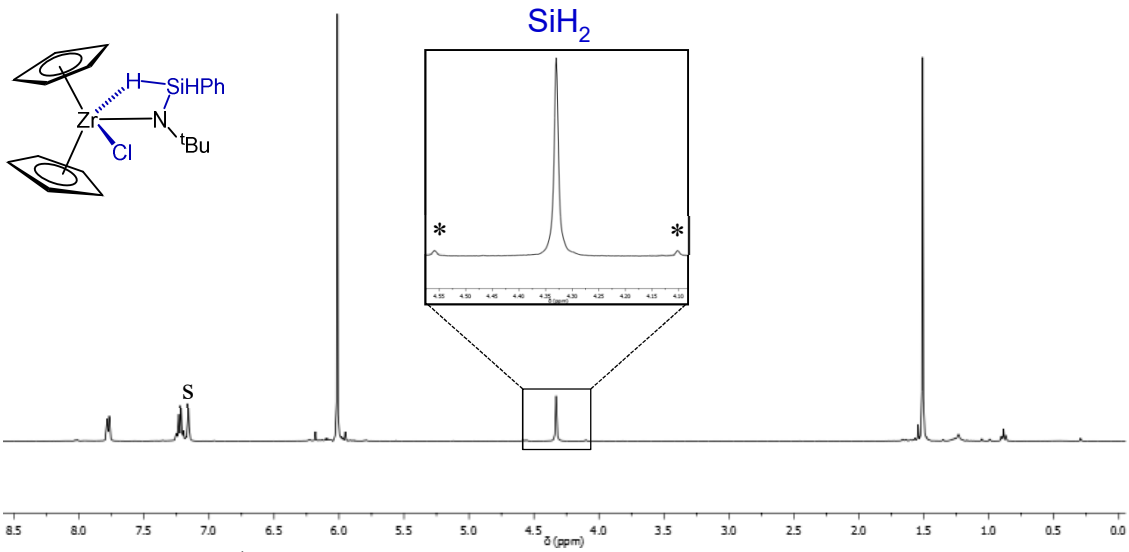
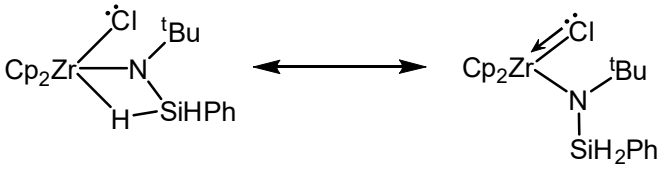


Figure 2.17: ^{1}H NMR spectrum (C_6D_6, 400.1 MHz, 298 K) of $Cp_2Zr(H)\{N(^tBu)Si(\mu\text{-}H)HPh\}$ (**10**) with the SiH resonance and its ^{29}Si satellites (*) enlarged.

Such a phenomenon has previously been observed by Berry and co-workers.[53] The SiH resonance of $Cp_2Zr(Cl)\{N(^tBu)Si(\mu\text{-}H)Me_2\}$ (**2.18**), prepared by reaction of chloromethane with $Cp_2Zr(H)\{N(^tBu)Si(\mu\text{-}H)Me_2\}$ (**2.16**), was found to have a chemical shift of 2.58 ppm (*cf.* 1.21 ppm for **2.16**). This higher frequency, and therefore weaker agostic interaction, was attributed to π-donation of the chloride ligand competing with the Si–H bond for the vacant orbital on zirconium. Equation 2.11 depicts how such π-donation could lead to a breaking of the β-agostic interaction in the extreme. Indeed, for the series $Cp_2Zr(X)\{N(^tBu)Si(\mu\text{-}H)Me_2\}$ (X = H, F, Cl, Br and I), the strength of the agostic interaction follows the order H>I>Br>Cl>F – the same trend followed for the Lewis acidity of boron trihalides.[99] Furthermore, Nikonov and co-workers have reported the weakening and breaking of the agostic interaction on introduction of π-donating ligands.[60] DFT analyses to investigate this further will be discussed in Section 2.7.3.1.



Equation 2.11[53]

The solid state IR spectrum of **10** exhibits two bands at 2116 and 2080 cm^{-1}, assigned to the two ν(Si–H) modes. Both stretches are at frequencies significantly higher than the agostic stretches in **6**, **7** and Berry's **2.18** (1941, 1893 and 1981 cm^{-1}, respectively)[53] and ν(Si–H_b) modes generally only appear up to 2000 cm^{-1}.[91] In the DFT computed IR spectrum of **10** the ν(Si–H) modes, appearing at 2104 and 2083 cm^{-1}, were coupled. Therefore these bands, unlike in **6**, cannot be attributed to distinct ν(Si–H_t) and ν(Si–H_b) modes. These observations are consistent with **10** containing a very weak agostic bond. This was further highlighted in the solid state structure of **10**.

Diffraction-quality crystals of **10** were grown from a saturated solution of benzene at room temperature, confirming the connectivity shown in Equation 2.10. The solid state structure of **10** is shown in Figure 2.18 and selected bond distances and angles in Table 2.5. **10** adopts a bent metallocene geometry analogous to that of **6**, **7**, **2.16** and **2.18**, with the nitrogen occupying the central coordination site of zirconocene and Cl, N, Si, H(1) and C(1) lying in the equatorial plane.[53]

As with the previously characterised β-agostic containing zirconocene silylamides, the angles about the planar nitrogen are distorted such that the silicon is bent towards the metal. The Zr–N–Si angle of 105.37(9)° is significantly smaller than would be expected if there was no agostic interaction, though around 7° larger than the Zr–N–Si angles of **6** and **7** and 6° larger than in $Cp_2Zr(Cl)\{N(^tBu)Si(\mu\text{-}H)Me_2\}$ (**2.18**), implying a longer Si–H_b and so weaker agostic interaction. Consistent with this, the Zr–Si bond distance of **10** (3.0860(6) Å) is *ca.* 0.14 Å longer than that of **6** and **7**, and 0.13 Å longer than that of **2.18**. The Zr–H(1) was found to be 2.61(3) Å; while there are inaccuracies in locating hydrogens in such heavy atom structures, this bond distance is *ca.* 0.4 Å longer than that

of **6** and **7**, and 0.34 Å longer than that of **2.18**. This significant increase in the β-Si–H···Zr agostic distance is unsurprising given the NMR and IR spectra discussed.

Furthermore, the Cl(1)-Zr(1)-H(1) angle of **10** is larger than the H(1)-Zr(1)-H(2) of **6** (156.2(6)° vs. 141.8(18)°). Presumably this is due to compound **10** falling somewhere between the two extremes depicted in Equation 2.13. Indeed, the angle Cl(1)-Zr(1)-N(1), at 95.62(5)°, is larger than the corresponding angle of **6** (H(1)-Zr(1)-N(1) = 78.2(14)°) and is closer to the angle of the non-agostic compound **11** (99.00(5)°) (*vide infra*). More to this point, the Zr–Cl bond distance of 2.4790(6) Å is shorter than that of **2.27** (2.523(1) Å), presumably due to a greater degree of π-donation of the chloride in **10** shortening the bond distance, and similar to that of **11** (2.4672(6) Å). This implies that the β-agostic conformation of **10** lies on the cusp of thermodynamic favourability, with respect to a non-agostic conformation.

Only one structurally characterised zirconocene compound that may have a longer Zr–H_b distance exists in the literature; $\{Cp_2ZrC(SiMe_3)C(\mu\text{-}H)(SiMe_3)\}_2O$ contains a Zr–H_b distance of 2.72(1) Å.[100] However, the agostic interaction between zirconium and hydrogen was only discussed as a possibility. Given the characterising data and comparisons to the literature, the β-agostic interaction in **10** can be seen to be present, though is weak and structural parameters approach those of a compound that would not contain a β-agostic interaction.

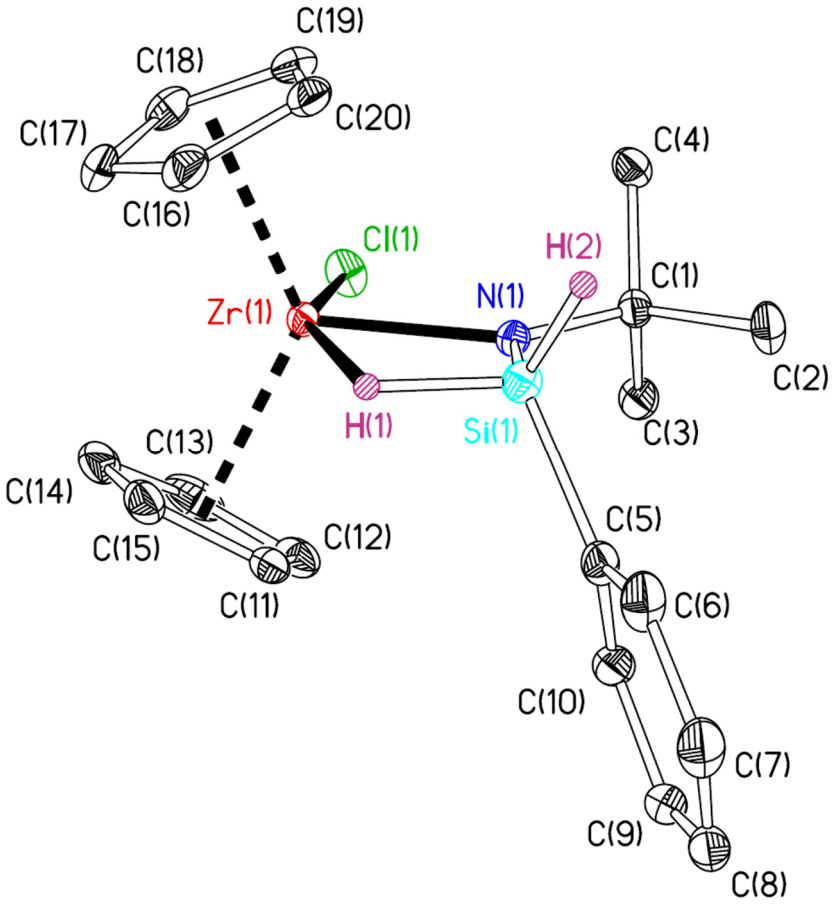


Figure 2.18: Displacement ellipsoid plots (20% probability) of $Cp_2Zr(Cl)\{N(^tBu)Si(\mu\text{-}H)HPh\}$ (**10**). C–H atoms are omitted for clarity. H(1) and H(2) are drawn as spheres of an arbitrary radius.

Table 2.5: Selected bond distances (Å) and angles (°) for $Cp_2Zr(Cl)\{N(^tBu)Si(\mu\text{-}H)HPh\}$ (**10**). $Cp_{cent(1)}$ and $Cp_{cent(2)}$ refer to the computed Cp ring centroids for the "lower" and "upper" Cp rings, respectively, as depicted in Figure 2.17.

Zr(1)-N(1)	2.1516(16)	Cl(1)-Zr(1)-H(1)	156.2(6)
Zr(1)-Cl(1)	2.4790(6)	Zr(1)-N(1)-Si(1)	105.37(9)
Zr(1)-H(1)	2.61(3)	N(1)-Si(1)-H(1)	100.5(11)
Zr(1)-Si(1)	3.0860(6)	Si(1)-H(1)-Zr(1)	93.5(13)
Zr(1)-$Cp_{cent(1)}$	2.25	H(1)-Zr(1)-N(1)	60.7(6)
Zr(1)-$Cp_{cent(2)}$	2.26	Cl(1)-Zr(1)-N(1)	95.62(5)
N(1)-Si(1)	1.6899(17)	Zr(1)-N(1)-C(1)	135.85(13)
Si(1)-H(1)	1.47(3)	C(1)-N(1)-Si(1)	121.30(13)
Si(1)-H(2)	1.35(3)	$Cp_{cent(1)}$-Zr(1)-$Cp_{cent(2)}$	127.1

2.7.3.1 Computational study of bonding in a zirconocene chloride-silylamide

As mentioned previously, the weakening of the agostic interaction in **10** and analogous chloride-silylamides has been attributed to π-donation of the chloride ligand competing with the Si–H bond for the vacant orbital on zirconium.[53] To gain a better understanding of the β-agostic Si–H···Zr interaction of **10**, as well as of $Cp_2Zr(H)\{N(^tBu)Si(\mu\text{-}H)HPh\}$ (**6**), single point, gas-phase DFT calculations (B3PW91/Def2-TZVP) were carried out on the model compounds $Cp_2Zr(Cl)\{N(Me)Si(\mu\text{-}H)HPh\}$, $Cp_2Zr(H)\{N(Me)Si(\mu\text{-}H)HPh\}$ and $Cp_2Zr(H)\{N(Ph)SiH_2Ph\}$ (used as a model of $Cp_2Zr(H)\{N(Xyl)SiH_2Ph\}$ (**8**)) and the wavefunctions analysed using the NBO (natural bond orbital) method.[101,102]

The NBO approach aids interpretation of the bonding in a transparent and intuitive way in terms of the closest idealised Lewis structure. In addition, selected NMR calculations were also performed, namely ^{29}Si chemical shifts and $^1J_{SiH}$ coupling constants, using the GIAO method in Gaussian09 and specialised basis sets of Jensen[103,104] for the non-metal atoms and Def2-TZVP for Zr. The DFT models mentioned above were based on the optimised geometries of the parent compounds (B3PW91/Def2-TZVP/d3-bj) and NBO and NMR calculations were also performed on $PhSiH_3$ for comparison. The results can be seen in Table 2.6 and both experimental and computed ^{29}Si NMR shifts were referenced to that of $SiMe_4$ (δ = 0 ppm).

Table 2.6: Experimental NMR data for $PhSiH_3$, $Cp_2Zr(H)\{N(^tBu)Si(\mu\text{-}H)HPh\}$ (**6**), $Cp_2Zr(Cl)\{N(^tBu)Si(\mu\text{-}H)HPh\}$ (**10**) and $Cp_2Zr(H)\{N(Xyl)SiH_2Ph\}$ (**8**) and DFT (B3PW91/Def2-TZVP) computed NMR (C_6D_6, RT, referenced to $SiMe_4$) and NBO data for $PhSiH_3$ and the model compounds $Cp_2Zr(H)\{N(Me)Si(\mu\text{-}H)HPh\}$, $Cp_2Zr(H)\{N(Me)Si(\mu\text{-}H)HPh\}$ and $Cp_2Zr(H)\{N(Ph)SiH_2Ph\}$. (^{a} = average value; values in bold, italics refer to the agostic Si–H).

	$PhSiH_3$	**$Cp_2Zr(H)\{N(Me)Si(\mu\text{-}H)HPh\}$**	**$Cp_2Zr(Cl)\{N(Me)Si(\mu\text{-}H)HPh\}$**	**$Cp_2Zr(H)\{N(Ph)SiH_2Ph\}$**
δ ^{29}Si (exp, ppm)	–61.1	–95.1	–69.7	–31.4
δ ^{29}Si (DFT, ppm)	–58.3	–102.9	–61.7	–30.9
$^1J_{SiH}$ (av., exp, Hz)	201	173	183	206
$^1J_{SiH}$ (DFT, Hz)	–	223.5	204.4	206.8
	–	***115.3***	***172.6***	215.8
	198.4^a	169.4^a	188.5^a	211.3^a
Si–H bond length (DFT, Å)	1.495^a	1.500	1.500	1.487
		1.540	***1.501***	1.493
Si–H NBO occupancy	1.982^a	1.973	1.975	1.961
		1.791	***1.897***	1.975
Si–H Mayer bond index[105]	0.944^a	0.918	0.924	0.918
		0.506	***0.808***	0.942

First, it can be noted that the DFT computed NMR parameters agree well with experimental values, with δ ^{29}Si within ± 8 ppm and the averaged $^{1}J_{SiH}$ coupling constant within ± 6 Hz. Furthermore, the computations allow for calculation of the individual $^{1}J_{SiH}$ coupling constants of the agostic and non-agostic Si–H moieties, which was not possible experimentally. For $Cp_2Zr(H)\{N(Me)Si(\mu\text{-}H)HPh)$ the coupling constant of the agostic Si–H is calculated to be 115.3 Hz, identical within error to that of $Cp_2Zr(H)\{N(^tBu)Si(\mu\text{-}H)Me_2\}$ (**2.16**, 113 Hz) and $Cp_2Zr(H)\{N(^tBu)Si(\mu\text{-}H)Ph_2\}$ (**7**, 121 Hz). In contrast, the coupling constant of the agostic Si–H of $Cp_2Zr(Cl)\{N(Me)Si(\mu\text{-}H)HPh\}$ is calculated to be 172.6 Hz, significantly greater in magnitude than of the aforementioned complexes and highlighting the weak nature of this agostic interaction. Given the solid state parameters of the parent chloride **10**, which show the agostic interaction of **10** to be one of the weakest characterised for a zirconocene complex, 172.6 Hz would be expected to be close to the limit between agostic and non-agostic $^{1}J_{SiH}$ coupling constants. As expected, the two $^{1}J_{SiH}$ coupling constants of $Cp_2Zr(H)\{N(Ph)SiH_2Ph\}$ are similar and >200 Hz.

To relate these observations back to orbital interpretations, attention is next turned to the NBO occupancies and Mayer bond indices,[105] with those of $Cp_2Zr(H)\{N(Me)Si(\mu\text{-}H)HPh\}$ considered before comparison to those of $Cp_2Zr(Cl)\{N(Me)Si(\mu\text{-}H)HPh\}$. The occupancy of the agostic Si–H NBO of $Cp_2Zr(H)\{N(Me)Si(\mu\text{-}H)HPh\}$ (1.791) is significantly lower than that of the non-agostic Si–H NBO (1.973), hence the longer Si–H bond length (1.540 *vs.* 1.500 Å). The reduction in occupancy can be seen to be due to formal donation to zirconium. Indeed, the natural localised molecular orbital (NLMO) corresponding to the agostic Si–H···Zr interaction has *ca.* 89% Si–H bond contribution and 8.6% Zr 4d contribution, which shows the interaction to be predominantly ligand-centred. Second order perturbation analysis gives

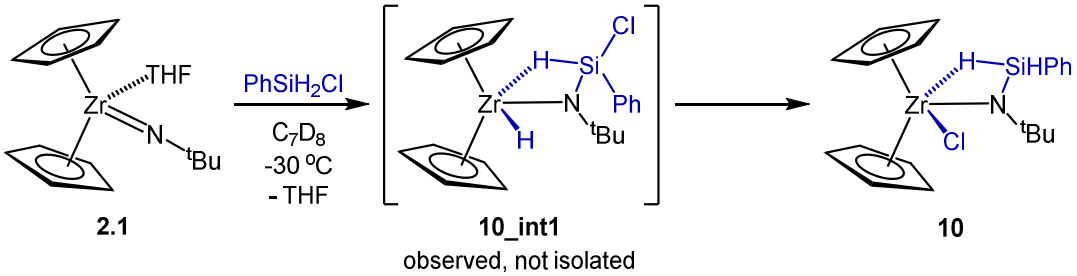
the energy of the agostic Si–H···Zr interaction as 40.1 kcal mol^{-1}; this value must not be considered alone, but only relative to comparable values (such as that of $Cp_2Zr(Cl)\{N(Me)Si(\mu\text{-}H)HPh\}$, *vide infra*). Another manifestation of the agostic interaction is a significant reduction in the Si–H Mayer bond index from 0.918, a value typical for a non-interacting Si–H bond, to 0.506.

For $Cp_2Zr(Cl)\{N(Me)Si(\mu\text{-}H)HPh\}$ the reduction in Si–H Mayer bond index and NBO occupancy for the agostic Si–H bond is, as expected, much less significant. Indeed, from second order perturbation analysis the energy of the agostic Si–H···Zr interaction is calculated to be just 17.7 kcal mol^{-1} (*cf.* 40.1 kcal mol^{-1} for $Cp_2Zr(H)\{N(Me)Si(\mu\text{-}H)HPh\}$) and the resulting NLMO has 94.7% Si–H contribution and only 3.4% Zr 4d contribution, so less covalency than in $Cp_2Zr(H)\{N(Me)Si(\mu\text{-}H)HPh\}$. Analysis of the NBOs shows that the in-plane 3p lone pair of the chloride ligand forms a π-bonding interaction with Zr ($Cl(3p_\pi)\rightarrow Zr(4d_\pi)$). This interaction involves two vacant orbitals of zirconium, one being that same orbital to which the agostic Si–H bond donates. Second order perturbation analysis calculates the component of the $Cl(3p_\pi)\rightarrow Zr(4d_\pi)$ interaction that competes with the agostic Si–H···Zr interaction to be 19.2 kcal mol^{-1}. This shows π-donation from the chloride ligand to zirconium to be the origin of the weakened agostic interaction of **10**, with respect to **6**, as was hypothesised previously in this Chapter and by Berry and co-workers.[53]

2.7.3.2 Mechanism of reaction

The reaction outlined in Equation 2.10 would appear to occur *via* 1,2-addition of the Si–Cl bond to the Zr=N bond. However, on following the reaction between $PhSiH_2Cl$ and **2.1** by ^1H NMR spectroscopy at –30 °C in toluene-d_8 a short-lived, first-formed intermediate, assigned to $Cp_2Zr(H)\{N(^tBu)Si(\mu\text{-}H)ClPh\}$ (**10_int1**, Scheme 2.3), was

observed. Though a satisfactory $^{13}C\{^{1}H\}$ NMR spectrum of **10_int1** could not be obtained, due to its short-lived nature, a ^{1}H NMR spectrum, obtained as a mixture of **10_int1**, **10** and **2.1** in a *ca.* 6:3:1 ratio, was recorded.



2.1 **10_int1** observed, not isolated **10**

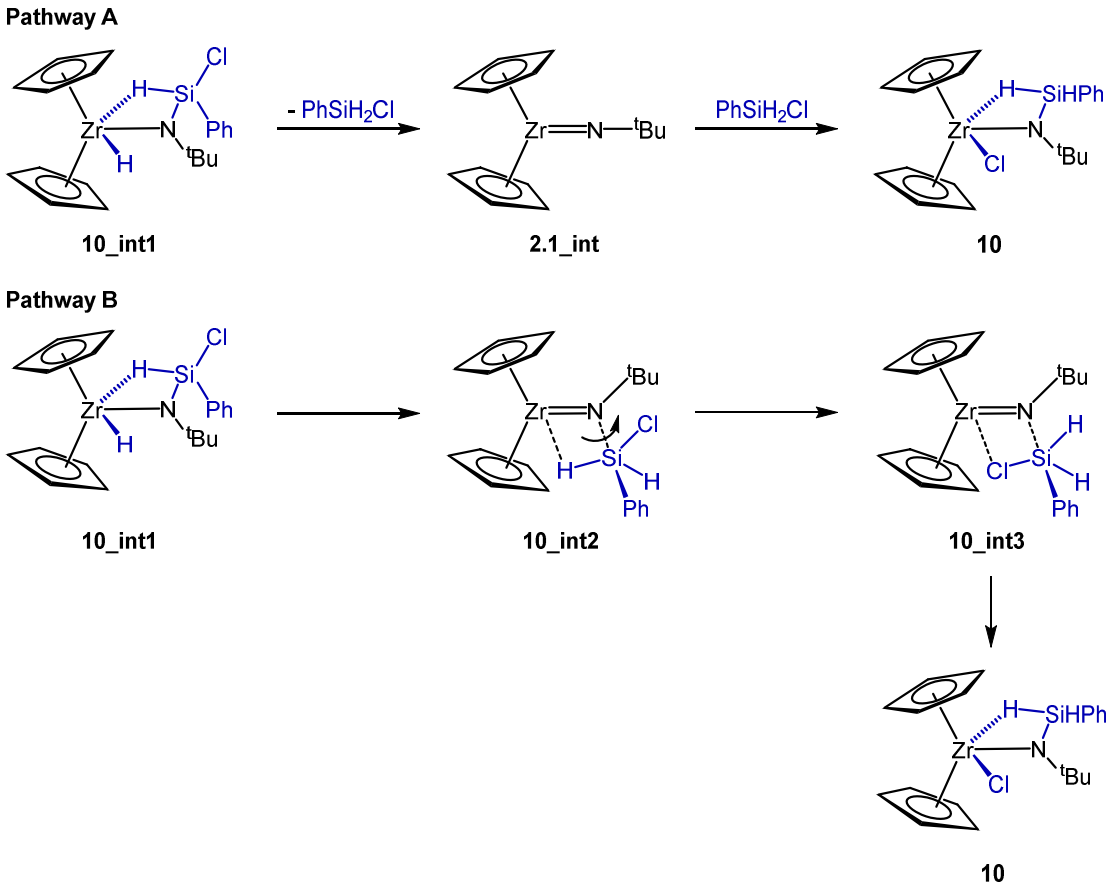
Scheme 2.3: Route of formation of **10** from the reaction between **2.2** and $PhSiH_2Cl$ v*ia* the observed intermediate **10_int1**.

The ^{1}H NMR spectrum of **10_int1** shows two Cp resonances at 5.85 and 5.66 ppm indicating a breakdown in symmetry from a C_s to a C_1 symmetric structure. Mutually coupled doublets at 5.70 and 2.23 ppm ($^{2}J_{HH}$ = 3.1 Hz) are assigned to the ZrH and β-Si–H···Zr environments, respectively. The presence of these doublets is consistent with the observed breakdown in symmetry, with the lack of fluxionality of the agostic hydrogen on the NMR timescale leading to the Si–Cl and Si–Ph bonds pointing in opposite directions, thereby rendering the two Cp moieties inequivalent. Though a ^{29}Si–^{1}H gradient experiment was not able to be carried out, a $^{1}J_{SiH}$ coupling constant of 154 Hz was established by analysis of the ^{29}Si satellites of the SiH resonance. This coupling constant is significantly larger than that of **7** and **2.16** (121 and 113 Hz, respectively), as well as other agostic complexes, indicating a lesser degree of Si–H bond lengthening and so a weaker agostic interaction.[48,49,53,59,60,77,78] The $^{2}J_{HH}$ coupling constant of 3.1 Hz is comparable to that of both **7** and **2.16** (3.7 and 3.1 Hz, respectively), with the ZrH and β-Si–H···Zr resonances appearing in similar regions to that of **7** (5.72 and 2.41 ppm).

The formation of **10_int1** as the kinetic, first-formed product can be rationalised given Si–H bonds are weaker than Si–Cl bonds and so Si–H bond activation would be expected

to have a lower energy barrier than Si–Cl activation (bond dissociation energy of Si–H and Si–Cl bonds are 293 and 417 kJ mol^{-1}, respectively).[106] Indeed, similar mechanistic assertions have been made for chlorosilane addition to a niobium imide, though the exact pathway could not be resolved.[48] This contrasts the observations made for the reaction of **2.3** with $PhSiH_2Cl$ to form **4** (*vide supra*). Furthermore, the analogous reaction between $PhSiH_2Cl$ and $Cp^*Ti\{MeC(N^iPr)_2\}(NNMe_2)$ was reported to proceed *via* 1,2-addition of the Si–Cl bond to the $Ti{=}N_\alpha$ bond to give $Cp^*Ti\{MeC(N^iPr)_2\}(Cl)\{N(NMe_2)SiH_2Ph\}$, with no intermediates or Si–H activation observed.[20] It is possible that the advent of the agostic interaction in **10_int1** affords the complex enough stability such that it can be observed before further reaction to give **10** occurs. Notably, **10_int1** was calculated by DFT to be 7.5 kcal mol^{-1} higher in free energy than **10** (Δ_rG(**2.1** + $PhSiH_2Cl$ → **10** + THF) = –32.1 kcal mol^{-1}).

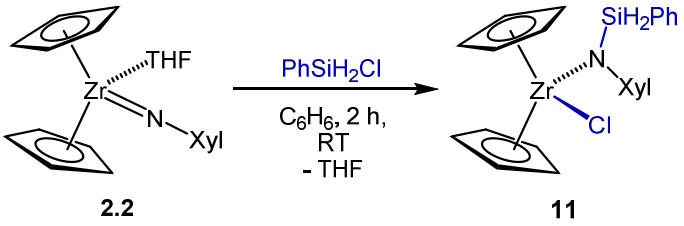
The isomerisation of **10_int1** to give **10** could occur through two possible pathways. Either the reformation of free $PhSiH_2Cl$ and Cp_2ZrN^tBu followed by 1,2-addition of the Si–Cl bond across the Zr=N multiple bond (Pathway A, Scheme 2.4), or the reformation of the Si–H bond to give the adduct **10_int2**, which could then undergo rotation about the N–Si interaction to give **10_int3** and subsequently undergo Si–Cl bond activation (Pathway B, Scheme 2.4). Such intermediates as **10_int2** and **10_int3** have been found, by computational calculations, along similar reaction pathways of silane activation, as has been presented earlier in this Chapter (Section 2.3), and so would likely offer a lower energy pathway than dissociation of the silane.[20] Furthermore, DFT calculations show **2.1_int** to be 29.0 kcal mol^{-1} higher in free energy than **10_int1**, implying an energy barrier of at least 29.0 kcal mol^{-1} for Pathway A, and results of reactions of silanes with compounds **6** – **11** discussed in Chapter 4 of this Thesis imply that Pathway B is kinetically favoured over Pathway A, and so is the mechanism invoked here.



Scheme 2.4: Possible pathways for the formation of **10** from **10_int1**.

2.7.4 Reaction of $Cp_2Zr(NXyl)(THF)$ (2.2) with chlorophenylsilane

On the NMR tube scale, reaction of $Cp_2Zr(NXyl)(THF)$ (**2.2**) with $PhSiH_2Cl$, in C_6D_6 at room temperature, gave quantitative conversion to the hydride silylamide compound $Cp_2Zr(Cl)\{N(Xyl)SiH_2Ph\}$ (**11**) after 15 minutes. On the preparative scale, a mixture of **2.2** and $PhSiH_2Cl$ in benzene was stirred for 2 h at RT, and **11** was isolated as a yellow powder in 64% yield (Equation 2.12). Unlike compounds **8** and **9**, **11** was found to be stable under vacuum and to handling. Compound **11** was characterised by NMR spectroscopy, IR spectroscopy, elemental analysis and X-ray analysis.



2.2 **11**

Equation 2.12

The ^{1}H NMR spectrum of **11** is analogous to that of compound **8**, with a single Cp resonance at 5.87 ppm, a single Me resonance at 2.06 ppm for the methyl groups of the xylyl moiety and a single resonance at 5.46 ppm for the SiH_2 protons. No proton resonance in the region expected for a hydride was observed, consistent with the formation of a zirconium chloride. The chemical shift of 5.46 ppm for the SiH_2 protons is slightly higher than that of **8** (5.26 ppm) and consistent with a terminal SiH_2 resonance, as would be expected considering the lack of agostic interaction in compounds **8** and **9** and that the agostic interaction of chlorides is weaker than that of hydrides (*vide supra*). Furthermore, $^{1}J_{SiH}$ coupling between the singlet at 5.46 ppm and a ^{29}Si resonance at –31.6 ppm was found, by a ^{29}Si-^{1}H gradient experiment, to be 209 Hz – typical for a terminal SiH_2 resonance.

Upon cooling of **11** in toluene-d_8 to –88 °C the Cp, methyl and SiH_2 resonances decoalesce in an analogous manner to **8** (see Appendix, Figure A5). Both the Cp and Me resonances are seen to decoalesce between –50 and –60 °C. The temperature at which the SiH_2 resonance decoalesces could not be determined due to overlap with Cp resonances, though at –88 °C the two SiH resonances could be observed at 5.66 and 5.36 ppm as mutually coupled doublets ($^{2}J_{HH}$ = 9.4 Hz). The chemical shifts of the SiH protons are comparable to those of **8** at –80 °C and are consistent with a lack of agostic interactions once conformationally rigid.

The solid state IR spectrum of **11** is consistent with the compound containing a terminal SiH_2 moiety, exhibiting bands assigned to the two v(Si–H) modes at 2189 and 2149 cm^{-1}.[22,53] The DFT computed IR spectrum of **11**, with the two v(Si–H) modes appearing at 2190 and 2148 cm^{-1}, confirms these assignments. These stretches are comparable to those of **9**, higher than those of **10** (2116 and 2080 cm^{-1}) and significantly higher than v(Si–H_b) of **6** and **7** (1941 and 1893 cm^{-1}, respectively).

Diffraction-quality crystals of **11** were grown from a saturated solution of hexane at 4 °C, confirming the connectivity shown in Equation 2.12. The solid state structure of **11** is shown in Figure 2.19 and selected bond distances and angles in Table 2.7. Compound **11** adopts a typical bent metallocene geometry, akin to **6**, **7**, **10** and $Cp_2Zr(Cl)\{N(^tBu)Si(\mu\text{-}H)Me_2\}$ (**2.18**).[53] In contrast to these structures only two of the three equatorial coordination sites of the zirconocene are occupied. In addition, Si(1), H(1), H(2) and C(1) lie out of the equatorial plane.

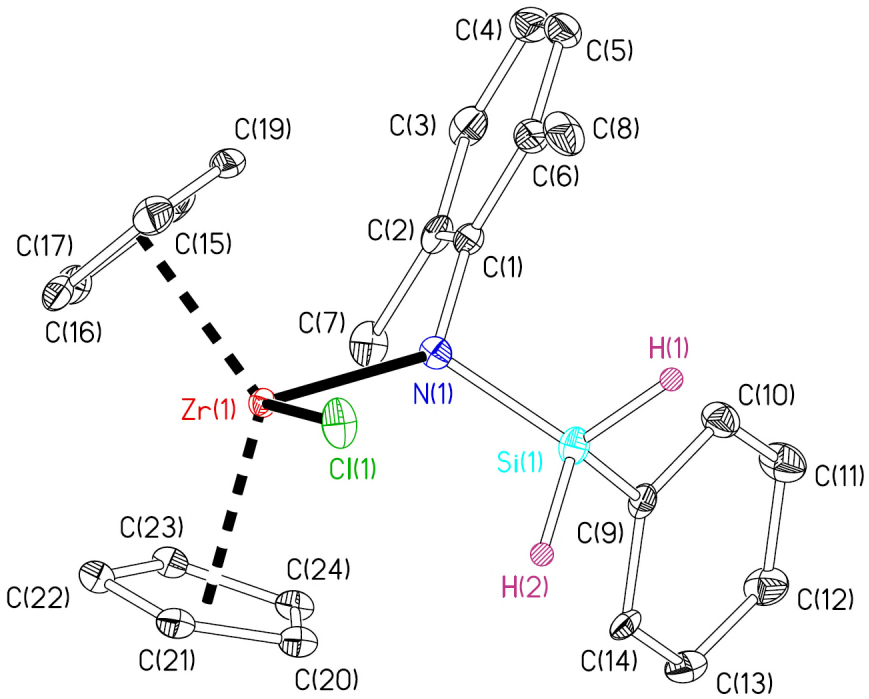


Figure 2.19: Displacement ellipsoid plots (20% probability) of $Cp_2Zr(Cl)\{N(Xyl)SiH_2Ph\}$ (**11**). C–H atoms are omitted for clarity. H(1) and H(2) are drawn as spheres of an arbitrary radius.

Table 2.7: Selected bond distances (Å) and angles (°) for $Cp_2Zr(Cl)\{N(Xyl)SiH_2Ph\}$ (**11**). $Cp_{cent(1)}$ and $Cp_{cent(2)}$ refer to the computed Cp ring centroids for the "lower" and "upper" Cp rings, respectively, as depicted in Figure 2.17.

Zr(1)-N(1)	2.1052(17)	Cl(1)-Zr(1)-N(1)	99.00(5)
Zr(1)-Cl(1)	2.4672(6)	Zr(1)-N(1)-Si(1)	122.83(9)
$Zr(1)-Cp_{cent(1)}$	2.21	Si(1)-N(1)-C(1)	107.33(13)
$Zr(1)-Cp_{cent(2)}$	2.24	C(1)-N(1)-Zr(1)	129.72(13)
N(1)-Si(1)	1.7556(18)	$Cp_{cent(1)}$-Zr(1)-$Cp_{cent(2)}$	126.6
Si(1)-H(1)	1.391(10)		
Si(1)-H(2)	1.397(10)		

Consistent with these observations, as well as spectroscopic observations, and also in contrast to **6**, **7**, **10** and **2.18**, it can be seen that **11** does not contain a β-Si–H···Zr agostic interaction. The Zr–N–Si angle of 122.83(9)° is much larger than is observed for **10** (105.37(9)°), indicating no distortion caused by interaction of the Si–H bond with the zirconium centre. Furthermore, the Zr–Si bond distance of 3.3943(6) Å in **11** is significantly longer than that of **10** and **6** (3.0860(6) Å and 2.9185(10) Å, respectively), with Zr–H(1) and Zr–H(2) distances of 4.297(19) and 3.33(2) Å, respectively – significantly longer than that of **10** and $\{Cp_2ZrC(SiMe_3)C(\mu\text{-}H)(SiMe_3)\}_2O$ (2.61(3) and 2.72(1) Å, respectively).[100]

The Zr–N bond distance of **11** (2.1052(17) Å) is shorter than that of both **6** and **10** (2.169(3) and 2.1516(16) Å, respectively). Meanwhile, the Zr–Cl bond distance of **11** (2.4672(6) Å) is similar to that of **10** (2.4790(6) Å). The shortening of the Zr–N can be attributed to the electron deficiency of the 16 VE metal centre. Whether the bond contains π-interactions that render the bond shorter is not clear. The planar nitrogen (with angles around the nitrogen totalling 359.9(3)°) and Cl(1)–Zr(1)–N(1)–C(1) dihedral angle of *ca*. 120.1° indicate the 2pπ lone pair lies somewhat in the equatorial plane. To investigate

this further the structure and frontier molecular orbitals (see Appendix, Figure A6) of **11** were calculated by DFT. The structure of **11** is consistent with that shown in Figure 2.19, showing no agostic interaction. The HOMO of **11** is a ligand based lone pair, with significant nitrogen 2pπ contribution, though contains negligible zirconium contribution showing there is no interaction between the nitrogen 2pπ lone pair and zirconium. Furthermore, the LUMO pertains to the putative π-acceptor MO of the zirconocene, with negligible nitrogen or chlorine contributions. Therefore the shortening of the Zr–N cannot be attributed to π-interactions. Notably, the chlorine lone pair lying in the equatorial plane (48% contribution, HOMO –9) contains little zirconium contribution (6%).

Notably, **11** crystallises with two stereoisomers in the unit cell, with the frozen rotation about the Zr–N bond rendering the two Cp moieties inequivalent, as shown by VT ^{1}H NMR spectroscopy, and so marking the zirconium a stereocentre. Furthermore, it can be seen that a frozen rotation about the N(1)–C(1) bond renders C(7) and C(8) inequivalent, as was observed in the ^{1}H NMR spectra of **11** below –50 °C. It can also be seen that rotation of the xylyl moiety would lead to steric clashes with the Cp moiety.

2.8 Other reactions

Further to the reactions of zirconocene hydrazides and imides, reactions of both the titanocene hydrazide $Cp_2Ti(NNPh_2)(py)$ (**2.20**) and imide $Cp_2Ti(N^tBu)(py)$ (**2.21**) with silanes $PhSiH_3$, Ph_2SiH_2, Et_3SiH, $^nBuSiH_3$ and $PhSiH_2Cl$, boranes HBPin, 9-BBN, thexyl borane, $HBAr^F_2$ ($Ar^F = C_6F_5$), dicyclohexyl borane, dimesityl borane and catechol borane (HBCat), carbon monoxide and isocyanides XylNC and ^{t}BuNC were attempted. In every case the ^{1}H NMR spectra contained an intractable mixture of very low intensity resonances and solutions were dark in colour.

In the cases of reactions with E–H (E = Si, B) bonds vigorous bubbling was observed on addition of the silane or borane and the ^{1}H NMR spectra revealed the presence of H_2. Assumedly each molecule of H_2 is formed by the combination of two transient titanium(IV) hydrides, giving also two titanium(III) species – explaining the presence of only very low intensity resonances in the ^{1}H NMR spectra. Indeed, EPR spectra of the reactions of **2.20** with $PhSiH_3$ and HBPin revealed the presence of multiple Ti(III) species. It is notable that Beckhaus and co-workers were able to isolate the hydride $(Cp^{Ad})_2Ti(H)\{N(NPh_2)BBN\}$ (**2.8**, Figure 2.1) from reaction of $(Cp^{Ad})_2Ti(NNPh_2)(py)$ (**2.7**) with 9-BBN.[15] Presumably, the large adamantyl groups act to prevent dihydrogen formation in the manner described above.

2.9 Conclusions

The reactions of $Cp_2Zr(NNPh_2)(DMAP)$ (**2.3**) with the borane HBPin and the silanes $PhSiH_3$ and Ph_2SiH_2 have been presented, resulting in the formation of hydride borylhydrazido(1–) and silylhydrazido(1–) compounds $Cp_2Zr(H)\{N(NPh_2)BPin\}$ **1**, $Cp_2Zr(H)\{N(NPh_2)SiH_2Ph\}$ (**2**) and $Cp_2Zr(H)\{N(NPh_2)SiHPh_2\}$ (**3**). The mechanism has been determined by DFT and found to proceed *via* DMAP dissociation, followed by adduct formation and E–H bond addition across the $Zr{=}N_\alpha$ bond, with subsequent isomerisation of first-formed products to yield the experimentally observed, crystallographically characterised compounds. The isomeric preference the compounds, by DFT analysis of a sterically minimised system, has been found to be a steric one. Reaction of **2.3** with the halosilane $PhSiH_2Cl$ has also been presented, resulting in the formation of the chloride silylhydrazido(1-) compound $Cp_2Zr(Cl)\{N(NPh_2)SiH_2Ph\}$ (**4**), apparently occurring *via* Si–Cl addition.

Compounds **1** – **3** were found to be inert towards hydride transfer to N_α and reductive N_α–N_β bond cleavage, with DFT calculations finding such transformations to be thermally inaccessible with free energy barriers of 39.3 and 35.6 kcal mol^{-1} for **1** and **2**, respectively. These observations contrast the facile reductive N_α–N_β bond cleavage found upon the reactions of **2.3** with CO (previously reported by Bergman)[12] and XylNC, a reaction that has been presented in this Chapter, which result in formation of $Cp_2Zr(NPh_2)(NCO)$ (**2.12**) and $Cp_2Zr(NPh_2)(NCNXyl)$ (**5**). As such, the mechanism of the reaction of **2.3** with CO was interrogated by DFT for comparison. Overall, while the free energy barriers to reductive N_α–N_β bond cleavage are similar between the CO, HBPin and $PhSiH_3$ reactions, relative to **2.3** and the relevant reagent, the advent of the stable hydride κ^2-boryl- and κ^2-silylhydrazido(1-) compounds in the cases of HBPin and $PhSiH_3$ (–16.6 and –7.5 kcal mol^{-1}, respectively) render the reductive N_α–N_β cleavage reaction thermally inaccessible.

In addition to these results, the first examples of irreversible Si–H addition across the M=N bond of any Group 4 imide have been presented. Reactions of $Cp_2Zr(N^tBu)(THF)$ (**2.1**) with $PhSiH_3$ and Ph_2SiH_2 result in the formation of the β-agostic hydride silylamide compounds $Cp_2Zr(H)\{N(^tBu)Si(\mu\text{-}H)HPh\}$ (**6**) and $Cp_2Zr(H)\{N(^tBu)Si(\mu\text{-}H)Ph_2\}$ (**7**). Interestingly, reactions of $Cp_2Zr(NXyl)(THF)$ (**2.2**) with $PhSiH_3$ and Ph_2SiH_2 result in the formation of the non-agostic hydride silylamide compounds $Cp_2Zr(H)\{N(Xyl)SiH_2Ph\}$ (**8**) and $Cp_2Zr(H)\{N(Xyl)SiHPh_2\}$ (**9**). The agostic and non-agostic isomers of both **6** and **8**, along with the related 'NPh' analogue, were interrogated by DFT analysis to investigate the origin of the isomeric preferences of the compounds. It was found that steric factors predominantly influenced the isomeric preference, while electronic factors had a minor effect.

Additionally, reactions of **2.1** and **2.2** with $PhSiH_2Cl$ were presented, resulting in the formation of $Cp_2Zr(Cl)\{N(^tBu)Si(\mu\text{-}H)HPh\}$ (**10**) and $Cp_2Zr(Cl)\{N(Xyl)SiH_2Ph\}$ (**11**). In contrast to literature examples of chlorosilane addition to Group 4 hydrazides, reaction of **2.1** with $PhSiH_2Cl$ was found to proceed *via* Si–H addition across the Zr=N bond, giving the short-lived, first-formed product $Cp_2Zr(H)\{N^tBu)Si(\mu\text{-}H)ClPh\}$ (**10_int1**).[67] Subsequently, **10_int1** was found to undergo a non-dissociative isomerisation to give **10**. NBO analysis on the DFT model compounds $Cp_2Zr(H)\{N(Me)Si(\mu\text{-}H)HPh\}$, $Cp_2Zr(Cl)\{N(Me)Si(\mu\text{-}H)HPh\}$ and $Cp_2Zr(H)\{N(Ph)SiH_2Ph\}$ was also conducted, showing the origin of the weakened agostic interaction of **10**, relative to **6**, to be due to competitive π-donation of the chloride ligand.

2.10 References

1 D. E. Wigley, *Prog. Inorg. Chem.*, 1994, **42**, 239–482.
2 P. Mountford, *Chem. Commun.*, 1997, 2127–2134.
3 C. Lorber, *Coord. Chem. Rev.*, 2016, **308**, 76–96.
4 L. H. Gade and P. Mountford, *Coord. Chem. Rev.*, 2001, **216**–**217**, 65–97.
5 A. P. Duncan and R. G. Bergman, *Chem. Rec.*, 2002, **2**, 431–445.
6 P. Bolton and P. Mountford, *Adv. Synth. Catal.*, 2005, **347**, 355–366.
7 N. Hazari and P. Mountford, *Acc. Chem. Res.*, 2005, **38**, 839–849.
8 A. L. Odom, *Dalton Trans.*, 2005, 225–233.
9 A. R. Fout, U. J. Kilgore and D. J. Mindiola, *Chem. Eur. J.*, 2007, **13**, 9428–9440.
10 A. V. Lee and L. L. Schafer, *Eur. J. Inorg. Chem.*, 2007, **2007**, 2245–2255.
11 T. E. Müller, K. C. Hultzsch, M. Yus, F. Foubelo and M. Tada, *Chem. Rev.*, 2008, **108**, 3795–3892.
12 P. J. Walsh, M. J. Carney and R. G. Bergman, *J. Am. Chem. Soc.*, 1991, **113**, 6343–6345.
13 P. J. Walsh, F. J. Hollander and R. G. Bergman, *J. Organomet. Chem.*, 1992, **428**, 13–47.
14 J. R. Dilworth, *Coord. Chem. Rev.*, 2017, **330**, 53–94.
15 M. Manßen, M.-F. Meyer, M. Schmidtmann and R. Beckhaus, *Organometallics*, 2018, **37**, 4515–4520.
16 Y. Li, Y. Shi and A. L. Odom, *J. Am. Chem. Soc.*, 2004, **126**, 1794–1803.
17 H. Herrmann, H. Wadepohl and L. H. Gade, *Dalton Trans.*, 2008, 2111.
18 D. J. Mindiola, *Angew. Chem., Int. Ed.*, 2008, **47**, 1557–1559.
19 J. D. Selby, C. Schulten, A. D. Schwarz, A. Stasch, E. Clot, C. Jones and P. Mountford, *Chem. Commun.*, 2008, 5101.
20 P. J. Tiong, A. Nova, E. Clot and P. Mountford, *Chem. Commun.*, 2011, **47**, 3147.
21 P. J. Tiong, A. Nova, L. R. Groom, A. D. Schwarz, J. D. Selby, A. D. Schofield, E. Clot and P. Mountford, *Organometallics*, 2011, **30**, 1182–1201.
22 L. C. Stevenson, S. Mellino, E. Clot and P. Mountford, *J. Am. Chem. Soc.*, 2015, **137**, 10140–10143.
23 S. Mellino, L. C. Stevenson, E. Clot and P. Mountford, *Organometallics*, 2017, **36**, 3329–3342.
24 A. D. Schwarz, A. Nova, E. Clot and P. Mountford, *Chem. Commun.*, 2011, **47**, 4926.
25 A. D. Schwarz, A. Nova, E. Clot and P. Mountford, *Inorg. Chem.*, 2011, **50**, 12155–12171.
26 L. R. Groom, A. D. Schwarz, A. Nova, E. Clot and P. Mountford, *Organometallics*, 2013, **32**, 7520–7539.
27 R. Thompson, C.-H. Chen, M. Pink, G. Wu and D. J. Mindiola, *J. Am. Chem. Soc.*, 2014, **136**, 8197–8200.
28 L. N. Grant, B. Pinter, T. Kurogi, M. E. Carroll, G. Wu, B. C. Manor, P. J. Carroll and D. J. Mindiola, *Chem. Sci.*, 2017, **8**, 1209–1224.
29 B. A. Clough and P. Mountford, *Organometallics*, 2018, **37**, 3558–3572.
30 B. A. Clough, S. Mellino, A. V. Protchenko, M. Slusarczyk, L. C. Stevenson, M. P. Blake, B. Xie, E. Clot and P. Mountford, *Inorg. Chem.*, 2017, **56**, 10794–10814.
31 P. J. Walsh, A. M. Baranger and R. G. Bergman, *J. Am. Chem. Soc.*, 1992, **114**,

1708–1719.
32 A. M. Baranger, P. J. Walsh and R. G. Bergman, *J. Am. Chem. Soc.*, 1993, **115**, 2753–2763.
33 M. Slusarczyk, DPhil Thesis, University of Oxford, 2018.
34 A. D. Schofield, A. Nova, J. D. Selby, A. D. Schwarz, E. Clot and P. Mountford, *Chem. Eur. J.*, 2011, **17**, 265–285.
35 J. D. Selby, C. D. Manley, M. Feliz, A. D. Schwarz, E. Clot and P. Mountford, *Chem. Commun.*, 2007, 4937.
36 H. Herrmann, J. Lloret Fillol, H. Wadepohl and L. H. Gade, *Angew. Chem., Int. Ed.*, 2007, **46**, 8426–8430.
37 P. J. Walsh, F. J. Hollander and R. G. Bergman, *Organometallics*, 1993, **12**, 3705–3723.
38 P. J. Walsh, F. J. Hollander and R. G. Bergman, *J. Am. Chem. Soc.*, 1988, **110**, 8729–8731.
39 A. D. Schofield, DPhil Thesis, University of Oxford, 2012.
40 B. Xie, DPhil Thesis, University of Oxford, 2018.
41 P. J. Walsh, F. J. Hollander and R. G. Bergman, *J. Organomet. Chem.*, 1992, **428**, 13–47.
42 P.-J. Tiong, A. D. Schofield, J. D. Selby, A. Nova, E. Clot and P. Mountford, *Chem. Commun.*, 2010, **46**, 85–87.
43 T. Gehrmann, J. Lloret-Fillol, H. Herrmann, H. Wadepohl and L. H. Gade, *Organometallics*, 2013, **32**, 3877–3889.
44 J. Chu, X. Han, C. E. Kefalidis, J. Zhou, L. Maron, X. Leng and Y. Chen, *J. Am. Chem. Soc.*, 2014, **136**, 10894–10897.
45 P. J. Tiong, DPhil Thesis, University of Oxford, 2012.
46 T. I. Gountchev and T. D. Tilley, *J. Am. Chem. Soc.*, 1997, **119**, 12831–12841.
47 J. Chu, E. Lu, Y. Chen and X. Leng, *Organometallics*, 2013, **32**, 1137–1140.
48 G. I. Nikonov, P. Mountford, S. K. Ignatov, J. C. Green, M. A. Leech, L. G. Kuzmina, A. G. Razuvaev, N. H. Rees, A. J. Blake, J. A. K. Howard and D. A. Lemenovskii, *J. Chem. Soc., Dalton Trans.*, 2001, 2903–2915.
49 S. K. Ignatov, N. H. Rees, A. A. Merkoulov, S. R. Dubberley, A. G. Razuvaev, P. Mountford and G. I. Nikonov, *Chem. Eur. J.*, 2008, **14**, 296–310.
50 S. K. Ignatov, A. Y. Khalimon, N. H. Rees, A. G. Razuvaev, P. Mountford and G. I. Nikonov, *Inorg. Chem.*, 2009, **48**, 9605–9622.
51 P. J. Walsh, M. J. Carney and R. G. Bergman, *J. Am. Chem. Soc.*, 1991, **113**, 6343–6345.
52 J. Unruangsri, H. Morgan, A. D. Schwarz, A. D. Schofield and P. Mountford, *Organometallics*, 2013, **32**, 3091–3107.
53 L. J. Procopio, P. J. Carroll and D. H. Berry, *J. Am. Chem. Soc.*, 1994, **116**, 177–185.
54 L. J. Procopio, P. J. Carroll and D. H. Berry, *J. Am. Chem. Soc.*, 1991, **113**, 1870–1872.
55 L. J. Procopio, P. J. Carroll and D. H. Berry, *Organometallics*, 1993, **12**, 3087–3093.
56 K. Yan, A. Pindwal, A. Ellern and A. D. Sadow, *Dalton Trans.*, 2014, **43**, 8644–8653.
57 K. Yan and A. D. Sadow, *Chem. Commun.*, 2013, **49**, 3212–3214.
58 K. Yan, J. J. Duchimaza Heredia, A. Ellern, M. S. Gordon and A. D. Sadow, *J. Am. Chem. Soc.*, 2013, **135**, 15225–15237.
59 K. Yan, A. Ellern and A. D. Sadow, *J. Am. Chem. Soc.*, 2012, **134**, 9154–9156.

60 N. A. McLeod, L. G. Kuzmina, I. Korobkov, J. A. K. Howard and G. I. Nikonov, *Dalton Trans.*, 2016, **45**, 2554–2561.
61 A. Reichert, M. Bolte, H.-W. Lerner and M. Wagner, *Dalton Trans.*, 2013, **42**, 688–694.
62 R. F. Jordan, C. S. Bajgur, W. E. Dasher and A. L. Rheingold, *Organometallics*, 1987, **6**, 1041–1051.
63 C. R. Groom, I. J. Bruno, M. P. Lightfoot and S. C. Ward, *Acta Crystallogr.*, 2016, **B72**, 171–179.
64 S. Gambarotta, C. Floriani, A. Chiesi-Villa and C. Guastini, *Inorg. Chem.*, 1983, **22**, 2029–2034.
65 S. L. Buchwald, B. T. Watson, M. W. Wannamaker and J. C. Dewan, *J. Am. Chem. Soc.*, 1989, **111**, 4486–4494.
66 D. A. Gately, J. R. Norton and P. A. Goodson, *J. Am. Chem. Soc.*, 1995, **117**, 986–996.
67 P. J. Tiong, A. Nova, A. D. Schwarz, J. D. Selby, E. Clot and P. Mountford, *Dalton Trans.*, 2012, **41**, 2277.
68 T. Gehrmann, S. A. Scholl, J. L. Fillol, H. Wadepohl and L. H. Gade, *Chem. Eur. J.*, 2012, **18**, 3925–3941.
69 M. E. Silver and R. C. Fay, *Organometallics*, 1983, **2**, 44–47.
70 S. Mellino, DPhil Thesis, University of Oxford, 2017.
71 M. Pierce-Butler and G. R. Willey, *J. Organomet. Chem.*, 1973, **54**, C19–C21.
72 C. J. Carmalt, A. C. Newport, I. P. Parkin, A. J. P. White and D. J. Williams, *J. Chem. Soc., Dalton Trans.*, 2002, 4055–4059.
73 D. A. Pennington, P. N. Horton, M. B. Hursthouse, M. Bochmann and S. J. Lancaster, *Polyhedron*, 2005, **24**, 151–156.
74 J. Y. Corey, *Chem. Rev.*, 2016, 116, 11291–11435.
75 A. Y. Khalimon, O. G. Shirobokov, E. Peterson, R. Simionescu, L. G. Kuzmina, J. A. K. Howard and G. I. Nikonov, *Inorg. Chem.*, 2012, **51**, 4300–4313.
76 L. C. Stevenson, DPhil Thesis, University of Oxford, 2015.
77 N. Eedugurala, Z. Wang, K. Yan, K. C. Boteju, U. Chaudhary, T. Kobayashi, A. Ellern, I. I. Slowing, M. Pruski and A. D. Sadow, *Organometallics*, 2017, **36**, 1142–1153.
78 K. C. Boteju, S. Wan, A. Venkatesh, A. Ellern, A. J. Rossini and A. D. Sadow, *Chem. Commun.*, 2018, **54**, 7318–7321.
79 M. Brookhart, M. L. H. Green and L.-L. Wong, *Prog. Inorg. Chem.*, 1988, **36**, 1–124.
80 C. Kayser, D. Frank, J. Baumgartner and C. Marschner, *J. Organomet. Chem.*, 2003, **667**, 149–153.
81 T. D. Tilley, *Organometallics*, 1985, **4**, 1452–1457.
82 N. Peulecke, A. Ohff, P. Kosse, A. Tillack, A. Spannenberg, R. Kempe, W. Baumann, V. V. Burlakov and U. Rosenthal, *Chem. – A Eur. J.*, 1998, **4**, 1852–1861.
83 W. A. Herrmann, N. W. Huber and J. Behm, *Chem. Ber.*, 1992, **125**, 1405–1407.
84 R. F. Jordan, P. K. Bradley, N. C. Baenziger and R. E. LaPointe, *J. Am. Chem. Soc.*, 1990, **112**, 1289–1291.
85 F.-C. Liu, J.-H. Chen, S.-C. Chen, K.-Y. Chen, G.-H. Lee and S.-M. Peng, *J. Organomet. Chem.*, 2005, **690**, 291–300.
86 P. Mountford, Unpublished Results.
87 B. Liu, T. Roisnel, J.-P. Guégan, J.-F. Carpentier and Y. Sarazin, *Chem. Eur. J.*, 2012, **18**, 6289–6301.

88 Y. Sarazin, D. Roşca, V. Poirier, T. Roisnel, A. Silvestru, L. Maron and J. F. Carpentier, *Organometallics*, 2010, **29**, 6569–6577.
89 I. Nagl, W. Scherer, M. Tafipolsky and R. Anwander, *Eur. J. Inorg. Chem.*, 1999, **1999**, 1405–1407.
90 J. Eppinger, M. Spiegler, W. Hieringer, W. A. Herrmann and R. Anwander, *J. Am. Chem. Soc.*, 2000, **122**, 3080–3096.
91 C. Meermann, G. Gerstberger, M. Spiegler, K. W. Törnroos and R. Anwander, *Eur. J. Inorg. Chem.*, 2008, **2008**, 2014–2023.
92 A. Y. Khalimon, R. Simionescu, L. G. Kuzmina, J. A. K. Howard and G. I. Nikonov, *Angew. Chem., Int. Ed.*, 2008, **47**, 7701–7704.
93 A. Y. Khalimon, R. Simionescu and G. I. Nikonov, *J. Am. Chem. Soc.*, 2011, **133**, 7033–7053.
94 W. A. Herrmann, J. Eppinger, M. Spiegler, O. Runte and R. Anwander, *Organometallics*, 1997, **16**, 1813–1815.
95 M. G. Klimpel, H. W. Görlitzer, M. Tafipolsky, M. Spiegler, W. Scherer and R. Anwander, *J. Organomet. Chem.*, 2002, **647**, 236–244.
96 M. Okazaki and S. Ebina, *Chem. Lett.*, 2014, **43**, 1089–1091.
97 B. Liu, T. Roisnel, J.-F. Carpentier and Y. Sarazin, *Chem. Eur. J.*, 2013, **19**, 2784–2802.
98 W. Scherer, V. Herz and C. Hauf, *Struct. Bond.*, 2012, **146**, 159–207.
99 I. S. Butler and J. F. Harrod, *Inorganic chemistry : principles and applications*, Benjamin Cummings, 1989.
100 U. Rosenthal, A. Ohff, M. Michalik, H. Gorls, V. V Burlakovil and V. B. Shurll, *Organometallics*, 1993, **12**, 5016–5019.
101 A. E. Reed, L. A. Curtiss and F. Weinhold, *Chem. Rev.*, 1988, **88**, 899–926.
102 F. Weinhold and C. R. Landis, *Valency and Bonding: A Natural Bond Orbital Donor-Acceptor Perspective*, Cambridge University Press, Cambridge, 2005.
103 F. Jensen, *J. Chem. Theory Comput.*, 2015, **11**, 132–138.
104 F. Jensen, *Theor. Chem. Acc.*, 2010, **126**, 371–382.
105 A. J. Bridgeman, G. Cavigliasso, L. R. Ireland and J. Rothery, *J. Chem. Soc., Dalton Trans.*, 2001, 2095–2108.
106 Y.-R. Luo and D. O'Hare, *Comprehensive Handbook of Chemical Bond Energies*, CRC Press, 2007.

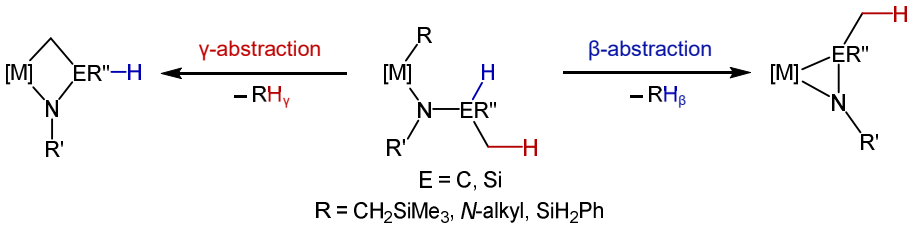
Chapter Three

Reactions of zirconocene hydride silylamides with terminal alkynes and ethylene

3.1 Introduction

Compounds bearing silylamide ligands have exhibited a rich reaction chemistry. Indeed, selected reactions of zirconocene silylamide compounds were discussed in Chapter 1 of this Thesis.[1–6] Reactive silylamido ligands usually contain β-agostic interactions, as found in $Cp_2Zr(H)\{N(^tBu)Si(\mu\text{-}H)HPh\}$ (**6**), $Cp_2Zr(H)\{N(^tBu)Si(\mu\text{-}H)Ph_2\}$ (**7**) and $Cp_2Zr(Cl)\{N(^tBu)Si(\mu\text{-}H)HPh\}$ (**10**), and very little has been reported for non-agostic β-hydrogen-containing silylamides akin to $Cp_2Zr(H)\{N(Xyl)SiH_2Ph\}$ (**8**), $Cp_2Zr(H)\{N(Xyl)SiHPh_2\}$ (**9**) and $Cp_2Zr(Cl)\{N(Xyl)SiH_2Ph\}$ (**11**).[5] Furthermore, the hallmark of β-agostic silylamide ligand chemistry is the abstraction or elimination of a β- or γ-hydrogen, followed by reaction with substrates, usually unsaturated, across the reactive Zr–Si or Zr–C bond.

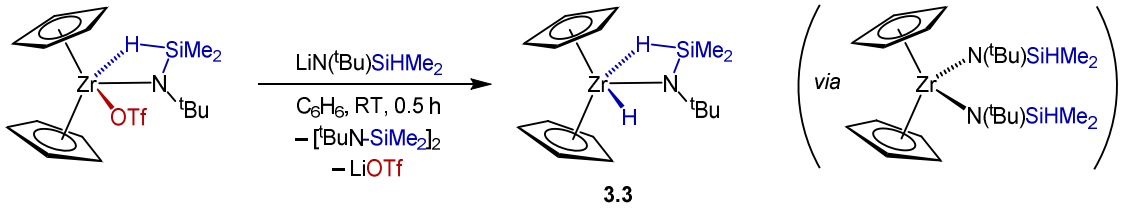
β- and γ-hydrogen abstraction and elimination reactions are ubiquitous in synthetic organometallic chemistry and catalysis, though are sometimes unwanted; for example they can disfavour σ-bond metathesis reactions, and the slow β-elimination of the disilylamido ligand $N(SiHMe_2)_2$ has been noted to allow its use in groups 2 and 3 and f-element chemistry.[7–14] Such hydrogen abstraction reactions require amenable R ligands placed *cis* to the β- or γ-hydrogen bearing ligand (R = alkyl, alkenyl, silyl, amide, Equation 3.1).[1–3,5,15–20]



Equation 3.1[5]

Berry and co-workers reported abstraction of the SiH hydrogen of $Cp_2Zr(CH_2SiMe_3)\{N(^tBu)Si(\mu\text{-}H)Me_2\}$ (**3.1**), with concurrent tetramethylsilane

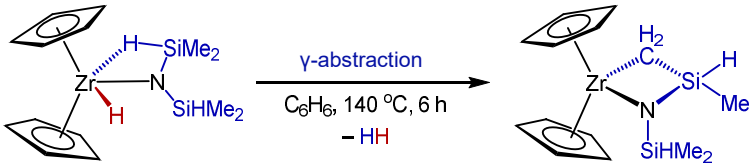
elimination, forming $Cp_2Zr\{\eta^2\text{-}N(^tBu)SiMe_2\}(PMe_3)$ (**3.2**) in the presence of PMe_3.[1] Reversible β-hydrogen abstraction by the SiH_2Ph ligand of the agostic molybdenum silyl silylamide $(ArN)(PMe_3)(PhH_2Si)Mo\{N(Ar)Si(\mu\text{-}H)HPh\}$ to give $(ArN)(PMe_3)Mo\{\eta^2\text{-}N(Ar)SiHPh\}$ and $PhSiH_3$ has also been reported by Nikonov and co-workers.[15,21,22] *N*-alkyl ligands of zirconocene amido and silylamide complexes have also been reported to induce β-abstraction.[1,5,19] As for β-elimination reactions of zirconocene silylamides, Sadow and co-workers reported the β-elimination of a transiently formed bis(disilylamido) complex to give $Cp_2Zr(H)\{N(^tBu)Si(\mu\text{-}H)Me_2\}$ (**3.3**) (Equation 3.2).[3]



3.3

Equation 3.2[3]

In contrast to these aforementioned systems, *hydride* silylamide complexes have not been observed to undergo β-hydrogen abstraction or elimination reactions. Rather, the zirconocene hydride silylamide $Cp_2Zr(H)\{N(SiHMe_2)Si(\mu\text{-}H)Me_2\}$ (**3.4**) was found to undergo γ-H abstraction and eliminate dihydrogen to give $Cp_2Zr\{\kappa^2\text{-}N(SiHMe_2)SiHMeCH_2\}$ (**3.5**), albeit under forcing conditions (Equation 3.3).[5] γ-Hydrogen abstraction has also been observed for silylamide complexes lacking β-hydrogens.[5,23–30] Abstraction of the β-SiH hydrogen of **3.4** was only observed by introduction of the Lewis acid $B(C_6F_5)_3$, forming $[Cp_2Zr\{N(Si(\mu\text{-}H)Me_2)_2\}][HB(C_6F_5)_3]$.[4] Furthermore, the reverse of β-H abstraction, dihydrogen insertion into the Zr–Si bond of **3.2** to give **3.3**, is spontaneous at room temperature.[1]



3.4 **3.5**

Equation 3.3[5]

Remarkably, the hydride silylamides Cp*Ta(H)(X){κ^2-(PhH$_2$Si)N(C$_6$H$_3$Me)$_2$N(SiMe$_3$) (X = Cl or Me), bearing both β- and γ-hydrogens underwent silane elimination to give Me$_3$SiH and the tantalum imides Cp*Ta(X){κ^2-N(C$_6$H$_3$Me)$_2$N(SiH$_2$Ph)}, akin to chemistry observed for hydride silylhydrazido(1-) complexes.[31–33] Notably, the dimeric tantalum hydride dimethyl*amide* [(Me$_2$N){(Me$_3$Si)$_2$N}Ta(μ-H)$_2$(μ-C-η^2-CHSiMe$_2$NSiMe$_3$)Ta(NMe$_2$)$_2$] (which can be thought of as (L)$_n$Ta(H)(NMe$_2$)) was shown to undergo hydride β-H abstraction to eliminate dihydrogen.[34] Such β-H abstractions have been shown to be common for dimethylamine ligands of d^0 complexes, as well as for other amide ligands, and a similar reaction has been reported for a transiently formed niobium hydride aryloxide.[17,19,35,36]

Overall, the β-hydrogen abstraction of silylamide ligands gives rise to reactive η^2-silanimines, which have exhibited interesting reaction chemistry. However, these require amenable, adjacent M–R ligands (e.g. R = CH$_2$SiMe$_3$, *N*-alkyl, R ≠ H) to facilitate abstraction, and other reaction pathways, such as γ-hydrogen abstraction, can prove more favourable. Hydride silylamides have hitherto not exhibited β-hydrogen abstraction, preferring these other reaction pathways or requiring insertion of small unsaturated molecules, such as ethylene or formaldehyde,[1] into the Zr–H bond to give an alkyl or alkoxide species prior to β-hydrogen abstraction.

This Chapter describes the reactions of Cp$_2$Zr(H){N(ᵗBu)Si(μ-H)HPh} (**6**) and Cp$_2$Zr(H){N(ᵗBu)Si(μ-H)Me$_2$} (**3.3**) with two, very different terminal alkynes, namely HCCC$_6$F$_5$ and HCCᵗBu. The compounds exhibit the first examples of β-hydrogen

abstraction of hydride silylamides to eliminate dihydrogen, with subsequent 1,2-insertion and C–H activation of $HCCC_6F_5$ and HCC^tBu, respectively, across transiently formed Zr–Si bonds. Accompanying kinetic and DFT studies will be described, including the reactions of **6** and **3.3** with PMe_3 and the reaction of $Cp_2Zr\{\eta^2\text{-}N(^tBu)SiMe_2\}(PMe_3)$ (**3.2**) with HCC^tBu, to confirm the reaction mechanism. Catalytic ethylene hydrogenation with **6** will also be discussed briefly.

It can be noted that all DFT calculations discussed in this chapter were performed by Professor Philip Mountford. Full details of these calculations are provided in Chapter 6, Section 6.4.

3.2 Reactions of $Cp_2Zr(H)\{N(^tBu)Si(\mu\text{-}H)HPh\}$ (6) and $Cp_2Zr(H)\{N(^tBu)Si(\mu\text{-}H)Me_2\}$ (3.3) with terminal alkynes

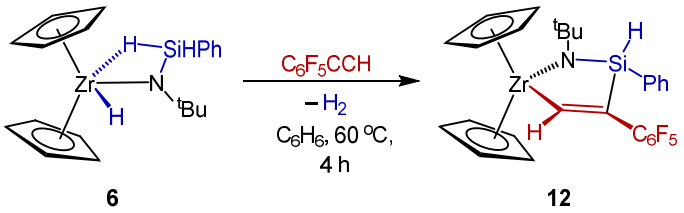
Berry and co-workers reported cycloaddition of internal alkynes with the η^2-silanimines **3.2** or $Cp_2Zr(CO)\{\eta^2\text{-}N(^tBu)SiMe_2\}$, though no reactivity with hydride or alkyl silylamides was reported.[2] Attempts to react compounds **6** – **9** with internal alkyne MeCCTol gave no reaction, even in excess or at elevated temperatures. Attention was then turned to reactions with terminal alkynes, of which there have been no previously reported reactions in the literature.

Reaction of *p*-tolylacetylene (HCCTol) with compound **6** gave a mixture of products, as judged by ^{1}H NMR spectroscopy in C_6D_6. Though no products could be fully assigned, dihydrogen, at 4.47 ppm, was observed in the spectrum. In addition, a singlet resonance at 8.40 ppm corresponding to a vinylic CH proton and a broad SiH_2 or SiH resonance at 4.30 ppm could be identified. It is notable that compounds **8** and **9** gave no reaction with HCCTol, even under forcing conditions, while reaction with compound **7** gave an intractable mixture of products. Given the propensity of HCCTol to form a mixture of products with **6**, the more electron deficient alkyne $HCCC_6F_5$ and the bulky, more electron-rich alkyne HCC^tBu were reacted with **6** in an attempt to observe more clean reactivity.

3.2.1 Reactions of $Cp_2Zr(H)\{N(^tBu)Si(\mu\text{-}H)HPh\}$ (6) and $Cp_2Zr(H)\{N(^tBu)Si(\mu\text{-}H)Me_2\}$ (3.3) with $HCCC_6F_5$

On the NMR tube scale, stoichiometric reaction of **6** and $HCCC_6F_5$, in C_6D_6 at 60 °C, led to complete consumption of the starting materials within 4 h. In contrast to the mixture of compounds observed for the reaction of **6** with HCCTol, $HCCC_6F_5$ gave 85%

conversion to the metallacycle $Cp_2Zr\{N(^tBu)Si(H)(Ph)C(C_6F_5)CH\}$ (**12**), as judged by ^1H NMR spectroscopy (Equation 3.4). On following the reaction *in situ* by ^1H NMR spectroscopy, H_2 could be seen to evolve as the reaction proceeded. On the preparative scale, **12** was isolated as a yellow gum and attempts to triturate the compound with pentane or crystallise the compound from ether, toluene or by layering were unsuccessful.



6 **12**

Equation 3.4

The ^1H NMR spectrum (Figure 3.1) of **12** shows two sharp, singlet resonances at 6.00 and 5.88 ppm corresponding to two magnetically inequivalent Cp groups. This indicates a breakdown in symmetry of the zirconocene complex from C_s to C_1 in the solution phase, caused by the chiral silicon of the metallacycle. A ^1H-^{13}C HSQC NMR experiment reveals a one-bond interaction between the singlet proton at 8.40 ppm, assigned to ZrCH, with a carbon resonance at 212.8 ppm. The high shift of this carbon resonance is indicative of a ZrC environment, as has previously been reported for related zirconacycles.[37,38] In addition, a ^1H-^{13}C HMBC NMR experiment shows a two-bond interaction between the ZrCH proton and a carbon resonance at 120.5 ppm, which contains no ^1H-^{13}C HSQC correlations and is assigned to the $ZrC(H)\underline{C}C_6F_5$ carbon.

The ZrCH resonance was absent in the ^1H NMR spectrum of the reaction of **6** with $DCCC_6F_5$, confirming assignment of this proton (Scheme 3.1). Furthermore, a ^{29}Si-^1H gradient experiment reveals a three-bond interaction between the singlet at 8.40 ppm and a ^{29}Si resonance at –41.7 ppm ($^3J_{SiH}$ = 19 Hz), consistent with the proposed structure, and the ^{29}Si satellites can be seen (indicated by * in Figure 3.1). The ^{29}Si-^1H gradient experiment also reveals a one-bond interaction between the triplet at 5.49 ppm and the

^{29}Si resonance at –41.7 ppm ($^{1}J_{SiH}$ = 204 Hz). This indicates the resonance at 5.49 ppm, which also reveals no single bond correlations to any ^{13}C resonances by ^{1}H–^{13}C HSQC or HMBC experiments, can be assigned to the SiH resonance of **12**.

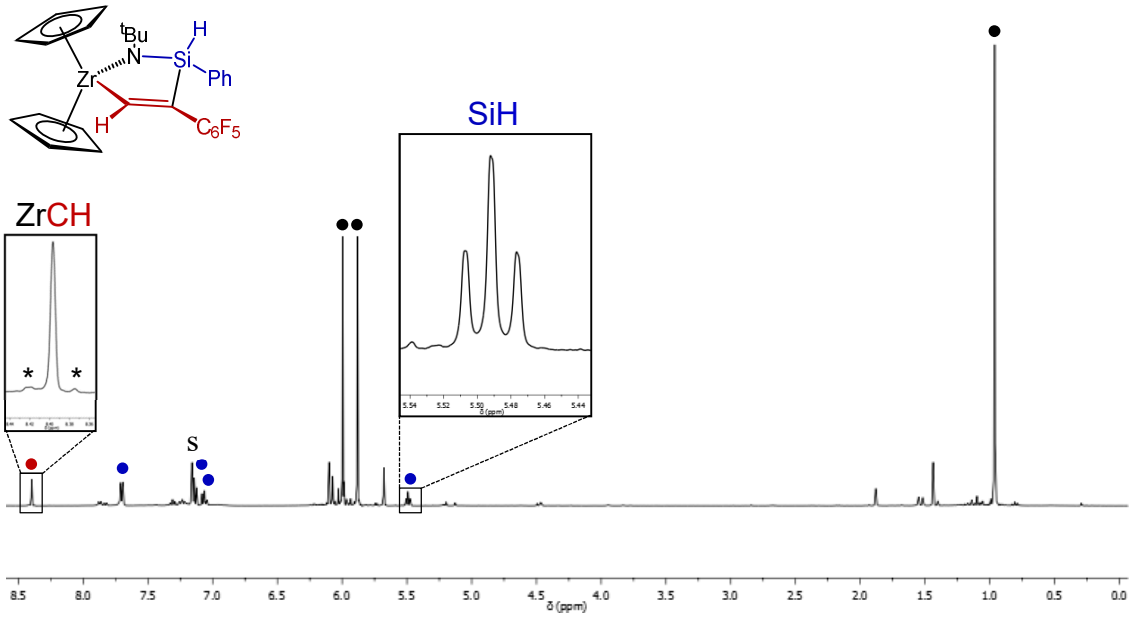
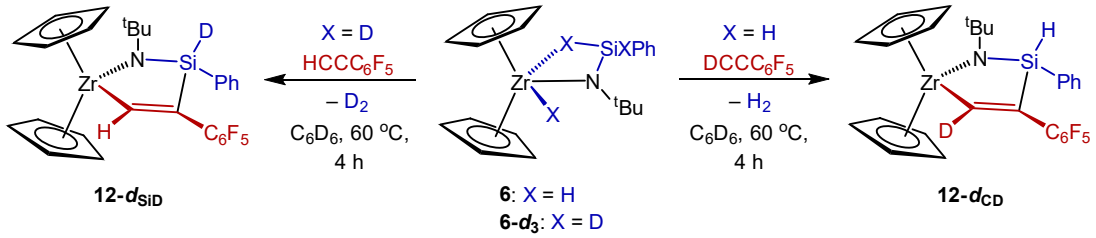


Figure 3.1: ^{1}H NMR spectrum (C_6D_6, 400.1 MHz, 298 K) of $Cp_2Zr\{N(^tBu)Si(H)(Ph)C(C_6F_5)CH\}$ (**12**) with the ZrCH resonance (and its ^{29}Si satellites, *) and SiH resonance enlarged.



12-d_{SiD} **6**: X = H **6-d_3**: X = D **12-d_{CD}**

Scheme 3.1: Reaction of **6** with $DCCC_6F_5$ to give **12-d_{CD}** (right) and reaction of **6-d_3** with $HCCC_6F_5$ to give **12-d_{SiD}** (left).

Reaction of **6-d_3** with $HCCC_6F_5$ confirms the assignment of this resonance (Scheme 3.1). Furthermore, the large $^{1}J_{SiH}$ coupling of 204 Hz (*cf.* $^{1}J_{SiH}$ = 173 Hz for **6**) indicates a loss of the agostic interaction. A ^{1}H-^{1}H COSY NMR experiment reveals only one interaction between the SiH triplet and another proton resonance – the ZrCH singlet at 8.40 ppm. This interaction cannot account for the 6.2 Hz coupling contained within the SiH triplet. As such, coupling must arise from interaction to a fluorine environment. Indeed, the ^{19}F

NMR spectrum reveals a 6.2 Hz doublet coupling of the *o*-C_6F_5 multiplet (not present in the $^{19}F\{^1H\}$ NMR spectrum, Figure 3.2). From the assigned structure of **12**, this coupling is noted as a $^5J_{HF}$ coupling. While such through-bond couplings have previously been observed, they require specific molecular conformations.[39] Therefore, this coupling must arise due to through-space interactions, though the lack of a molecular structure of **12** prevents analysis of the H···F distance. Previously, similar HF couplings in Group 4 transition metal complexes have exhibited H···F distances of 2.7 Å or less.[40–42]

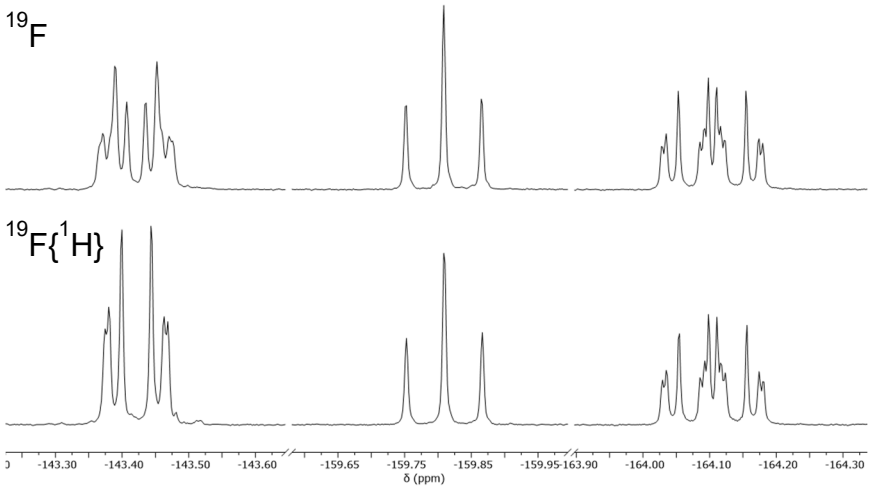


Figure 3.2: ^{19}F (top) and $^{19}F\{^1H\}$ (bottom) NMR spectra (C_6D_6, 376.5 MHz, 298 K) of $Cp_2Zr\{N(^tBu)Si(H)(Ph)C(C_6F_5)CH\}$ (**12**).

As previously discussed, ethylene was found to insert into the Zr–H bond of **3.3**, inducing ethane elimination *via* β-H abstraction, with subsequent cycloaddition of another molecule of ethylene across a transient Zr–Si bond.[1] If the same mechanism was followed in the stoichiometric reaction of **6** and $HCCC_6F_5$, the expected product would be $Cp_2Zr\{N(^tBu)Si(H)(Ph)C(H)(C_6F_5)CH_2\}$ (Figure 3.3). Alkynes have previously shown to insert into Zr–H bonds.[43,44] However, this is not the case here given **12** is the observed product and dihydrogen is seen to be released. Furthermore, terminal alkynes have been reported to undergo σ-bond metathesis with Zr–H bonds, releasing H_2 and forming acetylide complexes.[44] This cannot be the case here given the characterising data of **12**,

as well as the results of the deuterium labelling experiments. In fact, **12** resembles the products Berry and co-workers observed for the reaction of internal alkynes with η^2-silanimines.[2]

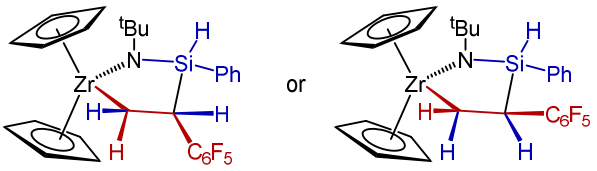
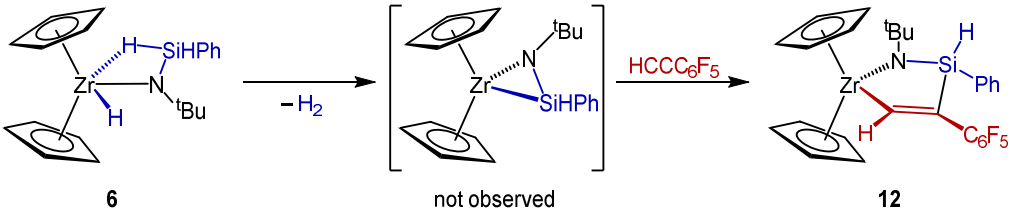


Figure 3.3: Two possible isomers of the expected product, $Cp_2Zr\{N(^tBu)Si(H)(Ph)C(H)(C_6F_5)CH_2\}$, if insertion of alkyne, followed by β-hydrogen abstraction and subsequent insertion into the Zr–Si bond were to occur.

Notably, two important mechanistic insights can be drawn from the reactions outlined in Scheme 3.1. First, reaction of $HCCC_6F_5$ with **6-*d*$_3$** and $DCCC_6F_5$ with **6** reveal that the dihydrogen eliminated in the reaction is produced exclusively from **6** and that the ZrCH proton in **12** originates exclusively from the alkyne, with no H/D exchange occurring. This, coupled with the observation that **12** resembles the product Berry and co-workers observed for the reaction of internal alkynes with η^2-silanimines, indicates dihydrogen elimination occurs initially, forming a transient η^2-silanimine, followed by cycloaddition of the alkyne to the transient Zr–Si bond (Scheme 3.2). Second, it can be noted that **6** does not release dihydrogen upon heating to 60 °C for 4 h in benzene (the conditions used for the reaction of **6** with $HCCC_6F_5$) and is stable under more forcing conditions. Therefore, it would appear that either the alkyne is directly facilitating dihydrogen elimination, or that the dihydrogen elimination from **6** occurs as a pre-equilibrium step to alkyne insertion to a transient Zr–Si bond and is sufficiently unfavourable to allow spontaneous dihydrogen elimination from **6** alone. However, these details are not clear based on the observations of deuterium labelling experiments alone.



6 not observed 12

Scheme 3.2: Mechanistic insights drawn from deuterium labelling experiments – sequential dihydrogen elimination followed by cycloaddition of $HCCC_6F_5$ to an unobserved η^2-silanimine intermediate to give **12**.

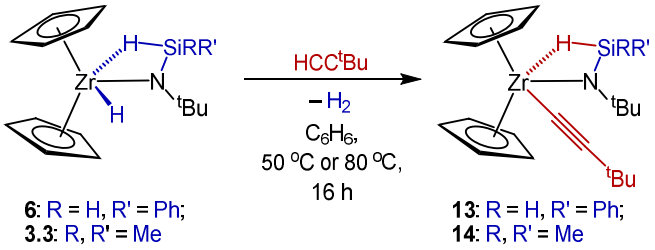
Unfortunately, attempts to gain further mechanistic insights into the reaction of **6** and $HCCC_6F_5$, which presents the first example of β-H abstraction by the hydride of a hydride silylamide, were hampered by varying quantities of impurities arising at different reaction temperatures and greater impurity levels with excess alkyne. Furthermore, reaction of the homologue, $Cp_2Zr(H)\{N(^tBu)Si(\mu\text{-}H)Ph_2\}$ (**7**), with $HCCC_6F_5$ led to an intractable mixture, assumedly due to the greater steric demand of the diphenylsilyl moiety, and so could not aid investigations. In contrast, neither $Cp_2Zr(H)\{N(Xyl)SiH_2Ph\}$ (**8**) nor $Cp_2Zr(H)\{N(Xyl)SiHPh_2\}$ (**9**) reacted with $HCCC_6F_5$, even under forcing conditions, indicating the different properties of compounds **6** and **8** influence their respective propensity to eliminate dihydrogen. Furthermore, while a mixture of $Cp_2Zr(H)\{N(^tBu)Si(\mu\text{-}H)Me_2\}$ (**3.3**) and $HCCC_6F_5$ gave no reaction at room temperature or 50 °C an intractable solution was formed after heating at 80 °C overnight.

Noting the implied mechanistic steps shown in Scheme 3.2, stoichiometric reaction of $HCCC_6F_5$ with the η^2-silanimine $Cp_2Zr\{\eta^2\text{-}N(^tBu)SiMe_2\}(PMe_3)$ (**3.2**) was attempted and was spontaneous at room temperature. While multiple products were still observed in the ^1H NMR spectrum, two major species had formed in equal amounts, as judged by the Cp region of the spectrum. One of these species contained a singlet resonance at 8.04 ppm, indicative of a vinylic ZrCH proton and 1,2-insertion of the alkyne into the Zr–Si bond of **3.2**. The other major species gave rise to a septet of relative integral 1H at 2.26 ppm coupled to a doublet resonance of relative integral 6H at 0.09 ppm ($^3J_{HH}$ = 2.8 Hz),

indicative of C–H activation and formation of the (CCC_6F_5)-analogue of $Cp_2Zr(CC^tBu)\{N(^tBu)Si(\mu\text{-}H)Me_2\}$ (**14**, *vide infra*). It would appear that the change in SiRR' group (R = H, R' = Ph or R, R' = Me) between **13_int** (*vide* infra) and **3.2** has resulted in a change of reactivity with $HCCC_6F_5$, with the former preferring 1,2-insertion over C–H activation and the latter showing no preference between the two.

3.2.2 Reactions of $Cp_2Zr(H)\{N(^tBu)Si(\mu\text{-}H)HPh\}$ (6) and $Cp_2Zr(H)\{N(^tBu)Si(\mu\text{-}H)Me_2\}$ (3.3) with HCC^tBu

On the NMR tube scale, reaction of **6** with one or more equivalents HCC^tBu, in C_6D_6 at 50 °C for 16 h, gave quantitative conversion to the acetylide silylamide $Cp_2Zr(CC^tBu)\{N(^tBu)Si(\mu\text{-}H)HPh\}$ (**13**), as judged by ^1H NMR spectroscopy (Equation 3.5). On the preparative scale, **13** was isolated as a pale yellow gum and attempts to crystallise the compound in pentane, ether or toluene were unsuccessful. Analogously, reaction of **3.3** with one or more equivalents HCC^tBu, in C_6D_6 at 80 °C for 16 h, gave ~80% conversion to the acetylide silylamide $Cp_2Zr(CC^tBu)\{N(^tBu)Si(\mu\text{-}H)Me_2\}$ (**14**) and ~20% conversion to another, unidentifiable, species on the NMR tube scale. On the preparative scale, iterative extractions with pentane were required to remove of the minor species from **14**, resulting in a very low isolated yield (<10%). However, stoichiometric reaction of $Cp_2Zr\{\eta^2\text{-}N(^tBu)SiMe_2\}(PMe_3)$ (**3.2**) and HCC^tBu resulted in insignificant amounts of the minor species being formed and allowed isolation of **14** in an acceptable yield (57%) as a pale yellow powder. This will be discussed in more detail in Section 3.2.3.



6: R = H, R' = Ph;
3.3: R, R' = Me

13: R = H, R' = Ph;
14: R, R' = Me

Equation 3.5

As with the reaction of **6** with $HCCC_6F_5$, on following both reactions *in situ* by ^{1}H NMR spectroscopy, H_2 could be seen to evolve as the reactions proceed and no intermediate species could be observed. It can also be noted that reaction of compound **7** with HCC^{t}Bu led to an intractable mixture, and that the same reaction with **8** gave no reaction even under forcing conditions.

The ^{1}H NMR spectrum of **13** (Figure 3.4, top) contrasts that of **12** and is analogous to compounds **6** and $Cp_2Zr(Cl)\{N(^tBu)Si(\mu\text{-}H)HPh\}$ (**10**). A single Cp resonance at 6.04 ppm and a single resonance at 4.38 ppm for the SiH_2 protons is observed, indicating C_s symmetry in the solution phase. Deuterium labelling of both the hydride silylamide and the alkyne confirm the assignment of the SiH_2 resonance and that one SiH proton originates from **6** and the other from HCC^{t}Bu (note the colour assignments of **13** in Equation 3.5) (*vide infra*). No proton resonance in the region expected for a zirconium hydride is observed, and two ^{t}Bu resonances, each of relative integral 9H, are observed, consistent with the incorporation of one equivalent of alkyne. The $^{13}C\{^1H\}$ NMR spectrum reveals a resonance at 132.3 ppm, assigned to Zr<u>C</u>C^{t}Bu, with no single or multiple bond correlations to protons. This chemical shift is similar to other *tert*-butyl acetylide ligands of zirconocene species and contrasts the high chemical shift (212.8 ppm) of the metallacyclic ZrCH carbon of **12**.[37] Furthermore, the solid state IR spectrum (Nujol mull) of **13** exhibits a sharp band at 2085 cm^{-1} assigned to ν(C≡C), similar to previously reported acetylide ligands.[5,37]

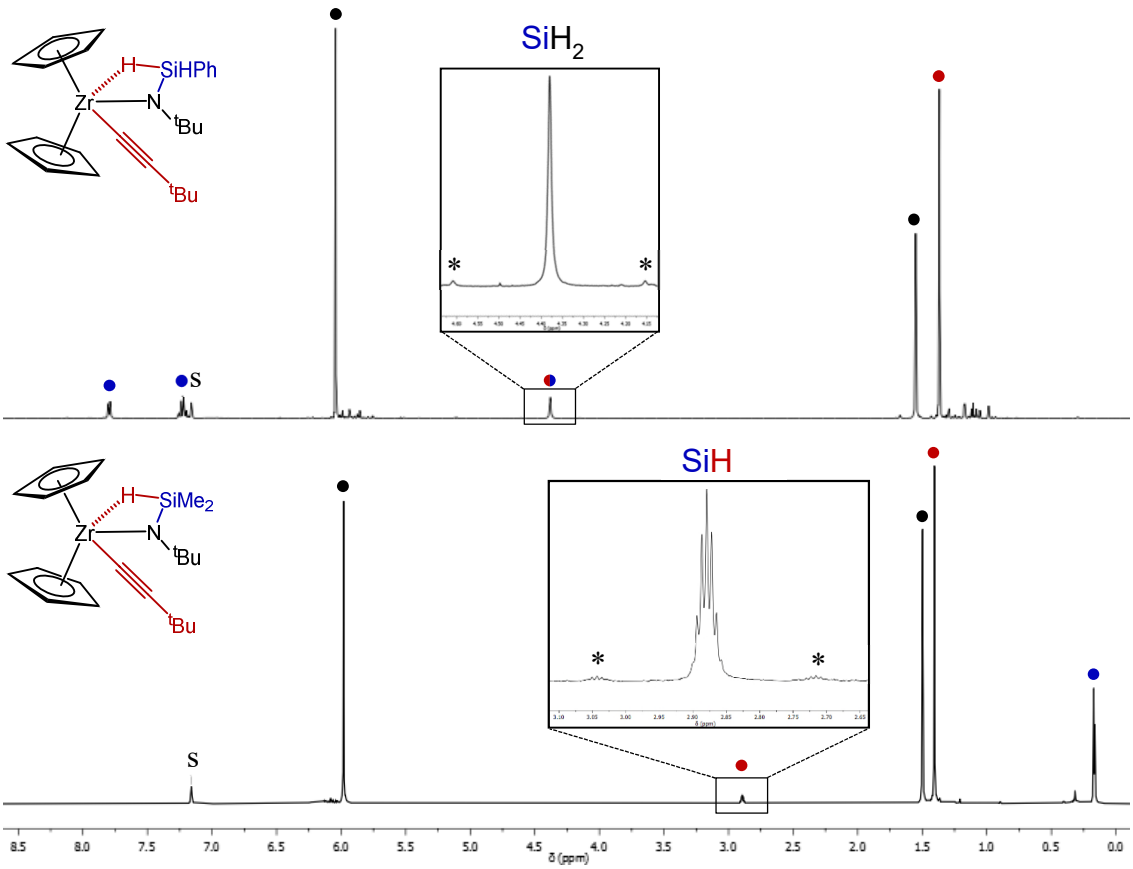


Figure 3.4: ^{1}H NMR spectra (C_6D_6, 400.1 MHz, 298 K) of $Cp_2Zr(CC^tBu)\{N(^tBu)Si(\mu\text{-}H)HPh\}$ (**13**, top) and $Cp_2Zr(CC^tBu)\{N(^tBu)Si(\mu\text{-}H)Me_2\}$ (**14**, bottom) with the SiH_2 and SiH resonances and their ^{29}Si satellites (*) enlarged.

The single resonance at 4.38 ppm for the SiH_2 protons indicates that the two SiH proton environments, terminal and β-agostic, are fluxional on the NMR timescale at room temperature, in an identical manner to **10** with a similar chemical shift (4.33 ppm). The one-bond interaction ($^{1}J_{SiH}$) between SiH_2 resonance and a ^{29}Si resonance at –75.1 ppm was found to be 182 Hz, identical to that of **10**. This shows that the strength of the β-agostic interaction of **13** is similar to that of **10** and weaker than that of **6**. For compound **10** this weakening was attributed to π-donation of the chloride ligand and similarly the weakening in **13** can be attributed to π-donation of the sp-hybridised acetylide ligand.[45]

Looking next at the characterising data of **14**, the NMR spectra are consistent with those of **13**. The $^{13}C\{^{1}H\}$ NMR spectrum shows a resonance at 130.8 ppm, assigned to $ZrCC^tBu$, with no single or multiple bond correlations to protons. While the IR spectrum

(Nujol mull) exhibits a band at 2081 cm^{-1} (ν(C≡C)), confirming the presence of an acetylide ligand, and a band at 1995 cm^{-1} assigned to ν(Si–H_b). The ^{1}H NMR spectrum (Figure 3.4, bottom) reveals a septet resonance at 2.88 ppm, assigned to the SiH proton, which is coupled to the $SiMe_2$ doublet at 0.14 ppm ($^{3}J_{HH}$ = 2.9 Hz). A ^{29}Si-^{1}H gradient experiment reveals a one-bond interaction between the septet at 2.88 ppm and a ^{29}Si resonance at –59.2 ppm ($^{1}J_{SiH}$ = 132 Hz), confirming the assignment of the SiH proton.

Table 3.1 contains key characterising data pertaining to the β-agostic interaction of **14** and a series of $Cp_2Zr(X)\{N(^{t}Bu)Si(\mu\text{-}H)Me_2\}$ (X = H, I, Br, C, F and OMe) compounds.[6,45] This allows for comparison of the strengths of the β-agostic interactions and, by extension, the π-donating abilities of the X ligands. As can be seen the SiH proton shift, $^{1}J_{SiH}$ coupling and ν(Si–H) of **14** are very similar to that of $Cp_2Zr(F)\{N(^{t}Bu)Si(\mu\text{-}H)Me_2\}$ (**3.9**), marking the acetylide ligand similar in character to a fluoride. Similar weakening of the agostic interaction with advent of an acetylide ligand in place of a hydride has been observed by Sadow and co-workers.[5]

Table 3.1: Spectroscopic data for $Cp_2Zr(X)\{N(^{t}Bu)Si(\mu\text{-}H)Me_2\}$ (X = H, I, Br, Cl, F, OMe and $CC^{t}Bu$ (**14**)).[6,45] Chemical shifts are shown in ppm, $^{1}J_{SiH}$ couplings in Hz and IR stretches in cm^{-1}.

Compound	^{1}H NMR	^{29}Si NMR		IR
	δ_{SiH}	δ_{Si}	$^{1}J_{SiH}$	ν(Si–H)
$Cp_2Zr(H)\{N(^{t}Bu)Si(\mu\text{-}H)Me_2\}$ (**3.3**)	1.21	–73.4	113	1912
$Cp_2Zr(I)\{N(^{t}Bu)Si(\mu\text{-}H)Me_2\}$ (**3.6**)	1.69	–62.0	119	1960
$Cp_2Zr(Br)\{N(^{t}Bu)Si(\mu\text{-}H)Me_2\}$ (**3.7**)	2.24	–56.1	123	1975
$Cp_2Zr(Cl)\{N(^{t}Bu)Si(\mu\text{-}H)Me_2\}$ (**3.8**)	2.58	–52.3	127	1981
$Cp_2Zr(F)\{N(^{t}Bu)Si(\mu\text{-}H)Me_2\}$ (**3.9**)	2.84	–42.0	135	1998
$Cp_2Zr(OMe)\{N(^{t}Bu)Si(\mu\text{-}H)Me_2\}$ (**3.10**)	3.69	–34.9	–[a]	2085
$Cp_2Zr(CC^{t}Bu)\{N(^{t}Bu)Si(\mu\text{-}H)Me_2\}$ (**14**)	2.88	–59.2	132	1995

[a] Parameter not recorded.

While attempts to grow diffraction-quality crystals of **13** were unsuccessful, single crystals of **14** were grown by slow evaporation of a concentrated C_6D_6 solution at room

temperature, confirming the connectivity shown in Equation 3.5. The solid state structure of **14** is shown in Figure 3.5 and selected bond distances and angles in Table 3.2. The SiH hydride was located in the Fourier difference map and positionally and isotropically refined. As expected, **14** adopts a typical bent metallocene geometry, with the nitrogen occupying the central coordination site of zirconocene and H(1), N, Si and C(7) lying in the equatorial plane.

With regards to the β-agostic interaction of **14**, the Zr–N–Si angle of 101.40(6)° is significantly larger than those of **3.3**, **3.8** and $Cp_2Zr(OTf)\{N(^tBu)Si(\mu\text{-}H)Me_2\}$ (**3.11**) (95.1(2), 99.1(1) and 96.59(10)°, respectively), as well as those of **6** and **7** (98.07(12) and 97.77(8)°, respectively), though is significantly smaller than that of $Cp_2Zr(Cl)\{N(^tBu)Si(\mu\text{-}H)HPh\}$ (**10**, 105.37(9)°) and $Cp_2Zr(OMe)\{N(^tBu)Si(\mu\text{-}H)Me_2\}$ (**3.10**, 107.0(6)°).[3,6,45] Furthermore, the Zr–H and Zr–Si bond distances of 2.35(2) and 2.9950(4) Å are longer than those of **3.3** (*ca*. 2.1 and 2.857(2) Å, respectively) and **3.8** (2.266(30) and 2.931(1) Å, respectively), but shorter than those of **10** (2.61(3) and 3.0860(6) Å, respectively). This is in line with the observations made from NMR and IR spectroscopic data that imply the agostic interaction is weaker in **14** than in **3.3** and **3.8**.

With regards to the acetylide ligand of **14**, the bonding parameters are unremarkable. The Zr(1)–C(7) bond distance of 2.2593(16) Å is similar to values found in zirconocene acetylide complexes, including zirconocene amide acetylide complexes and zirconocene acetylide complexes containing β-C–H agostic interactions.[37,46–50] Furthermore, the C(7)–C(8) bond distance of 1.208(2) Å is comparable within error to other zirconocene acetylide C≡C bonds, consistent with a triple bond.[37,46–50]

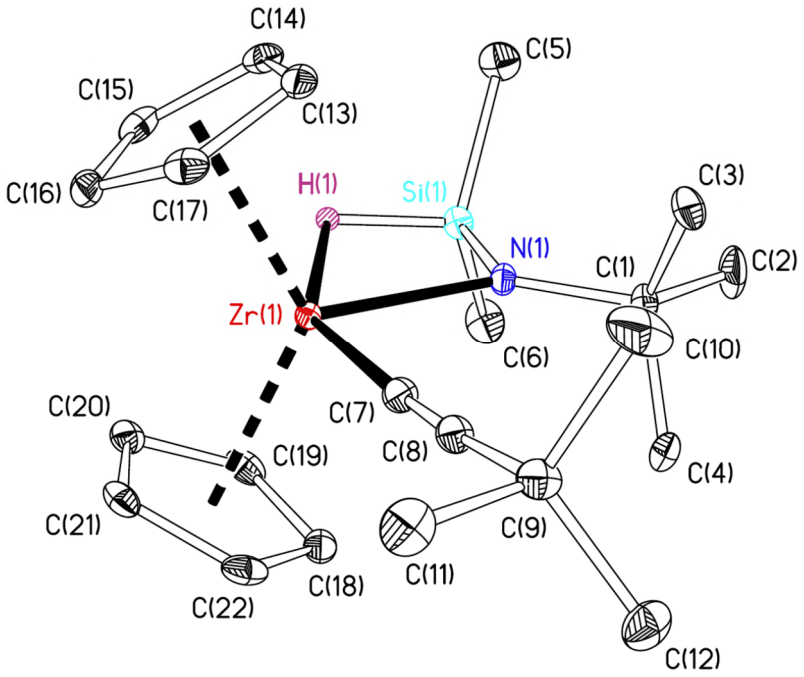


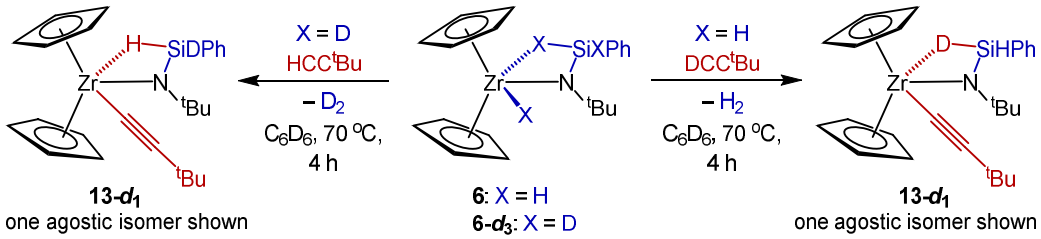
Figure 3.5: Displacement ellipsoid plot (20% probability) of $Cp_2Zr(CC^tBu)\{N(^tBu)Si(\mu\text{-}H)Me_2\}$ (**14**). C–H atoms are omitted for clarity. H(1) is drawn as a sphere of arbitrary radius.

Table 3.2: Selected bond distances (Å) and angles (°) for $Cp_2Zr(CC^tBu)\{N(^tBu)Si(\mu\text{-}H)Me_2\}$ (**14**). $Cp_{cent(1)}$ and $Cp_{cent(2)}$ refer to the computed Cp ring centroids for the "upper" and "lower" Cp rings, respectively, as depicted in Figure 2.2.

Zr(1)-N(1)	2.1539(13)	H(1)-Zr(1)-N(1)	61.1(5)
Zr(1)-H(1)	2.35(2)	C(7)-Zr(1)-N(1)	92.35(5)
Zr(1)-C(7)	2.2593(16)	H(1)-Zr(1)-C(7)	153.0(5)
Zr(1)-Si(1)	2.9950(4)	$Cp_{cent(1)}$-Zr(1)-$Cp_{cent(2)}$	126.3
Zr(1)-$Cp_{cent(1)}$	2.26	Zr(1)-N(1)-Si(1)	101.40(6)
Zr(1)-$Cp_{cent(2)}$	2.26	Si(1)-N(1)-C(1)	124.51(11)
N(1)-Si(1)	1.6985(14)	C(1)-N(1)-Zr(1)	134.02(11)
Si(1)-H(1)	1.41(2)	N(1)-Si(1)-H(1)	94.7(9)
C(7)-C(8)	1.208(2)	Si(1)-H(1)-Zr(1)	102.4(12)
		Zr(1)-C(7)-C(8)	175.96(14)
		C(7)-C(8)-C(9)	175.80(17)

The deuterium labelling experiments shown in Scheme 3.3 were performed. The reaction of **6** with DCC^{t}Bu and **6-*d*$_3$** with HCC^{t}Bu both yield **13-*d*$_1$** (drawn with either the H or D

in the agostic position in Scheme 3.3 in order to better show the reaction that has occurred in either case) and exclusively H_2 and D_2, respectively. These reactions are analogous to the reactions of **6** and **6-*d*$_3$** with $DCCC_6F_5$ and $HCCC_6F_5$, respectively, and analogous mechanistic insights can be drawn: β-hydrogen abstraction first occurs and H_2 is eliminated from compound **6**, forming a transient η^2-silanimine, with subsequent C–H activation of the alkyne across the Zr–Si bond. As noted previously, **6** is thermally stable under the same conditions presented in Equation 3.5, indicating that the presence of HCC^{t}Bu facilitates H_2 elimination. However, it is not clear from these reactions if the alkyne is directly involved in this, or H_2 elimination occurs as a pre-equilibrium step. Kinetic and DFT studies to probe the mechanistic details of this reaction are discussed in Sections 3.2.3 and 3.2.4, respectively (*vide infra*).



Scheme 3.3: Reaction of **6** with DCC^{t}Bu to give **13-*d*$_1$** (right) and reaction of **6-*d*$_3$** with HCC^{t}Bu to give **13-*d*$_1$** (left).

The C–H activation of a terminal alkyne across the Zr–Si bond of an η^2-silanimine has not previously been observed and it is noteworthy that $HCCC_6F_5$ undergoes the more commonly found 1,2-insertion into the proposed transient Zr–Si bond (this will be discussed in detail in Section 3.2.4).[1–3,5,6] Terminal alkynes are known to undergo insertion into transition metal–silicon bonds as a key step in the Crabtree-Ojima mechanism for hydrosilylation catalysis.[51,52] Related C–H activation of terminal alkynes across Zr–C bonds of three-membered zirconacycles has been observed, resulting in the formation of acetylides.[46,53] Furthermore, $HCCSiMe_3$ was found to undergo C–H activation across the Zr–C bond of the four-membered zirconacycle

$Cp_2Zr\{\kappa^2\text{-}N(SiHMe_2)SiHMeCH_2\}$ (**3.5**) to form $Cp_2Zr(CCSiMe_3)\{N(SiHMe_2)Si(\mu\text{-}H)Me_2\}$.[5] Notably, the zirconium silyl complex $Cp^*CpZr(Me)\{Si(SiMe_3)_3\}$ was found to be inert towards acetylene, despite the Zr–Si bonds readily reacting with Si–H bonds.[54,55] Most zirconium acetylides have been formed by reaction of terminal alkynes with Zr–X (X = N, P) bonds, or salt metathesis reactions.[37,47,48,56–63]

3.2.3 Kinetic study of the reaction of $Cp_2Zr(H)\{N(^tBu)Si(\mu\text{-}H)HPh\}$ (6) with HCC^tBu

First, it was observed that an increase in alkyne concentration led to faster reaction times, implying the alkyne is involved in the rate-determining step(s) of the reaction. In order to investigate this further, the order of the reaction in alkyne was determined. The initial rates method was used to determine the rate of hydride silylamide decay (d[**6**]/dt) reaction at time = 0, and the same reaction was repeated several times, keeping all conditions the same, varying only the equivalents of alkyne. Given the low boiling point of HCC^tBu (38 °C), it was necessary to conduct the reactions at room temperature. Example concentration-time plots are shown in Figure 3.6.

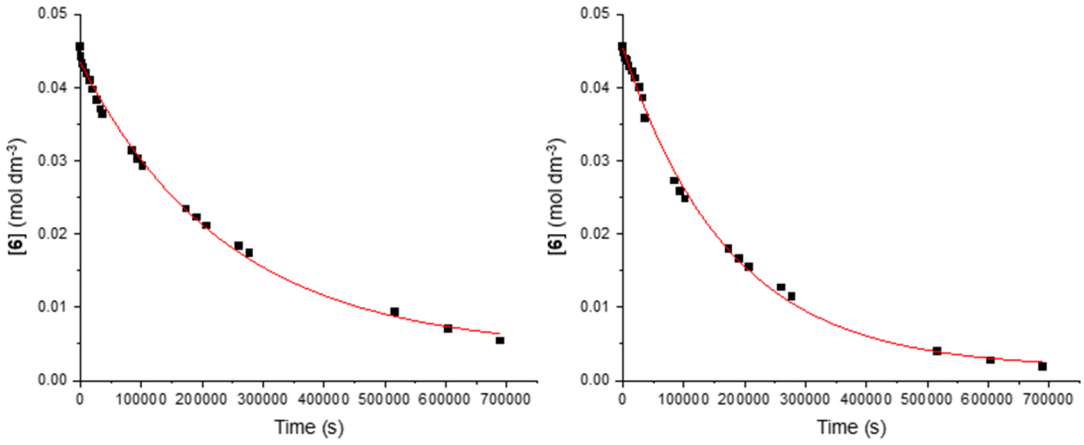


Figure 3.6: Plots of [**6**] *vs.* time for the reaction of **6** with 3 equivalents HCC^tBu (left, R^2 = 0.995) and 5.75 equivalents HCC^tBu (right, R^2 = 0.997).

The graphical software *Origin* was then used to fit these data points using a simple exponential function (Equation 3.6). The curve was then differentiated to give the gradient (Equation 3.7) and then the gradient was calculated at time = 0 s (Equation 3.8) to give the initial rate of reaction.

$$[\mathbf{6}] = y_0 + A_1 e^{-t/B_1} \quad (3.6)$$

$$\frac{d[\mathbf{6}]}{dt} = -\frac{A_1 e^{-t/B_1}}{B_1} \quad (3.7)$$

$$\left(\frac{d[\mathbf{6}]}{dt}\right)_{t=0} = -\frac{A_1}{B_1} \quad (3.8)$$

From Figure 3.7 it can be seen that the initial rate of reaction increases upon addition of increasing HCC^{t}Bu equivalents. However, the rate less than doubles with twice the equivalents of HCC^{t}Bu and the trend is not linear, but rather curved, with ever increasing HCC^{t}Bu equivalents enhancing the rate by an ever lower factor. At these high values of [HCC^{t}Bu]:[**6**] the onset of saturation kinetics accounts for these observations.

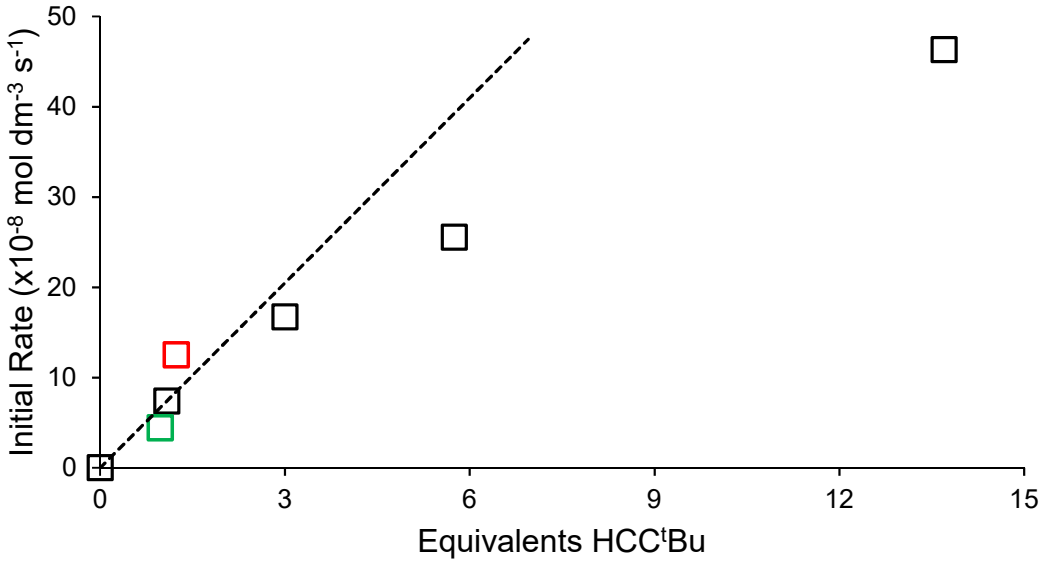


Figure 3.7: Plot of the initial rate of reaction of **6** (–d[**6**]/dt) with HCC^{t}Bu vs. equivalents of HCC^{t}Bu. The data point coloured red represents the reaction of **6** with 1.24 equiv. HCC^{t}Bu in the presence of 0.93 equiv. PMe_3. The data point coloured green represents the reaction of **6** with 0.98 equiv. DCC^{t}Bu.

In contrast, the corresponding double-reciprocal plot is linear over the range of HCC^{t}Bu used (Figure 3.8). Such phenomena have previously been observed for reactions involving dissociative pre-equilibrium steps prior to rate-determining steps.[64] Given these observations, the reaction scheme outlined in Scheme 3.4 can be invoked. Initially, dihydrogen is reversibly eliminated to form a reactive, transient η^2-silanimine complex (**13_int**) prior to rate-determining C–H activation of HCC^{t}Bu across the Zr–Si bond. Under such a mechanism, at steady state, Equations 3.9 – 3.15 can be written, with Equation 3.15 being consistent with the double reciprocal plot. It is notable that the concentration of H_2 will impact k_{obs} (Equation 3.14) and so it is assumed that the concentration of H_2 at t = 0 is small and constant between the different reactions. Indeed, the intensity of the H_2 resonance was negligible across all runs and data points, owing presumably to the long reaction times and agitation of the NMR tubes over the course of the reactions. Therefore it can be said that H_2 does not affect the observed initial rate constants in these reactions.

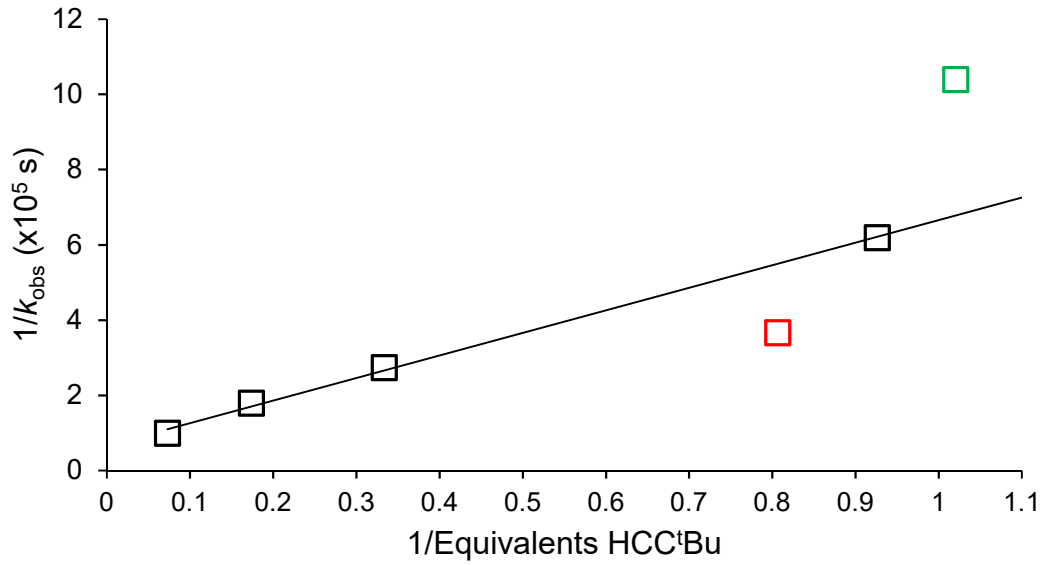
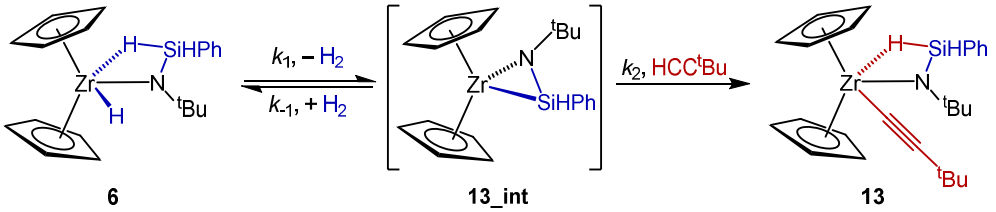


Figure 3.8: Double-reciprocal plot of $1/k_{obs}$ vs. 1/equivalents of HCC^{t}Bu. The linear fit (r^2 = 0.998) gives an intercept of $1/k_{obs}$ = 0.66(9) x 10^5 s.



Scheme 3.4: Experimentally implicated steps in the formation of **13** from **6** and HCC^{t}Bu.

$$Rate = \frac{\mathrm{d}[\mathbf{13}]}{\mathrm{d}t} = k_2[\mathrm{HCC^tBu}][\mathbf{13_int}] \tag{3.9}$$

At steady state,
$$\frac{\mathrm{d}[\mathbf{13_int}]}{\mathrm{d}t} = k_1[\mathbf{6}] - k_{-1}[\mathbf{13_int}][\mathrm{H_2}] - k_2[\mathrm{HCC^tBu}][\mathbf{13_int}] = 0 \tag{3.10}$$

$$[\mathbf{13_int}](k_{-1}[\mathrm{H_2}] + k_2[\mathrm{HCC^tBu}]) = k_1[\mathbf{6}] \tag{3.11}$$

$$[\mathbf{13_int}] = \frac{k_1[\mathbf{6}]}{(k_{-1}[\mathrm{H_2}] + k_2[\mathrm{HCC^tBu}])} \tag{3.12}$$

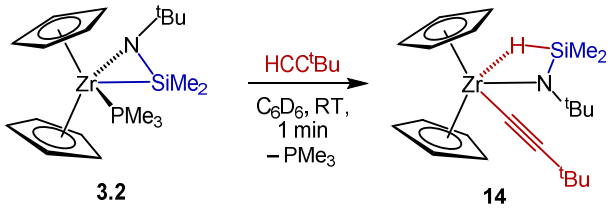
$$Rate = \frac{k_1k_2[\mathrm{HCC^tBu}][\mathbf{6}]}{(k_{-1}[\mathrm{H_2}] + k_2[\mathrm{HCC^tBu}])} = k_{obs}[\mathbf{6}] \tag{3.13}$$

$$k_{obs} = \frac{k_1k_2[\mathrm{HCC^tBu}]}{(k_{-1}[\mathrm{H_2}] + k_2[\mathrm{HCC^tBu}])} \tag{3.14}$$

$$\frac{1}{k_{obs}} = \frac{1}{k_1} + \left(\frac{k_{-1}[\mathrm{H_2}]}{k_1k_2}\right) \times \frac{1}{[\mathrm{HCC^tBu}]} \tag{3.15}$$

Given the implications of these findings, it was of interest to attempt to observe the explicit addition of HCC^{t}Bu to an η^2-silanimine, the explicit β-hydrogen abstraction and dihydrogen elimination of a hydride silylamide and explicitly observe an η^2-silanimine as an intermediate of these alkyne reactions. As both **13_int** and the dimethyl analogue **14_int** could not be observed during the reactions of **6** and **3.3** with HCC^{t}Bu, assumedly due to these being too high in energy and therefore reactive, stabilised forms of the η^2-silanimines were required, such as $Cp_2Zr\{N(^tBu)SiMe_2\}(PMe_3)$ (**3.2**) or $Cp_2Zr\{\eta^2\text{-}Si(Me_2)N(^tBu)SiMe_2(\mu\text{-}H)\}$, which was stabilised by the β-agostic Si–H

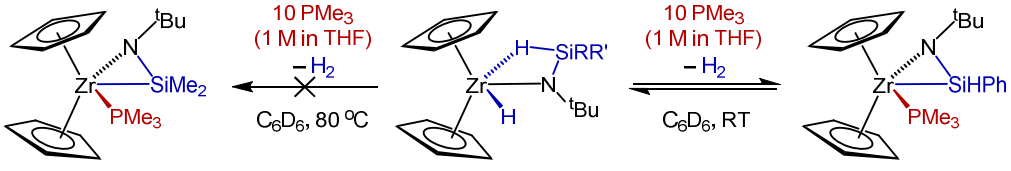
interaction.[1,6] Stoichiometric reaction of **3.2** and HCC^{t}Bu formed **14** instantly at room temperature, as judged by ^{1}H NMR, and, on the preparative scale, allowed isolation of **14** in a 57% yield, as previously mentioned (Equation 3.16).



3.2 **14**

Equation 3.16

Further to this reaction, attempts to observe the β-hydrogen abstraction and dihydrogen elimination of both **6** and **3.3** by addition of PMe_3 were made. Previously, Sadow and co-workers reported H_2 elimination from the hydride silylamide **3.3**, by addition of PMe_3 at 140 °C, to form $Cp_2Zr\{\eta^2\text{-}N(^t\text{Bu})SiH(Me)CH_2\}$ and $[Cp_2Zr(NSiHMe_2)]_n$, *via* γ-H abstraction of either the $SiMe_2$ or *tert*-butyl groups and not β-elimination.[3] On the NMR tube scale, addition of one equivalent of PMe_3 to **6** in C_6D_6 gave minimal conversion of **6** to $Cp_2Zr\{\eta^2\text{-}N(^t\text{Bu})SiHPh\}(PMe_3)$ (**15**), as judged by ^{1}H NMR spectroscopy. Addition of a further 9 equivalents gave ~60% conversion of **6** to **15**, after 3 days at room temperature, with no further conversion observed and small amounts of decomposition (Scheme 3.5). Heating of the reaction mixture to 80 °C led to complete decomposition of **15**. These observations indicate the formation of **15** and dihydrogen to be in equilibrium with **6** and PMe_3. Indeed, Δ_rG for forming **15** from **6** and PMe_3 is calculated by DFT to be just –1.5 kcal mol^{-1}, consistent with experimental observations.



3.2

6: R = H, R' = Ph;
3.3: R, R' = Me

15
60% conversion

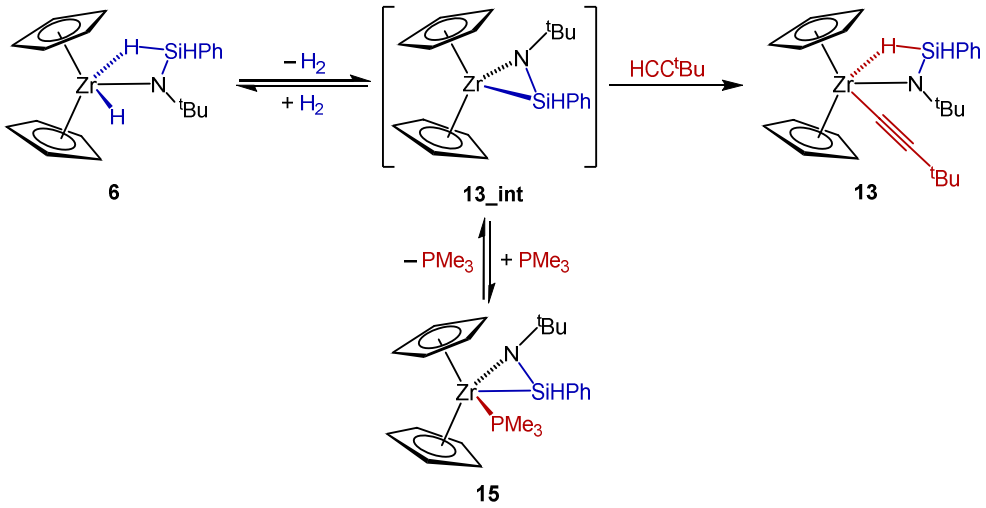
Scheme 3.5: Reactions of **6** and **3.3** with PMe_3 to form **15** in equilibrium and give no reaction, respectively.

In contrast, no reaction was observed on the addition of 10 equivalents PMe_3 to **3.3**, even upon heating at 80 °C for several days, consistent with reports by Sadow and co-workers.[3] The reverse reaction, addition of H_2 to **3.2**, is spontaneous at room temperature.[1] Additionally, the reaction of **3.3** with HCC^{t}Bu is accessible at 80 °C, indicating the lack of reaction with PMe_3 is due to unfavourable thermodynamic factors in the formation of **3.2**. This is consistent with the reaction of HCC^{t}Bu with **3.2** being rapid compared to reaction with **3.3**.

Compound **15** was characterised by ^{1}H, ^{13}C{^{1}H}, ^{31}P and ^{29}Si NMR spectroscopy. The ^{1}H NMR spectrum of **15** (recorded from the *in situ* reaction mixture) is consistent with the proposed structure and shows two Cp resonances at 5.60 and 5.50 ppm. This indicates a breakdown in symmetry, as was seen for **12** and consistent with the formation of a η^2-silanimine complex containing a chiral Si environment. The ^{t}Bu resonance is found at 1.27 ppm (*cf.* 1.30 ppm for **6**) and a new PMe_3 resonance was observed at 1.00 ppm (*cf.* 0.80 ppm for free PMe_3), similar to that observed for Berry's η^2-silanimine $Cp_2Zr\{\eta^2\text{-}N(^t\text{Bu})SiMe_2\}$ (**3.2**, 0.98 ppm). The SiH resonance is found at 4.29 ppm as a doublet ($^3J_{HP}$ = 5.8 Hz) consistent with a loss of the β-agostic interaction and coordination of PMe_3. The ^{31}P{^{1}H} NMR spectrum reveals a single, new resonance at –2.8 ppm (*cf.* –62.5 ppm for free PMe_3); this compares to a resonance of 0.8 ppm for **3.2**.[1] A ^{29}Si-^{1}H gradient experiment reveals a one-bond interaction between the doublet at 4.29 ppm and a ^{29}Si resonance at –74.2 ppm ($^1J_{SiH}$ = 185 Hz). This coupling constant is small, considering no agostic interaction is present.

It can be seen that the presence of PMe_3 significantly stabilises the η^2-silanimine **13_int**. Indeed, the reduction in free energy upon PMe_3 coordination is calculated by DFT to be 8.7 kcal mol^{-1}. Therefore, if PMe_3 were present in the reaction of **6** with HCC^{t}Bu, **15**

could appear as an off-route, base-trapped intermediate species on the reaction pathway (Scheme 3.6). As such, reaction of **6** with 1.2 equivalents HCC^{t}Bu, in the presence of 0.93 equivalents PMe_3, was followed *in situ* by ^{1}H NMR spectroscopy. The concentration-time plot of **6**, **13** and **15** can be seen in Figure 3.9 and is in accordance with the mechanism proposed in Scheme 3.6. The concentration of **15** rises initially and then falls, indicative of **15** being an off-route, base-trapped intermediate species. As can be seen from the red data points in Figures 3.7 and 3.8, the initial rate of decay is increased by addition of PMe_3. Meanwhile the initial rate of formation of **13** was close to what would be expected in the absence of PMe_3, consistent with **6** and **15** being close in free energy and there being no substantial free energy barrier between **15** and **13_int**.



Scheme 3.6: Proposed reaction scheme for the formation of **13** from **6** and HCC^{t}Bu, in the presence of PMe_3, with **15** as an off-route, base-trapped intermediate.

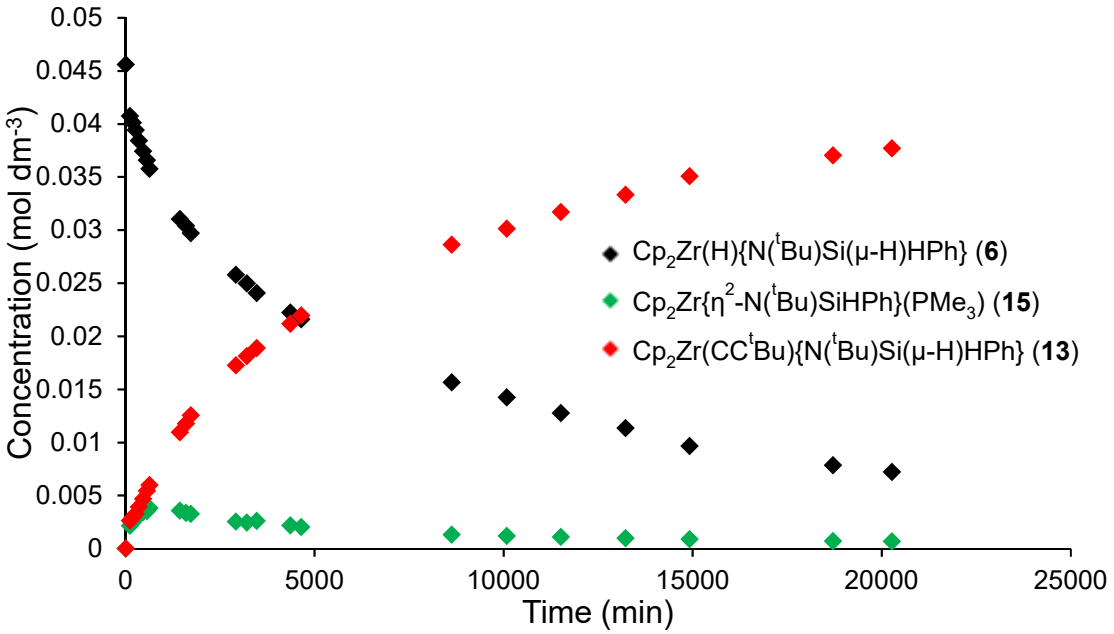
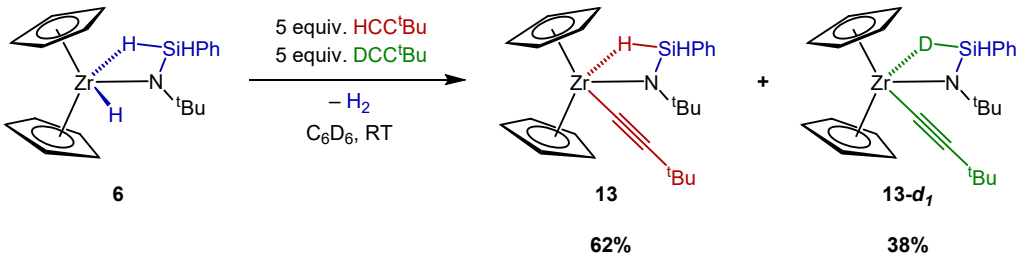


Figure 3.9: Concentration-time profiles for the reaction of $Cp_2Zr(H)\{N(^tBu)Si(\mu\text{-}H)HPh\}$ (**6**) with 1.24 equiv. HCC^tBu in the presence of 0.93 equiv. PMe_3.

The reactions of **3.2** with HCC^tBu and **6** with PMe_3 confirm the feasibility of the individual reaction steps implied in Scheme 3.4. Furthermore, the observation of **15** as an intermediate in the reaction of **6** with HCC^tBu and the accompanying rate-acceleration in the presence of PMe_3 support the proposed mechanism. Following these reactions, the kinetic isotope effects (KIEs) of both the C–H activation and dihydrogen elimination steps for reaction of **6** with HCC^tBu were investigated independently.

A competition kinetic isotope effect for the alkyne was carried out by reacting 5 equivalents of each HCC^tBu and DCC^tBu at room temperature in C_6D_6 (Equation 3.17). It is important to note that addition of 20 equivalents DCC^tBu to **8** and 20 equivalents HCC^tBu to **8-*d*$_1$** gave no change to the SiH_2 and SiHD integrals, respectively, even when heated to 100 °C. Therefore, no CH/SiD or CD/SiH exchange processes occur and influence the SiH_2/SiHD integral.



Equation 3.17

The integral from the competition KIE experiment was found to be 1.49, compared to 1.84 and 0.92 for the SiH_2 and SiHD resonances of **8** and **8-*d*$_1$**, respectively, giving a maximum KIE of 1.6. The KIE for C–H activation was also investigated using the initial rates method. Reaction of **6** with 0.98 equivalents DCC^{t}Bu was monitored at room temperature to approximately three half-lives and the initial rate was calculated to be 4.4 × 10^{-8} mol dm^{-3} s^{-1} with a $1/k_{obs}$ value of 10.4 × 10^5 s^{-1} (green data point in Figures 3.7 and 3.8) . By extrapolation of the trend line shown in Figure 3.8, $1/k_{obs}$ and the initial rate for the reaction of **6** with 0.98 equivalents HCC^{t}Bu could be calculated. These were found to be 6.8(2) × 10^5 s^{-1} and 6.7(2) × 10^{-8} mol dm^{-3} s^{-1}, respectively, giving a primary KIE of ~1.5, in good agreement with the value obtained from the competition experiment. This small primary KIE could imply an early transition state and/or that the transition state for the C–H activation step is non-linear, with the C–H bond of the alkyne approaching side-on to the Zr–Si bond.[65] Similar primary KIEs have been reported for proton transfers occurring *via* non-linear transition states.[66,67]

Next, the kinetic isotope effect of dihydrogen elimination was investigated. Considering H_2/D_2 plays no role in the C–H activation step of the reaction and HCC^{t}Bu plays no role in the dihydrogen elimination step, and noting the derived rate equation shown in Equation 3.13, reactions of **6** or **6-*d*$_3$** with 20 equivalents HCC^{t}Bu were conducted and followed by ^{1}H NMR spectroscopy at 338 K in C_6D_6. The concentration-time plots for the reactions of **6** (blue) and **6-*d*$_3$** (red) can be seen in Figure 3.10. Attempts were made

to fit these data points using a simple exponential function (Equation 3.6); however, this was not possible. This is likely due to fluctuations in the concentration of H_2 or D_2 in solution over the course of the reaction, given dihydrogen inhibition is invoked the proposed mechanism (Scheme 3.4) and that, over the short reaction times in excess alkyne and elevated temperatures, supersaturation of H_2 is possible. Overlays of the plots of $-\ln([\mathbf{6}]/[\mathbf{6}]_0)$ *vs.* time and $[H_2]$ *vs.* time show this (Figure 3.11, *vide infra*). This was not found to be a problem in the room temperature reactions of **6** with varying concentrations of HCC^{t}Bu, as the concentration of H_2 remained negligible throughout the reactions.

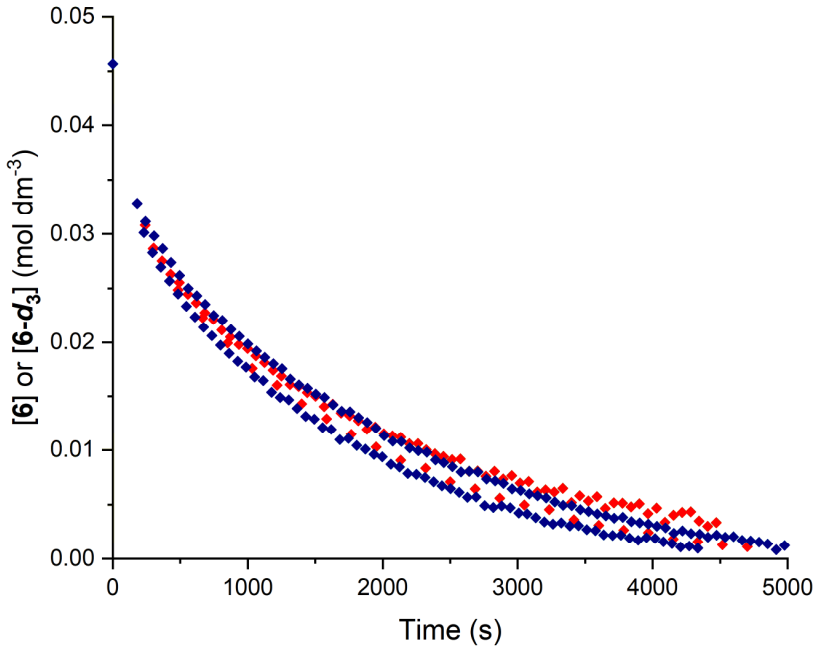


Figure 3.10: Concentration-time plots for the reactions of **6** (blue) and **6-*d*$_3$** (red) with 20 equivalents HCC^{t}Bu at 338 K in C_6D_6.

While values for the initial rates of reactions could not be extracted, visually there appears to be no significant isotope effect for dihydrogen elimination at 338 K in the presence of excess HCC^{t}Bu. The absence of a significant isotope effect, despite H_2 elimination impacting the rate of reaction, is likely due to its reversible nature and this KIE actually being an equilibrium isotope effect (EIE). This would be consistent with the proposed mechanism and EIEs have been observed for reversible H–H and C–H elimination

reactions, as well as pre-equilibrium C–H elimination reaction steps.[68–71] An EIE of approximately 1 would reflect a lack of difference in zero point energy gain for deuterium *vs*. hydrogen between each side of the equilibrium shown in Scheme 3.4.

EIEs arise due to deuterium preferring to reside in the higher frequency oscillator, as the zero point energy (ZPE) difference between E–H and E–D bonds increases with increasing overall vibrational frequencies of the E–H/E–D bonds.[72,73] If ΔZPE is greater on the left side of the equilibrium, K_{eq} will be lower for deuterium than hydrogen and a normal EIE will be observed. Conversely, an inverse EIE will be observed if ΔZPE is greater on the right side. An EIE of 1 will be observed if there is no difference in ΔZPE. Importantly, stretching frequencies and other isotopically sensitive frequency modes, such as bending modes, all need to be accounted for. Analysis of just the stretching frequencies can be misleading, as is conceivably the case in this reaction, with ν(H–H) > ν(Si–H) and ν(Zr–H) implying an inverse EIE should be observed. However, adding other isotopically sensitive frequency modes into the equation may be the reason an absence of a significant EIE is observed, as has been implicated previously for EIEs.[70,74,75]

It can be observed in Figure 3.10 that there are reasonable differences in the reaction rates between respective protonated and deuterated runs. While there is, of course, normal experimental error, there is also the error associated in varying concentration profile of H_2 or D_2 between reactions, which cannot be controlled. Indeed, the concentration of H_2 in the slower of the two reactions of **6** was found to be higher throughout the reaction. Furthermore, an additional source of error lies in the equivalencies of HC^{t}Bu used, which is difficult to control on addition to **6** due to its volatility (boiling point 38 °C). On inspection of the ^{1}H NMR data it could be observed that the actual equivalents HC^{t}Bu added to the reactions of **6** were not both 20, but rather 20 for the faster of the two

reactions and 17 for the slower. For reactions of **6-*d*$_3$** the equivalencies were found to be 19 and 17.5 for the faster and slower reactions. While the order of the reaction will be less than one at such high equivalencies (see Figure 3.7) it will still be significant and affect the rate of reaction somewhat. However, these errors do not impact the conclusions drawn from the data.

As mentioned, it is proposed that the variation of significant concentrations of hydrogen throughout the reactions of **6** with excess alkyne at high temperatures acts to slow the reaction rate. This would be consistent with the proposed mechanism and so explicit evidence of this phenomenon would be supportive in this kinetic study. Indeed, an overlay of [H_2] *vs.* time and –ln([**6**]/[**6**]$_0$) *vs.* time for reaction of **6** with 20 equivalents HCC^{t}Bu at 326 K explicitly demonstrates this (Figure 3.11). As can be seen the data points for the semi-logarithmic plot deviate from the best-fit line, and the gradient of the data inversely correlates to the concentration of H_2. This is fully consistent with the rate equation shown in Equation 3.13.

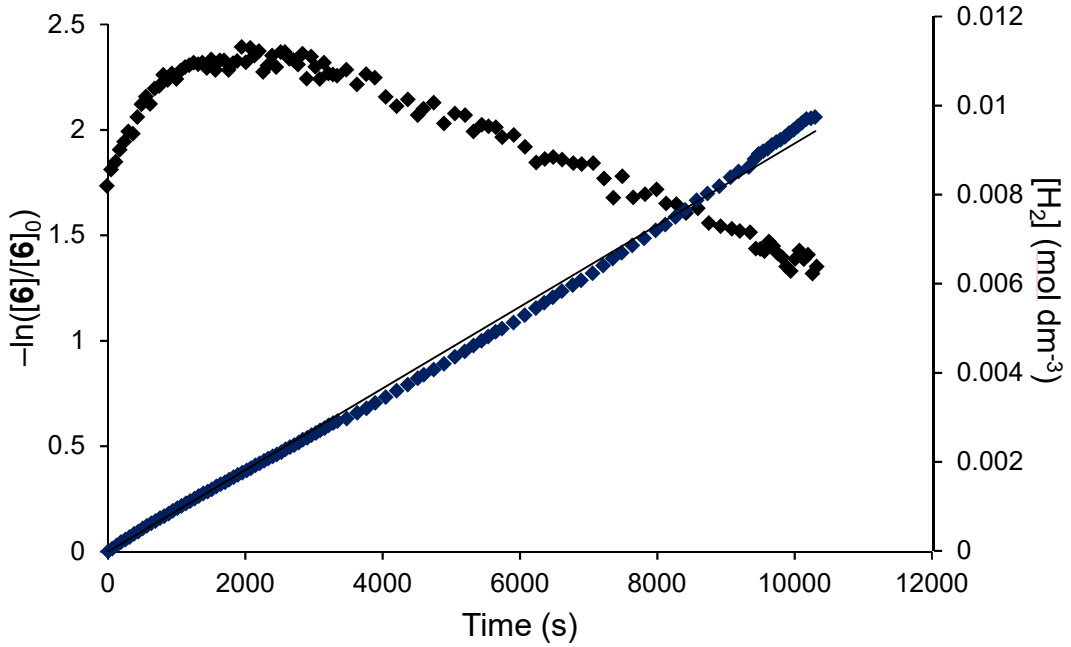


Figure 3.11: An overlay of the first order semi-logarithmic plot for the reaction of $Cp_2Zr(H)\{N(^tBu)Si(\mu\text{-}H)HPh\}$ (**6**) with 20 equivalents HCC^tBu at 326 K (left axis, blue, $r^2 = 0.997$) and the concentration of H_2 (mol dm^{-3}) during the reaction (right axis, black).

In instances such as these variable time normalisation analysis (VTNA) has been employed to account for these fluctuations, unambiguously assign the order of each reaction component and give k_{obs}.[76,77] This technique normalises the time between each pair of data points by averaging the concentration of each reaction component, raised to its respective order in the rate equation, of the two data points (Equation 3.18 shows the time normalisation equation). This effectively removes this kinetic effect of the components from the reaction profile and, if raised to the correct order, will lead to visually straight lines in a concentration *vs.* normalised time plot.

$$\Sigma[\mathrm{A}]^{\alpha}[\mathrm{B}]^{\beta}\Delta t = \sum_{i=1}^{n}\left(\frac{[\mathrm{A}]_i + [\mathrm{A}]_{i-1}}{2}\right)^{\alpha}\left(\frac{[\mathrm{B}]_i + [\mathrm{B}]_{i-1}}{2}\right)^{\beta}(t_i - t_{i-1}) \qquad (3.18)^{77}$$

As such, VTNA was applied to the reaction of **6** with excess HCC^tBu. The linear plot of [**13**] *vs.* $\Sigma[\mathbf{6}]^1[H_2]^{-1}\Delta t$ for the reactions at 326 K is shown in Figure 3.12 (VTNA plots at 329, 332, 335 and 338 K can been seen in the Appendix, Figure A7), showing the order of the reaction in **6** and H_2 to be 1 and –1, respectively. Other values for the orders of **6**

and H_2 gave non-linear plots. This is consistent with the mechanism proposed in Scheme 3.4 and rate equation shown in Equation 3.13.

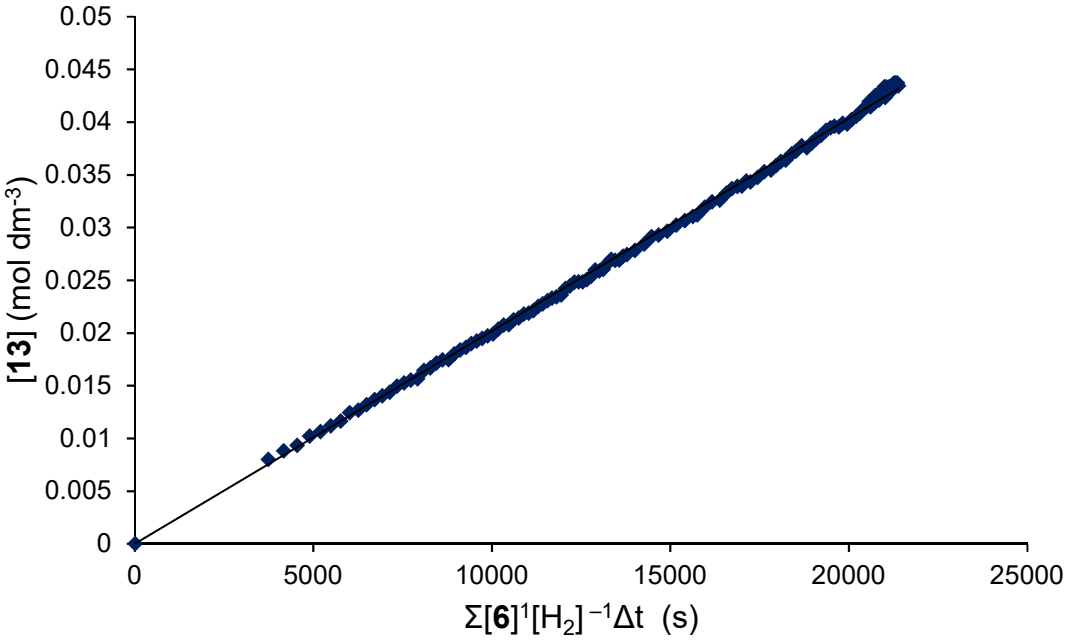


Figure 3.12: Variable time normalisation analysis (VTNA) of the reaction of $Cp_2Zr(H)\{N(^tBu)Si(\mu\text{-}H)HPh\}$ (**6**) with 20 equivalents HCC^tBu to give $Cp_2Zr(CC^tBu)\{N(^tBu)Si(\mu\text{-}H)HPh\}$ (**13**) and H_2 at 326 K, with the normalised time being $\Sigma[\mathbf{6}]^1[H_2]^{-1}\Delta t$. ($r^2 = 0.999$).

The slope of the plot shown in Figure 3.12 formally represents k_{obs}, however, there will be an error associated with this value due to the long T_1 relaxation time of dihydrogen preventing accurate measurement of its concentration. This error was exemplified when attempting to extract activation parameters from the reactions over the temperature range 326 – 338 K, as at different temperatures the T_1 relaxation time of H_2 varies such that the observed concentrations of H_2, and, by extension, rate constants, cannot be compared between reactions. As such, use of the rate constants extracted from these plots gave ill-fitting data by Eyring analysis. Reports of convex Arrhenius plots have been made for reactions which follow the same form as proposed for the reaction of **6** with HCC^tBu – an equilibrium preceding an irreversible reaction step.[78]

3.2.3.1 Summary of the kinetic study

Several studies have been carried out in order to probe the mechanism of the reaction of $Cp_2Zr(H)\{N(^tBu)Si(\mu\text{-}H)HPh\}$ (**6**) with HCC^tBu to give $Cp_2Zr(CC^tBu)\{N(^tBu)Si(\mu\text{-}H)HPh\}$ (**13**). The reaction is shown to be first order in both **6** and HCC^tBu, and –1 order in dihydrogen. A double reciprocal plot of the initial rate constants of the reactions of **6** with varying equivalents of HCC^tBu (Figure 3.8) shows that HCC^tBu addition is preceded by an equilibrium step – hypothesised to be dihydrogen elimination from **6** to form the transient η^2-silanimine intermediate $Cp_2Zr\{\eta^2\text{-}N(^tBu)SiHPh\}$ (**13_int**). Reaction of **6** with excess PMe_3 to form $Cp_2Zr\{\eta^2\text{-}N(^tBu)SiHPh\}(PMe_3)$ (**15**, Scheme 3.5), reaction of $Cp_2Zr\{\eta^2\text{-}N(^tBu)SiMe_2\}(PMe_3)$ (**3.2**) with HCC^tBu to form $Cp_2Zr(CC^tBu)\{N(^tBu)Si(\mu\text{-}H)Me_2\}$ (**14**, Equation 3.16)) and reaction of **6** with HCC^tBu in the presence of PMe_3 to allow observation of **15** as an intermediate in the reaction (Figure 3.9, Scheme 3.6) confirm this hypothesis.

The observation of a small primary KIE for C–H activation (~1.5) implies an early or non-linear transition state for this reaction step (Figure 3.7, Equation 3.18). While extraction of accurate values for the KIE of the dihydrogen elimination step was not possible, visually, no significant isotope effect could be observed for this reaction step, which is attributed to a lack of difference in the gain in zero point energy reduction for deuterium on either side of the equilibrium. Furthermore, variable time normalisation analysis (VTNA) was employed to explicitly show the influence of H_2 on the reaction and derive the orders in reaction of **6** and H_2 (1 and –1, respectively).

Overall, the proposed mechanism for the reaction of **6** with HCC^tBu (and, by extension, $Cp_2Zr(H)\{N(^tBu)Si(\mu\text{-}H)Me_2\}$ (**3.3**) with HCC^tBu) is shown in Scheme 3.4. First, the

hydride abstracts the β-hydrogen of the silylamide to eliminate dihydrogen giving the unobserved intermediate **13_int**. The Zr–Si bond of **13_int** can then either react with dihydrogen to reform **6**, the microscopic reverse of dihydrogen elimination, or undergo irreversible C–H activation with HCC^{t}Bu to form the product **13**.

3.2.4 DFT studies of the reactions of $Cp_2Zr(H)\{N(^tBu)Si(\mu\text{-}H)HPh\}$ (6) with HCC^{t}Bu and $HCCC_6F_5$

While the kinetic studies of the reaction of **6** with HCC^{t}Bu show that dihydrogen elimination occurs as a pre-equilibrium step prior to C–H activation across a transiently formed Zr–Si bond, and both steps contribute to the observed rate of reaction, little information has been gained on the relative barriers of the reaction steps. Furthermore, no knowledge has been gained on the divergent reactivity of HCC^{t}Bu and $HCCC_6F_5$ with **6**. Therefore, to probe these further, the mechanisms of dihydrogen elimination from **6**, and subsequent C–H activation and 1,2-insertion of both HCC^{t}Bu and $HCCC_6F_5$ (Figure 3.13 and Figure 3.16), were calculated. Attempts were made to calculate barriers for 2,1-insertion of the alkynes; however, transition state structures would invariably lead to preferential C–H activation, showing this to be the preferred route of this reaction due to steric effects.

On the pathway to dihydrogen elimination, **6** necessarily undergoes a rotation about the Zr–N bond, *via* **6_int** (not shown), to form **6_alt** (G_{rel} = 2.8 kcal mol^{-1}). This is the reverse of the isomerisation seen upon formation of **6** from $Cp_2ZrN^tBu(THF)$ (**3.12**) and $PhSiH_3$ in Chapter 2 of this Thesis, and has a barrier of 16.8 kcal mol^{-1}. With the β-agostic SiH adjacent to the zirconium hydride, and both hydrogens and the silicon in the plane of the zirconocene, β-H abstraction and dihydrogen elimination occurs *via* **TS2** with a barrier of 20.5 kcal mol^{-1} to form **13_int** (G_{rel} = 7.2 kcal mol^{-1}).

The H–H distance is calculated to reduce from 1.799 Å in **6_alt** to 0.776 Å in **TS2**, very similar to that of molecular dihydrogen, and the Zr–Si distance from 2.856 to 2.592 Å, very similar to that of **13_int** (2.580 Å) and shorter than was found experimentally for $Cp_2Zr\{\eta^2\text{-}N(^tBu)SiMe_2\}(PMe_3)$ (2.654(1) Å).[4] Additionally, the Si–H distance increases from 1.558 to 2.848 Å, showing a complete loss of the Si–H bond. These parameters indicate **TS2** is a late transition state. The KIE for the reversible dihydrogen elimination step **6** to **13_int** in the reaction of **6** with HCC^tBu is calculated to be 1.1 at 65 °C. This is consistent with the negligible KIE (or, more accurately, EIE) observed from the data shown in Figure 3.10.

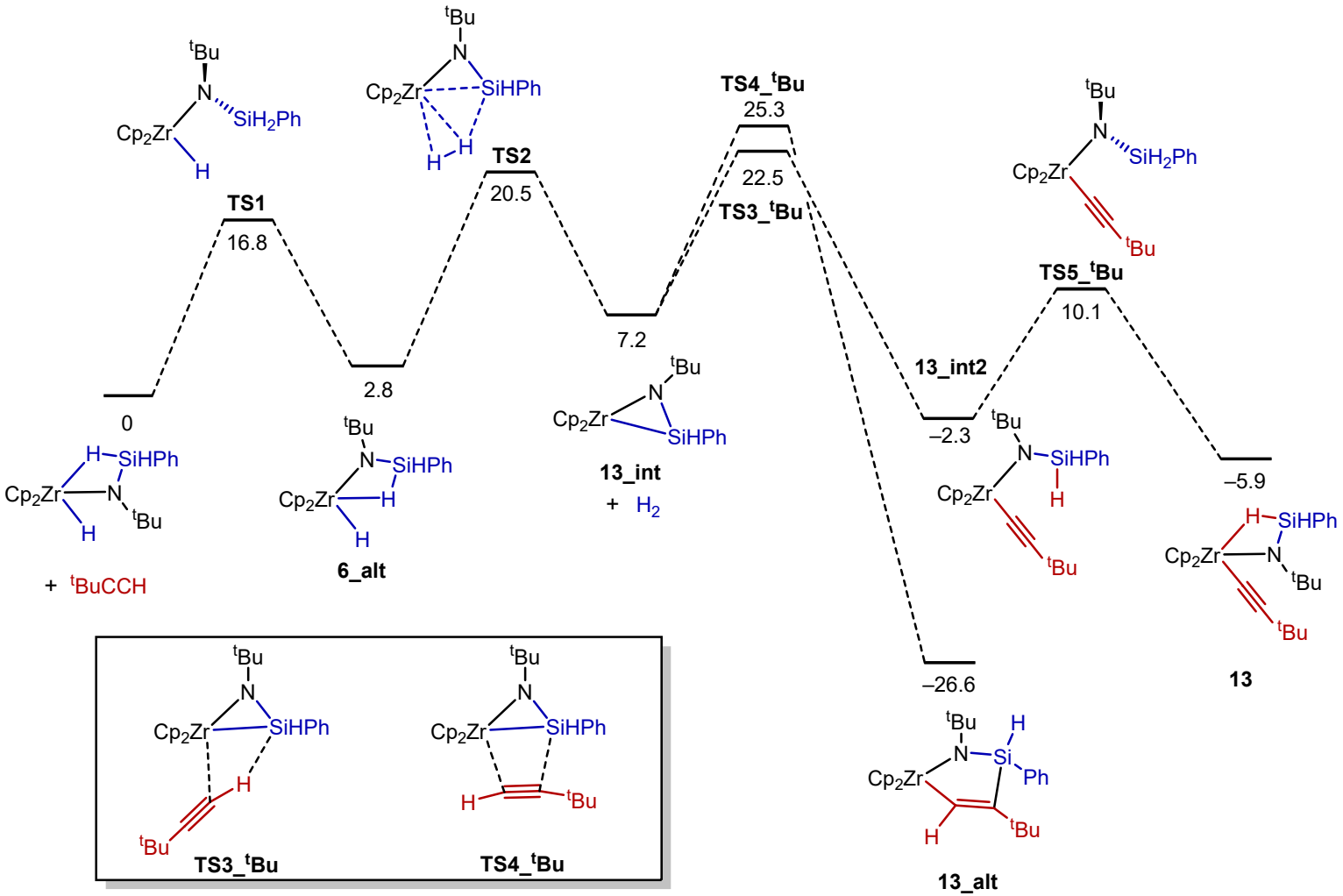


Figure 3.13: DFT (B3PW91/Def2-TZVP/d3-bj/SCRF) mechanism for the C–H activation and 1,2-insertion reactions of HC^{t}Bu with **6**, forming H_2 and either **13** or **13_alt**, respectively. Gibbs free energies (kcal mol^{-1}, T = 298.15 K) for minima and transition states (labelled **TSx** or **TSx_^{t}Bu**) are shown relative to **6** and HC^{t}Bu.

The structure of the dimethyl analogue of the putative intermediate **13_int**, $Cp_2Zr\{\eta^2\text{-}N(^tBu)SiMe_2\}$ (**14_int**), has previously been calculated by Bi and co-workers, though under a similar level of DFT (B3LYP).[1,79] The structural parameters of the two are near identical. When compared to the base stabilised η^2-silanimine $Cp_2Zr\{\eta^2\text{-}N(^tBu)SiMe_2\}(PMe_3)$ (**3.2**), as mentioned, the Zr–Si distance is shorter in **13_int**. Additionally, the Zr–N distance is slightly shorter in **13_int** (2.063 vs. 2.167(3) Å), consistent with an electron deficient zirconium centre. Notably, the hydride and phenyl moieties of the silicon lie almost planar with the Zr–Si bond, leaving the bond accessible. Given the reactivity η^2-silanimines have exhibited with small molecules it was of interest to gain further understanding of the bonding of such species. The model species $Cp_2Zr\{\eta^2\text{-}N(Me)SiHPh\}$ was used for calculations of the molecular orbitals, containing a methyl group bound to the nitrogen in place of the *tert*-butyl group of **13_int**. Key orbital representations and associated energies are shown in Figure 3.14.

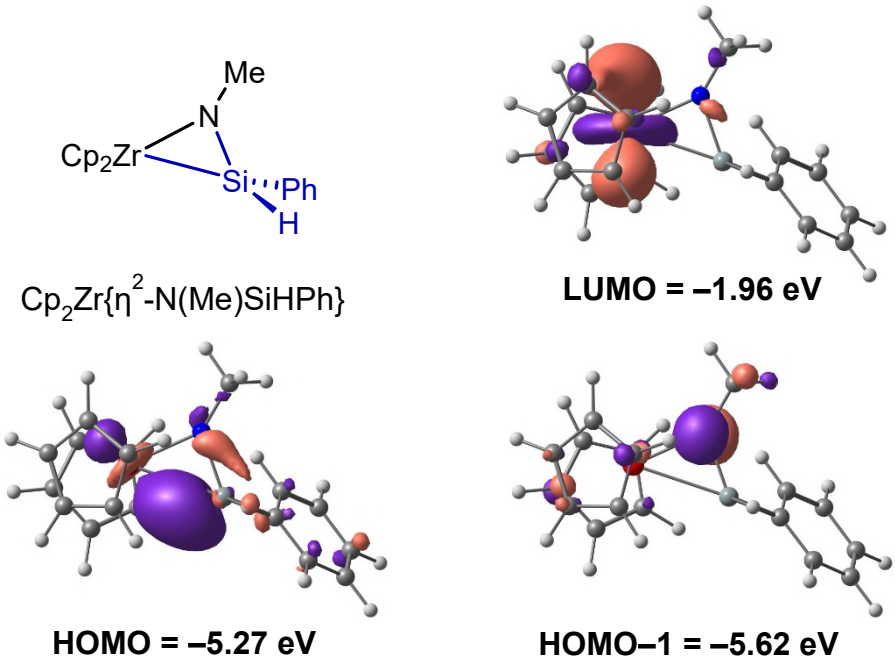


Figure 3.14: DFT (B3PW91/Def2-TZVP) model compound $Cp_2Zr\{\eta^2\text{-}N(Me)SiHPh\}$ and associated isosurfaces and energies of the LUMO, HOMO and HOMO–1 molecular orbitals.

The non-bonding molecular orbital composed predominantly of the nitrogen 2p lone pair, with some participation from the Cp moieties (e_{1g} (π)), typical of bent metallocene M–N-containing compounds,[80–82] is found as the HOMO–1 of $Cp_2Zr\{\eta^2$-N(Me)SiHPh$\}$. Slightly higher in energy (–5.27 *vs.* –5.62 eV), and found as the HOMO, is the molecular orbital representing the Zr–Si bond. This MO has *ca.* 40% participation from Si and 30% from Zr (b_2-based), indicating a rather covalent bond. The main density of the bond does not lie along the Zr–Si vector, due to the 3-membered ZrNSi ring, and orientates out of the open face of $ZrSiHC_{Ph}$ plane. The low-lying LUMO pertains to the Zr-based $1a_1$-type non-bonding orbital and is typical of 16 VE Cp_2ZrL_2 complexes – Figure 3.15 shows the interaction diagram for a generic Cp_2ML_2 complex.[83,84] Here, the $2a_1$ and $1b_2$ orbitals of the metallocene interact with the SALCs of the L_2 moiety to form bonding and anti-bonding MOs, while the $1a_1$ orbital of the metallocene is non-bonding. The HOMO–LUMO gap is seen to be 3.31 eV, and the HOMO pertaining to the Zr–Si bond and the LUMO to the vacant Zr-based a_1 orbital is consistent with the observed reactivity of η^2-silanimines. Furthermore, the orientations of the HOMO and LUMO – pointing out of the face of the $ZrSiHC_{i\text{-}Ph}$ plane – help facilitate addition across and insertion into the Zr–Si bond.

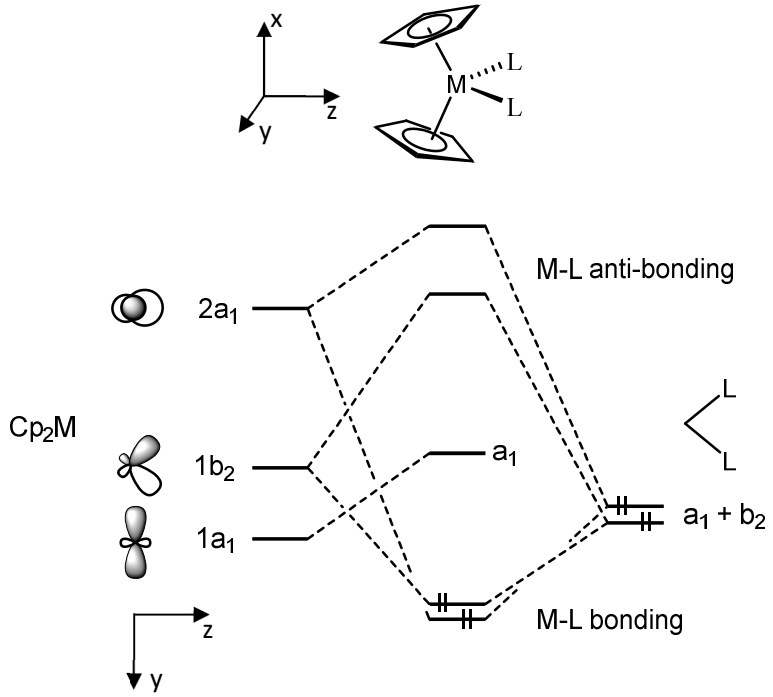


Figure 3.15: Interaction diagram for a 16 VE Cp_2ML_2 complex.[83,84]

Progressing from the formation of the η^2-silanimine **13_int**, HCC^{t}Bu can approach in two orientations, either with the ^{t}Bu moiety adjacent to Cp_2Zr or SiHPh. The former leads to the experimentally observed C–H activation reaction *via* **TS3_^{t}Bu**, **13_int2** and **TS5_^{t}Bu**, with an activation barrier of 22.5 kcal mol^{-1} and an overall Δ_rG = –5.9 kcal mol^{-1}. The latter leads to 1,2-insertion of the alkyne into the Zr–Si bond *via* **TS4_^{t}Bu**, with an activation barrier of 25.3 kcal mol^{-1} and an overall Δ_rG = –26.6 kcal mol^{-1}. While 1,2-insertion is thermodynamically favourable over C–H activation, it is not kinetically competitive. Furthermore, conversion between **13** and the 1,2-insertion product, **13_alt**, is inaccessible with a barrier of 31.2 kcal mol^{-1}, consistent with only C–H activation being observed. The higher activation barrier for 1,2-insertion can be attributed to steric clashes of the ^{t}Bu moiety with the phenyl group of the silanimine, which impact the reaction before significant rehybridization of the C≡C bond – as judged by the Si–C and Zr–C distances 3.72 and 2.97 Å, respectively, indicating an angled approach of the alkyne to

prevent clashes, short C≡C distance (1.22 Å) and linear alkyne (<CCC and <CCH = 169.4°) in **TS4_^{t}Bu**.

Towards C–H activation, the transition state **TS3_^{t}Bu** appears early along the reaction pathway and the approach of the C–H bond is side-on. The CCH angle is rather linear 168.3° with a C–H bond distance of 1.13 Å, the Zr–Si bond distance is similar to that of **13_int** (2.58 Å) at 2.63 Å, indicative of an early transition state. Furthermore, the H–Si and Zr–C distances of 2.46 and 2.76 Å are much longer than in the first-formed product **13_int2** (1.49 and 2.19 Å, respectively). Amplification of the side-on approach of the C–H bond to the Zr–Si bond is observed on analysis of the imaginary vibrational frequency of **TS3_^{t}Bu**. Consistent with the early, bent transition state, the KIE for C–H activation is calculated to be small, at 1.3 at 298 K. This is slightly smaller than, but comparable to, the value of 1.5 and 1.6 gained from initial rate analysis and competition reaction between HCC^{t}Bu and DCC^{t}Bu, respectively.

As mentioned above, the first-formed product of C–H activation is **13_int2** (G_{rel} = –2.3 kcal mol^{-1}). **13_int2** contains no β-agostic interaction as shown by a long Zr–H distance of 3.39 Å. Rotation about the Zr–N bond, with a barrier of 12.4 kcal mol^{-1}, leads to formation of **13** (G_{rel} = –5.9 kcal mol^{-1}), the structure of which is consistent with the crystallographic structure of $Cp_2Zr(CC^{t}Bu)\{N(^{t}Bu)Si(\mu\text{-}H)Me_2\}$ (**14**). Overall, the calculated mechanism for the reaction of **6** with HCC^{t}Bu is in agreement with the mechanism asserted through experimental findings. Furthermore, the calculations are consistent with the lack of observation of both 1,2- and 2,1-insertion products.

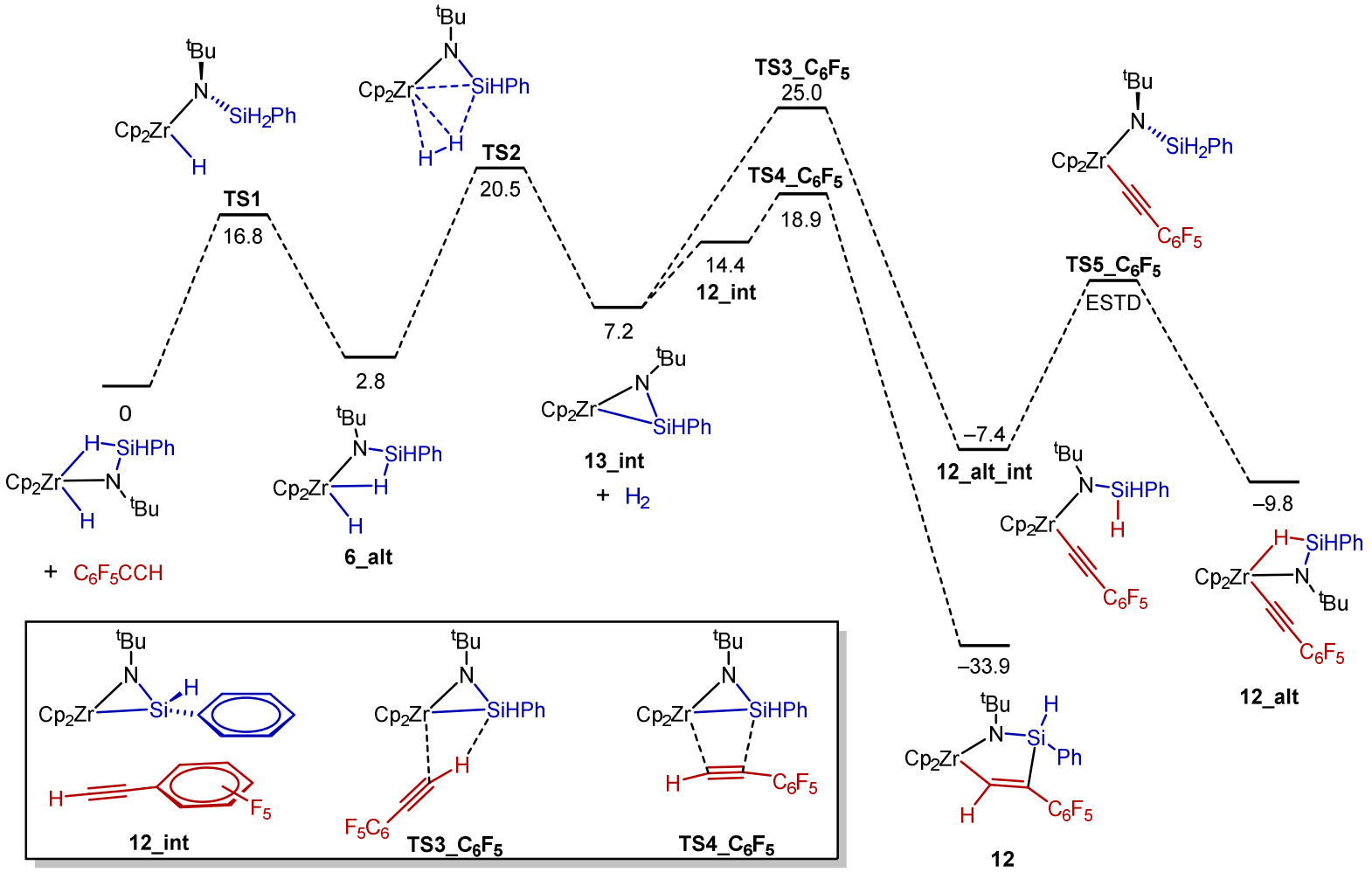


Figure 3.16: DFT (B3PW91/Def2-TZVP/d3-bj/SCRF) mechanism for the 1,2-insertion and C–H activation reactions of $HCCC_6F_5$ with **6**, forming H_2 and either **12** or **12_alt**, respectively. Gibbs free energies (kcal mol^{-1}, T = 298.15 K) for minima and transition states (labelled **TSx** or **TSx_C$_6$F$_5$**) are shown relative to **6** and $HCCC_6F_5$.

Attention is now turned to the DFT calculated mechanism of **6** with $HCCC_6F_5$ (Figure 3.16), which is consistent with experimental observation. Initially, the reaction proceeds in an identical manner to that with HCC^tBu – *via* dihydrogen elimination to form **13_int**. As with HCC^tBu, $HCCC_6F_5$ can approach in two orientations: either with the aryl group adjacent to Cp_2Zr; or adjacent to SiHPh. The former leads to C–H activation *via* **TS3**, **12_alt_int** and **TS5_C6F5** with an activation barrier of 25.0 kcal mol^{-1} and an overall Δ_rG = –9.8 kcal mol^{-1}. The first formed product, **12_alt_int** (G_{rel} = –7.4 kcal mol^{-1}), is a non-agostic isomer of **12_alt** and is isostructural with **13_int2**. Rotation about the Zr–N bond leads to formation of the final product **12_alt**, which is isostructural with **13**.

Approach of $HCCC_6F_5$ with the aryl group adjacent to SiHPh leads to 1,2-insertion of the alkyne into the Zr–Si bond *via* **12_int** and **TS4_C6F5**, with a relatively low activation barrier of 18.9 kcal mol^{-1} and an overall Δ_rG = –33.9 kcal mol^{-1}. This shows 1,2-insertion of the alkyne to be both kinetically and thermodynamically favourable over C–H activation, as well as irreversible. This is in contrast to the reaction with HCC^tBu, where C–H activation is kinetically favoured. It can also be noted that the calculated barrier of reaction of **6** with $HCCC_6F_5$ (20.5 kcal mol^{-1}) is lower than with HCC^tBu (22.5 kcal mol^{-1}). Consistent with this, a competition experiment between $HCCC_6F_5$ and HCC^tBu, carried out with 10 equivalents of each alkyne with one equivalent of **6**, showed no formation of **13** and only formation of **12** and the impurities associated with reaction of **6** with $HCCC_6F_5$.

On analysis of **TS4_C6F5**, it can be seen that π-π interactions of the Ph and C_6F_5 rings stabilise the transition state – the centroid-centroid distance is 3.43 Å, within the 3.8 Å limit of such interactions, and the two rings are parallel-displaced.[85] The transition state is also early along the reaction pathway, with little distortion of the alkyne (C≡C = 1.22

Å, <CCC = 174.3° and <CCH = 174.8°) and long Zr–C and Si–C distances (3.23 and 3.52 Å, respectively, vs. 2.24 and 1.90 Å in **12**). These Zr–C and Si–C distances of 3.23 and 3.52 Å compare to 2.97 and 3.72 Å in **TS4_^{t}Bu** showing that while $HCCC_6F_5$ can approach near-parallel with the Zr–Si bond, presumably due to π-π interactions, a lack of steric clash and greater electrostatic attraction due to electron-withdrawing effect of the C_6F_5 on the C≡C bond, HCC^{t}Bu must approach at a significant angle.

Notably, **TS4_C_6F_5** is preceded by the intermediate **12_int**, with G_{rel} = 14.4 kcal mol^{-1} (Figure A8). The average distance from the Zr centre to the carbon atoms of the C≡C linkage is long, at 4.20 Å (*cf.* 3.30 Å in **TS4_C_6F_5**), indicating this species is not a π-adduct. π-Adducts have been observed on the pathway to alkyne insertion reactions into M–E bonds, though contain much shorter Zr···$C_{C≡C}$ distances (<3 Å), and the Zr···$C_{C≡C}$ distances of zirconocene complexes containing structurally characterised η^2-bound alkynes with near-linear alkyne linkages are <3 Å.[69,86–88] However, the distance between the centroids of the parallel-displaced aryl rings is 3.51 Å, within the 3.8 Å limit for π-π stacking interactions and only slightly longer than observed in **TS4_C_6F_5** (3.43 Å).[85] This indicates the π-π stacking is the stabilising force of this intermediate and, considering the distance between the aryl rings does not change greatly between **12_int** and **TS4_C_6F_5** but the Zr···$C_{C≡C}$ distances do, acts as an anchor for the reaction.

Upon following the intrinsic reaction coordinate forward from **TS4**, **12** is formed with G_{rel} = –33.9 kcal mol^{-1}. As mentioned previously, coupling between the *ortho*-fluorine of the aryl group and the SiH proton is seen in both the ^{1}H and ^{19}F NMR spectra. The H···F distance in the ground state structure between the hydride and adjacent *ortho*-fluorine is 2.90 Å, but rotation of the C_6F_5 ring can bring the atoms closer. Previously, Group 4 transition metal complexes have exhibiting through-space couplings contain H···F

distances of 2.7 Å or less.[40–42] Overall, the computed mechanism for the reaction of **6** with $HCCC_6F_5$ is consistent with the experimental findings that 1,2-insertion is favoured over C–H activation and 2,1-insertion, and that reaction of **6** with $HCCC_6F_5$ is kinetically favoured over reaction with HCC^tBu. Electronic and steric factors appear to lead to the difference in reactivity between HCC^tBu and $HCCC_6F_5$.

3.2.5 DFT studies of dihydrogen elimination from $Cp_2Zr(H)\{N(Xyl)SiH_2Ph\}$ (8)

Noting the lack of reaction of the xylylsilalmides **8** and **9** with terminal alkynes, the mechanism of dihydrogen elimination from **8** was calculated by DFT and is shown Figure 3.17. The mechanism is analogous to that of **6**, with formation of the unfavourable agostic conformation **8_alt1** (G_{rel} = 13.2 kcal mol^{-1}), with the agostic Si–H residing in the central coordination site of the zirconocene, being first accessed. Subsequently and consistent with not being observed experimentally, dihydrogen elimination occurs with a thermally inaccessible free energy barrier of 32.2 kcal mol^{-1} relative to **8** (19.0 kcal mol^{-1} relative to **8_alt1**), forming the η^2-silanimine $Cp_2Zr\{\eta^2\text{-}N(Xyl)SiHPh\}$ (G_{rel} = 9.8 kcal mol^{-1}).

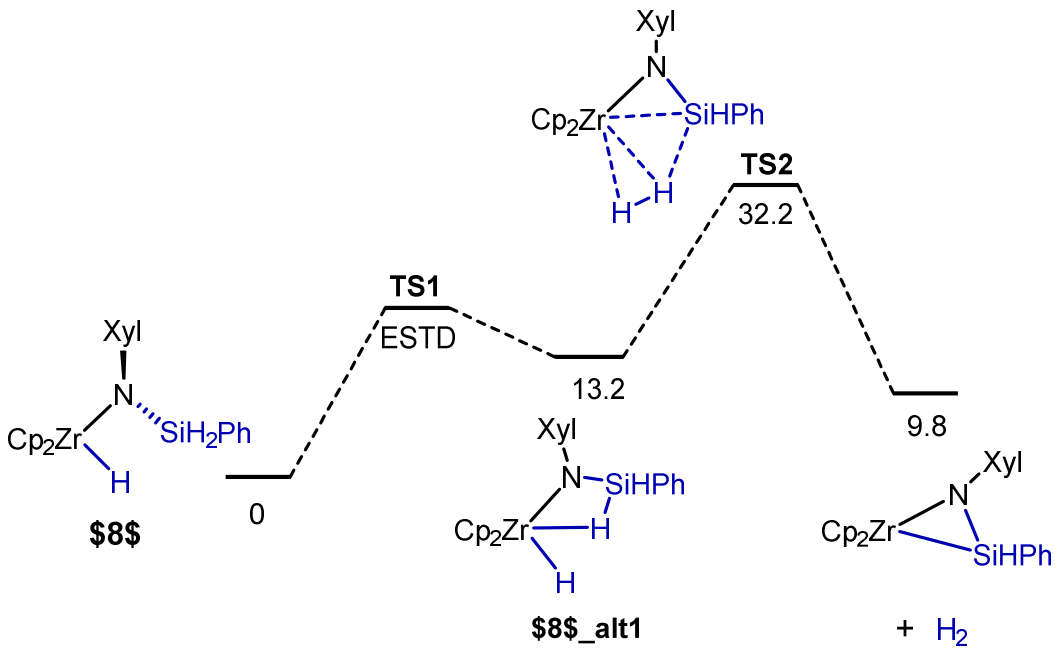


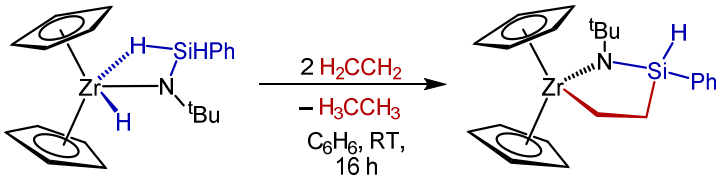
Figure 3.17: DFT (B3PW91/Def2-TZVP/d3-bj/SCRF) mechanism for dihydrogen elimination from **8**, forming H_2 and the η^2-silanimine $Cp_2Zr\{\eta^2$-N(Xyl)SiHPh$\}$. Gibbs free energies (kcal mol^{-1}, T = 298.15 K) for minima and transition states (labelled **TSx**) are shown relative to **8**.

Notably, while this free energy barrier of 32.2 kcal mol^{-1} compares to 20.5 kcal mol^{-1} for **6**, the relative free energy barriers with respect to **8_alt1** and **6_alt** are similar at 19.0 kcal mol^{-1} and 17.7 kcal mol^{-1}, respectively. As such, the majority of the 11.7 kcal mol^{-1} disparity in energy barrier, and so reason for lack of reactivity of **8**, can be attributed predominantly to the 10.4 kcal mol^{-1} disparity in relative free energy, with respect to **8** and **6**, of the intermediates **8_alt1** and **6_alt**. In turn, this is attributed predominantly to the steric bulk of the xylyl group, as discussed in Chapter 2 of this Thesis.

3.3 Reactions of $Cp_2Zr(H)\{N(^tBu)Si(\mu\text{-}H)HPh\}$ (6) with ethylene

Next, attention is turned to the reactions of $Cp_2Zr(H)\{N(^tBu)Si(\mu\text{-}H)HPh\}$ (**6**) and $Cp_2Zr(H)\{N(Xyl)SiH_2Ph\}$ (**8**) with ethylene, as well as the reaction of **6** with a mixed feedstock of ethylene and hydrogen. As discussed in Chapter 1 of this Thesis, Berry and co-workers reacted the hydride silylamide $Cp_2Zr(H)\{N(^tBu)Si(\mu\text{-}H)Me_2\}$ (**3.3**) with ethylene to form the zirconacycle $Cp_2Zr\{N(^tBu)SiMe_2CH_2CH_2\}$ (**3.13**).[1] This reaction is proposed to proceed by insertion of ethylene into the Zr–H bond to give a transient alkyl silylamide, which rapidly releases ethane by β-hydrogen abstraction to form a transient η^2-silanimine $Cp_2Zr\{\eta^2\text{-}N(^tBu)SiMe_2\}$ (**14_int**). Insertion of a second equivalent of ethylene into the transient Zr–Si bond then forms the product. Insertion of ethylene into M–Si bonds of η^2-silanimines has also been observed by the groups of Sadow and Nikonov.[5,15] In the case of Nikonov, net C–H bond activation of ethylene was observed, proposed to proceed *via* ethylene insertion, with subsequent hydrogen transfer to molybdenum to form the hydride product.

The reaction of **6** with 1 bar over-pressure of ethylene was followed by ^1H NMR spectroscopy. A colour change from pale yellow to bright yellow over the course of 16 h at room temperature accompanied smooth formation of the zirconacycle $Cp_2Zr\{N(^tBu)Si(H)(Ph)CH_2CH_2\}$ (**16**), with concomitant formation of ethane, as expected (Equation 3.19). Notably, small amounts of butane and hexane were also observed, indicating the viability of more than one insertion event at the zirconium centre prior to elimination of the alkane. Such insertion events would resemble that of the propagation reaction of Ziegler-Natta polymerisations.[89] On the preparative scale, **16** was isolated as a waxy yellow solid that could not be crystallised. Reaction of **6** with an excess of 1-hexene gave no reaction.



6 **16**

Equation 3.19

The ^{1}H NMR spectrum of **16** (Figure 3.18) shows two sharp, singlet resonances at 5.91 and 5.84 ppm corresponding to two chemically inequivalent Cp groups. This indicates C_1 symmetry, consistent with the proposed structure, analogous to $Cp_2Zr\{N(^tBu)Si(H)(Ph)C(C_6F_5)CH\}$ (**12**) and $Cp_2Zr\{\eta^2\text{-}N(^tBu)SiHPh\}(PMe_3)$ (**15**). Four resonances, each of relative integral 1H, appear between 1 and 2 ppm, and are assigned to the four aliphatic protons of the $ZrCH_2CH_2Si$ linkage. This is consistent with the symmetry of the compound and with the chemical shifts of the aliphatic protons of Berry and Sadow's zirconocycles $Cp_2Zr\{N(^tBu)SiMe_2CH_2CH_2\}$ (**3.13**) and $Cp_2Zr\{N(SiHMe_2)SiMe_2CH_2CH_2\}$ (**3.14**).[1,5] A ^{1}H-^{1}H COSY experiment reveals a three-bond interaction between the SiCH multiplet resonance at 1.16 – 1.09 ppm and the SiH proton resonance at 5.23 ppm, which is similar to the chemical shift of that of **12** (5.49 ppm). The $^{13}C\{^{1}H\}$ NMR spectrum reveals resonances at 38.4 and 10.0 ppm assigned to the $ZrCH_2$ and $SiCH_2$ resonances, respectively. These are similar to those of **3.13** and **3.14** at 39.1 and 11.2 ppm, and 37.9 and 18.7 ppm, respectively. A ^{29}Si-^{1}H gradient experiment reveals a one-bond interaction between the resonance at 5.23 ppm and a ^{29}Si resonance at –35.1 ppm ($^{1}J_{SiH}$ = 192 Hz) – similar to the ^{29}Si chemical shift and Si–H coupling of **12** (–41.7 ppm, $^{1}J_{SiH}$ = 204 Hz).

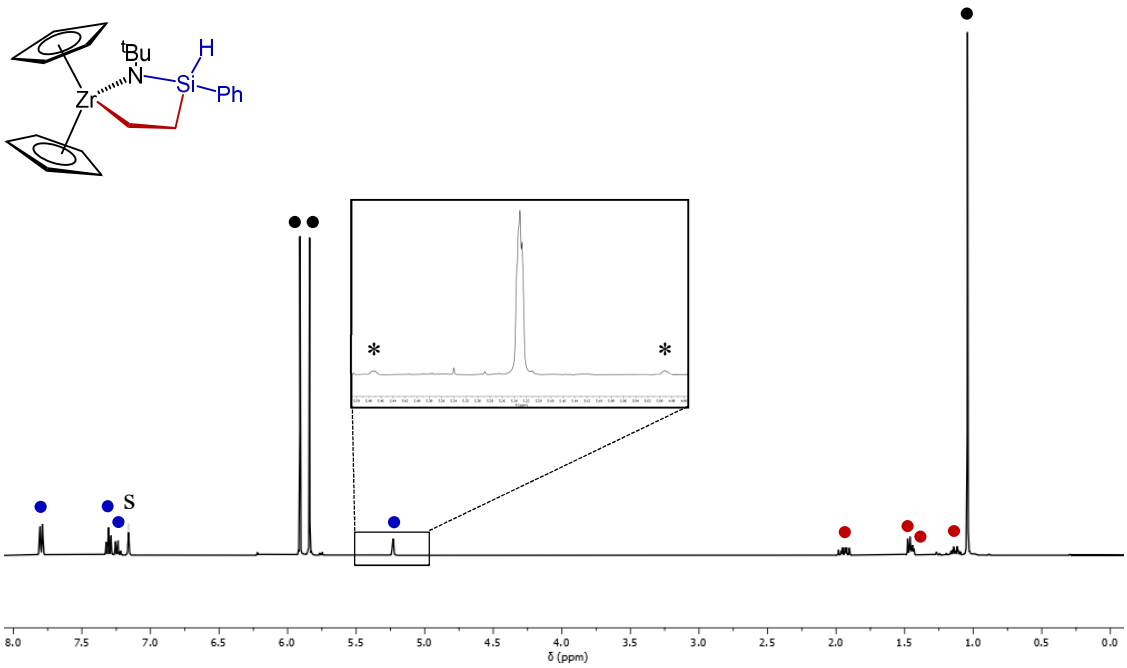
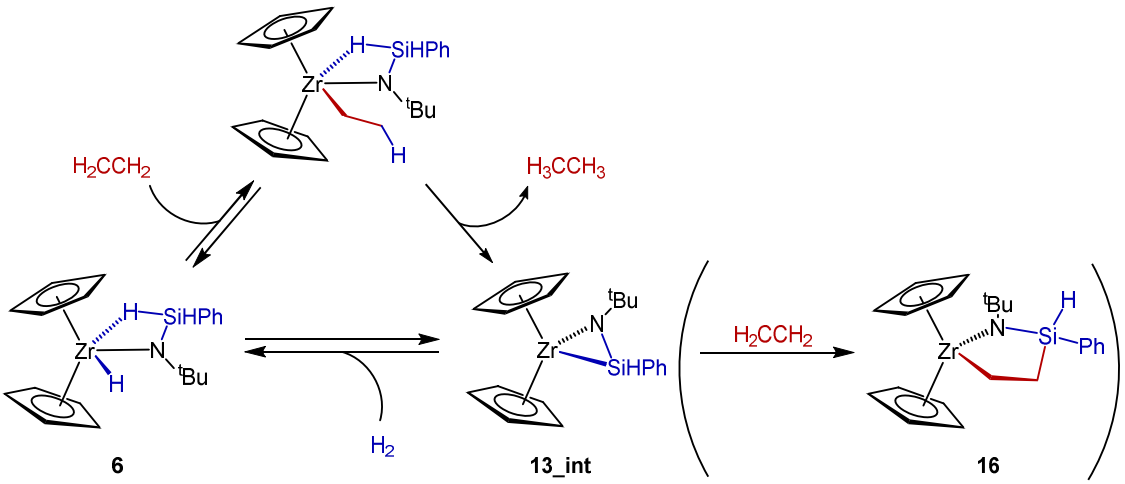


Figure 3.18: ^{1}H NMR spectrum (C_6D_6, 400.1 MHz, 298 K) of $Cp_2Zr\{N(^tBu)Si(H)(Ph)CH_2CH_2\}$ (**16**) with the SiH resonance (and its ^{29}Si satellites, *) enlarged.

Following the reaction of **6**, the reaction of $Cp_2Zr(H)\{N(Xyl)SiH_2Ph\}$ (**8**) with ethylene was attempted. No reaction was observed, even upon increasing the pressure to 2 bar over-pressure and temperature to 80 °C. It could be that insertion of ethylene into the Zr–H bond of **8** is thermally inaccessible and therefore no reaction is observed, or that the insertion product $Cp_2Zr(CH_2CH_3)\{N(Xyl)SiH_2Ph\}$ is significantly higher in free energy than ethylene and **8**, such that any equilibrium between the two would lie completely on the side of ethylene and **8**, and abstraction of the β-H of the silylamide by the alkyl is thermally inaccessible, and therefore no reaction is observed. It has already been noted that β-H abstraction by the hydride of **8** appears thermally inaccessible, given the lack of reaction with terminal alkynes (indeed, the activation energy for this process was calculated to be 32.5 kcal mol^{-1}), though the advent of an alkyl species would greatly reduce the free energy required for β-H abstraction.[1] It is not clear which factor prevents reaction between **8** and ethylene.

Notably, Bi and co-workers carried out DFT studies on the mechanisms of H_2 addition across and ethylene insertion into the Zr–Si bond of the transient η^2-silanimine $Cp_2Zr\{\eta^2\text{-}N(^tBu)SiMe_2\}$ (**14_int**).[1,79] H_2 addition was calculated to have a slightly lower activation energy than ethylene insertion (0.7 kcal mol^{-1}). Considering this, and that the mechanism of reaction of ethylene with **6** proceeds *via* the analogous η^2-silanimine $Cp_2Zr\{\eta^2\text{-}N(^tBu)SiHPh\}$ (**13_int**) and concomitant release of ethane, a catalytic cycle for the hydrogenation of ethylene with **6** can be drawn (Scheme 3.7). Catalyst decomposition by competing ethylene insertion into the Zr–Si bond of **13_int** to irreversibly form **16** must also be considered, given the similar activation energies of ethylene and H_2 insertion. Indeed, only catalytic reactions ran with excess H_2 did not lead to complete conversion of **6** to **16** before complete consumption of ethylene.



Scheme 3.7: Proposed catalytic cycle for the hydrogenation of ethylene by **6**, with the catalyst decomposition pathway also shown.

Addition of 1 bar overpressure of H_2 followed by addition of ethylene, set to 1.5 bar overpressure, to a frozen, degassed C_6D_6 solution of 0.01 mmol **6** in a Young's tap NMR tube, was carried out. Given the partial pressure, measured volume of the headspace of the specific NMR tube used and the ideal gas equation, the molar quantities of H_2 and ethylene added were calculated to be 0.16 and 0.04 mmol, respectively, equating to 25 mol% **6**, though there are of course large errors in these values due to the experimental

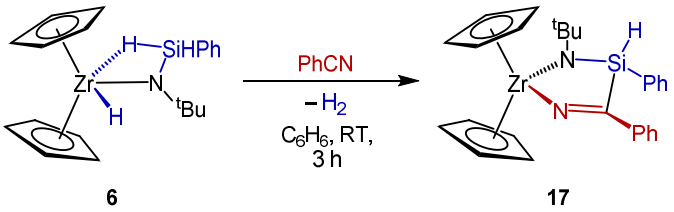
setup. Nevertheless, it can be said that **6** was present in a catalytic quantity. After 66 h at room temperature complete consumption of ethylene was observed, along with an intense resonance for ethane at 0.80 ppm and minor resonances attributable to butane and hexane, indicating catalytic turnover (Figure A9).

The reaction is extremely slow, although mass transport of ethylene and hydrogen into solution in an NMR tube will limit the rate somewhat, and 40% conversion of **6** to **16** was observed. Taking this into account and the limitations of the experimental setup, the reaction was not pursued further. However, it can be noted that homogeneous transition metal olefin hydrogenation catalysts, such as Vaska's complex and Wilkinson's catalyst, traditionally undergo reaction solely at the metal centre and are redox active.[90,91] As such there have been far fewer examples of Group 4 catalysts than later transition metal catalysts, due to the relative rarity of the d^2 metal undergoing oxidative addition.[92] One example of a masked Ti^{II} precatalyst has recently been reported, utilising oxidative C–H addition to access an active Ti^{IV} species of the type $L_nTi(H)\{CH_2C(H)RR'\}$, which bears similarities to **6**.[93] In the hydrogenation of ethylene by **6**, H_2 addition across the transient Zr–Si bond removes the requirement for a Zr^{II} intermediate and allows the system to turnover.

3.4 Other reactions

The nitriles PhCN, ^{t}BuCN and C_6F_5CN were reacted with **6**. Addition of all nitriles led to consumption of **6** within several hours at room temperature. Mixtures of which no products could be confidently assigned in the ^{1}H NMR spectra of the reactions with ^{t}BuCN and C_6F_5CN. Stoichiometric reaction of **6** and PhCN gave ~75% conversion to a single species, as judged by ^{1}H NMR spectroscopy, with concomitant release of H_2. The product revealed two singlet resonances at 6.15 and 6.05 ppm, assigned to two

inequivalent Cp rings, akin to the zirconacycle $Cp_2Zr\{N(^tBu)Si(H)(Ph)C(C_6F_5)CH\}$ (**12**). Phenyl resonances that could be attributed to two inequivalent C_6H_5 moieties could be observed, as could a single SiH resonance of relative integral one at 6.42 ppm (*cf.* 5.49 ppm for **12**), which revealed no correlations in a ^{13}C-^{1}H HSQC experiment. A ^{13}C-^{1}H HMBC experiment revealed correlations between a carbon resonance at 192.5 ppm and the SiH resonance at 6.42 ppm and *o*-$NCC_6\underline{H}_5$ resonance centred at 7.70 ppm. This carbon resonance displayed no single bond correlations to any protons by ^{13}C-^{1}H HSQC. These observations are consistent with formation of $Cp_2Zr\{N(^tBu)Si(H)(Ph)C(Ph)N\}$ (**17**), which is tentatively proposed to be the product of this reaction, *via* dihydrogen elimination from **6** and subsequent insertion of the N≡C bond into the transiently formed Zr–Si bond, analogous to the reaction of **6** with $HCCC_6F_5$ (Equation 3.20). Analogous insertion of nitriles into the Mo–Si bond of an η^2-silanimine has been observed previously, with similar couplings and chemical shifts seen for proton and carbon environments as described here.[21] Insertion of nitriles into the Zr–Si bond of zirconocene silyls has also previously been reported.[54] Unfortunately, compound **17** was unstable in solution and sensitive to handling, and so the reaction was not pursued further.



6 **17**

Equation 3.20

3.5 Conclusions

The reactions of the zirconocene hydride silylamides $Cp_2Zr(H)\{N(^tBu)Si(\mu\text{-}H)HPh\}$ (**6**) and $Cp_2Zr(H)\{N(^tBu)Si(\mu\text{-}H)Me_2\}$ (**3.3**) with the terminal alkynes $HCCC_6F_5$ and HCC^tBu have been described. With $HCCC_6F_5$, $Cp_2Zr\{N(^tBu)Si(H)(Ph)C(C_6F_5)CH\}$ (**12**) was formed by reaction with **6** and a mixture of products was formed from **3.3**. With HCC^tBu, $Cp_2Zr(CC^tBu)\{N(^tBu)Si(\mu\text{-}H)HPh\}$ (**13**) and $Cp_2Zr(CC^tBu)\{N(^tBu)Si(\mu\text{-}H)Me_2\}$ (**14**) were formed from **6** and **3.3**, respectively. Deuterium labelling experiments and kinetic studies were carried out, in addition to the reactions of **6** with excess PMe_3 to form $Cp_2Zr\{\eta^2\text{-}N(^tBu)SiHPh\}(PMe_3)$ (**15**) and $Cp_2Zr\{\eta^2\text{-}N(^tBu)SiHPh\}(PMe_3)$ (**3.2**) with HCC^tBu to form **14**, in order to probe the reaction mechanism.

The reactions are proposed to proceed by β-hydrogen abstraction by the hydride ligand to eliminate dihydrogen, forming a transient η^2-silanimine, followed by either insertion of the C≡C bond into, or C–H activation across, the transient Zr–Si bond to give the observed products. These reactions present the first examples of β-hydrogen abstraction by the hydride ligand of a hydride silylamide and the first examples (in the case of reactions with HCC^tBu) of C–H activation of a terminal alkyne across the Zr–Si bond of an η^2-silanimine. It is notable that the non-agostic zirconocene hydride silylamides $Cp_2Zr(H)\{N(Xyl)SiH_2Ph\}$ (**8**) and $Cp_2Zr(H)\{N(Xyl)SiHPh_2\}$ (**9**) remained inert towards the terminal alkynes indicating β-hydrogen abstraction and dihydrogen elimination are thermally inaccessible. Indeed, DFT calculations showed the free energy barrier for dihydrogen elimination from **8** to be 32.2 kcal mol^{-1}.

DFT studies to probe the mechanisms and relative free energy barriers of dihydrogen elimination, C≡C insertion into the Zr–Si bond and C–H activation across the Zr–Si bond

of the reactions of **6** with $HCCC_6F_5$ and HCC^tBu were also carried out. These were consistent with experimental observations. Dihydrogen elimination was calculated to occur with an energy barrier of 20.5 kcal mol^{-1}, and analysis of the molecular orbitals of the model η^2-silanimine $Cp_2Zr\{\eta^2\text{-}N(Me)SiHPh\}$ showed the HOMO to pertain to the Zr–Si bond and LUMO the Zr-based a_1 orbital, both orientating out of the $ZrSiHC_{Ph}$ plane – consistent with reactions occurring across the Zr–Si bond. C–H activation of HCC^tBu and 1,2-insertion of $HCCC_6F_5$ were calculated to occur with free energy barriers of 22.5 and 20.5 kcal mol^{-1}, relative to **6** and respective alkyne, with steric and electronic factors contributing to the divergent reactivity.

Additional to the reactions with terminal alkynes, reaction of **6** with ethylene was also carried out resulting in the formation of $Cp_2Zr\{N(^tBu)Si(H)(Ph)CH_2CH_2\}$ (**16**), consistent with previous reactions. As with terminal alkynes, **8** was found to be inert to ethylene. Evidence for the catalytic hydrogenation of ethylene by **6** was presented, requiring excess H_2 to prevent catalyst decomposition by addition of ethylene across the Zr–Si bond of the η^2-silanimine intermediate. The hydrogenation of ethylene by early transition metal complexes is rare, relative to later transition metals, and the transient Zr–Si bond was shown to be key to the reaction. Finally, attempts to react **6** with nitriles were described. While no species could be isolated, the NMR tube scale reaction of **6** with PhCN indicated predominant formation of the zirconacycle $Cp_2Zr\{N(^tBu)Si(H)(Ph)C(Ph)N\}$ (**17**), mimicking the reaction of **6** with $HCCC_6F_5$.

3.6 References

1 L. J. Procopio, P. J. Carroll and D. H. Berry, *J. Am. Chem. Soc.*, 1991, **113**, 1870–1872.
2 L. J. Procopio, P. J. Carroll and D. H. Berry, *Organometallics*, 1993, **12**, 3087–3093.
3 K. Yan, A. Ellern and A. D. Sadow, *J. Am. Chem. Soc.*, 2012, **134**, 9154–9156.
4 K. Yan, J. J. Duchimaza Heredia, A. Ellern, M. S. Gordon and A. D. Sadow, *J. Am. Chem. Soc.*, 2013, **135**, 15225–15237.
5 K. Yan and A. D. Sadow, *Chem. Commun.*, 2013, **49**, 3212–3214.
6 K. Yan, A. Pindwal, A. Ellern and A. D. Sadow, *Dalton Trans.*, 2014, **43**, 8644–8653.
7 R. A. Anderson and V. V. Mainz, *Inorg. Chem.*, 1980, **19**, 2165–2169.
8 W. A. Herrmann, J. Eppinger, M. Spiegler, O. Runte and R. Anwander, *Organometallics*, 1997, **16**, 1813–1815.
9 R. Anwander, O. Runte, J. Eppinger, G. Gerstberger, E. Herdtweck and M. Spiegler, *J. Chem. Soc., Dalton Trans.*, 1998, 847–858.
10 J. Eppinger, M. Spiegler, W. Hieringer, W. A. Herrmann and R. Anwander, *J. Am. Chem. Soc.*, 2000, **122**, 3080–3096.
11 M. G. Klimpel, H. W. Görlitzer, M. Tafipolsky, M. Spiegler, W. Scherer and R. Anwander, *J. Organomet. Chem.*, 2002, **647**, 236–244.
12 B. Liu, T. Roisnel, J.-P. Guégan, J.-F. Carpentier and Y. Sarazin, *Chem. Eur. J.*, 2012, **18**, 6289–6301.
13 J. F. Hartwig, *J. Am. Chem. Soc.*, 1996, **118**, 7010–7011.
14 W. Scherer, D. J. Wolstenholme, V. Herz, G. Eickerling, A. Brück, P. Benndorf and P. W. Roesky, *Angew. Chem., Int. Ed.*, 2010, **49**, 2242–2246.
15 A. Y. Khalimon, R. Simionescu and G. I. Nikonov, *J. Am. Chem. Soc.*, 2011, **133**, 7033–7053.
16 S. K. Ignatov, N. H. Rees, A. A. Merkoulov, S. R. Dubberley, A. G. Razuvaev, P. Mountford and G. I. Nikonov, *Chem. Eur. J.*, 2008, **14**, 296–310.
17 W. A. Nugent, D. W. Ovenall and S. J. Holmes, *Organometallics*, 1983, **2**, 161–162.
18 A. Koperniku, P. J. Foth, G. M. Sammis and L. L. Schafer, *J. Am. Chem. Soc.*, 2019, **141**, 18944–18948.
19 S. L. Buchwald, B. T. Watson, M. W. Wannamaker and J. C. Dewan, *J. Am. Chem. Soc.*, 1989, **111**, 4486–4494.
20 M. Okazaki and S. Ebina, *Chem. Lett.*, 2014, **43**, 1089–1091.
21 A. Y. Khalimon, R. Simionescu, L. G. Kuzmina, J. A. K. Howard and G. I. Nikonov, *Angew. Chem., Int. Ed.*, 2008, **47**, 7701–7704.
22 N. A. McLeod, L. G. Kuzmina, I. Korobkov, J. A. K. Howard and G. I. Nikonov, *Dalton Trans.*, 2016, **45**, 2554–2561.
23 S. J. Simpson, H. W. Turner and R. A. Andersen, *J. Am. Chem. Soc.*, 1979, **101**, 7728–7729.
24 S. J. Simpson and R. A. Andersen, *Inorg. Chem.*, 1981, **20**, 3627–3629.
25 D. C. Bradley, H. Chudzynska, J. D. J. Backer-Dirks, M. B. Hursthouse, A. A. Ibrahim, M. Motevalli and A. C. Sullivan, *Polyhedron*, 1990, **9**, 1423–1427.
26 P. Berno, R. Minhas, S. Hao and S. Gambarotta, *Organometallics*, 1994, **13**, 1052–1054.
27 C. P. Gerlach and J. Arnold, *Organometallics*, 1996, **15**, 5260–5262.

28 H. Cai, X. Yu, T. Chen, X. T. Chen, X. Z. You and Z. Xue, *Can. J. Chem.*, 2003, **81**, 1398–1405.
29 M. Niemeyer, *Inorg. Chem.*, 2006, **45**, 9085–9095.
30 O. Bénaud, J. C. Berthet, P. Thuéry and M. Ephritikhine, *Inorg. Chem.*, 2010, **49**, 8117–8130.
31 T. I. Gountchev and T. D. Tilley, *J. Am. Chem. Soc.*, 1997, **119**, 12831–12841.
32 P. J. Tiong, A. Nova, A. D. Schwarz, J. D. Selby, E. Clot and P. Mountford, *Dalton Trans.*, 2012, **41**, 2277.
33 L. C. Stevenson, S. Mellino, E. Clot and P. Mountford, *J. Am. Chem. Soc.*, 2015, **137**, 10140–10143.
34 L. Wang, S. C. Hunter, Z. Song, C. A. Steren, T. Chen, Z. Wei, H. Cai and Z.-L. Xue, *Chem. Eur. J.*, 2014, **20**, 6033–6039.
35 A. Koperniku, P. J. Foth, G. M. Sammis and L. L. Schafer, *J. Am. Chem. Soc.*, 2019, **141**, 18944–18948.
36 M. A. Lockwood, M. C. Potyen, B. D. Steffey, P. E. Fanwick and I. P. Rothwell, *Polyhedron*, 1995, **14**, 3293–3313.
37 B. Xie, DPhil Thesis, University of Oxford, 2018.
38 V. V. Burlakov, P. Arndt, W. Baumann, A. Spannenberg and U. Rosenthal, *Organometallics*, 2004, **23**, 4160–4165.
39 M. Hennig, M. L. Munzarová, W. Bermel, L. G. Scott, V. Sklenář and J. R. Williamson, *J. Am. Chem. Soc.*, 2006, **128**, 5851–5858.
40 J. C. Hierso, *Chem. Rev.*, 2014, 114, 4838–4867.
41 M. C. W. Chan, S. C. F. Kui, J. M. Cole, G. J. McIntyre, S. Matsui, N. Zhu and K.-H. Tam, *Chem. Eur. J.*, 2006, **12**, 2607–2619.
42 S. C. F. Kui, N. Zhu and M. C. W. Chan, *Angew. Chem., Int. Ed.*, 2003, **42**, 1628–1632.
43 M. J. Butler, A. J. P. White and M. R. Crimmin, *Organometallics*, 2018, **37**, 949–956.
44 P. J. Chirik and J. E. Bercaw, *Organometallics*, 2005, **24**, 5407–5423.
45 L. J. Procopio, P. J. Carroll and D. H. Berry, *J. Am. Chem. Soc.*, 1994, **116**, 177–185.
46 M. Horáček, P. Štěpnička, J. Kubišta, R. Gyepes and K. Mach, *Organometallics*, 2004, **23**, 3388–3397.
47 S. K. Podiyanachari, R. Fröhlich, C. G. Daniliuc, J. L. Petersen, G. Kehr, G. Erker, N. Suzuki, S. Yuasa, K. Hagimori, S. Inoue, T. Asada, T. Takemoto and Y. Masuyama, *Dalton Trans.*, 2012, **41**, 10811–10816.
48 G. Erker, W. Frömberg, R. Benn, R. Mynott, K. Angermund and C. Kruger, *Organometallics*, 1989, **8**, 911–920.
49 R. Choukroun, B. Donnadieu, J. S. Zhao, P. Cassoux, C. Lepetit and B. Silvi, *Organometallics*, 2000, **19**, 1901–1911.
50 P. J. Walsh, F. J. Hollander and R. G. Bergman, *J. Organomet. Chem.*, 1992, **428**, 13–47.
51 B. Marciniec, in *Hydrosilylation*, Springer Netherlands, 2008, pp. 53–86.
52 M. Zaranek, B. Marciniec and P. Pawluć, *Org. Chem. Front.*, 2016, **3**, 1337–1344.
53 D. Kissounko, A. Epshteyn, J. C. Fettinger and L. R. Sita, *Organometallics*, 2006, **25**, 531–535.
54 H. G. Woo and T. Don Tilley, *J. Organomet. Chem.*, 1990, **393**, C6–C9.
55 H. G. Woo, R. H. Heyn and T. D. Tilley, *J. Am. Chem. Soc.*, 1992, **114**, 5698–5707.

56 H. Ferreira, A. R. Dias, M. T. Duarte, J. R. Ascenso and A. M. Martins, *Inorg. Chem.*, 2007, **46**, 750–755.
57 A. D. Jenkins, M. F. Lappert and R. C. Srivastava, *J. Organomet. Chem.*, 1970, **23**, 165–172.
58 D. G. Black, D. C. Swenson, R. F. Jordan and R. D. Rogers, *Organometallics*, 1995, **14**, 3539–3550.
59 Z. Hou, T. L. Breen and D. W. Stephan, *Organometallics*, 1993, **12**, 3158–3167.
60 W. H. Bernskoetter, J. A. Pool, E. Lobkovsky and P. J. Chirik, *J. Am. Chem. Soc.*, 2005, **127**, 7901–7911.
61 H. M. Hoyt and R. G. Bergman, *Angew. Chem., Int. Ed.*, 2007, **46**, 5580–5582.
62 R. Jimenez, M. C. Barral, V. Moreno and A. Santos, *J. Organomet. Chem.*, 1979, **182**, 353–359.
63 D. L. Reger, M. E. Tarquini and L. Lebioda, *Organometallics*, 1983, **2**, 1763–1769.
64 A. D. Schofield, A. Nova, J. D. Selby, C. D. Manley, A. D. Schwarz, E. Clot and P. Mountford, *J. Am. Chem. Soc.*, 2010, **132**, 10484–10497.
65 H. Kwart, *Acc. Chem. Res.*, 1982, **15**, 401–408.
66 M. G. Cushion, J. Meyer, A. Heath, A. D. Schwarz, I. Fernández, F. Breher and P. Mountford, *Organometallics*, 2010, **29**, 1174–1190.
67 A. L. Reznichenko and K. C. Hultzsch, *J. Am. Chem. Soc.*, 2012, **134**, 3300–3311.
68 G. Parkin, *J. Label. Compd. Radiopharm.*, 2007, **50**, 1088–1114.
69 B. A. Clough and P. Mountford, *Organometallics*, 2018, **37**, 3558–3572.
70 L. C. Stevenson, DPhil Thesis, University of Oxford, 2015.
71 J. L. Polse, R. A. Andersen and R. G. Bergman, *J. Am. Chem. Soc.*, 1995, **117**, 5393–5394.
72 T. H. Lowry and K. S. Richardson, *Mechanism and theory in organic chemistry*, Harper & Row, New York, 1987.
73 M. G. Omez-Gallego and M. A. Sierra, *Chem. Rev*, 2011, **111**, 4857–4963.
74 D. Rabinovich and G. Parkin, *J. Am. Chem. Soc.*, 1993, **115**, 353–354.
75 T. Hascall, D. Rabinovich, V. J. Murphy, M. D. Beachy, R. A. Friesner and G. Parkin, *J. Am. Chem. Soc.*, 1999, **121**, 11402–11417.
76 J. Burés, *Angew. Chem., Int. Ed.*, 2016, **55**, 16084–16087.
77 C. D. T. Nielsen and J. Burés, *Chem. Sci.*, 2019, 10, 348–353.
78 D. G. Truhlar and A. Kohen, *Proc. Natl. Acad. Sci. U. S. A.*, 2001, **98**, 848–851.
79 S. Bi, S. Zhu and Z. Zhang, *Eur. J. Inorg. Chem.*, 2007, **2007**, 2046–2054.
80 J. D. Selby, M. Feliz, A. D. Schwarz, E. Clot and P. Mountford, *Organometallics*, 2011, **30**, 2295–2307.
81 J. C. Green, M. L. H. Green, J. T. James, P. C. Konidaris, G. H. Maunder and P. Mountford, *J. Chem. Soc., Chem. Commun.*, 1992, 1361–1365.
82 B. A. Clough, S. Mellino, A. V. Protchenko, M. Slusarczyk, L. C. Stevenson, M. P. Blake, B. Xie, E. Clot and P. Mountford, *Inorg. Chem.*, 2017, **56**, 10794–10814.
83 J. W. Lauher and R. Hoffmann, *J. Am. Chem. Soc.*, 1976, **98**, 1729–1742.
84 J. C. Green, *Chem. Soc. Rev.*, 1998, **27**, 263.
85 C. Janiak, *J. Chem. Soc., Dalton Trans.*, 2000, 3885–3896.
86 G. Erker, S. Venne-Dunker, G. Kehr, N. Kleigrewe, R. Fröhlich, C. Mück-Lichtenfeld and S. Grimme, *Organometallics*, 2004, **23**, 4391–4395.
87 S. Kumar Podiyanachari, G. Kehr, C. Mück-Lichtenfeld, C. G. Daniliuc and G. Erker, *J. Am. Chem. Soc.*, 2013, **135**, 17444–17456.

88 V. V. Burlakov, A. Spannenberg, P. Arndt, U. Rosenthal and M. Nieger, *Acta Crystallogr.*, 2015, **E71**, 71–72.
89 P. Cossee, *J. Catal.*, 1964, **3**, 80–88.
90 L. Vaska and R. E. Rhodes, *J. Am. Chem. Soc.*, 1965, **87**, 4970–4971.
91 J. F. Young, J. A. Osborn, F. H. Jardine and G. Wilkinson, *Chem. Commun.*, 1965, 131–132.
92 E. P. Beaumier, A. J. Pearce, X. Y. See and I. A. Tonks, *Nat. Rev. Chem.*, 2019, **3**, 15–34.
93 J. R. Aguilar-Calderón, A. J. Metta-Magaña, B. Noll and S. Fortier, *Angew. Chem., Int. Ed.*, 2016, **55**, 14101–14105.

Chapter Four

Reactions of zirconocene hydride silylamides with boranes and silanes

4.1 Introduction

As discussed previously in this Thesis, the hallmark chemistry of the silylamide ligand in organometallic systems is β- or γ-H abstraction by amenable metal-bound R ligands (R = alkyl, amide, silyl) followed by reaction of substrates, usually unsaturated, at the newly formed M–Si or M–C bond.[1–20] In Chapter 3, the class of amenable R ligands for β-H abstraction was extended to hydrides. Furthermore, the scope of unsaturated substrates reacted with the transient Zr–Si bonds of η^2-silanimines was extended to terminal alkynes and nitriles. To this date, the reaction of E–H bonds (E = B, Si, H) with complexes bearing silylamide ligands have been comparatively limited.

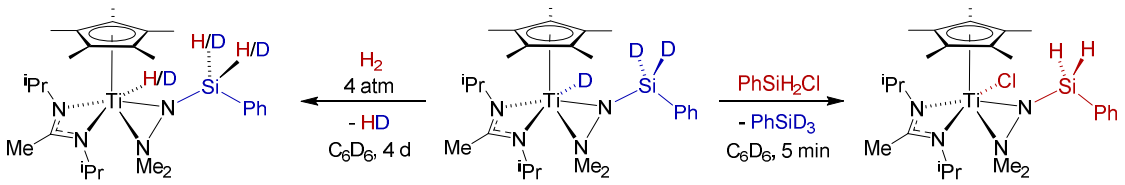
Sadow and co-workers have shown the ability of the SiH hydrogen of $Cp_2Zr(H)\{N(Si(\mu\text{-}H)Me_2)(SiHMe_2)\}$ (**4.1**) to be abstracted by $B(C_6F_5)_3$ forming $[Cp_2Zr\{N(Si(\mu\text{-}H)Me_2)_2\}][HB(C_6F_5)_3]$, which could then react with DMAP to cleave one of the Si–H bonds and form $[Cp_2Zr\{N(Si(\mu\text{-}H)Me_2)SiMe_2(DMAP)\}][HB(C_6F_5)_3]$.[14] No other reports of reactions of boranes with zirconocene silylamides have been made and no reactions of B–H bonds with zirconocene silylamides have been reported. Addition of amine-boranes to alkaline earth silylamides has been reported to result in protonation of the amide group by the amine-borane N–H bond as an entry point to active species for the dehydrocoupling of amine-boranes.[21,22] Formation of the titanium organoborohydride $Ti(N_2^{iPr}N^{Me})\{(\mu\text{-}H)_2BC_8H_{14}\}(NPh_2)$ ($N_2^{iPr}N^{Me}$ = $N(Me)(CH_2CH_2N^iPr)_2$) was reported by reaction of one equivalent of 9-BBN dimer with the titanium silylamide $Ti(N_2^{iPr}N^{Me})\{N(H)SiH_2Ph\}(NPh_2)$ (**4.2**).[23] The reaction proceeded *via* B–H addition across the Ti–N bond to form a transient titanium hydride, which was then trapped by the second 9-BBN monomer.

Similar formation of Group 4 borohydrides *via* intermediate hydride species has been reported.[24–26] Shore and co-workers reported the observation of $Cp_2Zr(H)\{(\mu\text{-}H)_2BR\}$ (R = C_4H_8 or C_5H_{10}) as an intermediate species in the formation of the zirconocene organoborohydride $Cp_2Zr\{(\mu\text{-}H)_2BR\}\{(\mu\text{-}H)B(R)CH_2Ph\}$ from $Cp_2Zr(Cl)\{(\mu\text{-}H)_2BR\}$ and Ph_2CH_2MgCl in an unusual reaction.[26] $Cp_2Zr\{(\mu\text{-}H)_2BR\}\{(\mu\text{-}H)B(R)CH_2Ph\}$ (R = C_4H_8 or C_5H_{10}) was shown to exist in equilibrium with $Cp_2Zr(H)\{(\mu\text{-}H)_2BR\}$ and $RBCH_2Ph$ in solution. Explicit addition of boranes to metal hydrides to form borohydrides has also been observed.[27–31] Zirconium borohydride complexes have also been prepared *via* salt metathesis reactions between zirconium chlorides and alkali salts of the borohydride.[32–35]

In terms of the reactions of B–H bonds with metal–silicon bonds, there have been few reports. Most notably, Berry and co-workers reported the insertion of the B–H bond of $L{\cdot}BH_3$ (L = NEt_3, *N*-methylmorpholine) into the Ta–Si bond of $Cp_2Ta(PMe_3)\{Si(^tBu)_2H\}$ to form the κ^2-silylborohydride complex $Cp_2Ta\{(\mu\text{-}H)_2BHSi(^tBu)_2H\}$.[27] Given the recurrence of the transient Zr–Si bond in reactions of zirconocene silylamides, the possibility of B–H bond insertion can be imagined.

Turning to Si–H and H–H bond reactivity, there have been multiple reports of reactions of silylamides and related silylhydrazides with silanes and dihydrogen. The titanium silylhydrazido(1-) compound $Cp^*Ti\{MeC(N^iPr)_2\}\{N(NMe_2)SiH_2Ph\}(H)$ (**4.3**) was shown to readily undergo silane exchange with added $RSiH_3$ or $PhSiH_2Cl$ *via* $PhSiH_3$ elimination to form the intermediate hydrazide $Cp^*Ti\{MeC(N^iPr)_2\}(NNMe_2)$ (**4.4**).[36,37] Use of the deuterated isotopologue of **4.3**, **4.3-*d*$_3$**, with $PhSiH_2Cl$ confirmed reaction *via* 1,2-elimination of $PhSiD_3$ and subsequent 1,2-addition of $PhSiH_2Cl$ as the only pathway for this reaction (Scheme 4.1). Further to this, reaction of **4.3-*d*$_3$** with H_2 exhibited the ability of the Ti–H/D bond to undergo σ-bond metathesis with the H–H bond (Scheme

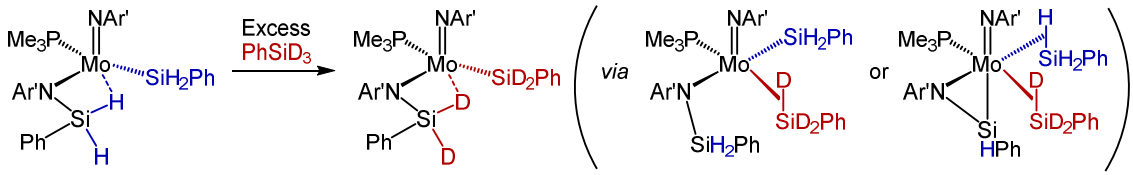
4.1). Such σ-bond metathesis has also been exhibited by Chirik and co-workers by the reaction of $(\eta^5\text{-}C_5H_3\text{-}1,3\text{-}(SiMe_3)_2)_2Ti\{N(R)D\}(D)$ (R = $SiMe_3$ or 2,4,6-$C_6H_2Me_3$) with H_2.[38]



4.3-*d*$_3$

Scheme 4.1: Reactions of Cp*Ti{MeC(N^{i}Pr)$_2$}{N(NMe$_2$)SiD$_2$Ph}(D) (**4.3-*d*$_3$**) with silanes and H_2.[36,37]

Mountford and co-workers also found the silylamido compound Ti($N_2^{iPr}N^{Me}$){N(H)SiH_2Ph}(NPh_2) (**4.2**) could undergo reaction with $PhSiD_3$ to give a mixture of **4.2**, Ti($N_2^{iPr}N^{Me}$){N(H)SiD_2Ph}(NPh_2) (**4.2-*d*$_2$**) and partially deuterated isotopologue Ti($N_2^{iPr}N^{Me}$){N(H)SiHDPh}(NPh_2) (**4.2-*d*$_1$**).[23,39] This was proposed to proceed *via* a silylamide intermediate. Nikonov and co-workers showed that (Ar'N)$_2$Mo{N(^{t}Bu)$SiMe_2$(μ-H)}(H) (Ar' = Dipp) undergoes Mo–H/Si–D exchange with $PhSiD_3$ *via* σ-bond metathesis, with no evidence of addition of $PhSiD_3$ to the Mo=N imido bond, followed by silane elimination.[3] Exchange experiments between (Ar'N)Mo(PMe_3){N(Ar')SiPhH(μ-H)}(SiH_2Ph) and $PhSiD_3$ showed incorporation of deuterium into the Si–H sites of the agostic silylamido moiety, as well as exchange of the silyl ligand (Equation 4.1).[16] This was proposed to occur *via* two pathways, one of which involved an η^2-silanimine intermediate.



Equation 4.1

Given the aforementioned reactions of B–H bonds with metal hydrides, silylamides and silyls, there is a wealth of potential reactivity for boranes with the hydride silylamides

$Cp_2Zr(H)\{N(^tBu)Si(\mu\text{-}H)HPh\}$ (**6**), $Cp_2Zr(H)\{N(^tBu)Si(\mu\text{-}H)Ph_2\}$ (**7**), $Cp_2Zr(H)\{N(^tBu)Si(\mu\text{-}H)Me_2\}$ (**4.5**) and $Cp_2Zr(H)\{N(Xyl)SiH_2Ph\}$ (**8**), either through borohydride formation, B–H activation across the Zr–N bond of the silylamide or insertion of B–H bond into a transiently formed Zr–Si bond. Encouraged by this, reactions of these zirconocene hydride silylamides with secondary and primary boranes and $BH_3{\cdot}SMe_2$ were carried out. Furthermore, similarly motivated by the small, but rich and diverse class of literature reactions of silanes with silylamido and silylhydrazido(1-) compounds, reactions of **6** – **8**, $Cp_2Zr(H)\{N(Xyl)SiHPh_2\}$ (**9**), $Cp_2Zr(H)\{N(NPh_2)SiH_2Ph\}$ (**2**) and $Cp_2Zr(H)\{N(NPh_2)SiHPh_2\}$ (**3**), and their deuterated isotopologues, with silanes, deutero-silanes and dihydrogen were also carried out.

It can be noted that all DFT calculations discussed in this chapter were performed by Professor Philip Mountford. Full details of these calculations are provided in Chapter 6, Section 6.4.

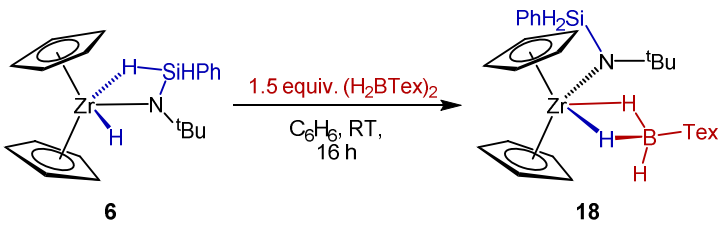
4.2 Reactions of hydride silylamides with boranes

Initially, secondary boranes 9-BBN, dicyclohexyl borane, dimesityl borane, catechol borane, pinacol borane and Piers' borane ($HB(C_6F_5)_2$)[40] were reacted on the NMR tube scale with **6** and **7**. No reaction was observed in the cases of catechol borane and pincaol borane, even up to temperatures of 80 °C, while decomposition to intractable mixtures was observed in the case of all other boranes. For reactions of these secondary boranes with **8**, no reaction was observed in the case of pinacol borane, while intractable mixtures were formed in the cases of catechol borane, dicyclohexyl borane, dimesityl borane and Piers' borane. Upon addition of 9-BBN to **8**, no colour change was observed, though one major species was formed, as judged by ^1H and $^{11}B\{^1H\}$ NMR spectroscopy. The ^1H NMR spectrum showed a single, broad Cp resonance centred at 5.74 ppm and a single

SiH_2 resonance at 5.37 ppm with a $^1J_{SiH}$ coupling constant of 205 Hz. The $^{11}B\{^1H\}$ NMR spectrum showed a single resonance at 7.8 ppm, indicative of a four-coordinate boron (i.e. organoborohydride formation).[41] However, the compound was highly sensitive to handling and vacuum preventing isolation and further characterisation. Attention was then turned to the primary borane thexylborane ([(μ-H)HBTex]$_2$).

4.2.1 Reactions of $Cp_2Zr(H)\{N(^tBu)Si(\mu\text{-}H)HPh\}$ (6) and $Cp_2Zr(H)\{N(Xyl)SiH_2Ph\}$ (8) with thexylborane

On the NMR tube scale, addition of 0.5 equivalents thexylborane dimer to **6** resulted in an equilibrium between the starting materials and the borohydride $Cp_2Zr\{(\mu\text{-}H)_2B(H)Tex\}\{N(^tBu)SiH_2Ph\}$ (**18**). Compound **18** was found to be unstable in solution, decomposing over the course of several days, but stable as a solid for several weeks when stored at room temperature under an inert atmosphere. On the preparative scale, **6** was reacted with 1.5 equivalents thexylborane dimer, which was required to give full conversion to **18**, and **18** was isolated as a pale yellow powder in 41% yield (Equation 4.2). Attempts to analyse the thermodynamics of the equilibrium by VT NMR were unsuccessful as an equilibrium was not reached for two days at room temperature when dissolving **18** in C_6D_6 and similar times were required at elevated temperatures, over which time **18** decomposed.

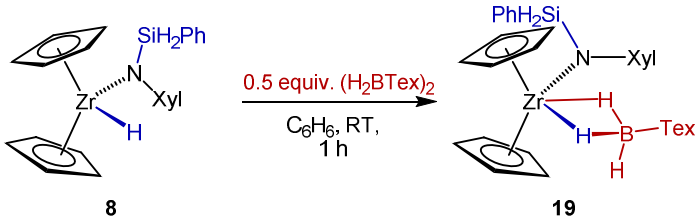


6 **18**

Equation 4.2

In contrast to the equilibrium formed upon reaction of **6** with 0.5 equivalents thexylborane dimer, reaction of **8** with 0.5 equivalents thexylborane dimer was found to

give rapid and quantitative formation of $Cp_2Zr\{(\mu\text{-}H)_2B(H)Tex\}\{N(Xyl)SiH_2Ph\}$ (**19**, Equation 4.3) when followed by ^1H NMR spectroscopy. Presumably, the lack of β-agostic interaction in **8** allows for quantitative formation of **19**. With **18**, the free energy penalty in breaking the β-agostic interaction (3.7 kcal mol^{-1}, see Appendix, Figure A3), as well as the free energy penalty in breaking the thexylborane dimer, presumably offsets the free energy gain in κ^2-adduct formation, resulting in an equilibrium mixture being formed. On the preparative scale, **19** was isolated as a pale yellow powder in a 38% yield. These reactions mimic those of metal hydrides with boranes discussed in Section 4.1.[23–31] It can also be noted that $Cp_2Zr(H)\{N(^tBu)Si(\mu\text{-}H)Ph_2\}$ (**7**) did not react with thexylborane.



8 **19**

Equation 4.3

The ^1H NMR spectrum of **18** shows a single Cp resonance at 5.97 ppm and a single resonance for the SiH_2 protons at 5.11 ppm, indicating the compound is C_s symmetric in the solution phase. A ^{29}Si-^1H gradient experiment reveals a one-bond interaction between the singlet at 5.11 ppm and a ^{29}Si resonance at –51.6 ppm ($^1J_{SiH}$ = 191 Hz). This coupling constant and the ^1H NMR chemical shift of the SiH_2 protons of **18** are significantly different to those of **6** ($^1J_{SiH}$ = 173 Hz and δ = 3.30 ppm), consistent with the loss of the β-agostic interaction. No proton resonance in the region expected for a hydride is observed in the ^1H NMR spectrum and the ^{11}B NMR spectrum of **18** shows a single broad, multiplet resonance at 10.0 ppm (*cf.* 24.5 ppm for thexylborane). These observations are consistent with κ^2-organoborohydride formation and concurrent loss of the agostic interaction.[41,42]

The NMR spectra of **19** are analogous to **18**; the SiH_2 protons appear at 5.40 ppm in the ^1H NMR spectrum and the ^{29}Si resonance is found at –29.5 ppm, with a $^1J_{SiH}$ coupling of 206 Hz, similar to that of **8** (205 Hz). No hydride resonance is observable in the ^1H NMR spectrum and the ^{11}B NMR spectrum reveals a single broad, multiplet resonance at 1.38 ppm.[41] The solid state IR spectrum (Nujol mull) of **18** exhibits three bands corresponding to ν(B–H), at 2405, 2131 and 2065 cm^{-1}. Consistent with literature values for κ^2-borohydrides, the band at 2405 cm^{-1} is assigned to a terminal B–H stretch (ν(B–H_t)), while the bands at 2131 and 2065 cm^{-1} are assigned to the two metal-bridging B–H stretches (ν(B–H_b)).[43] Bands at 2016 and 1976 cm^{-1} are assigned to ν(Si–H) and are at a higher frequency than the β-agostic ν(Si–H) modes of **6** and **7** (1941 and 1893 cm^{-1}, respectively), consistent with a lack of β-agostic interaction.

Diffraction-quality crystals of **18** were grown from a saturated solution of hexane at 5 °C, confirming the connectivity shown in Equation 4.2. The solid state structure of **18** is shown in Figure 4.1 and selected bond distances and angles in Table 4.1. Compound **18** adopts a bent metallocene geometry, with a κ^2-bound borohydride moiety and a non-agostic silylamide ligand. The Zr–N distance of 2.1937(18) Å of **18** is slightly longer than that of **6** (2.169(3) Å), perhaps due to the outer coordination site being more sterically encumbered than the central coordination site of zirconocene. Although there are inherent inaccuracies regarding location of hydrogens in heavy atom structures such as that of **18**, the boron and silicon hydrides were located in the Fourier difference map and positionally and isotropically refined. The Zr(1)–H(4) distance of 3.03(3) Å is *ca.* 0.8 Å longer than the agostic Zr–H distances of **6** and **7**, and 0.4 Å longer than that of **10**. Furthermore, the Zr–N–Si angle of 111.52(10)° (*cf. ca.* 98° for **6** and **7**) shows minimal bending of the silicon towards zirconium, clearly indicating a lack of β-agostic interaction, consistent with NMR and IR spectra.

The Zr–H(1) and Zr–H(2) distances of 2.11(2) and 2.14(3) Å, respectively, are significantly longer than the Zr–H distance of **6** (1.90(5) Å), but similar to those of the zirconocene κ^2-organoborohydride $Cp_2Zr(H)\{(\mu\text{-}H)_2BHMe\}$ (2.04(4) and 2.00(3) Å).[35] The Zr–B distance of 2.514(3) Å is also similar to the Zr–B distance of $Cp_2Zr(H)\{(\mu\text{-}H)_2BHMe\}$ (2.558(4) Å). The Zr–H(1) and Zr–H(2), and B–H(1) and B–H(2) distances being, respectively, identical within error shows the symmetric binding of the borohydride to zirconium. Notably, the four-membered M(1)–H(1)–B(1)–H(2) ring is planar for most group 4 κ^2-borohydrides and κ^2-organoborohydrides not containing BC_α–H···M agostic interactions.[23,24,26,27,44] However, that of **18** is not, with the H(1)–B(1)–H(2) plane lying 39.8° out of plane with the H(1)–Zr(1)–H(2) plane. Analysis of the structure shows this is necessary to avoid steric clashes between the thexyl moiety and the Cp ring of C(22) – C(26).

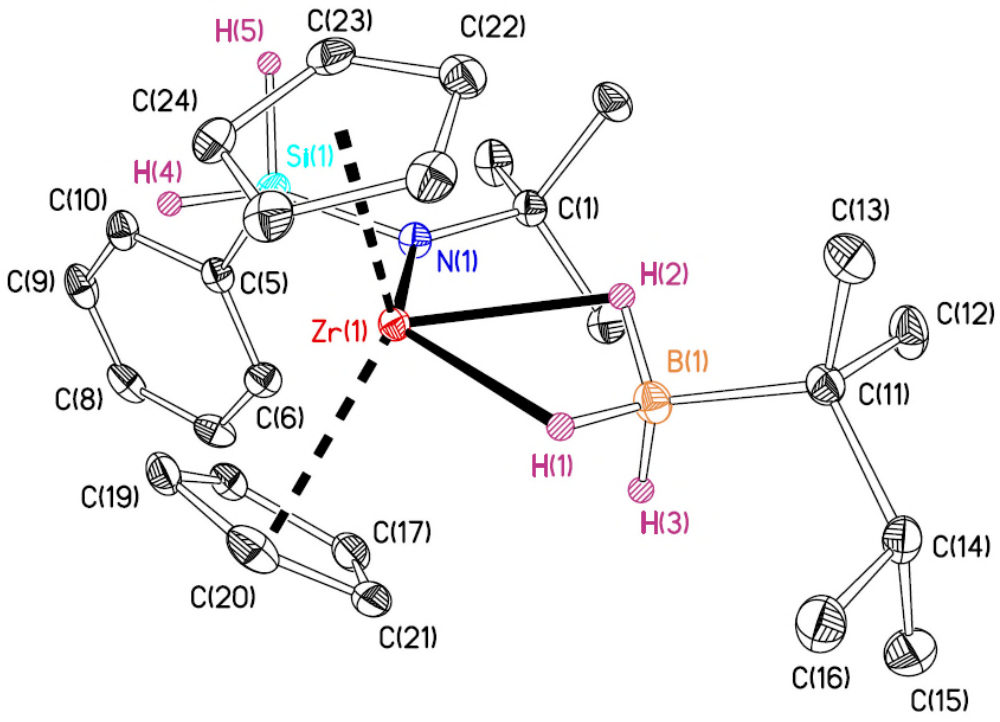
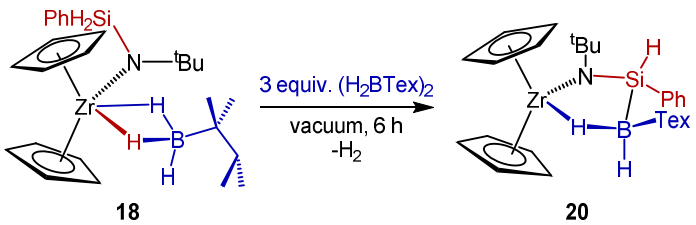


Figure 4.1: Displacement ellipsoid plots (20% probability) of $Cp_2Zr\{(\mu\text{-}H)_2B(H)Tex\}\{N(^tBu)SiH_2Ph\}$ (**18**). C–H atoms are omitted for clarity. H(1) – H(5) are drawn as spheres of an arbitrary radius.

Table 4.1: Selected bond distances (Å) and angles (°) for $Cp_2Zr\{(\mu\text{-}H)_2B(H)Tex\}\{N(^tBu)SiH_2Ph\}$ (**18**). $Cp_{cent(1)}$ and $Cp_{cent(2)}$ refer to the computed Cp ring centroids for the "lower" and "upper" Cp rings, respectively, as depicted in Figure 4.1.

Zr(1)-N(1)	2.1937(18)	H(1)-Zr(1)-N(1)	129.7(6)
Zr(1)-H(1)	2.11(2)	H(2)-Zr(1)-N(1)	82.3(8)
Zr(1)-H(2)	2.14(3)	H(1)-Zr(1)-H(2)	50.4(9)
Zr(1)-B(1)	2.514(3)	$Cp_{cent(1)}$-Zr(1)-$Cp_{cent(2)}$	126.1
Zr(1)-$Cp_{cent(1)}$	2.27	Zr(1)-N(1)-Si(1)	111.52(10)
Zr(1)-$Cp_{cent(2)}$	2.25	Si(1)-N(1)-C(1)	117.37(15)
N(1)-Si(1)	1.7110(19)	C(1)-N(1)-Zr(1)	130.16(14)
B(1)-H(1)	1.20(2)		
B(1)-H(2)	1.10(3)		
B(1)-H(3)	1.13(3)		
Si(1)-H(4)	1.42(3)		
Si(1)-H(5)	1.40(3)		

As previously mentioned, **18** was found to be unstable in solution. In order to investigate this decomposition, a solution of **18** with 3 equivalents thexylborane was left for several days and subsequently dried under vacuum for 6 hours. This led to the formation of several yellow single crystals of $Cp_2Zr\{N(^tBu)Si(H)(Ph)B(Tex)H(\mu\text{-}H)\}$ (**20**) suitable for analysis by X-ray diffraction (Equation 4.4). However, no tractable ^1H NMR spectrum could be obtained from this sample and attempts to regrow the crystals on a larger scale were unsuccessful.



18 **20**

Equation 4.4

The solid state structure of **20** is shown in Figure 4.2 and selected bond distances and angles in Table 4.2. Compound **20** adopts a four-coordinate bent metallocene geometry, with the central coordination site of zirconium vacant and a five-membered Zr–N–Si–B–H metallacycle. The molecule is of C_1 symmetry with a chiral silicon, and, in the solid state, a chiral boron. Both the phenyl group of the silicon and thexyl group of the boron are equatorial, minimising steric clashes. The nitrogen is planar in geometry but distorted, with a small Zr–N–Si angle of 93.68(8)°, as to allow for formation of the five-membered ring. The Zr–N bond distance is also significantly shorter in **20** than **18** (2.0689(18) vs. 2.1937(18) Å), presumably due to the more electron poor, coordinatively unsaturated zirconium. The Zr–H bond distance of **20** (2.04(3) Å) is not significantly shorter than the Zr–H bond distances of **18** (*cf.* 2.11(2) and 2.14(3) Å), nor is the B–(μ-H) bond distance (1.17(3) *vs*. 1.20(2) and 1.10(3) Å).

The Si–B distance of **20**, at 2.112(3) Å, is slightly longer than comparable structurally characterised two-centre two-electron silylborohydride Si–B bonds, such as that of $Cp_2Ta\{(\mu\text{-}H)_2BHSi(^tBu)_2H\}$ (2.02(1) Å).[27,45–57] This may be attributed to the strain of the 5-membered ring, but may also be due to interaction of the Si–B bond with the vacant central bonding orbital of the zirconocene. Indeed, the Zr–Si distance of 2.7844(6) Å, while significantly longer than the Zr–Si distance of Berry's η^2-silanimine $Cp_2Zr\{\eta^2\text{-}N(^tBu)SiMe_2\}(PMe_3)$ (**4.6**, 2.654(1) Å), is shorter than some crystallographically characterised Zr–Si bonds of zirconocenes, such as that of $Cp_2Zr(S_2CNEt_2)(SiMe_3)$ (2.815(1) Å).[1,58] This implies there may be some interaction of the Si–B bond with the vacant central bonding orbital of the zirconocene. Indeed, assertions of an agostic Si–C bond have been made for a similar five-membered zirconocacycle with a Zr–Si distance of 2.935(2) Å.[59] This will be discussed in more detail in Section 4.2.3.

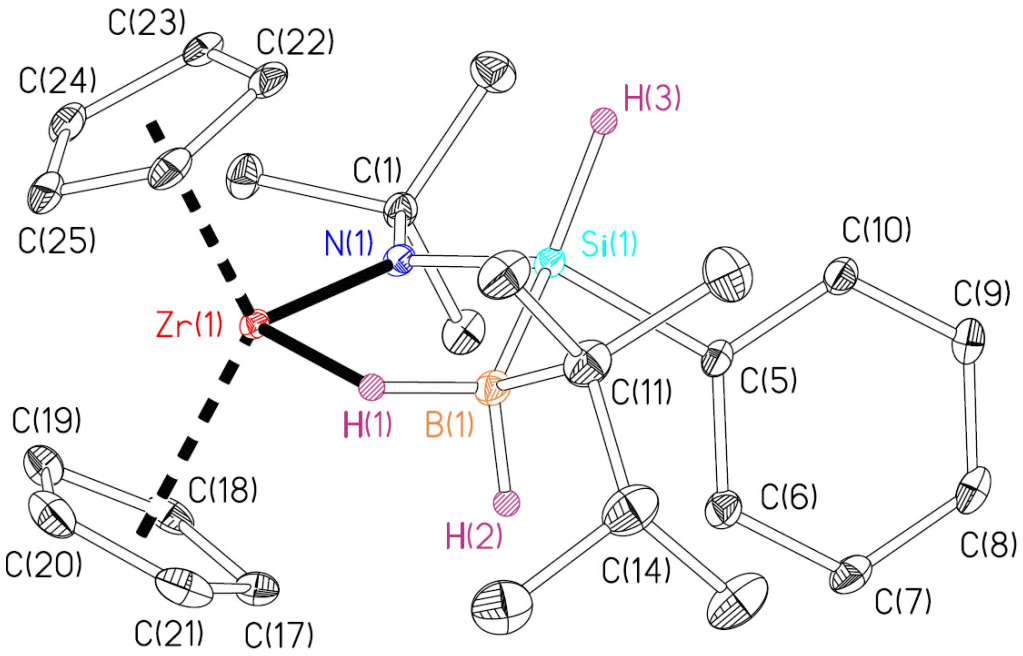


Figure 4.2: Displacement ellipsoid plot (20% probability) of $Cp_2Zr\{N(^tBu)Si(H)(Ph)B(Tex)H(\mu\text{-}H)\}$ (**20**). C–H atoms are omitted for clarity. H(1) – H(3) are drawn as spheres of an arbitrary radius.

Table 4.2: Selected bond distances (Å) and angles (°) for $Cp_2Zr\{N(^tBu)Si(H)(Ph)B(Tex)H(\mu\text{-}H)\}$ (**20**). $Cp_{cent(1)}$ and $Cp_{cent(2)}$ refer to the computed Cp ring centroids for the "lower" and "upper" Cp rings, respectively, as depicted in Figure 4.2.

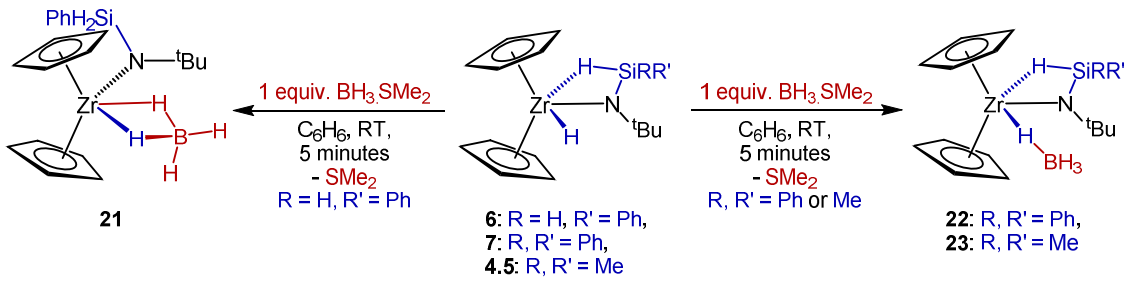
Zr(1)-N(1)	2.0689(18)	H(1)-Zr(1)-N(1)	108.9(8)
Zr(1)-H(1)	2.04(3)	Zr(1)-N(1)-Si(1)	93.68(8)
Zr(1)-Si(1)	2.7844(6)	N(1)-Si(1)-B(1)	107.52(10)
Zr(1)-$Cp_{cent(1)}$	2.25	Si(1)-B(1)-H(1)	119.2(14)
Zr(1)-$Cp_{cent(2)}$	2.25	B(1)-H(1)-Zr(1)	103.9(17)
N(1)-Si(1)	1.7352(19)	$Cp_{cent(1)}$-Zr(1)-$Cp_{cent(2)}$	126.7
Si(1)-B(1)	2.112(3)	Si(1)-N(1)-C(1)	125.28(15)
B(1)-H(1)	1.17(3)	C(1)-N(1)-Zr(1)	140.75(14)
B(1)-H(2)	1.11(3)		
Si(1)-H(3)	1.42(3)		

The reaction of **18** to **20** must proceed *via* loss of dihydrogen, given the molecular formula of **18**. Furthermore, the structure of **20** resembles that of a borane-adduct of an η^2-silanimine, which would result from insertion of the B–H bond into a Zr–Si bond,

similar to Berry's reaction of borane with a Ta–Si bond.[27] As such, the reaction may proceed in an analogous manner to that of reactions of **6** with $HCCC_6F_5$ and HCC^tBu (see Chapter 3 of this Thesis). However, given the lack of reproducibility of this reaction and difficulty in isolating of **20**, the reaction could not be investigated further. Instead, attention was turned to the reaction of hydride silylamides with $BH_3{\cdot}SMe_2$.

4.2.2 Reactions of $Cp_2Zr(H)\{N(^tBu)Si(\mu\text{-}H)HPh\}$ (6), $Cp_2Zr(H)\{N(^tBu)Si(\mu\text{-}H)Ph_2\}$ (7) and $Cp_2Zr(H)\{N(^tBu)Si(\mu\text{-}H)Me_2\}$ (4.5) with $BH_3{\cdot}SMe_2$

On the NMR tube scale, stoichiometric reaction of **6**, **7** and **4.5** with $BH_3{\cdot}SMe_2$ gave rapid, quantitative conversion to the borohydride compounds $Cp_2Zr\{(\mu\text{-}H)_2BH_2\}\{N(^tBu)SiH_2Ph\}$ (**21**), $Cp_2Zr\{(\mu\text{-}H)BH_3\}\{N(^tBu)Si(\mu\text{-}H)Ph_2\}$ (**22**), and $Cp_2Zr\{(\mu\text{-}H)BH_3\}\{N(^tBu)Si(\mu\text{-}H)Me_2\}$ (**23**), respectively, at room temperature, as judged by ^1H and ^{11}B NMR spectroscopy. On the preparative scale, benzene solutions of either **6**, **7** or **4.5** were stirred with 5 equivalents $BH_3{\cdot}SMe_2$ for 5 minutes, and **21**, **22** and **23** were isolated as pale yellow single crystals from concentrated solutions of either hexane or toluene in 41 – 47% yield (Scheme 4.2). Excess $BH_3{\cdot}SMe_2$ was used in preparative scale reactions to slow a further reaction, which will be discussed in Section 4.2.3.



Scheme 4.2: Reactions of $Cp_2Zr(H)\{N(^tBu)Si(\mu\text{-}H)RR'\}$ (R = H, R' = Ph (**6**), R, R' = Ph (**7**) and R, R' = Me (**4.5**)) with $BH_3{\cdot}SMe_2$ to give $Cp_2Zr\{(\mu\text{-}H)_2BH_2\}\{N(^tBu)SiH_2Ph\}$ (**21**, left) or $Cp_2Zr\{(\mu\text{-}H)BH_3\}\{N(^tBu)Si(\mu\text{-}H)RR'\}$ (R, R' = Ph (**22**) or Me (**23**), right), respectively.

The ^{1}H NMR spectrum of **21** (Figure 4.3, top) shows a single Cp resonance at 5.91 ppm and a single resonance at 4.75 ppm for the SiH_2 protons, indicating the compound is C_s symmetric in the solution phase on the NMR timescale. A ^{29}Si-^{1}H gradient experiment reveals a one-bond interaction between the singlet at 4.75 ppm and a ^{29}Si resonance at –58.4 ppm ($^{1}J_{SiH}$ = 189 Hz). This coupling constant and the proton shift of the SiH_2 group are similar to those of **18** (191 Hz and 5.11 ppm) and indicate a loss of the β-agostic interaction. The lack of a proton resonance attributable to a hydride in the ^{1}H NMR spectrum, combined with the apparent loss of β-agostic interaction, is consistent with κ^2-borohydride formation. Furthermore, the ^{1}H{^{11}B} NMR spectrum of **21** shows a singlet resonance of relative integral 4H at 1.04 ppm, consistent with borohydride formation. This also shows that the bridging and terminal BH environments are fluxional on the NMR timescale. Attempts to decoalesce the bridging and terminal BH environments by cooling a toluene-d_8 solution of **21** to –88 °C were unsuccessful, highlighting the facile exchange of environments. Reaction of **6-*d*$_3$** with BD_3·THF to give **21-*d*$_6$** confirmed the assignments of the SiH_2 and BH_4 environments.

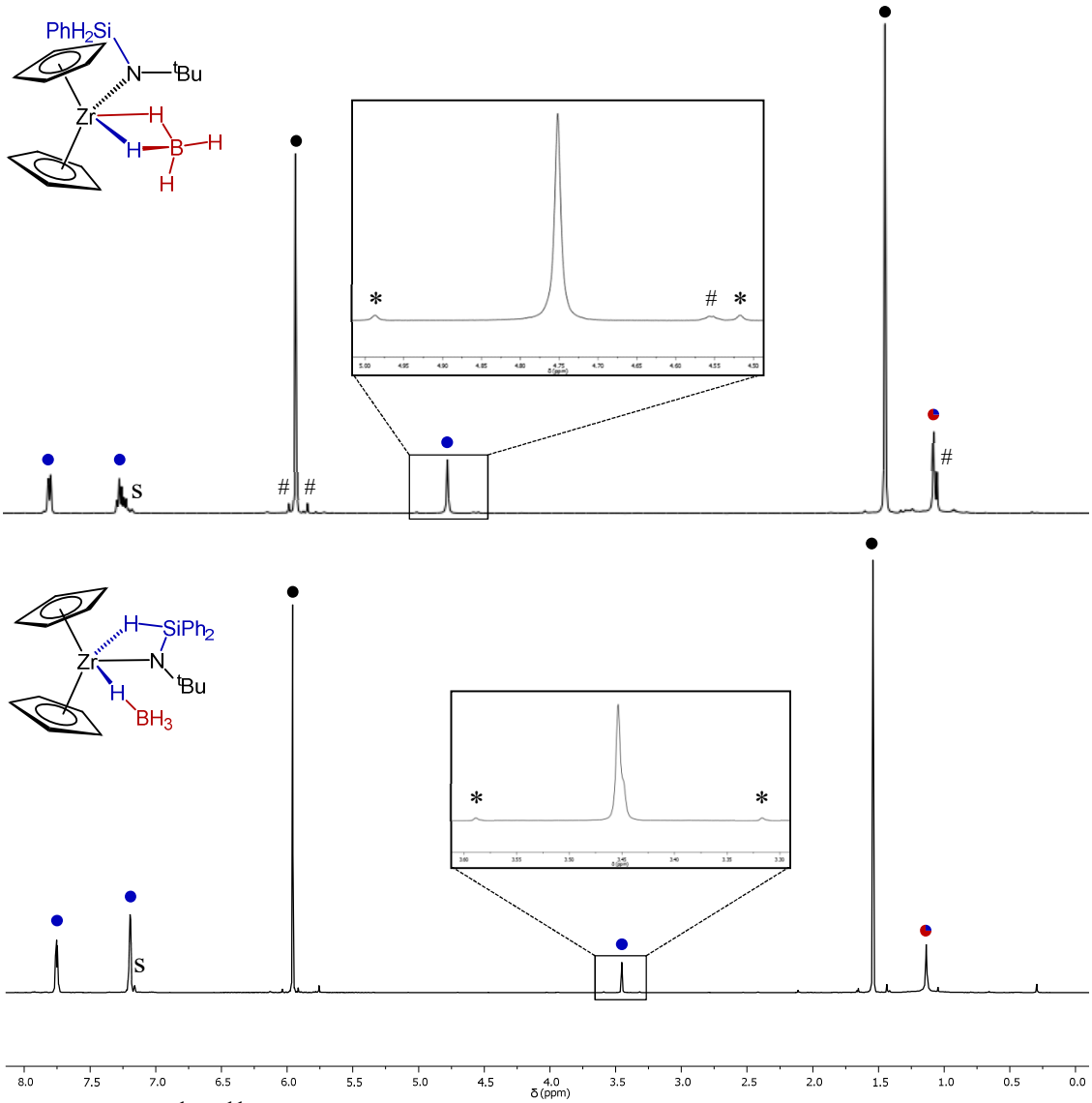


Figure 4.3: $^{1}H\{^{11}B\}$ NMR spectra (C_6D_6, 400.1 MHz, 298 K) of $Cp_2Zr\{(\mu\text{-}H)_2BH_2\}\{N(^tBu)SiH_2Ph\}$ (**21**, top) and $Cp_2Zr\{(\mu\text{-}H)BH_3\}\{N(^tBu)Si(\mu\text{-}H)Ph_2\}$ (**22**, bottom) with the SiH_2 resonances and their ^{29}Si satellites (*) enlarged. # indicates a thermal decomposition product of **21**.

Similar to the NMR spectra of **21**, the ^{1}H NMR spectra of **22** and **23** reveal no hydride resonances and the $^{1}H\{^{11}B\}$ NMR spectra show singlet resonances at 1.14 and 1.07 ppm, respectively, each of relative integral 4H. The ^{11}B NMR spectra also reveal resonances at –11.5 and –15.5 ppm, respectively, with a $^{1}J_{BH}$ coupling constant of 86 Hz for **23**, consistent with borohydride formation.[33] In contrast to **21**, the SiH proton resonances of **22** and **23** appear at much lower chemical shifts (3.45 and 1.53 ppm, respectively, *vs.* 4.75 ppm). Furthermore, for **22** the one-bond interaction, $^{1}J_{SiH}$, between the singlet at

3.45 ppm and the ^{29}Si resonance at –57.6 ppm was found to be just 136 Hz (*cf.* 189 Hz for **14**) and for **23** $^{1}J_{SiH}$ was found to be 115 Hz.

These coupling constants and SiH proton chemical shifts are relatively close to those of the respective hydrides of **22** and **23** (**7** and **4.5**), implying that the β-agostic interaction is maintained in both compounds and the borohydride is κ^1-bound rather than κ^2-bound.[42] Indeed, as was done for the acetylide $Cp_2Zr(CC^tBu)\{N(^tBu)Si(\mu\text{-}H)Me_2\}$ (**14**), the strength of the agostic interaction in **23** can be compared to a number of $Cp_2Zr(X)\{N(^tBu)Si(\mu\text{-}H)Me_2\}$ compounds (Table 4.3). As can be seen, the β-agostic interaction in **23** is very close in strength to that of **4.5**, which may indicate weak binding of the borane. The IR spectra of both **22** and **23** are also consistent with κ^1-bound borohydrides. Compound **23** exhibits bands at 2381 and 2347 cm^{-1} for $\nu(B\text{–}H_t)$ modes, a band at 2038 cm^{-1} for $\nu(B\text{–}H_b)$ and a band at 1738 cm^{-1} for $\nu(Zr\text{–}H_b)$.[43]

Table 4.3: Spectroscopic data for $Cp_2Zr(X)\{N(^tBu)Si(\mu\text{-}H)Me_2\}$ (X = H (**4.5**), I, Br, Cl, F, CC^tBu (**14**) and $(\mu\text{-}H)BH_3$ (**23**)).[42] Chemical shifts are shown in ppm, $^{1}J_{SiH}$ couplings in Hz and IR stretches in cm^{-1}.

Compound	^{1}H NMR	^{29}Si NMR		IR
	δ_{SiH}	δ_{Si}	$^{1}J_{SiH}$	ν(Si–H)
$Cp_2Zr(H)\{N(^tBu)Si(\mu\text{-}H)Me_2\}$ (**4.5**)	1.21	–73.4	113	1912
$Cp_2Zr(I)\{N(^tBu)Si(\mu\text{-}H)Me_2\}$	1.69	–62.0	119	1960
$Cp_2Zr(Br)\{N(^tBu)Si(\mu\text{-}H)Me_2\}$	2.24	–56.1	123	1975
$Cp_2Zr(Cl)\{N(^tBu)Si(\mu\text{-}H)Me_2\}$	2.58	–52.3	127	1981
$Cp_2Zr(F)\{N(^tBu)Si(\mu\text{-}H)Me_2\}$	2.84	–42.0	135	1998
$Cp_2Zr(CC^tBu)\{N(^tBu)Si(\mu\text{-}H)Me_2\}$ (**14**)	2.88	–59.2	132	1995
$Cp_2Zr\{(\mu\text{-}H)BH_3\}\{N(^tBu)Si(\mu\text{-}H)Me_2\}$ (**23**)	1.53	–58.4	115	1893

Diffraction-quality crystals of **21**, **22** and **23** were grown from saturated solutions of either hexane or toluene at 4 or –30 °C, and confirm the connectivities shown in Scheme 4.2. The solid state structures of **21**, **22** and **23** are shown in Figure 4.4 and selected bond distances and angles in Table 4.4. The structural parameters of **21** are largely similar to

those of **18**, such as the Zr–H(5) distance (2.96(4) Å) and Zr–N–Si angle (110.92(12)°), which indicate a lack of β-agostic interaction. In contrast to **18**, the Zr(1)–H(1)–B(1)–H(2) ring is planar in **21**, which is to be expected as there are no steric clashes between the Cp rings and borane. This gives rise to a longer Zr–B distance (2.614(4) *vs.* 2.514(3) Å). This Zr–B distance is also longer than in other zirconocene κ^2-borohydrides, such as $Cp_2Zr(H)\{(\mu\text{-}H)_2BHMe\}$ (2.558(4) Å) and $\{Me_4C_2(C_5H_4)_2\}Zr\{(\mu\text{-}H)_2BH_2\}_2$ (2.594(2) and 2.597(2) Å).[35,60] The Zr–(μ-H) bond distances **21** are similar to those of these κ^2-borohydrides and **18**.

Consistent with NMR and IR spectroscopic data, both **22** and **23** contain a β-Si–H···Zr agostic interaction and a κ^1-borohydride moiety. The nitrogen occupies the central coordination site of the zirconocene, with H(1), H(2), B(1), N(1), C(1), Si(1) and H(5) lying in the equatorial plane. The small Zr–N–Si angles of **22** and **23** (97.37(6) and 96.00(10) °, respectively) are similar to those of the hydrides **7** and **4.5** (97.77(8) and 95.1(2)°, respectively) and clearly indicate bending of the Si–H bond towards the metal.[42] Furthermore, the Zr–H(5) bond distance of **22** at 2.15(2) Å is identical, within error, to the equivalent Zr–(μ-H) bond distance of **7** (2.17(2) Å), and within the expected range for bridging zirconocene hydrides.[13,42,61,62] Similarly, the Zr–H(5) bond distance of **23** (2.137 Å) is similar to the *ca*. 2.1 Å Zr–(μ-H) bond distance of **4.5**, which was calculated from an idealised Si–H bond. The Zr–Si distances of 2.9075(4) and 2.8703(9) Å for **22** and **23** are also similar to those of **7** and **4.5**.

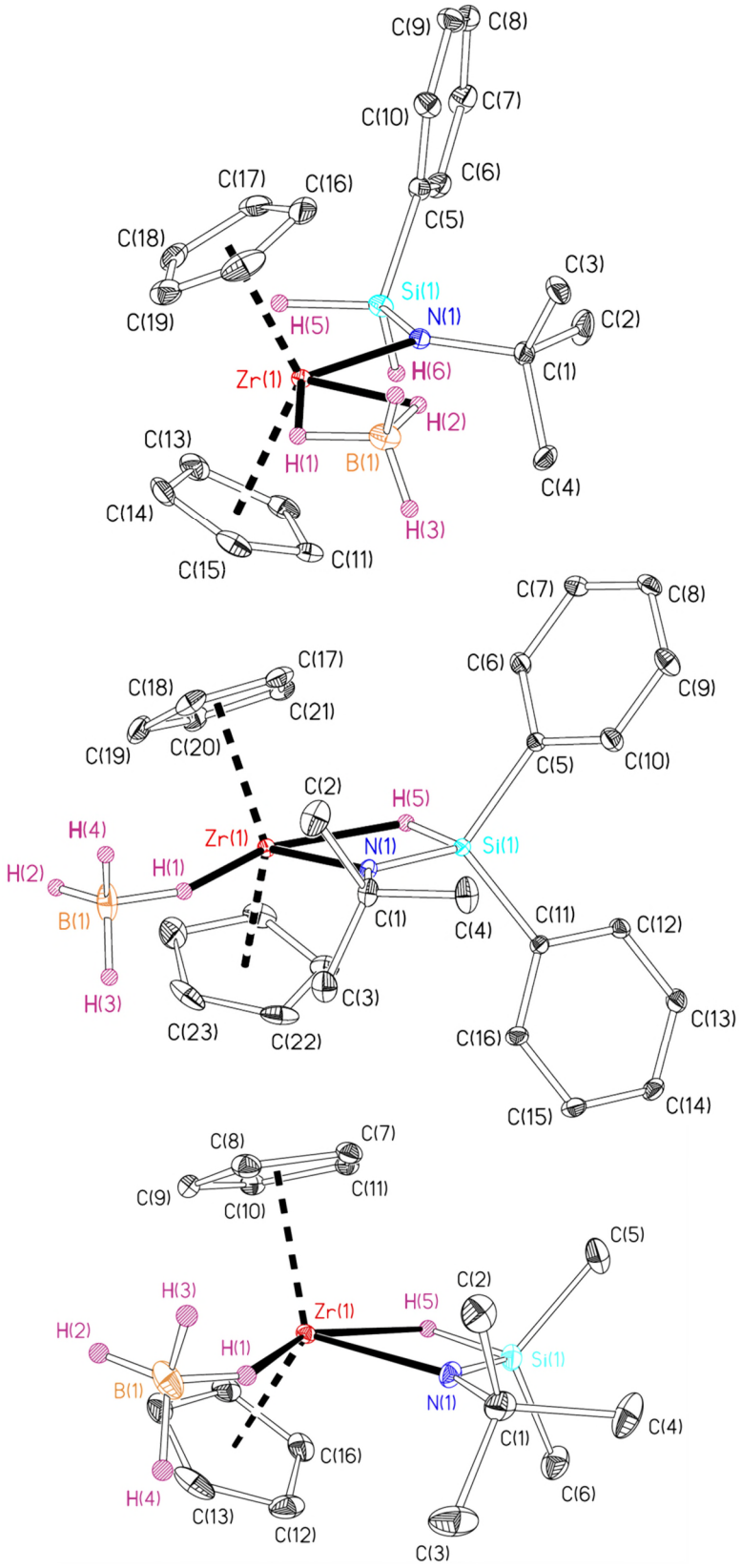


Figure 4.4: Displacement ellipsoid plots (20% probability) of $Cp_2Zr\{(\mu\text{-}H)_2BH_2\}\{N(^tBu)SiH_2Ph\}$ (**21**, top), $Cp_2Zr\{(\mu\text{-}H)BH_3\}\{N(^tBu)Si(\mu\text{-}H)Ph_2\}$ (**22**, middle) and $Cp_2Zr\{(\mu\text{-}H)BH_3\}\{N(^tBu)Si(\mu\text{-}H)Me_2\}$ (**23**, bottom). C–H atoms are omitted for clarity. H(1) – H(6) are drawn as spheres of an arbitrary radius.

Table 4.4: Selected bond distances (Å) and angles (°) for $Cp_2Zr\{(\mu\text{-}H)_2BH_2\}\{N(^tBu)SiH_2Ph\}$ (**21**), $Cp_2Zr\{(\mu\text{-}H)BH_3\}\{N(^tBu)Si(\mu\text{-}H)Ph_2\}$ (**22**) and $Cp_2Zr\{(\mu\text{-}H)BH_3\}\{N(^tBu)Si(\mu\text{-}H)Me_2\}$ (**23**). $Cp_{cent(1)}$ and $Cp_{cent(2)}$ refer to the computed Cp ring centroids for the "lower" and "upper" Cp rings, respectively, of **21** and the "upper" and "lower" Cp rings, respectively, of **22** and **23** as depicted in Figure 4.4.

Parameter	21	22	23
Zr(1)-N(1)	2.178(2)	2.1624(12)	2.153(2)
Zr(1)-H(1)	2.12(4)	2.00(2)	2.03(3)
Zr(1)-H(2)	2.06(4)	3.31(3)	3.23(3)
Zr(1)-H(5)	2.96(4)	2.15(2)	2.137
$Zr(1)\text{-}Cp_{cent(1)}$	2.24	2.23	2.24
$Zr(1)\text{-}Cp_{cent(2)}$	2.24	2.22	2.22
N(1)-Si(1)	1.709(2)	1.6872(13)	1.689(2)
B(1)-H(1)	1.25(5)	1.21(2)	1.25(3)
B(1)-H(2)	1.19(4)	1.107(10)	1.16(4)
B(1)-H(3)	1.07(6)	1.116(10)	1.13(4)
B(1)-H(4)	1.11(5)	1.119(10)	1.16(4)
Si(1)-H(5)	1.43(4)	1.51(2)	1.549
Si(1)-H(6)	1.38(4)	-	-
H(1)-Zr(1)-H(5)	187.5(14)	146.1(9)	144.9
H(1)-Zr(1)-N(1)	131.3(12)	80.7(7)	77.1(7)
H(2)-Zr(1)-N(1)	77.0(12)	-	-
H(1)-Zr(1)-H(2)	54.3(17)	-	-
H(5)-Zr(1)-N(1)	56.1(8)	65.5(5)	67.9
$Cp_{cent(1)}\text{-}Zr(1)\text{-}Cp_{cent(2)}$	128.5	126.2	127.8
Zr(1)-N(1)-Si(1)	110.92(12)	97.37(6)	96.00(10)
Si(1)-N(1)-C(1)	118.7(2)	125.66(11)	126.15(17)
C(1)-N(1)-Zr(1)	129.33(19)	136.93(10)	137.59(17)
N(1)-Si(1)-H(5)	105.8(16)	93.4(8)	95.1
Zr(1)-H(1)-B(1)	99(3)	150.4(17)	138.80(18)
Zr(1)-H(2)-B(1)	104(3)	-	-

The Zr–H(1) bond distances of **22** and **23**, at 2.00(2) and 2.03(3) Å, are similar to those of **18** and **22**, as well as the zirconocene κ^1-organoborohydride

$Cp_2Zr\{(\mu\text{-}H)B(C_4H_8)CH_2Ph\}\{(\mu\text{-}H)_2BC_4H_8\}$ (1.95(3) Å), and significantly longer than that of **7** (1.69(3) Å).[26] The Zr–H(2) distances of 3.31(3) and 3.23(3) Å clearly indicate a lack of bonding interaction. This, along with the large Zr–H(1)–B angles of 150.4(17) and 138.80(18)° (*cf.* 99(3) and 94.6(12)° for **21** and **18**), confirm the borohydride is κ^1-bound. It can also be observed that the B–H(1) bond distance of **22**, at 1.21(2) Å, is significantly longer than the terminal B–H bond distances, the longest of which is 1.119(10) Å, indicating the bridging hydrogen maintains some zirconium hydride character.

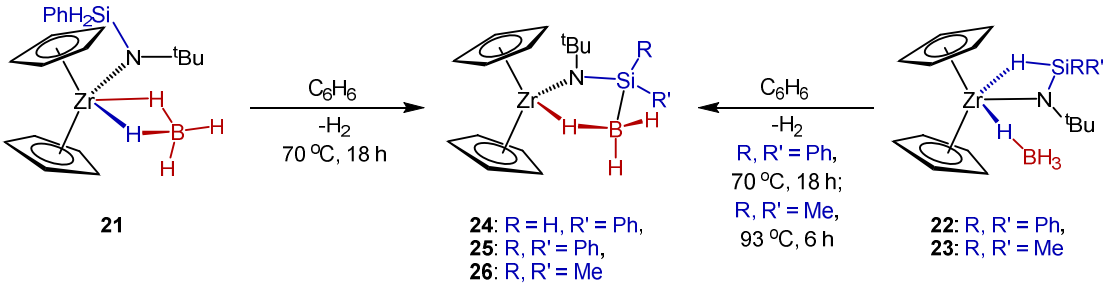
κ^1-Borohydrides are less common than κ^2- and κ^3-borohydrides. Indeed, the Cambridge Crystallographic Database contains no structurally authenticated Group 4 κ^1-borohydrides, only κ^1-organoborohydrides, such as $Cp_2Zr\{(\mu\text{-}H)B(C_4H_8)CH_2Ph\}\{(\mu\text{-}H)_2BC_4H_8\}$.[26] Notably, this borohydride quantitatively dissociates in solution at room temperature to give $Cp_2Zr(H)\{(\mu\text{-}H)_2BC_4H_8\}$ and $B(C_4H_8)CH_2Ph$, and in the solid state $B(C_4H_8)CH_2Ph$ could be removed under vacuum. Only upon cooling to –60 °C was $Cp_2Zr\{(\mu\text{-}H)B(C_4H_8)CH_2Ph\}\{(\mu\text{-}H)_2BC_4H_8\}$ observed. This is in contrast to **22** and **23**, which are stable to vacuum.

By DFT, Δ_rG(**6** + $BH_3{\cdot}SMe_2$ → **21** + SMe_2) = –3.6 kcal mol^{-1} and compound **21** was calculated to be 0.3 kcal mol^{-1} more stable than the κ^1-borohydride conformation of **21** (**21_alt**), with an energy barrier between **21** and **21_alt** of 1.3 kcal mol^{-1}. Though these energy differences are minimal and there are errors associated with these calculations, it is clear from experimental data that **21** has a thermodynamic preference to contain no β-agostic interaction. In contrast, compounds **22** and **23** maintain β-agostic interactions. The origin of this preference may be steric, with breaking of the β-agostic interaction and the associated free rotation about the Zr–N and N–Si bonds bringing about steric clashes

that the gain in free energy from the increase in entropy cannot overcome. This is unlikely given the steric profiles of the silyl moieties of **21** (SiH_2Ph) and **23** ($SiHMe_2$). Alternatively, it can be said that the increased σ-donation of the second phenyl group in **22** in place of the hydride in **21**, or two methyl groups in **23**, will act to increase the polarity of the Si–H bond, thereby raising the energy of the σ orbital and lowering the energy of the σ* orbital, which increases the negative hyperconjugation from the Zr–N bond and therefore the strength and stability of the β-agostic interaction.[63] Previously, substitution of the silyl moiety has been noted to increase the strength of β-agostic interactions.[64] This stronger β-agostic interaction could overcome the strength of the second bridging B–H–Zr bond.

4.2.3 Thermal decomposition of $Cp_2Zr\{(\mu\text{-}H)_2BH_2\}\{N(^tBu)SiH_2Ph\}$ (21), $Cp_2Zr\{(\mu\text{-}H)BH_3\}\{N(^tBu)Si(\mu\text{-}H)Ph_2\}$ (22) and $Cp_2Zr\{(\mu\text{-}H)BH_3\}\{N(^tBu)Si(\mu\text{-}H)Me_2\}$ (23)

As with **18**, compounds **21**, **22** and **23** were thermally unstable in solution. Quantitative formation of the zirconacycles $Cp_2Zr\{N(^tBu)Si(H)(Ph)BH_2(\mu\text{-}H)\}$ (**24**), $Cp_2Zr\{N(^tBu)Si(Ph)_2BH_2(\mu\text{-}H)\}$ (**25**) and $Cp_2Zr\{N(^tBu)Si(Me)_2BH_2(\mu\text{-}H)\}$ (**26**), with concurrent formation of dihydrogen, was observed on following the decomposition of **21**, **22** and **23**, respectively, by ^1H and ^{11}B NMR spectroscopy. These reactions occurred over the course of several days at room temperature and 3 h at 80 °C for **21** and **22**. In contrast, **23** was seen to be stable for multiple weeks at room temperature and complete decomposition occurred over 18 hours at 80 °C. On the preparative scale, benzene solutions of **21** and **22** were heated to 70 °C for 18 h, while a benzene solution of **23** was heated to 93 °C for 6 h. Compounds **24**, **25** and **26** were isolated as yellow or orange crystals or powders in 40 – 49% yields (Scheme 4.3).



21 **24**: R = H, R' = Ph, **25**: R, R' = Ph, **26**: R, R' = Me **22**: R, R' = Ph, **23**: R, R' = Me

Scheme 4.3: Thermal decomposition reactions of $Cp_2Zr\{(\mu\text{-}H)_2BH_2\}\{N(^tBu)SiH_2Ph\}$ (**21**, left), $Cp_2Zr\{(\mu\text{-}H)BH_3\}\{N(^tBu)Si(\mu\text{-}H)Ph_2\}$ (**22**, right) and $Cp_2Zr\{(\mu\text{-}H)BH_3\}\{N(^tBu)Si(\mu\text{-}H)Me_2\}$ (**23**, right) to give $Cp_2Zr\{N(^tBu)Si(H)(Ph)BH_2(\mu\text{-}H)\}$ (**24**), $Cp_2Zr\{N(^tBu)Si(Ph)_2BH_2(\mu\text{-}H)\}$ (**25**) and $Cp_2Zr\{N(^tBu)Si(Me)_2BH_2(\mu\text{-}H)\}$ (**26**), respectively.

The $^1H\{^{11}B\}$ NMR spectrum (Figure 4.5) of **24** shows two sharp, singlet resonances at 5.97 and 5.82 ppm corresponding to two chemically inequivalent Cp groups. This indicates a breakdown in symmetry of the zirconocene complex from C_s symmetric in compound **21** to C_1 symmetric for **24** in solution, consistent with the chiral silicon of the proposed zirconacycle. This phenomenon was also observed in the ^1H NMR spectrum of the zirconacycles $Cp_2Zr\{N(^tBu)Si(H)(Ph)C(C_6F_5)CH\}$ (**12**) and $Cp_2Zr\{N(^tBu)Si(H)(Ph)C(C_6H_5)N\}$ (**17**). The protons of the BH_3 moiety appear at 1.20 ppm as a time-averaged doublet of relative integral 3H, showing the terminal and bridging BH environments to be exchanging on the NMR timescale at room temperature. The SiH resonance of **24** is observed at 4.55 ppm as a binomial quartet and a ^1H-^1H COSY experiment gave a $^3J_{HH}$ coupling constant of 2.7 Hz between this SiH resonance and the BH_3 resonance, consistent with the formation of a Si–B bond. The absence of the resonances at 4.55 and 1.20 ppm in the $^1H\{^{11}B\}$ NMR spectrum of **24-*d*$_4$** confirmed the assignments of the SiH and BH proton resonances. The ^{11}B NMR spectrum reveals a quartet resonance at –6.2 ppm ($^1J_{BH}$ = 86 Hz), consistent with a four-coordinate boron environment with three hydrides.

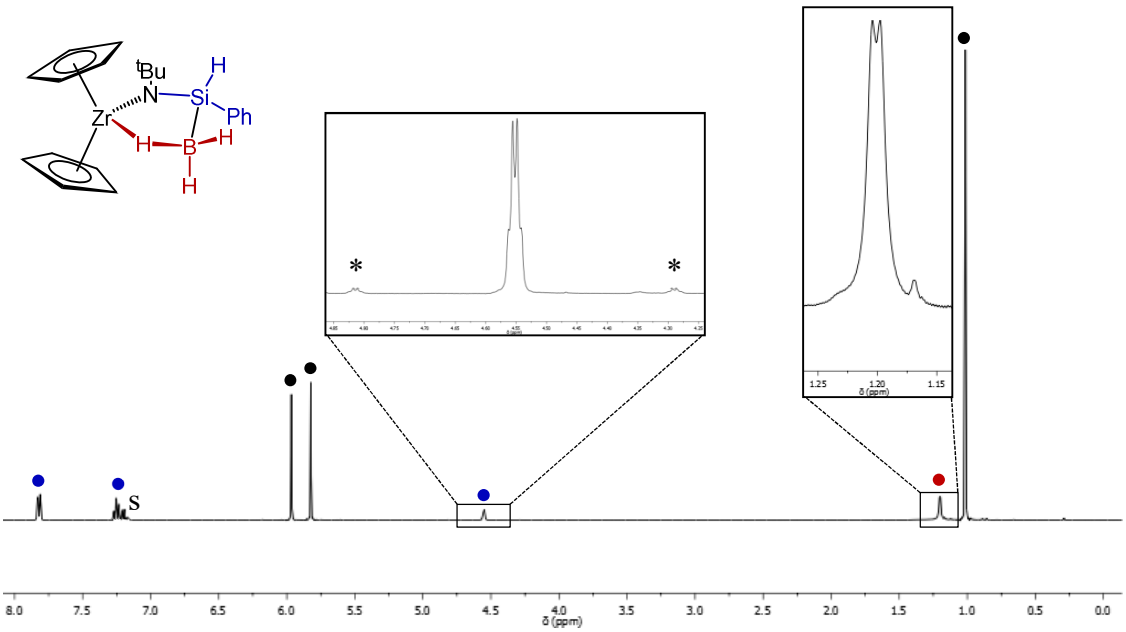


Figure 4.5: $^{1}H\{^{11}B\}$ NMR spectrum (C_6D_6, 400.1 MHz, 298 K) of $Cp_2Zr\{N(^tBu)Si(H)(Ph)BH_2(\mu\text{-}H)\}$ (**24**) with the SiH_2, and ^{29}Si satellites (*), and BH_3 resonances enlarged.

The ^{1}H NMR spectra of **25** and **26** reveal Cp resonances at 5.92 and 5.80 ppm, respectively, indicating C_s symmetry. In both spectra no resonance attributable to an SiH proton environment could be observed, and for **26** the methyl resonances (6H) of the silyl moiety appeared as a singlet at 0.34 ppm, consistent with the absence of an Si–H bond. The $^{1}H\{^{11}B\}$ NMR spectra revealed time-averaged singlet resonances of relative integral 3H at 1.43 and 1.20 ppm for **25** and **26**, respectively, consistent with the proposed structures.

The solid state structures of **24**, **25** and **26** are shown in Figure 4.6 and selected bond distances and angles in Table 4.5. As with **20**, compounds **24**, **25** and **26** adopt four-coordinate bent metallocene geometry, with the central coordination site of zirconium vacant and with a five-membered Zr–N–Si–B–H metallacycle. Similar to **20**, while the nitrogen atoms of **24** – **26** are planar in geometry with small Zr–N–Si angles (94.06(4) – 93.21(10)°) such that the silicon is bent towards the metal and borane, allowing for formation of the five-membered ring. The Zr–H bond distances (2.02(2) – 2.12(4) Å) are

also similar to those observed previously in this Chapter. Furthermore, as with **20**, the Zr–N bond distances of **24** – **26** are significantly shorter than those of **21** – **23** (2.0633(10) – 2.0856(12) *vs*. 2.1624(12) – 2.178(2) Å), owing, presumably, to the electron deficient zirconium.

As discussed for **18**, the small Zr–N bond distances and small Zr–N–Si bond angles lead to short Zr–Si distances (2.7886(3) and 2.7972(4) Å for **24** and **25**, respectively) that are shorter than some previously characterised Zr–Si bonds.[1,58] This indicates an agostic interaction of the Si–B bond is likely.[59] The Si–B bond distances of **24** – **26** are significantly shorter than that of **20** (2.0836(15) – 2.0951(17) *vs*. 2.112(3) Å), perhaps owing to the lack of σ-donating thexyl moiety rendering the boranes more electron deficient in **24 – 26**. These Si–B bond distances are, however, significantly longer than that of $Cp_2Ta\{(\mu\text{-}H)_2BHSi(^tBu)_2H\}$ (2.02(1) Å) and other silylborohydride Si–B bonds, which may be due to interaction with zirconium.[27,45–57]

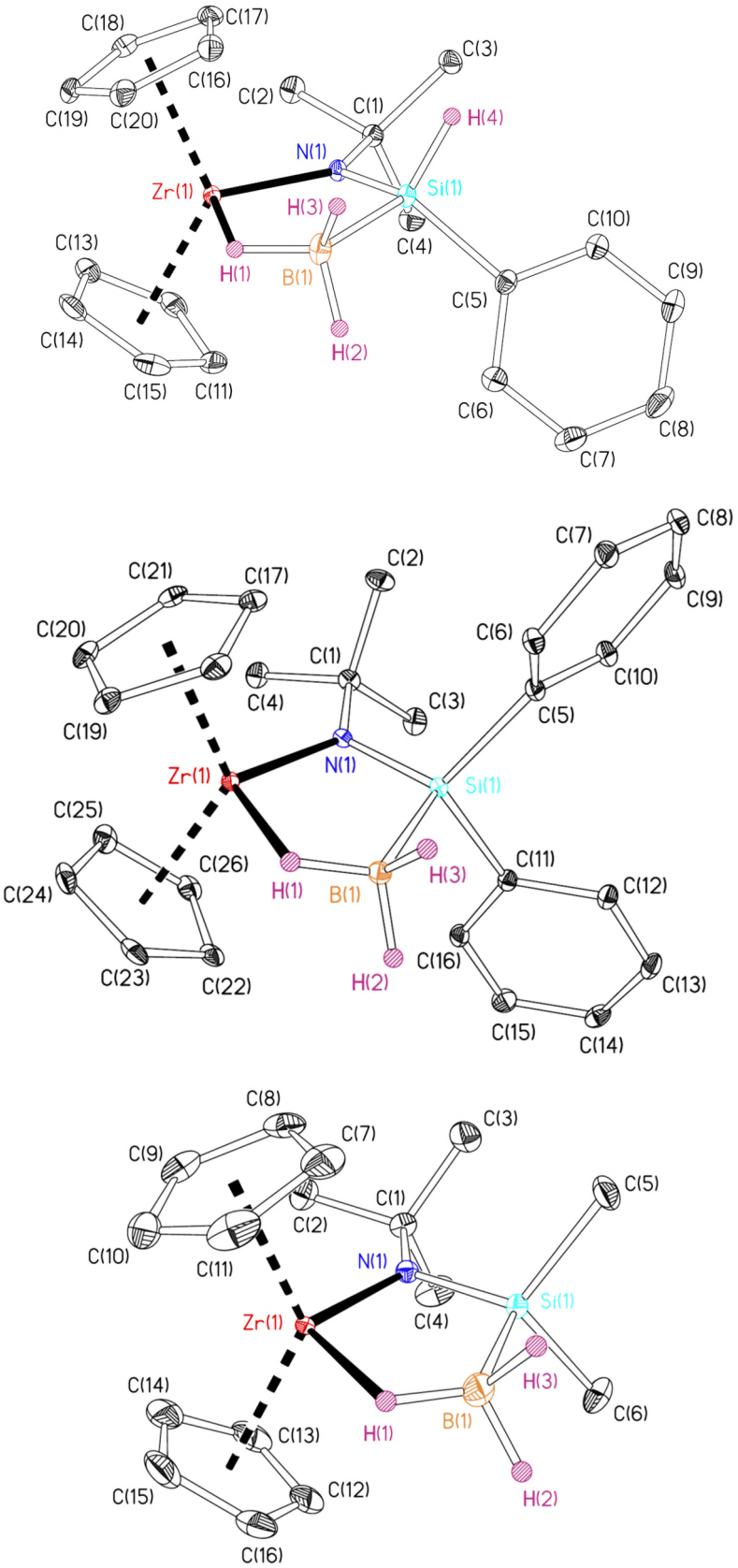


Figure 4.6: Displacement ellipsoid plots (20% probability) of $Cp_2Zr\{N(^tBu)Si(H)(Ph)BH_2(\mu\text{-}H)\}$ (**24**, top), $Cp_2Zr\{N(^tBu)Si(Ph)_2BH_2(\mu\text{-}H)\}$ (**25**, middle) and $Cp_2Zr\{N(^tBu)Si(Me)_2BH_2(\mu\text{-}H)\}$ (**26**, bottom). C–H atoms are omitted for clarity. H(1) – H(4) are drawn as spheres of an arbitrary radius.

Table 4.5: Selected bond distances (Å) and angles (°) for $Cp_2Zr\{N(^tBu)Si(H)(Ph)BH_2(\mu\text{-}H)\}$ (**24**), $Cp_2Zr\{N(^tBu)Si(Ph)_2BH_2(\mu\text{-}H)\}$ (**25**) and $Cp_2Zr\{N(^tBu)Si(Me)_2BH_2(\mu\text{-}H)\}$ (**26**). $Cp_{cent(1)}$ and $Cp_{cent(2)}$ refer to the computed Cp ring centroids for the "lower" and "upper" Cp rings, respectively, of **24** and the "upper" and "lower" Cp rings, respectively, of **25** and **26** as depicted in Figure 4.6.

Parameter	24	25	26
Zr(1)-N(1)	2.0633(10)	2.0856(12)	2.075(2)
Zr(1)-H(1)	2.040(17)	2.02(2)	2.12(4)
Zr(1)-Si(1)	2.7886(3)	2.7972(4)	2.774(1)
$Zr(1)\text{-}Cp_{cent(1)}$	2.24	2.24	2.24
$Zr(1)\text{-}Cp_{cent(2)}$	2.24	2.25	2.25
N(1)-Si(1)	1.7354(10)	1.7328(13)	1.728(2)
Si(1)-B(1)	2.0836(15)	2.0951(17)	2.089(4)
B(1)-H(1)	1.214(18)	1.18(2)	1.20(4)
B(1)-H(2)	1.161(18)	1.13(2)	1.103(5)
B(1)-H(3)	1.07(2)	1.07(3)	1.103(5)
Si(1)-H(4)	1.362(16)	–	–
H(1)-Zr(1)-N(1)	111.2(5)	110.2(6)	112.7(12)
Zr(1)-N(1)-Si(1)	94.06(4)	93.74(5)	93.21(10)
N(1)-Si(1)-B(1)	108.87(5)	108.67(6)	109.03(14)
Si(1)-B(1)-H(1)	123.8(8)	122.5(10)	129(2)
B(1)-H(1)-Zr(1)	101.3(11)	102.7(13)	95(2)
Si(1)-N(1)-C(1)	125.78(8)	128.18(10)	127.1(2)
C(1)-N(1)-Zr(1)	139.93(8)	137.36(1)	139.7(2)
$Cp_{cent(1)}\text{-}Zr(1)\text{-}Cp_{cent(2)}$	128.3	126.8	130.3

To investigate the potential agostic $Si_\beta\text{–}B_\gamma\cdots Zr$ interaction and elongation of the Si–B bond further, single point, gas-phase DFT calculations (B3PW91/Def2-TZVP) were carried out on $Cp_2Zr\{N(Me)Si(H)(Ph)BH_2(\mu\text{-}H)\}$, as a model of **24**, using the optimised geometry of **24** (B3PW91/Def2-TZVP/d3-bj) but with ^{t}Bu replaces by Me. The molecular orbitals were computed and wavefunctions analysed using the natural bond orbital (NBO) method.[65,66] The Wiberg and Mayer bond indices[67] of relevant atom pairs (number as in

the solid state structure of **24**, Figure 4.6) of $Cp_2Zr\{N(Me)Si(H)(Ph)BH_2(\mu\text{-}H)\}$ are shown in Table 4.6).

Table 4.6: DFT (B3PW91/Def2-TZVP) computed interatomic distances (Å) and Mayer bond indices for the model compound $Cp_2Zr\{N(Me)Si(H)(Ph)BH_2(\mu\text{-}H)\}$.

Parameter	Dist. (Å)	Wiberg bond index	Mayer bond index[67]
Zr(1)-N(1)	2.047	1.086	1.086
Zr(1)-H(1)	2.005	0.328	0.328
Zr(1)-B(1)	2.530	0.539	0.539
Zr(1)-Si(1)	2.752	0.323	0.323
N(1)-Si(1)	1.761	1.086	1.086
Si(1)-B(1)	2.073	0.772	0.772
Si(1)-H(4)	1.502	0.907	0.907
B(1)-H(1)	1.268	0.603	0.603
B(1)-H(2)	1.217	0.917	0.917
B(1)-H(3)	1.218	0.911	0.911

The Wiberg and Mayer bond indices for the Si(1)-B(1) and B(1)-H(1) (agostic B–H bond) are significantly less than one, indicating delocalisation of the bonds. Concurrently, significant, non-zero bond indices are found for Zr(1)-H(1) (Zr···H), Zr(1)-B(1) (Zr···B) and Zr(1)-Si(1) (Zr···Si), indicating agostic interactions of both the B–H and Si–B bonds. Meanwhile, the bond indices of the N–Si, Si–H and terminal B–H bonds are normal. The HOMO, LUMO and LUMO+1, shown in the Appendix, Figure A10, give further insight into the agostic interactions and it can be noted that metal-ligand interaction can often be more easily traced through antibonding molecular orbitals, rather than the respective bonding molecular orbital. The HOMO, as expected, is comprised predominantly of the nitrogen-based lone pair. Most notably, the LUMO is antibonding between Zr and Si–B–

H and the LUMO+1 has Zr–H some σ* character, providing further evidence of Si_β–B_γ agostic interaction, as well as B–H agostic interaction.

Given the observations made from bond index and molecular orbital computations, NBO analysis was carried out to probe the nature of the agostic interaction between the Si_β–B_γ bond and Zr, and origin of the Si–B bond elongation. Previously, similar Si_β–C_γ···M interactions and, in particular, the lengthening of these Si–C bonds have been attributed to either negative hyperconjugation of the σ(M–E_α) bond into σ*(Si_β–C_γ), due to a large ionic component of the M–E_α bond (E = C or N),[68–70] or donation from σ(Si_β–C_γ) to an empty valence orbital of the metal centre.[71–74] First, it can be noted that the occupancy of the Zr–N NBO is computed to be 1.920 and >95% of the natural localised molecular orbital (NLMO) relating to the Zr–N bond is composed of the Zr–N NBO, indicating very little negative hyperconjugation. Second order perturbation analysis finds the energy of negative hyperconjugation from the σ(Zr–N_α) bond into σ*(Si_β–B_γ) to be 1.22 kcal mol^{-1}, a value much smaller than that of the interaction of the Si–B bond with Zr (*vide infra*), further showing that there is no significant negative hyperconjugation.

The occupancies of the Si–B and agostic B–H NBOs are 1.734 and 1.748, respectively, with the occupancies depleted by donation to Zr. For comparison the occupancies of the two terminal B–H NBOs are 1.955 and 1.962. Consistent with this, the NLMOs relating to the Si_β–B_γ···Zr and B–H···Zr have 84.8% Si–B NBO and 12.9% Zr, and 86.8% B–H NBO and 11.9% Zr contributions, respectively, showing the agostic interactions to be ligand-centred as expected (see Appendix, Figure A11). Second order perturbation analysis shows the energy of these interactions to be 88.3 and 85.2 kcal mol^{-1}, respectively, comprised of donation of each bonding orbital to two empty valence orbitals of Zr. The minor (17.0 kcal mol^{-1}) component of the B–H···Zr interaction donates to the same vacant orbital of Zr as the major (72.3 kcal mol^{-1}) component of the Si_β–B_γ···Zr

interaction. These analyses have confirmed a $Si_{\beta}–B_{\gamma}\cdots Zr$ interaction is present and that the lengthening of the Si–B bond, with respect to other silylborohydride Si–B bonds, is due not to negative hyperconjugation, but donation from the Si–B bond to Zr.

As is clear from the structures of **24** – **26** the compounds represent borane adducts of η^2-silanimines resulting from insertion of the borane into a Zr–Si bond. There has been one example of such a reaction, as discussed in Section 4.1. Berry and co-workers observed the insertion of the B–H bond of $L{\cdot}BH_3$ (L = NEt_3, *N*-methylmorpholine) into the Ta–Si bond of $Cp_2Ta(PMe_3)\{Si(^tBu)_2H\}$ to form the κ^2-silylborohydride complex $Cp_2Ta\{(\mu\text{-}H)_2BHSi(^tBu)_2H\}$.[27] Si–B bonds are more typically synthesised by addition of silyllithium reagents to haloboranes, pinacol borane (HBPin) or BPin derivatives.[75–78] Hartwig and co-workers reported the iridium-catalysed Si–B bond formation using dipinacolborane (B_2Pin_2) and a range of tertiary silanes.[79] However, transition-metal mediated Si–B bond formation remains a relatively uncommon reaction.

Si–B bonds are of interest due to their application in the functionalisation of a wide variety of unsaturated organic molecules, as well as strained ring systems and carbenoids, as highlighted in a review by Oestreich and co-workers.[78] These reactions are usually transition-metal catalysed, with catalysis proceeding *via* such pathways as oxidative addition to the metal centre or transmetallation. No further reactions of compounds **24** – **26** were attempted. Given the uncommon nature of the Si–B bond forming reactions shown in Scheme 4.3, kinetic studies were undertaken to probe the mechanism of reaction.

4.2.4 Kinetic studies of the thermal decomposition of $Cp_2Zr\{(\mu\text{-}H)BH_3\}\{N(^tBu)Si(\mu\text{-}H)Me_2\}$ (23)

The thermal decompositions of **21** – **23** to give **24** – **26** and dihydrogen were followed *in situ* by a ^1H NMR array. For the reactions of **21** and **22** no intermediate species could be observed (*vide infra*). In contrast, for the reaction of **23** intermediate species could be observed. A concentration-time plot for the thermal decomposition of **23** at 90 °C is shown in Figure 4.7. Concentration-time plots extracted from reactions carried out at 93, 96, 99 and 102 °C, with identical initial concentration of **23**, followed the same profile as at 90 °C.

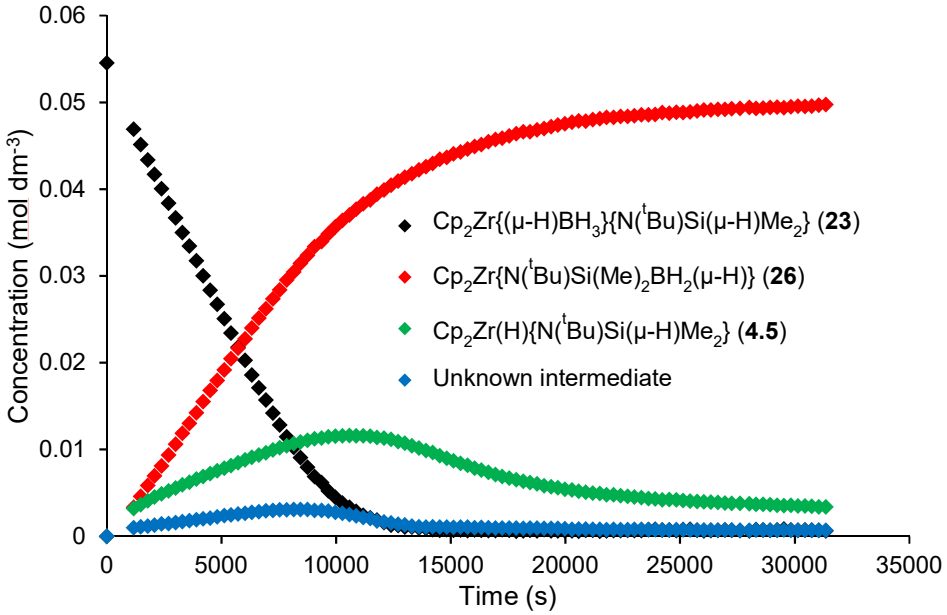
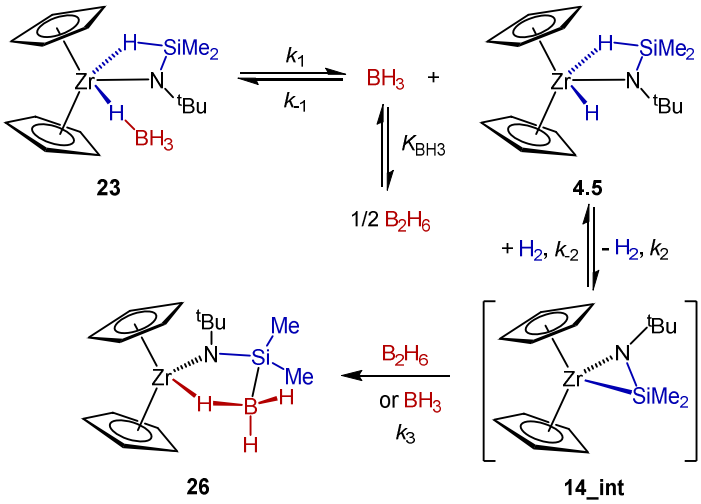


Figure 4.7: Concentration-time profiles for thermal decomposition of $Cp_2Zr\{(\mu\text{-}H)BH_3\}\{N(^tBu)Si(\mu\text{-}H)Me_2\}$ (**23**) to give $Cp_2Zr\{N(^tBu)Si(Me)_2BH_2(\mu\text{-}H)\}$ (**26**) and H_2 in toluene-d_8 at 90 °C.

Two intermediate species were observed, the major intermediate species (green plot) was characterised as $Cp_2Zr(H)\{N(^tBu)Si(\mu\text{-}H)Me_2\}$ (**4.5**), while the minor intermediate species (blue plot) could not be identified. Given the concentration of this minor intermediate reached only 0.0031 mol dm^{-3} (6% conversion) mechanistic pathways involving this unknown species will not be discussed. It can also be noted that the

concentration of dihydrogen rose and fell with a profile similar to that for reaction of **6** with HCC^{t}Bu. Given the major reaction pathway can be said to follow **23** → **4.5** + [BH_3] → **26**, with BH_3 dissociation implied by the presence of **4.5**, and the dihydrogen elimination previously observed for **4.5** and **6** upon reaction with terminal alkynes, the outline mechanism shown in Scheme 4.4 can be drawn. Initially, BH_3 reversibly dissociates from **23** forming **4.5** prior to reversible β-hydrogen abstraction and dihydrogen elimination forming the putative η^2-silanimine intermediate $Cp_2Zr\{\eta^2\text{-}N(^tBu)SiMe_2\}$ (**14_int**), which is not observed. This dihydrogen elimination would be expected to be reversible given observations made in Chapter 3 of this Thesis and DFT calculations discussed in Section 4.2.6. Subsequently, **26** forms by insertion of borane into the Zr–Si bond of **14_int**.



Scheme 4.4: Possible pathway for the thermal decomposition of $Cp_2Zr\{(\mu\text{-}H)_2BH_2\}\{N(^tBu)SiHMe_2\}$ (**23**) to give $Cp_2Zr\{N(^tBu)Si(Me)_2BH_2(\mu\text{-}H)\}$ (**26**) and H_2, *via* $Cp_2Zr(H)\{N(^tBu)Si(\mu\text{-}H)Me_2\}$ (**4.5**) and $Cp_2Zr\{\eta^2\text{-}N(^tBu)SiMe_2\}$ (**14_int**) with dimerisation of BH_3 also considered.

With regards to the dissociation of BH_3 from **23**, an identical pathway has previously been invoked for an aluminium borohydride,[80] and zirconocene borohydrides such as $Cp_2Zr\{(\mu\text{-}H)_2B(H)Tex\}\{N(^tBu)SiH_2Ph\}$ (**18**) have been shown to exist in equilibrium with their corresponding hydrides and boranes in solution.[26] It is notable that BH_3 is not observed in solution, but rather as Lewis base stabilised adducts (such as $BH_3{\cdot}SMe_2$) or

as dimeric B_2H_6.[80] Indeed, Δ_rG(**23** → **4.5** + BH_3) = 19.7 kcal mol^{-1} at 363 K, compared to Δ_rG(**23** → **4.5** + 0.5 B_2H_6) = 5.1 kcal mol^{-1}, showing B_2H_6 formation to provide a 14.6 kcal mol^{-1} reduction in free energy at 363 K. Furthermore, this dimerisation would reduce the maximum activation energy for the overall reaction proposed in Scheme 4.4 dramatically (this will be discussed further in Section 4.2.6). While still thermodynamically unfavourable, loss of B_2H_6, which has a boiling point of 180.5 K, from the reaction solution to the headspace or by trace amounts of O_2 in the reaction vessel scavenging B_2H_6, could drive the reaction forward and lead to the appearance of **4.5**.

Attempts to observe B_2H_6 during the course of the reaction were made by monitoring the reaction by ^{11}B NMR spectroscopy at 90 °C in toluene-d_8. The ^{11}B NMR chemical shift of B_2H_6 has previously been reported as 16.6 ppm at 100 °C in C_6D_6.[80] Consistent with this, a resonance with low intensity could initially be observed at 17.6 ppm in the reaction (see Appendix, Figure A12). No other intermediate species were observed. This resonance quickly reduced in intensity, which may be indicative of the aforementioned pathways for loss of borane from the reaction solution. Indeed, upon preparative scale synthesis of **26** in a Schlenk tube open to a flow of nitrogen, complete conversion of **23** to **26** could not be realised, instead forming a mixture of **26** and **4.5**. Only upon addition of $BH_3{\cdot}SMe_2$ and further heating, or reaction of **23** in a sealed ampoule, could complete conversion to **26** be observed. Given these observations and DFT calculations, BH_3 dimerisation is invoked in Scheme 4.4. The concentration of BH_3 can be expressed in terms of its equilibrium with B_2H_6 (Equations 4.5 and 4.6), although whether BH_3 must reform before reaction with **14_int** is not clear. S_N2 reaction at tetrahedral boron has been shown previously and so a concerted addition and cleavage of B_2H_6 could occur,

facilitated by bridging interaction of a B–H bond with the Zr-based LUMO of **14_int** (see Chapter 3, Section 3.2.4).[81–84]

$$K_{\mathrm{BH_3}} = \frac{[\mathrm{B_2H_6}]}{[\mathrm{BH_3}]^2} \tag{4.5}$$

$$[\mathrm{BH_3}] = {K_{\mathrm{BH_3}}}^{-\frac{1}{2}}[\mathrm{B_2H_6}]^{\frac{1}{2}} \tag{4.6}$$

Under the mechanism shown in Scheme 4.4, with a steady-state approximation for the unobserved, putative intermediate **14_int**, rate laws for the reaction could be obtained (Equations 4.7 – 4.16). While it is unclear whether BH_3 or B_2H_6 reacts with **14_int** to form **26**, Equation 4.6 shows how the concentrations of the two species are related and so the use of either in this kinetic discussion has no impact on the conclusions drawn. Therefore, BH_3 is used for ease.

At equilibrium for BH_3 dissociation:

$$k_1[\mathbf{23}] = k_{-1}[\mathrm{BH_3}][\mathbf{4.5}] \; (= \; k_{-1}[\mathbf{4.5}]^{\,2}) \tag{4.7}$$

$$[\mathbf{4.5}] = \frac{k_1}{k_{-1}}\frac{[\mathbf{23}]}{[\mathrm{BH_3}]} = K_{eq}\frac{[\mathbf{23}]}{[\mathrm{BH_3}]} \tag{4.8}$$

$$[\mathrm{BH_3}] = \frac{k_1}{k_{-1}}\frac{[\mathbf{23}]}{[\mathbf{4.5}]} = K_{eq}\frac{[\mathbf{23}]}{[\mathbf{4.5}]} \tag{4.9}$$

For formation of **26**:

$$Rate = \frac{\mathrm{d}[\mathbf{26}]}{\mathrm{d}t} = k_3[\mathbf{14_int}][\mathrm{BH_3}] \tag{4.10}$$

At steady state:

$$\frac{\mathrm{d}[\mathbf{14_int}]}{\mathrm{d}t} = k_2[\mathbf{4.5}] - k_{-2}[\mathbf{14_int}][\mathrm{H_2}] \tag{4.11}$$

$$- k_3[\mathrm{BH_3}][\mathbf{14_int}] = 0$$

$$[\mathbf{14_int}](k_{-2}[\mathrm{H_2}] + k_3[\mathrm{BH_3}]) = k_2[\mathbf{4.5}] \tag{4.12}$$

$$[\mathbf{14_int}] = \frac{k_2[\mathbf{4.5}]}{(k_{-2}[\mathrm{H_2}] + k_3[\mathrm{BH_3}])} \tag{4.13}$$

$$Rate = \frac{k_2k_3[\mathbf{4.5}][\mathrm{BH_3}]}{(k_{-2}[\mathrm{H_2}] + k_3[\mathrm{BH_3}])} \tag{4.14}$$

From Equation 4.7:

$$Rate = \frac{K_{eq}k_2k_3[\mathbf{23}]}{(k_{-2}[\mathrm{H_2}] + k_3[\mathrm{BH_3}])} \quad (4.15)$$

From Equation 4.9:

$$Rate = \frac{K_{eq}k_2k_3[\mathbf{23}]}{\left(k_{-2}[\mathrm{H_2}] + K_{eq}k_3\frac{[\mathbf{23}]}{[\mathbf{4.5}]}\right)} \quad (4.16)$$

These rate laws can be used to rationalise phenomena of the concentration-time plot shown in Figure 4.7. First, it is notable that depleting [BH_3] (and so [B_2H_6]) leads to an increase in [**4.5**] (Equation 4.8), as would be expected. Next, when k_{-2}[H_2] >> k_3[BH_3], the rate of reaction is proportional to [**4.5**][BH_3] (Equation 4.14), and so, due to Equation 4.7, the reaction would be expected to be second order in **4.5**. Indeed, at the latter stages of the reaction, when [**23**] ≈ 0 mol dm^{-3}, the decay of **4.5** follows second order decay with a linear trend for 1/[**4.5**] *vs.* time (see Appendix, Figure A13).

Using the same rationale and Equation 4.16, when k_{-2}[H_2] >> $K_{eq}k_3$[**23**]/[**4.5**], which would be the case when [**4.5**] > [**23**], and significant quantities of **23** were still present in solution, it can be said that the rate is proportional to [**23**]. Consistent with this, the decay of **23** was repeatedly observed to follow a linear trend for –ln([**23**]/[**23**]$_t$) *vs.* time, when [**4.5**] > [**23**], for three half-lives (see Appendix, Figure A14). Furthermore, for the reaction of **23** in the presence of ~0.8 equivalents of **4.5** (Figure 4.8), the decay of **23** appeared to follow first order kinetics to beyond three half-lives (Figure 4.9). It can be noted that the order of H_2, which would be expected to be –1, could not be accurately evaluated by variable time normalisation analysis (VTNA) during the periods in which the decay of **23** appeared first order, with a range of orders in H_2 giving satisfactory, linear fits for [**26**] *vs.* normalised time. This is likely due to the concentration of H_2 being relatively constant over the time period interrogated, leading to minimal influences on the corrected time depending on the order of H_2 used.

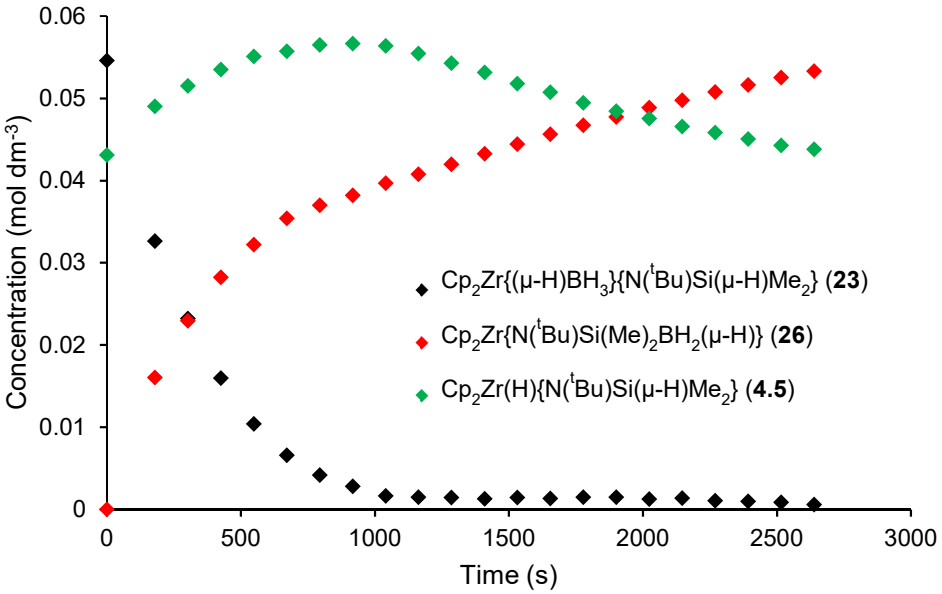


Figure 4.8: Concentration-time profiles for thermal decomposition of $Cp_2Zr\{(\mu\text{-}H)BH_3\}\{N(^tBu)Si(\mu\text{-}H)Me_2\}$ (**23**) to give $Cp_2Zr\{N(^tBu)Si(Me)_2BH_2(\mu\text{-}H)\}$ (**26**) and H_2 in the presence of ~0.8 equivalents $Cp_2Zr(H)\{N(^tBu)Si(\mu\text{-}H)Me_2\}$ (**4.5**) toluene-d_8 at 99 °C.

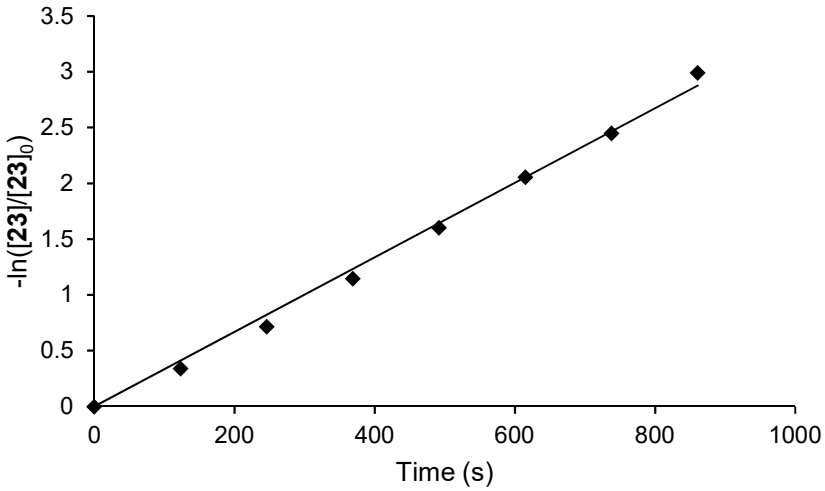


Figure 4.9: First order semi-logarithmic plot for the decay of **23** during the thermal decomposition of **23** to give **26** and H_2 in the presence of ~0.8 equivalents **4.5** toluene-d_8 at 99 °C. ($r^2 = 0.995$).

Additional experiments were undertaken to probe the mechanism of reaction further. First, thermal decomposition of **23** in the presence of 20 equivalents of THF was carried out (see Appendix, Figure A15), but had little effect on the rate of reaction or concentrations of **23**, **4.5** or **26** at any time. THF could coordinate to free BH_3 to form BH_3·THF and provide an alternative pathway for BH_3 stabilisation and subsequent

reaction with **14_int**. However, DFT calculations show $\Delta_rG(BH_3 + THF \rightarrow BH_3{\cdot}THF) = -12.7$ kcal mol^{-1} (*cf.* $\Delta_rG(2\ BH_3 \rightarrow B_2H_6) = -14.6$ kcal mol^{-1}) and so presumably a gross excess of THF would be required to influence the reaction kinetics.

Thermal decomposition of **23** in the presence of 20 equivalents of $BH_3{\cdot}SMe_2$ was also carried out (Figure 4.10, bold data points). As can be seen the rate of formation of **26** is somewhat increased, presumably owing to the abundance of BH_3, which could react with **14_int** as $BH_3{\cdot}SMe_2$ or as BH_3, formed by dissociation of $BH_3{\cdot}SMe_2$. It can be noted the initial concentration profiles of **4.5** are similar between reaction with and without excess $BH_3{\cdot}SMe_2$. This presumably is the case due to the balancing of excess borane promoting formation of **23** by reaction with **4.5** and promoting formation of **26**, which removes **4.5** from the equilibrium with **23**. Depletion of **23** in the presence of $BH_3{\cdot}SMe_2$ occurs at a higher conversion of **26** and subsequent to depletion of **23** the decay of **4.5** appears first order to three half-lives (Figure 4.11). This is expected as, using Equation 4.14, when $k_{-2}[H_2] << k_3[BH_3]$ the rate equation can be simplified to k_2[**4.5**].

Overall, the pathway shown in Scheme 4.4 is proposed as the mechanism of reaction for the thermal decomposition of **23**. The appearance of **4.5** as an intermediate species, as well as the observation of B_2H_6 by ^{11}B NMR and several observations rationalised through rate expressions are consistent with this proposed mechanism. Attention was next turned to the mechanism of the thermal decomposition of $Cp_2Zr\{(\mu\text{-}H)_2BH_2\}\{N(^tBu)SiH_2Ph\}$ (**21**) to give $Cp_2Zr\{N(^tBu)Si(H)(Ph)BH_2(\mu\text{-}H)\}$ (**24**) and H_2.

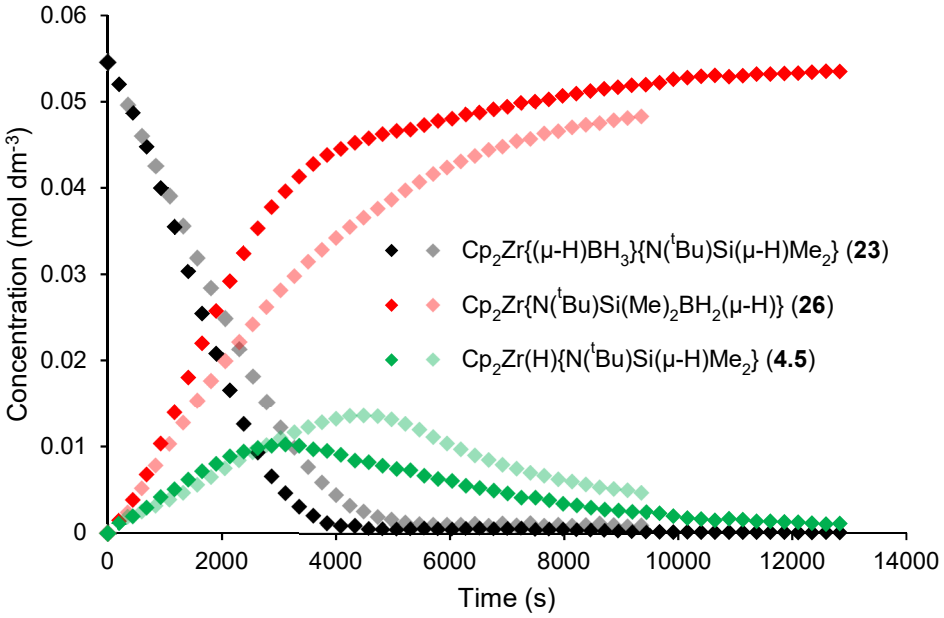


Figure 4.10: Concentration-time profiles for thermal decomposition of $Cp_2Zr\{(\mu\text{-}H)BH_3\}\{N(^tBu)Si(\mu\text{-}H)Me_2\}$ (**23**) to give $Cp_2Zr\{N(^tBu)Si(Me)_2BH_2(\mu\text{-}H)\}$ (**26**) and H_2 in the presence of 20 equivalents $BH_3{\cdot}SMe_2$ (bold points) and with no excess $BH_3{\cdot}SMe_2$ (faded points) in toluene-d_8 at 99 °C.

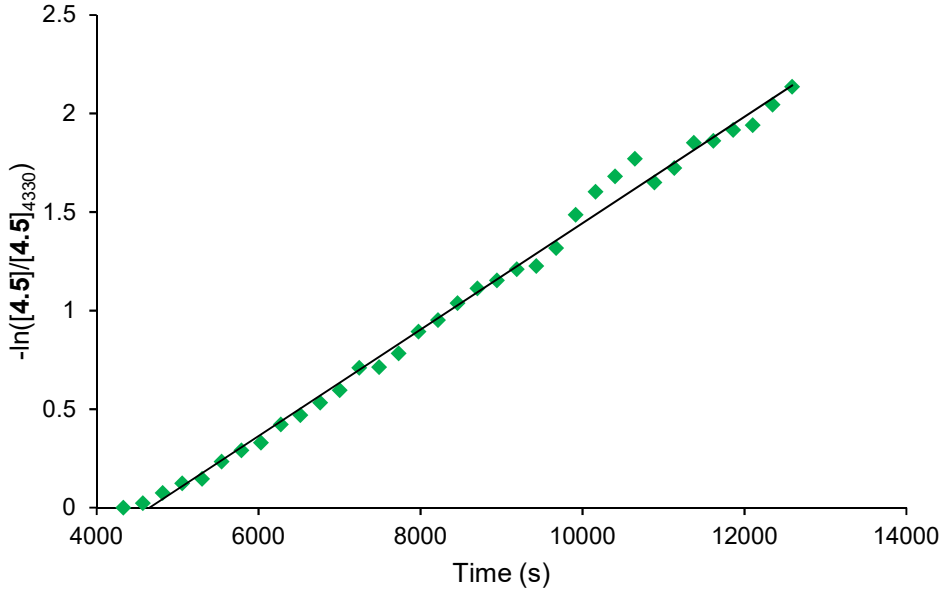


Figure 4.11: First order semi-logarithmic plot for the decay of $Cp_2Zr(H)\{N(^tBu)Si(\mu\text{-}H)Me_2\}$ (**4.5**) in the presence excess $BH_3{\cdot}SMe_2$ during the thermal decomposition of **23** to give **26** and H_2 in the presence of 20 equivalents $BH_3{\cdot}SMe_2$ when [**23**] ≈ 0 mol dm^{-3} in toluene-d_8 at 99 °C. (r^2 = 0.994).

4.2.5 Kinetic studies of the thermal decomposition of $Cp_2Zr\{(\mu\text{-}H)_2BH_2\}\{N(^tBu)SiH_2Ph\}$ (21)

Unlike with the thermal decomposition of **23**, no intermediate species were observed upon monitoring the thermal decomposition of **21** by ^1H or ^{11}B NMR array, only the smooth conversion of **21** to **24** with concurrent formation of H_2. Initially, this gives little insight into the mechanism of reaction. As such, further experiments were undertaken in attempt to elucidate the mechanism. While $Cp_2Zr(H)\{N(^tBu)Si(\mu\text{-}H)HPh\}$ (**6**), the result of borane dissociation from **21** and the analogue of **4.5**, is not seen to form during the reaction, possible borane dissociation was investigated by monitoring the stoichiometric reaction of **6-*d*$_3$** and $BH_3{\cdot}SMe_2$ at room temperature in C_6D_6. It must be noted that after addition of $BH_3{\cdot}SMe_2$ volatiles were removed under reduced pressure to remove SMe_2.

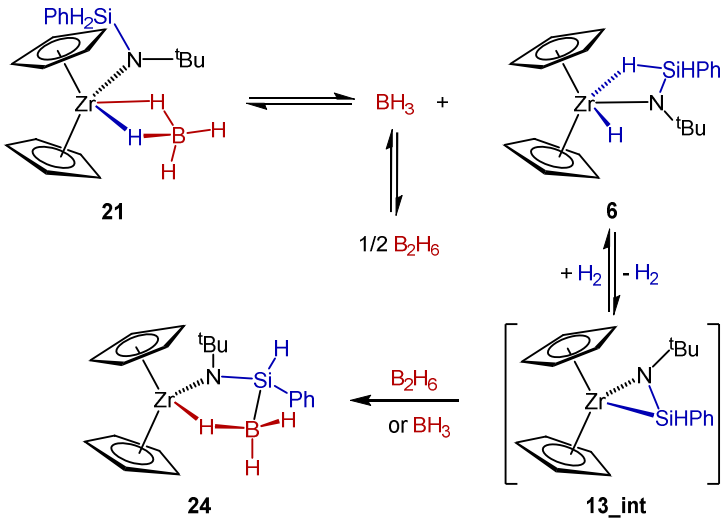
Formation of a partially deuterated isotopologue of **21** was observed and after 10 minutes the relative integral of the SiH_2/SiHD proton resonance was 0.6. However, after 1.5 hours the relative integral of the SiH_2/SiHD resonance was seen to increase to a close-to-statistical value of 1.2. This increase in SiH proton resonance integral is the result of hydrogen-deuterium exchange. For exchange to occur in this manner, after formation of the borohydride, BH_3 must be able to dissociate from **21**. After dissociation, the B–H bonds of the borane could directly undergo exchange with the Si–D bonds, which has previously been shown in the absence of a metal centre, or intramolecular exchange between Zr–H and Si–D bonds (see Section 4.3.2).[23] As **6** is not observed by NMR spectroscopy, it can be inferred that the dissociation of the borane occurs in a thermodynamically unfavourable equilibrium. Indeed, DFT calculations show Δ_rG(**21** → **6** + BH_3) = 20.0 kcal mol^{-1} 356 K, with no transition state found, showing dissociation to

be accessible, but significantly thermodynamically unfavourable. Next the effect of THF and excess $BH_3{\cdot}SMe_2$ were investigated.

The thermal decomposition of **21** was observed to occur significantly faster in THF-d_8 than in C_6D_6. After heating a C_6D_6 solution of **21** to 50 °C for 18 h, 70% conversion to **24** was observed by ^{1}H NMR spectroscopy. Comparatively, after heating a THF-d_8 solution of **21** to 50 °C for 2 h, 90% conversion to **24** was observed. THF is known to coordinate to BH_3 to form $BH_3{\cdot}$THF, and so would act to stabilise the free BH_3 released upon dissociation from **21**. BH_3 could also dimerise to give B_2H_6, which is thermodynamically favourable over THF coordination and presumably would occur in C_6D_6, though the low levels of BH_3 in solution implied by the lack of observed intermediates and the abundance of THF would overcome this thermodynamic preference. Rate enhancement in THF would therefore be expected if the thermodynamically unfavourable and reversible borane dissociation were occurring along the reaction pathway from **21** to **24** and were important to the overall rate of reaction, and so this can be inferred.

Reaction of **21** in the presence of 20 equivalents $BH_3{\cdot}SMe_2$ in THF-d_8 gave only 15% conversion to **24** after 2 h at 50 °C. Again, this observation is consistent with reversible borane dissociation occurring along the reaction pathway and being important to the overall rate of reaction, as an excess of borane would act to shift the equilibrium of borane dissociation towards the side of **21**. This also suggests that subsequent reaction of borane to form **24** does not significantly impact the rate of reaction in comparison to borane dissociation. This is in contrast to the thermal decomposition of **23**, where addition of $BH_3{\cdot}SMe_2$ increased the rate of formation of **26**, presumably due to addition of borane to **14_int** being important to the rate of reaction, as discussed.

Given the aforementioned observations, the reaction pathway implied for the conversion of **23** to **26** and H_2, and the proposed mechanism for the reaction of **6** with HCC^{t}Bu, the pathway shown in Scheme 4.5 can be drawn. This pathway is identical to that for the thermal decomposition of **23**. Initially, BH_3 reversibly dissociates from **21** forming transient **6** prior to reversible β-hydrogen abstraction and dihydrogen elimination forming the putative η^2-silanimine intermediate $Cp_2Zr\{\eta^2\text{-}N(^t\text{Bu})SiHPh\}$ (**13_int**). Subsequently, **24** forms by insertion of BH_3 or B_2H_6 into the Zr–Si bond of **13_int**. As for reaction of **23** and a comparable reaction discussed in the literature,[80] reversible BH_3 dimerisation is invoked. DFT computations, discussed in more detail in Section 4.2.6, calculate BH_3 dimerisation to lower the free energy of activation of the reaction by up to 14.7 kcal mol^{-1} to a minimum of 25.8 kcal mol^{-1} at 356 K, depending on the barrier for borane insertion into the Zr–Si bond of **13_int**, which is not thought to be rate determining given the aforementioned reactions with excess $BH_3{\cdot}SMe_2$.



Scheme 4.5: Possible pathway for the thermal decomposition of $Cp_2Zr\{(\mu\text{-}H)_2BH_2\}\{N(^t\text{Bu})SiH_2Ph\}$ (**21**) to give $Cp_2Zr\{N(^t\text{Bu})Si(H)(Ph)BH_2(\mu\text{-}H)\}$ (**24**) and H_2, *via* $Cp_2Zr(H)\{N(^t\text{Bu})Si(\mu\text{-}H)HPh\}$ (**6**) and $Cp_2Zr\{\eta^2\text{-}N(^t\text{Bu})SiHPh\}$ (**13_int**) with dimerisation of BH_3 also considered.

To further investigate the possibility of this pathway, or other pathways, the orders of the reaction in **21** and H_2 were determined. Given the implication of multiple

rate-determining equilibria, the reaction was monitored by ^{1}H NMR array in toluene-d_8 at multiple temperatures to additionally investigate the effect of temperature on the order of reaction. For each temperature (347, 350, 353, 356 and 359 K) plots of [**21**] *vs.* time, [**21**]$^{0.5}$ *vs.* time, –ln([**21**]/[**21**]$_0$) *vs.* time and 1/[**21**] *vs*. time were drawn (see Appendix, Figure A16 for those at 350 K).

The first order semi-logarithmic plots to approximately three half-lives, disregarding the first few data points to allow for as close to constant concentration of H_2 as possible, gave the best, but unsatisfactory, fits and are shown in Figure 4.12. Similar to the reaction of **6** with 20 equivalents HCC^{t}Bu (see Chapter 3, Section 3.2.3), H_2 could be seen to be inhibiting the reaction (Figure A17). As such, variable time normalisation analysis (VTNA), which has previously been used for reactions involving multiple equilibria and reaction components, was employed to determine the order of the reaction in **21** and H_2.[85,86] The premise of VTNA was described in Chapter 3 and while not suitable for the thermal decomposition of **23**, due to the rate laws of its decay being varied by the relative effects of species at different times of the reaction, the technique was able to be used here. At each temperature, the order in **21** was found to be 0.75 and the order in H_2 found to be –0.75 as judged by linear plots over the course of the entire reactions (Figure 4.13). Furthermore, VTNA plots to take into account the concentration of H_2, with an order in the reaction of –0.75 (Figure A18), and the concentration of **21**, with an order of 0.75 (Figure A19), for two independent thermal decompositions of **21** at identical [**21**]$_0$ at 356 K gave near perfectly overlapping data. This VTNA leads to an observed rate equation as shown in Equation 4.17.

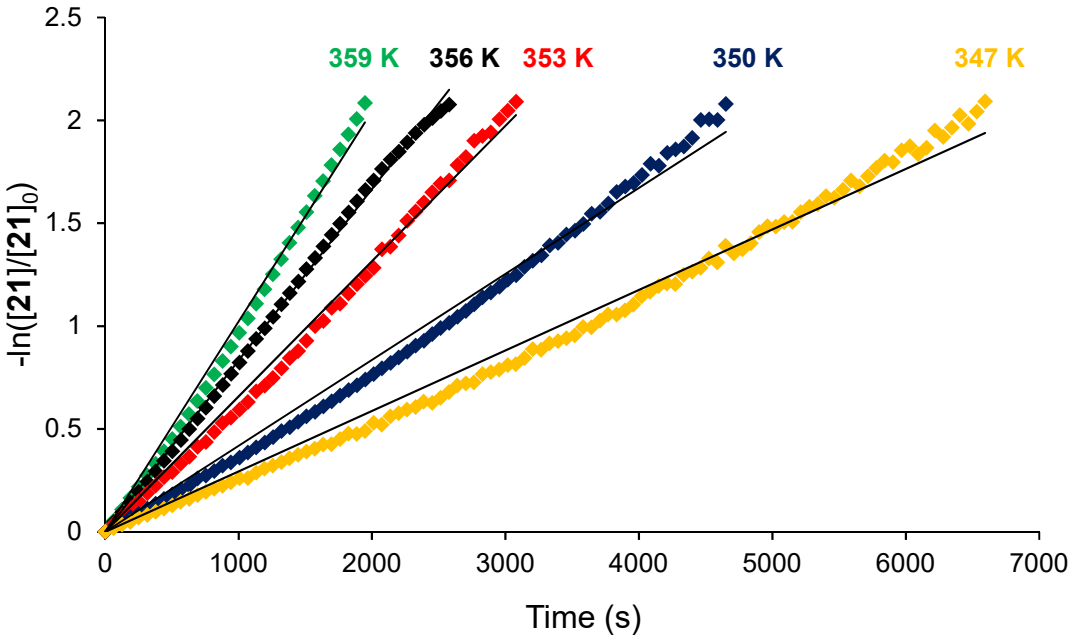


Figure 4.12: Semi-logarithmic plots for the thermal decomposition of $Cp_2Zr\{(\mu\text{-}H)_2BH_2\}\{N(^tBu)SiH_2Ph\}$ (**21**) to give $Cp_2Zr\{N(^tBu)Si(H)(Ph)BH_2(\mu\text{-}H)\}$ (**24**) and H_2 in toluene-d_8. (avg. r^2 = 0.993, range 0.990 – 0.999).

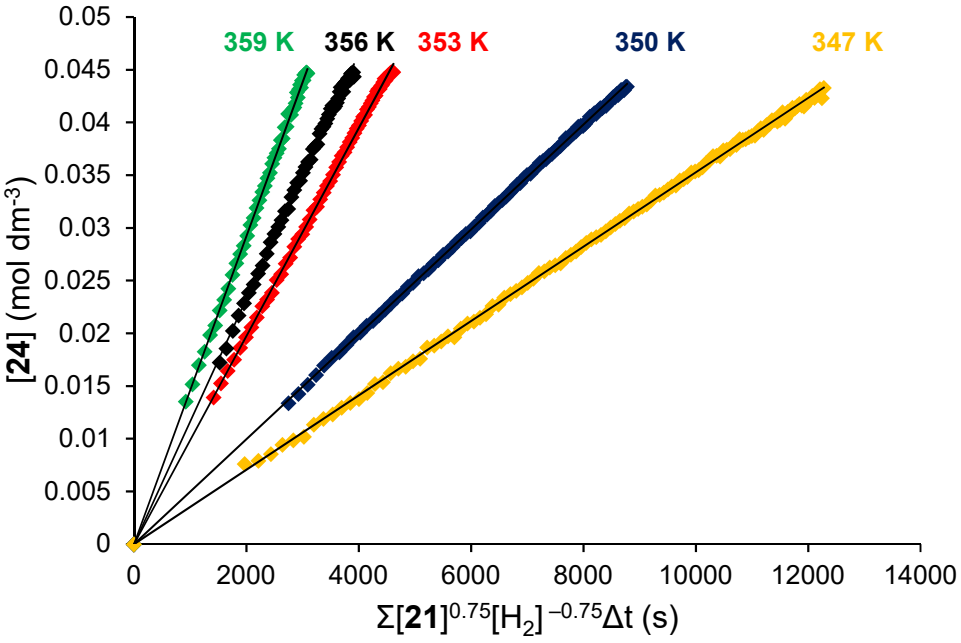


Figure 4.13: Variable time normalisation analysis (VTNA) plots of the thermal decomposition of $Cp_2Zr\{(\mu\text{-}H)_2BH_2\}\{N(^tBu)SiH_2Ph\}$ (**21**) to give $Cp_2Zr\{N(^tBu)Si(H)(Ph)BH_2(\mu\text{-}H)\}$ (**24**) and H_2 in toluene-d_8, with the normalised time being $\Sigma[\mathbf{6}]^{0.75}[H_2]^{-0.75}\Delta t$. (avg. r^2 = 0.999, range 0.998 – 1.000).

$$\frac{\mathrm{d}[\mathbf{24}]}{\mathrm{d}t} = k_{obs}[\mathbf{21}]^{0.75}[H_2]^{-0.75} \qquad (4.17)$$

The observation of non-integer orders of **21** and H_2 in the reaction is consistent with multiple rate-sensitive equilibria occurring and so the mechanism shown in Scheme 4.5, but does offer direct evidence. The non-integer orders presumably arise from the concentrations of intermediate species being intimately related to the concentration of **21**. Similar phenomena have been observed for reactions involving multiple equilibria.[85] The exact order of **21** and H_2 in the reaction will depend on the extent to which individual reaction steps contribute to the rate equation. Notably, the fact that the orders remain constant over the temperature range investigated implies that only one pathway occurs in the reaction, as the entropic contributions to the activation energies of varying pathways would lead to changes in respective influences on the rate of reaction and observed order of **21** and H_2. Although temperature effects can be similar for different pathways.

While the gradient of the plots shown in Figure 4.13 formally represents k_{obs}, use of these values in an Eyring analysis gave ill-fitting data, potentially due to the varying T_1 relaxation times of dihydrogen at varying temperatures giving inconsistent, inaccurate values for $[H_2]$. This was also seen for the reaction of **6** with HCC^{t}Bu, and non-linear Arrhenius plots have been reported for reactions involving pre-equilibrium steps.[87]

Further to the establishment of the rate equation shown in Equation 4.17, the kinetic isotope effect (KIE) of the reaction was investigated. Due to the observed hydrogen-deuterium exchange between B–H/D and Si–H/D sites, selective deuterium labelling of **21** was not possible, and only the perdeuterated isotopologue **21-*d*$_6$** could be prepared. The concentration-time plots for the thermal decomposition of **21** (blue) and **21-*d*$_6$** (red) at 356 K in toluene-d_8 are shown in Figure 4.14. The initial concentrations of **21** and **21-*d*$_6$** were kept constant across the reactions, and, given the consistency of the data, it would appear the concentration profiles of H_2 or D_2 were relatively consistent between respective protonated and deuterated experiments.

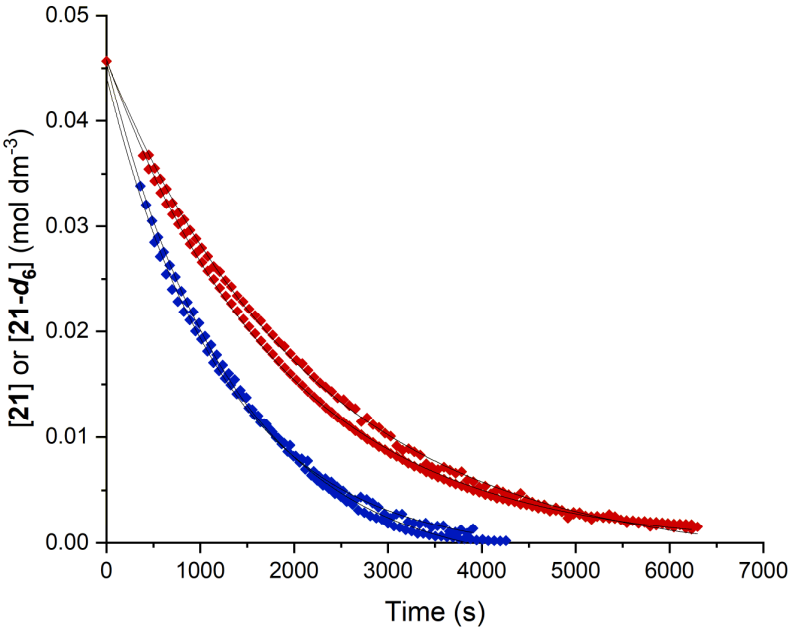


Figure 4.14: Plots of $[Cp_2Zr\{(\mu\text{-}H)_2BH_2\}\{N(^tBu)SiH_2Ph\}]$ ([**21**], blue) and $[Cp_2Zr\{(\mu\text{-}D)_2BD_2\}\{N(^tBu)SiD_2Ph\}]$ ([**21-*d*$_6$**], red) *vs.* time plotted in *Origin*. Values for A_1 and B_1 extracted from the best-fit lines shown for **21** are A_1 = 0.0483(3) and 0.0453(3), and B_1 = 1339(19) and 1254(21) giving initial rates of 3.61(6) and 3.61(7) x 10^{-5} mol dm^{-3} s^{-1}. For **21-*d*$_6$** the best-fit lines gave A_1 = 0.0462(1) and 0.0476(2), and B_1 = 1862(14) and 2184(23) giving initial rates of 2.48(2) and 2.18(2) x 10^{-5} mol dm^{-3} s^{-1}. (Avg. r^2 = 0.999, range 0.998 – 0.999).

The graphical software *Origin* was used to fit all data points using a simple exponential function, thus describing the decay of **21** or **21-*d*$_6$** throughout the kinetic study (Equation 4.18). The curve was then differentiated to give the gradient (Equation 4.19) and then the gradient was calculated at time = 0 s (Equation 4.20) to give the initial rate of reaction.

$$[\mathbf{21}] = y_0 + A_1 e^{-t/B_1} \qquad (4.18)$$

$$\frac{d[\mathbf{21}]}{dt} = -\frac{A_1 e^{-t/B_1}}{B_1} \qquad (4.19)$$

$$\left(\frac{d[\mathbf{21}]}{dt}\right)_{t=0} = -\frac{A_1}{B_1} \qquad (4.20)$$

The initial rates of reaction were found to be 3.61(6) and 3.61(7) x 10^{-5} mol dm^{-3} s^{-1} for the thermal decomposition of **21** and 2.48(2) and 2.18(2) x 10^{-5} mol dm^{-3} s^{-1} for perdeuterated **21-*d*$_6$**, giving a kinetic isotope effect of 1.46 – 1.66 at 356 K. This small kinetic isotope effect could reflect the presence of multiple isotope-sensitive equilibria,

rather than the KIE of a single reaction step. This would be consistent with the mechanism in Scheme 4.5, but offers little insight into the mechanism. The exact extent of the equilibrium isotope effect will relate to the various zero point energy (ZPE) differences between sides of the rate-determining equilibria, as discussed in Chapter 3, Section 3.2.3. Such equilibrium isotope effects (EIEs) have been observed for reversible H–H and C–H elimination reactions, as well as pre-equilibrium C–H elimination reaction steps.[23,88–90] Furthermore, it can be noted that secondary isotope effects are observed upon rehybridisation of E–H bonds between sp^3 and sp^2 hybridised, due to the out-of-plane bending vibrations.[91] However, these are usually small and could be negated over the course of this reaction given multiple rehybridisations are implied for the borane.

Overall, several experiments have been conducted to investigate the mechanism of the thermal decomposition of $Cp_2Zr\{(\mu\text{-}H)_2BH_2\}\{N(^tBu)SiH_2Ph\}$ (**21**) to give $Cp_2Zr\{N(^tBu)Si(H)(Ph)BH_2(\mu\text{-}H)\}$ (**24**) and H_2. Reaction in C_6D_6, THF-d_8 and with excess $BH_3{\cdot}SMe_2$ implied borane dissociation is occurring along the reaction pathway and influential on the rate of reaction, while subsequent reaction of borane to form **24** does not significantly impact the rate of reaction in comparison to borane dissociation. The reaction was found, by VTNA, to be 0.75 and –0.75 order in **21** and H_2, respectively, and a kinetic isotope effect, using the per-deuterated isotopologue **21-*d*$_6$**, of 1.46 – 1.66 was observed at 356 K. These results are consistent with multiple, rate-sensitive equilibria being present along the reaction pathway. Furthermore, the observation that the orders of **21** and H_2 in the reaction did not vary over the temperature range 347 – 359 K imply only one pathway is occurring in this reaction.

Using these observations, conclusions drawn from the thermal decomposition of $Cp_2Zr\{(\mu\text{-}H)BH_3\}\{N(^tBu)Si(\mu\text{-}H)Me_2\}$ (**23**) and the mechanism of reaction of

$Cp_2Zr(H)\{N(^tBu)Si(\mu\text{-}H)HPh\}$ (**6**) with terminal alkynes discussed in Chapter 3 of this Thesis, the pathway shown in Scheme 4.5 was drawn. While consistent with experimental observations, direct observation of intermediate species was not possible by ^1H or ^{11}B NMR array. Therefore, to investigate this pathway further and the analogous pathway for **23**, DFT calculations were undertaken.

4.2.6 DFT studies on the thermal decompositions of $Cp_2Zr\{(\mu\text{-}H)_2BH_2\}\{N(^tBu)SiH_2Ph\}$ (21) and $Cp_2Zr\{(\mu\text{-}H)BH_3\}\{N(^tBu)Si(\mu\text{-}H)Me_2\}$ (23)

The DFT calculated mechanism for both $Cp_2Zr\{(\mu\text{-}H)_2BH_2\}\{N(^tBu)SiH_2Ph\}$ (**21**, black text) and $Cp_2Zr\{(\mu\text{-}H)BH_3\}\{N(^tBu)Si(\mu\text{-}H)Me_2\}$ (**23**, magenta text) at 356 K is shown in Figure 4.15 and is based on the proposed pathways shown in Schemes 4.4 and 4.5. First, the mechanism of thermal decomposition of **21** is discussed, followed by that of **23**.

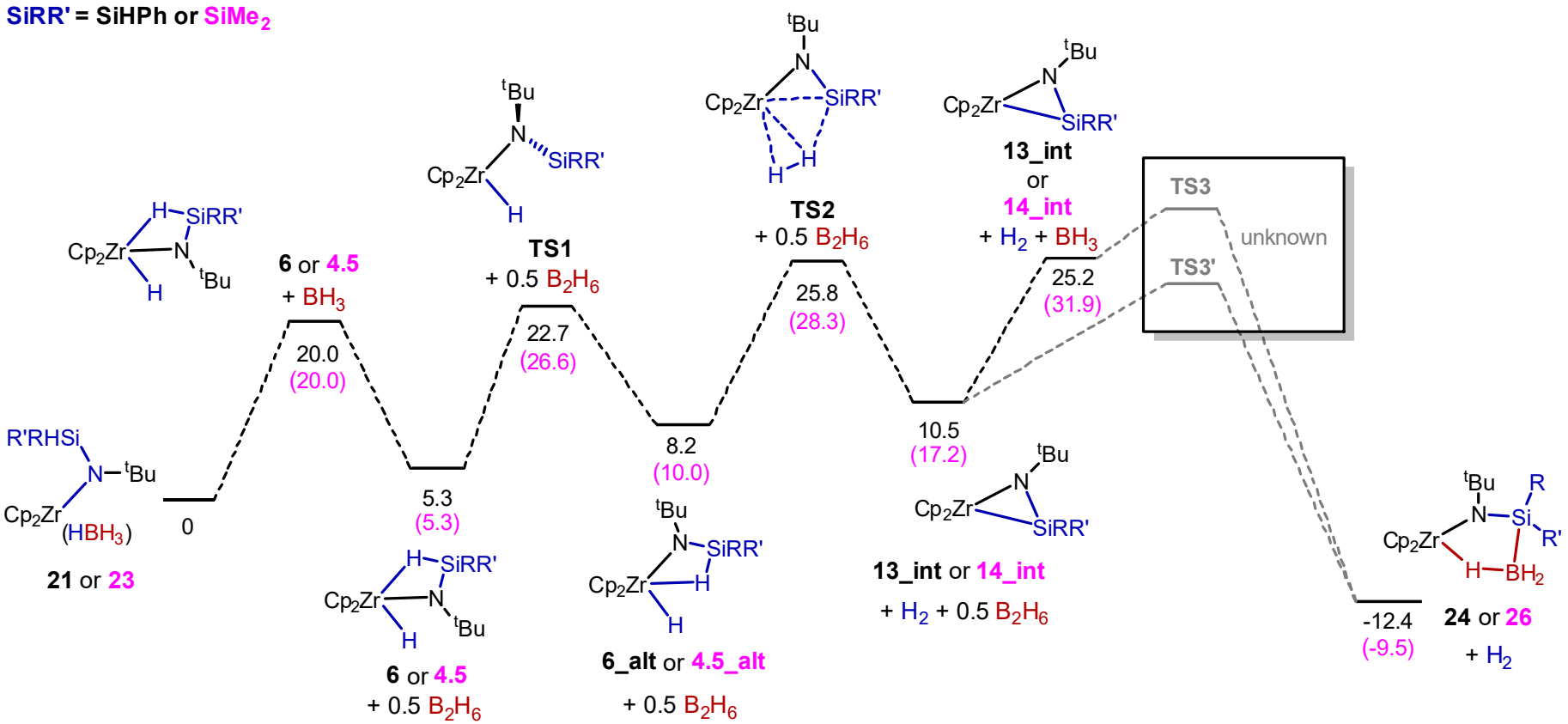


Figure 4.15: DFT (B3PW91/Def2-TZVP/d3-bj/SCRF) mechanism for the thermal decompositions of $Cp_2Zr\{(\mu\text{-}H)_2BH_2\}\{N(^tBu)SiH_2Ph\}$ (**21**, black text) and $Cp_2Zr\{(\mu\text{-}H)BH_3\}\{N(^tBu)Si(\mu\text{-}H)Me_2\}$ (**23**, magenta text) to form H_2 and $Cp_2Zr\{N(^tBu)Si(H)(Ph)BH_2(\mu\text{-}H)\}$ (**24**) and $Cp_2Zr\{N(^tBu)Si(Me)_2BH_2(\mu\text{-}H)\}$ (**26**), respectively. Gibbs free energies (kcal mol^{-1}, T = 356 K) for minima and transition states (labelled **TSx**) are shown relative to **21** (black) or **23** (pink).

Initially, borane dissociation from **21** occurs with Δ_rG = 20.0 kcal mol^{-1} forming the hydride $Cp_2Zr(H)\{N(^tBu)Si(\mu\text{-}H)HPh\}$ (**6**) and monomeric BH_3. Dimerisation of BH_3 then occurs, providing a free energy reduction of 14.7 kcal mol^{-1} to the reaction system, with G_{rel}(**6** + 0.5 B_2H_6) = 5.3 kcal mol^{-1}. From here, β-hydrogen abstraction and dihydrogen elimination occurs, as has been described in Chapter 3, Section 3.2.4 of this Thesis. Rotation about the Zr–N bond of **6** occurs *via* **TS1** with a free energy barrier of 22.7 kcal mol^{-1}, with respect to **21**, allowing formation of **6_alt** (G_{rel} = 8.2 kcal mol^{-1}). With the agostic hydrogen adjacent to the hydride, β-H abstraction and dihydrogen elimination occurs *via* **TS2** with a barrier of 25.8 kcal mol^{-1}, forming the η^2-silanimine $Cp_2Zr\{\eta^2\text{-}N(^tBu)SiHPh\}$ (**13_int**, G_{rel} = 10.5 kcal mol^{-1}). This barrier may represent the activation energy of the reaction (*vide infra*) and it can be noted that if BH_3 dimerisation did not occur **TS2** would be thermally inaccessible, with G_{rel} = 40.5 kcal mol^{-1}, highlighting the importance of stabilisation of BH_3 early along the reaction pathway.

From **13_int** and B_2H_6 two options are available: either B_2H_6 can dissociate to give BH_3, which then react with **13_int** to form **24**, or B_2H_6 can react directly with **13_int**. In the former case, dissociation of B_2H_6 leads to a 14.7 kcal mol^{-1} increase in free energy of the reaction system, leading to G_{rel} = 25.2 kcal mol^{-1}. Unfortunately, transition state **TS3** and associated energy barrier for insertion into the Zr–Si bond could not be located, but would be expected to have a small, though appreciable, energy barrier. For direct reaction of B_2H_6 with **13_int** the transition state, **TS3'**, again proved elusive and so it cannot be said for certain which route provides the lowest energy barrier. From experimental observations, it would appear insertion of borane to **13_int** is not rate-determining and given **TS3** would inevitably have a higher free energy than **TS2**, direct reaction with B_2H_6, *via* **TS3'**, may offer the lower energy pathway. However, nothing can be said for certain. Regardless of the nature of borane insertion, $Cp_2Zr\{N(^tBu)Si(H)(Ph)BH_2(\mu\text{-}H)\}$

(**24**) is formed with G_{rel} = –12.4 kcal mol^{-1}. Overall, the mechanism is in agreement with the mechanism asserted through experimental findings (Scheme 4.5), calculating the reaction to proceed with an energy barrier as low as 25.8 kcal mol^{-1} and implying no intermediates should be observed during the reaction.

Turning next to the mechanism for thermal decomposition of **23**, borane dissociation occurs with a free energy barrier of 20.0 kcal mol^{-1} at 356 K (19.7 kcal mol^{-1} at 363 K, a temperature at which kinetic investigations into the reaction were carried out) forming the hydride $Cp_2Zr(H)\{N(^tBu)Si(\mu\text{-}H)Me_2\}$ (**4.5**) and unstable, free BH_3. Again, dimerisation of BH_3 provides a 14.7 kcal mol^{-1} reduction in free energy with G_{rel}(**4.5** + 0.5 B_2H_6) = 5.3 kcal mol^{-1} (5.1 kcal mol^{-1} at 363 K). It is notable that while significantly thermodynamically unfavourable, the experimental observation of **4.5** during the reaction presumably occurs due to the high energy barrier for dihydrogen elimination (*vide infra*) allowing B_2H_6 to be lost from the reaction solution before dihydrogen elimination, driving forward the equilibrium between **23** and **4.5**, and leading to **4.5** having a relatively long lifetime, with respect to **6**.

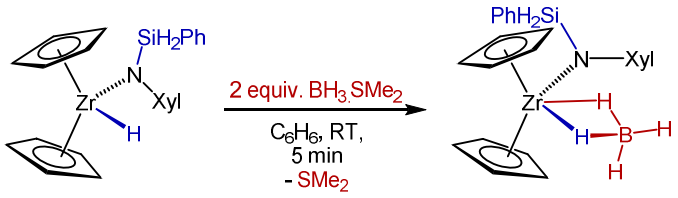
From **4.5**, β-hydrogen and dihydrogen elimination occurs in an identical manner to **6**. Rotation about the Zr–N bond of **4.5** occurs *via* **TS1**, with a free energy barrier of 26.6 kcal mol^{-1} (26.5 kcal mol^{-1} at 363 K), allowing formation of **4.5_alt** with G_{rel} = 10.0 kcal mol^{-1} (10.0 kcal mol^{-1} at 363 K). β-H abstraction and dihydrogen elimination then occurs *via* **TS2** with a barrier of 28.3 kcal mol^{-1} (28.2 kcal mol^{-1} at 363 K), forming the η^2-silanimine $Cp_2Zr\{\eta^2\text{-}N(^tBu)SiMe_2\}$ (**14_int**). Remarkably, **14_int**, with G_{rel} = 17.2 kcal mol^{-1} (16.9 kcal mol^{-1} at 363 K) is 6.7 kcal mol^{-1} higher in relative free energy than **13_int** and dihydrogen elimination requires 2.5 kcal mol^{-1} more free energy. This is consistent with the thermal decomposition of **23** occurring slower at the same temperature as that of **21**. On inspection of **14_int** and **13_int** the metrics of the ZrNSi metallacycle

are near identical, with Zr–Si bond distances of 2.578 and 2.580 Å, respectively, and also very similar to the structure of **14_int** previously calculated by Bi and co-workers under a similar level of DFT (B3LYP).[92] The metrics surrounding the respective **TS2** structures are also very similar, with no notable differences. The origin of these free energy differences is not immediately obvious, though the steric bulk of the second methyl group of **14_int** in place of hydrogen in **13_int** could factor, as could stabilising delocalisation of electron into the phenyl ring of **13_int**, which is not possible in **14_int**. Indeed the HOMO of $Cp_2Zr\{\eta^2\text{-}N(Me)SiHPh\}$ (a model of **13_int**) was found to have some C_{Ph} contribution (see Chapter 3, Section 3.2.4).

Moving forward from **14_int** and B_2H_6, and as for **13_int** and B_2H_6, either BH_3 can reform and insert into the Zr–Si bond of **14_int**, or B_2H_6 can directly insert. The transition states of both these pathways could not be calculated, as discussed for **13_int**, though formation of BH_3 from B_2H_6 prior to its insertion was calculated to lead to G_{rel}(**14_int** + BH_3 + H_2) = 31.9 kcal mol^{-1} (31.5 kcal mol^{-1} at 363 K). This implies a high barrier for BH_3 insertion and so it could be that B_2H_6 insertion offers a lower energy pathway, though little can be confirmed surrounding the insertion event. Subsequent to insertion, **24** is formed and calculated to be thermodynamically stable with G_{rel} = –9.5 kcal mol^{-1} (–9.6 kcal mol^{-1} at 363 K). Overall, the mechanism is consistent with that proposed through experimental findings, with the high barrier to dihydrogen elimination rationalising the loss of B_2H_6 from the reaction solution and the observation of significant quantities of **4.5** as an intermediate by ^{1}H NMR, which is not seen for **21**.

4.2.7 Reaction of $Cp_2Zr(H)\{N(Xyl)SiH_2Ph\}$ (8) with $BH_3{\cdot}SMe_2$

On the NMR tube scale, as with the reaction of **6** and **7** with $BH_3{\cdot}SMe_2$, stoichiometric reaction of $Cp_2Zr(H)\{N(Xyl)SiH_2Ph\}$ (**8**) and $BH_3{\cdot}SMe_2$, in C_6D_6 at room temperature, gave instant, quantitative formation of $Cp_2Zr\{(\mu\text{-}H)_2BH_2\}\{N(Xyl)SiH_2Ph\}$ (**27**). On the preparative scale, **8**, generated *in situ*, was stirred with two equivalents $BH_3{\cdot}SMe_2$ in benzene for 5 minutes at room temperature. Compound **27** was isolated as a colourless crystalline solid from concentrated hexane solutions at 4 °C in a 55% yield (Equation 4.21).



8 **27**

Equation 4.21

The ^1H NMR spectrum of **27** showed a single Cp resonance and a single SiH_2 resonance at 5.74 and 5.40 ppm, respectively, indicating C_s symmetry in solution. The $^1J_{SiH}$ coupling constant was found, by a ^{29}Si-^1H gradient experiment, to be 206 Hz (*cf.* 205 and 189 Hz for **8** and $Cp_2Zr\{(\mu\text{-}H)_2BH_2\}\{N(^tBu)SiH_2Ph\}$ (**21**), respectively) with the ^{29}Si resonance appearing at –30.0 ppm, consistent with an absence of a β-agostic interaction.[3,42] As with other borohydrides characterised in this Chapter, no resonance attributable to a zirconium hydride could be observed. Furthermore, a singlet resonance of relative integral 4H at 0.93 was observed in the $^1H\{^{11}B\}$ NMR, similar to **21**, and a single quintet ($^1J_{BH}$ = 84 Hz) was observed at –17.5 ppm in the ^{11}B NMR spectrum (*cf.* –4.5 ppm and $^1J_{BH}$ = 85 Hz for **21**), consistent with borohydride formation. The bridging and terminal BH environments, which undergo fast exchange on the NMR timescale at room temperature, could not be decoalesced upon cooling to –88 °C.

The solid state structure of **27** is shown in Figure 4.16, with selected bond distances and angles shown in Table 4.7, confirming the connectivity shown in Equation 4.21. Analogous to **21**, **27** adopts a bent metallocene structure with a κ^2-bound borohydride moiety. While, as in **21**, H(1), H(2), B(1) and N(1) lie in the equatorial plane of the zirconocene, the silylamido ligand is rotated with respect to that of **21** such that H(5), Si(1), and C(1) do not lie in the equatorial plane. The bulky xylyl moiety would clash with the borohydride moiety if the ligand adopted the same orientation as in **21** and instead adopts a similar orientation to that in **8**. The Zr–N (2.133(3) Å) and Zr–B (2.597(4) Å) distances of **27**, are shorter than those of **21** (2.178(2) and 2.614(4) Å, respectively), though the Zr–H(1) and Zr–H(2) distances are identical within error.

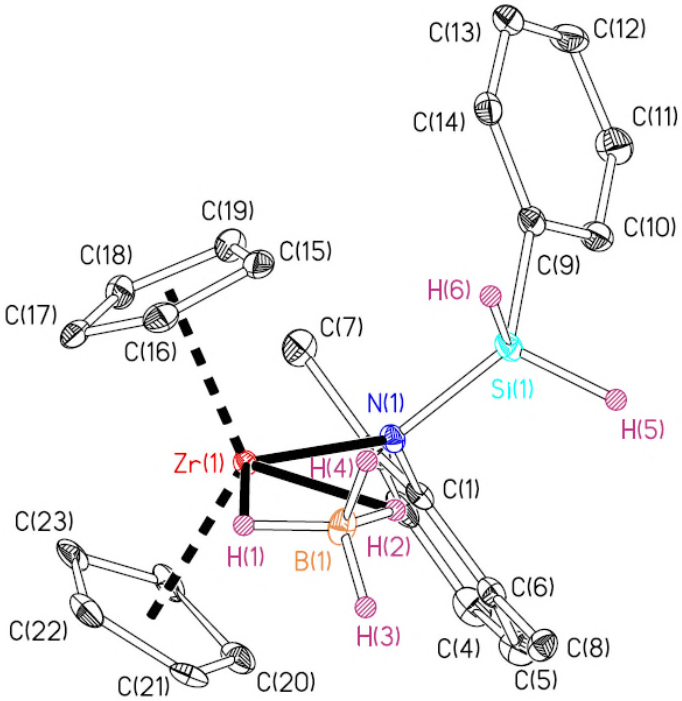
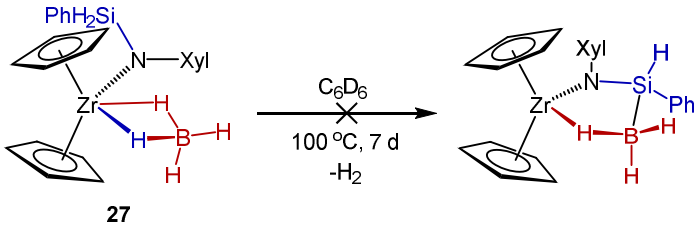


Figure 4.16: Displacement ellipsoid plot (20% probability) of $Cp_2Zr\{(\mu\text{-}H)_2BH_2\}\{N(Xyl)SiH_2Ph\}$ (**27**). C–H atoms are omitted for clarity. H(1) – H(6) are drawn as spheres of an arbitrary radius.

Table 4.7: Selected bond distances (Å) and angles (°) for $Cp_2Zr\{(\mu\text{-}H)_2BH_2\}\{N(Xyl)SiH_2Ph\}$ (**27**). $Cp_{cent(1)}$ and $Cp_{cent(2)}$ refer to the computed Cp ring centroids for the "upper" and "lower" Cp rings, respectively, as depicted in Figure 4.16.

Zr(1)-N(1)	2.133(3)	H(1)-Zr(1)-N(1)	127.7(4)
Zr(1)-H(1)	2.20(5)	H(2)-Zr(1)-N(1)	76.1(3)
Zr(1)-H(2)	2.21(5)	H(1)-Zr(1)-H(2)	51.6(4)
$Zr(1)\text{-}Cp_{cent(1)}$	2.23	$Cp_{cent(1)}\text{-}Zr(1)\text{-}Cp_{cent(2)}$	126.6
$Zr(1)\text{-}Cp_{cent(2)}$	2.22	Zr(1)-N(1)-Si(1)	123.23(15)
N(1)-Si(1)	1.757(3)	Si(1)-N(1)-C(1)	107.7(2)
B(1)-H(1)	1.141(10)	C(1)-N(1)-Zr(1)	128.9(2)
B(1)-H(2)	1.142(10)		
B(1)-H(3)	1.095(10)		
B(1)-H(4)	1.094(10)		
Si(1)-H(5)	1.393(10)		
Si(1)-H(6)	1.390(10)		

Unlike **21**, **27** was seen to be stable in solution up to 100 °C for seven days in C_6D_6 and was not seen to release dihydrogen and undergo the thermal decomposition shown in Equation 4.22 when monitored by ^1H NMR spectroscopy. Furthermore, formation of $Cp_2Zr(H)\{N(Xyl)SiH_2Ph\}$ (**8**), *via* borane dissociation, was not observed, even at 100 °C, unlike what was seen for $Cp_2Zr\{(\mu\text{-}H)BH_3\}\{N(^tBu)Si(\mu\text{-}H)Me_2\}$ (**23**) and $Cp_2Zr\{(\mu\text{-}H)B(C_4H_8)CH_2Ph\}\{(\mu\text{-}H)_2BC_4H_8\}$.[26]



27

Equation 4.22

The formation of **27** from **8** and $BH_3{\cdot}SMe_2$ was calculated by DFT to occur with Δ_rG = –9.6 kcal mol^{-1} at room temperature, 6.0 kcal mol^{-1} more favourable than formation of

21, which is unsurprising given the lack of agostic interaction in **8**. Accordingly, dissociation of BH_3 from **27** is 6.0 kcal mol^{-1} more "uphill" in free energy than from **24**, with Δ_rG = 28.4 kcal mol^{-1}. The stability of **27** can be attributed not only to this, but, given the proposed mechanism of the thermal decompositions of compounds **21** and **23**, and of the reactions of **6** and **4.5** with terminal alkynes presented in Chapter 3, also to the inaccessible 32.2 kcal mol^{-1} free energy barrier of dihydrogen elimination from **8** discussed in Chapter 3, Section 3.2.5.

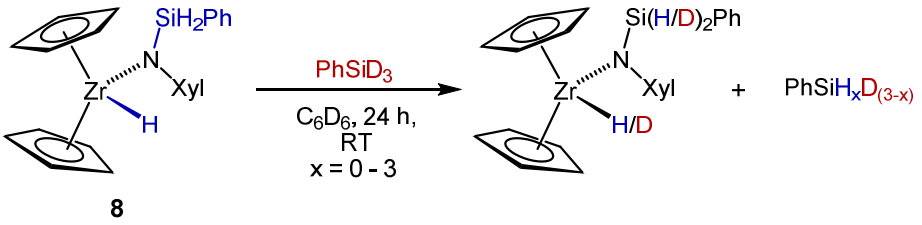
4.3 Reactions of hydride silylamides and silylhydrazides with silanes and chlorosilanes

As discussed in Section 4.1, the reactions of silanes and halosilanes with hydride hydrazido(1–), silyl silylamide and amide silylamide compounds has led to a variety of mechanistic pathways.[3,16,23,36–39] Encouraged by these results, the reactions of the hydride silylamide compounds $Cp_2Zr(H)\{N(^tBu)Si(\mu\text{-}H)RPh\}$ (R = H (**6**), Ph (**7**)) and $Cp_2Zr(H)\{N(Xyl)SiH(R)Ph\}$ (R = H (**8**), Ph (**9**)), as well as the hydride silylhydrazido(1–) compounds $Cp_2Zr(H)\{N(NPh_2)SiH(R)Ph\}$ (R = H (**2**), Ph (**3**)), with silanes and chlorosilanes were investigated. To begin, the reactions of **8** and **9** will be discussed, as these reactions gave the deepest mechanistic insights and kinetic resolution between competing reaction pathways. Subsequently, reactions of **6** and **7**, and **2** and **3** will be discussed.

4.3.1 Reactions of $Cp_2Zr(H)\{N(Xyl)SiH_2Ph\}$ (8) and $Cp_2Zr(H)\{N(Xyl)SiHPh_2\}$ (9) with silanes, chlorosilanes and dihydrogen

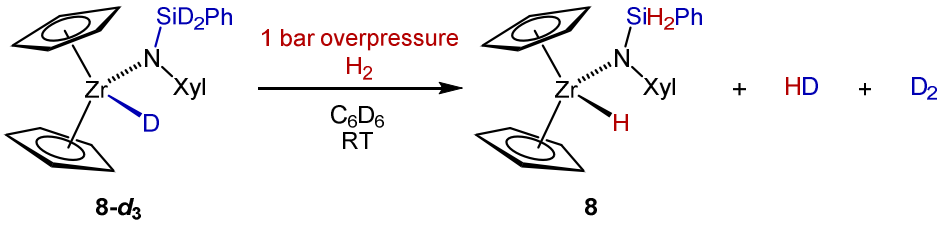
On following the stoichiometric reaction of **8** and $PhSiD_3$, in C_6D_6, by ^1H NMR spectroscopy, incorporation of deuterium into both the Zr–H and Si–H sites of **8** could be observed, along with the appearance of a Si–H resonance envelope based at *ca.* 4.2 ppm

attributable to $PhSiH_3$ and its partially deuterated isotopologues $PhSiH_xD_{(3-x)}$ (x = 1 or 2) (Equation 4.23). A statistical distribution of hydrogen and deuterium across the various Si–H and Zr–H sites was reached after 24 h at room temperature as judged by ^1H NMR spectroscopy. Identical observations were made from the reaction of **8-*d*$_3$** with one equivalent $PhSiH_3$. Furthermore, reaction of a C_6D_6 solution of **8-*d*$_3$** with 1 bar overpressure dihydrogen, in a sealed Young's tap NMR tube, led to complete incorporation of hydrogen into the Zr–D and Si–D sites after several days at room temperature (Equation 4.24). Resonances attributable to HD could be seen in the ^1H NMR spectrum, along with resonances for HD and D_2 in the ^2H NMR spectrum.



8

Equation 4.23



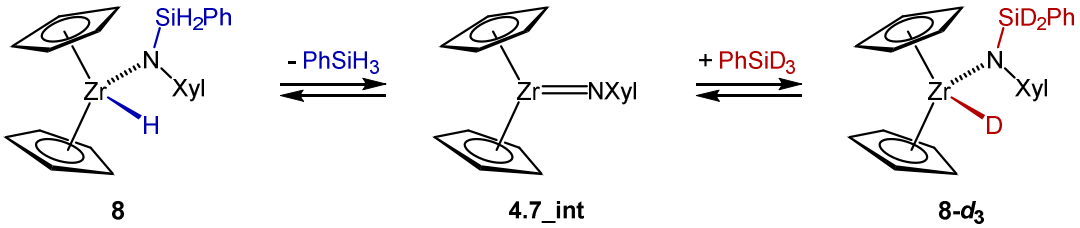
8-*d*$_3$ **8**

Equation 4.24

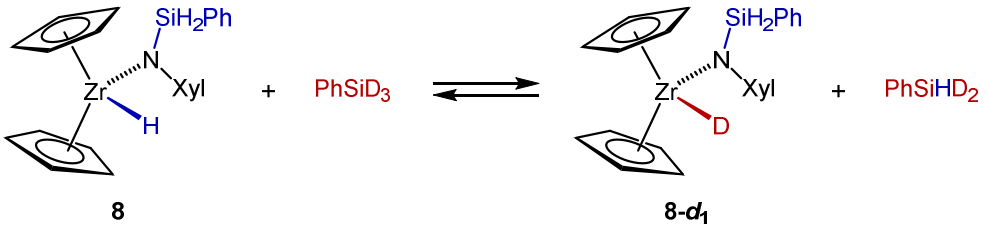
In principal, a number of individual mechanistic steps can take place in the reaction of **8** with $PhSiD_3$, as summarised in Pathways A – D in Scheme 4.6. Pathway A results in net $PhSiH_3$/$PhSiD_3$ exchange *via* the base-free imide $Cp_2Zr(NXyl)$ (**4.7_int**), analogous to the exchange seen for $Cp^*Ti\{MeC(N^iPr)_2\}\{N(NMe_2)SiH_2Ph\}(H)$ (**4.3**). Si–H/Si–D exchange is only enabled through Pathway B (σ-bond metathesis) forming an initial isotopologue **8-*d*$_1$**. The first-formed Zr–D bond of **8-*d*$_1$** can subsequently scramble into the Si–H bonds *via* either dissociative Pathway C (related to Pathway A and proceeding *via* **4.7_int**) or non-dissociative Pathway D, which invokes the silane adduct **8-*d*$_1$_int**.

Species akin to **8-*d*$_1$_int** are invariably found as intermediates (stationary points) along the reaction coordinate for Si–H addition to (L)M=NR bonds and immediately precede the Si–H cleavage event.[23,36,37,39] Indeed, such adducts were found in the DFT calculated mechanism for silane addition to both $Cp_2Zr(NXyl)(THF)$ (**4.7**) and $Cp_2Zr(N^tBu)(THF)$ (**4.8**) (see Appendix, Figures A4 and A2, respectively). Notably, the transition state (**TS1**) and free energy barriers between the base-free imides $Cp_2Zr{=}NXyl$ and $Cp_2Zr{=}N^tBu$ and these silane adducts were not able to be calculated. From Δ_rH, however, the upper bounds for the free energy barrier of silane elimination from **8** and **6** can be calculated and compared to the energy barrier for adduct formation. For **8**, silane elimination has a maximum free energy barrier of 37.7 kcal mol^{-1}, compared to the computed 27.7 kcal mol^{-1} barrier for adduct formation, and for **6**, silane elimination has a maximum free energy barrier of 37.5 kcal mol^{-1}, compared to the computed 27.8 kcal mol^{-1} barrier for adduct formation. These calculations imply Pathway D should have a lower free energy barrier than Pathways A and C.

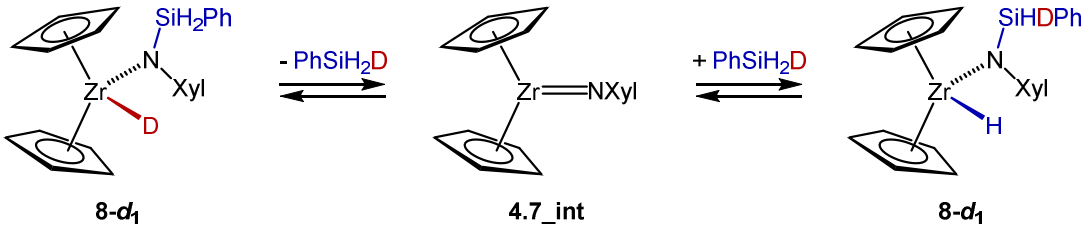
Pathway A: net $PhSiH_3/PhSiD_3$ exchange *via* reversible 1,2-addition



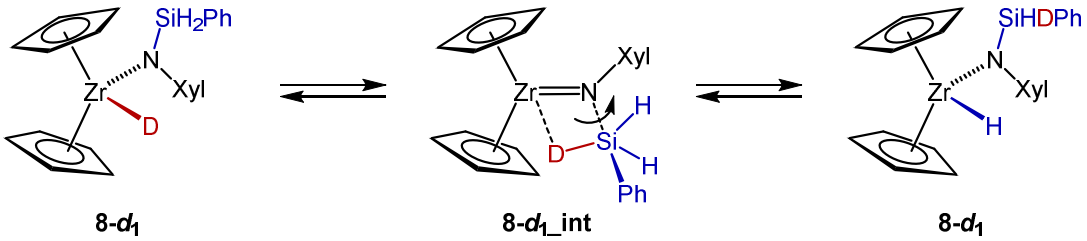
Pathway B: intermolecular Zr-H/Si-D σ-bond metathesis



Pathway C: intramolecular Zr-H/Si-D exchange *via* a dissociative pathway



Pathway D: intramolecular Zr-H/Si-D exchange *via* a non-dissociative pathway

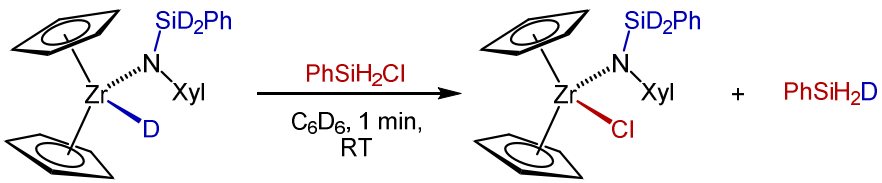


Scheme 4.6: Plausible pathways for silane and Zr–H(D)/Si–H(D) exchange reactions of $Cp_2Zr(H)\{N(Xyl)SiH_2Ph\}$ (**8**).

Notably, it can be observed that in the reaction of **8-*d*$_3$** with $PhSiH_3$ hydrogen is incorporated more rapidly into the Zr–D site than the Si–D sites, with the relative integrals of ZrH and SiH_2 reaching 0.61 and 0.11, respectively, after one hour. This indicates σ-bond metathesis occurs as the kinetically most favoured route of exchange reaction, with other, slower exchange pathways available to allow observation of Si–H/D exchange. Additionally, it can be observed that reaction of **8-*d*$_3$** with $PhSiH_2Cl$ gives immediate conversion to $Cp_2Zr(Cl)\{N(Xyl)SiD_2Ph\}$ (**11-*d*$_2$**, Equation 4.25), confirming the occurrence of σ-bond metathesis. This is in contrast to the reactions of

4.3-*d*$_3$ with $PhSiH_2Cl$ which gave Cp*Ti{MeC(N^{i}Pr)$_2$}{N(NMe$_2$)SiH$_2$Ph)}(Cl) and $PhSiD_3$ *via* transiently formed Cp*Ti{MeC(N^{i}Pr)$_2$}(NNMe$_2$) (analogous to Pathway A in Scheme 4.6).[36,37]

The difference between the reactions of **8** and **4.3** is most likely related to the Δ_rG (more specifically, the respective activation free energy) for silane elimination. Indeed, silane elimination from the DFT model compound of **4.3**, Cp*Ti{MeC(N^{i}Pr)$_2$}{N(NMe$_2$)SiH$_2$Me}(H), was calculated to be 21.6 kcal mol^{-1}, compared to a minimum of 27.7 kcal mol^{-1}, assuming no barrier for silane elimination from the silane adduct **Int1** in Figure A4 (see Appendix), and a maximum of 37.7 kcal mol^{-1} for **8** at 298.15 K. No incorporation of deuterium into the Si–H sites of **11** was observed when reacted with $PhSiD_3$, even upon heating to 80 °C, which can be expected as the formation of **8** from **11** is calculated to be significantly endergonic (Δ_rG = 18.2 kcal mol^{-1} for **11** + $PhSiH_3$ → **8** + $PhSiH_2Cl$).

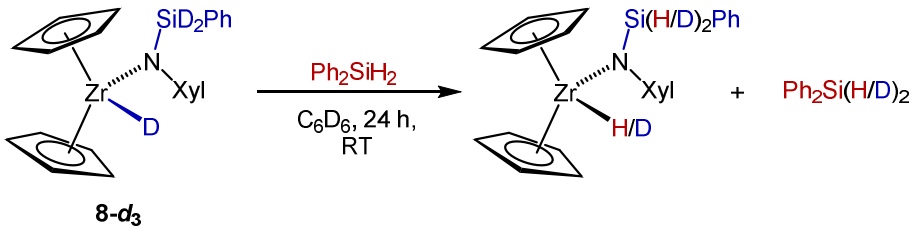


8-*d*$_3$ **11-*d*$_2$**

Equation 4.25

With σ-bond metathesis (Pathway B) established as the most facile exchange pathway, further investigations into Pathways A, C and D were required. Reaction of **8-*d*$_3$** with Ph_2SiH_2 showed incorporation of hydrogen into the Zr–D and Si–D sites of **8-*d*$_3$** (Equation 4.26). A statistical distribution was reached after 24 h at room temperature and, as with the reaction of **8-*d*$_3$** with $PhSiH_3$, incorporation at the Zr–D site was seen to be faster than at the Si–D sites. Notably, $Cp_2Zr(H)\{N(Xyl)SiHPh_2\}$ (**9**), nor any of its isotopologues, were formed in the reaction. Incorporation of hydrogen

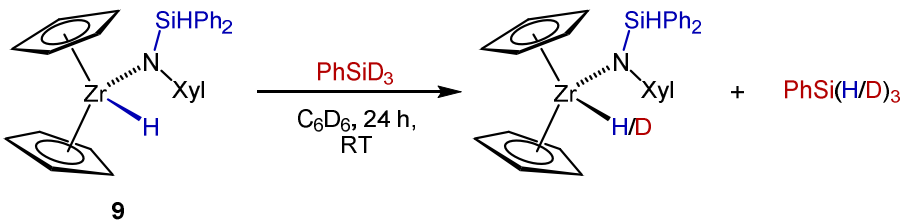
into the Si–D sites therefore appears to occur *via* Pathway D (non-dissociative exchange). However, Pathway C could still be occurring, if addition of $PhSi(H/D)_3$ to **4.7_int** to form **8** is sufficiently kinetically and thermodynamically favourable over the addition of Ph_2SiH_2 to **4.7_int** to form **9**.



8-*d*$_3$

Equation 4.26

A competition experiment between $PhSiH_3$ and Ph_2SiH_2 was carried out by reacting $Cp_2Zr(NXyl)(THF)$ (**4.7**) with 5 equivalents $PhSiH_3$ and Ph_2SiH_2 in order to test the kinetic preference for the addition of either silane. Rapid formation of **8** and **9** was observed in a 3:1 ratio and this ratio did not change over time, showing that, while the addition is $PhSiH_3$ is kinetically favoured over Ph_2SiH_2, the preference is not overwhelming. The computed Δ_rG for **8** + Ph_2SiH_2 → **9** + $PhSiH_3$ is –3.3 kcal mol^{-1}. These results confirm that dissociative exchange (Pathways A and C), while thermodynamically viable, is kinetically inaccessible and cannot account for the experimental observations. Furthermore, stoichiometric reaction of **9** with $PhSiD_3$ gave only deuteration at Zr–H, with a statistical distribution of deuterium between the Zr and silane reached after 4 days at room temperature. This reaction shows that Pathway A, C and D are not accessible for **9** at room temperature (Equation 4.27) and explicitly demonstrates Zr–H/Si–D σ-bond metathesis (Pathway B).

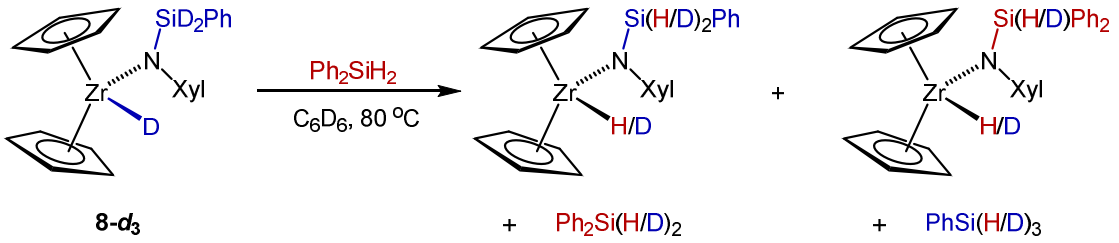


9

Equation 4.27

These experiments show that Pathways A and C cannot be occurring in the reaction of **8-*d*$_3$** with Ph_2SiH_2 or $PhSiD_3$ at room temperature and silane elimination from **8** and **9** is inaccessible at room temperature. Therefore, Pathway D must account for the incorporation of hydrogen into the Si–D sites of **8-*d*$_3$**. To confirm the invoked Pathway D occurs intramolecularly, **8-*d*$_3$** was reacted with 2.5 equivalents $PhSiH_3$ for 45 minutes at room temperature in C_6D_6 before the excess silane was removed *in vacuo* and the residue redissolved. At this time, the relative integrals of ZrH and SiH protons were observed to be 0.89 and 0.19, respectively. After 24 hours, hydrogen had been redistributed between the Zr and Si sites to give relative integrals of 0.48 and 0.71, respectively. As dissociation of the silane cannot occur at room temperature, this supports the occurrence of Pathway D and that the barrier to silane elimination is greater than adduct formation.

Upon heating the reaction mixture of **8-*d*$_3$** and Ph_2SiH_2 to 80 °C, the slow formation of **9** and its isotopologues, could be observed confirming that Pathways A and C are accessible under forcing conditions and are kinetically inaccessible at room temperature (Equation 4.28). The Δ_rG values for silane elimination from **6** and **7** reduce by *ca.* 2.5 kcal mol^{-1} at 80 ^oC and a similar phenomenon would be expected for **8** and **9**. This entropic contribution and the general Boltzmann effects of temperature account for the observation of Pathways A and C at 80 °C. A similar observation can be made for the reaction of **9** with $PhSiD_3$ at 80 °C, where Pathways A, C and D are observed under these more forcing conditions. However, kinetic resolution between the dissociative and non-dissociative pathways for silane exchange of **9** was not possible and noticeable decomposition of **8** and **9** occurs under these reaction conditions.



Equation 4.28

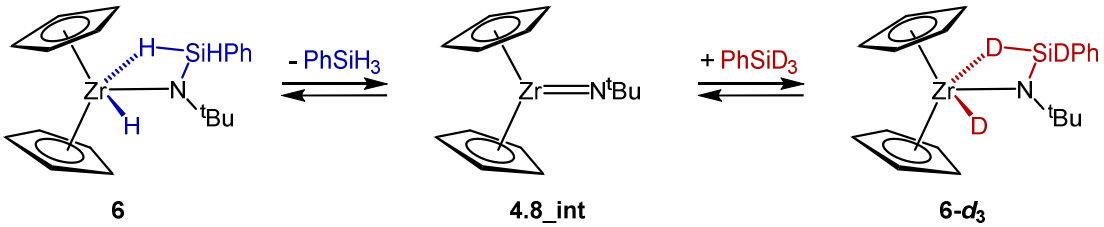
These reactions have shown the various pathways of silane exchange available to the silylxylylamido compounds **8** and **9**, showing kinetic discrimination between each pathway for **8**. σ-Bond metathesis is the most facile route (Pathway B), followed by intramolecular Zr–H(D)/Si–D(H) exchange *via* a non-dissociative route (Pathway D), with dissociative exchange of silane (Pathways A and C) only occurring at elevated temperatures. DFT calculations are consistent with these observations. Notably, this is in contrast to what was seen for compound **4.3** where dissociative exchange was the most facile route, with this being attributed to the respective free energy barriers to silane elimination.[36] Furthermore, this is the first explicit example of non-dissociative exchange pathway, which was shown in the absence of silane and at room temperature – conditions under which dissociative exchange is inaccessible.

4.3.2 Reactions of $Cp_2Zr(H)\{N(^tBu)Si(\mu\text{-}H)HPh\}$ (6) and $Cp_2Zr(H)\{N(^tBu)Si(\mu\text{-}H)Ph_2\}$ (7) with silanes and chlorosilanes

Analogous reactions to those carried out for **8** and **9** were carried out for $Cp_2Zr(H)\{N(^tBu)Si(\mu\text{-}H)HPh\}$ (**6**) and $Cp_2Zr(H)\{N(^tBu)Si(\mu\text{-}H)Ph_2\}$ (**7**). Stoichiometric reaction of $PhSiD_3$ and **6** gave incorporation of deuterium into both the Zr–H and Si–H sites of **6**, with a statistical distribution being reached after 24 h. This is analogous to what was observed for **8** and analogously pathways A – D (Scheme 4.7) could, in principal, take place. Additionally, Pathway E (Scheme 4.8), involving the reversible elimination of dihydrogen from **6** *via* **13_int**, could also be occurring as a

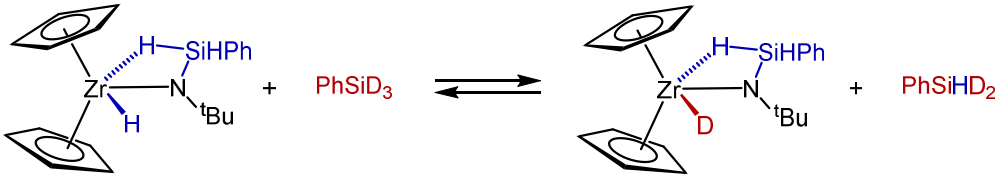
pathway for intramolecular Zr–H/Si–H exchange. This pathway is calculated to have a thermally accessible free energy barrier of 20.5 kcal mol^{-1} and dihydrogen elimination is observed from **6** on reaction with terminal alkynes. Such a pathway was not proposed for the xylylsilylamides **8** and **9** as the free energy barrier for dihydrogen elimination from **8** is calculated to be 32.2 kcal mol^{-1}. Additional reactions were conducted to investigate these pathways.

Pathway A: net $PhSiH_3/PhSiD_3$ exchange *via* reversible 1,2-addition



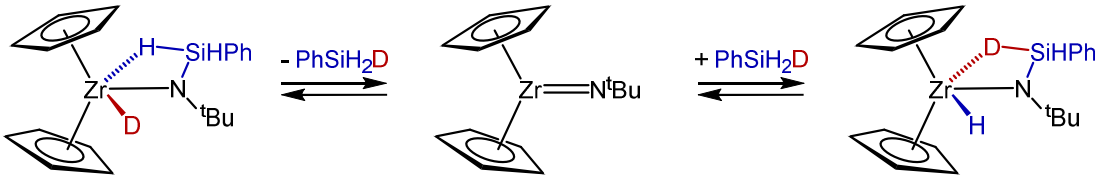
6 **4.8_int** **6-d_3**

Pathway B: intermolecular Zr-H/Si-D σ-bond metathesis



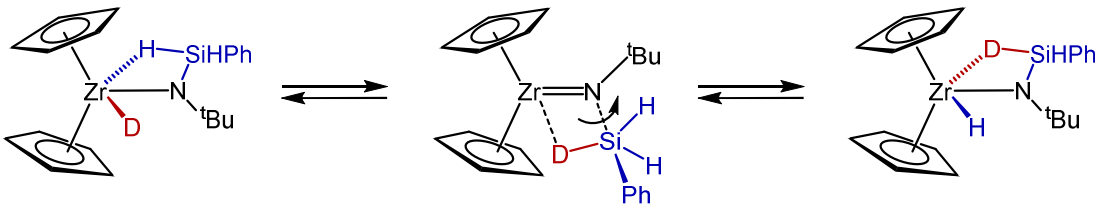
6 **6-d_1**

Pathway C: intramolecular Zr-H/Si-D exchange *via* a dissociative pathway



6-d_1 **4.8_int** **6-d_1** (one isomer shown)

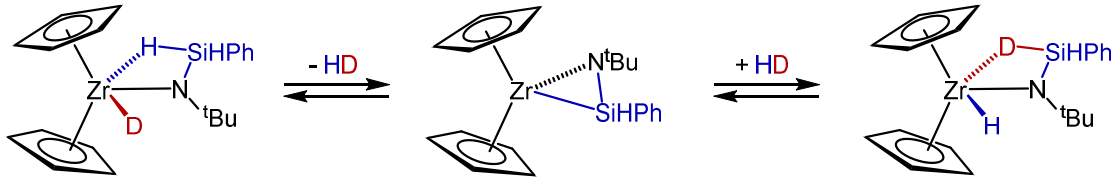
Pathway D: intramolecular Zr-H/Si-D exchange *via* a non-dissociative pathway



6-d_1 **6-d_1_int** **6-d_1** (one isomer shown)

Scheme 4.7: Plausible pathways for silane and Zr–H(D)/Si–H(D) exchange reactions of $Cp_2Zr(H)\{N(^tBu)Si(\mu\text{-}H)HPh\}$ (**6**).

Pathway E: intramolecular Zr-H/Si-D exchange *via* dihydrogen formation



6-*d*$_1$ **13_int** **6-*d*$_1$** (one isomer shown)

Scheme 4.8: Pathway for intramolecular silane and Zr–H/Si–D exchange reactions of **6** *via* dihydrogen formation.

Addition of $PhSiD_3$ to the chloride silylamide $Cp_2Zr(Cl)\{N(^tBu)Si(\mu\text{-}H)HPh\}$ (**10**) gave no reaction, even upon heating to 80 °C, consistent with the overall exchange reaction **10** + $PhSiH_3$ → **6** + $PhSiH_2Cl$ being significantly endergonic (Δ_rG = 12.8 kcal mol^{-1}), as expected, and $PhSiH_2Cl$ elimination from **10** to give $[Cp_2Zr(N^tBu)]$ (**4.8_int**) having Δ_rG = 36.5 kcal mol^{-1}. Furthermore, reaction of **6-*d*$_3$** with $PhSiH_2Cl$ gave instant conversion to **10-*d*$_2$**, with no incorporation of hydrogen into the Si–D sites, confirming Pathway B.

As with the reaction of **8-*d*$_3$** with Ph_2SiH_2, reaction of **6-*d*$_3$** with Ph_2SiH_2 at room temperature showed incorporation of hydrogen into the Zr–D and Si–D sites of **6-*d*$_3$**. A statistical distribution was reached after 24 h at room temperature and neither **7** nor any of its isotopologues were observed. The computed Δ_rG for **6** + Ph_2SiH_2 → **7** + $PhSiH_3$ is –1.5 kcal mol^{-1}, indicating silane exchange reactions (Pathways A and C), whilst thermodynamically viable, are kinetically inaccessible. Therefore intramolecular Zr–H/Si–H exchange pathways must account for the experimental observations. Both Pathway D and E can be proposed here. Pathway D was invoked to occur for the xylylsilylamide **8**, though Pathway E is calculated to occur with a free energy barrier of 20.5 kcal mol^{-1} for **6**, much lower than that of adduct formation (27.8 kcal mol^{-1}), implying the occurrence of Pathway E.

On heating the reaction mixtures of **6-*d*3** with Ph_2SiH_2 and **7** and $PhSiD_3$ to 80 °C formation of **7** and **6**, respectively, as well as their related isotopologues, were formed. This shows the dissociative pathways A and C to be viable under these conditions. As mentioned previously, the calculated Δ_rG values reduce by *ca.* 2.5 kcal mol^{-1} at 80 ºC, this entropic phenomenon, and general Boltzmann effects of temperature, account for these observations. It is also notable that in the reaction of **6** with $PhSiD_3$ the level of incorporation of deuterium at the Si–H sites consistently matched the level of incorporation of deuterium at the Zr–H sites, indicating Pathway D and/or E were occurring at either a faster or identical rate as Pathway B. This is contrary to what was observed for **8** with $PhSiD_3$, where Pathway B was seen to occur at a faster rate than Pathway D.

4.3.3 Reactions of $Cp_2Zr(H)\{N(NPh_2)SiH_2Ph\}$ (2) and $Cp_2Zr(H)\{N(NPh_2)SiHPh_2\}$ (3) with silanes and chlorosilanes

Reactions of the hydride silylhydrazido(1–) compounds $Cp_2Zr(H)\{N(NPh_2)SiH_2Ph\}$ (**2**) and $Cp_2Zr(H)\{N(NPh_2)SiHPh_2\}$ (**3**) with silanes and chlorosilanes were carried out in an analogous manner to those of **6** – **9**. Reactivity was identical to that shown previously with four reaction pathways analogous to those shown in Schemes 4.6 and 4.7 invoked. As with the reactions of **6** and **7**, incorporation of deuterium into the Zr–H and Si–H sites (and hydrogen into the Zr–D and Si–D sites) was observed to occur at the same rate, indicating Pathway D was occurring at a faster or identical rate as Pathway B. In this instance no pathway such as Pathway E shown for **6** in Scheme 4.8 is proposed as a possible explanation for the relative rates, as no dihydrogen elimination chemistry has been observed for **2** or **3**.

4.4 Conclusions

First, this Chapter described the reactions of zirconocene hydride silylamide complexes with boranes. The reactions of $Cp_2Zr(H)\{N(^tBu)Si(\mu\text{-}H)HPh\}$ (**6**) and $Cp_2Zr(H)\{N(Xyl)SiH_2Ph\}$ (**8**) with the primary borane thexylborane led to the formation of the κ^2-organoborohydrides $Cp_2Zr\{(\mu\text{-}H)_2B(H)Tex\}\{N(^tBu)SiH_2Ph\}$ (**18**) and $Cp_2Zr\{(\mu\text{-}H)_2B(H)Tex\}\{N(Xyl)SiH_2Ph\}$ (**19**), respectively. While **19** was formed quantitatively, **18** was formed in equilibrium and was unstable in solution and under vacuum, decomposing to a number of compounds. One decomposition product, $Cp_2Zr\{N(^tBu)Si(H)(Ph)B(Tex)H(\mu\text{-}H)\}$ (**20**), was able to be crystallised from the decomposition mixture.

The reactions of **6**, $Cp_2Zr(H)\{N(^tBu)Si(\mu\text{-}H)Ph_2\}$ (**7**), $Cp_2Zr(H)\{N(^tBu)Si(\mu\text{-}H)Me_2\}$ (**4.5**) and **8** with $BH_3{\cdot}SMe_2$ were also described. For **6** and **8**, these led to the quantitative formation of the κ^2-borohydrides $Cp_2Zr\{(\mu\text{-}H)_2BH_2\}\{N(^tBu)SiH_2Ph\}$ (**21**) and $Cp_2Zr\{(\mu\text{-}H)_2BH_2\}\{N(Xyl)SiH_2Ph\}$ (**27**), respectively. For **7** and **4.5**, the κ^1-borohydrides $Cp_2Zr\{(\mu\text{-}H)BH_3\}\{N(^tBu)Si(\mu\text{-}H)Ph_2\}$ (**22**) and $Cp_2Zr\{(\mu\text{-}H)BH_3\}\{N(^tBu)Si(\mu\text{-}H)Me_2\}$ (**23**) were formed, respectively. These complexes maintained the β-agostic interaction and represent the first structurally characterised Group 4 κ^1-borohydride complexes.

While compound **27** was found to be thermally stable, compounds **21** – **23** were not. Compounds **21** – **23** decomposed to quantitatively form the zirconacycles $Cp_2Zr\{N(^tBu)Si(R)(R')BH_2(\mu\text{-}H)\}$ (R = H, R' = Ph (**24**), R, R' = Ph (**25**) and R, R' = Me (**26**)) and dihydrogen. Structural characterisation and DFT calculations showed these complexes to contain agostic Si–B···Zr and B–H···Zr interactions. Kinetic studies to probe the mechanisms of the thermal decompositions of **21** and **23** were described. These

studies were summarised in Sections 4.2.4 and 4.2.5, with the pathways shown in Schemes 4.4 and 4.5 being proposed. DFT calculations for the thermal decompositions of **21** and **23** were supportive of the proposed pathways. These reactions closely resemble the reactions presented in Chapter 3 of this Thesis, and the invoked insertion of borane into a Zr–Si bond, the exact nature of which could not be determined, is a rare example of such a reaction.

Next, the reactions of zirconocene hydride silylamide complexes **6** – **9** and the silylhydrazido(1–) complexes $Cp_2Zr(H)\{N(NPh_2)SiH_2Ph\}$ (**2**) and $Cp_2Zr(H)\{N(NPh_2)SiHPh_2\}$ (**3**) with silanes and chlorosilanes were described and observations were supported by DFT calculations. For all compounds three reaction mechanisms were found to be occurring as summarised in Schemes 4.6 and 4.7: dissociative exchange of the silane *via* imido or hydrazido intermediates (Pathway A/C); σ-bond metathesis between Zr–H/D bonds and Si–H/D or Si–Cl bonds of the free silanes (Pathway B); or non-dissociative exchange *via* silane adducts (Pathway D). Pathways A and C were found to be the least kinetically accessible for all complexes. For the silylxylylamides **8** and **9**, Pathway B was found to be kinetically favoured over Pathway D. In contrast for **2**, **3**, **6** and **7** this was not observed and for **6** and **7** a pathway involving the formation of a dihydrogen σ-adduct (Pathway E) was proposed, due to the previously observed reactivity of these complexes and DFT computed mechanism of dihydrogen elimination from **6**.

4.5 References

1 L. J. Procopio, P. J. Carroll and D. H. Berry, *J. Am. Chem. Soc.*, 1991, **113**, 1870–1872.
2 L. J. Procopio, P. J. Carroll and D. H. Berry, *Organometallics*, 1993, **12**, 3087–3093.
3 N. A. McLeod, L. G. Kuzmina, I. Korobkov, J. A. K. Howard and G. I. Nikonov, *Dalton Trans.*, 2016, **45**, 2554–2561.
4 A. Y. Khalimon, R. Simionescu, L. G. Kuzmina, J. A. K. Howard and G. I. Nikonov, *Angew. Chem., Int. Ed.*, 2008, **47**, 7701–7704.
5 S. J. Simpson, H. W. Turner and R. A. Andersen, *J. Am. Chem. Soc.*, 1979, **101**, 7728–7729.
6 S. J. Simpson and R. A. Andersen, *Inorg. Chem.*, 1981, **20**, 3627–3629.
7 D. C. Bradley, H. Chudzynska, J. D. J. Backer-Dirks, M. B. Hursthouse, A. A. Ibrahim, M. Motevalli and A. C. Sullivan, *Polyhedron*, 1990, **9**, 1423–1427.
8 P. Berno, R. Minhas, S. Hao and S. Gambarotta, *Organometallics*, 1994, **13**, 1052–1054.
9 C. P. Gerlach and J. Arnold, *Organometallics*, 1996, **15**, 5260–5262.
10 H. Cai, X. Yu, T. Chen, X. T. Chen, X. Z. You and Z. Xue, *Can. J. Chem.*, 2003, **81**, 1398–1405.
11 M. Niemeyer, *Inorg. Chem.*, 2006, **45**, 9085–9095.
12 O. Bénaud, J. C. Berthet, P. Thuéry and M. Ephritikhine, *Inorg. Chem.*, 2010, **49**, 8117–8130.
13 K. Yan, A. Ellern and A. D. Sadow, *J. Am. Chem. Soc.*, 2012, **134**, 9154–9156.
14 K. Yan, J. J. Duchimaza Heredia, A. Ellern, M. S. Gordon and A. D. Sadow, *J. Am. Chem. Soc.*, 2013, **135**, 15225–15237.
15 K. Yan and A. D. Sadow, *Chem. Commun.*, 2013, **49**, 3212–3214.
16 A. Y. Khalimon, R. Simionescu and G. I. Nikonov, *J. Am. Chem. Soc.*, 2011, **133**, 7033–7053.
17 S. K. Ignatov, N. H. Rees, A. A. Merkoulov, S. R. Dubberley, A. G. Razuvaev, P. Mountford and G. I. Nikonov, *Chem. Eur. J.*, 2008, **14**, 296–310.
18 W. A. Nugent, D. W. Ovenall and S. J. Holmes, *Organometallics*, 1983, **2**, 161–162.
19 A. Koperniku, P. J. Foth, G. M. Sammis and L. L. Schafer, *J. Am. Chem. Soc.*, 2019, **141**, 18944–18948.
20 S. L. Buchwald, B. T. Watson, M. W. Wannamaker and J. C. Dewan, *J. Am. Chem. Soc.*, 1989, **111**, 4486–4494.
21 M. S. Hill, M. Hodgson, D. J. Liptrot and M. F. Mahon, *Dalton Trans.*, 2011, **40**, 7783–7790.
22 P. Bellham, M. S. Hill, G. Kociok-Köhn and D. J. Liptrot, *Chem. Commun.*, 2013, **49**, 1960–1962.
23 L. C. Stevenson, DPhil Thesis, University of Oxford, 2015.
24 J. Knizek and H. Nöth, *Eur. J. Inorg. Chem.*, 2011, **2011**, 1888–1900.
25 A. L. Johnson, M. G. Davidson and M. F. Mahon, *J. Chem. Soc., Dalton Trans.*, 2006, 5405–5411.
26 F.-C. Liu, J. Liu, E. A. Meyers and S. G. Shore, *Inorg. Chem.*, 1999, **38**, 2169–2173.
27 Q. Jiang, P. J. Carroll and D. H. Berry, *Organometallics*, 1993, **12**, 177–183.
28 D. Baudry, A. Dormond, B. Lachot, M. Visseaux and G. Zucchi, *J. Organomet.*

Chem., 1997, **547**, 157–165.
29 D. Barbier-Baudry, A. Dormond and M. Visseaux, *J. Organomet. Chem.*, 2000, **609**, 21–28.
30 W. J. Evans, J. M. Perotti and J. W. Ziller, *Inorg. Chem.*, 2005, **44**, 5820–5825.
31 D. Pun, E. Lobkovsky and P. J. Chirik, *Chem. Commun.*, 2007, 3297–3299.
32 S. C. P. Joseph, F. G. N. Cloke, P. B. Hitchcock and C. J. Cardin, *Organometallics*, 1995, **14**, 3566–3569.
33 P. A. Lummis, R. McDonald, M. J. Ferguson and E. Rivard, *Dalton Trans.*, 2015, **44**, 7009–7020.
34 L. H. Rude, M. Corno, P. Ugliengo, M. Baricco, Y. S. Lee, Y. W. Cho, F. Besenbacher, J. Overgaard and T. R. Jensen, *J. Phys. Chem. C*, 2012, **116**, 20239–20245.
35 W. K. Kot, N. M. Edelstein and A. Zalkin, *Inorg. Chem.*, 1987, **26**, 1339–1341.
36 P. J. Tiong, A. Nova, A. D. Schwarz, J. D. Selby, E. Clot and P. Mountford, *Dalton Trans.*, 2012, **41**, 2277.
37 P. J. Tiong, DPhil Thesis, University of Oxford, 2012.
38 T. E. Hanna, I. Keresztes, E. Lobkovsky, W. H. Bernskoetter and P. J. Chirik, *Organometallics*, 2004, **23**, 3448–3458.
39 L. C. Stevenson, S. Mellino, E. Clot and P. Mountford, *J. Am. Chem. Soc.*, 2015, **137**, 10140–10143.
40 D. J. Parks, R. E. Rupert and W. E. Piers, *Angew. Chem., Int. Ed.*, 1995, **34**, 809–811.
41 F. A. Perras and D. L. Bryce, *Chem. Sci.*, 2014, **5**, 2428–2437.
42 L. J. Procopio, P. J. Carroll and D. H. Berry, *J. Am. Chem. Soc.*, 1994, **116**, 177–185.
43 T. J. Marks and J. R. Kolb, *Chem. Rev.*, 1977, **77**, 263–293.
44 E. Ding, B. Du, F. C. Liu, S. Liu, E. A. Meyers and S. G. Shore, *Inorg. Chem.*, 2005, **44**, 4871–4878.
45 H. Braunschweig, M. Colling, C. Kollann and U. Englert, *J. Chem. Soc., Dalton Trans.*, 2002, 2289–2296.
46 G. Dübek, D. Franz, C. Eisenhut, P. J. Altmann and S. Inoue, *Dalton Trans.*, 2019, **48**, 5756–5765.
47 S. Khoo, Y. L. Shan, M. C. Yang, Y. Li, M. Der Su and C. W. So, *Inorg. Chem.*, 2018, **57**, 5879–5887.
48 S. M. I. Al-Rafia, A. C. Malcolm, R. Mc Donald, M. J. Ferguson and E. Rivard, *Chem. Commun.*, 2012, **48**, 1308–1310.
49 S. Kaufmann, S. Schäfer, M. T. Gamer and P. W. Roesky, *Dalton Trans.*, 2017, **46**, 8861–8867.
50 A. Jana, D. Leusser, I. Objartel, H. W. Roesky and D. Stalke, *Dalton Trans.*, 2011, **40**, 5458–5463.
51 V. D. Thalangamaarachchige, N. J. Silva, D. K. Unruh, A. J. A. Aquino and C. Krempner, *Tetrahedron*, 2019, **75**, 1861–1864.
52 H. Cui, M. Wu and P. Teng, *Eur. J. Inorg. Chem.*, 2016, **2016**, 4123–4127.
53 M. Y. Abraham, Y. Wang, Y. Xie, P. Wei, H. F. Schaefer, P. V. R. Schleyer and G. H. Robinson, *J. Am. Chem. Soc.*, 2011, **133**, 8874–8876.
54 B. J. Guddorf, A. Hepp and F. Lips, *Chem. Eur. J.*, 2018, **24**, 10334–10338.
55 R. Rodriguez, T. Troadec, T. Kato, N. Saffon-Merceron, J.-M. Sotiropoulos and A. Baceiredo, *Angew. Chem., Int. Ed.*, 2012, **51**, 7158–7161.
56 H. Wang, T. L. Chan and Z. Xie, *Chem. Commun.*, 2018, **54**, 385–388.
57 R. Azhakar, G. Tavčar, H. W. Roesky, J. Hey and D. Stalke, *Eur. J. Inorg.*

Chem., 2011, **2011**, 475–477.
58 T. D. Tilley, *Organometallics*, 1985, **4**, 1452–1457.
59 A. D. Horton and A. G. Orpen, *Organometallics*, 1991, **10**, 3910–3918.
60 F. Schaper and H.-H. Brintzinger, *Acta Crystallogr. Sect. C Cryst. Struct. Commun.*, 2000, **56**, e78–e78.
61 R. F. Jordan, P. K. Bradley, N. C. Baenziger and R. E. LaPointe, *J. Am. Chem. Soc.*, 1990, **112**, 1289–1291.
62 F.-C. Liu, J.-H. Chen, S.-C. Chen, K.-Y. Chen, G.-H. Lee and S.-M. Peng, *J. Organomet. Chem.*, 2005, **690**, 291–300.
63 W. Scherer, V. Herz and C. Hauf, *Struct. Bond.*, 2012, **146**, 159–207.
64 M. Brookhart, M. L. H. Green and L.-L. Wong, *Prog. Inorg. Chem.*, 1988, **36**, 1–124.
65 A. E. Reed, L. A. Curtiss and F. Weinhold, *Chem. Rev.*, 1988, **88**, 899–926.
66 F. Weinhold and C. R. Landis, *Valency and Bonding: A Natural Bond Orbital Donor-Acceptor Perspective*, Cambridge University Press, Cambridge, 2005.
67 A. J. Bridgeman, G. Cavigliasso, L. R. Ireland and J. Rothery, *J. Chem. Soc., Dalton Trans.*, 2001, 2095–2108.
68 E. Clot and O. Eisenstein, *Struct. Bond.*, 2004, **113**, 1–32.
69 W. Scherer and G. S. McGrady, *Angew. Chem., Int. Ed.*, 2004, 43, 1782–1806.
70 G. I. Nikonov, *J. Organomet. Chem.*, 2001, **635**, 24–36.
71 P. D. Bolton, E. Clot, N. Adams, S. R. Dubberley, A. R. Cowley and P. Mountford, *Organometallics*, 2006, **25**, 2806–2825.
72 N. Koga and K. Morokuma, *J. Am. Chem. Soc.*, 1988, **110**, 108–112.
73 D. L. Clark, J. C. Gordon, P. J. Hay, R. L. Martin and R. Poli, *Organometallics*, 2002, **21**, 5000–5006.
74 E. D. Brady, D. L. Clark, J. C. Gordon, P. J. Hay, D. W. Keogh, R. Poli, B. L. Scott and J. G. Watkin, *Inorg. Chem.*, 2003, **42**, 6682–6690.
75 H. Nöth and G. Höllerer, *Chem. Ber.*, 1966, **99**, 2197–2205.
76 W. Biffar, H. Nöth and R. Schwerthöffer, *Liebigs Ann. der Chemie*, 1981, **1981**, 2067–2080.
77 M. Suginome, *Organometallics*, 2000, **19**, 4647–4649.
78 M. Oestreich, E. Hartmann and M. Mewald, *Chem. Rev.*, 2013, 113, 402–441.
79 T. A. Boebel and J. F. Hartwig, *Organometallics*, 2008, **27**, 6013–6019.
80 X. Chen, Y. Zhang, Y. Wang, W. Zhou, D. A. Knight, T. B. Yisgedu, Z. Huang, H. K. Lingam, B. Billet, T. J. Udovic, G. M. Brown, S. G. Shore, C. Wolverton and J. C. Zhao, *Chem. Sci.*, 2012, **3**, 3183–3191.
81 D. E. Walmsley, W. L. Budde and M. F. Hawthorne, *J. Am. Chem. Soc.*, 1971, **93**, 3150–3155.
82 R. G. Potter, D. M. Camaioni, M. Vasiliu and D. A. Dixon, *Inorg. Chem.*, 2010, **49**, 10512–10521.
83 H. Kameo, Y. Baba, S. Sakaki, Y. Tanaka and H. Matsuzaka, *Inorg. Chem.*, 2020, **59**, 4282–4291.
84 G. C. Lloyd-Jones and N. P. Taylor, *Chem. Eur. J.*, 2015, **21**, 5423–5428.
85 J. Burés, *Angew. Chem., Int. Ed.*, 2016, **55**, 16084–16087.
86 C. D. T. Nielsen and J. Burés, *Chem. Sci.*, 2019, 10, 348–353.
87 D. G. Truhlar and A. Kohen, *Proc. Natl. Acad. Sci. U. S. A.*, 2001, **98**, 848–851.
88 G. Parkin, *J. Label. Compd. Radiopharm.*, 2007, **50**, 1088–1114.
89 B. A. Clough and P. Mountford, *Organometallics*, 2018, **37**, 3558–3572.
90 J. L. Polse, R. A. Andersen and R. G. Bergman, *J. Am. Chem. Soc.*, 1995, **117**, 5393–5394.

91 M. G. Omez-Gallego and M. A. Sierra, *Chem. Rev*, 2011, **111**, 4857–4963.
92 S. Bi, S. Zhu and Z. Zhang, *Eur. J. Inorg. Chem.*, 2007, **2007**, 2046–2054.

Chapter Five

Titanium permethylpentalene chemistry

5.1 Introduction

5.1.1 Overview

The work presented in this Chapter sits separate from the zirconocene chemistry presented in Chapters 2, 3 and 4, and concerns the chemistry of titanium permethylpentalene (Pn*) complexes. As such, a brief overview of pentalene ligand, its nomenclature, synthesis, coordination chemistry and its application as a ligand in Group 4 complexes will be given. The pentalene ligand has been cited for comparisons between the (η^8-Pn)M and bent-metallocene Cp_2M motifs. To this end, particular interest will be paid to the use of pentalene as an η^8-bound ancillary ligand to metal complexes that display notable small molecule reactivity with respect to their metallocene analogous. Lastly in this introduction, metallocene analogues of interest with regard to the work presented in this Chapter, such as the Tebbe reagent ($Cp_2Ti(\mu\text{-}CH_2)(\mu\text{-}Cl)AlMe_2$) and Petasis reagent ($Cp_2TiMe_2$), will also briefly be discussed.

5.1.2 Nomenclature

In this Chapter, "pentalene" may refer to dihydropentalene, C_8H_8, pentalene, C_8H_6, or the pentalene dianion $[C_8H_6]^{2-}$. Appropriate prefixes are added to donate substituents. Figure 5.1 shows the numbering system and nomenclature of the carbocyclic framework of pentalene, shown as the dianion $[C_8H_6]^{2-}$. Carbons 1, 3, 5 and 7 pertain to the non-wingtip (NWT) positions; carbons 2 and 6 pertain to the wingtip (WT) positions; and carbons 4 and 8 pertain to the bridgehead positions.

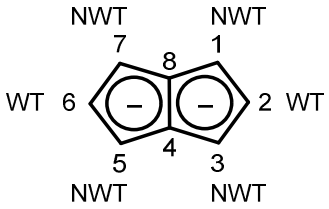
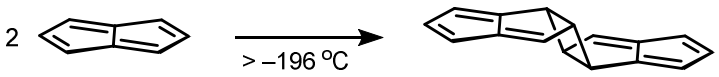


Figure 5.1: The numbering system and nomenclature of the pentalene carbocyclic ring. NWT = non-wingtip and WT = wingtip.

5.1.3 Synthesis of pentalene and pentalene-derivatives

The neutral pentalene molecule, C_8H_6, is an 8π anti-aromatic planar molecule with a bond-alternant C_{2h} structure.[1–3] Given its anti-aromaticity it is highly unstable and dimerises by [2+2] cycloaddition to give $[C_8H_6]_2$ at temperatures above –196 °C (Equation 5.1).[3–7] This dimerisation prevents access to the 10π aromatic pentalene dianion, which is of interest for its use in organometallic chemistry, by alkali metal reduction. In comparison, the isoelectronic molecule cyclooctatetraene (C_8H_8, COT), which, due to the absence of the transannular bond of pentalene, can adopt a tub-shaped conformation to alleviate the anti-aromaticity and give thermal stability, is easily reduced by alkali metals to the $[COT]^{2-}$ dianion.[8,9] Due to this, efforts have focussed on the synthesis of dihydropentalenes, which can be doubly deprotonated to form $[Pn]^{2-}$ synthons.

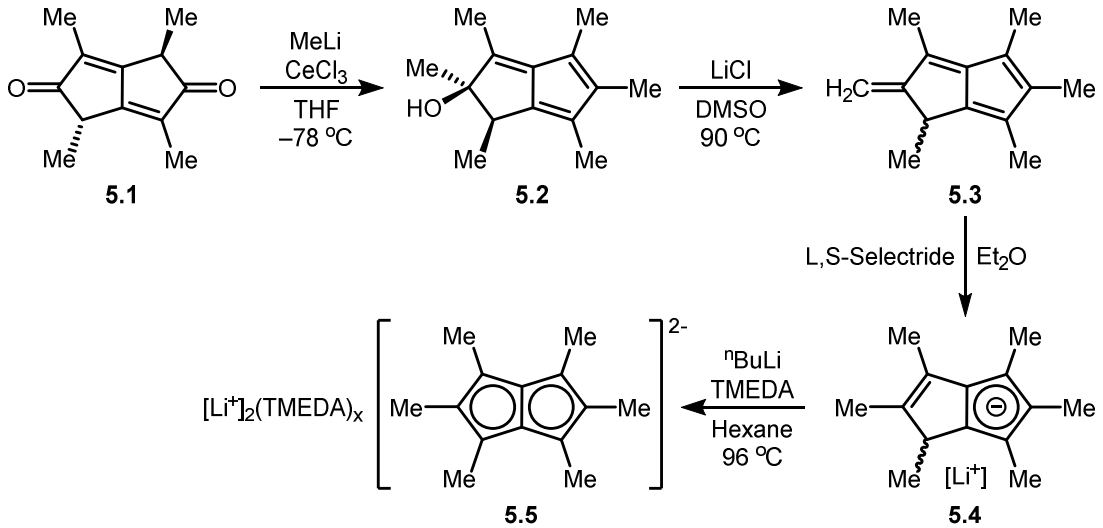


Equation 5.1[3,5]

Several flash vacuum pyrolysis reactions yielding dihydropentalene have been reported using isodicyclopentadienes and COT at temperatures of 550 – 600 °C.[10–12] The ring expansion of dibromocyclopropane substituted cyclohelpatrienes also leads to dihydropentalene and mono-subsituted derivatives.[13,14] A third route involves intramolecular cyclisation of 6-(2-aminovinyl)fulvenes.[15,16] Subsequent deprotonation of dihydropentalenes with ^{n}BuLi·DME affords $C_8H_6[Li(DME)]_2$ and mono-substituted

derivatives. $C_8H_6[Li(DME)]_2$ has also been used to access substituted derivatives of dihydropentalene.[12,17] For example addition of 2 equivalents $^{i}Pr_3SiOTf$ yielded 1,5-$C_8H_6(Si^{i}Pr_3)$ ($Pn^{\dagger}H_2$).[12] Subsequent addition of 2 equivalents KNH_2 provided the dipotassiated dianion $Pn^{\dagger}K_2$. This alkyl substitution removes the problems of solubility of Pn and diastereomer formation of mono-substituted $Pn^{1\text{-}R}$ derivatives.

Most relevant to this Chapter is the multi-step synthesis of permethylpentalene, $[Pn^*]^{2-}$, reported by O'Hare and co-workers (Scheme 5.1).[18–20] Here, methylation of *trans*-2,4,6,8-tetramethylbicyclo[3.3.0]octa-1,5-diene-3,7-dione (**5.1**) and subsequent, *in situ*, dehydration gives **5.3**, the exocyclic isomer of the neutral permethylpentalene molecule, C_8Me_6. Addition of a hydride, delivered by L,S-selectride, at the exocyclic double bond to give **5.4**, followed by deprotonation by reflux in excess ^{n}BuLi yields Pn^*Li_2 (**5.5**) on a 15 g scale.



Scheme 5.1: Synthesis of Pn^*Li_2 (**5.5**) from *trans*-2,4,6,8-tetramethylbicyclo[3.3.0]octa-1,5-diene-3,7-dione (**5.1**).[18–20]

5.1.4 Pentalene coordination chemistry

The pentalene dianion (Pn^{2-}) can coordinate to metals in a variety of bonding modes, the most prevalent of which are shown in Figure 5.2.[18,21] η^1,η^1-Bond is typically observed when coordinated to p-block elements such as in 1,5-$Pn^*(SnMe_3)_2$ (**5.6**), which is

synthesised by salt metathesis of **5.5** with trimethyltin chloride and used in the synthesis of [Pn*TiCl(μ-Cl)]$_2$ (**5.7**) by its addition to TiCl$_4$·2THF.[22] In the η^5-bonding modes shown, the pentalene can be thought of as two allyl anions centred at either wingtip with a bridgehead doublebond that acts as a μ-L ligand.[21] While the *trans*-(η^5,η^5) bonding mode is more common, the *cis*-(η^5,η^5) bonding mode can be achieved through pre-organisation of the bimetallic precursors.[17,23–29] Bimetallic double-sandwich complexes of the type Pn$^R_2$M$_2$ (Pn^R = Pn, Pn* or Pn†; M = Ti, V, Cr, Mo, Mn, Fe, Co, Rh, Ni or Pd) have been synthesised.[17,23,32,33,24–31]

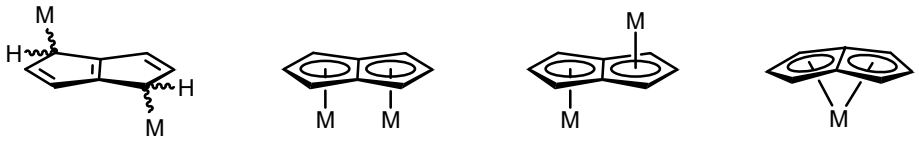


Figure 5.2: Bonding modes of the pentalene dianion (Pn^{2-}) ligand.[18,21]

Most common in the presence of a single early transition metal or rare earth metal centre is the η^8-bonding mode of the pentalene dianion.[34–38] Here, the two five-membered rings fold at the C–C bridgehead bond to allow bonding interaction between all eight carbons and a single metal centre. Naturally, this draws comparisons to the bent-metallocene Cp$_2$M motif, though the pentalene ligand donates two fewer electrons to the metals valence electron count (10 *vs.* 12 electrons using ionic valence electron count).[39,40] Notably, the folding of the pentalene ligand disrupts its aromaticity, though this is more than compensated for by the formation of the cumulatively strong poly-haptic bonds. The "fold-angle", illustrated in Figure 5.3, is a key metric for such complexes and is affected by such things as the size of the metal, coordination environment of the metal and electronic demands of the appending ligand set.[38,41–43]

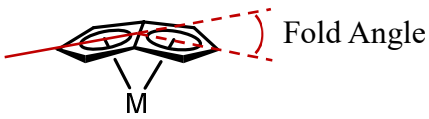


Figure 5.3: Illustration of the fold angle for η^8-Pn complexes.

The frontier molecular orbitals of a nominal η^8-PnM fragment are shown in Figure 5.4 alongside those of a Cp_2M fragment.[21,39,40,44] Both are C_{2v} symmetric and both contain two a_1 and one b_2 MOs that are analogous. Notably, due to the two fewer electrons the Pn ligand donates compared to the two Cp ligands, η^8-PnM contains an additional MO of b_1 symmetry that lies orthogonal to the plane of the three aforementioned MOs.

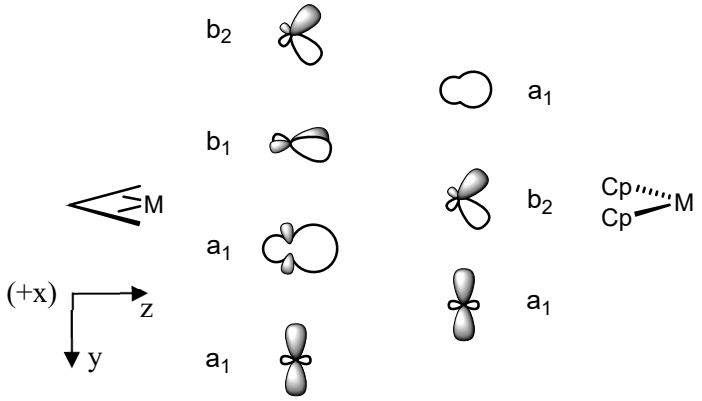


Figure 5.4: Simplified frontier molecular orbital diagram for η^8-PnM (left) and Cp_2M (right).[21,39,40]

This leads to such complexes avoiding co-planar ligand arrangement that is observed for Cp_2ML_3 complexes.[21,45,46] Instead, η^8-$PnML_3$ complexes, such as $Pn^{\dagger}TaMe_3$, form trigonal pyramidal geometries and η^8-$PnML_4$ complexes, such as $PnZrCl_2(THF)_2$, form square pyramidal geometries, with respect to the metal centre ML_n fragment (Figure 5.5).[41,43] Furthermore, the additional, orthogonal frontier molecular orbital allows electron deficient complexes to dimerise.[22] For example, while Cp_2TiCl_2 is a monomeric 16 VE complex, monomeric Pn^*TiCl_2 would be a 14 VE complex; dimerisation to the bridging complex $[Pn^*TiCl(\mu\text{-}Cl)]_2$ (**5.7**) achieves a 16 VE count for each titanium centre.[22,47]

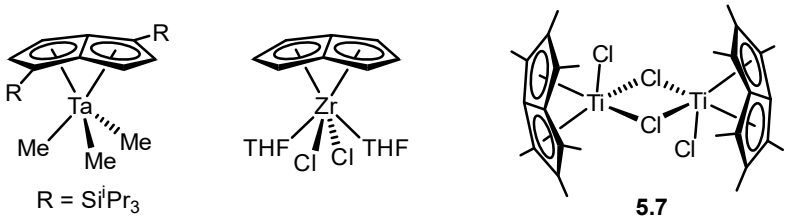


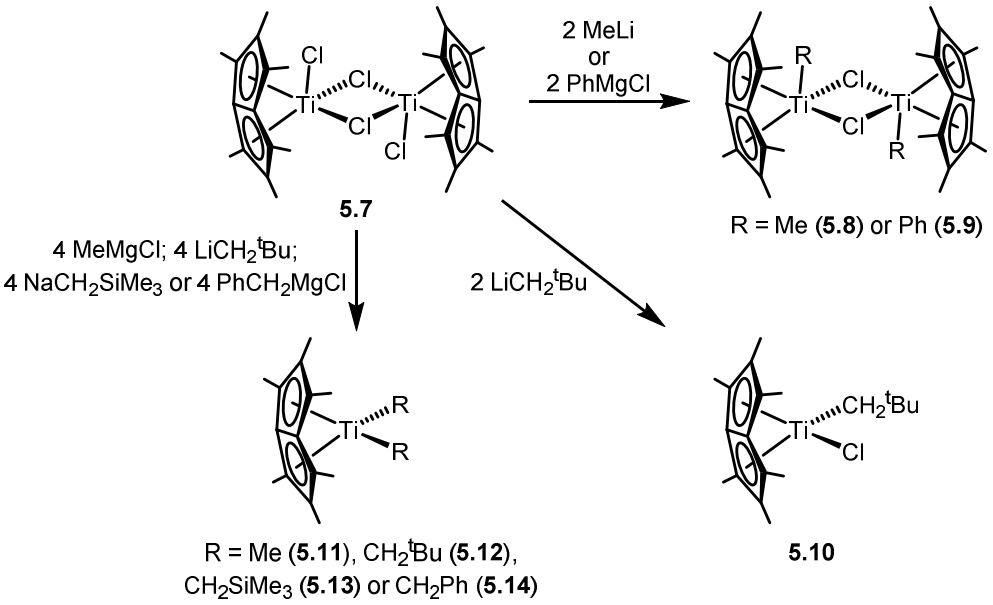
Figure 5.5: Coordination environments of η^8-Pn complexes.[22,41,43]

5.1.5 Selected synthesis and small molecule reactivity of Group 4 pentalene complexes

Cloke and co-workers reported the reactivity of the double-sandwich titanium complex $Pn^{\dagger}_2Ti_2$, synthesised by reduction of the mixed-valence Ti(III)/Ti(IV) dimer $[Pn^{\dagger}Ti]_2(\mu\text{-}Cl)_3$ with potassium amalgam, with a variety of small molecules.[33,48–53] Reaction with CO_2 gave the dicarbonyl double-sandwich complex $Pn^{\dagger}_2\{Ti(CO)\}_2$, with concomitant formation of the oxo-bridged dimer $[\eta^8\text{-}Pn^{\dagger}Ti(\mu\text{-}O)]_2$.[48,50] Both isocyanides and carbodiimides formed adducts bridging across the titanium centres. Two equivalents phenyl isocyanate reacted to give the unsymmetrical dimeric phenyl-carbonimidate bridged complex $[(\eta^8\text{-}Pn^{\dagger})Ti]_2(\mu,\kappa^2\text{:}\kappa^2\text{-}O_2CNPh)$.[51] This was formed by insertion of oxygen into the Ti=Ti double bond, with release of phenyl isocyanide, and subsequent addition of the second equivalent phenyl isocyanate to the Ti–O–Ti motif. Addition of the N-heterocyclic carbene 1,3,4,5-tetramethylimidazol-2-ylidene to $Pn^{\dagger}_2Ti_2$ led to formation of a tuck-in complex by coordination of the carbene to one titanium centre and C–H activation.[52,53] Dihydrogen could subsequently activate across the Ti–C bond, as could the C–H bond of HCC^tBu.

O'Hare and co-workers have reported the synthesis and reactivity of several η^8-Pn* Group 4 complexes.[54,55] The titanium dichloride dimer $[Pn^*TiCl(\mu\text{-}Cl)]_2$ (**5.7**) acts as a useful precursor towards many alkyl complexes that have been the subject of reactivity studies.[22,42,54–56] Addition of two or four equivalents lithiated alkyl species results in the formation of monomeric or dimeric alkyl or bis(alkyl) species, as summarised in Scheme 5.2. 14 VE complexes of the type Pn*Ti(R)Cl were not observed in their monomeric form for R = Me and Ph, but rather were found to dimerise through bridging chloride interactions to form more stable 16 VE complexes $[Pn^*Ti(R)]_2(\mu\text{-}Cl)_2$ (R = Me (**5.8**) and Ph (**5.9**)).[55] However, in the case of R = $CH_2{}^tBu$ (**5.10**) the steric bulk of the R ligand

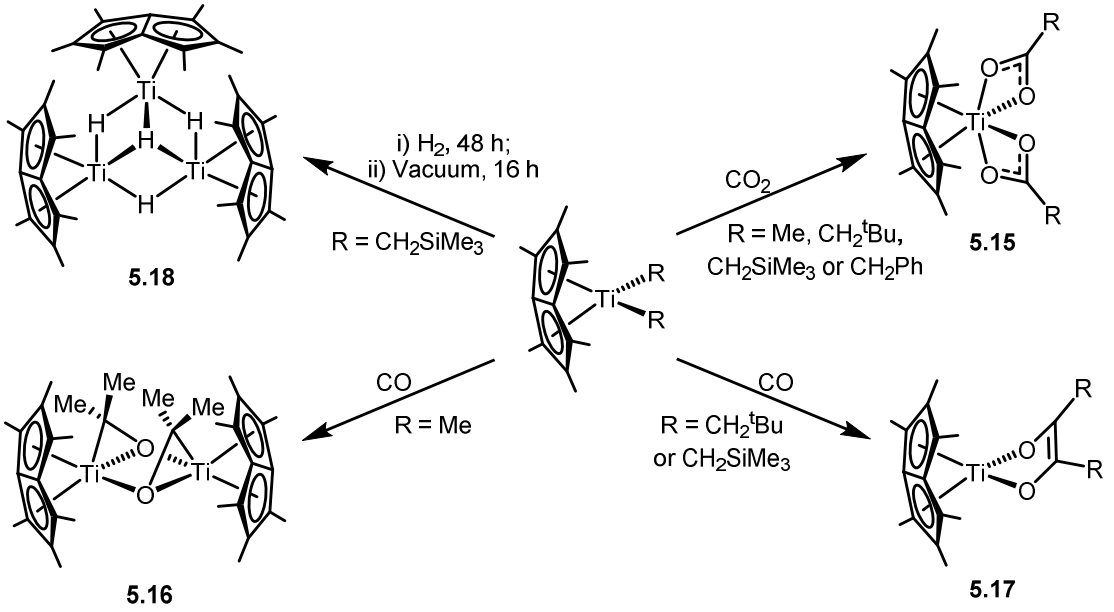
prevented dimer formation. Notably, **5.8** and **5.9** were found to be thermally unstable, but **5.10** not, with the dimeric structure crucial to the decomposition pathway.



Scheme 5.2: Synthesis of alkylated titanium permethylpentalene complexes.[54,55]

While no reactivity was reported for the aforementioned monoalkyl complexes, the monomeric bis(alkyl) complexes Pn*TiR_2 (R = Me (**5.11**), $CH_2{}^tBu$ (**5.12**), CH_2SiMe_3 (**5.13**) and CH_2Ph (**5.14**)) were reacted with CO_2, CO and H_2 (Scheme 5.3).[54,55] With CO_2, double insertion into the Ti–C bonds was observed, forming complexes of the type Pn*Ti(κ^2-$O_2CR)_2$ (**5.15**). This contrasts the reactivity of Cp_2TiMe_2, which undergoes only a single insertion with CO_2. With CO, divergent reactivity was observed for **5.11** and **5.12**/**5.13**. Compound **5.11** reacted to form the dimeric titanoxirane [Pn*Ti(μ-η^1(O):$\eta^2$$OC(Me)_2$)]$_2$ (**5.16**), while **5.12** and **5.13** reacted, by the coupling of two molecules of CO, to form ene-diolate complexes of the type Pn*Ti(κ^2-OC(R)C(R)O) (**5.17**). Reaction of **5.13** with H_2 for 2 days, followed by exposure to a dynamic vacuum for 16 hours gave the mixed valence Ti(III)/Ti(III)/Ti(IV) hydride cluster Pn*$_3$$Ti_3$($\mu_2$-H)$_3$($\mu_3$-H) (**5.18**).[55,56] Other Pn*M hydride clusters of titanium and zirconium have been synthesised by addition of $LiAlH_4$ to **5.7** and [Pn*Zr(μ-Cl)$_{3/2}$]$_2$(μ-Cl)$_2$Li·THF_x (**5.19**).[56] Compounds **5.11** – **5.14** have also been employed as ethylene polymerisation

catalysts, as have many pentalene-cyclopentadienyl complexes of the type $Pn^{R}MCp^{R'}(X)$ (Pn^{R} = Pn, $Pn^{\dagger}$, Pn*; M = Ti, Zr, Hf).[42,55–57]

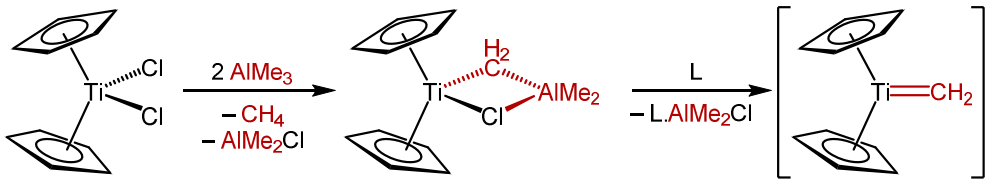


Scheme 5.3: Reactions of $Pn^{*}TiR_2$ complexes with CO_2, CO and H_2.[54–56]

Reduced Group 4 pentalene complexes have also been targeted due to the rich chemistry exhibited by masked titanocene and zirconocene compounds, as well as dinitrogen-activated metallocene complexes.[58–62] Reduction of **5.19** by KC_8 in aromatic solvents gave triple-decker complexes of the type $[Pn^{*}Zr]_2(\mu\text{-}\eta^6\text{:}\eta^6\text{-}C_6H_5R)$ (R = H or Me), contrasting the dinitrogen activation of $Cp^{*}_2ZrCl_2$, to form $(Cp^{*}_2ZrN_2)_2(\mu\text{-}N_2)$, under reducing conditions.[61–63] Reaction of $[Pn^{*}TiCl(\mu\text{-}Cl)]_2$ (**5.7**) with stoichiometric amounts of KC_8 gave the mixed-valence Ti(III)/Ti(IV) dimer $[Pn^{*}Ti]_2(\mu\text{-}Cl)_3$.[56] With 4 equivalents KC_8 the homoleptic triple-decker metallocene complex $(\eta^8\text{-}Pn^{*})Ti(\mu\text{-}\eta^5\text{:}\eta^5\text{-}Pn^{*})Ti(\eta^8\text{-}Pn^{*})$ was formed, with associated by-products. Notably, with magnesium, the dinitrogen bridged complex $[Pn^{*}Ti]_2(\mu\text{-}N_2)\cdot MgCl_2\cdot 3THF$ was formed. The N–N bond of this complex was predicted to have a bond order of only 1.113. No reactivity has been reported for this complex.

5.1.6 Group 4 metallocene alkylidene chemistry

The chemistry of Group 4 η^8-pentalene compounds has drawn comparisons with analogous metallocene compounds and so reactions that can be mimicked by permethylpentalene complexes are of interest in order to investigate the impact the different electron and steric properties of the ligand has on the observed chemistry. A commonly used and much lauded reaction is methylidene group transfer by transient Group 4 metallocene methylidenes, formed *in situ* from precursors, the most well-known of which is the Tebbe reagent ($Cp_2Ti(\mu\text{-}CH_2)(\mu\text{-}Cl)AlMe_2$, **5.20**).[64–69] First synthesised in 1978 by addition of 2 equivalents $AlMe_3$ to Cp_2TiCl_2, the Tebbe reagent has been utilised for the metallo-Wittig-type methylidenation of a range of substrates such as aldehydes, ketone and esters with good functional group selectivity, as well as olefin methathesis and cycloaddition of alkenes and internal alkynes.[64–73] Usually, addition of a base, such as pyridine or THF is required to generate the reactive methylidene species $[Cp_2Ti{=}CH_2]$.[69,72]



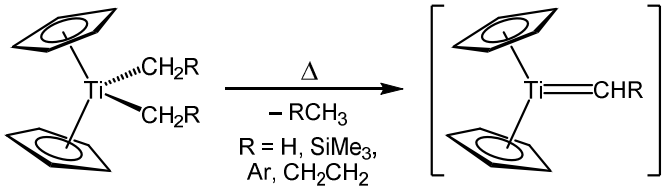
5.20

Scheme 5.4: Synthesis of the Tebbe reagent, $Cp_2Ti(\mu\text{-}CH_2)(\mu\text{-}Cl)AlMe_2$ (**5.20**) and subsequent formation of the reactive methylidene $[Cp_2Ti{=}CH_2]$ by addition of a base.[64,69,72]

Since this seminal report, several other titanium complexes that can form alkylidene species *in situ* have been reported. Tebbe and co-workers also reported the synthesis of $Cp_2Ti(\mu\text{-}CH_2)(\mu\text{-}Cl)Al(CH_2{}^tBu)_2$ by addition of $Al(CH_2{}^tBu)_3$ to **5.20**.[68] Higher homologues of the Tebbe reagent have also been synthesised, such as $Cp_2Ti\{\mu\text{-}C(H)C(H)(CH_3)_2\}(\mu\text{-}Cl)Al({}^iBu)_2$, by reaction of Cp_2TiCl_2 with $Al{}^iBu_3$. Furthermore, $Cp_2Ti\{\mu\text{-}C(H)Et\}(\mu\text{-}Cl)Al({}^iBu)_2$ was synthesised by addition of DIBAL-H

to the alkenyl complex $Cp_2Ti\{C(H)=C(H)CH_3\}Cl$, though this did contain Ti(III) by-products.[74]

The Tebbe reagent is highly unstable and is usually synthesised *in situ*, rather than isolated. Indeed, despite being reported in 1978, the complex has only been recently crystallographically characterised.[75] By comparison, the Petasis reagent, Cp_2TiMe_2 (**5.21**), is air- and moisture-stable.[71] When heated, Cp_2TiMe_2 eliminates methane to form the reactive methylidene species $[Cp_2Ti{=}CH_2]$ and has been employed in a similar manner to the Tebbe reagent.[65,66,69,71,76,77] Similarly, $Cp_2Ti(CH_2SiMe_3)_2$ (**5.22**) and $Cp_2Ti(CH_3)(CH_2SiMe_3)$ (**5.23**) release tetramethylsilane or methane when heated to form transient alkylidenes.[71]

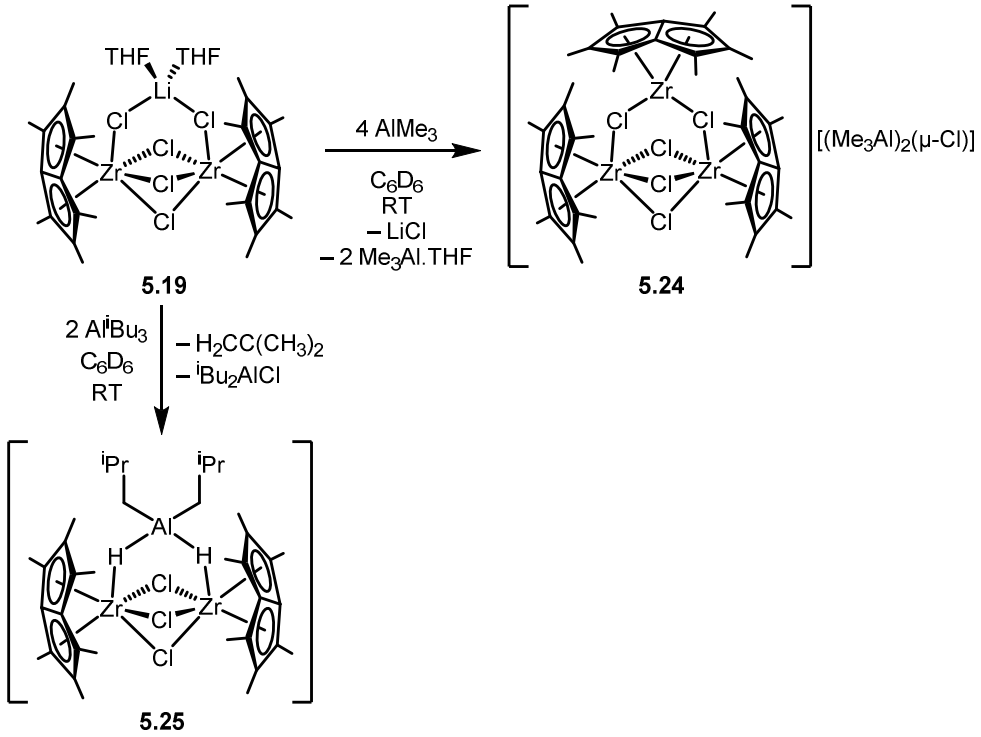


Equation 5.2

Grubbs and co-workers reported the titanocycles $Cp_2Ti(\kappa^2\text{-}CH_2C(Me)_2CH_2)$ and $Cp_2Ti(\kappa^2\text{-}CH_2C(^tBu)CH_2)$, synthesised by addition of the appropriate alkene to **5.20**, to generate $[Cp_2Ti{=}CH_2]$ upon heating.[69,72,73] Magnesium, palladium and platinum analogues of the Tebbe reagent are also known,[78,79] as are several alkylidene-bridged zirconocene-aluminium and base-stabilised alkylidene complexes.[65,72,74,80–82]

The rich chemistry of Group 4 metallocene alkylidenes provides the impetus to synthesise analogous permethylpentalene compounds. To this end, synthesis of a permethylpentalene zirconium analogue of the Tebbe reagent was recently attempted by the O'Hare group (Scheme 5.5).[83] Reaction of $[Pn^*Zr(\mu\text{-}Cl)_{3/2}]_2(\mu\text{-}Cl)_2Li\cdot THF_2$ (**5.19**) with excess $AlMe_3$ in benzene led to deposition of the crystalline species $[\{Pn^*Zr(\mu\text{-}Cl)_{3/2}\}_2(\mu\text{-}Cl)_2(ZrPn^*)][(AlMe_3)_2(\mu\text{-}Cl)]$ (**5.24**). Here, the formation of the

thermodynamically favourable trimeric zirconium cation could not be overcome. The hetero-trimetallic species $\{Pn^*Zr(\mu\text{-}Cl)_{3/2}\}_2(\mu\text{-}H)_2\{Al(^iBu)_2\}$ (**5.25**) was formed upon reaction of **5.19** with 2 equivalents Al^iBu_3, with concomitant isobutene and $^iBu_2AlCl$ formation. Similar hydride formation, by β-hydrogen elimination, has been seen upon reaction of $AlEt_3$ with Cp_2TiCl_2, which formed $[Cp_2TiHAl(Et)_2]_2$.[65,84]



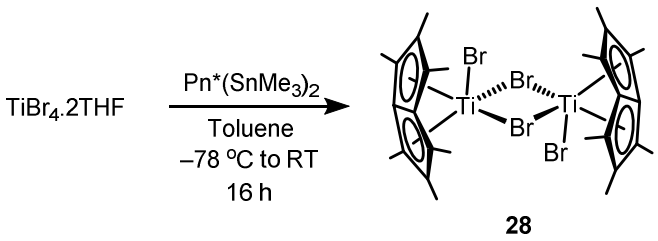
Scheme 5.5: Reactions of $[Pn^*Zr(\mu\text{-}Cl)_{3/2}]_2(\mu\text{-}Cl)_2Li\cdot THF_2$ (**5.19**) with $AlMe_3$ and Al^iBu_3.

In this Chapter, the synthesis of the bromo-analogue of **5.7**, namely $[Pn^*TiBr(\mu\text{-}Br)]_2$ (**28**), will be described. Subsequently attempts to synthesise the titanium permethylpentalene analogue of the Tebbe reagent and analogous alkylidene precursors are discussed. Furthermore, the reactions of small molecules with permethylpentalene alkyl complexes, in attempt to observe reactivity akin to the Petasis reagent, are described.

5.2 Synthesis of [Pn*TiBr(μ-Br)]$_2$ (28)

[Pn*TiCl(μ-Cl)]$_2$ (**5.7**) is a useful synthon towards many alkyl complexes of which the small molecule reactivity and ethylene polymerisation has been investigated.[22,42,54–57] Furthermore, structural differences pertaining to the pentalene ligand have been noted on altering the metal of Pn^RML_n complexes and for L = Cl or Me. The bromo-analogue of **5.7** has, however, not previously been synthesised and would represent an alternative synthon for titanium permethylpentalene complexes, as well as allow for investigation of the structural effects such a change brings.

[Pn*TiBr(μ-Br)]$_2$ (**28**) was synthesised in an analogous manner to **5.7**.[22] A toluene solution of 1,5-Pn*(SnMe$_3$)$_2$ (**5.6**), formed *in situ* by addition of Me$_3$SnCl to Pn*Li$_2$ (**5.5**), was added in equimolar quantities to a toluene solution of TiBr$_4$·2THF at –78 °C, followed by stirring at room temperature for 16 h. Crystallisation of a concentrated, –30 °C toluene solution of the crude reaction mixture allowed isolation of **28** as a dark blue, crystalline solid in a 71% yield on a ~2 g scale (Equation 5.3).



28

Equation 5.3

The ^{1}H NMR spectrum of **28** is analogous to that of **5.7** exhibiting two resonances of relative intensity 2:1 at 1.90 and 1.43 ppm (*cf.* 1.89 and 1.62 ppm for **5.7**) for the NWT-Me and WT-Me groups of the Pn* moieties, respectively.[22] This indicates C_{2v} symmetry in solution phase, contrasting the C_{2h} symmetry observed in the solid state (*vide infra*). This could arise through either rotation of the Pn* ligands about the axis that runs through titanium centres, or exchange of the bridging and terminal bromide ligands,

on the NMR timescale. Cooling a toluene-d_8 solution of **28** to –88 °C did not decoalesce or broaden the resonances – identical to what was observed for **5.7**.

The solid state structure of **28** is shown in Figure 5.6, confirming the connectivity shown in Equation 5.3, and selected bond distances and angles in Table 5.1, with those of **5.7** included for comparison.[22] As expected and analogous to **5.7**, **28** adopts a dimeric structure with two bridging bromides and two terminal bromides – one bound to each titanium centre – thus alleviating the electron deficiency the 14-electron monomer would experience. The fold angle (Figure 5.3) of **28** (31.0°) is less than in **5.7** (32.3(3)°) and the average Ti–Pn*$_{cent}$ distance longer (1.970(2) *vs.* 1.955(2) Å). Increase in the fold angle of a series of tantalum complexes, Pn†TaCl$_x$Me$_{3-x}$, upon increasing values of x has been observed and attributed to the greater electron-withdrawing character of chloride rendering the metal centre more electron deficient – a similar assertion can be made here.[43]

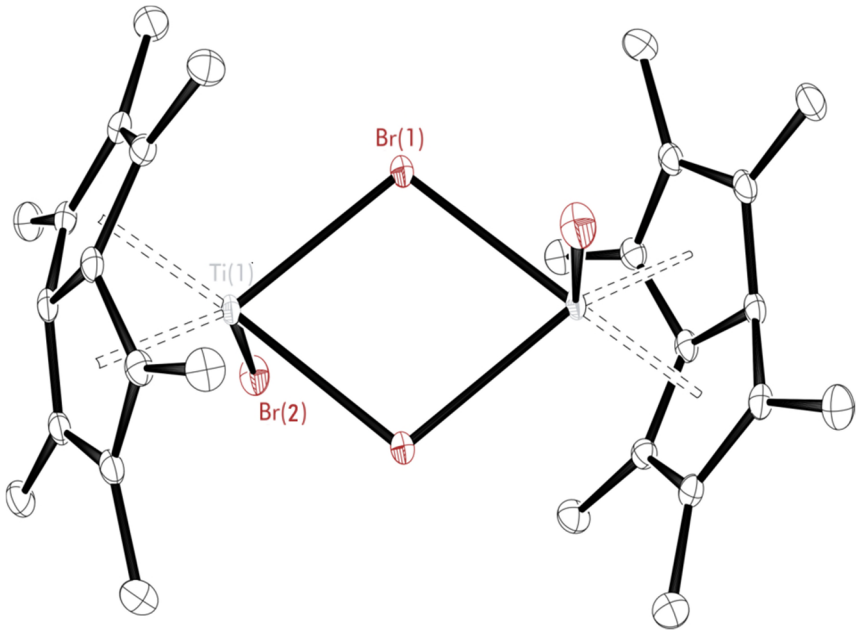


Figure 5.6: Displacement ellipsoid plot (50% probability) of [Pn*TiBr(μ-Br)]$_2$ (**28**). H atoms are omitted for clarity.

Table 5.1: Selected bond distances (Å) and angles (°) for [Pn*TiBr(μ-Br)]$_2$ (**28**) and [Pn*TiCl(μ-Cl)]$_2$ (**5.7**). ([a]Average value)

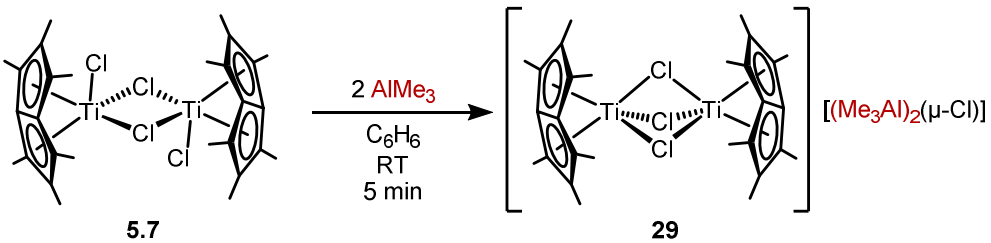
Parameter	28	5.7
Ti–Pn*$_{cent}$[a]	1.970(2)	1.955(2)
Ti–(μ-X)[a]	2.6478(5)	2.485(1)
Ti–X(2)[a]	2.5321(5)	2.3595(10)
Ti–Ti	4.053(7)	3.806(8)
Fold angle[a]	31.0	32.3(3)
Ti–(μ-X)–Ti[a]	99.873(13)	99.94(3)
(μ-X)–Ti–(μ-X)[a]	80.128(13)	80.06(3)

The average Ti–Pn*$_{cent}$ distance of **28** (1.970(2) Å) can be noted to be significantly shorter than the average Ti–Cp$_{cent}$ distance in comparable titanocene dibromide complexes, such as Cp_2TiBr_2 and $(Cp^{Ad})_2TiBr_2$ (2.057 and 2.066 Å, respectively).[85,86] Such a phenomenon has previously been attributed to the lower steric demand of the Pn* ligand compared to two Cp or Cp-derived ligands.[22] The Ti–Br(2) bond distance of 2.5321(5) Å is longer than in the titanocene dibromide Cp_2TiBr_2 (2.489(2) – 2.498(2) Å), but in good agreement with other Ti(IV) metallocene Ti–Br bonds, such as those of $(Cp^{Ad})_2TiBr_2$ (2.5366(6) Å, Ad = adamantyl, $C_{10}H_{15}$) and $\{(C_5H_4)C(CH_3)_2C(CH_3)_2(C_5H_4)\}TiBr_2$ (2.508(1) – 2.536(1) Å).[85–87] Next, attention was turned to the reactions of **28** and **5.7** with alkyl aluminium reagents in attempts to synthesise permethylpentalene analogues of the Tebbe reagent ($Cp_2Ti(\mu\text{-}CH_2)(\mu\text{-}Cl)AlMe_2$, **5.20**).

5.3 Reactions of titanium permethylpentalene complexes with alkylaluminium reagents

5.3.1 Reactions of [Pn*TiCl(μ-Cl)]$_2$ (5.7) and [Pn*TiBr(μ-Br)]$_2$ (29)

Upon addition of 2 or 4 equivalents $AlMe_3$ to [Pn*TiCl(μ-Cl)]$_2$ (**5.7**), in benzene, an instant colour change from dark red to dark green was observed. From this solution orange crystals of [(Pn*Ti)$_2$(μ-Cl)$_3$][(Me$_3$Al)$_2$(μ-Cl)] (**29**, Equation 5.4) were deposited within minutes and the ^{1}H NMR spectrum of an NMR tube scale reaction ran in C_6D_6 contained a number of intractable, low intensity resonances, indicating the majority of material had been crystallised. Compound **29** was found to be insoluble in benzene and other hydrocarbon solvents. Dissolution in THF-d_8 and pyridine-d_5 led to the reformation of **5.7**, as judged by ^{1}H NMR spectroscopy. Dissolution of **29** in C_6D_5Br was, however, possible and, as the ^{1}H NMR spectrum differs significantly to that of **5.7** and $AlMe_3$, **29** is proposed to stable with respect to reformation of the constituents in C_6D_5Br solution. Compound **29** exhibits a single resonance at 0.00 ppm for the $AlMe_3$ protons, which shows a single bond correlation to a resonance at –4.5 ppm in the $^{13}C\{^1H\}$ NMR spectrum. Resonances attributable to the permethylpentalene protons are observed as overlapping singlets at 1.86 ppm (**5.7** exhibits resonances at 2.12 and 1.87 ppm for the NWT-ME and WT-Me groups, respectively, in C_6D_5Br).



5.7 **29**

Equation 5.4

The solid state structure of **29** is shown in Figure 5.7, confirming the connectivity shown in Equation 5.4, and selected bond distances and angles in Table 5.2. The structure is *C*$_2$

symmetric with the Pn* ligands staggered in the solid state. The average Ti–(μ-Cl) bond distance (2.4750(5) Å) is shorter than in **5.7** (2.485(1) Å), as are the average Ti –Pn*$_{cent}$ distance (1.936(3) *vs.* 1.955(2) Å) and the Ti–Ti distance (3.2628(4) *vs.* 3.806(8) Å). Furthermore, the fold angle (33.1°) is greater than in **5.7** (32.3(3)°). These observations can be attributed to the greater electron deficiency of the titanium centres of the cation, due to the abstraction of one chloride ligand, as well as reduced steric encumbrance at the metal, due to the bridging of all three chlorides.[56]

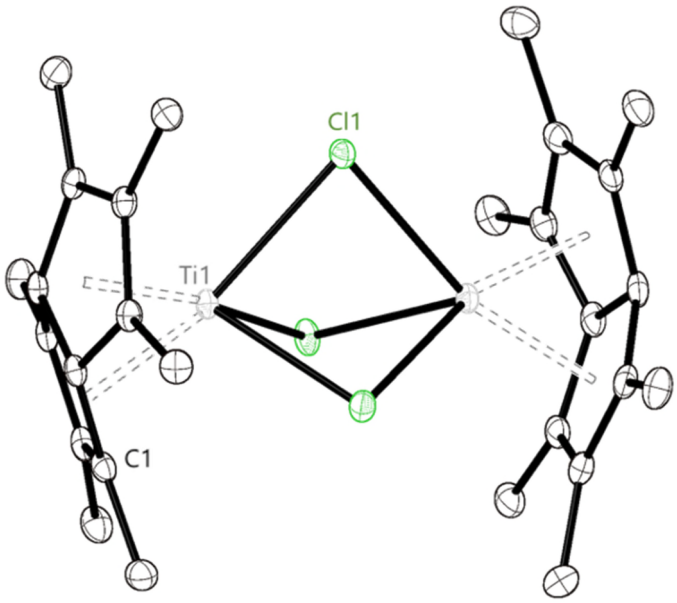


Figure 5.7: Displacement ellipsoid plot (20% probability) of [(Pn*Ti)$_2$(μ-Cl)$_3$][(Me$_3$Al)$_2$(μ-Cl)] (**29**). H atoms and the [(Me$_3$Al)$_2$(μ-Cl)] fragment are omitted for clarity.

Table 5.2: Selected bond distances (Å) and angles (°) for [(Pn*Ti)$_2$(μ-Cl)$_3$][(Me$_3$Al)$_2$(μ-Cl)] (**29**). ([a]Average value)

Ti–(μ-Cl)[a]	2.4750(5)	Fold angle[a]	33.1
Ti–Pn*$_{cent}$[a]	1.936(3)	Ti–(μ-Cl)–Ti[a]	82.472(16)
Al–(μ-Cl)[a]	2.3508(9)	(μ-Cl)–Ti–(μ-Cl)[a]	81.262(17)
Ti–Ti	3.2628(4)	Al–(μ-Cl)–Al	114.44(3)

Further to comparisons with **5.7**, the neutral, mixed-valence Ti(III)/Ti(IV) dimer [Pn*Ti]$_2$(μ-Cl)$_3$ has previously been structurally characterised, as has the methylidene

bridged dimer [Pn*Ti(μ-Cl)$_2$](μ-CH$_2$) (**5.26**), containing comparable dimeric structures with three bridging ligands.[55,88] [Pn*Ti]$_2$(μ-Cl)$_3$ was crystallised with two whole molecules in the asymmetric unit, one exhibited eclipsing Pn* ligands and the other staggered, while **5.26** exhibited eclipsed Pn* ligands. The average Ti–(μ-Cl) bond distance is shorter in **29** than in [Pn*Ti]$_2$(μ-Cl)$_3$ and **5.26** (2.4834(7) and 2.4813(7) Å, respectively), as is the average Ti–Pn*$_{cent}$ distance (1.936(3) *vs.* 1.951(2) and 1.959 Å), presumably due to the electron deficiency of the cationic dimer of **29**.

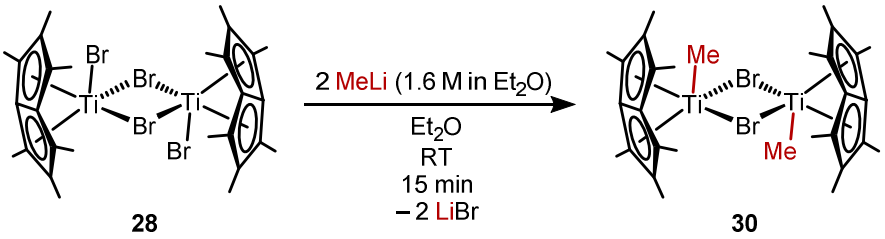
Formation of **29** arises by abstraction of one chloride ligand from the [Pn*TiCl(μ-Cl)]$_2$ dimer, with no methylation of either titanium centre. Presumably, the sterically crowded nature of **5.7** renders abstraction of the chloride kinetically favourable over methylation – an issue not encountered for Cp$_2$TiCl$_2$, where the planar arrangement of the three frontier bonding orbitals of the titanocene allow for relatively facile interaction of the methyl with titanium – and subsequent formation of the thermodynamically stable ionic species **29** renders methylation inaccessible. Indeed, this reaction resembles that of [Pn*Zr(μ-Cl)$_{3/2}$]$_2$(μ-Cl)$_2$Li·THF$_x$ (**5.19**) with excess AlMe$_3$, where no methylation of zirconium was observed and only the abstraction of chloride, and THF and LiCl, to form [{Pn*Zr(μ-Cl)$_{3/2}$}$_2$(μ-Cl)$_2$(ZrPn*)][(AlMe$_3$)$_2$(μ-Cl)] (Scheme 5.5).[83] Presumably, the same issues are present here.

Further to the reaction of **5.7** with AlMe$_3$, reaction of [Pn*TiBr(μ-Br)]$_2$ (**28**) with 2 or 4 equivalents AlMe$_3$ was carried out on the NMR tube scale in C$_6$D$_6$, C$_6$D$_5$Br and THF-*d*$_8$. In each case, no reaction was observed to occur, even with excess AlMe$_3$ and at elevated temperatures intractable mixtures were formed. Reaction of both **5.7** and **28** with 2 and 4 equivalents Al^{i}Bu$_3$ were also carried out on the NMR tube scale in C$_6$D$_6$.

While **28** gave no reaction, **5.7** reacted immediately with the reaction solution turning from dark red to orange. The ^{1}H NMR spectrum of the reaction revealed an intractable mixture from which only isobutene could be identified. Slow evaporation of the C_6D_6 solution reliably yielded orange single crystals. However, the solid state structure could not be resolved from the diffraction data, despite repeated attempts. Carrying out the reaction of the preparative scale was also unsuccessful. As mentioned previously, Turner observed formation of $\{Pn^*Zr(\mu\text{-}Cl)_{3/2}\}_2(\mu\text{-}H)_2\{Al(^{i}Bu)_2\}$ from the reaction of $[Pn^*Zr(\mu\text{-}Cl)_{3/2}]_2(\mu\text{-}Cl)_2Li\cdot THF_x$ (**5.19**) with $Al^{i}Bu_3$, with concomitant isobutene and $(^{i}Bu)_2AlCl$ formation.[83] Given the observation of isobutene on reaction of **5.7** with $Al^{i}Bu_3$, a similar reaction could be occurring, though no further evidence of this could be obtained.

5.3.2 Synthesis of [Pn*TiMe(μ-Br)$_2$]$_2$ (30)

Noting the inability of $AlMe_3$ to methylate $[Pn^*TiCl(\mu\text{-}Cl)]_2$ (**5.7**) or $[Pn^*TiBr(\mu\text{-}Br)]_2$ (**29**), it was of interest to attempt synthesis of Tebbe reagent analogues with the mono-methylated titanium permethylpentalene halides $[Pn^*TiMe(\mu\text{-}Cl)]_2$ (**5.8**) and $[Pn^*TiMe(\mu\text{-}Br)]_2$ (**30**). This would bypass the necessity of the first methylation event and prevent formation of **29**. Similar to the synthesis of **5.8**,[55] **30** was synthesised by addition of 2 equivalents MeLi to a diethyl ether solution of $[Pn^*TiBr(\mu\text{-}Br)]_2$ (**28**) and isolated as a dark green crystalline solid from toluene solution in a 45% yield (Equation 5.5).



28 **30**

Equation 5.5

The ^{1}H NMR spectrum of **30** (Figure 5.8, top) is analogous to that of **5.8**, exhibiting three sharp resonances of relative intensity 12:6:3 assigned to the NWT-Me, WT-Me and Ti–Me resonances, respectively.[55] As seen for **28**, this indicates C_{2v} symmetry in solution phase, which contrasts the C_{2h} symmetry in the solid state (*vide infra*) and indicates a fluxional process, which is fast on the NMR timescale, equates the four NWT-ME and two WT-Me, respectively. The Ti–Me proton resonance appears at 0.51 ppm and exhibits a single bond correlation to a carbon resonance at 43.9 ppm, consistent with **5.8**.

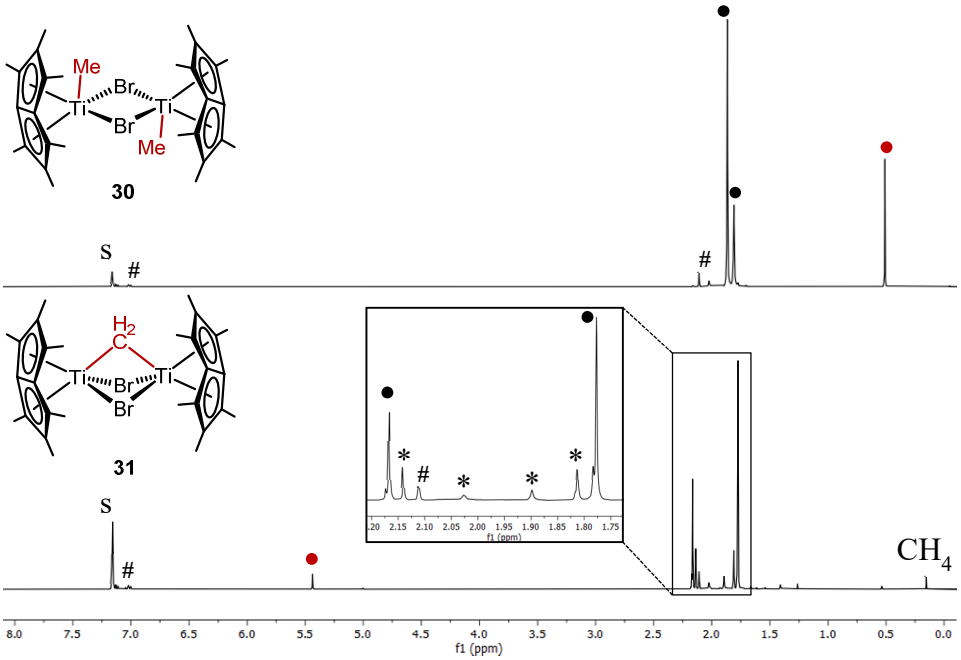


Figure 5.8: ^{1}H NMR spectrum (C_6D_6, 400.1 MHz, 298 K) of [Pn*TiMe(μ-Br)]$_2$ (**30**, top) and [Pn*Ti(μ-Br)]$_2$(μ-CH_2) (**31**, bottom) with the Pn* region of the latter enlarged. (# denotes residual toluene and * indicates resonances attributable to minor species formed as by-products in the thermal decomposition of **30**).

The solid state structure of **30** is shown in Figure 5.9, confirming the connectivity shown in Equation 5.5, and selected bond distances and angles in Table 5.3, with those of **5.8** included for comparison.[55] The average Ti–Pn*$_{cent}$ distance (1.969(2) Å) is identical to that of both **28** and **5.8** (1.970(2) and 1.969(5) Å, respectively). Meanwhile, the fold angle of **30** is slightly larger than that of both **28** and **5.8** (31.2 *vs.* 31.0 and 30.6°, respectively). This is contrary to expectation, where the trend in relative electronegativity of the

ancillary methyl, bromide or chloride ligands for the three complexes follows **5.8** > **28** > **30** (Pauling electronegativities: Me = 2.55, Br = 2.96 and Cl = 3.16), and so the fold angle would be expected to decrease along this series.[89,90] Indeed, **5.8** exhibited a 2.0 – 2.3° decrease in fold angle with respect to [Pn*TiCl(μ-Cl)]$_2$ (**5.7**).[22,55] The Ti–C(15) (Ti–CH_3) bond distance of **30** (2.202(5) Å) is similar to that of **5.8** and the titanocene methyl chloride {$Me_2Si(C_5H_4)_2$}Ti(Me)Cl (2.188(5) and 2.197(11) Å, respectively).[55,91] As expected, the Ti–Ti distance increases with respect to **5.8**, with similar Ti–(μ-X)–Ti and (μ-X)–Ti–(μ-X) angles.

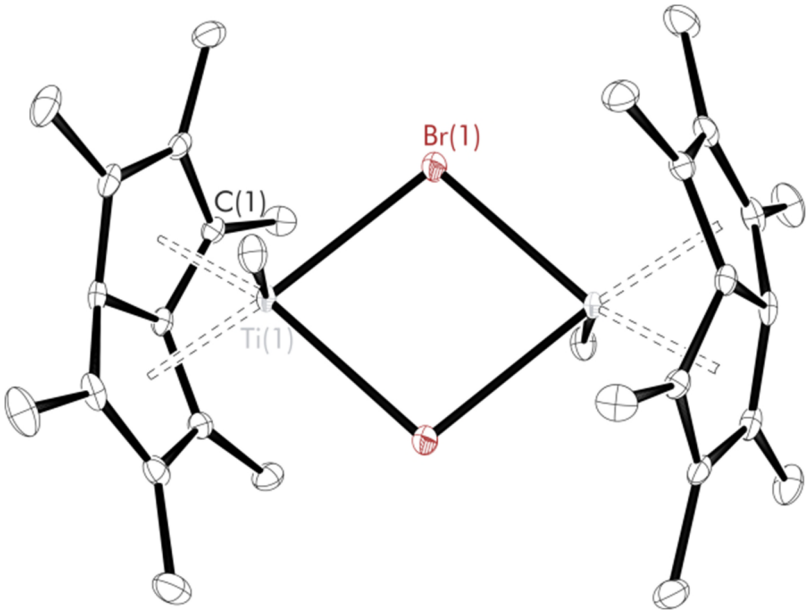


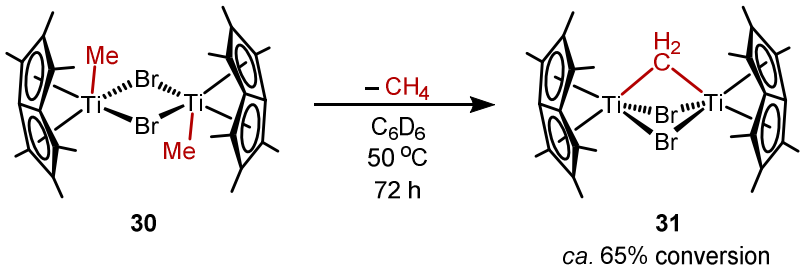
Figure 5.9: Displacement ellipsoid plot (20% probability) of [Pn*TiMe(μ-Br)]$_2$ (**30**). H atoms are omitted for clarity.

Table 5.3: Selected bond distances (Å) and angles (°) for [Pn*TiMe(μ-Br)]$_2$ (**30**) and [Pn*TiMe(μ-Br)]$_2$ (**5.8**). ([a]Average value)

Parameter	30	5.8
Ti–Pn*$_{cent}$[a]	1.969(2)	1.969(5)
Ti–(μ-X)[a]	2.6353(5)	2.508(1)
Ti–C(15)[a]	2.202(2)	2.188(5)
Ti–Ti	4.009(1)	3.840(2)
Fold angle[a]	31.2	30.6
Ti–(μ-X)–Ti[a]	98.875(14)	99.95(4)
(μ-X)–Ti–(μ-X)[a]	81.127(14)	80.05(4)

As mentioned in Section 5.1.5, **5.8** was found to be thermally unstable. Elimination of methane forms the methylidene-bridged dimer [Pn*Ti(μ-Cl)]$_2$(μ-CH$_2$) (**5.26**), which was structurally characterised. Similarly, **30** was found to be thermally unstable. Over the course of 3 days at 50 °C in benzene, complete decomposition of **30** was observed, accompanied by a colour change from dark green to dark purple. Analysis of the ^{1}H NMR spectrum revealed formation of methane and one major species (*ca.* 65%), alongside several minor species, which could not be identified (Figure 5.8, bottom). This contrasts the decomposition of **5.8** which gives quantitative conversion to **5.26**, as judged by ^{1}H NMR spectroscopy. The major species of the decomposition of **30** is proposed to be the bromo-analogue of **5.26**, namely [Pn*Ti(μ-Br)]$_2$(μ-CH$_2$) (**31**, Equation 5.6), exhibiting three sharp resonances of relative integral 2:12:24 at 5.44, 2.17 and 1.78 ppm, respectively. Most notable is the resonance assigned to the bridging CH$_2$ moiety, at 5.44 ppm. This resonance is consistent with that found for **5.26** (5.18 ppm) and {Ti[μ-(η^5-C$_5$Me$_4$SiMe$_2$-O)]Me}$_2$(μ-CH$_2$) (5.90 ppm), as is the carbon resonance (191.8 *vs.* 183.2 and 196.9 ppm, respectively).[55,92] On the preparative scale, attempts to remove

the by-products from **31** were unsuccessful, as were attempts to crystallise **31**, preventing further characterisation.



30 **31**

ca. 65% conversion

Equation 5.6

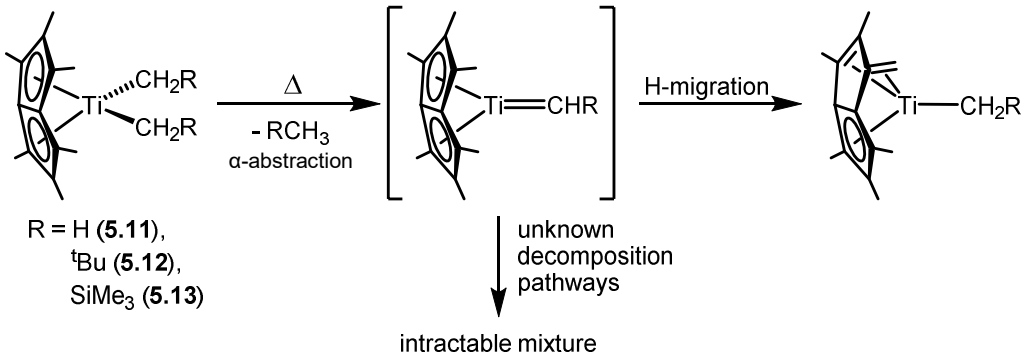
5.3.3 Reactions of [Pn*TiMe(μ-Cl)]$_2$ (5.8) and [Pn*TiMe(μ-Br)]$_2$ (30)

Following on from the synthesis of **30**, reactions of both **5.8** and **30** with $AlMe_3$ and Al^iBu_3 were carried out in C_6D_6. No reaction was observed in any case and after several days at room temperature or at elevated temperatures resonances attributable to the thermal decomposition of **5.8** and **30** were observed. The use of excess alkylaluminium reagents as well as a mixture of $AlMe_3$ and Me_2AlCl, to mimic the *in situ* reaction mixture during Tebbe reagent formation, brought about no changes in these observations.

Previously, reaction of $AlMe_3$ with Pn*TiCp(Cl) and Pn*TiCp(Me) has resulted in the formation of the chloride- and methyl-bridged heterobimetallic complexes Pn*TiCp(μ-Cl)$AlMe_3$ and Pn*TiCp(μ-CH_3)$AlMe_3$, respectively.[56] Despite the ^{1}H NMR spectrum of Pn*TiCp(μ-CH_3)$AlMe_3$ exhibiting a single metal-methyl resonance, indicating reversible coordination of an $[AlMe_4]^-$ anion, the complex was prone to loss of the volatile $AlMe_3$ fragment, indicating the complex was loosely bound. Furthermore, formation of analogues of Pn*TiCp(μ-Cl)$AlMe_3$ for **5.8** and **30** would require dissociation of the dimer, which would have an associated energy penalty. These insights may explain the lack of reactivity was observed for **5.8** or **30**.

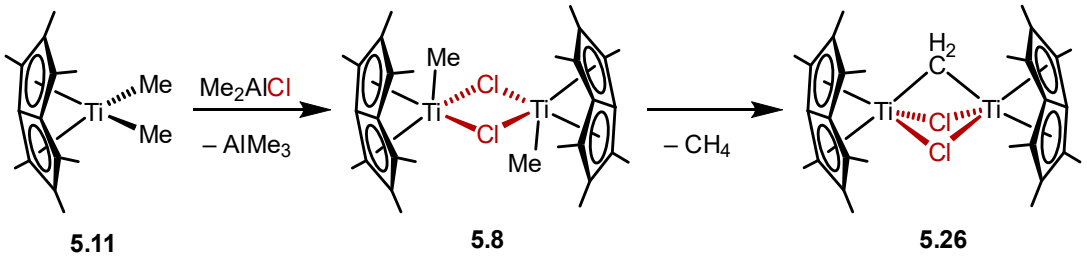
5.4 Thermolysis of titanium permethylpentalene bis(alkyl) complexes

Given the apparent inaccessibility of Pn*-Tebbe reagent analogues through dihalides or mono(halide)-mono(methyl) complexes, synthesis *via* thermolysis of titanium permethylpentalene bis(alkyl) complexes was explored. As discussed in Section 5.1.6, the Petasis reagent (Cp_2TiMe_2, **5.21**) and analogues $Cp_2Ti(CH_2SiMe_3)_2$ (**5.22**) and $Cp_2Ti(Me)(CH_2SiMe_3)$ (**5.23**), are thermally unstable towards α-hydrogen abstraction of one alkyl ligand by the other to release an alkane and form a transient alkylidene species, as are many other analogous titanocene compounds.[71] Similarly, Pn*$TiMe_2$ (**5.11**), Pn*$Ti(CH_2{}^tBu)_2$ (**5.12**) and Pn*$Ti(CH_2SiMe_3)_2$ (**5.13**) were found to be thermally unstable, decomposing to an intractable mixture from which only CH_4, CMe_4 and $SiMe_4$, respectively, could be identified.[54,55] From these observations it can be proposed that decomposition proceeds *via* α-hydrogen abstraction, though γ-hydrogen could be occurring for **5.12** and **5.13**, forming transient alkylidene species (Scheme 5.6). Previously, unsuccessful attempts to trap decomposition species of **5.12** with PMe_3 were made.[55] Subsequent to proposed alkylidene formation, hydrogen migration from a methyl group of the permethylpentalene to form fulvene/"tuck-in" complexes, akin to what is observed for alkyl-substituted Cp-derivatives, is thought to be inaccessible due to the large deformation of the ring system required (Scheme 5.6).[54–56,93–95] As such, little is known about the onwards decomposition.



Scheme 5.6: Possible decomposition pathways of titanium permethylpentalene bis(alkyl) complexes **5.11** – **5.13** *via* α-hydrogen abstraction to form transient alkylidene complexes.

Reactions of **5.11** and **5.13** with stoichiometric amounts of Me_2AlCl were carried out in C_6D_6, as were reactions with excess Me_2AlCl. For **5.13** no reaction was observed at room temperature, consistent with decomposition only occurring at elevated temperatures (90 °C). Upon heating, intractable mixtures akin to those observed in the absence of Me_2AlCl were observed, with no discernible evidence for reaction between **5.13** and Me_2AlCl, and a dark, unidentifiable precipitate was formed. In the case of **5.11**, slow conversion to a number of species, as well as a dark precipitate, was observed at room temperature, with full consumption of **5.11** seen after two weeks, as judged by ^1H NMR spectroscopy. From this mixture, only CH_4 and the methylidene bridged dimer $[Pn^*Ti(\mu\text{-}Cl)]_2(\mu\text{-}CH_2)$ (**5.26**) could be identified, which had formed in significant quantities. Notably, CH_4 is not seen to be released from **5.11** at room temperature.[54] This indicates the pathway shown in Scheme 5.7 could be occurring.



Scheme 5.7: Possible pathway of formation of $[Pn^*Ti(\mu\text{-}Cl)]_2(\mu\text{-}CH_2)$ (**5.26**) from the reaction of Me_2AlCl with Pn^*TiMe_2 (**5.11**).

Considering the prevalence of 16VE dimers of titanium permethylpentalene complexes, and that no 14VE dimers have been reported and would assumedly be rather unstable, a permethylpentalene Tebbe reagent analogue containing two bridging chloride interactions would be expected to be significantly more stable than with one bridging chloride interaction (Figure 5.10).

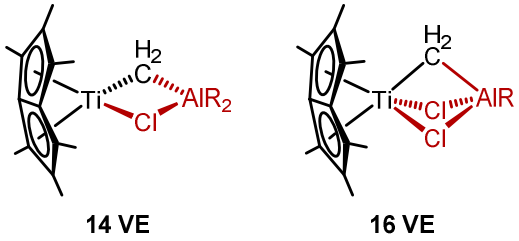


Figure 5.10: Hypothetical permethylpentalene Tebbe reagent analogues.

As such, reaction of **5.11** with the alkylaluminium dichloride reagent $EtAlCl_2$ was carried out on the NMR tube scale. After addition of $EtAlCl_2$ the resonances attributable to the Pn* moieties reduced greatly in intensity and small amounts of precipitate could be observed. After several days small amounts of **5.26** could be identified and attempts to crystallise any species from the solution, or identify the precipitate formed, were unsuccessful.

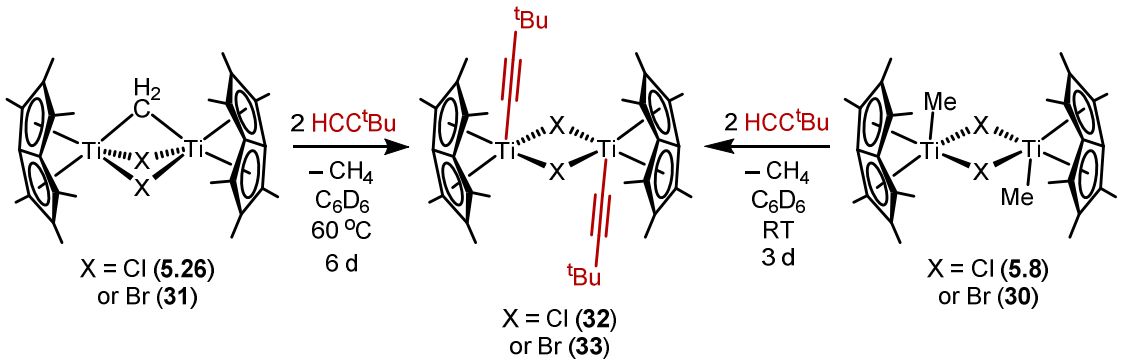
5.5 Small molecule reactivity of titanium permethylpentalene alkyl complexes

To probe the reactivity of the methylidene bridged dimer **5.26**, which bears some resemblance to the Tebbe reagent, several reactions with small molecules were carried out. Reactions with cyclohexanone, 1-hexene, propylene oxide and internal alkynes, such as $MeCCSiMe_3$ and MeCCTol – substituents that would be expected to undergo cycloaddition with a transient methylidene species – either did not react or gave intractable mixtures at room temperature or at elevated temperatures. Terminal alkynes have also been seen to undergo cycloaddition, as well as C–H activation with

titanium-carbon bonds, as well as titanium-oxygen and titanium-nitrogen multiple bonds.[96–100] Therefore, the terminal alkyne HCC^{t}Bu was reacted with **5.26** as well as with **31**, generated *in situ*.

On the NMR tube scale, reaction of **5.26** or **31** with 2 equivalents HCC^{t}Bu, at 60 °C, in C_6D_6, for 6 days, led to complete consumption of the starting materials with concomitant colour change from dark purple to dark blue. Reaction of **5.26** showed *ca*. 90% conversion to a single species containing three singlet resonances of relative integral 24:12:18 at 2.13, 1.78 and 1.29 ppm, respectively. Similarly, **31** gave predominant conversion to a single species containing three singlet resonances of relative integral 24:12:18 at 2.09, 1.65 and 1.26 ppm, respectively, though analysis of whether other reactions were occurring was prevented by the presence of significant impurities associated with synthesis of **31** (see Section 5.3.2). Notably, methane could be observed in both reaction mixtures and no intermediate species could be seen.

If reaction were occurring through a transient methylidene species, formed by asymmetric dissociation of **5.26** or **31** to [Pn*Ti=CH_2] and [Pn*TiX_2] (X = Cl or Br), the dihalide dimers [Pn*TiX(μ-X)]$_2$ (X = Cl (**5.7**) and Br (**28**)) would be expected to be observed. However, they are not, indicating reaction does not occur through this pathway. Indeed, the ^{1}H NMR spectra of the products, along with the observation of methane, is consistent with the formation of the acetylide dimers [Pn*Ti(CC^{t}Bu)(μ-X)]$_2$ (X = Cl (**32**) and Br (**33**), Scheme 5.8). Structural characterisation of **33** confirmed this (*vide infra*).



Scheme 5.8: Reactions of $[Pn^*Ti(\mu\text{-}X)]_2(\mu\text{-}CH_2)$ (X = Cl (**5.26**) or Br (**31**)) and $[Pn^*TiMe(\mu\text{-}X)]_2$ (X = Cl (**5.8**) or Br (**30**)) with HCC^tBu to form $[Pn^*Ti(CC^tBu)(\mu\text{-}X)]_2$ (X = Cl (**32**) or Br (**33**)).

Given no intermediates are observed in the reactions, the reaction can be said to occur by activation of the C–H bond of the relatively acidic alkyne across one Ti–CH_2 bond to form transient, asymmetric dimers of the type $[Pn^*Ti(CC^tBu)](\mu\text{-}X)_2[(Me)TiPn^*]$. Subsequently, the C–H bond of the second equivalent of HCC^tBu can react across the Ti–CH_3 bond to give the observed acetylide products and methane. Presumably, this second activation would be much more rapid than the first due to the less sterically crowded Ti–CH_2 bond and greater flexibility of the dimer. Previously, Cloke and co-workers reported a similar C–H activation of HCC^tBu across the Ti–C bond of a "double-sandwich" pentalene titanium tuck-in complex to form an acetylide compound.[53] Furthermore, C–H activation of HCC^tBu across the Ti–C bond of a titanocene ethylene complex has been reported, as have similar activations across zirconocene Zr–C bonds.[97,101–103]

Consistent with the proposed pathway, reaction of $[Pn^*TiMe(\mu\text{-}Cl)]_2$ (**5.8**) and $[Pn^*TiMe(\mu\text{-}Br)]_2$ (**30**) with 2 equivalents HCC^tBu, at room temperature for 3 days, formed **32** and **33**, respectively (Scheme 5.8). Formation of **32** was accompanied by similar levels of impurity as observed previously, while formation of **33** was accompanied by formation of small amounts of side-products. Attempts to remove the side products from **32** and **33** on the preparative scale were unsuccessful, leading to

significant decomposition. Presumably, the more facile reaction with **5.8** and **30** than **5.26** and **31** can be attributed to the sterically more accessible Ti–C bonds, due to the Pn* ligands 'canting' towards the methylidene bridge in **5.26** and **31**.[55]

Diffraction quality crystals of **33** were grown by slow evaporation of a benzene solution. The solid state structure is shown in Figure 5.11, confirming the connectivity shown in Scheme 5.8, and selected bond distances and angles in Table 5.4, with those of **30** for comparison. As with **28** and **30**, the structure is C_{2h} symmetric in the solid state, contrasting the C_{2v} symmetry exhibited in solution, as judged by the singlet resonances attributable to the NWT-Me (2.09 ppm) and WT-Me (1.65 ppm) protons in the ^{1}H NMR spectrum. The structural parameters are unremarkable compared to those of **30** – the average Ti–Pn*$_{cent}$ distance is identical, as is the fold angle, and the Ti–(μ-Br) distances are similar. The Ti–C(15) (Ti–CC^{t}Bu or Ti–CH_3) is shorter in **33** than **30** (2.113(3) *vs.* 2.202(2) Å), as expected with the hybridisations of the carbon bonding orbitals. The acetylide moiety is near-linear and the C≡C bond distance of 1.207(4) Å is consistent with a triple bond and with other titanocene acetylides. The Ti–CC^{t}Bu bond distance is within error of the range of comparable structures (2.108 – 2.08 Å).[104–109] The slight lengthening compared to some structures could be attributed to the need for the ^{t}Bu moiety to avoid steric clashes with the Me moieties of the Pn* ligand – a similar assertion was made for Cloke and co-worker's Pn†-double-sandwich titanium acetylide, which exhibited a Ti–CC^{t}Bu bond distance of 2.150(8) Å.[53]

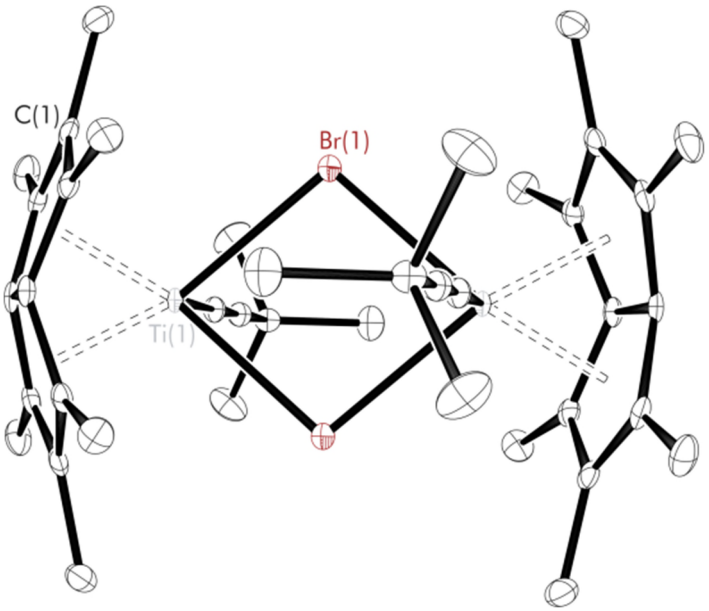


Figure 5.11: Displacement ellipsoid plot (20% probability) of [Pn*Ti(CC^{t}Bu)(μ-Br)]$_2$ (**33**). H atoms are omitted for clarity.

Table 5.4: Selected bond distances (Å) and angles (°) for [Pn*Ti(CC^{t}Bu)(μ-Br)]$_2$ (**33**) and [Pn*TiMe(μ-Br)]$_2$ (**30**). (^{a}Average value)

Parameter	**33**	**30**
Ti–Pn*$_{cent}$[a]	1.970(2)	1.969(2)
Ti–(μ-Br)[a]	2.6189(4)	2.6353(5)
Ti–C(15)[a]	2.113(3)	2.202(2)
C(15)≡C(16)[a]	1.207(4)	–
Ti–Ti	3.992(1)	4.009(1)
Fold angle[a]	31.2	31.2
Ti–(μ-X)–Ti[a]	99.317(17)	98.875(14)
(μ-X)–Ti–(μ-X)[a]	80.683(17)	81.127(14)
Ti–C(15)–C(16)[a]	176.8(3)	–
C(15)–C(16)–C(17)[a]	179.6(3)	–

Following the reactions of the methylidene bridged dimers **5.26** and **31** with small molecules, attempts to react bis(alkyl) complexes Pn*TiMe$_2$ (**5.11**) and Pn*Ti(CH$_2$SiMe$_3$)$_2$ (**5.13**) with small, unsaturated molecules, which react by addition to the Ti=CHR bond of transient alkylidenes formed by thermolysis of the Petasis reagent and its analogues, were undertaken. Reactions with cyclohexanone, 1-hexene, propylene

oxide and internal alkynes, such as $MeCCSiMe_3$ and MeCCTol all gave either no reaction or an intractable mixture at room temperature or elevated temperatures, with no evidence of reaction through transient alkylidene species.

5.6 Conclusions

The synthesis of $[Pn^*TiBr(\mu\text{-}Br)]_2$ (**28**), conducted in an identical manner to the chloride-analogue, $[Pn^*TiCl(\mu\text{-}Cl)]_2$ (**5.7**), has been described and the compound was structurally characterised. Subsequently, reactions of **28** and **5.7** with alkylaluminium reagents, $AlMe_3$ and Al^iBu_3, were carried out in attempt to form a permethylpentalene analogue of the Tebbe reagent ($Cp_2Ti(\mu\text{-}CH_2)(\mu\text{-}Cl)AlMe_2$, **5.20**). Analogous to what has been observed for the zirconium equivalent, $[(Pn^*Ti)_2(\mu\text{-}Cl)_3][(Me_3Al)_2(\mu\text{-}Cl)]$ (**29**) formed upon reaction of **5.7** with two equivalents $AlMe_3$ in benzene and was structurally characterised. This reaction proceeded by the abstraction of one chloride ligand from **5.7**, which would be expected as the first step towards Tebbe reageant synthesis. Reaction of **5.7** with Al^iBu_3 gave an intractable mixture from which single crystals could be reliably grown, though the structure could not be solved satisfactorily. Furthermore, reactions of **28** were unsuccessful.

Attention was next turned to the reactions of the "pre-methylated" complexes $[Pn^*TiMe(\mu\text{-}Cl)]_2$ (**5.8**) and $[Pn^*TiMe(\mu\text{-}Br)]_2$ (**30**), the synthesis of which was described here, with alkylaluminium reagents. Compounds **5.8** and **30** were found not to react with $AlMe_3$ or Al^iBu_3, instead undergoing the same thermal decomposition as is observed in the absence of the reagents. Additionally, reactions of Pn^*TiMe_2 (**5.11**) and $Pn^*Ti(CH_2SiMe_3)_2$ (**5.13**) with the alkylaluminium chloride reagents Me_2AlCl and $EtAlCl_2$ were carried out. No evidence of a Tebbe reagent analogue was found and with **5.11** only non-quantitative formation of the methylidene bridged dimer

[Pn*Ti(μ-Cl)]$_2$(μ-CH$_2$) (**5.26**) could be observed by ^{1}H NMR spectroscopy, indicating chloride transfer to titanium.

Attempts to observe reactivity of a titanium permethylpentalene alkylidene were made through reactions of **5.26**, [Pn*Ti(μ-Br)]$_2$(μ-CH$_2$) (**31**), **5.11** and **5.13** with a variety of small molecules. Intractable mixtures were formed in many cases, but reaction of two equivalents HCC^{t}Bu with **5.26** or **31** led to the formation of the halide-bridged acetylide dimers [Pn*Ti(CC^{t}Bu)(μ-X)]$_2$ (X = Cl (**32** or Br (**33**)) by C–H activation. Reaction of HCC^{t}Bu with the methyl complexes **5.8** and **30** gave **32** and **33**, respectively, confirming that the methylidene moiety of **5.26** and **31** does not react through a transient Ti=CH$_2$ bond. No evidence for formation of a permethylpentalene Tebbe reagent analogue was found, nor was evidence for the possibility of reaction of titanium permethylpentalene complexes through transient terminal alkylidene species.

5.7 References

1 P. C. den Boer-Veenendaal and D. H. W. den Boer, *Mol. Phys.*, 1961, **4**, 33–38.
2 P. C. den Boer, D. H. W. den Boer, C. A. Coulson and T. H. Goodwin, *Tetrahedron*, 1963, **19**, 2163–2170.
3 T. Bally, S. Chai, M. Neuenschwander and Z. Zhu, *J. Am. Chem. Soc.*, 1997, **119**, 1869–1875.
4 M. J. S. Dewar and C. de Llano, *J. Am. Chem. Soc.*, 1969, **91**, 789–795.
5 K. Hafner, R. Dönges, E. Goedecke and R. Kaiser, *Angew. Chem., Int. Ed.*, 1973, **12**, 337–339.
6 B. A. Hess and L. J. Schaad, *J. Am. Chem. Soc.*, 1971, **93**, 305–310.
7 S. A. R. Knox and F. G. A. Stone, *Acc. Chem. Res.*, 1974, **7**, 321–328.
8 H. S. Kaufman, I. F. Ankuchen and H. Mark, *Nature*, 1948, **161**, 165–165.
9 F. Klärner, *Angew. Chem., Int. Ed.*, 2001, **40**, 3977–3981.
10 T. J. Katz, M. Rosenberger and R. K. O'Hara, *J. Am. Chem. Soc.*, 1964, **86**, 249–252.
11 M. Jones and L. O. Schwab, *J. Am. Chem. Soc.*, 1968, **90**, 6549–6550.
12 F. G. N. Cloke, M. C. Kutcha, R. M. Harker, P. B. Hitchcock and J. S. Parry, *Organometallics*, 2000, **19**, 5795–5798.
13 M. S. Baird and C. B. Reese, *Tetrahedron Lett.*, 1976, **17**, 2895–2898.
14 S. C. Jones, P. Roussel, T. Hascall and D. O'Hare, *Organometallics*, 2006, **25**, 221–229.
15 R. Kaiser and K. Hafner, *Angew. Chem., Int. Ed.*, 1970, **9**, 892–893.
16 R. Kaiser and K. Hafner, *Angew. Chem.*, 1973, **85**, 361–362.
17 S. C. Jones, DPhil Thesis, University of Oxford, 2003.
18 A. E. Ashley, DPhil Thesis, University of Oxford, 2006.
19 A. E. Ashley, A. R. Cowley and D. O'Hare, *European J. Org. Chem.*, 2007, **2007**, 2239–2242.
20 A. E. Ashley, A. R. Cowley and D. O'Hare, *Chem. Commun.*, 2007, 1512–1514.
21 F. G. N. Cloke, J. C. Green, A. F. R. Kilpatrick and D. O'Hare, *Coord. Chem. Rev.*, 2017, 344, 238–262.
22 R. T. Cooper, F. M. Chadwick, A. E. Ashley and D. O'Hare, *Organometallics*, 2013, **32**, 2228–2233.
23 S. C. Jones and D. O'Hare, *Chem. Commun.*, 2003, **3**, 2208–2209.
24 A. E. Ashley, R. T. Cooper, G. G. Wildgoose, J. C. Green and D. O'Hare, *J. Am. Chem. Soc.*, 2008, **130**, 15662–15677.
25 M. C. Kuchta, F. G. N. Cloke and P. B. Hitchcock, *Organometallics*, 1998, **17**, 1934–1936.
26 F. G. N. Cloke, J. C. Green, C. N. Jardine and M. C. Kuchta, *Organometallics*, 1999, **18**, 1087–1090.
27 G. Balazs, F. G. N. Cloke, L. Gagliardi, J. C. Green, A. Harrison, P. B. Hitchcock, A. R. M. Shahi and O. T. Summerscales, *Organometallics*, 2008, **27**, 2013–2020.
28 B. Michaels, Part II Thesis, University of Oxford, 2019.
29 O. T. Summerscales, C. J. Rivers, M. J. Taylor, P. B. Hitchcock, J. C. Green and F. G. N. Cloke, *Organometallics*, 2012, **31**, 8613–8617.
30 S. C. Binding, J. C. Green, W. K. Myers and D. O'Hare, *Inorg. Chem.*, 2015, **54**, 11935–11940.
31 T. J. Katz, N. Acton and J. Mcginnis, *J. Am. Chem. Soc.*, 1972, **94**, 6205–6206.

32 T. J. Katz and N. Acton, *J. Am. Chem. Soc.*, 1972, 94, 3281–3283.
33 A. F. R. Kilpatrick, J. C. Green, F. G. N. Cloke and N. Tsoureas, *Chem. Commun.*, 2013, **49**, 9434–9436.
34 F. Geoffrey and N. Cloke, in *Pure and Applied Chemistry*, International Union of Pure and Applied Chemistry, 2001, vol. 73, pp. 233–238.
35 R. Gleiter, S. Bethke, J. Okubo and K. Jonas, *Organometallics*, 2001, **20**, 4274–4278.
36 R. B. King, *Appl. Organomet. Chem.*, 2003, **17**, 393–397.
37 S. Bendjaballah, S. Kahlal, K. Costuas, E. Bévillon and J.-Y. Saillard, *Chem. Eur. J.*, 2006, **12**, 2048–2065.
38 K. Jonas, B. Gabor, R. Mynott, K. Angermund, O. Heinemann and C. Krüger, *Angew. Chem., Int. Ed.*, 1997, **36**, 1712–1714.
39 J. W. Lauher and R. Hoffmann, *J. Am. Chem. Soc.*, 1976, **98**, 1729–1742.
40 J. C. Green, *Chem. Soc. Rev.*, 1998, **27**, 263.
41 K. Jonas, P. Kolb, G. Kollbach, B. Gabor, R. Mynott, K. Angermund, O. Heinemann and C. Krüger, *Angew. Chem., Int. Ed.*, 1997, **36**, 1714–1718.
42 F. M. Chadwick, R. T. Cooper, A. E. Ashley, J. C. Buffet and D. M. O'Hare, *Organometallics*, 2014, **33**, 3775–3785.
43 F. G. N. Cloke, P. B. Hitchcock, M. C. Kuchta and N. A. Morley-Smith, *Polyhedron*, 2004, **23**, 2625–2630.
44 B. J. C Green, M. L. H Green and C. K. Prout, *A Bonding Model for Bent Bis-(n-cyclopentadienyl) Metal Compounds*, 1972.
45 M. L. H. Green, *Pure Appl. Chem.*, 1972, **30**, 373–388.
46 L. J. Procopio, P. J. Carroll and D. H. Berry, *J. Am. Chem. Soc.*, 1994, **116**, 177–185.
47 A. Clearfield, D. K. Warner, C. Herman Saldarriaga-Molina, R. Ropal and I. Bernal, *Can. J. Chem.*, 1975, **53**, 1622–1629.
48 A. F. R. Kilpatrick and F. G. N. Cloke, *Chem. Commun.*, 2014, **50**, 2769–2771.
49 A. F. R. Kilpatrick, J. C. Green and F. G. N. Cloke, *Organometallics*, 2015, **34**, 4830–4843.
50 A. F. R. Kilpatrick, J. C. Green and F. G. N. Cloke, *Organometallics*, 2015, **34**, 4816–4829.
51 A. F. R. Kilpatrick, J. C. Green and F. G. N. Cloke, *Organometallics*, 2017, **36**, 352–362.
52 N. Tsoureas, J. C. Green and F. G. N. Cloke, *Chem. Commun.*, 2017, **53**, 13117–13120.
53 N. Tsoureas, J. C. Green and F. G. N. Cloke, *Dalton Trans.*, 2018, **47**, 14531–14539.
54 R. T. Cooper, F. M. Chadwick, A. E. Ashley and D. O'Hare, *Chem. Commun.*, 2015, **51**, 11856–11859.
55 R. T. Cooper, DPhil Thesis, University of Oxford, 2012.
56 D. A. X. Fraser, DPhil Thesis, University of Oxford, 2018.
57 D. A. X. Fraser, Z. R. Turner, J. C. Buffet and D. O'Hare, *Organometallics*, 2016, **35**, 2664–2674.
58 J. A. Pool, E. Lobkovsky and P. J. Chirik, *Nature*, 2004, **427**, 527–530.
59 T. E. Hanna, I. Keresztes, E. Lobkovsky, W. H. Bernskoetter and P. J. Chirik, *Organometallics*, 2004, **23**, 3448–3458.
60 D. J. Knobloch, E. Lobkovsky and P. J. Chirik, *Nat. Chem.*, 2010, **2**, 30–35.
61 J. M. Manriquez and J. E. Bercaw, *J. Am. Chem. Soc.*, 1974, 96, 6229–6230.
62 J. M. Manriquez, R. D. Banner, R. E. Marsh and J. E. Bercaw, *J. Am. Chem.*

Soc., 1976, **98**, 3042–3044.
63 A. F. R. Kilpatrick, J. C. Green, Z. R. Turner, J. C. Buffet and D. O'Hare, *Chem. Commun.*, 2017, **53**, 12048–12051.
64 F. N. Tebbe, G. W. Parshall and G. S. Reddy, *J. Am. Chem. Soc.*, 1978, **100**, 3611–3613.
65 T. Takeda, *Modern carbonyl olefination*, Wiley-VCH, 2004.
66 T. Takeda, *Bull. Chem. Soc. Jpn.*, 2005, **78**, 195–217.
67 F. N. Tebbe, G. W. Parshall and D. W. Ovenall, *J. Am. Chem. Soc.*, 1979, **101**, 5074–5075.
68 U. Klabunde, F. N. Tebbe, G. W. Parshall and R. L. Harlow, *J. Mol. Catal.*, 1980, **8**, 37–51.
69 R. C. Hartley and G. J. McKiernan, *J. Chem. Soc. Perkin 1*, 2002, 2, 2763–2793.
70 T. R. Howard, J. B. Lee and R. H. Grubbs, *J. Am. Chem. Soc.*, 1980, 102, 6876–6878.
71 N. A. Petasis, S.-P. Lu, E. I. Bzowej, D.-K. Fu, J. P. Staszewski, I. Akritopoulou-Zanze, M. A. Patane and Y.-H. Hu, *Pure Appl. Chem*, 1996, **68**, 667–670.
72 J. D. Meinhart, E. V. Anslyn and R. H. Grubbs, *Organometallics*, 1989, **8**, 583–589.
73 L. Clawson, S. L. Buchwald and R. H. Grubbs, *Tetrahedron Lett.*, 1984, **25**, 5733–5736.
74 F. W. Hartner and J. Schwartz, *J. Am. Chem. Soc.*, 1981, **103**, 4979–4981.
75 R. Thompson, E. Nakamaru-Ogiso, C. H. Chen, M. Pink and D. J. Mindiola, *Organometallics*, 2014, **33**, 429–432.
76 N. A. Petasis and E. I. Bzowej, *J. Am. Chem. Soc.*, 1990, **112**, 6392–6394.
77 N. A. Petasis and Y. H. Hu, *J. Org. Chem.*, 1997, **62**, 782–783.
78 B. de Heisteeg, G. Schat, O. S. Akkerman and F. Bickelhaupt, *Tetrahedron Lett.*, 1987, **28**, 6493–6496.
79 F. Ozawa, J. W. Park, P. B. Mackenzie, W. P. Schaefer, L. M. Henling and R. H. Grubbs, *J. Am. Chem. Soc.*, 1989, **111**, 1319–1327.
80 C. E. Tucker and P. Knochel, *J. Am. Chem. Soc.*, 1991, **113**, 9888–9890.
81 S. M. Clift and J. Schwartz, *J. Am. Chem. Soc.*, 1984, **106**, 8300–8301.
82 F. M. Hartner, S. M. Clift, J. Schwartz and T. H. Tulip, *Organometallics*, 1987, **6**, 1346–1350.
83 Z. R. Turner and D. O'Hare, *Unpublished Results*.
84 F. N. Tebbe and L. J. Guggenberger, *J. Chem. Soc. Chem. Commun.*, 1973, 227–228.
85 T. Oswald, N. Lauterbach, M. Schmidtmann and R. Beckhaus, *Acta Crystallogr. Sect. C Struct. Chem.*, 2018, **74**, 442–451.
86 N. Klouras, V. Nastopoulos, I. Demakopoulos and I. Leban, *Zeitschrift fur Anorg. und Allg. Chemie*, 1993, **619**, 1927–1930.
87 A. J. Edwards, N. J. Burke, C. M. Dobson, K. Prout and S. J. Heyes, *J. Am. Chem. Soc.*, 1995, **117**, 4637–4653.
88 R. J. West, Part II Thesis, University of Oxford, 2008.
89 R. J. Boyd and S. L. Boyd, *J. Am. Chem. Soc.*, 1992, **114**, 1652–1655.
90 J. Emsley, *The Elements*, Oxford University Press, 2000.
91 R. Gomez, T. Cuenca, P. Royo and E. Hovestreydt, *Organometallics*, 1991, **10**, 2516–2518.
92 O. Buitrago, C. R. De Arellano, G. Jiménez and T. Cuenca, *Organometallics*, 2004, **23**, 5873–5876.
93 C. McDade, J. C. Green, J. E. Bercaw and J. C. Green, *Organometallics*, 1982, **1**,

1629–1634.
94 H. Van Der Heijden and B. Hessen, *J. Chem. Soc. Chem. Commun.*, 1995, 145–146.
95 H. Van Der Heijden and B. Hessen, *Inorganica Chim. Acta*, 2003, **345**, 27–36.
96 F. Sato, H. Urabe and S. Okamoto, *Chem. Rev.*, 2000, **100**, 2835–2886.
97 S. A. Cohen and J. E. Bercaw, *Organometallics*, 1985, **4**, 1006–1014.
98 T. T. Nguyen, G. D. Kortman and K. L. Hull, *Organometallics*, 2016, **35**, 1713–1725.
99 B. Xie, DPhil Thesis, University of Oxford, 2018.
100 B. D. Ward, A. Maisse-François, P. Mountford and L. H. Gade, *Chem. Commun.*, 2004, **4**, 704–705.
101 K. Yan and A. D. Sadow, *Chem. Commun.*, 2013, **49**, 3212–3214.
102 M. Horáček, P. Štěpnička, J. Kubišta, R. Gyepes and K. Mach, *Organometallics*, 2004, **23**, 3388–3397.
103 D. Kissounko, A. Epshteyn, J. C. Fettinger and L. R. Sita, *Organometallics*, 2006, **25**, 531–535.
104 W. Frosch, S. Back, H. Müller, K. Köhler, A. Driess, B. Schiemenz, G. Huttner and H. Lang, *J. Organomet. Chem.*, 2001, **619**, 99–109.
105 S. Back, T. Stein, W. Frosch, I. Y. Wu, J. Kralik, M. Büchner, G. Huttner, G. Rheinwald and H. Lang, *Inorganica Chim. Acta*, 2001, **325**, 94–102.
106 Y. Hayashi, M. Osawa, K. Kobayashi and Y. Wakatsuki, *Chem. Commun.*, 1996, **0**, 1617–1618.
107 P. Štěpnička, R. Gyepes, I. Císařová, M. Horáček, J. Kubišta and K. Mach, *Organometallics*, 1999, **18**, 4869–4880.
108 F. G. Kirchbauer, P. M. Pellny, H. Sun, V. V. Burlakov, P. Arndt, W. Baumann, A. Spannenberg and U. Rosenthal, *Organometallics*, 2001, **20**, 5289–5296.
109 S. Back, H. Pritzkow and H. Lang, *Organometallics*, 1998, **17**, 41–44.

Chapter Six

Experimental details and characterising data

6.1 General methods and instrumentation

All manipulations were carried out using standard Schlenk line or dry-box techniques under an atmosphere of argon or dinitrogen. Solvents were either degassed by sparging with dinitrogen and dried by passing through a column of the appropriate drying agent[1] or refluxed over sodium (toluene), potassium (THF) or Na/K alloy (Et_2O) and distilled. Deuterated solvents were dried over potassium (C_6D_6 and toluene-d_8), sodium (THF-d_8) or CaH_2 (pyridine-d_5 and C_6D_5Br) distilled under reduced pressure and stored under argon in Teflon valve ampoules. Unless otherwise stated NMR samples were prepared under dinitrogen in 5 mm Wilmad 507-PP tubes fitted with J. Young Teflon valves. ^{1}H, $^{1}H\{^{11}B\}$, $^{13}C\{^{1}H\}$, ^{11}B, $^{11}B\{^{1}H\}$, ^{19}F, $^{19}F\{^{1}H\}$, ^{31}P, ^{29}Si and ^{2}H spectra were recorded on Bruker Ascend 400, Bruker Avance III 500 NMR or a Bruker AVC 500 spectrometer fitted with a ^{13}C cryoprobe. ^{1}H and $^{13}C\{^{1}H\}$ and spectra were referenced internally to residual protio-solvent (^{1}H) or solvent (^{13}C) resonances, and are reported relative to tetramethylsilane ($\delta = 0$ ppm). ^{2}H NMR spectra were referenced to the natural abundance deuterium resonance of the protio solvent. ^{19}F, ^{11}B, ^{29}Si and ^{31}P spectra were referenced externally to $CFCl_3$, $Et_2O{\cdot}BF_3$, $SiMe_4$ and H_3PO_4 respectively. Assignments were confirmed as necessary with the use of two dimensional ^{1}H-^{1}H, ^{13}C-^{1}H, ^{19}F-^{19}F, ^{13}C-^{19}F and ^{1}H-^{29}Si NMR correlation experiments. Chemical shifts are quoted in δ (ppm) and coupling constants in Hz. IR spectra were recorded on a Thermo Scientific Nicolet iS5 FTIR spectrometer and samples prepared in a dry-box using NaCl plates as a Nujol mull or as a thin film. The data are quoted in wavenumbers (cm^{-1}). Elemental analyses were carried out by the Elemental Analysis Service at the London Metropolitan University.

6.2 Literature preparations

$Cp_2Zr(NNPh_2)(DMAP)$,[2] $Cp_2Zr(NPh_2)(NCO)$,[2] $Cp_2Zr(N^tBu)(THF)$,[3] $Cp_2Zr(N^tBu)(DMAP)$,[4] $Cp_2Zr(NXyl)(THF)$,[3] NaCp,[5] $Cp_2Ti(N^tBu)(py)$,[6] $Cp_2Ti(NNPh_2)(py)$,[7] $PhSiD_3$,[8] $HN(^tBu)SiMe_2H$,[9] $Cp_2Zr(H)\{N(^tBu)SiMe_2(\mu\text{-}H)\}$,[10] $Cp_2Zr(PMe_3)\{\eta^2\text{-}N(^tBu)SiMe_2\}$,[10] DCC^tBu,[11] $TiCl_4.2THF$,[12] Pn^*Li_2,[13,14] $[Pn^*TiCl(\mu\text{-}Cl)]_2$,[15] $[Pn^*TiMe(\mu\text{-}Cl)]_2$[16] and $[Pn^*Ti(\mu\text{-}Cl)]_2(\mu\text{-}CH_2)$[16] were synthesised according to literature procedures.

$HBMes_2$ was kindly donated by Dr. Simona Mellino. $HCCC_6F_5$ and $DCCC_6F_5$ were kindly provided by Dr. Bowen Xie. 1,1-diphenylhydrazine was obtained from Sigma-Aldrich as the hydrogen chloride salt, from which the free hydrazine was obtained by basification, drying and removal of residual solvent, followed by distillation under inert atmospheric conditions. All other reagents were purchased from commercial suppliers and (for liquid reagents) degassed before use, unless specified otherwise. HCC^tBu, HCCTol, H_2N^tBu and H_2NXyl were dried over CaH_2 and distilled before use. DMAP was sublimed under dynamic vacuum at 100 °C and transferred to the dry-box.

6.3 X-ray data collection and processing parameters

Crystals were mounted on glass fibers using perfluoropolyether oil and cooled rapidly in a stream of cold N_2 using an Oxford Cryosystems Cryostream unit. Diffraction data were measured using either an Enraf-Nonius KappaCCD or Agilent Technologies Supernova diffractometer using Mo-K_α or Cu-K_α radiation, respectively. As appropriate, absorption and decay corrections were applied to the data and equivalent reflections merged.[17] The structures were solved with SIR92[18] or Superflip,[19] and further refinements and all other crystallographic calculations were performed using the CRYSTALS program suite.[20]

Other details of the structure solution and refinements are given in the CIF data, which can be made available on request.

6.4 Computational details

DFT calculations described in this Thesis were performed by Dr Eric Clot (Institut Charles Gerhardt, Université de Montpellier) and Professor Philip Mountford (University of Oxford). Geometry optimisations were performed with the Gaussian09 package (rev. D.01)[21] at the B3PW91 level of hybrid density functional theory,[22,23] with inclusion of Grimme's D3(bj) dispersion correction[24,25] in the optimisation process except for sterically-pruned model systems. For geometry optimisations in the gas phase all atoms were represented by the Def2-SVP basis set.[26] For sterically-pruned model systems additional single-point calculations were carried out on the optimised geometry using the Def2-TZVP basis set.[27] For systems with realistic steric bulk, the single-point calculations, again with a Def2-TZVP basis set, took into account both solvent and dispersion effects. All calculations for zirconium systems included the appropriate effective core pseudopotential.[28] The solvent (benzene) influence was taken into consideration through single point calculations on the gas-phase optimized geometry with SCRF calculations within the SMD model.[29] For the SCRF calculations all the atoms were treated with a Def2-TZVP basis set.[27] Influence of the dispersion forces was also considered by computing the D3(bj) corrections.[24,25] SCF energies reported in this work are for gas-phase model systems using the Def2-TZVP basis set. For larger systems (Def2-TZVP basis sets) the Gibbs free energies and enthalpies were obtained by summing the SMD energy, the gas-phase Gibbs or enthalpy contribution at 298.15 K (or another temperature where specified) obtained from the geometry optimisations, and the D3(bj) correction. NBO analyses were carried out using NBO 6.0,[30] on wavefunctions

computed with B3PW91 and the Def2-TZVP family of basis sets for all atoms. NMR chemical shifts were computed using the GIAO method as implemented in Gaussian09 at the B3PW91 level. Non-metal atoms were described with the pcSseg-2 and pcJ-2 NMR basis sets of Jensen (for shielding tensors and spin-spin coupling constants, respectively),[31,32] and Zr was treated as described above. The ^{11}B and ^{29}Si NMR shifts are referenced with respect to the experimental values of 0.0 ppm for $BF_3{\cdot}OEt_2$ and $SiMe_4$, respectively.

6.5 Experimental details and characterising data for Chapter Two

$Cp_2Zr(H)\{N(NPh_2)BPin\}$ (1). To a stirred solution of $Cp_2Zr(NNPh_2)(DMAP)$ (**2.3**, 0.400 g, 0.761 mmol) in toluene (20 mL), at 0 °C, was added dropwise pinacol borane (0.121 mL, 0.837 mmol). The solution was stirred for 10 mins at 0 °C before being allowed to warm to RT and stirred for a further 1 h. Volatiles were removed under reduced pressure and the resulting solid extracted with hexane (3 x 10 mL) and concentrated. Pale yellow diffraction-quality crystals grew upon cooling to 4 °C and were washed with cold hexane and dried *in vacuo* to afford **1**. Yield: 0.295 g (73%).

^{1}H NMR (C_6D_6, 400.1 MHz, 298 K): δ 7.97 – 7.93 (4 H, m, *o*-NC_6H_5), 7.08 – 7.03 (4 H, m, *m*-NC_6H_5), 6.84 – 6.80 (2 H, m, *p*-NC_6H_5), 5.67 (10 H, s, C_5H_5), 5.22 (1 H, s, ZrH), 1.18 (12 H, s, Me) ppm. ^{13}C{^{1}H} NMR (C_6D_6, 100.6 MHz, 293 K): δ 154.0 (*i*-NC_6H_5), 128.2 (*m*-NC_6H_5), 125.3 (*p*-NC_6H_5), 125.3 (*o*-NC_6H_5), 106.3 (C_5H_5), 82.2 (CMe), 24.8 (CMe) ppm. ^{11}B NMR (C_6D_6, 128.4 MHz, 293 K): δ 26.1 (s) ppm. IR (NaCl plates, Nujol mull, cm^{-1}): 1592 (w, ν(Zr-H)), 1485 (s), 1414 (s), 1279 (w), 1260 (m), 1142 (s), 1087 (m), 1068 (m), 1028 (m), 1014 (s), 969 (w), 802 (s). Anal. found (calcd. for $C_{28}H_{33}N_2O_2BZr$): C, 63.14 (63.26); H, 6.38 (6.26); N, 5.22 (5.27)%.

$Cp_2Zr(H)\{N(NPh_2)SiH_2Ph\}$ (2). To a stirred solution of $Cp_2Zr(NNPh_2)$(DMAP) (**2.3**, 0.300 g, 0.571 mmol) in benzene (10 mL) at RT was added dropwise a solution of $PhSiH_3$ (0.106 mL, 0.857 mmol) in benzene (5 mL). The solution was then heated to 40 °C and allowed to stir for 1 d after which time the volatiles were removed under reduced pressure to afford a yellow sticky solid which was then triturated with hexane (5 mL) and dried *in vacuo* to afford **2**, with 1 equivalent DMAP, as a yellow powder. Yield: 0.235 g (65%). Diffraction-quality crystals were grown from a concentrated benzene solution at RT.

^{1}H NMR (C_6D_6, 400.1 MHz, 298 K): δ 7.90 – 7.86 (2 H, m, *o*-SiC_6H_5), 7.70 – 7.67 (4 H, m, *o*-NC_6H_5), 7.32 – 7.28 (3 H, overlapping 2 x m, *m*-SiC_6H_5, *p*-SiC_6H_5) 7.03 – 6.98 (4 H, m, *m*-NC_6H_5), 6.82 – 6.78 (2 H, m, *p*-NC_6H_5), 5.53 (2 H, s, SiH_2), 5.51 (10 H, s, C_5H_5), 5.03 (1 H, s, ZrH) ppm. $^{13}C\{^1H\}$ NMR (C_6D_6, 100.6 MHz, 293 K): δ 153.7 (*i*-NC_6H_5), 136.0 (*o*-SiC_6H_5), 135.6 (*i*-SiC_6H_5), 130.4 (*p*-SiC_6H_5), 128.7 (*m*-NC_6H_5), 128.5 (*m*-SiC_6H_5), 125.8 (*p*-NC_6H_5), 125.3 (o-NC_6H_5), 105.8 (C_5H_5) ppm. ^{29}Si NMR (HMBC ^{1}H-observed, C_6D_6, 499.9 MHz, 298 K): δ –32.9 ($^1J_{SiH}$ = 202 Hz, SiH_2Ph) ppm. IR (NaCl plates, Nujol mull, cm^{-1}): 2110 (s, ν(Si–H)), 2072 (m, ν(Si–H)), 1594 (s), 1584 (m, ν(Zr-H)), 1537 (w), 1519 (w), 1485 (s), 1428 (m), 1226 (w), 1117 (w), 1049 (w), 1021 (w), 1011 (w), 966 (m), 884 (m), 871 (s), 834 (s), 817 (s), 802 (s). Compound **2** repeatedly gave unsatisfactory and irreproducible combustion analyses which is attributed to the variable amounts of inseparable DMAP present.

$Cp_2Zr(D)\{N(NPh_2)SiD_2Ph\}$ (2-*d*$_3$). To a stirred solution of $Cp_2Zr(NNPh_2)$(DMAP) (**2.3**, 0.300 g, 0.571 mmol) in benzene (10 mL) at RT was added dropwise a solution of $PhSiD_3$ (0.106 mL, 0.857 mmol) in benzene (5 mL). The solution was then heated to 40 °C and allowed to stir for 1 d after which time the volatiles were removed under reduced pressure to afford a yellow sticky solid which was then triturated with hexane (5 mL) and dried *in vacuo* to afford **2-*d*$_3$**, with 1 equivalent DMAP, as a yellow powder. Yield: 0.207 g (57%).

^{2}H NMR (C_6H_6, 76.7 MHz, 298 K): δ 5.52 (s, SiD_2), 5.02 (s, ZrD) ppm.

$Cp_2Zr(H)\{N(NPh_2)SiHPh_2\}$ (3). To a stirred solution of $Cp_2Zr(NNPh_2)$(DMAP) (**2.3**, 0.300 g, 0.571 mmol) in benzene (10 mL) at RT was added dropwise a solution of Ph_2SiH_2 (0.158 mL, 0.857 mmol) in benzene (5 mL). The solution was then heated to 60 °C and allowed to stir for 2 d after which time the volatiles were removed under reduced pressure to afford a yellow sticky solid which was then triturated with hexane (5 mL) and dried *in vacuo* to afford **3**, with 1 equivalent DMAP, as a yellow powder. Yield: 0.248 g (61%). Diffraction-quality crystals were grown from a concentrated benzene solution at RT.

^{1}H NMR (C_6D_6, 400.1 MHz, 298 K): δ 7.68 – 7.59 (8 H, overlapping 2 x m, *o*-NC_6H_5, *o*-SiC_6H_5), 7.22 – 7.18 (6 H, overlapping 2 x m, *m*-SiC_6H_5, *p*-SiC_6H_5), 6.97 – 6.92 (4 H, m, *m*-NC_6H_5), 6.80 – 6.76 (2 H, m, *p*-NC_6H_5), 6.25 (1 H, s, SiH), 5.52 (10 H, s, C_5H_5), 5.02 (1 H, s, ZrH) ppm. ^{13}C{^{1}H} NMR (C_6D_6, 100.6 MHz, 293 K): δ 154.4 (*i*-NC_6H_5), 137.7 (*i*-SiC_6H_5), 135.8 (*o*-SiC_6H_5), 129.8 (*p*-SiC_6H_5), 128.5 (*m*-NC_6H_5), 128.2 (*m*-SiC_6H_5), 126.0 (*o*-NC_6H_5), 125.6 (*p*-NC_6H_5), 105.9 (C_5H_5) ppm. ^{29}Si NMR (HMBC ^{1}H-observed, C_6D_6, 499.9 MHz, 298 K): δ –20.7 ($^{1}J_{SiH}$ = 201 Hz, $SiHPh_2$) ppm. IR (NaCl plates, Nujol mull, cm^{-1}): 2125 (m, ν(Si–H)), 1586 (m, ν(Zr-H)), 1540 (w), 1486 (s), 1427 (m), 1261 (s), 1203 (w), 1181 (w), 1156 (m), 1108 (s), 1062 (s), 1014 (s), 927 (w), 863 (m), 825 (s), 801 (s), 761 (s), 739 (m), 733 (m), 706 (s), 695 (s), 681 (m), 640 (w), 597 (m), 583 (m). Compound **3** repeatedly gave unsatisfactory and irreproducible combustion analyses which is attributed to the variable amounts of inseparable DMAP present.

$Cp_2Zr(Cl)\{N(NPh_2)SiH_2Ph\}$ (4). To a stirred solution of $Cp_2Zr(NNPh_2)$(DMAP) (**2.3**, 0.300 g, 0.571 mmol) in benzene (10 mL), at 0 °C, was added dropwise a solution of $PhSiH_2Cl$ (76.0 µL, 0.571 mmol) in benzene (5 mL). The reaction was allowed to warm

to room temperature and after 1 h the volatiles were removed under reduced to afford a yellow sticky solid, which was then triturated with hexane (5 mL) and dried *in vacuo* to afford **4**, with 1 equivalent DMAP, as an orange powder. Yield: 0.271 g (71%). Diffraction-quality crystals were grown from a concentrated benzene solution at RT.

^{1}H NMR (C_6D_6, 400.1 MHz, 298 K): δ 7.87 – 7.83 (4 H, m, *o*-NC_6H_5), 7.67 – 7.63 (2 H, m, *o*-SiC_6H_5), 7.23 – 7.19 (3 H, overlapping 2 x m, *m*-SiC_6H_5, *p*-SiC_6H_5), 7.07 – 7.02 (4 H, m, *m*-NC_6H_5), 6.87 – 6.82 (2 H, m, *p*-NC_6H_5), 5.78 (10 H, s, C_5H_5), 5.42 (2 H, s, SiH_2) ppm. ^{13}C{^{1}H} NMR (C_6D_6, 100.6 MHz, 293 K): δ 152.4 (*i*-NC_6H_5), 136.0 (*o*-SiC_6H_5), 135.2 (*i*-SiC_6H_5), 130.5 (*p*-SiC_6H_5), 128.7 (*m*-NC_6H_5), 128.5 (*m*-SiC_6H_5), 125.6 (*p*-NC_6H_5), 124.5 (o-NC_6H_5), 113.3 (C_5H_5) ppm. ^{29}Si NMR (HMBC ^{1}H-observed, C_6D_6, 499.9 MHz, 298 K): δ –29.9 ($^{1}J_{SiH}$ = 208 Hz, SiH_2Ph) ppm. IR (NaCl plates, Nujol mull, cm^{-1}): 2360 (w), 2142 (w, ν(Si–H)), 2102 (m, ν(Si–H)), 1588 (m), 1485 (m), 1120 (w), 1048 (w), 1013 (m), 948 (m), 895 (m), 834 (m), 813 (s), 800 (s), 773 (m), 707 (m), 630 (w), 600 (w). Compound **4** repeatedly gave unsatisfactory and irreproducible combustion analyses which is attributed to the variable amounts of inseparable DMAP present.

Alternative NMR tube scale synthesis of $Cp_2Zr(Cl)\{N(NPh_2)SiH_2Ph\}$ (4). To a solution of $Cp_2Zr(H)\{N(NPh_2)SiH_2Ph\}$ (**2**, 10.0 mg, 20.5 μmol) in C_6D_6 (0.6 mL) in an NMR tube equipped with a J. Young Teflon valve at RT was added $PhSiH_2Cl$ (2.8 μL, 21.0 μmol). Immediate, quantitative formation of **4** was observed by ^{1}H NMR spectroscopy, with concomitant formation of $PhSiH_3$. No colour change was observed.

Alternative NMR tube scale synthesis of $Cp_2Zr(H)(NH^tBu)$ (2.14). A freeze-pump-thaw-degassed solution of $Cp_2Zr(N^tBu)$(DMAP) (**2.13**, 10.0 mg, 24.1 μmol) in C_6D_6 (0.6 mL) in an NMR tube equipped with a J. Young Teflon valve was exposed to H_2 (1 bar overpressure) at RT. The reaction was heated to 80 °C for 3 days

bringing about a colour change from yellow to pale yellow. ^{1}H NMR spectroscopy showed that the reaction had reached an equilibrium mixture containing 56% **2.13** and 44% **2.14** with the ^{1}H NMR data matching those previously reported.[4]

NMR tube scale synthesis of $Cp_2Zr(NPh_2)\{NCNXyl\}$ (5). To a solution of $Cp_2Zr(NNPh_2)(DMAP)$ (**2.3**, 30.0 mg, 57.1 μmol) in C_6D_6 (0.6 mL) in an NMR tube equipped with a J. Young Teflon valve was added XylNC (7.5 mg, 57.1 μmol) at RT. The product **5** was quantitatively formed immediately and subsequently characterised by ^{1}H and ^{13}C NMR spectroscopy at RT. Attempts to isolate **5** on the preparative scale were unsuccessful.

^{1}H NMR (C_6D_6, 400.1 MHz, 298 K): δ 7.15 – 7.11 (4 H, m, *o*-NC_6H_5), 7.08 (2 H, d, $^{3}J_{HH}$ = 7.5 Hz, *m*-Xyl), 6.93 (1 H, t, $^{3}J_{HH}$ = 7.5 Hz, *p*-Xyl), 6.90 – 6.86 (6 H, overlapping 2 x m, *m*-NC_6H_5, *p*-NC_6H_5), 5.72 (10 H, s, C_5H_5), 2.58 (6 H, s, CH_3) ppm. ^{13}C{^{1}H} NMR (C_6D_6, 100.6 MHz, 293 K): δ 157.6 (*i*-Xyl), 150.6 (*i*-NC_6H_5), 131.8 (*o*-Xyl), 128.9 (*m*-NC_6H_5), 128.7 (*m*-Xyl), 126.9 (*o*-NC_6H_5), 122.9 (*p*-NC_6H_5), 122.2 (*p*-Xyl), 112.7 (C_5H_5), 19.9 (CH_3) ppm.

$Cp_2Zr(H)\{N(^{t}Bu)SiH(\mu\text{-}H)Ph\}$ (6). To a stirred solution of $Cp_2Zr(N^{t}Bu)(THF)$ (**2.1**, 0.149 g, 0.409 mmol) in benzene (10 mL) at RT was added dropwise a solution of $PhSiH_3$ (53.0 μL, 0.429 mmol) in benzene (5 mL). After 1 h the volatiles were removed under reduced pressure to afford a yellow oil which was then triturated with hexane (2 mL) and dried *in vacuo* to afford **6** as a yellow powder. Yield: 71 mg (43%). Diffraction-quality crystals were grown from a concentrated benzene solution at RT.

^{1}H NMR (C_6D_6, 400.1 MHz, 298 K): δ 7.69 – 7.67 (2 H, m, *o*-SiC_6H_5), 7.21 – 7.19 (3 H, overlapping 2 x m, *m*-SiC_6H_5, *p*-SiC_6H_5), 5.75 (10 H, s, C_5H_5), 5.69 (1 H, s, ZrH), 3.30 (2 H, s, SiH_2), 1.30 (9 H, s, CMe_3) ppm. ^{1}H NMR (C_7D_8, 400.1 MHz, 185 K): δ 7.71 –

7.68 (2 H, m, *o*-SiC_6H_5), 7.20 – 7.17 (3 H, overlapping 2 x m, *m*-SiC_6H_5, *p*-SiC_6H_5), 5.68 (10 H, s, C_5H_5), 5.55 (1 H, s, ZrH), 4.57 (1 H, br s, SiH), 1.74 (1 H, br s, Si(μ-H)Zr), 1.36 (9 H, s, CMe_3) ppm. $^{13}C\{^1H\}$ NMR (C_6D_6, 100.6 MHz, 293 K): δ 135.3 (*i*-SiC_6H_5), 134.8 (*o*-SiC_6H_5), 130.6 (*p*-SiC_6H_5), 128.6 (*m*-SiC_6H_5), 106.2 (C_5H_5), 54.8 ($\underline{C}Me_3$), 35.0 ($C\underline{Me}_3$) ppm. ^{29}Si NMR (HMBC ^1H-observed, C_6D_6, 499.9 MHz, 298 K): δ –95.1 ($^1J_{SiH}$ = 173 Hz, SiH_2Ph) ppm. IR (NaCl plates, Nujol mull, cm^{-1}): 2089 (m, ν(Si–H_t)), 1941 (m, ν(Si–H_b)), 1576 (m, ν(Zr-H)), 1261 (m), 1204 (m), 1050 (m), 1016 (s), 887 (s), 799 (s), 756 (w), 727 (m), 703 (m), 687 (w). Anal. found (calcd. for $C_{20}H_{27}NSiZr$): C, 59.82 (59.94); H, 6.86 (6.79); N, 3.43 (3.50)%.

$Cp_2Zr(D)\{N(^tBu)SiD(\mu\text{-}D)Ph\}$ (6-*d*$_3$). To a stirred solution of $Cp_2Zr(N^tBu)(THF)$ (**2.1**, 0.149 g, 0.409 mmol) in benzene (10 mL) at RT was added dropwise a solution of $PhSiD_3$ (53.0 μL, 0.429 mmol) in benzene (5 mL). After 1 h the volatiles were removed under reduced pressure to afford a yellow oil which was then triturated with hexane (2 mL) and dried *in vacuo* to afford **6-*d*$_3$** as a yellow powder. Yield: 75 mg (45%).

^2H NMR (C_6H_6, 76.7 MHz, 298 K): δ 5.66 (s, ZrD), 3.27 (s, SiD_2) ppm. IR (NaCl plates, Nujol mull, cm^{-1}): 1521 (m, ν(Si-D_t)), 1410 (m, ν(Si-D_b)), 1352 (m), 1261 (m), 1204 (m), 1128 (m, ν(Zr-D)), 1111 (m), 1070 (m), 1016 (m), 841 (m), 797 (s), 744 (m), 707 (m), 640 (m), 550 (m).

$Cp_2Zr(H)\{N(^tBu)Si(\mu\text{-}H)Ph_2\}$ (7). To a stirred solution of $Cp_2Zr(N^tBu)(THF)$ (**2.1**, 0.201 g, 0.551 mmol) in benzene (10 mL) at RT was added dropwise a solution of Ph_2SiH_2 (0.107 mL, 0.578 mmol) in benzene (5 mL). After 1 h the volatiles were removed under reduced pressure to afford a colourless oil which was then triturated with hexane (2 mL) and dried *in vacuo* to afford **7** as a colourless powder. Yield: 0.134 g (51%). Diffraction-quality crystals were grown from a concentrated hexane solution at –30 °C.

^{1}H NMR (C_6D_6, 400.1 MHz, 298 K): δ 7.76 – 7.73 (4 H, m, *o*-SiC_6H_5), 7.21 – 7.19 (6 H, overlapping 2 x m, *m*-SiC_6H_5, *p*-SiC_6H_5), 5.76 (10 H, s, C_5H_5), 5.72 (1 H, d, $^{2}J_{HH}$ = 3.7 Hz, ZrH), 2.41 (1 H, d, $^{2}J_{HH}$ = 3.7 Hz, SiH), 1.44 (9 H, s, CMe_3) ppm. $^{13}C\{^{1}H\}$ NMR (C_6D_6, 100.6 MHz, 293 K): δ 136.1 (*o*-SiC_6H_5), 135.7 (*i*-SiC_6H_5), 130.0 (*p*-SiC_6H_5), 128.4 (*m*-SiC_6H_5), 106.1 (C_5H_5), 55.3 ($\underline{C}Me_3$), 35.4 ($C\underline{Me_3}$) ppm. ^{29}Si NMR (HMBC ^{1}H-observed, C_6D_6, 499.9 MHz, 298 K): δ –81.1 ($^{1}J_{SiH}$ = 121 Hz, $SiHPh_2$) ppm. IR (NaCl plates, Nujol mull, cm^{-1}): 1893 (m, ν(Si–H_b)), 1614 (m, ν(Zr–H)), 1583 (m), 1260 (m), 1201 (m), 1107 (m), 1085 (m), 1015 (m), 822 (s), 807 (s), 732 (m), 700 (m), 662 (m), 555 (m). Anal. found (calcd. for $C_{26}H_{31}NSiZr$): C, 65.36 (65.49); H, 6.62 (6.55); N, 2.91 (2.94)%.

$Cp_2Zr(H)\{N(Xyl)SiH_2Ph\}$ (8). To a stirred solution of $Cp_2Zr(NXyl)(THF)$ (**2.2**, 0.203 g, 0.492 mmol) in benzene (10 mL) at RT was added dropwise a solution of $PhSiH_3$ (67.0 μL, 0.541 mmol) in benzene (5 mL). After 1 h the volatiles were removed under reduced pressure to afford **8** as a yellow, waxy solid, which could not be solidified. Yield: 0.097 g (44%).

^{1}H NMR (C_6D_6, 400.1 MHz, 298 K): δ 7.55 – 7.53 (2 H, m, *o*-SiC_6H_5), 7.13 – 7.10 (3 H, overlapping 2 x m, *m*-SiC_6H_5, *p*-SiC_6H_5), 6.99 (2 H, d, $^{3}J_{HH}$ = 7.4 Hz, *m*-Xyl), 6.85 (1 H, t , $^{3}J_{HH}$ = 7.4 Hz, *p*-Xyl), 5.70 (10 H, s, C_5H_5), 5.49 (1 H, s, ZrH), 5.26 (2 H, s, SiH_2), 2.12 (6 H, s, Me) ppm. ^{1}H NMR (C_7D_8, 400.1 MHz, 193 K): δ 7.70 – 7.67 (2 H, m, *o*-SiC_6H_5), 7.17 – 7.11 (3 H, overlapping 2 x m, *m*-SiC_6H_5, *p*-SiC_6H_5), 7.11 – 7.02 (2 H, m, *m*-Xyl), 6.95 (1 H, t , $^{3}J_{HH}$ = 7.4 Hz, *p*-Xyl), 5.85 (5 H, br s, C_5H_5), 5.45 (1 H, s, ZrH), 5.37 (6 H, overlapping 2 x br s, C_5H_5, SiH), 5.13 (1 H, br s, SiH), 2.26 (3 H, br s, Me), 2.06 (3 H, br s, Me) ppm. $^{13}C\{^{1}H\}$ NMR (C_6D_6, 100.6 MHz, 293 K): δ 157.8 (*i*-Xyl), 136.9 (*i*-SiC_6H_5), 135.3 (*o*-SiC_6H_5), 131.6 (*o*-Xyl), 129.8 (*p*-SiC_6H_5), 128.7 (*m*-Xyl), 127.9 (*m*-SiC_6H_5), 122.7 (*p*-Xyl), 108.1 (C_5H_5), 21.0 (Me) ppm. ^{29}Si NMR (HMBC

^{1}H-observed, C_6D_6, 499.9 MHz, 298 K): δ –31.4 ($^{1}J_{SiH}$ = 206 Hz, SiH_2Ph) ppm. Compound **8** repeatedly gave unsatisfactory and irreproducible combustion analyses.

NMR tube scale synthesis of $Cp_2Zr(D)\{N(Xyl)SiD_2Ph\}$ (8-*d*$_3$). To a solution of $Cp_2Zr(NXyl)(THF)$ (**2.2**, 10.0 mg, 24.2 μmol) in C_6D_6 (0.6 mL) in an NMR tube equipped with a J. Young Teflon valve was added $PhSiD_3$ (3.4 μL, 26.8 μmol) at RT. After 5 minutes the solution had turned pale yellow and the product **8-*d*$_3$** was quantitatively formed. Volatiles were removed under reduced pressure and the residue was redissolved in C_6D_6 (0.6 mL). Compound **8-*d*$_3$** was subsequently characterised by ^{2}H NMR spectroscopy at RT.

^{2}H NMR (C_6H_6, 76.7 MHz, 298 K): δ 5.46 (s, ZrD), 5.25 (s, SiD_2) ppm.

$Cp_2Zr(H)\{N(Xyl)SiHPh_2\}$ (9). To a stirred solution of $Cp_2Zr(NXyl)(THF)$ (**2.2**, 0.200 g, 0.485 mmol) in benzene (10 mL) at RT was added dropwise a solution of Ph_2SiH_2 (91.0 μL, 0.490 mmol) in benzene (5 mL). After 1 h the volatiles were removed under reduced pressure to afford **9** as a yellow, waxy solid, which could not be solidified. Yield: 0.148 g (58%).

^{1}H NMR (C_6D_6, 400.1 MHz, 298 K): δ 7.60 – 7.58 (4 H, m, *o*-SiC_6H_5), 7.12 – 7.09 (6 H, overlapping 2 x m, *m*-SiC_6H_5, *p*-SiC_6H_5), 6.80 (2 H, d, $^{3}J_{HH}$ = 7.5 Hz, *m*-Xyl), 6.69 (1 H, t , $^{3}J_{HH}$ = 7.5 Hz, *p*-Xyl), 6.01 (1 H, s, SiH), 5.69 (10 H, s, C_5H_5), 5.56 (1 H, s, ZrH), 2.14 (6 H, s, Me) ppm. $^{13}C\{^{1}H\}$ NMR (C_6D_6, 100.6 MHz, 293 K): δ 157.5 (*i*-Xyl), 137.9 (*i*-SiC_6H_5), 135.9 (*o*-SiC_6H_5), 132.1 (*o*-Xyl), 129.5 (*p*-SiC_6H_5), 128.3 (*m*-Xyl), 127.5 (*m*-SiC_6H_5), 122.5 (*p*-Xyl), 108.1 (C_5H_5), 21.9 (Me) ppm. ^{29}Si NMR (HMBC ^{1}H-observed, C_6D_6, 499.9 MHz, 298 K): δ –20.0 ($^{1}J_{SiH}$ = 205 Hz, $SiHPh_2$) ppm. IR (NaCl plates, Nujol mull, cm^{-1}): 2126 (m, ν(Si–H)), 1587 (m, ν(Zr–H)), 1372 (m), 1257 (m), 1215 (w), 1176

(s), 1105 (s), 1094 (s), 1013 (m), 838 (s), 796 (s), 763 (m), 729 (m), 698 (m), 687 (m). Compound **9** repeatedly gave unsatisfactory and irreproducible combustion analyses.

$Cp_2Zr(Cl)\{N(^tBu)SiH(\mu\text{-}H)Ph\}$ (10). To a stirred solution of $Cp_2Zr(N^tBu)(THF)$ (**2.1**, 0.200 g, 0.548 mmol) in benzene (10 mL) at RT was added dropwise a solution of $PhSiH_2Cl$ (0.077 mL, 0.576 mmol) in benzene (5 mL). After 18 h the volatiles were removed under reduced pressure to afford an orange solid which was then triturated with hexane (2 mL) and dried *in vacuo* to afford **10** as an orange powder. Yield: 0.117 g (49%). Diffraction-quality crystals were grown from a concentrated benzene solution at RT.

^1H NMR (C_6D_6, 400.1 MHz, 298 K): δ 7.79 – 7.76 (2 H, m, *o*-SiC_6H_5), 7.25 – 7.20 (3 H, overlapping 2 x m, *m*-SiC_6H_5, *p*-SiC_6H_5), 6.01 (10 H, s, C_5H_5), 4.33 (2 H, s, SiH_2), 1.51 (9 H, s, CMe_3) ppm. ^1H NMR (C_7D_8, 400.1 MHz, 185 K): δ 7.82 – 7.79 (2 H, m, *o*-SiC_6H_5), 7.22 – 7.18 (3 H, overlapping 2 x m, *m*-SiC_6H_5, *p*-SiC_6H_5), 5.92 (10 H, s, C_5H_5), 4.84 (1 H, br s, SiH), 3.61 (1 H, br s, Si(μ-H)Zr), 1.56 (9 H, s, CMe_3) ppm. $^{13}C\{^1H\}$ NMR (C_6D_6, 100.6 MHz, 293 K): δ 136.6 (*i*-SiC_6H_5), 134.4 (*o*-SiC_6H_5), 130.4 (*p*-SiC_6H_5), 128.8 (*m*-SiC_6H_5), 114.7 (C_5H_5), 57.5 ($\underline{C}Me_3$), 34.2 ($C\underline{Me_3}$) ppm. ^{29}Si NMR (HMBC ^1H-observed, C_6D_6, 499.9 MHz, 298 K): δ –69.7 ($^1J_{SiH}$ = 183 Hz, SiH_2Ph) ppm. IR (NaCl plates, Nujol mull, cm^{-1}): 2116 (w, ν(Si–H)), 2080 (m, ν(Si–H)), 1621 (br w), 1261 (m), 1218 (m), 1184 (m), 1111 (m), 1014 (m), 890 (m), 805 (s), 721 (m), 763 (w), 721 (m), 689 (w). Anal. found (calcd. for $C_{20}H_{26}NSiClZr$): C, 55.02 (55.20); H, 6.13 (6.02); N, 3.08 (3.22)%.

NMR tube scale synthesis of $Cp_2Zr(H)\{N(^tBu)Si(\mu\text{-}H)ClPh\}$ (10_int1). To a pre-cooled (–30 °C) solution of $Cp_2Zr(N^tBu)(THF)$ (**2.1**, 10.0 mg, 27.4 μmol) in an NMR tube equipped with a J. Young Teflon valve in toluene-d_8 (0.6 mL) was added $PhSiH_2Cl$ (3.7 μL, 27.8 μmol). The reaction was monitored by ^1H NMR spectroscopy using a

pre-cooled (–30 °C) NMR probe and **10_int1** was characterised by ^{1}H NMR spectroscopy as a 6:3:1 mixture with **10** and **2.1**, respectively. On warming to RT, **10_int1** converted quantitatively to **10**.

^{1}H NMR ($C_6D_5CD_3$, 400.1 MHz, 243 K): δ 7.87 – 7.85 (2 H, m, *o*-SiC_6H_5), 7.18 – 7.16 (3 H, overlapping 2 x m, *m*-SiC_6H_5, *p*-SiC_6H_5), 5.85 (5 H, s, C_5H_5), 5.70 (1 H, d, $^{2}J_{HH}$ = 3.1 Hz, ZrH), 5.66 (5 H, s, C_5H_5), 2.23 (1 H, d, $^{2}J_{HH}$ = 3.1 Hz, SiH), 1.30 (9 H, s, CMe_3) ppm.

$Cp_2Zr(Cl)\{N(Xyl)SiH_2Ph\}$ (11). To a stirred solution of $Cp_2Zr(NXyl)(THF)$ (**2.2**, 203 mg, 0.493 mmol) in benzene (10 mL) at RT was added dropwise a solution of $PhSiH_2Cl$ (0.069 mL, 0.518 mmol) in benzene (5 mL). After 2 h the volatiles were removed under reduced pressure to afford a yellow, waxy solid which was then triturated with hexane (4 mL) and dried *in vacuo* to afford **11** as a yellow powder. Yield: 0.153 g (64%). Diffraction-quality crystals were grown from a concentrated hexane solution at 4 °C.

^{1}H NMR (C_6D_6, 400.1 MHz, 298 K): δ 7.32 – 7.29 (2 H, m, *o*-SiC_6H_5), 7.11 – 7.06 (1 H, m, *p*-SiC_6H_5), 7.04 – 7.00 (2 H, m, *m*-SiC_6H_5), 6.98 – 6.96 (2 H, m, *m*-Xyl), 6.90 – 6.86 (1 H, m, *p*-Xyl), 5.87 (10 H, s, C_5H_5), 5.46 (2 H, s, SiH_2), 2.06 (6 H, s, Me) ppm. ^{1}H NMR (C_7D_8, 400.1 MHz, 185 K): δ 7.32 – 7.29 (2 H, m, *o*-SiC_6H_5), 7.06 – 6.96 (6 H, overlapping 4 x m, *p*-SiC_6H_5, *m*-SiC_6H_5, *m*-Xyl, *p*-Xyl), 6.10 (5 H, s, C_5H_5), 5.66 (1 H, d, $^{2}J_{HH}$ = 9.4 Hz, SiH), 5.47 (5 H, s, C_5H_5), 5.36 (1 H, d, $^{2}J_{HH}$ = 9.4 Hz, SiH), 2.41 (3 H, s, Me), 1.70 (3 H, s, Me) ppm. $^{13}C\{^{1}H\}$ NMR (C_6D_6, 100.6 MHz, 293 K): δ 157.9 (*i*-Xyl), 136.0 (*o*-SiC_6H_5), 135.7 (*i*-SiC_6H_5), 132.7 (*o*-Xyl), 129.9 (*p*-SiC_6H_5), 129.0 (*m*-Xyl), 127.8 (*m*-SiC_6H_5), 123.5 (*p*-Xyl), 114.6 (C_5H_5), 20.7 (Me) ppm. ^{29}Si NMR (HMBC ^{1}H-observed, C_6D_6, 499.9 MHz, 298 K): δ –31.6 ($^{1}J_{SiH}$ = 209 Hz, SiH_2Ph) ppm. IR (NaCl plates, Nujol mull, cm^{-1}): 2189 (m, ν(Si–H)), 2149 (m, ν(Si–H)), 1261 (m), 1179 (m),

1115 (m), 1100 (m), 1017 (m), 945 (m), 882 (m), 870 (m), 837 (s), 818 (s), 810 (s), 768 (s), 761 (m), 740 (m), 732 (m), 703 (m), 694 (m), 599 (m). Anal. found (calcd. for $C_{24}H_{26}NSiClZr$): C, 59.53 (59.65); H, 5.56 (5.42); N, 2.96 (2.90)%.

6.6 Experimental details and characterising data for Chapter Three

$Cp_2Zr\{N(^tBu)Si(H)(Ph)C(C_6F_5)CH\}$ (12). To a stirred solution of $Cp_2Zr(N^tBu)(THF)$ (**3.12**, 0.202 g, 0.554 mmol) in benzene (10 mL) at RT was added dropwise a solution of $PhSiH_3$ (71.0 µL, 0.575 mmol) in benzene (5 mL). After 1 h the volatiles were removed under reduced pressure and the yellow residue redissolved in benzene (10 mL). To the stirred solution was added $HCCC_6F_5$ (0.110 g, 0.573 mmol) at RT and the solution was heated to 60 °C. After 4 h volatiles were removed under reduced pressure and the resulting yellow oil washed with hexane (4 x 10 mL) and dried *in vacuo* to afford **12** as a yellow, waxy solid, which could not be solidified. Yield: 0.127 g (38%).

^1H NMR (C_6D_6, 499.9 MHz, 298 K): δ 8.40 (1 H, s, ZrCH), 7.71 – 7.69 (2 H, m, *o*-SiC_6H_5), 7.16 – 7.13 (2 H, m, *m*-SiC_6H_5), 7.08 – 7.04 (1 H, m, *p*-SiC_6H_5), 6.00 (5 H, s, C_5H_5), 5.88 (5 H, s, C_5H_5), 5.49 (1 H, t, J_{HF} = 6.2 Hz, SiH), 0.96 (9 H, s, CMe_3) ppm. $^{13}C\{^1H\}$ NMR (C_6D_6, 125.7 MHz, 298 K): δ 212.8 (ZrC), 140.2 (*i*-SiC_6H_5), 134.8 (*o*-SiC_6H_5), 129.7 (*p*-SiC_6H_5), 128.2 (*m*-SiC_6H_5), 120.5 (ZrC<u>C</u>), 112.9 (C_5H_5), 112.8 (C_5H_5), 58.1 (<u>C</u>Me_3), 33.9 (C<u>Me</u>$_3$). Those resonances belonging to the aromatic C_6F_5 ring could not be satisfactorily assigned. $^{19}F\{^1H\}$ NMR (C_6D_6, 376.5 MHz, 298 K): δ –143.4 (2 F, m, *o*-C_6F_5), –159.8 (1 F, t, $^3J_{FF}$ = 21.3 Hz, *p*-C_6F_5), –164.1 (2 F, m, *m*-C_6F_5) ppm. ^{29}Si NMR (HMBC ^1H-observed, C_6D_6, 499.9 MHz, 298 K): δ –41.7 ($^1J_{SiH}$ = 204 Hz, $^3J_{SiH}$ = 19 Hz, $HCC(Ar^F)SiHPh$) ppm. IR (NaCl plates, Nujol mull, cm^{-1}): 2089 (m, ν(Si–H)), 1814 (w), 1712 (w), 1628 (w), 1515 (s), 1463 (s), 1426 (s), 1384 (m), 1361 (m), 1300 (w), 1261 (m), 1224 (m), 1182 (s), 1104 (s), 1017 (s), 986 (s), 965 (s), 797 (s), 735 (w),

699 (m), 641 (m). Compound **12** repeatedly gave unsatisfactory and irreproducible combustion analyses.

NMR tube scale synthesis of $Cp_2Zr\{N(^tBu)Si(H)(Ph)C(C_6F_5)CD\}$ (12-d_{CD}). To a solution of $Cp_2Zr(N^tBu)(THF)$ (**3.12**, 10.0 mg, 27.4 μmol) in an NMR tube equipped with a J. Young Teflon valve in C_6D_6 (0.6 mL) was added $PhSiH_3$ (3.5 μL, 28.4 μmol) at RT. After 1 h the volatiles were removed under reduced pressure and the residue redissolved in C_6D_6 (0.6 mL). $DCCC_6F_5$ (5.3 mg, 27.4 μmol) was added at RT and the solution heated to 60 °C for 4 h. 85% of the product **12-d_{CD}** was formed, along with 15% unidentifiable species, as judged by ^1H NMR spectroscopy and subsequently volatiles were removed under reduced pressure. The yellow residue was redissolved in C_6H_6 (0.6 mL) and **12-d_{CD}** was characterised by ^2H NMR spectroscopy at RT.

^2H NMR (C_6H_6, 76.7 MHz, 298 K): δ 8.41 (s, ZrCD) ppm.

NMR tube scale synthesis of $Cp_2Zr\{N(^tBu)SiDPhC(Ar^F)CH\}$ (12-d_{SiD}). To a solution of $Cp_2Zr(N^tBu)(THF)$ (**3.12**, 10.0 mg, 27.4 μmol) in an NMR tube equipped with a J. Young Teflon valve in C_6D_6 (0.6 mL) was added $PhSiD_3$ (3.5 μL, 27.6 μmol) at RT. After 1 h the volatiles were removed under reduced pressure and the residue redissolved in C_6D_6 (0.6 mL). $HCCC_6F_5$ (5.3 mg, 27.4 μmol) was added at RT and the solution heated to 60 °C for 4 h. 85% of the product **12-d_{SiD}** was formed, along with 15% unidentifiable species. The ^1H NMR spectrum revealed the absence of the triplet resonance at 5.49 ppm.

NMR tube scale reaction between $Cp_2Zr\{\eta^2\text{-}N(^tBu)SiMe_2\}(PMe_3)$ and $HCCC_6F_5$. To a solution of $Cp_2Zr\{\eta^2\text{-}N(^tBu)SiMe_2\}(PMe_3)$ (**3.2**, 10.0 mg, 23.4 μmol) in an NMR tube equipped with a J. Young Teflon valve in C_6D_6 (0.6 mL) was added $HCCC_6F_5$ (4.5 mg, 23.4 μmol). After 1 h the volatiles were removed under reduced pressure and the residue redissolved in C_6D_6 (0.6 mL). The ^1H and $^{19}F\{^1H\}$ NMR spectra showed two major

species (~80% conversion) formed in a 1:1 ratio along with several minor species (~20% conversion). The two species could not be fully disambiguated in the ^{1}H and $^{19}F\{^{1}H\}$ NMR spectra, but are tentatively proposed to be $Cp_2Zr\{N(^{t}Bu)SiMe_2C(C_6F_5)CH\}$ and $Cp_2Zr(CCC_6F_5)\{N(^{t}Bu)Si(\mu\text{-}H)Me_2\}$.

^{1}H NMR (C_6D_6, 400.1 MHz, 298 K): δ 8.04 (1 H, s, ZrCH), 5.93 (10 H, s, C_5H_5), 5.85 (10 H, s, C_5H_5), 2.26 (1 H, sept., $^{3}J_{HH}$ = 2.8 Hz, SiH), 1.46 (9 H, s, $NCMe_3$), 1.02 (9 H, s, $NCMe_3$), 0.19 (6 H, s, $SiMe_2$), 0.09 (6 H, d, $^{3}J_{HH}$ = 2.8 Hz, $SiH\underline{Me_2}$) ppm. $^{19}F\{^{1}H\}$ NMR (C_6D_6, 376.5 MHz, 298 K): δ –139.7 to –139.8 (2 F, m, *o*-C_6F_5), –142.5 to –142.6 (2 F, m, *o*-C_6F_5), –158.8 (1 F, t, $^{3}J_{FF}$ = 21.6 Hz, *p*-C_6F_5), –159.9 (1 F, t, $^{3}J_{FF}$ = 21.4 Hz, *p*-C_6F_5), –163.6 to –163.7 (2 F, m, *m*-C_6F_5), –164.0 to –164.1 (2 F, m, *m*-C_6F_5) ppm.

$Cp_2Zr(CC^{t}Bu)\{N(^{t}Bu)SiH(\mu\text{-}H)Ph\}$ (13). To a stirred solution of $Cp_2Zr(N^{t}Bu)(THF)$ (**3.12**, 0.200 g, 0.548 mmol) in benzene (10 mL) at RT was added dropwise a solution of $PhSiH_3$ (71.0 µL, 0.575 mmol) in benzene (5 mL). After 1 h the volatiles were removed under reduced pressure and the yellow residue redissolved in benzene (10 mL). To the stirred solution was added $HCC^{t}Bu$ (0.340 mL, 2.76 mmol) at RT and the solution was heated to 50 °C. After 16 h volatiles were removed under reduced pressure and the resulting yellow oil extracted in hexane (3 x 10 mL). The combined extracts were dried *in vacuo* to afford **13** as a pale yellow, waxy solid, which could not be solidified. Yield: 0.161 g (59%).

^{1}H NMR (C_6D_6, 400.1 MHz, 298 K): δ 7.80 – 7.78 (2 H, m, *o*-SiC_6H_5), 7.26 – 7.18 (3 H, overlapping 2 x m, *m*-SiC_6H_5, *p*-SiC_6H_5), 6.04 (10 H, s, C_5H_5), 4.38 (2 H, s, SiH_2), 1.55 (9 H, s, $NCMe_3$), 1.37 (9 H, s, $CCCMe_3$) ppm. $^{13}C\{^{1}H\}$ NMR (C_6D_6, 125.7 MHz, 298 K): δ 137.1 (*i*-SiC_6H_5), 134.5 (*o*-SiC_6H_5), 132.3 ($Zr\underline{C}CCMe_3$), 130.2 (*p*-SiC_6H_5), 128.7 (*m*-SiC_6H_5), 112.2 (C_5H_5), 56.9 ($N\underline{C}Me_3$), 34.9 ($NC\underline{Me_3}$), 31.6 ($ZrCCC\underline{Me_3}$), 29.1

(ZrCC$\underline{C}$Me$_3$) ppm. ^{29}Si NMR (HMBC ^{1}H-observed, C_6D_6, 499.9 MHz, 298 K): δ -75.1 ($^1J_{SiH}$ = 182 Hz, SiH_2Ph) ppm. IR (NaCl plates, Nujol mull, cm^{-1}): 2085 (s, ν(C≡C)), 2034 (br, w), 1963 (w), 1420 (m), 1357 (m), 1246 (s), 1188 (m), 1108 (m), 1021 (s), 966 (w), 891 (s), 800 (s), 759 (m), 721 (s). Compound **12** repeatedly gave unsatisfactory and irreproducible combustion analyses.

NMR tube scale synthesis of Cp$_2$Zr(CC^{t}Bu){N(^{t}Bu)SiH(μ-D)Ph}/ Cp$_2$Zr(CC^{t}Bu){N(^{t}Bu)SiD(μ-H)Ph} (13-*d*$_1$). To a solution of Cp$_2$Zr(N^{t}Bu)(THF) (**3.12**, 10.0 mg, 27.4 μmol) in an NMR tube equipped with a J. Young Teflon valve in C_6D_6 (0.6 mL) was added $PhSiH_3$ (3.5 μL, 28.4 μmol) at RT. After 1 h the volatiles were removed under reduced pressure and the residue redissolved in C_6D_6 (0.6 mL). DCC^{t}Bu (3.4 μL, 27.4 μmol) was added at RT and the solution heated to 70 °C for 4 h. Quantitative formation of the product **13-*d*$_1$** was observed by ^{1}H NMR spectroscopy and subsequently volatiles were removed under reduced pressure. The yellow residue was redissolved in C_6H_6 (0.6 mL) and **13-*d*$_1$** was subsequently characterised by ^{2}H NMR spectroscopy at RT.

^{2}H NMR (C_6H_6, 76.7 MHz, 298 K): δ 4.37 (s, SiD) ppm.

Alternative NMR tube scale synthesis of Cp$_2$Zr(CC^{t}Bu){N(^{t}Bu)SiH(μ-D)Ph}/ Cp$_2$Zr(CC^{t}Bu){N(^{t}Bu)SiD(μ-H)Ph} (13-*d*$_1$). To a solution of Cp$_2$Zr(N^{t}Bu)(THF) (**3.12**, 10.0 mg, 27.4 μmol) in an NMR tube equipped with a J. Young Teflon valve in C_6D_6 (0.6 mL) was added $PhSiD_3$ (3.5 μL, 27.6 μmol) at RT. After 1 h the volatiles were removed under reduced pressure and the residue redissolved in C_6D_6 (0.6 mL). HCC^{t}Bu (3.4 μL, 27.6 μmol) was added at RT and the solution heated to 70 °C for 4 h. Quantitative formation of the product **13-*d*$_1$** was observed by ^{1}H NMR spectroscopy and subsequently

volatiles were removed under reduced pressure. The yellow residue was redissolved in C_6H_6 (0.6 mL) and the ^2H NMR spectrum matched that reported above.

$Cp_2Zr(CC^tBu)\{N(^tBu)Si(\mu\text{-}H)Me_2\}$ (14). To a stirred solution of $Cp_2Zr\{\eta^2\text{-}N(^tBu)SiMe_2\}(PMe_3)$ (**3.2**, 0.180 g, 0.422 mmol) in benzene (15 mL) at RT was added HCC^tBu (0.519 mL, 4.22 mmol). After 10 minutes the volatiles were removed under reduced pressure and the yellow residue extracted in pentane (2 x 5 mL). The combined extracts were concentrated and cooled to –30 °C, resulting in the formation of **14** as a pale yellow powder, which was subsequently washed with cold pentane (5 mL) and dried *in vacuo*. Yield: 0.104 g (57%). Diffraction-quality crystals were grown by slow evaporation of a concentrated C_6D_6 solution at RT.

^1H NMR (C_6D_6, 400.1 MHz, 298 K): δ 5.97 (10 H, s, C_5H_5), 2.88 (1 H, sept., $^3J_{HH}$ = 2.9 Hz, SiH), 1.47 (9 H, s, $NCMe_3$), 1.38 (9 H, s, $ZrCCCMe_3$), 0.14 (6 H, d, $^3J_{HH}$ = 2.9 Hz, $SiH\underline{Me}_2$) ppm. $^{13}C\{^1H\}$ NMR (C_6D_6, 125.7 MHz, 298 K): δ 130.8 ($Zr\underline{C}CCMe_3$), 127.2 ($ZrC\underline{C}CMe_3$), 111.4 (C_5H_5), 57.2 ($N\underline{C}Me_3$), 35.0 ($NC\underline{Me}_3$), 31.7 ($ZrCCC\underline{Me}_3$), 29.1 ($ZrCC\underline{C}Me_3$), 1.4 ($SiHMe_2$) ppm. ^{29}Si NMR (HMBC ^1H-observed, C_6D_6, 499.9 MHz, 298 K): δ -59.2 ($^1J_{SiH}$ = 132 Hz, $SiHMe_2$) ppm. IR (NaCl plates, Nujol mull, cm^{-1}): 2081 (m, ν(C≡C)), 1995 (w, ν(Si–H)), 1355 (s), 1245 (s), 1195 (m), 1014 (m), 982 (m), 902 (w), 843 (w), 799 (s), 755 (w), 726 (m). An elemental analysis was not carried out because of the coronavirus epidemic and its impact on technical services.

Kinetic measurements for the reaction of $Cp_2Zr(H)\{N(^tBu)SiH(\mu\text{-}H)Ph\}$ (6) with varying equivalents of HCC^tBu to form $Cp_2Zr(CC^tBu)\{N(^tBu)SiH(\mu\text{-}H)Ph\}$ (13). To a solution of $Cp_2Zr(N^tBu)(THF)$ (**3.12**, 10.0 mg, 27.4 μmol) in an NMR tube equipped with a J. Young Teflon valve in C_6D_6 (0.6 mL) was added $PhSiH_3$ (3.5 μL, 28.4 μmol) or $PhSiD_3$ (3.5 μL, 27.6 μmol) at RT. After 1 h the volatiles were removed under reduced

pressure and the residue redissolved in C_6D_6 (0.6 mL). HCC^{t}Bu (3.6 μL, 29.6 μmol; 10.1 μL, 82.2 μmol; 19.4 μL, 0.158 mmol; or 46.2 μL, 0.375 mmol) was added at RT and the reactions monitored by ^{1}H NMR until approximately three half-lives had been completed. The initial rates were obtained from plots of **6** *vs.* time using *Origin*.

Note: to avoid the problem of boiling the alkyne such that the equivalencies were affected, and to avoid the problem of H_2 supersaturation, the reactions were run in parallel at room temperature in NMR tubes of identical volume. Conducting the reactions at room temperature led to long reaction times and so ^{1}H NMR spectra were taken over the course of several days. Following the reactions in this manner allowed for extraction of concentration-time plots

Kinetic measurements for the reaction of Cp$_2$Zr(H){N(^{t}Bu)SiH(μ-H)Ph} (6) with HCC^{t}Bu and PMe$_3$ to form Cp$_2$Zr(CC^{t}Bu){N(^{t}Bu)SiH(μ-H)Ph} (13). To a solution of Cp$_2$Zr(N^{t}Bu)(THF) (**3.12**, 10.0 mg, 27.4 μmol) in an NMR tube equipped with a J. Young Teflon valve in C_6D_6 (0.6 mL) was added $PhSiH_3$ (3.5 μL, 28.4 μmol) at RT. After 1 h the volatiles were removed under reduced pressure and the residue redissolved in C_6D_6 (0.6 mL). HCC^{t}Bu (4.2 μL, 34.0 μmol) and PMe_3 (1 M in THF, 25.5 μL, 25.5 μmol) were added at RT and the reactions monitored by ^{1}H NMR until approximately three half-lives had been completed. The initial rates were obtained from plots of **6** *vs.* time using *Origin*.

Kinetic isotope effect measurements for the reaction of Cp$_2$Zr(H){N(^{t}Bu)SiH(μ-H)Ph} (6) with HCC^{t}Bu or DCC^{t}Bu to form Cp$_2$Zr(CC^{t}Bu){N(^{t}Bu)SiH(μ-H)Ph} (13) or Cp$_2$Zr(CC^{t}Bu){N(^{t}Bu)SiH(μ-D)Ph}/Cp$_2$Zr(CC^{t}Bu){N(^{t}Bu)SiD(μ-H)Ph} (13-*d*$_1$). To a solution of Cp$_2$Zr(N^{t}Bu)(THF) (**3.12**, 10.0 mg, 27.4 μmol) in an NMR tube equipped with a J. Young Teflon valve in C_6D_6 (0.6 mL) was added $PhSiH_3$ (3.5 μL, 28.4 μmol) at RT. After 1 h the volatiles were removed under reduced pressure and the residue

redissolved in C_6D_6 (0.6 mL). HCC^{t}Bu (3.6 µL, 29.6 µmol) or DCC^{t}Bu (3.3 µL, 26.9 mmol) was added at RT and the reactions monitored by ^{1}H NMR until approximately three half-lives had been completed. The initial rates were obtained from plots of **6** *vs.* time using *Origin*.

NMR tube scale synthesis of Cp$_2$Zr{η^2-N(^{t}Bu)SiHPh}(PMe$_3$) (15). To a solution of Cp$_2$Zr(N^{t}Bu)(THF) (**3.12**, 10.0 mg, 27.4 µmol) in an NMR tube equipped with a J. Young Teflon valve in C_6D_6 (0.6 mL) was added $PhSiH_3$ (3.5 µL, 28.4 µmol) at RT. After 1 h the volatiles were removed under reduced pressure and the residue redissolved in C_6D_6 (0.6 mL). PMe_3 (1 M in THF, 0.274 mL, 0.274 mmol) was added at RT. After 3 days 60% of the product **15** had formed, as judged by ^{1}H NMR spectroscopy, and a colour change from pale yellow to bright yellow was observed. Compound **15** was subsequently characterised by ^{1}H, ^{13}C{^{1}H}, ^{31}P and ^{29}Si spectroscopy. Attempts to isolate **15** on the preparative scale were unsuccessful.

^{1}H NMR (C_6D_6, 400.1 MHz, 298 K): δ 7.62 – 7.60 (2 H, m, o-SiC_6H_5), 7.23 – 7.21 (2 H, m, *m*-SiC_6H_5), 7.08 – 7.04 (1 H, m, *p*-SiC_6H_5), 5.60 (5 H, s, C_5H_5), 5.50 (5 H, s, C_5H_5), 4.29 (1 H, d, $^3J_{HP}$ = 5.8 Hz, SiH), 1.27 (9 H, s, CMe_3), 1.00 (9 H, d, $^3J_{HP}$ = 6.7 Hz, PMe_3) ppm. ^{13}C{^{1}H} NMR (C_6D_6, 125.7 MHz, 298 K): δ 134.8 (*i*-SiC_6H_5), 134.2 (*o*-SiC_6H_5), 128.6 (*m*-SiC_6H_5), 126.8 (*p*-SiC_6H_5), 105.3 (C_5H_5), 104.0 (C_5H_5), 56.5 (N<u>C</u>Me$_3$), 34.2 (NC<u>Me</u>$_3$), 19.7 (d, $^1J_{CP}$ = 23.0 Hz, P<u>Me</u>$_3$) ppm. ^{31}P NMR (C_6D_6, 162.0 MHz, 298 K): δ –2.6 (m, PMe_3) ppm. ^{29}Si NMR (HMBC ^{1}H-observed, C_6D_6, 499.9 MHz, 298 K): δ –74.2 ($^1J_{SiH}$ = 185 Hz, SiHPh) ppm.

Competition reaction of Cp$_2$Zr(H){N(^{t}Bu)SiH(µ-H)Ph} (6) with HCC^{t}Bu and DCC^{t}Bu. To a solution of Cp$_2$Zr(N^{t}Bu)(THF) (**3.12**, 10.0 mg, 27.4 µmol) in an NMR tube equipped with a J. Young Teflon valve in C_6D_6 (0.6 mL) was added $PhSiH_3$ (3.5 µL,

28.4 μmol) at RT. After 1 h the volatiles were removed under reduced pressure and a solution of HCC^{t}Bu (16.9 μL, 0.137 mmol) and DCC^{t}Bu (17.1 μL, 0.137 mmol) in C_6D_6 (0.6 mL) was added at RT. After three days the reaction was complete and ^{1}H NMR integration showed the products to be 62% **13** and 38% **13-*d*$_1$**.

Note: after the reaction was complete the integral of the SiH_2 resonance was established, with respect to the integral of the acetylide ^{t}Bu resonance, by ^{1}H NMR spectroscopy. An elongated T_1 relaxation time (120 seconds) was implemented to eliminate any false readings arising from the slow relaxation times of SiH protons compared to the CH protons of the ^{t}Bu group. This integral was then compared to the integral of the SiH_2 and SiHD resonances from the reactions of **6** with HCC^{t}Bu and DCC^{t}Bu, respectively.

Kinetic isotope effect measurements for the reaction of Cp$_2$Zr(H){N(^{t}Bu)SiH(μ-H)Ph} (6) or Cp$_2$Zr(D){N(^{t}Bu)SiD(μ-D)Ph} (6-*d*$_3$) with HCC^{t}Bu to form Cp$_2$Zr(CC^{t}Bu){N(^{t}Bu)SiH(μ-H)Ph} (13) or Cp$_2$Zr(CC^{t}Bu){N(^{t}Bu)SiH(μ-D)Ph}/Cp$_2$Zr(CC^{t}Bu){N(^{t}Bu)SiD(μ-H)Ph} (13-*d*$_1$). To a solution of Cp$_2$Zr(N^{t}Bu)(THF) (**3.12**, 10.0 mg, 27.4 μmol) in an NMR tube equipped with a J. Young Teflon valve in C_6D_6 (0.6 mL) was added $PhSiH_3$ (3.5 μL, 28.4 μmol) or $PhSiD_3$ (3.5 μL, 27.6 μmol) at RT. After 1 h the volatiles were removed under reduced pressure and the residue redissolved in C_6D_6 (0.6 mL). HCC^{t}Bu (67.4 μL, 0.548 mmol) was added and the NMR tube was transferred to a temperature-regulated (338 K) probe. The reaction was monitored using an array which recorded spectra (4 scans) every 63 s. The decay of **6** or **6-*d*$_3$** and formation of **13** or **13-*d*$_1$** was calculated by measuring the integral of C_5H_5.

Kinetic measurements for the reaction of Cp$_2$Zr(H){N(^{t}Bu)SiH(μ-H)Ph} (6) with HCC^{t}Bu to form Cp$_2$Zr(CC^{t}Bu){N(^{t}Bu)SiH(μ-H)Ph} (13) at varying temperatures. The general procedure is as follows. To a solution of Cp$_2$Zr(N^{t}Bu)(THF) (**3.12**, 10.0 mg,

27.4 μmol) in an NMR tube equipped with a J. Young Teflon valve in C_6D_6 (0.6 mL) was added $PhSiH_3$ (3.5 μL, 28.4 μmol) or $PhSiD_3$ (3.5 μL, 27.6 μmol) at RT. After 1 h the volatiles were removed under reduced pressure, the residue redissolved in C_6D_6 (0.6 mL) and HCC^{t}Bu (67.4 μL, 0.548 mmol) added. A blank C_6D_6 sample was added to the NMR probe at RT, locked and shimmed, and the probe heated to the relevant temperature (326, 329, 332, 335, 338 K). After thermal equilibration, the experimental sample replaced the blank sample and an array was set up to record a ^{1}H NMR spectrum (4 scans) every 63 s. The decay of **6** and formation of **13** was calculated by measuring the integral of C_5H_5. Reactions were performed in duplicate.

$Cp_2Zr\{N(^tBu)Si(H)(Ph)CH_2CH_2\}$ (16). To a stirred solution of $Cp_2Zr(N^tBu)(THF)$ (**3.12**, 0.200 g, 0.548 mmol) in benzene (10 mL) at RT in a Rotaflo ampoule, was added dropwise a solution of $PhSiH_3$ (71.0 μL, 0.575 mmol) in benzene (5 mL). After 1 h the volatiles were removed under reduced pressure and the yellow residue redissolved in benzene (10 mL). The solution was freeze-pump-thaw degassed three times before being exposed to ethylene at 1 bar over-pressure. The sealed ampoule was stirred for 16 h before being transferred to a Schlenk flask. Volatiles were removed under reduced pressure and the residue dried *in vacuo* to afford **16** as a yellow, waxy solid, which could not be solidified. Yield 0.164 g (70%).

^{1}H NMR (C_6D_6, 499.9 MHz, 298 K): δ 7.81 – 7.78 (2 H, m, *o*-SiC_6H_5), 7.33 – 7.29 (2 H, m, *m*-SiC_6H_5), 7.26 – 7.21 (1 H, m, *p*-SiC_6H_5), 5.91 (5 H, s, C_5H_5), 5.84 (5 H, s, C_5H_5), 5.24 – 5.22 (1 H, m, SiH), 1.98 – 1.90 (1 H, m, CH), 1.48 – 1.46 (1 H, m, CH), 1.45 – 1.43 (1 H, m, CH), 1.16 – 1.09 (1 H, m, CH), 1.04 (9 H, s, CMe_3) ppm. ^{13}C{^{1}H} NMR (C_6D_6, 125.7 MHz, 298 K): δ 1403.5 (*i*-SiC_6H_5), 134.2 (*o*-SiC_6H_5), 129.0 (*p*-SiC_6H_5), 128.4 (*m*-SiC_6H_5), 111.8 (C_5H_5), 111.2 (C_5H_5), 57.4 ($\underline{C}Me_3$), 38.4 ($ZrCH_2$), 34.1 ($C\underline{Me_3}$), 10.0 ($SiCH_2$) ppm. ^{29}Si NMR (HMBC ^{1}H-observed, C_6D_6, 499.9 MHz, 298 K): δ -35.1

($^1J_{S\text{-}H}$ = 192 Hz, SiHPh) ppm. An elemental analysis was not carried out because of the coronavirus epidemic and its impact on technical services.

Catalytic hydrogenation of ethylene by $Cp_2Zr(H)\{N(^tBu)SiH(\mu\text{-}H)Ph\}$ (6). To a solution of $Cp_2Zr(N^tBu)(THF)$ (**3.12**, 3.6 mg, 10.0 μmol) in an NMR tube equipped with a J. Young Teflon valve in C_6D_6 (0.6 mL) was added $PhSiH_3$ (1.3 μL, 10.5 μmol) at RT. After 1 h the volatiles were removed under reduced pressure and the residue redissolved in C_6D_6 (0.6 mL). The solution was freeze-pump-thaw degassed three times before being exposed to dihydrogen at 1 bar over-pressure, followed by exposure to ethylene at 1.5 bar over-pressure. The reaction was monitored by ^1H NMR until complete consumption of ethylene was observed.

NMR tube scale synthesis of $Cp_2Zr\{N(^tBu)Si(H)(Ph)C(Ph)N\}$ (17). To a solution of $Cp_2Zr(N^tBu)(THF)$ (**3.12**, 10.0 mg, 27.4 μmol) in an NMR tube equipped with a J. Young Teflon valve in C_6D_6 (0.6 mL) was added $PhSiH_3$ (3.5 μL, 28.4 μmol) at RT. After 1 h the volatiles were removed under reduced pressure and the residue redissolved in C_6D_6 (0.6 mL). PhCN (2.8 μL, 27.4 μmol) was added at RT. After 3 h, a colour change from pale yellow to yellow was observed and 75% of the product **17** was formed, along with 25% unidentifiable species, as judged by ^1H NMR spectroscopy. Compound **17** was subsequently characterised by ^1H and ^{13}C NMR spectroscopy at RT. Attempts to isolate **17** on the preparative scale were unsuccessful.

^1H NMR (C_6D_6, 400.1 MHz, 298 K): δ 7.89 – 7.87 (2 H, m, *o*-SiC_6H_5), 7.71 – 7.69 (2 H, m, *o*-NCC_6H_5), 7.24 – 7.20 (2 H, m, *m*-SiC_6H_5), 7.16 – 7.13 (1 H, m, *p*-NCC_6H_5), 7.11 – 7.07 (2 H, m, *m*-NCC_6H_5), 7.01 – 6.95 (1 H, m, *p*-SiC_6H_5,), 6.42 (1 H, s, SiH), 6.15 (5 H, s, C_5H_5), 6.05 (5 H, s, C_5H_5), 1.06 (9 H, s, CMe_3) ppm. $^{13}C\{^1H\}$ NMR (C_6D_6, 125.7 MHz, 298 K): δ 192.5 (ZrN<u>C</u>(C_6H_5)Si), 142.3 (*i*-SiC_6H_5), 140.6 (*i*-NCC_6H_5), 134.6 (*o*-SiC_6H_5),

129.2 (*p*-SiC_6H_5), 128.5 (*m*-SiC_6H_5), 128.4 (*m*-NCC_6H_5), 128.0 (*p*-NCC_6H_5), 126.8 (*o*-NCC_6H_5), 113.2 (C_5H_5), 113.0 (C_5H_5), 56.1 (N<u>C</u>Me_3), 34.3 (NC<u>Me_3</u>) ppm.

6.7 Experimental details and characterising data for Chapter Four

$Cp_2Zr\{(\mu\text{-}H)_2B(H)Tex\}\{N(^tBu)SiH_2Ph\}$ (18). To a stirred solution of $Cp_2Zr(H)\{N^tBu(SiH_2Ph)\}$ (**6**, 0.192 g, 0.480 mmol) in benzene (5 mL) at RT was added dropwise a solution of H_2BTex (0.141 g, 1.440 mmol) in benzene (5 mL). After 16 h the volatiles were removed under reduced pressure and the resulting solid extracted with hexane (3 x 10 mL). The combined extracts were concentrated and cooled to –30 °C, resulting in the formation of **18** as a pale yellow powder, which was subsequently washed with cold hexane (2 mL) and dried *in vacuo*. Yield: 0.097 g (41%). Diffraction-quality crystals were grown from a concentrated hexane solution at 5 °C.

^{1}H NMR (C_6D_6, 400.1 MHz, 298 K): δ 7.88 – 7.86 (2 H, m, *o*-SiC_6H_5), 7.31 – 7.27 (2 H, m, *m*-SiC_6H_5), 7.24 – 7.20 (1 H, m, *p*-SiC_6H_5), 5.97 (10 H, s, C_5H_5), 5.11 (2 H, s, SiH_2), 1.73 (1 H, sept, $^3J_{HH}$ = 6.7 Hz, C<u>H</u>$(Me)_2$), 1.41 (9 H, s, CMe_3), 1.26 (6 H, s, BC(<u>Me</u>)$_2$CH$(Me)_2$), 1.17 (6 H, d, $^3J_{HH}$ = 6.7 Hz, CH(<u>Me</u>)$_2$) ppm. ^{13}C{^{1}H} NMR (C_6D_6, 100.6 MHz, 293 K): δ 140.5 (*i*-SiC_6H_5), 134.0 (*o*-SiC_6H_5), 129.4 (*p*-SiC_6H_5), 128.6 (*m*-SiC_6H_5), 112.9 (C_5H_5), 56.6 (<u>C</u>Me_3), 40.0 (<u>C</u>H$(Me)_2$), 34.4 (C<u>Me_3</u>), 33.3 (br, B<u>C</u>$(Me)_2$CH$(Me)_2$), 28.0 (BC(<u>Me</u>)$_2$CH$(Me)_2$), 19.9 (CH(<u>Me</u>)$_2$) ppm. ^{11}B NMR (C_6D_6, 128.4 MHz, 293 K): δ 10.0 (m) ppm. ^{29}Si NMR (HMBC ^{1}H-observed, C_6D_6, 499.9 MHz, 298 K): δ -51.6 ($^1J_{SiH}$ = 191 Hz, SiH_2Ph) ppm. IR (NaCl plates, Nujol mull, cm^{-1}): 2405 (m, ν(B–H)), 2131 (s, ν(B–H)), 2065 (s, ν(B–H)), 2016 (m, ν(Si–H)), 1976 (m, ν(Si–H)), 1355 (s), 1328 (m), 1299 (m), 1262 (m), 1208 (w), 1174 (m), 1108 (m), 1025 (m), 1017 (m), 966 (s), 892 (s), 837 (w), 811 (s), 759 (m), 717 (s), 685 (m). Anal. found (calcd. for $C_{26}H_{42}NSiBZr$): C, 61.08 (62.61); H, 8.97 (8.49); N, 2.71 (2.81)%.

$Cp_2Zr\{(\mu\text{-}H)_2BHTex\}\{N(Xyl)SiH_2Ph\}$ (19). To a stirred solution of $Cp_2Zr(NXyl)(THF)$ (**4.7**, 0.175 g, 0.424 mmol) in benzene (10 mL) at RT was added dropwise $PhSiH_3$ (53.0 µL, 0.429 mmol). After 1 h the volatiles were removed under reduced pressure and the resulting yellow oil dissolved in benzene (10 mL). H_2BTex (42.0 mg, 0.428 mmol) in benzene (5 mL) was added dropwise at RT. After 1 h the volatiles were removed under reduced pressure and the resulting orange oil washed with hexane (5 x 10 mL) and dried *in vacuo* to afford **19** as a pale yellow solid. Yield: 88 mg (38%).

^1H NMR (C_6D_6, 400.1 MHz, 298 K): δ 7.25 – 7.23 (2 H, m, *o*-SiC_6H_5), 7.11 – 7.07 (1 H, m, *p*-SiC_6H_5), 7.05 – 7.02 (2 H, m, *m*-SiC_6H_5), 6.99 – 6.97 (2H, m, *m*-Xyl), 6.92 – 6.88 (1 H, m, *p*-Xyl), 5.80 (10 H, s, C_5H_5), 5.40 (2 H, s, SiH_2), 2.10 (6 H, s, Me_{Xyl}), 1.76 (1 H, sept, $^3J_{HH}$ = 6.8 Hz, C<u>H</u>$(Me)_2$), 1.32 (6 H, s, BC(<u>Me</u>)$_2$CH$(Me)_2$), 1.23 (6 H, d, $^3J_{HH}$ = 6.8 Hz, CH(<u>Me</u>)$_2$) ppm. $^{13}C\{^1H\}$ NMR (C_6D_6, 100.6 MHz, 298 K): δ 158.2 (*i*-Xyl), 136.5 (*i*-SiC_6H_5), 135.8 (*o*-SiC_6H_5), 134.1 (*o*-Xyl), 129.6 (*p*-SiC_6H_5), 129.2 (*m*-Xyl), 127.7 (*m*-SiC_6H_5), 123.2 (*p*-Xyl), 113.1 (C_5H_5), 39.7 (<u>C</u>H$(Me)_2$), 28.9 (BC(<u>Me</u>)$_2$CH$(Me)_2$), 20.9 (Xyl<u>C</u>H_3), 20.1 (CH(<u>Me</u>)$_2$) ppm. ^{11}B NMR (C_6D_6, 128.4 MHz, 293 K): δ 1.38 (m) ppm. ^{29}Si NMR (HMBC ^1H-observed, C_6D_6, 499.9 MHz, 298 K): δ -29.5 ($^1J_{SiH}$ = 206 Hz, SiH_2Ph) ppm. Anal. found (calcd. for $C_{30}H_{42}NSiBZr$): C, 62.82 (65.90); H, 8.21 (7.74); N, 3.04 (2.56)%.

$Cp_2Zr\{N(^tBu)SiHPhBHTex(\mu\text{-}H)\}$ (20). To a solution of $Cp_2Zr\{(\mu\text{-}H)_2B(H)Tex\}\{N(^tBu)SiH_2Ph\}$ (**19**, 27.4 mg, 54.9 µmol) in an NMR tube equipped with a J. Young Teflon valve in C_6D_6 (0.5 mL) was added H_2BTex (16.1 mg, 0.164 mmol) at RT. After 5 days volatiles were removed under reduced pressure and the residue dried *in vacuo* for 6 h after which time several yellow diffraction-quality crystals of the product **20** had grown. Compound **20** was characterised by single crystal X-ray diffraction. The reaction could not be reproduced on the preparative scale.

$Cp_2Zr\{(\mu\text{-}H)_2BH_2\}\{N(^tBu)SiH_2Ph\}$ (21). To a stirred solution of $Cp_2Zr(N^tBu)(THF)$ (**4.8**, 0.200 g, 0.548 mmol) in benzene (10 mL) at RT was added dropwise a solution of $PhSiH_3$ (71.0 µL, 0.575 mmol) in benzene (5 mL). After 1 h the volatiles were removed under reduced pressure and the yellow residue redissolved in benzene (10 mL). To the stirred solution was added $BH_3{\cdot}SMe_2$ (0.260 mL, 2.74 mmol) at RT. After 5 minutes volatiles were removed under reduced pressure and the resulting solid extracted into hexane (3 x 10 mL). The combined extracts were concentrated and cooled to 4 °C, resulting in the formation of **21** as pale yellow diffraction-quality crystals, which were subsequently washed with hexane (2 mL) and dried *in vacuo*. Yield: 0.106 g (47%).

^1H NMR (C_6D_6, 400.1 MHz, 298 K): δ 7.80 – 7.78 (2 H, m, *o*-SiC_6H_5), 7.28 – 7.23 (2 H, m, *m*-SiC_6H_5), 7.22 – 7.18 (1 H, m, *p*-SiC_6H_5), 5.91 (10 H, s, C_5H_5), 4.75 (2 H, s, SiH_2), 1.41 (9 H, s, CMe_3). $^1H\{^{11}B\}$ NMR (C_6D_6, 400.1 MHz, 298 K): δ 1.04 (4 H, s, BH_4) ppm. $^{13}C\{^1H\}$ NMR (C_6D_6, 100.6 MHz, 298 K): δ 138.8 (*i*-SiC_6H_5), 134.1 (*o*-SiC_6H_5), 129.8 (*p*-SiC_6H_5), 128.7 (*m*-SiC_6H_5), 113.2 (C_5H_5), 56.9 ($\underline{C}Me_3$), 34.2 ($C\underline{Me_3}$) ppm. ^{11}B NMR (C_6D_6, 128.4 MHz, 293 K): δ - 4.5 (quint., $^1J_{BH}$ = 85 Hz) ppm. ^{29}Si NMR (HMBC ^1H-observed, C_6D_6, 499.9 MHz, 298 K): δ -58.4 ($^1J_{SiH}$ = 189 Hz, SiH_2Ph) ppm. IR (NaCl plates, Nujol mull, cm^{-1}): 2433 (m), 2390 (s), 2244 (w), 2175 (w), 2115 (m), 2076 (m), 1891 (w), 1428 (m), 1360 (m), 1212 (w), 1179 (m), 1127 (m), 1107 (m), 1050 (m), 1019 (m), 966 (m), 896 (s), 810 (s), 754 (m), 714 (s). Anal. found (calcd. for $C_{20}H_{30}NSiBZr$): C, 57.86 (57.94); H, 7.22 (7.29); N, 3.31 (3.38)%.

NMR tube scale synthesis of $Cp_2Zr\{(\mu\text{-}D)_2BD_2\}\{N(^tBu)SiD_2Ph\}$ (21-d_6). To a solution of $Cp_2Zr(N^tBu)(THF)$ (**4.8**, 10.0 mg, 27.4 µmol) in an NMR tube equipped with a J. Young Teflon valve in C_6D_6 (0.6 mL) was added $PhSiD_3$ (3.5 µL, 27.6 µmol) at RT. After 1 h the volatiles were removed under reduced pressure and the residue redissolved

in C_6D_6 (0.6 mL). BD_3·THF (1.0 M in THF, 0.055 mL, 55.0 μmol) was added at RT. After 5 minutes volatiles were removed under reduced pressure and the resulting solid redissolved in C_6D_6 (0.6 mL). The ^1H NMR spectrum revealed the absence of the resonance at 4.75 ppm and the $^1H\{^{11}B\}$ NMR spectrum revealed the absence of the resonances at 4.75 and 1.04 ppm.

$Cp_2Zr\{(\mu\text{-}H)BH_3\}\{N(^tBu)Si(\mu\text{-}H)Ph_2\}$ (22). To a stirred solution of $Cp_2Zr(N^tBu)(THF)$ (**4.8**, 0.200 g, 0.548 mmol) in benzene (10 mL) at RT was added dropwise a solution of Ph_2SiH_2 (0.103 mL, 0.555 mmol) in benzene (5 mL). After 1 h the volatiles were removed under reduced pressure and the yellow residue redissolved in benzene (10 mL). To the stirred solution was added BH_3·SMe_2 (0.260 mL, 2.74 mmol) at RT. After 5 minutes volatiles were removed under reduced pressure and the resulting solid extracted into toluene (3 x 5 mL). The combined extracts were concentrated and cooled to –30 °C, resulting in the formation of **22** as pale yellow diffraction-quality crystals, which were subsequently washed with toluene (2 mL) and dried *in vacuo*. Yield: 0.110 g (41%).

^1H NMR (C_6D_6, 499.9 MHz, 298 K): δ 7.76 – 7.74 (4 H, m, *o*-SiC_6H_5), 7.21 – 7.19 (6 H, overlapping 2 x m, *m*-SiC_6H_5, *p*-SiC_6H_5), 5.96 (10 H, s, C_5H_5), 3.45 (1 H, s, SiH), 1.54 (9 H, s, CMe_3). $^1H\{^{11}B\}$ NMR (C_6D_6, 499.9 MHz, 298 K): δ 1.14 (4 H, s, BH_4) ppm. $^{13}C\{^1H\}$ NMR (C_6D_6, 125.7 MHz, 298 K): δ 136.2 (*i*-SiC_6H_5), 136.1 (*o*-SiC_6H_5), 130.2 (*p*-SiC_6H_5), 128.5 (*m*-SiC_6H_5), 112.8 (C_5H_5), 57.3 ($\underline{C}Me_3$), 35.4 ($C\underline{Me_3}$) ppm. ^{11}B NMR (C_6D_6, 128.4 MHz, 293 K): δ – 11.5 (m) ppm. ^{29}Si NMR (HMBC ^1H-observed, C_6D_6, 499.9 MHz, 298 K): δ – 57.6 ($^1J_{SiH}$ = 136 Hz, $SiHPh_2$) ppm. IR (NaCl plates, Nujol mull, cm^{-1}): 2374 (br, s), 2142 (m), 2001 (br, s), 1851 (s), 1586 (w), 1427 (s), 1358 (s), 1224 (m), 1195 (s), 1103 (s), 1059 (s), 1019 (s), 998 (m), 810 (br, s), 738 (s), 719 (s), 701 (s),

671 (m). Anal. found (calcd. for $C_{26}H_{34}NSiBZr$): C, 63.53 (63.64); H, 7.10 (6.98); N, 2.88 (2.85)%.

$Cp_2Zr\{(\mu\text{-}H)BH_3\}\{N(^tBu)Si(\mu\text{-}H)Me_2\}$ (23). To a stirred solution of $Cp_2Zr(H)\{N(^tBu)Si(\mu\text{-}H)Me_2\}$ (**4.5**, 0.200 g, 0.567 mmol) in benzene (10 mL) at RT was added $BH_3{\cdot}SMe_2$ (0.108 mL, 1.13 mmol) at RT. After 5 minutes volatiles were removed under reduced pressure and the resulting solid extracted into toluene (3 x 5 mL). The combined extracts were concentrated and cooled to 4 °C, resulting in the formation of **23** as pale yellow diffraction-quality crystals, which were subsequently washed with toluene (2 mL) and dried *in vacuo*. Yield: 0.095 g (46%).

^1H NMR (C_6D_6, 499.9 MHz, 298 K): δ 5.88 (10 H, s, C_5H_5), 1.53 (1 H, sept., $^3J_{HH}$ = 2.6 Hz, SiH), 1.29 (9 H, s, CMe_3), 0.01 (6 H, d, $^3J_{HH}$ = 2.6 Hz, $SiH\underline{Me_2}$) ppm. $^1H\{^{11}B\}$ NMR (C_6D_6, 499.9 MHz, 298 K): δ 1.07 (4 H, s, BH_4) ppm. $^{13}C\{^1H\}$ NMR (C_6D_6, 125.7 MHz, 298 K): δ 112.0 (C_5H_5), 57.4 ($\underline{C}Me_3$), 34.4 ($C\underline{Me_3}$), 1.2 ($SiHMe_2$) ppm. ^{11}B NMR (C_6D_6, 128.4 MHz, 293 K): δ - 15.5 (quint., $^1J_{BH}$ = 86 Hz) ppm. ^{29}Si NMR (HMBC ^1H-observed, C_6D_6, 499.9 MHz, 298 K): δ - 58.4 ($^1J_{SiH}$ = 115 Hz, $SiHMe_2$) ppm. IR (NaCl plates, Nujol mull, cm^{-1}): 2381 (br, s), 2347 (br, m), 2038 (br, m), 1893 (s), 1738 (br, w), 1355 (m), 1250 (w), 1200 (m), 1159 (m), 1057 (s), 1015 (m), 850 (w), 835 (w), 818 (s), 797 (s), 763 (m), 709 (w). An elemental analysis was not carried out because of the coronavirus epidemic and its impact on technical services.

$Cp_2Zr\{N(^tBu)SiHPhBH_2(\mu\text{-}H)\}$ (24). To a stirred solution of $Cp_2Zr(N^tBu)(THF)$ (**4.8**, 0.200 g, 0.548 mmol) in benzene (10 mL) at RT was added dropwise a solution of $PhSiH_3$ (0.071 mL, 0.575 mmol) in benzene (5 mL). After 1 h the volatiles were removed under reduced pressure and the yellow residue redissolved in benzene (10 mL). To the stirred solution was added $BH_3{\cdot}SMe_2$ (52.0 µL, 0.548 mmol) at RT. After 1 h the volatiles were

removed under reduced pressure and the resulting solid redissolved in benzene (10 mL) and heated at 70 °C. After 18 h the volatiles were removed under reduced pressure and the resulting solid extracted into hexane (4 x 10 mL). The combined extracts were concentrated and cooled to 4 °C, resulting in the formation of **24** as yellow diffraction-quality crystals, which were subsequently washed with hexane (2 mL) and dried *in vacuo*. Yield: 0.090 g (40%).

^{1}H NMR (C_6D_6, 400.1 MHz, 298 K): δ 7.83 – 7.80 (2 H, m, *o*-SiC_6H_5), 7.27 – 7.22 (2 H, m, *m*-SiC_6H_5), 7.21 – 7.16 (1 H, m, *p*-SiC_6H_5), 5.97 (5 H, s, C_5H_5), 5.82 (5 H, s, C_5H_5), 4.55 (1 H, q, $^{3}J_{HH}$ = 2.7 Hz, SiH), 1.01 (9 H, s, CMe_3). ^{1}H{^{11}B} NMR (C_6D_6, 400.1 MHz, 298 K): δ 1.20 (3 H, d, $^{3}J_{HH}$ = 2.7 Hz, BH_3) ppm. ^{13}C{^{1}H} NMR (C_6D_6, 100.6 MHz, 298 K): δ 138.1 (*i*-SiC_6H_5), 136.1 (*o*-SiC_6H_5), 129.0 (*p*-SiC_6H_5), 128.2 (*m*-SiC_6H_5), 111.9 (C_5H_5), 111.7 (C_5H_5), 58.8 ($\underline{C}Me_3$), 34.0 ($C\underline{Me_3}$) ppm. ^{11}B NMR (C_6D_6, 128.4 MHz, 293 K): δ -6.2 (q, $^{1}J_{BH}$ = 86 Hz) ppm. ^{29}Si NMR (HMBC ^{1}H-observed, C_6D_6, 499.9 MHz, 298 K): δ -63.2 ($^{1}J_{SiH}$ = 210 Hz, SiHPh) ppm. IR (NaCl plates, Nujol mull, cm^{-1}): 2392 (s), 2360 (s), 2060 (s), 2010 (w), 1987 (m), 1428 (m), 1356 (s), 1299 (m), 1189 (s), 1113 (s), 1100 (s), 1020 (s), 856 (s), 838 (s), 801 (br, s), 735 (s), 698 (s), 681 (m). Anal. found (calcd. for $C_{20}H_{28}NSiBZr$): C, 58.16 (58.23); H, 6.99 (6.84); N, 3.33 (3.40)%.

NMR tube scale synthesis of $Cp_2Zr\{N(^tBu)SiDPhBD_2(\mu\text{-}D)\}$ (24-*d*$_4$). To a solution of $Cp_2Zr(N^tBu)(THF)$ (**4.8**, 10.0 mg, 27.4 μmol) in an NMR tube equipped with a J. Young Teflon valve in C_6D_6 (0.6 mL) was added $PhSiD_3$ (3.5 μL, 27.6 μmol) at RT. After 1 h the volatiles were removed under reduced pressure and the residue redissolved in C_6D_6 (0.6 mL). BD_3·THF (1.0 M in THF, 0.028 mL, 28.0 μmol) was added at RT. After 5 minutes volatiles were removed under reduced pressure and the resulting solid redissolved in C_6D_6 (0.6 mL) and heated for 18 h at 80 °C. The ^{1}H NMR spectrum

revealed the absence of the resonance at 4.55 ppm and the $^{1}H\{^{11}B\}$ NMR spectrum revealed the absence of the resonances at 4.55 and 1.20 ppm.

$Cp_2Zr\{N(^tBu)SiPh_2BH_2(\mu\text{-}H)\}$ (25). To a stirred solution of $Cp_2Zr(N^tBu)(THF)$ (**4.8**, 0.200 g, 0.548 mmol) in benzene (10 mL) at RT was added dropwise a solution of Ph_2SiH_2 (0.103 mL, 0.555 mmol) in benzene (5 mL). After 1 h the volatiles were removed under reduced pressure and the yellow residue redissolved in benzene (10 mL). To the stirred solution was added $BH_3{\cdot}SMe_2$ (52.0 µL, 0.548 mmol) at RT. After 1 h the volatiles were removed under reduced pressure and the resulting solid redissolved in benzene (10 mL) and heated at 70 °C. After 18 h the volatiles were removed under reduced pressure and the resulting solid was washed with hexane (2 x 10 mL) and dried *in vacuo* to yield **25** as a yellow powder. Yield: 0.127 g (47%). Diffraction-quality crystals were grown by slow evaporation of a concentrated C_6D_6 solution.

^{1}H NMR (C_6D_6, 400.1 MHz, 298 K): δ 7.94 – 7.92 (4 H, m, *o*-SiC_6H_5), 7.29 – 7.25 (4 H, m, *m*-SiC_6H_5), 7.23 – 7.19 (2 H, m, *p*-SiC_6H_5), 5.92 (10 H, s, C_5H_5), 1.05 (9 H, s, CMe_3). $^{1}H\{^{11}B\}$ NMR (C_6D_6, 400.1 MHz, 298 K): δ 1.43 (3 H, s, BH_3) ppm. $^{13}C\{^{1}H\}$ NMR (C_6D_6, 100.6 MHz, 298 K): δ 139.8 (*i*-SiC_6H_5), 137.1 (*o*-SiC_6H_5), 128.6 (*p*-SiC_6H_5), 127.7 (*m*-SiC_6H_5), 112.1 (C_5H_5), 60.0 ($\underline{C}Me_3$), 34.9 ($C\underline{Me_3}$) ppm. ^{11}B NMR (C_6D_6, 128.4 MHz, 293 K): δ – 1.8 (q, $^{1}J_{BH}$ = 72 Hz) ppm. IR (NaCl plates, Nujol mull, cm^{-1}): 2431 (m), 2380 (m), 2315 (w), 1992 (w), 1424 (m), 1359 (m), 1308 (w), 1189 (s), 1118 (w), 1094 (s), 1020 (s), 809 (s), 742 (m), 716 (s), 700 (s), 669 (s). Anal. found (calcd. for $C_{26}H_{32}NSiBZr$): C, 56.37 (63.91); H, 6.50 (6.60); N, 2.36 (2.87)%.

$Cp_2Zr\{N(^tBu)SiMe_2BH_2(\mu\text{-}H)\}$ (26). To a stirred solution of $Cp_2Zr(H)\{N(^tBu)Si(\mu\text{-}H)Me_2\}$ (**4.5**, 0.200 g, 0.567 mmol) in benzene (10 mL) at RT was added $BH_3{\cdot}SMe_2$ (0.108 mL, 1.13 mmol) at RT. After 5 minutes volatiles were removed

under reduced pressure and the resulting solid extracted into toluene (3 x 5 mL). In a sealed Rotaflo ampoule, the combined extracts were stirred and heated to 93 °C. After 6 h the solution was filtered, concentrated and cooled to –30 °C, resulting in the formation of **26** as orange diffraction-quality crystals which were washed with toluene (2 mL) and dried *in vacuo*. Yield: 0.101 g (49%).

^{1}H NMR (C_6D_6, 400.1 MHz, 298 K): δ 5.80 (10 H, s, C_5H_5), 1.07 (9 H, s, CMe_3), 0.34 (6 H, s, $SiMe_2$) ppm. ^{1}H{^{11}B} NMR (C_6D_6, 499.9 MHz, 298 K): δ 1.20 (3 H, s, BH_3) ppm. ^{13}C{^{1}H} NMR (C_6D_6, 125.7 MHz, 298 K): δ 111.6 (C_5H_5), 59.3 ($\underline{C}Me_3$), 34.5 ($C\underline{Me_3}$), 4.9 ($SiMe_2$) ppm. ^{11}B NMR (C_6D_6, 128.4 MHz, 293 K): δ –1.4 (q, $^{1}J_{BH}$ = 88 Hz) ppm. IR (NaCl plates, Nujol mull, cm^{-1}): 2396 (m), 2364 (m), 2111 (w), 1998 (w), 1355 (s), 1305 (w), 1235 (m), 1191 (s), 116 (m), 1024 (s), 843 (m), 802 (s), 757 (s), 712 (s), 670 (w). An elemental analysis was not carried out because of the coronavirus epidemic and its impact on technical services.

Kinetic measurements for the conversion of $Cp_2Zr\{(\mu\text{-}H)BH_3\}\{N(^tBu)Si(\mu\text{-}H)Me_2\}$ (23) to $Cp_2Zr\{N(^tBu)Me_2BH_2(\mu\text{-}H)\}$ (26) and H_2. The general procedure is as follows. In a dry-box, a toluene-d_8 solution (0.5 mL) of $Cp_2Zr\{(\mu\text{-}H)BH_3\}\{N(^tBu)Si(\mu\text{-}H)Me_2\}$ (**23**, 10.0 mg, 27.3 μmol) was transferred to an NMR tube equipped with a J. Young Teflon valve. To this solution, either THF (44.3 μL, 0.546 mmol), $BH_3{\cdot}SMe_2$ (51.8 μL, 0.546 mmol) or $Cp_2Zr(H)\{N(^tBu)Si(\mu\text{-}H)Me_2\}$ (7.7 mg, 21.8 μmol) was added when appropriate. A blank toluene-d_8 sample was added to the NMR probe at RT, locked and shimmed, and the probe heated to the relevant temperature (366, 369, 375, or 375 K). After thermal equilibration, the experimental sample replaced the blank sample and an array was set up to record ^{1}H NMR spectra (4 scans) with a set delay between the recordings of each spectrum (e.g. 63 s). The concentrations of species were measured using the C_5H_5 integrals.

Reaction of $Cp_2Zr(D)\{N(^tBu)Si(\mu\text{-}D)DPh\}$ (6-*d*$_3$) with $BH_3\cdot SMe_2$. To a C_6D_6 (0.6 mL) solution of $Cp_2Zr(D)\{N(^tBu)Si(\mu\text{-}D)DPh\}$ (**6-*d*$_3$**, 10.0 mg, 24.8 μmol) in an NMR tube equipped with a J. Young Teflon valve was added $BH_3\cdot SMe_2$ (2.3 μL, 24.8 μmol). The solution was shaken and the volatiles immediately removed under reduced pressure. The residue was redissolved in C_6D_6 (0.6 mL) and the relative integral of the SiH/SiHD resonance was monitored by ^{1}H NMR spectroscopy.

Kinetic measurements for the conversion of $Cp_2Zr\{(\mu\text{-}H)_2BH_2\}\{N(^tBu)SiH_2Ph\}$ (21) to $Cp_2Zr\{N(^tBu)SiHPhBH_2(\mu\text{-}H)\}$ (24) and H_2. The general procedure is as follows. In a dry-box, a toluene-*d*$_8$ solution (0.6 mL) of $Cp_2Zr\{(\mu\text{-}H)_2BH_2\}\{N(^tBu)SiH_2Ph\}$ (**21**, 10.0 mg, 24.1 μmol) was transferred to an NMR tube equipped with a J. Young Teflon valve. A blank toluene-*d*$_8$ sample was added to the NMR probe at RT, locked and shimmed, and the probe heated to the relevant temperature (347, 350, 353, 356, 359 K). After thermal equilibration, the experimental sample replaced the blank sample and an array was set up to record a ^{1}H NMR spectrum (4 scans) with a set delay between the recordings of each spectrum (e.g. 63 s). The concentrations of **21** and **24** were measured using the C_5H_5 integrals.

Investigation of the effect of solvent and $BH_3\cdot SMe_2$ on the rate of conversion of $Cp_2Zr\{(\mu\text{-}H)_2BH_2\}\{N(^tBu)SiH_2Ph\}$ (21) to $Cp_2Zr\{N(^tBu)SiHPhBH_2(\mu\text{-}H)\}$ (24) and H_2. In parallel, in a dry-box, a C_6D_6 and two THF-*d*$_8$ solutions (0.6 mL) of $Cp_2Zr\{(\mu\text{-}H)_2BH_2\}\{N(^tBu)SiH_2Ph\}$ (**21**, 10.0 mg, 24.1 μmol) were transferred to NMR tubes equipped with J. Young Teflon valves. To one THF-*d*$_8$ solution was added $BH_3\cdot SMe_2$ (45.7 μL, 0.482 mmol). The solutions were heated to 50 °C and ^{1}H NMR spectra recorded at certain time intervals. The progress of the reactions was measured using the C_5H_5 integrals of **21** and **24**.

Kinetic isotope effect measurements for the reaction of $Cp_2Zr\{(\mu\text{-}H)_2BH_2\}\{N(^tBu)SiH_2Ph\}$ (21) to $Cp_2Zr\{N(^tBu)SiHPhBH_2(\mu\text{-}H)\}$ (24) and H_2 or $Cp_2Zr\{(\mu\text{-}D)_2BD_2\}\{N(^tBu)SiD_2Ph\}$ (21-*d*$_6$) to $Cp_2Zr\{N(^tBu)SiDPhBD_2(\mu\text{-}D)\}$ (24-*d*$_4$) and D_2. A toluene-d_8 solution (0.6 mL) of $Cp_2Zr\{(\mu\text{-}H)_2BH_2\}\{N(^tBu)SiH_2Ph\}$ (**21**, 10.0 mg, 24.1 μmol) or $Cp_2Zr\{(\mu\text{-}D)_2BD_2\}\{N(^tBu)SiD_2Ph\}$ (**21-*d*$_6$**, 10.1 mg, 24.1 μmol) was transferred to an NMR tube equipped with a J. Young Teflon valve. A blank toluene-d_8 sample was added to the NMR probe at RT, locked and shimmed, and the probe heated to 356 K. After thermal equilibration, the experimental sample replaced the blank sample and an array was set up to record a ^{1}H NMR spectrum (4 scans) with a set delay between the recordings of each spectrum (e.g. 63 s). The concentrations of species were measured using the C_5H_5 integrals.

$Cp_2Zr\{(\mu\text{-}H)_2BH_2\}\{N(Xyl)SiH_2Ph\}$ (27) To a stirred solution of $Cp_2Zr(NXyl)(THF)$ (**4.7**, 0.177 g, 0.429 mmol) in benzene (10 mL) at RT was added dropwise $PhSiH_3$ (56.0 μL, 0.454 mmol). After 1 h the volatiles were removed under reduced pressure and the resulting yellow oil dissolved in benzene (10 mL). $BH_3.SMe_2$ (81.0 μL, 0.854 mmol) was added to the stirred solution at RT. After 5 minutes the volatiles were removed under reduced pressure and the resulting solid extracted into hexane (4 x 10 mL). The combined extracts were concentrated and cooled to 4 °C, resulting in the formation of **27** as a colourless crystalline solid which was subsequently washed with hexane (2 mL) and dried *in vacuo*. Yield: 0.109 g (55%).

^{1}H NMR (C_6D_6, 400.1 MHz, 298 K): δ 7.25 – 7.23 (2 H, m, *o*-SiC_6H_5), 7.10 – 7.06 (1 H, m, *p*-SiC_6H_5), 7.03 – 6.99 (2 H, m, *m*-SiC_6H_5), 6.97 – 6.96 (2H, m, *m*-Xyl), 6.90 – 6.86 (1 H, m, *p*-Xyl), 5.74 (10 H, s, C_5H_5), 5.40 (2 H, s, SiH_2), 2.04 (6 H, s, Me) ppm. ^{1}H{^{11}B} NMR (C_6D_6, 400.1 MHz, 298 K): δ 0.93 (4 H, s, BH_4) ppm. ^{13}C{^{1}H} NMR (C_6D_6, 100.6 MHz, 298 K): δ 158.5 (*i*-Xyl), 136.1 (*i*-SiC_6H_5), 135.9 (*o*-SiC_6H_5), 133.5 (*o*-Xyl), 129.8

(*p*-SiC_6H_5), 129.2 (*m*-Xyl), 127.8 (*m*-SiC_6H_5), 123.3 (*p*-Xyl), 113.1 (C_5H_5), 20.8 (Me) ppm. ^{11}B NMR (C_6D_6, 128.4 MHz, 293 K): δ –17.4 (quint., $^1J_{BH}$ = 84 Hz) ppm. ^{29}Si NMR (HMBC ^1H-observed, C_6D_6, 499.9 MHz, 298 K): δ –30.0 ($^1J_{SiH}$ = 206 Hz, SiH_2Ph) ppm. IR (NaCl plates, Nujol mull, cm^{-1}): 2422 (s), 2375 (s), 2227 (w), 2143 (br, s), 1588 (w), 1428 (w), 1344 (s), 1262 (m), 1247 (w), 1177 (s), 1117 (s), 1100 (m), 1015 (s), 945 (s), 885 (s), 867 (s), 843 (s), 814 (m), 735 (m), 703 (s), 692 (m), 598 (m). Anal. found (calcd. for $C_{24}H_{30}NSiBZr$): C, 62.09 (62.31); H, 6.35 (6.54); N, 3.14 (3.03)%.

NMR tube scale reaction of $Cp_2Zr(H)\{N(Xyl)SiH_2Ph\}$ (8) with $PhSiD_3$. To a C_6D_6 (0.6 mL) solution of $Cp_2Zr(NXyl)(THF)$ (**4.7**, 10.0 mg, 24.2 μmol) in an NMR tube equipped with a J. Young Teflon valve was added $PhSiH_3$ (3.0 μL, 24.2 μmol) at RT. After 1 h the volatiles were removed under reduced pressure and the residue redissolved in C_6D_6 (0.6 mL). $PhSiD_3$ (3.1 μL, 24.2 μmol) was added at RT and the ^1H NMR spectrum was monitored for 24 h, after which time statistical distribution of hydrogen and deuterium across the various Si–H and Zr–H sites was reached. The appearance of a Si–H resonance envelope based at *ca.* 4.2 ppm attributable to $PhSiH_3$ and its partially deuterated isotopomers $PhSiH_xD_{(3-x)}$ (x = 1 or 2) was also observed.

NMR tube scale reaction of $Cp_2Zr(D)\{N(Xyl)SiD_2Ph\}$ (8-*d*$_3$) with $PhSiH_3$. To a C_6D_6 (0.6 mL) solution of $Cp_2Zr(NXyl)(THF)$ (**4.7**, 10.0 mg, 24.2 μmol) in an NMR tube equipped with a J. Young Teflon valve was added $PhSiD_3$ (3.1 μL, 24.2 μmol) at RT. After 1 h the volatiles were removed under reduced pressure and the residue redissolved in C_6D_6 (0.6 mL). $PhSiH_3$ (3.0 μL, 24.2 μmol) was added at RT and the ^1H NMR spectrum was monitored for 24 h, after which time statistical distribution of hydrogen and deuterium across the various Si–H and Zr–H sites was reached.

NMR tube scale reaction of $Cp_2Zr(D)\{N(Xyl)SiD_2Ph\}$ (8-*d*$_3$) with H_2. To a C_6D_6 (0.6 mL) solution of $Cp_2Zr(NXyl)(THF)$ (**4.7**, 10.0 mg, 24.2 μmol) in an NMR tube equipped with a J. Young Teflon valve was added $PhSiD_3$ (3.1 μL, 24.2 μmol) at RT. After 1 h the volatiles were removed under reduced pressure and the residue redissolved in C_6D_6 (0.6 mL). The solution was freeze-pump-thaw-degassed and then exposed to H_2 (1 bar overpressure) at RT. The ^{1}H NMR spectrum was monitored for several days, after which time the relative integrals of the Si–H and Zr–H resonances grew to 2 and 1, respectively, indicating complete incorporation of hydrogen into the Si–D and Zr–D sites. A resonance attributable to HD was also observed. Running the reaction in C_6H_6 (0.6 mL), the ^{2}H NMR spectrum revealed resonances attributable to HD and D_2.

NMR tube scale reaction of $Cp_2Zr(D)\{N(Xyl)SiD_2Ph\}$ (8-*d*$_3$) with $PhSiH_2Cl$. To a C_6D_6 (0.6 mL) solution of $Cp_2Zr(NXyl)(THF)$ (**4.7**, 10.0 mg, 24.2 μmol) in an NMR tube equipped with a J. Young Teflon valve was added $PhSiD_3$ (3.1 μL, 24.2 μmol) at RT. After 1 h the volatiles were removed under reduced pressure and the residue redissolved in C_6D_6 (0.6 mL). $PhSiH_2Cl$ (3.2 μL, 24.2 μmol) was added at RT and the ^{1}H NMR spectrum immediately contained resonances attributable to $Cp_2Zr(Cl)\{N(Xyl)SiH_2Ph\}$ (**11**), with the complete absence of resonances attributable to Si–H environments, indicating quantitative formation of $Cp_2Zr(Cl)\{N(Xyl)SiD_2Ph\}$ (**11-*d*$_2$**).

NMR tube scale reaction of $Cp_2Zr(Cl)\{N(Xyl)SiH_2Ph\}$ (11) with $PhSiD_3$. To a C_6D_6 (0.6 mL) solution of $Cp_2Zr(Cl)\{N(Xyl)SiH_2Ph\}$ (**11**, 10.0 mg, 20.7 μmol) in an NMR tube equipped with a J. Young Teflon valve was added $PhSiD_3$ (2.6 μL, 20.7 μmol) at RT. The ^{1}H NMR spectrum showed no changed after 24 h and heating to 80 °C for 24 h also brought no change to the ^{1}H NMR spectrum, indicating no reaction had occurred.

NMR tube scale reaction of $Cp_2Zr(D)\{N(Xyl)SiD_2Ph\}$ (8-*d*$_3$) with Ph_2SiH_2. To a C_6D_6 (0.6 mL) solution of $Cp_2Zr(NXyl)(THF)$ (**4.7**, 10.0 mg, 24.2 μmol) in an NMR tube equipped with a J. Young Teflon valve was added $PhSiD_3$ (3.1 μL, 24.2 μmol) at RT. After 1 h the volatiles were removed under reduced pressure and the residue redissolved in C_6D_6 (0.6 mL). Ph_2SiH_2 (4.5 μL, 24.2 μmol) was added at RT and the ^{1}H NMR spectrum was monitored for 24 h, after which time statistical distribution of hydrogen and deuterium across the various Si–H and Zr–H sites of **8** was reached. No resonances attributable to $Cp_2Zr(H)\{N(Xyl)SiHPh_2\}$ (**9**), or any of its isotopomers, were observed until the reaction was heated to 80 °C.

NMR tube scale reaction of $Cp_2Zr(H)\{N(Xyl)SiHPh_2\}$ (9) with $PhSiD_3$. To a C_6D_6 (0.6 mL) solution of $Cp_2Zr(NXyl)(THF)$ (**4.7**, 10.0 mg, 24.2 μmol) in an NMR tube equipped with a J. Young Teflon valve was added Ph_2SiH_2 (4.5 μL, 24.2 μmol) at RT. After 1 h the volatiles were removed under reduced pressure and the residue redissolved in C_6D_6 (0.6 mL). $PhSiD_3$ (3.1 μL, 24.2 μmol) was added at RT and the ^{1}H NMR spectrum was monitored for 24 h, after which time the relative intensity of the Zr–H resonance of **9** had reduced to 0.25, while the relative intensity of the Si–H resonance was unchanged. No reduction of the relative intensity of the Si–H resonance of **9** and no resonances attributable to $Cp_2Zr(H)\{N(Xyl)SiH_2Ph\}$ (**8**), or any of its isotopomers, were observed until the reaction was heated to 80 °C.

Competition reaction of $Cp_2Zr(NXyl)(THF)$ with $PhSiH_3$ and $PhSiH_2$. $Cp_2Zr(NXyl)(THF)$ (**4.7**, 10.0 mg, 24.2 μmol) was dissolved in a solution of $PhSiH_3$ (14.9 μL, 0.121 mmol) and Ph_2SiH_2 (22.5 μL, 0.121 mmol) in C_6D_6 (0.6 mL) and transferred to an NMR tube equipped with a J. Young Teflon valve. The ^{1}H NMR spectrum showed the immediate formation of $Cp_2Zr(H)\{N(Xyl)SiH_2Ph\}$ (**8**) and $Cp_2Zr(H)\{N(Xyl)SiHPh_2\}$ (**9**) in a 3:1 ratio. This ratio did not change over time.

Intramolecular hydrogen-deuterium exchange of $Cp_2Zr(H)\{N(Xyl)SiD_2Ph\}$ (8-*d*$_1$). To a C_6D_6 (0.6 mL) solution of $Cp_2Zr(NXyl)(THF)$ (**4.7**, 10.0 mg, 24.2 μmol) in an NMR tube equipped with a J. Young Teflon valve was added $PhSiD_3$ (3.1 μL, 24.2 μmol) at RT. After 1 h the volatiles were removed under reduced pressure and the residue redissolved in C_6D_6 (0.6 mL). $PhSiH_3$ (7.7 μL, 60.5 μmol) was added at RT and after 45 mins volatiles were removed under reduced pressure. The residue was redissolved in C_6D_6 (0.6 mL) and analysis of the ^{1}H NMR spectrum showed the relative integrals of the Zr–H and Si–H resonances to be 0.89 and 0.19, respectively. After 24 h at RT, the ^{1}H NMR spectrum showed the relative integrals of the Zr–H and Si–H resonances to be 0.48 and 0.71, respectively.

Reactions of $Cp_2Zr(H)\{N(^tBu)Si(\mu\text{-}H)HPh\}$ (6), $Cp_2Zr(D)\{N(^tBu)Si(\mu\text{-}D)DPh\}$ (6-*d*$_3$), $Cp_2Zr(H)\{N(^tBu)Si(\mu\text{-}H)Ph_2\}$ (7), or $Cp_2Zr(Cl)\{N(^tBu)Si(\mu\text{-}H)HPh\}$ (10) with silanes. The general procedure is as follows. To a C_6D_6 (0.6 mL) solution of either $Cp_2Zr(H)\{N(^tBu)Si(\mu\text{-}H)HPh\}$ (**6**, 10.0 mg), $Cp_2Zr(D)\{N(^tBu)Si(\mu\text{-}D)DPh\}$ (**6-*d*$_3$**, 10.0 mg), $Cp_2Zr(H)\{N(^tBu)Si(\mu\text{-}H)Ph_2\}$ (**7**, 10.0 mg), or $Cp_2Zr(Cl)\{N(^tBu)Si(\mu\text{-}H)HPh\}$ (**10**, 10.0 mg) in an NMR tube equipped with a J. Young Teflon valve was added stoichiometric amounts of either $PhSiH_3$, $PhSiD_3$, Ph_2SiH_2, or $PhSiH_2Cl$ at RT. The reactions were either left at RT or heated to 60 or 80 °C, and the ^{1}H NMR spectra of the reaction solutions were monitored to observe the change in relative integral of Zr–H and Si–H resonances belonging to respective species and the change in relative amounts of **6**, **7**, **10** or their respective isotopomers.

Reactions of $Cp_2Zr(H)\{N(NPh_2)SiH_2Ph\}$ (2), $Cp_2Zr(D)\{N(NPh_2)SiD_2Ph\}$ (2-*d*$_3$), $Cp_2Zr(H)\{N(NPh_2)SiHPh_2\}$ (3), or $Cp_2Zr(Cl)\{N(NPh_2)SiH_2Ph\}$ (4) with silanes. The general procedure is as follows. To a C_6D_6 (0.6 mL) solution of either $Cp_2Zr(H)\{N(NPh_2)SiH_2Ph\}$ (**2**, 10.0 mg), $Cp_2Zr(D)\{N(NPh_2)SiD_2Ph\}$ (**2-*d*$_3$**, 10.0 mg),

$Cp_2Zr(H)\{N(NPh_2)SiHPh_2\}$ (**3**, 10.0 mg), or $Cp_2Zr(Cl)\{N(NPh_2)SiH_2Ph\}$ (**4**, 10.0 mg) in an NMR tube equipped with a J. Young Teflon valve was added stoichiometric amounts of either $PhSiH_3$, $PhSiD_3$, Ph_2SiH_2, or $PhSiH_2Cl$ at RT. The reactions were either left at RT or heated to 60 or 80 °C, and the ^{1}H NMR spectra of the reaction solutions were monitored to observe the change in relative integral of Zr–H and Si–H resonances belonging to respective species and the change in relative amounts of **2**, **3**, **4** or their respective isotopomers.

6.8 Experimental details and characterising data for Chapter Five

[Pn*TiBr(μ-Br)]$_2$ (28) To a stirred suspension of $Pn^*Li_2\cdot(TMEDA)_{0.1}$ (**5.5**, 1.30 g, 6.13 mmol) in toluene (50 mL) at RT was added a solution of Me_3SnCl (2.44 g, 12.3 mmol) in toluene (50 mL). After 16 h, the suspension was filtered through Celite and eluted with toluene (3 x 50 mL). The solution was concentrated to 50 mL and cooled to –78 °C, then transferred dropwise to a stirred solution of $TiBr_4\cdot2THF$ (3.14 g, 6.13 mmol) in toluene at –78 °C. The reaction mixture was slowly warmed to RT and stirred for a further 16 h before being filtered through Celite and eluted with toluene (3 x 50 mL). The solution was concentrated and cooled to –30 °C, resulting in the formation of **28** as a red-brown crystalline solid, suitable for X-ray diffraction, which was subsequently washed with cold toluene (–78 °C, 25 mL) and dried *in vacuo*. Yield: 1.71 g (71%).

^{1}H NMR (C_6D_6, 400.1 MHz, 298 K): δ 1.90 (24 H, s, {**1,3,5,7**}-Me_8), 1.43 (12 H, s, {**2,6**}-Me_8) ppm. $^{13}C\{^1H\}$ NMR (C_6D_6, 100.6 MHz, 298 K): δ 146.1 (**4,8**), 133.2 (**2,6**), 128.2 (**1,3,5,7**), 13.6 ({**1,3,5,7**}-Me_8), 10.4 ({**2,6**}-Me_8) ppm. Anal. found (calcd. for $C_{28}H_{36}Ti_2Br_4$): C, 41.80 (42.68); H, 4.52 (4.60)%.

[(Pn*Ti)$_2$(μ-Cl)$_3$][(Me$_3$Al)$_2$(μ-Cl)] (29) To a stirred solution of $[Pn^*TiCl(\mu\text{-}Cl)]_2$ (**5.7**, 107 mg, 0.175 mmol) in benzene (5 mL) at RT was added $AlMe_3$ (75.0 μL, 0.39 mmol).

After addition stirring was immediately stopped and the solution turned from dark red to dark green. After 5 minutes, orange crystals, suitable for X-ray diffraction, of **29** were deposited and the solution decanted away. The crystalline solid was washed with benzene (3 x 5 mL) and dried *in vacuo*. Yield: 127 mg (48%).

^{1}H NMR (C_6D_5Br, 400.1 MHz, 298 K): δ 1.86 (36 H, overlapping 2 x s, {**1,3,5,7**}-Me_8), {**2,6**}-Me_8), 0.00 (18 H, $AlMe_3$) ppm. $^{13}C\{^{1}H\}$ NMR (C_6D_6, 100.6 MHz, 298 K): δ 148.4 (**4,8**), 137.9 (**2,6**), 129.0 (**1,3,5,7**), 12.2 ({**1,3,5,7**}-Me_8), 10.8 ({**2,6**}-Me_8), –4.5 ($AlMe_3$) ppm.

[Pn*TiMe(μ-Br)]$_2$ (30) To a stirred solution of [Pn*TiBr(μ-Br)]$_2$ (**28**, 258 mg, 0.328 mmol) in Et_2O (40 mL) at RT was added MeLi (1.6 M in Et_2O, 0.41 mL, 0.656 mmol). The solution immediately turned from dark blue to dark green and after 15 minutes the volatiles were removed under reduced pressure. The resulting green solid was washed with pentane (3 x 10 mL) and extracted into toluene (2 x 10 mL). The combined extracts were concentrated and cooled to –30 °C, resulting in the formation of **30** as dark green diffraction-quality crystals, which were subsequently washed with cold toluene (5 mL) and dried *in vacuo*. Yield: 97 mg (45%).

^{1}H NMR (C_6D_6, 400.1 MHz, 298 K): δ 1.87 (24 H, s, {**1,3,5,7**}-Me_8), 1.82 (12 H, s, {**2,6**}-Me_8), 0.51 (6 H, s, TiMe) ppm. $^{13}C\{^{1}H\}$ NMR (C_6D_6, 100.6 MHz, 298 K): δ 136.2 (**4,8**), 131.2 (**2,6**), 119.1 (**1,3,5,7**), 43.9 (TiMe), 12.9 ({**1,3,5,7**}-Me_8), 11.2 ({**2,6**}-Me_8) ppm.

NMR tube scale synthesis of [Pn*Ti(μ-Br)]$_2$(μ-CH_2) (31). A solution of [Pn*TiMe(μ-Br)]$_2$ (**30**, 20.0 mg, 30.4 μmol) in C_6D_6 (0.6 mL), in an NMR tube equipped with a J. Young Teflon valve, was heated to 50 °C. After 72 h complete consumption of the starting material was observed, with concomitant colour change from dark green to dark purple. ~65% conversion to the product **30** was observed by ^{1}H NMR spectroscopy,

with ~35% unidentifiable by-products. Compound **30** was characterised *in situ*, as a mixture with the aforementioned intractable species, by ^{1}H and ^{13}C{^{1}H} NMR spectroscopy at RT.

^{1}H NMR (C_6D_6, 400.1 MHz, 298 K): δ 5.44 (2 H, s, (μ-CH_2)), 2.17 (12 H, s, {**2,6**}-Me_8), 1.78 (24 H, s, {**1,3,5,7**}-Me_8) ppm. ^{13}C{^{1}H} NMR (C_6D_6, 100.6 MHz, 298 K): δ 191.8 (μ-CH_2), 135.2 (**4,8**), 133.3 (**2,6**), 115.7 (**1,3,5,7**), 12.9 ({**1,3,5,7**}-Me_8), 12.3 ({**2,6**}-Me_8) ppm.

NMR tube scale synthesis of [Pn*Ti(CC^{t}Bu)(μ-Cl)]$_2$ (32). To a solution of [Pn*Ti(μ-Cl)]$_2$(μ-CH_2) (**5.26**, 20.0 mg, 36.2 μmol) in C_6D_6 (0.6 mL), in an NMR tube equipped with a J. Young Teflon valve, was added HCC^{t}Bu (8.9 μL, 72.4 μmol). The reaction mixture was heated to 60 °C for 6 days, after which time complete consumption of the starting material was observed, with a concomitant colour change from dark purple to dark blue. ~90% conversion to the product **32** was observed by ^{1}H NMR spectroscopy. Volatiles were removed under reduced pressure and the residue redissolved in C_6D_6 (0.6 mL).

^{1}H NMR (C_6D_6, 400.1 MHz, 298 K): δ 2.13 (24 H, s, {**1,3,5,7**}-Me_8), 1.78 (12 H, s, {**2,6**}-Me_8), 1.29 (18 H, s, CMe_3) ppm.

Alternative NMR tube scale synthesis of [Pn*Ti(CC^{t}Bu)(μ-Cl)]$_2$ (32). To a solution of [Pn*TiMe(μ-Cl)]$_2$ (**5.7**, 20.0 mg, 35.1 μmol) in C_6D_6 (0.6 mL), in an NMR tube equipped with a J. Young Teflon valve, was added HCC^{t}Bu (8.6 μL, 70.2 μmol). After 3 days at RT complete consumption of the starting material was observed, with a concomitant colour change from dark purple to dark blue. ~90% conversion to the product **32** was observed by ^{1}H NMR spectroscopy. Volatiles were removed under reduced pressure and the residue redissolved in C_6D_6 (0.6 mL).

NMR tube scale synthesis of [Pn*Ti(CC^{t}Bu)(μ-Br)]$_2$ (33). To a solution of [Pn*TiMe(μ-Br)]$_2$ (**30**, 20.0 mg, 30.4 μmol) in C_6D_6 (0.6 mL), in an NMR tube equipped with a J. Young Teflon valve, was added HCC^{t}Bu (7.4 μL, 60.8 μmol). After 3 days at RT formation of **33** was observed by ^{1}H NMR spectroscopy, with a concomitant colour change from dark purple to dark blue. Volatiles were removed under reduced pressure and the residue redissolved in C_6D_6 (0.6 mL). Slow evaporation of a C_6D_6 solution of **33** at RT led to formation of diffraction-quality crystals.

^{1}H NMR (C_6D_6, 400.1 MHz, 298 K): δ 2.09 (24 H, s, {**1,3,5,7**}-Me$_8$), 1.65 (12 H, s, {**2,6**}-Me$_8$), 1.26 (18 H, s, CMe$_3$) ppm.

Alternative NMR tube scale synthesis of [Pn*Ti(CC^{t}Bu)(μ-Br)]$_2$ (33). A solution of [Pn*TiMe(μ-Br)]$_2$ (**30**, 20.0 mg, 30.4 μmol) in C_6D_6 (0.6 mL), in an NMR tube equipped with a J. Young Teflon valve, was heated to 50 °C for 3 days to form [Pn*Ti(μ-Br)]$_2$(μ-CH$_2$) (**31**) *in situ*. Volatiles were then removed under reduced pressure, the residue redissolved in C_6D_6 (0.6 mL) and HCC^{t}Bu (7.4 μL, 60.8 μmol) was added. The reaction mixture was heated to 60 °C for 6 days, after which time complete consumption of the starting material was observed, with a concomitant colour change from dark purple to dark blue. Compound **33** could be observed, along with impurities associated with those formed from the thermal decomposition of [Pn*TiMe(μ-Br)]$_2$ (**30**).

6.9 References

1 A. B. Pangborn, M. A. Giardello, R. H. Grubbs, R. K. Rosen and F. J. Timmers, *Organometallics*, 1996, **15**, 1518–1520.

2 P. J. Walsh, M. J. Carney and R. G. Bergman, *J. Am. Chem. Soc.*, 1991, **113**, 6343–6345.

3 P. J. Walsh, F. J. Hollander and R. G. Bergman, *J. Am. Chem. Soc.*, 1988, **110**, 8729–8731.

4 B. Xie, DPhil Thesis, University of Oxford, 2018.

5 T. K. Panda, M. T. Gamer and P. W. Roesky, *Organometallics*, 2003, **22**, 877–878.

6 S. C. Dunn, P. Mountford and D. A. Robson, *J. Chem. Soc., Dalton Trans.*, 1997, 293–304.

7 J. D. Selby, M. Feliz, A. D. Schwarz, E. Clot and P. Mountford, *Organometallics*, 2011, **30**, 2295–2307.

8 V. V. Avrorin, G. E. Fominykh, I. S. Ignat'Ev, E. N. Sinotova and T. A. Kochina, *Russ. J. Gen. Chem.*, 2014, **84**, 2125–2129.

9 G. H. Wiseman, D. R. Wheeler and D. Seyferth, *Organometallics*, 1986, **5**, 146–152.

10 L. J. Procopio, P. J. Carroll and D. H. Berry, *J. Am. Chem. Soc.*, 1991, **113**, 1870–1872.

11 J. Wang, A. K. Dash, M. Kapon, J.-C. Berthet, M. Ephritikhine and M. S. Eisen, *Chem. Eur. J.*, 2002, **8**, 5384–5396.

12 L. E. Manzer, *Inorg. Synth.*, 1982, **21**, 135–140.

13 A. E. Ashley, A. R. Cowley and D. O'Hare, *European J. Org. Chem.*, 2007, **2007**, 2239–2242.

14 A. E. Ashley, A. R. Cowley and D. O'Hare, *Chem. Commun.*, 2007, 1512–1514.

15 R. T. Cooper, F. M. Chadwick, A. E. Ashley and D. O'Hare, *Organometallics*, 2013, **32**, 2228–2233.

16 R. T. Cooper, DPhil Thesis, University of Oxford, 2012.

17 Z. Otwinowski and W. Minor, *Methods Enzymol.*, 1997, **276**, 307–326.

18 A. Altomare, G. Cascarano, C. Giacovazzo, A. Guagliardi, M. C. Burla, G. Polidori and M. Camalli, *J. Appl. Crystallogr.*, 1994, **27**, 435–435.

19 L. Palatinus and G. Chapuis, *J. Appl. Crystallogr.*, 2007, **40**, 786–790.

20 P. W. Betteridge, J. R. Carruthers, R. I. Cooper, K. Prout and D. J. Watkin, *J. Appl. Crystallogr.*, 2003, **36**, 1487–1487.

21 M. J. Frisch, G. W. Trucks, H. B. Schlegel, G. E. Scuseria, M. A. Robb, J. R. Cheeseman, G. Scalmani, V. Barone, B. Mennucci, G. A. Petersson, H. Nakatsuji, M. Caricato, X. Li, H. P. Hratchian, A. F. Izmaylov, J. Bloino, G. Zheng, J. L. Sonnenberg, M. Hada, M. Ehara, M. Toyota, R. Fukuda, J. Hasegawa, M. Ishida, T. Nakajima, Y. Honda, O. Kitao, H. Nakai, T. Vreven, J. A. Montgomery Jr., J. E. Perelta, F. Ogliaro, M. J. Bearpark, J. Heyd, E. N. Brothers, K. N. Kudin, V. N. Staroverov, R. Kobayashi, J. Normand, K. Raghavachari, A. P. Rendell, J. C. Burant, S. S. Iyengar, J. Tomasi, M. Cossi, N. Rega, N. J. Millam, M. Klene, J. E. Knox, J. B. Cross, V. Bakken, C. Adamo, J. Jaramillo, R. Gomperts, R. E. Stratmann, O. Yazyev, A. J. Austin, R. Cammi, C. Pomelli, J. W. Ochterski, R. L. Maritn, K. Morokuma, V. G. Zakrzewski, G. A. Voth, P. Salvador, J. J. Dannenberg, S. Dapprich, A. D. Daniels, O. Farkas, J. B. Foresman, J. V. Ortiz, J. Cioslowski and D. J. Fox, *Gaussian 09, Revis. D.01, Gaussian Inc., Wallingford CT*, 2013.

22 A. D. Becke, *J. Chem. Phys.*, 1993, **98**, 5648–5652.
23 J. P. Perdew and Y. Wang, *Phys. Rev. B*, 1992, **45**, 13244–13249.
24 S. Grimme, J. Antony, S. Ehrlich and H. Krieg, *J. Chem. Phys.*, 2010, **132**, 154104.
25 S. Grimme, S. Ehrlich and L. Goerigk, *J. Comput. Chem.*, 2011, **32**, 1456–1465.
26 A. Schäfer, H. Horn and R. Ahlrichs, *J. Chem. Phys.*, 1992, **97**, 2571–2577.
27 F. Weigend and R. Ahlrichs, *Phys. Chem. Chem. Phys.*, 2005, **7**, 3297–3305.
28 D. Andrae, U. Häußermann, M. Dolg, H. Stoll and H. Preuß, *Theor. Chim. Acta*, 1990, **77**, 123–141.
29 A. V. Marenich, C. J. Cramer and D. G. Truhlar, *J. Phys. Chem. B*, 2009, **113**, 6378–6396.
30 E. D. Glendening, J. K. Badenhoop, A. E. Reed, J. Carpenter, J. A. Bohmann, C. M. Morales, C. R. Landis and F. Weinhold, *NBO 6.0, Theoretical Chemistry Institute, University of Wisconsin, Madison*, 2013.
31 F. Jensen, *J. Chem. Theory Comput.*, 2015, **11**, 132–138.
32 F. Jensen, *Theor. Chem. Acc.*, 2010, **126**, 371–382.

Appendix

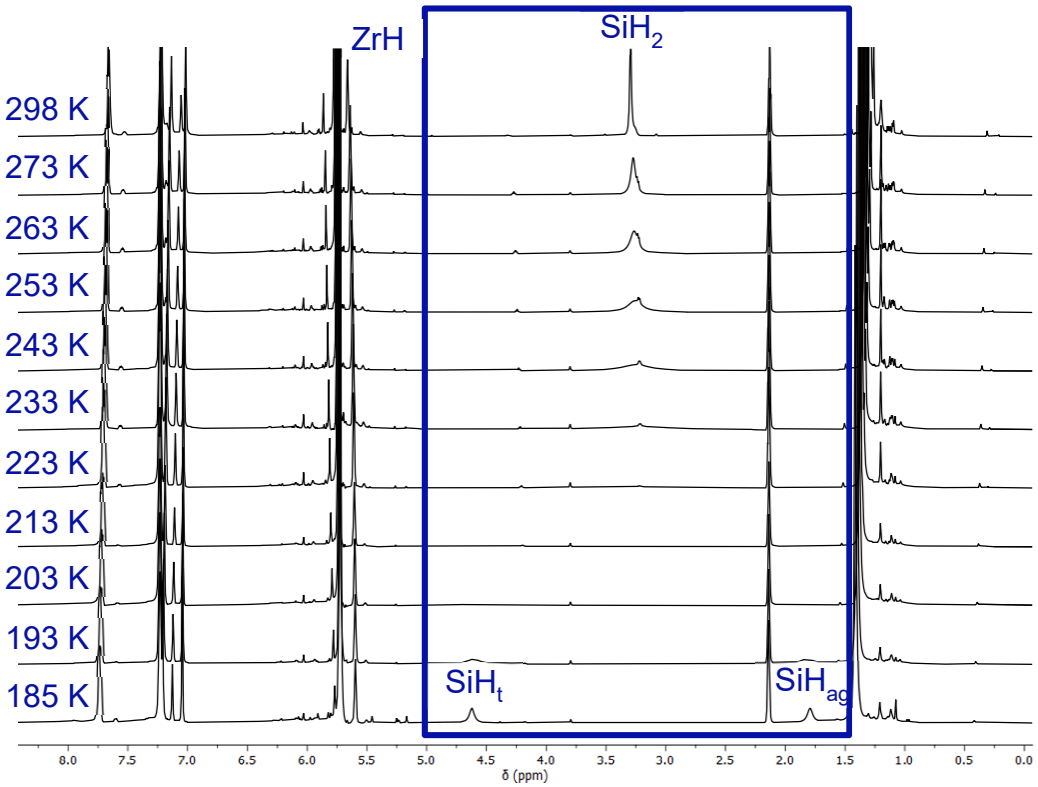


Figure A1: ^{1}H NMR spectra (C_7D_8, 400.1 MHz) of $Cp_2Zr(H)\{N(^tBu)Si(\mu\text{-}H)HPh\}$ (**6**) across the temperature range 298 K – 185 K. Highlighted within the blue box are the SiH_2, SiH_t (t = terminal) and SiH_{ag} (ag = agostic) resonances. Coalescence temperature = 218 ± 5 K.

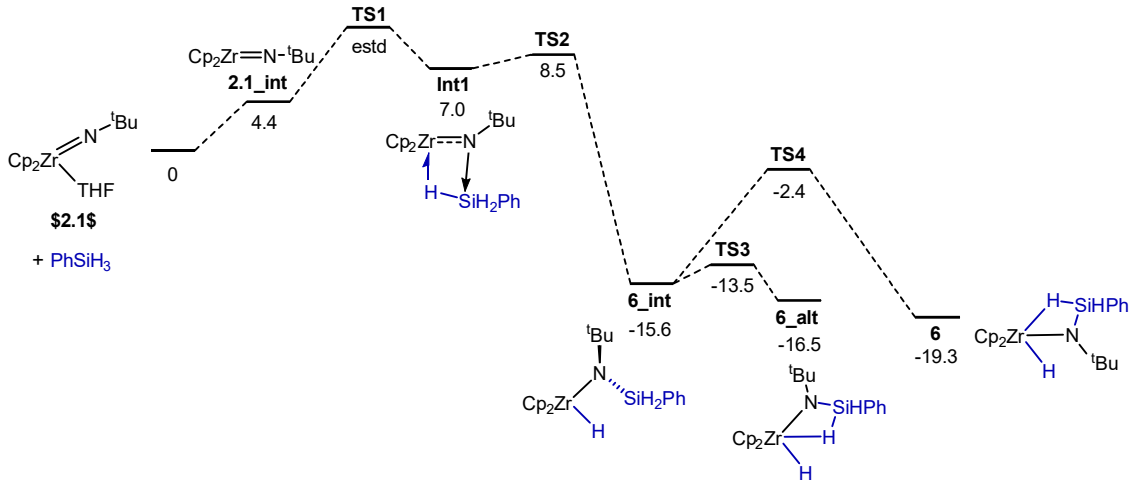


Figure A2: DFT (B3PW91/Def2-TZVP/d3-bj/SCRF) mechanism for the reaction of **2.1** with $PhSiH_3$ forming **6** and THF. Gibbs free energies (kcal mol^{-1}, T = 298.15 K) for minima, maxima and transition states (labelled **Intx** or **TSx**) are shown relative to **2.1** and $PhSiH_3$.

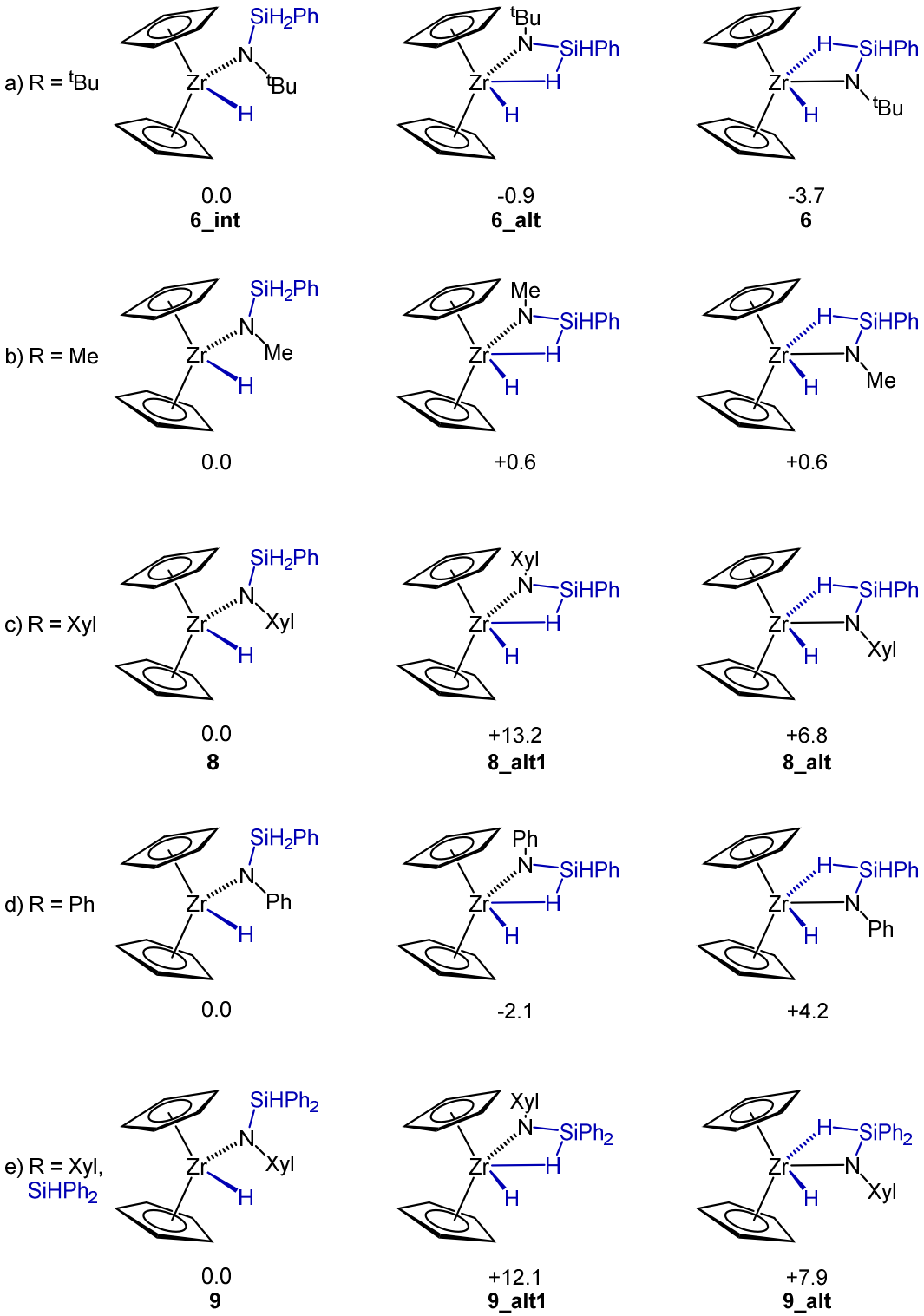


Figure A3: Three possible isomers of $Cp_2Zr(H)\{N(R)SiH_2Ph\}$ (R = ^{t}Bu, Xyl, Me and Ph) and $Cp_2Zr(H)\{N(Xyl)SiHPh_2\}$ and their associated free energies (kcal mol^{-1}, 298.15 K, in C_6H_6), relative to the respective non-agostic isomer, as calculated by DFT (B3PW91/Def2-TZVP/d3-bj/SCRF).

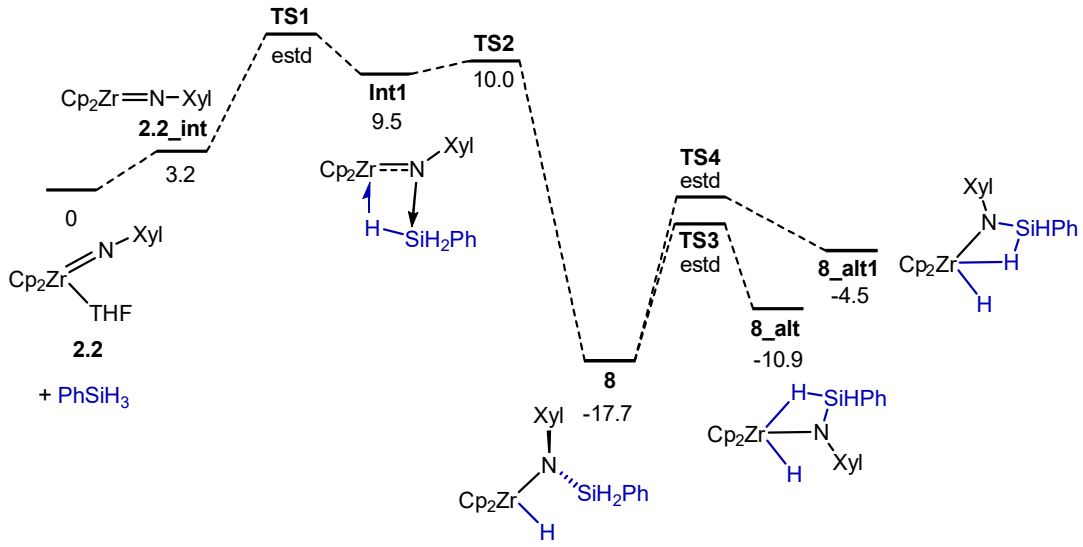


Figure A4: DFT (B3PW91/Def2-TZVP/d3-bj/SCRF) mechanism for the reaction of **2.2** with $PhSiH_3$ forming **8** and THF, as well as the unobserved isomerisation to agostic isomers **8_alt** and **8_alt1**. Gibbs free energies (kcal mol^{-1}, T = 298.15 K) for minima, maxima and transition states (labelled **Intx** or **TSx**) are shown relative to **2.2** and $PhSiH_3$.

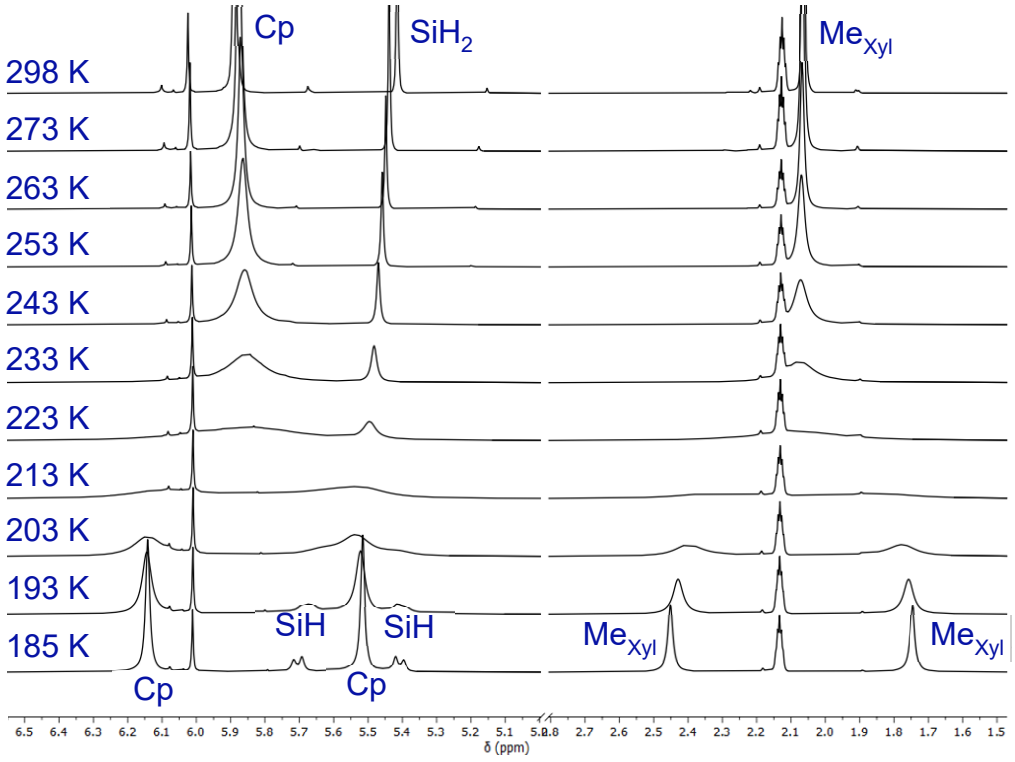


Figure A5: ^1H NMR spectra (C_7D_8, 400.1 MHz) of $Cp_2Zr(Cl)\{N(Xyl)SiH_2Ph\}$ (**11**) across the temperature range 298 K – 185 K. Decoalescence of the Me_{Xyl}, SiH and Cp environments is observed.

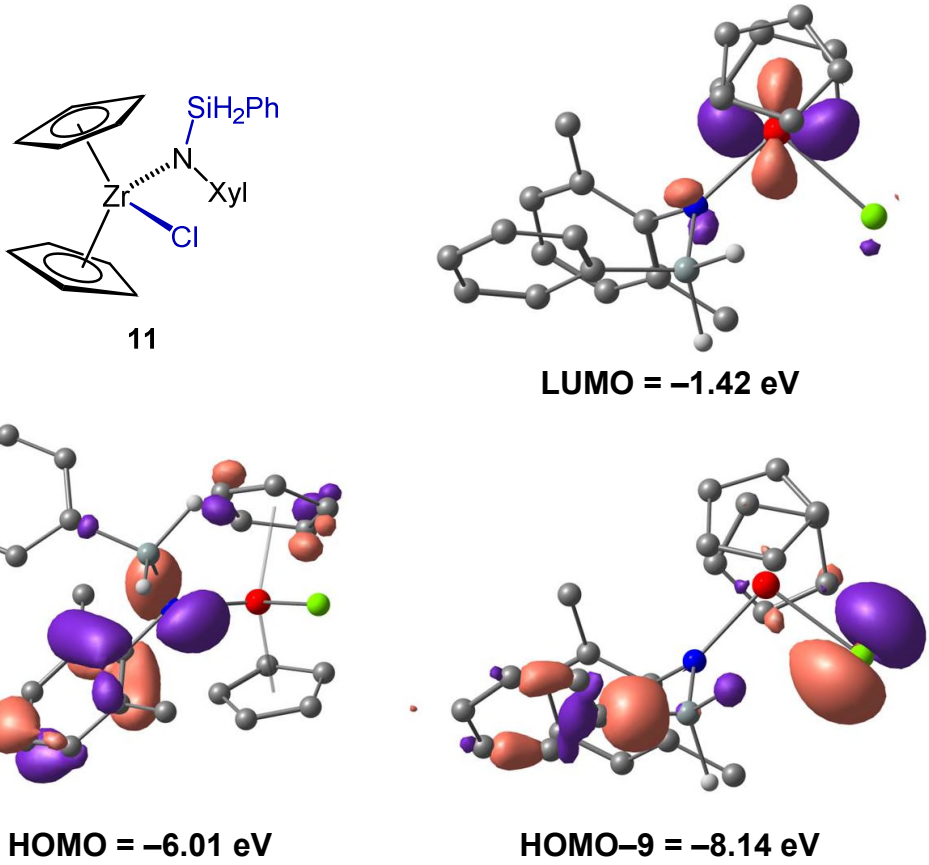


Figure A6: DFT (B3PW91/Def2-TZVP) structure of compound $Cp_2Zr(Cl)\{N(Xyl)SiH_2Ph\}$ (**11**) and associated isosurfaces and energies of the LUMO, HOMO and HOMO–9 molecular orbitals.

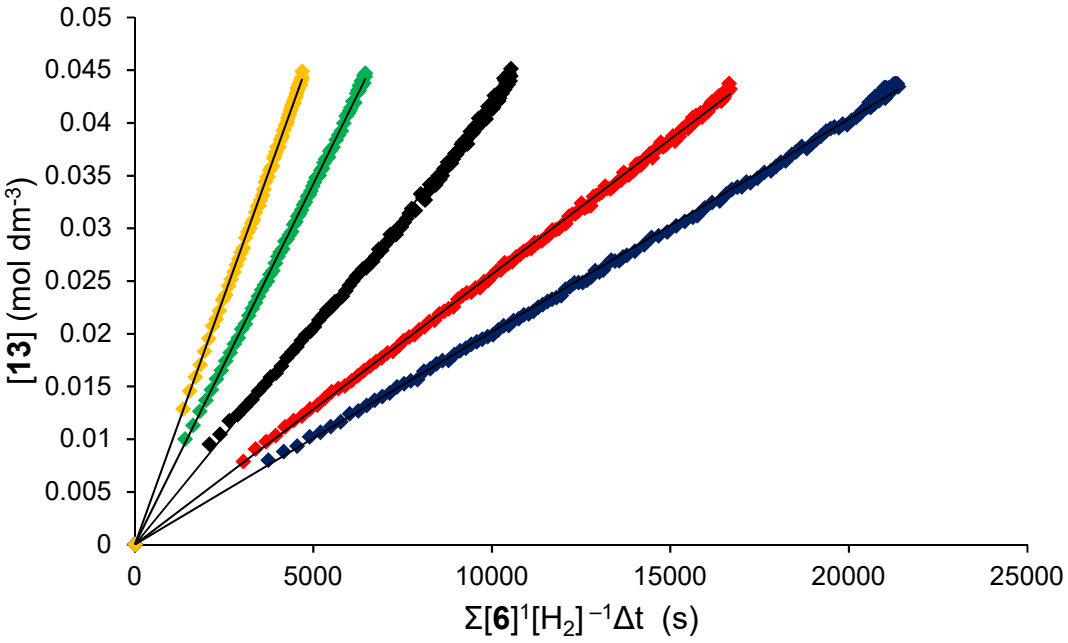


Figure A7: Variable time normalisation analysis (VTNA) of the reactions of $Cp_2Zr(H)\{N(^tBu)Si(\mu\text{-}H)HPh\}$ (**6**) with 20 equivalents HCC^tBu at 326 (blue), 329 (red), 332 (black), 335 (green) and 338 (yellow) K, with the normalised time being $\Sigma[\mathbf{6}]^1[H_2]^{-1}\Delta t$. (avg. $r^2 = 0.999$, range 0.998 – 1.000).

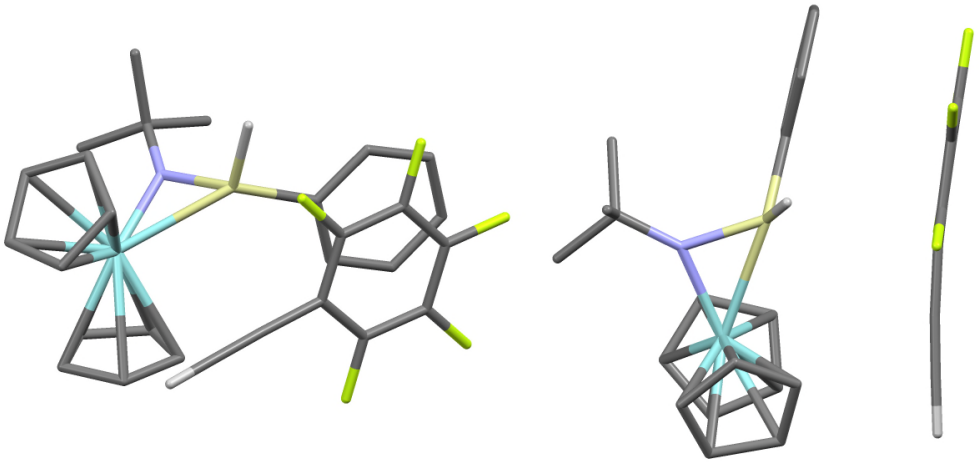


Figure A8: DFT (B3PW91/Def2-TZVP/d3-bj/SCRF) structures of the π–π interaction-containing intermediate **12_int** on the reaction pathway of $Cp_2Zr(H)\{N(^tBu)Si(\mu\text{-}H)HPh\}$ (**6**) and $HCCC_6F_5$ to form $Cp_2Zr\{N(^tBu)Si(H)(Ph)C(C_6F_5)CH\}$ (**12**) and H_2. Centroid–centroid distance of the two aryl rings is 3.51 Å.

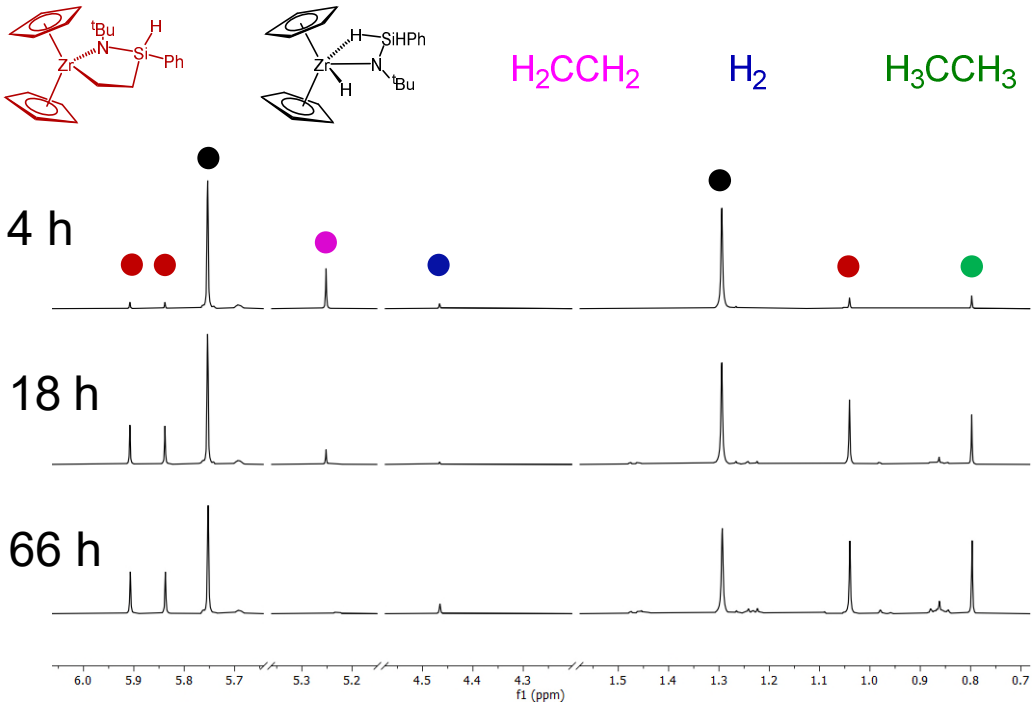


Figure A9: *In situ* ^{1}H NMR spectra of the catalytic hydrogenation of ethylene with 25 mol% $Cp_2Zr(H)\{N(^tBu)Si(\mu\text{-}H)HPh\}$ (**6**) at room temperature in C_6D_6.

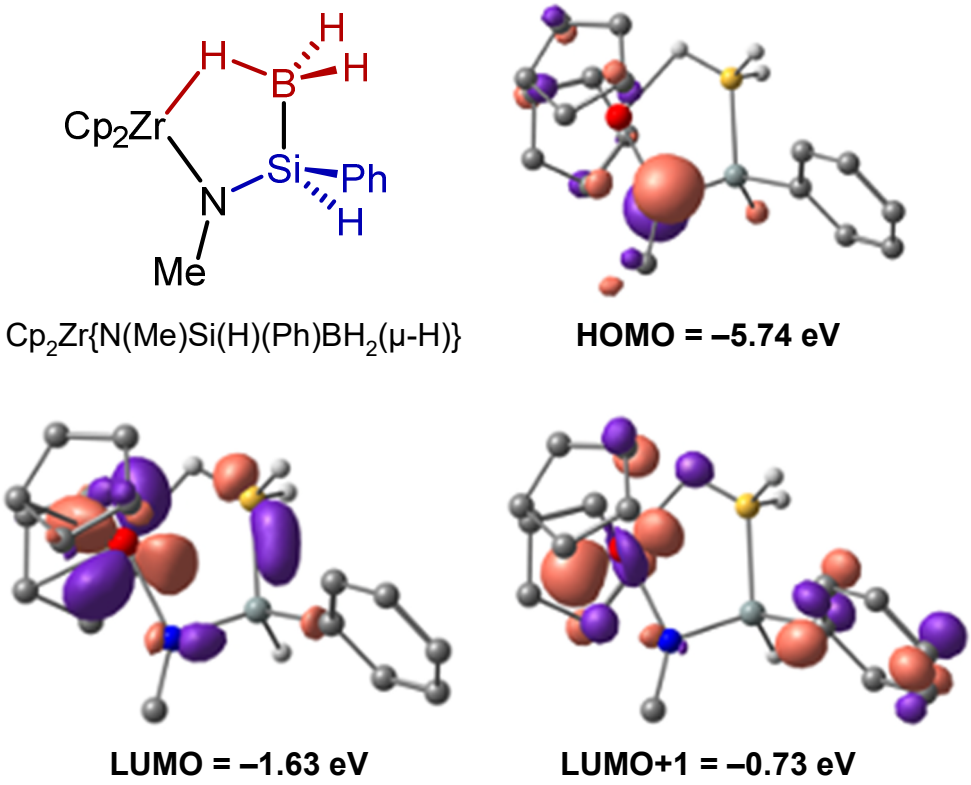


Figure A10: DFT (B3PW91/Def2-TZVP) structure of the DFT model compound $Cp_2Zr\{N(Me)Si(H)(Ph)BH_2(\mu\text{-}H)\}$ and associated isosurfaces and energies of the HOMO, LUMO and LUMO+1 molecular orbitals.

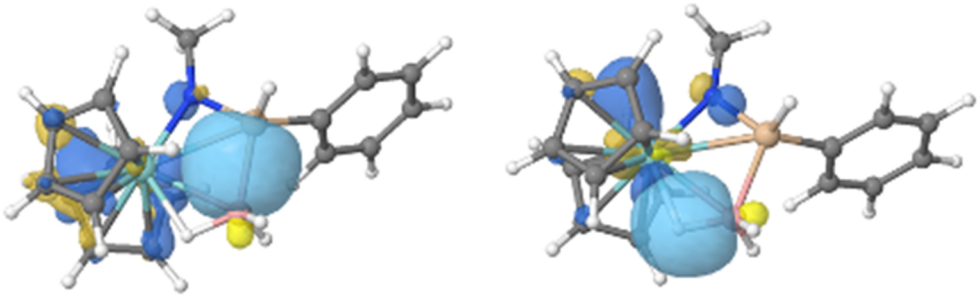


Figure A11: DFT (B3PW91/Def2-TZVP) computed NLMOs pertaining to the agostic $Si_{\beta}–B_{\gamma}\cdots Zr$ (left) and B–H···Zr (right) interactions of $Cp_2Zr\{N(Me)Si(H)(Ph)BH_2(\mu\text{-}H)\}$, as represented by overlapping the NBO isosurfaces of the Si–B and B–H bonds (light colours) with the relevant empty valence NBO isosurface of Zr (dark colours).

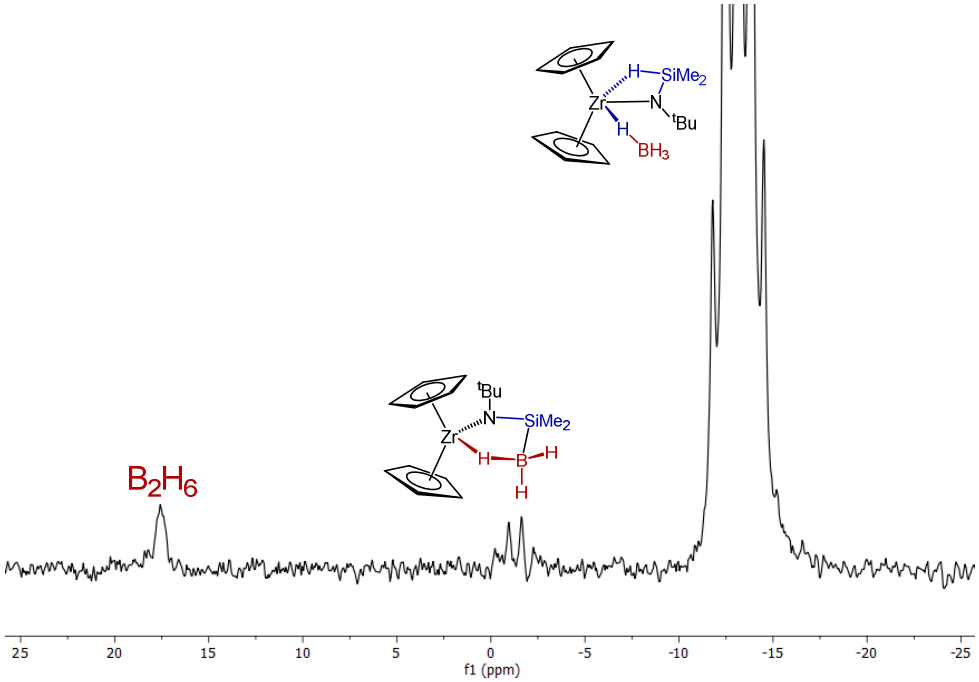


Figure A12: *In situ* ^{11}B NMR (C_7D_8, 128.4 MHz, 363 K) spectra for the thermal decomposition of $Cp_2Zr\{(\mu\text{-}H)BH_3\}\{N(^tBu)Si(\mu\text{-}H)Me_2\}$ (**23**) to give $Cp_2Zr\{N(^tBu)Si(Me)_2BH_2(\mu\text{-}H)\}$ (**26**) and H_2 at t = 1180 s.

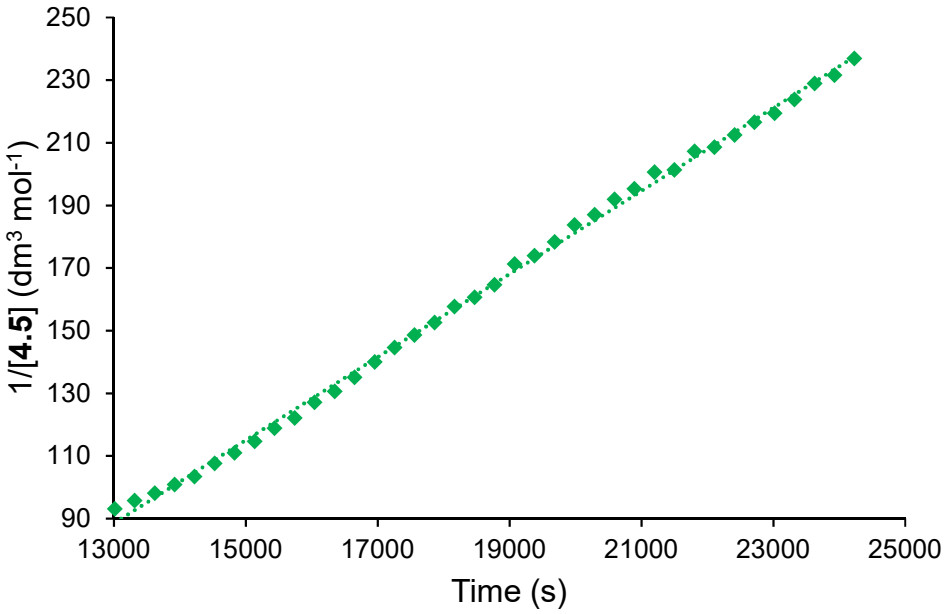


Figure A13: Second order semi-reciprocal plot for the decay of $Cp_2Zr(H)\{N(^tBu)Si(\mu\text{-}H)Me_2\}$ (**4.5**) during the thermal decomposition of **23** to give **26** and H_2 in toluene-d_8 at 90 °C, between 13007 and 24228 s, when [**23**] ≈ 0 mol dm^{-3}. (r^2 = 0.998).

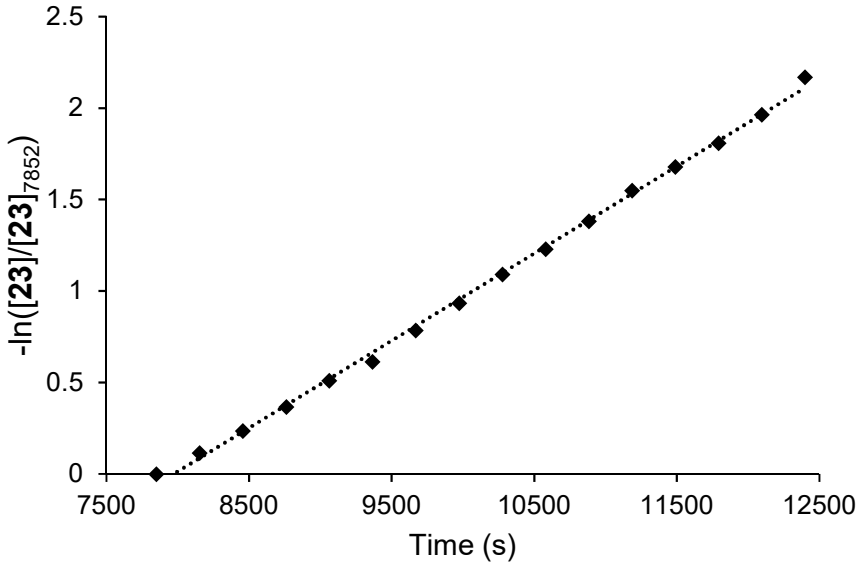


Figure A14: First order semi-logarithmic plot for the decay of $Cp_2Zr\{(\mu\text{-}H)BH_3\}\{N(^tBu)Si(\mu\text{-}H)Me_2\}$ (**23**) during the thermal decomposition of **23** to give **26** and H_2 in toluene-d_8 at 90 °C, between 7852 and 12401 s, when [**23**] ≤ [**4.5**]. (r^2 = 0.998).

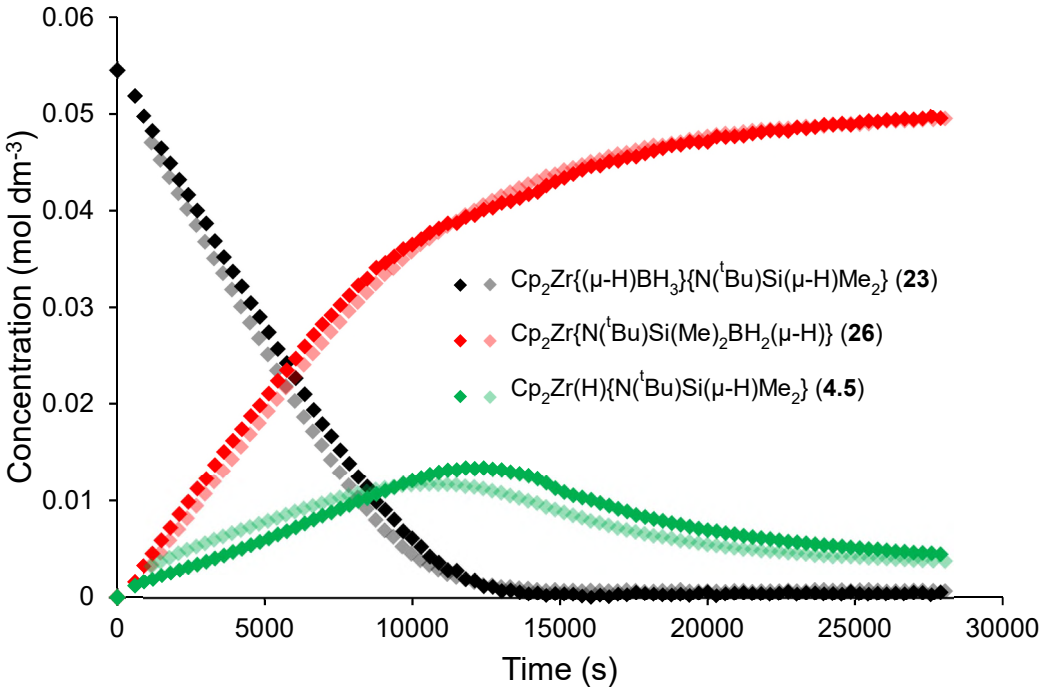


Figure A15: Concentration-time profiles for thermal decomposition of $Cp_2Zr\{(\mu\text{-}H)BH_3\}\{N(^tBu)Si(\mu\text{-}H)Me_2\}$ (**23**) to give $Cp_2Zr\{N(^tBu)Si(Me)_2BH_2(\mu\text{-}H)\}$ (**26**) and H_2 in the presence of 20 equivalents THF (bold points) and with no THF (faded points) in toluene-d_8 at 90 °C.

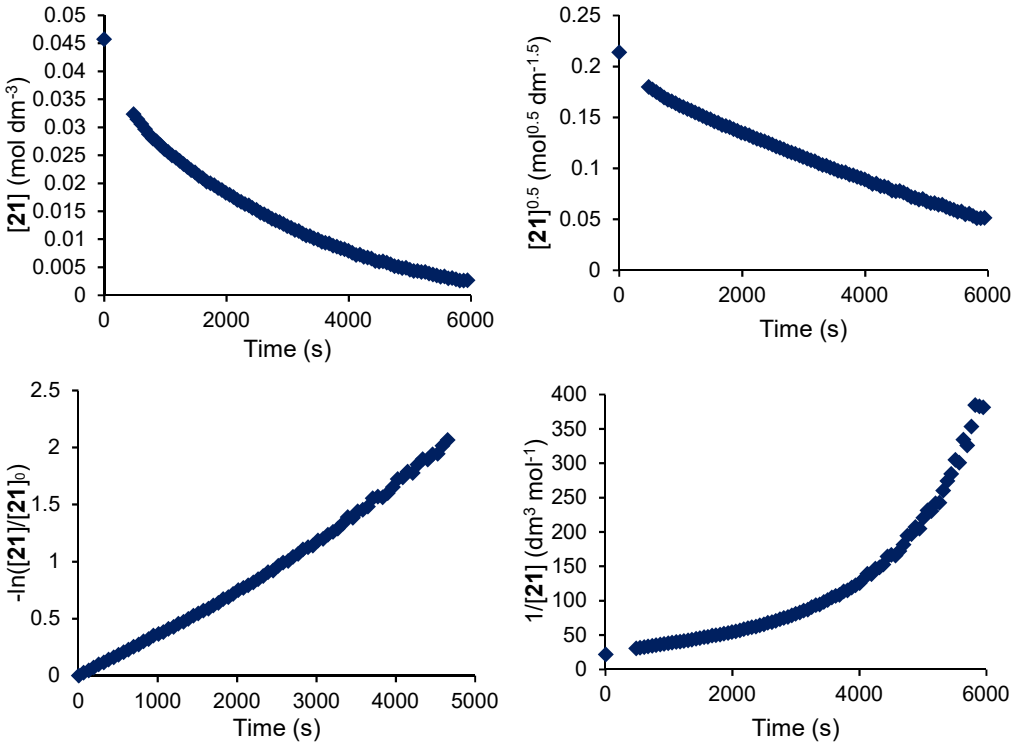


Figure A16: For the thermal decomposition of $Cp_2Zr\{(\mu\text{-}H)_2BH_2\}\{N(^tBu)SiH_2Ph\}$ (**21**) to give $Cp_2Zr\{N(^tBu)Si(H)(Ph)BH_2(\mu\text{-}H)\}$ (**24**) and H_2, in toluene-d_8 at 350 K, are shown: top left – concentration-time plot for the decay of **21**; top right – half order plot for the decay of **21**; bottom left – first order semi-logarithmic plot for the decay of **21** and; bottom right – second order semi-reciprocal plot for the decay of **21**.

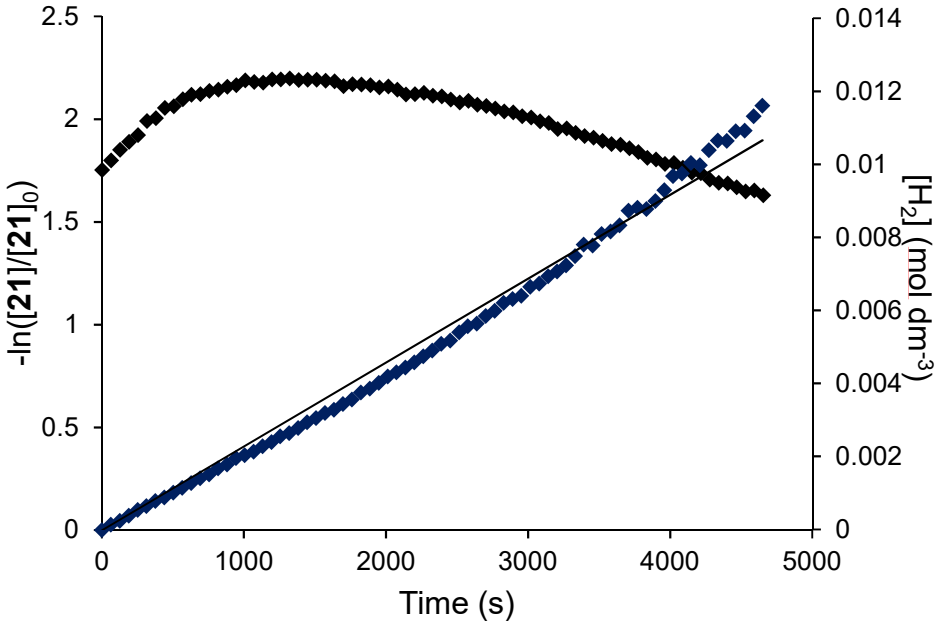


Figure A17: An overlay of the first order semi-logarithmic plot for the thermal decomposition of $Cp_2Zr\{(\mu\text{-}H)_2BH_2\}\{N(^tBu)SiH_2Ph\}$ (**21**) to give $Cp_2Zr\{N(^tBu)Si(H)(Ph)BH_2(\mu\text{-}H)\}$ (**24**) and H_2, in toluene-d_8 at 350 K, (left axis, blue, $r^2 = 0.988$) and the concentration of H_2 (mol dm^{-3}) during the reaction (right axis, black).

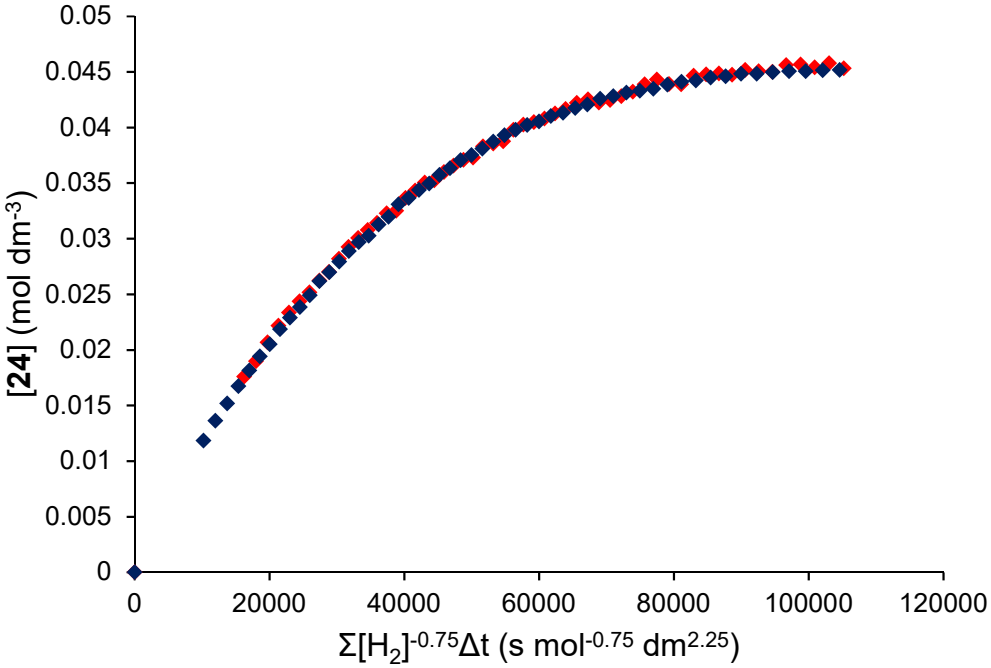


Figure A18: Overlays of the concentration-normalised time plots for two independent runs of the thermal decomposition of $Cp_2Zr\{(\mu\text{-}H)_2BH_2\}\{N(^tBu)SiH_2Ph\}$ (**21**) to give $Cp_2Zr\{N(^tBu)Si(H)(Ph)BH_2(\mu\text{-}H)\}$ (**24**) and H_2, in toluene-d_8 at 356 K. The normalised time axis takes into account only the concentration of dihydrogen, with an order in the reaction of –0.75.

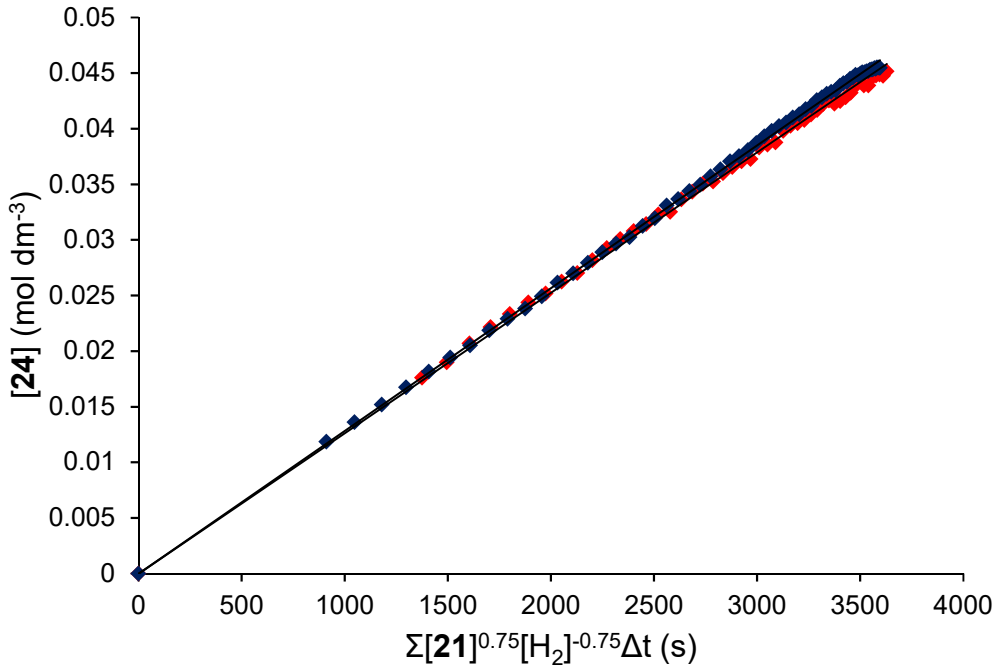


Figure A19: Overlays of the concentration-normalised time plots for two independent runs of the thermal decomposition of $Cp_2Zr\{(\mu\text{-}H)_2BH_2\}\{N(^tBu)SiH_2Ph\}$ (**21**) to give $Cp_2Zr\{N(^tBu)Si(H)(Ph)BH_2(\mu\text{-}H)\}$ (**24**) and H_2, in toluene-d_8 at 356 K. The normalised time axis takes into account both the concentration of dihydrogen, with an order in the reaction of –0.75, and **21**, with an order of 0.75. (r^2 = 0.999 and 0.998)